Crystallography Reports, Vol. 46, No. 4, 2001, pp. 521–522. Translated from Kristallografiya, Vol. 46, No. 4, 2001, pp. 583–584.

In Memory of Boris Konstantinovich Vainshtein (on the Occasion of His 80th Anniversary)

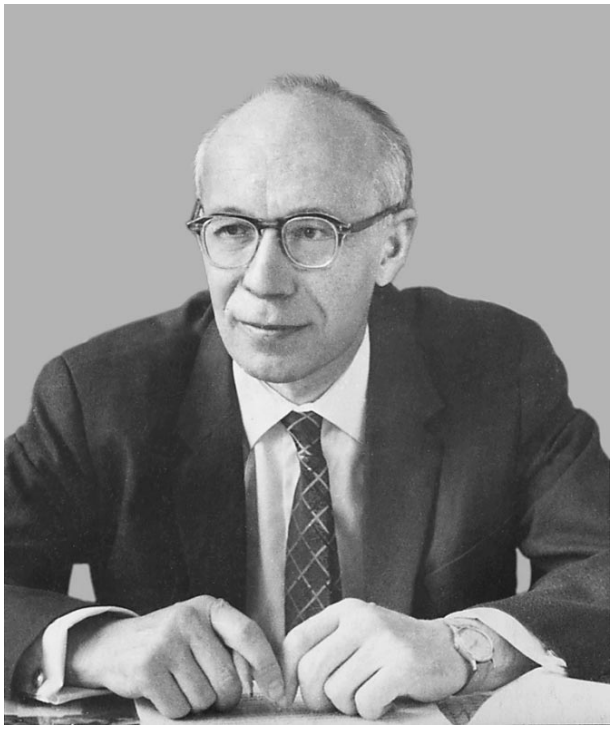

On July 10, 2001, Boris Konstantinovich Vainshtein, an outstanding physicist–crystallographer and member of the Russian Academy of Sciences, would have celebrated his eightieth birthday.

Academician Vainshtein, an outstanding scientist and a remarkable person, has made a great contribution to the creation and development of modern crystallography. He was a talented organizer of science and the director of the Shubnikov Institute of Crystallography for more than 34 years.

Boris Konstantinovich Vainshtein was born in Moscow in 1921. He graduated with distinction from two higher schools—the Physics Faculty of Moscow State University (1945) and the Metallurgy Faculty of the Moscow Institute of Steel and Alloys (1947) and received a diploma as a physicist and an engineer-researcher.

Vainshtein's natural gifts and manysidedness was revealed even in his student years. He was a brilliant student, deeply interested in physics, mathematics, and literature; he also painted, wrote verses, edited a newspaper, and played chess.

In 1945, Vainshtein entered the postgraduate course of the Institute of Crystallography and was bound forever with this institute. In 1950, he defended his Candidate and, in 1955, Doctoral dissertations in physics and mathematics. In 1959, he organized and headed the Laboratory of Protein Structure. In 1962, Vainshtein was elected a Corresponding Member and, in 1976, a Full Member of the USSR Academy of Sciences.

Being appointed the director of the Institute of Crystallography in 1962, Vainshtein continued the scientific traditions laid by A.V. Shubnikov and developed crystallography as a science combining studies along three main integral parts—crystal growth, crystal structure, and crystal properties. The great organizational talent characteristic of Vainshtein flourished during his directorship—he managed to gather around him people devoted to science and transformed the Institute of Crystallography into unique scientific center well known throughout the world.

The first studies performed by Vainshtein were dedicated to electron diffraction. He was the first to use the Fourier analysis of the electrostatic potential and derived the basic formulas of the electron diffraction structure analysis; he was also the first to determine the

1063-7745/01/4604-0521$21.00 © 2001 MAIK "Nauka/Interperiodica"

positions of light hydrogen atoms in a number of structures. Later, Vainshtein also solved many problems of the theory of X-ray diffraction analysis, which allowed him to start studying and successfully solve the structure of a number of complicated objects—various amino acids, peptides, and complicated natural biopolymers–proteins. Vainshtein and his coworkers determined the structures of synthetic polypeptides and some amino acids. He also made an important contribution to the theory of X-ray diffraction from polymer molecules and liquid crystals. Analyzing structures of biocrystals, he also widely used electron microscopy, developed the direct method of three-dimensional reconstruction of the structure, and applied it to structure determination of protein molecules and bacteriophages. Vainshtein and his colleagues have studied the three-dimensional structures of more than twenty of the most complicated active compounds, antibiotics, proteins, and viruses.

Boris Konstantinovich Vainshtein is the author of more than 400 scientific articles, reviews, and monographs. His well-known monographs *Structure Analysis by Electron Diffraction* (1956) and *Diffraction of X-rays by Chain Molecules* (1963) were soon translated into English. One of his last works was the four-volume *Modern Crystallography* (1994) written by his initiative, with his active participation as an author and editor, which was also immediately translated into English.

Vainshtein published a series of articles on the most general problems of crystallography, which included the relation of crystallography to the adjacent fields of the knowledge, the place of crystallography among other sciences, the relation and mutual influence of both fundamental and applied crystallography. Vainshtein was also the editor of crystallographic articles in the Large Soviet Encyclopedia and himself wrote many articles for this edition. He was the editor-in-chief of the journal *Kristallografiya* (Crystallography Reports) and the member of the editorial boards of various Russian and foreign journals.

For many years, Vainshtein had been the recognized leader in crystallography in our country. Being the assistant academician–secretary of the Department of General Physics and Astronomy of the USSR (Russian) Academy of Sciences and the chairman of the Councils on Physics of Crystals and Electron Microscopy, he coordinated all the studies performed in these fields in our country.

The many-sided scientific activity of Vainshtein had won him the worldwide recognition. Since 1957, Vainshtein had participated in all the Congresses of the International Union of Crystallography and in many other international conferences, seminars, and meetings. Vainshtein was the chairman of the Organizing Committee of the Seventh International Congress and Symposium organized by the International Union of Crystallography (IUCr) in Moscow in 1966. For a number of years, he was a member of the Executive Committee and the vice president of the International Union of Crystallography of the IUCr.

Vainshtein's scientific and organizational achievements were highly estimated and he was awarded high governmental decorations: the Order of Lenin, the Order of the October Revolution, two Orders of the Red Banner of Labor, the Order for Merits before Russia, and many medals.

Vainshtein scientific work brought him numerous decorations and honorary degrees, including the highest national and international crystallographic awards—the Fedorov and the Ewald prize and medals. He was elected a member of many foreign scientific societies and institutions. He was a member of the Leopoldina Academy in Germany, a foreign member of the Polish Academy of Sciences, a corresponding member of the Academy of Sciences and Arts of Barcelona, a member of the New York Academy of Sciences, a doctor *Honoris Causa* of Stockholm University, a doctor of science of the University of Keele, an honorary doctor of the University of York, an honorary member of the Roland Eótvós Physical Society of Hungary, and an associate fellow of the Catalonian Institute of Sciences.

In Vainshtein's directorship, scientific activity always prevailed over administrative activity. Penetrating into the crux of the problems solved at the institute, he determined the main directions in the activity of all the laboratories. Vainshtein always stimulated and supported new researches.

The name of Vainshtein will always remain in the history of the Russian and world crystallography. The best tribute to Vainshtein as a scientist and an organizer of science would be new achievements of Russian crystallography and, first of all, of the Institute of Crystallography, where he had worked for more than 50 years and headed for almost 35 years.

This issue of *Kristallografiya* (Crystallography Reports) is dedicated to the memory of Vainshtein and is comprised of articles presented by the scientists from the Institute of Crystallography and, thus, reflects the major directions of the present research at this institute.

Some other articles dedicated to the memory of Vainshtein will also be published in the next issue.

Translated by L. Man

Crystallography Reports, Vol. 46, No. 4, 2001, p. 523. Translated from Kristallografiya, Vol. 46, No. 4, 2001, pp. 585–586.

To the Memory of Academician Vainshtein

It has now been five years that Boris Konstantinovich left us, a period sufficient for letting go of the charisma of this great man and to make an attempt to estimate objectively the influence of his personality, ideas, and deeds on the development of modern crystallography.

Boris Konstantinovich Vainshtein won world recognition in his own lifetime. His famous monographs are in constant use in those research laboratories all over the world which apply the diffraction methods and study the structure of condensed matter of any nature.

A great poet once said that the places where once a great man lived remain sacred even after a thousand years. Such a sacred place for Vainshtein himself had always been the Institute of Crystallography of the Russian Academy of Sciences, which he had directed for 34 years—from 1962 and up to the last day of his life in October 1996. (In this connection, a curious analogy crosses the mind—two centuries ago Catherine the Great, who determined the main trends in the development of the Russian state, governed Russia for 34 years, from 1762 to 1796.)

To evaluate Vainshtein's activity, let us have a look at the Institute of Crystallography today.

Vainshtein's intuition prompted to him the prospects and importance of studying biological objects and various media of organic origin still in the mid1950s. These studies required the rapid development of the methods of structure analysis, the use of new radiation sources, the design of special apparatuses, new methods for synthesis of preparations, etc. To provide such studies, new research units were formed at the institute beginning with the Laboratories of Protein Structure and Liquid Crystals, Sectors of X-ray Diffractometry, Automation of Structural Studies to the Laboratory of X-ray Optics and Synchrotron Radiation and the Research Center of Space Materials Science in the city of Kaluga.

Similar to any other developing organism, the Institute of Crystallography bears the trace of Vainshtein's personality, a scientist who, with his intellect, intuition, organization talent, and deeds, started and developed this important research field.

Indeed, during Shubnikov's and Belov's time, the face of the Institute of Crystallography was determined by crystal growth (mainly of crystals analogous to natural ones), the study of their classical properties (optical, mechanical, and electrical), the classical X-ray structure analysis, and the crystal chemistry of the natural minerals.

The Institute of Crystallography guided by Vainshtein had became famous with its research of growth, structure, and properties of bioorganic objects; new methods of studying the atomic and real structure of condensed matter (including the X-ray diffraction analysis of proteins, small-angle scattering, electron microscopy, X-ray diffractometry, topography, etc.); and new technologies for growing new crystals that had no natural analogues such as lasing crystals.

It is important that Vainshtein, who created and developed new fields of the crystallographic science, also cared about and efficiently used the scientific potential of the Institute of Crystallography that he inherited from Shubnikov.

Today, being a unique physical institute possessing the culture and the basis for studying biological and organic objects, the unique set of physical and, first of all, diffraction methods for studying atomic and real structure of crystals and the properties of condensed matter of any nature and almost unlimited possibilities for synthesis of new organic and inorganic materials (from the crystallization methods from aqueous solutions to the molecular-beam epitaxy and the method of molecular architecture based on the Langmuir–Blodgett technique), the Institute of Crystallography has really become a unique scientific organization.

Finally, Vainshtein's intuition and his great efforts provided the Institute of Crystallography one of the key positions in the implementation of scientific and technological projects most important for our state and associated with large setups (megascience). This concerns the development and use of the specialized sources of synchrotron radiation of neutrons and the studies in materials science under the microgravitation conditions.

All the above demonstrates the possibilities of the Institute of Crystallography at the modern stage of science development. The current possibilities of the Institute of Crystallography are the direct result of the creative scientific and organizational work and the intellect of one of the outstanding scientists of this institute—Academician Boris Konstantinovich Vainshtein.

We, the present generation of Russian crystallographers, are obliged to run Vainshtein's scientific heritage as carefully and reasonably as it was run earlier by Vainshtein, a brilliant scientist and a wonderful person.

M.V. Kovalchuk

Director of the Shubnikov Institute of Crystallography of the Russian Academy of Sciences,

Corresponding Member of the Russian Academy of Sciences

1063-7745/01/4604-0523$21.00 © 2001 MAIK "Nauka/Interperiodica"

Crystallography Reports, Vol. 46, No. 4, 2001, pp. 524–526. From Kristallografiya, Vol. 46, No. 4, 2001, pp. 587–590.

Dedicated to the memory of B.K. Vainshtein

On Complexity*

A. L. Mackay

School of Crystallography, Birkbeck College (University of London), Malet Street, London WC1E 7HX

Received February 28, 2000

Abstract—What is the complexity of inorganic crystal structures, how may it be measured, and is there a limit? We present some speculations for discussion. *© 2001 MAIK "Nauka/Interperiodica".*

> "There are indeed whole branches of mathematics dealing with the assessment of complexity, which no one has the ability or the imagination to make use of for grasping the biological situation. The difficulty of applying topological analysis to embryonic development, for instance, is that morphological form may change considerably, while its topological status remains unchanged."
>
> *Joseph Needham (1936)*

OBSERVATIONS

The Inorganic Crystal Structure Database contains some 50 000 structures (many of which are duplicated), which can be searched according to various parameters. Figure 1 shows a plot of the numbers of structures containing 1, 2, 3, …, N different elements. A cursory examination shows that many of the structures with large values of N contain solid solutions, different elements occupying the same sites, but the result is nevertheless clear. There is a sharp limit to complexity. A similar conclusion appears from a plot of the cell volumes of cubic structures (Fig. 2). A closer inspection shows that structures with very large units cells are mainly modulations (polytypes) or hierarchic assemblies of smaller units.

A naive application of combinatorics would lead to the expectation that numbers would rise with factorial N or at least as the Fibonacci series. For example, the number of polyhedra with N vertices goes up as $N(4) = 1$, $N(5) = 2$, $N(6) = 7$, $N(8) = 257$, …, and N. Sloan [1] has collected many examples of such series.

The centenary of Planck's discovery of the quantum of action recalls the "ultraviolet catastrophe," which his postulation of the quantization of energy was designed to avoid. A preliminary consideration by Wien of the equilibrium distribution of wavelengths of the electromagnetic radiation in a black enclosure fitted observation at low frequencies but increased indefinitely with the square of the frequency, quite contrary to experiment. The theory assumed that each mode of oscillation carried the same amount of energy and that the number of high-frequency modes increased without limit. Planck resolved the situation by postulating that the energy should be quantized and distributed between the modes. This function is also plotted in Fig. 1 and shows a striking similarity with the observed distribution. Is this a coincidence? In fact, in a one-dimensional crystal, the number of atoms in a repeat must be an integer and similar effects are to be expected in three-dimensions. Space is "quantized" by atomicity, and not all dimensions of unit cells are possible.

The problem could be considered thermodynamically. For example, a soup of many elements does not

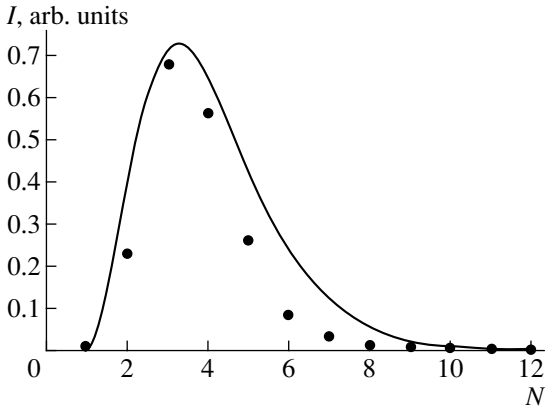

Fig. 1. Points denote the numbers of inorganic crystal structures with 1, 2, 3, ... N different elements. $N = 3$ has a maximum of 19000. The line follows the Planck distribution of energy in an absolutely black body.

* This article was submitted by the author in English.

1063-7745/01/4604-0524$21.00 © 2001 MAIK "Nauka/Interperiodica"

produce very complex crystals but minimizes the configurational entropy by forming ordered crystal of several simpler compositions. We may try to force complexity for a binary mixture by choosing an atomic ratio of τ (the golden number), which is as far from a rational ratio as possible, but the maximum order is achieved by the formation of a quasi-crystal with a strong local order.

PROGRAM

G.J. Chaitin [2] has proposed that the complexity of a structure and the amount of information that it contains might be measured by the length of the computer program necessary to generate it. This carries reasonably into the biological field where a protein molecule, as a sequence of amino acids, may be described numerically either directly as this sequence or as the equivalent sequence of DNA triplets, bearing in mind the redundancy of the code and the fact that several triplets may code for the same amino acid.

A protein, such as lysozyme, might be regarded as a region in the chemical phase diagram of the C, H, O, N, S, P system, but this would be inpractical and the difficulty of navigating a stoichiometric mixture to the representative region in the phase diagram would be quite impossible. In any case, it must be metastable and in a local minimum. However, there is no corresponding code for inorganic structures composed of discrete ions, although a method of coding periodic networks has been developed using the Delaney–Dress symbol (Delgado *et al.* [3]). An isolated organic molecule might be described topologically as a connectivity matrix, the Wiswesser notation being one possible way of linearizing and compressing it, but this ignores crystalline ordering.

It is possible to define the complexity of an inorganic crystal structure (or a molecular structure for that matter) by the number of parameters necessary to describe it. Only so many bits can be allocated to the statement of the space group and only so many to the coordinates of the atoms in the asymmetric unit. Since the frequency distribution of structures among the space groups is nonuniform, the coding can be further compressed by Huffman's method.

Shannon [4], in developing information theory, estimated the "entropy" of printed English text. Text can be specified by the number of bits necessary to transmit it, but the language has about 50% redundancy so that *a priori* knowledge of the language can serve to identify and correct some mistakes in transmission. Similarly, crystal chemistry embodies a foreknowledge of what is possible and what is not as regards the spatial combination of atoms. If our recognition of 50000 structures represents perhaps 50% (or some other percentage) of all that are possible, then the information necessary to specify any one would be less than about 16 bits, whereas the amount to specify the topology and approximate parameters of the atoms in the asymmetric unit of a crystal structure, without recognizing standard subcomponents and using previous experience, should take more. Pauling's rules [5] embody the chemical experience corresponding to a native knowledge of English in Shannon's example.

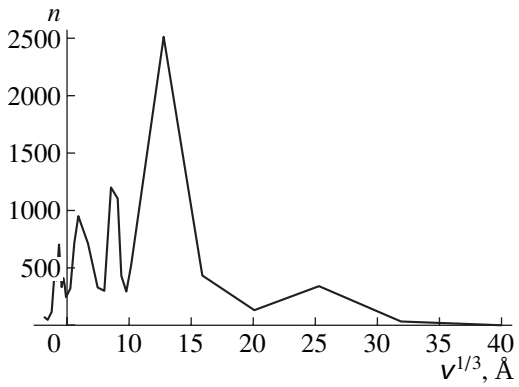

Fig. 2. The number of inorganic crystal structures against the cube root of the unit cell volume scale to approximate numbers of atoms per edge (volume of average atom approximately 20 Å^3).

It is now within the bounds of possibility to create arbitrarily ordered assemblies of atoms by developments of molecular beam techniques. Thus, large amounts of information could be written into a metastable structure. Stereolithography is also being miniaturized and is approaching the atomic scale. We may thus have to distinguish between stable and metastable configurations of atoms.

HIERARCHIC STRUCTURES—THE DETECTION OF SUBCOMPONENT STRUCTURES

Two classes of inorganic structures were early recognized on the basis of the occurrence of different strengths of bonding, calculated following Pauling's rules [5]—those where each atom was more strongly bonded to a central atom of a group than to the surrounding world and thus where the structure could be seen as an assembly of subunits and those where atoms had no particular local affiliation.

No crystal is infinite, and for a crystal of $10 \times 10 \times 10$ unit cells, half of them are on the outside. There is, thus, no absolute identity of situation. Identity is further relaxed in hierarchic structures: either as clusters of clusters or like rope, as fibers of fibers. In quasi-crystals, absolute identity is also replaced by quasi-identity, identity of surroundings out to a certain range. Absolute identity comes in at the quantum level with Bose condensates, where conditions are very different from the Bragg world of odd-style crystallography [6].

In looking for significant substructure, besides discrete groups, one may perceive fibers or chains or extended sheets as the building motif. Silicates are clas-

sified in this way. With experience, one may also detect an extended curved surface, such as the periodic minimal surfaces or nodal surfaces. The presence of some of these may be signalled in X-ray diffraction patters by certain particularly strong structure factors. It is possible to demonstrate the presence of simple components in a three-dimensional electron density plot. For example, by taking a plane section it could be shown that the carbon atoms in a benzene ring were coplanar, as was done long ago by K. Lonsdale. Now it is possible to take more complex sections and to show, for example, that the silicon atoms in a zeolite lie on a cage surface. This can be done by drawing the surface and coloring it according to the local electron density (as demonstrated by S. Leoni and R. Nesper [7]). In the cubic case, some of these surfaces correspond to the maxima of the structure-factor expressions (which combine the density waves for all symmetrically related reflections). Recently, Brenner *et al*. [8] have drawn attention to the significance of strong single reflections in certain X-ray powder diagrams recognized already by the pioneers of structure analysis.

DELONE OR BRAVAIS?

Traditional crystallography, embedded in the 230 space groups of the International Tables for Crystallography, considers infinite arrays of atoms and asks under what symmetry operations are they invariant. It specifies local order from global order. Delone [9] (and later his colleagues) and Peter Engel worked from local order outwards. The theory uses two parameters (r, R). Given points with local surroundings identical to a distance of R from each center and with another identical point no further than distance r away, they asked to what distance do the local surroundings of these given points have to be identical to require that the whole structure has the symmetry of one of the 230 space groups. The necessary range is remarkably limited to about $4R$ (with $6R$ being required deal with certain polytypes). This approach is thus suitable for including glasses and quasi-crystals within the framework of crystallography.

Traditional crystallography has been dominated by the use of X-ray diffraction, which emphasizes periodicity, but electron microscopy and various other imaging techniques which do not lose the phase information can now carry over to the recognition of more general forms of order. A.V. Shubnikov, for example, foreshadowed the appearance of quasi-crystal with hierarchic symmetry by examining the property of self-similarity.

What is seen as "order" depends to a great extent on the viewer. As we pass from order, which corresponds to an absolute free energy minimum, to ordered structures, which are in local minima, the skill required to detect the generating algorithm increases, so that "intelligence is that faculty of mind by which order is perceived in a situation previously considered disordered" [10]. We can see that 11.001001001001001001… is a simple repetition of "001" units (and is 22/7), but it is not obvious that 1.01101010000010011111…. is the binary expression of the square root of 2. It is possible that the theorem that the expansion of a rational fraction is periodic could be extended to three-dimensional atomic arrangements, but the opposite is true, namely, that a binary compound AB_x, where x is irrational, cannot be periodic but may be hierarchic quasi-crystal.

We must conclude that complexity is still a somewhat subjective concept dependent on current techniques and theories.

ACKNOWLEDGMENTS

We are pleased to acknowledgment the use of the ICSD through facilities at the Daresbury Laboratory provided to the academic community by the SERC.

REFERENCES

1. N. J. A. Sloan, *A Handbook of Integer Sequences* (Academic, New York, 1973); www.research.att.com/@njas/sequences/.
2. G. J. Chaitin, Sci. Am., May, p. 47 (1975).
3. O. Delgado, A. W. M. Dress, D. H. Huson, *et al.*, Nature **400**, 644 (1999).
4. C. E. Shannon and W. Weaver, *The Mathematical Theory of Communication* (Univ. of Illinois Press, Urbana, 1949).
5. L. Pauling, *The Nature of the Chemical Bond* (Cornell Univ. Press, Ithaca, 1960), p. 543.
6. W. L. Bragg and H. Lipson, Z. Kristallogr. **95**, 323 (1936).
7. S. Leoni and R. Nesper, in *Proceedings of the Congress of the International Union of Crystallography, Glasgow, 1999.*
8. S. Brenner, L. McClusker, and C. Bärlocher, J. Appl. Crystallogr. **30**, 1167 (1997).
9. B. N. Delone (Delaunay), N. Padurov, and A. Aleksandrov, *Mathematical Foundations of Structural Analysis of Crystals* (Gostekhteorizdat, Leningrad, 1934).
10. H. A. Fatmi and R. W. Young, Nature **228**, 97 (1970).

Crystallography Reports, Vol. 46, No. 4, 2001, pp. 527–533. Translated from Kristallografiya, Vol. 46, No. 4, 2001, pp. 591–597.

CRYSTALLOGRAPHIC SYMMETRY

Dedicated to the memory of B.K. Vainshtein

Tetrahedral Structures with Icosahedral Order and Their Relation to Quasicrystals

V. E. Dmitrienko* and M. Kléman**

** Shubnikov Institute of Crystrallography, Russian Academy of Sciences, Leninskiĭ pr. 59, Moscow, 117333 Russia*

e-mail: dmitrien@ns.crys.ras.ru

*** Laboratoire de Minéralogie-Cristallographie, Universités Paris VI et Paris VII, 4 place Jussieu, Paris Cedex 05, 75252 France*

Received March 1, 2001

Abstract—The possible existence of quasicrystals in tetrahedral phases is considered. It is shown that one of the well-known crystalline silicon phases (the BC8 phase or silicon III) is characterized by the icosahedral local order with three-quarters of the interatomic bonds being directed along the fivefold axes of an icosahedron. This crystal is considered as an approximant of an icosahedral quasicrystal. Higher order approximants and other tetrahedral structures related to quasicrystals are also constructed. It is shown that in these structures, the formation of the intrinsic phason disorder with the preservation of the energetically favorable coordination number four is possible. The *ab initio* quantum-mechanical calculations for carbon and silicon show that, although all the considered phases are metastable, their energies only slightly differ from the energies of the corresponding stable phases. © *2001 MAIK "Nauka/Interperiodica".*

INTRODUCTION

Boris Konstantinovich Vainshtein was always deeply interested in the fundamental problems of crystallography and keeping in contact with people studying these problems. Therefore, it seems to be not accidental that the first true crystallographic paper on quasicrystals entitled *De nive quinquagula* (On Pentagonal Snowflakes) was dedicated to the 60th birthday of Vainshtein and written by a friend of his, the famous British scientist Mackay, several years prior to the discovery of quasicrystals [1]. Earlier, the quasiperiodic functions and surface tilings were studied only by mathematicians [2, 3], so that nothing indicated the future revolution in crystallography which would follow the discovery of icosahedral quasicrystals in metal alloys [4]. In the following years, Vainshtein always encouraged the development of this direction at the Institute of Crystallography. He was the initiator of complementing the new edition of *Modern Crystallography* [5] with the chapter entitled *Quasicrystals*. The joint work over this chapter had become for one of the authors of this article (V.E.D.) the unique possibility of getting acquainted with the phenomenal scientific intuition and capacity for work characteristic of Vainshtein. Of course, it would have been very useful to discuss such a surprising turn in the problem of existence of quasicrystals in tetrahedral systems considered in the present article with such scientists as Vainshtein and V.L. Indenbom, but, alas, it is not possible. Thus, we can only hope that someone else would take interest in this problem.

The basic achievements of the science of quasicrystals have already been included into textbooks on crystallography [5, 6], but they all relate to quasicrystals in metal alloys. In addition to icosahedral quasicrystals [4], other quasicrystals were also discovered—octagonal, decagonal, and dodecagonal [7–9]—whose point symmetry groups included the eight-, ten-, and twelvefold rotation or screw axes, respectively. All these quasicrystals have dense atomic structures characterized by the noncrystallographic symmetry with the atoms usually being surrounded by ten to sixteen nearest neighbors in the first coordination sphere. Since there are no covalent bonds, the atoms can be considered as spheres of different diameters. In the tetrahedral structures, each atom has four neighbors related to it by directional covalent bonds (the classical example here is the diamond structure). Therefore, it is still unclear how to apply the attractive ideas of the theory of metal quasicrystals to the systems with tetrahedral coordination. This problem is closely related to the structure of amorphous substances which can also have metal or covalent bonds; this has also been exhaustively studied for many years.

1063-7745/01/4604-0527$21.00 © 2001 MAIK "Nauka/Interperiodica"

One of the most often used approaches to the problem is based on the well-known fact that there exists a class of structures characterized by high atomic density—the so-called tetrahedrally close-packed structures—that can be geometrically transformed into the structures with tetrahedral coordination. In the tetrahedrally close packed structures, all the interstitials are tetrahedral; i.e., all the atoms are located at the vertices of slightly distorted tetrahedra (see review [10]). These tetrahedra should necessarily be distorted because the three-dimensional space cannot be tiled with ideal tetrahedra. An example here is the so-called Frank–Kasper crystalline phases observed in numerous metal alloys [11]. One of the most often encountered structural motifs in these structures is an icosahedron with the coordination number of the central atom 12 (coordination numbers 14, 15, and 16 are also possible). In the tetrahedrally close-packed structures, each tetrahedron shares the faces with four neighboring tetrahedra. Therefore, performing the dual transformation (placing "new" atoms into the centers of each tetrahedron and removing all the "old" atoms), one arrives at a new structure with tetrahedrally coordinated atoms [11]. Of course, in this type of structure, the bond lengths differ from one another and the bond angles differ from the ideal tetrahedral angle $\theta_{tetr} = \arccos(-1/3) \approx 109.47°$, which is not favorable in terms of energy. One more serious drawback of these dual structures is the formation of large cavities. To the atoms with the icosahedral coordination there correspond cavities in the shape of distorted dodecahedra. Even larger cavities are formed at the atomic sites characterized by the coordination numbers 14, 15, and 16. Therefore, the average atomic density of these structures is rather low. Nevertheless, such metastable structures can be obtained experimentally, e.g., for silicon (they are related to the class of clathrate compounds).

A similar approach has long been used in precomputer modeling of amorphous structures. The icosahedral and dodecahedral motifs are rather typical of the spherical models of metal glasses [12] and amorphous semiconductors [13], respectively. A more consistent theory providing the construction of both crystalline and amorphous tetrahedrally close packed structures is based on the fact that the curved space (a three-dimensional sphere in the four-dimensional space) can be tiled with ideal tetrahedra; this tiling has an icosahedral symmetry. The "flattening" of this curved space results in tetrahedrally close packed structures with local icosahedral motifs in the plane three-dimensional space, which is inevitably accompanied by the formation of specific defects—disclinations [14]. A similar construction is also possible for tetrahedral structures [15] (for details see the review articles [16, 17]).

Some icosahedral quasicrystals are also related to the Frank–Kasper phases, e.g., the Al–Li–Cu alloys. Therefore, it was suggested to apply the dual construction considered above to tetrahedral quasicrystals [18] (see also recent publications [19, 20]). Another traditional method applied to quasicrystals—the projection from a multidimensional space—showed that the attempts to construct icosahedral crystals with the coordination number four have failed and that many atoms are characterized by coordination numbers three and even two; in other words, there are too many dangling bonds [21]. Dangling bonds are also obtained in the comparatively simple decoration of the rhombohedral Penrose tiling [22]. A more sophisticated decoration of rhombohedra with dodecahedra and the related polyhedra provides the construction of quasicrystal structures with almost no dangling bonds (less than 1%) [23, 24], but, in these models, the order is formed at such long distances that they should be considered rather as models of amorphous structures.

The progress in the experimental studies of this field was considerably hindered by the absence of the so-called *approximants*—crystals with a local atomic order close to that in quasicrystals. With an increase of the approximant order, their unit cells also increase, so that their structures and properties become even more similar to those of quasicrystals. At the same time, the structures of approximants can be studied by the traditional methods of X-ray diffraction analysis. For conventional metal quasicrystals, numerous approximants are known whose structures can be determined by the standard methods. This fact provided for the rapid progress in understanding the nature of quasicrystals. Recently, it was also shown that there are quasicrystal approximants for structures with tetrahedral coordination [25]. Below, we describe in detail these crystalline phases and their specific phason-type defects.

ICOSAHEDRAL ORDERING AND THE BC8 PHASE OF SILICON

The metastable silicon phase BC8 (or silicon III) has long been known [26]. Under pressures exceeding 10 GPa, the diamond structure of silicon (silicon I) is transformed into the β-tin (white tin) structure (silicon II) structure. The removal of the pressure does not lead to the initial structure; instead, silicon II is transformed into a metastable cubic phase, silicon III, with 16 atoms in the body-centered unit cell (the lattice parameter a = 6.636 Å, sp. gr. $Ia\bar{3}$). Since the corresponding primitive rhombohedral unit cell (used in the *ab initio* calculations of the structure and the electronic properties) contains eight atoms, this body-centered cubic phase is called the BC8 phase. At room temperature, this phase is rather stable but annealing at comparatively low temperature (about 100°C) results in its transformation, first, into the hexagonal lonsdaleite-type structure and, then, into the stable diamond structure. The BC8 phase is observed for germanium; similar phases are also known for binary compounds. The articles on the "exotic phases" in semiconductors were reviewed in [27].

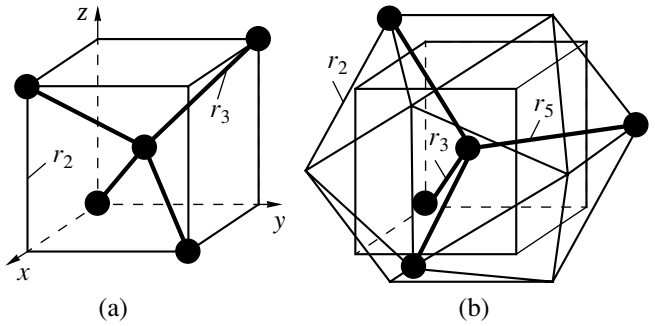

Fig. 1. Illustrating tetrahedral ordering in the (a) diamond structure and (b) BC8 phase. Covalent bonds are indicated by bold lines. In the ideal structure, the icosahedron edges are exactly equal to the cube edges (for simplicity, the unseen edges of an icosahedron are not indicated). The cubes in (a) and (b) are the same, their edges are twice shorter than the lattice constant of the diamond structure and τ^2 times shorter than the lattice constant of the BC8 phase. In both cases, the center of inversion is located in the middle of the bond directed along the threefold axis.

All the atoms in the BC8 structures occupy the crystallographic position 16(*c*) and lie on threefold axes. This structure is well described on the Internet [28]. Only recently, was it shown [25] that this structure is characterized by the "hidden" icosahedral order—three-quarters of all the covalent bonds are directed almost along the fivefold axes of an icosahedron (Fig. 1). Each atom has two types of bonds denoted by letters A and B. The type-A bonds are directed along the threefold axes as in the diamond structure. The orientations of three B-type bonds depend on the value of the parameter *x*. Replacing the experimental value $x = 0.1003$ by the ideal value $x_{ic} = \tau^{-2}/4 \approx 0.0955$, where $\tau = (1 + \sqrt{5})/2$ (the so-called golden mean), one can make B bonds parallel to the fivefold axes of an icosahedron, i.e., to the $\langle 01\tau \rangle$-type directions. The motifs typical of the icosahedral symmetry can be distinctly seen only if the structure is projected along these crystallographically unusual directions (Fig. 2). The angles between the bonds slightly differ from one another, and, instead of one tetrahedral angle $\theta_{tetr} \approx 109.47°$ (as in the diamond structure), the BC8 structure has two angles: $\theta_{BB} = \arccos[(1-2\tau)/5] \approx 116.56°$ and $\theta_{AB} = \arccos(-1/\sqrt{12\tau + 9}) \approx 100.81°$.

Similar to any approximant of an icosahedral crystal, the ideal structure of the BC8 phase can be obtained by projecting the points of a certain six-dimensional cubic lattice onto the real space [25, 29]. In our case, the six-dimensional lattice is a body-centered one, whereas for conventional quasicrystals and their approximants, the six-dimensional lattices are either primitive or face-centered. The lengths of the A and B bonds, r_3 and r_5, are related to the constant a_r of the quasilattice in the same way as in the conventional metal quasicrystals, $r_5 = a_r/\tau$ and $r_3 = a_r\sqrt{3}/\sqrt{4\tau + 3}$. The lattice constant a_{BC8} of the BC8 phase corresponds to the lattice constant of the 1/0 approximant, namely, $a_{BC8} = a_{1/0} = 2\tau a_r/\sqrt{1 + \tau^2}$ (the fact that BC8 is an approximant was first established in [22]). Thus, a_r for silicon should be about 3.9 Å. It should be indicated that another interatomic distance characteristic of quasicrystals and their approximants—$r_2 = 2a_r/\sqrt{4\tau + 3}$ (this distance is equal to the edge of the cube and the icosahedron in Fig. 1)—is absent in the BC8 structure, although it cannot be excluded that it would be detected in higher order approximants. Due to the partial similarity symmetry inherent in approximants, the BC8 structure has many distances $\tau^n r_5$, $\tau^n r_3$, and $\tau^n r_2$ with $n = 1, 2$, whereas the quasicrystals can have any distances with $n > 1$.

It should be indicated that exactly the same structure for the BC8 phase can also be obtained at another value of the atomic coordinates, $x = x'_{ic} = \tau x_{ic} \approx 0.1545$, but,

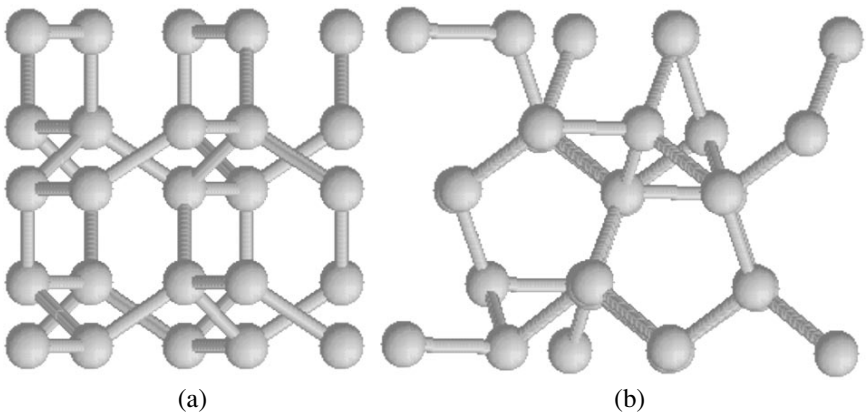

Fig. 2. (a) The BC8 structure viewed along the *z*-axis. The atoms and the bonds are shown. The maximum horizontal and vertical distances between the atoms correspond to the lattice constant. (b) The same structure viewed along the fivefold axis. One can see regular pentagons and half of a decagon, but it should be kept in mind that the structures are not planar.

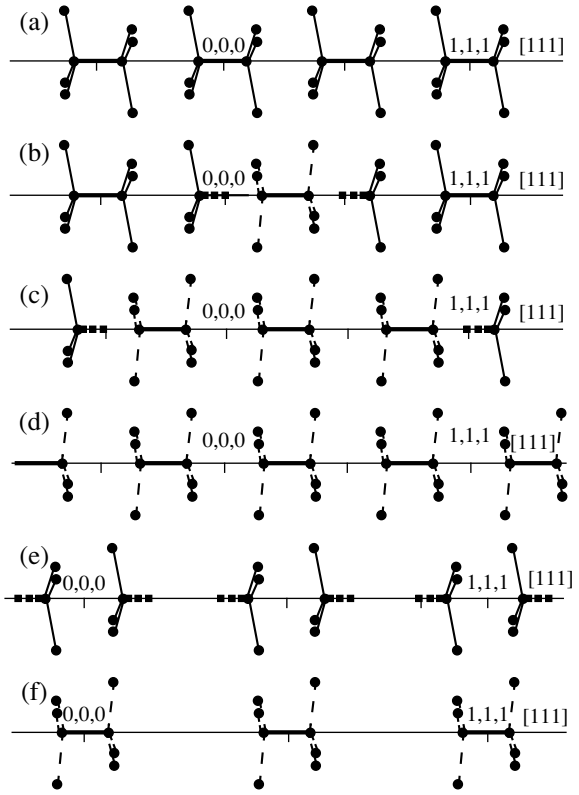

Fig. 3. Illustrating the formation of phasonlike defects in the 1/0 (the BC8 phase) and the 1/1 approximants. The A bonds are shown by bold lines; the B bonds, by solid lines; the C bonds, by dashed lines; and the dangling bonds, by bold dashed lines. (a–d) The BC8 phase; all the atoms are in the 16(*c*) positions on threefold axes. (a) The chain of atoms in the vicinity of one of the threefold axes of the ideal structure. (b) Two atoms jump toward one another forming a new A bond and two dangling bonds. (c) Dangling bonds "propagating" along the chain. (d) The whole chain is switched into a new state; there are no dangling bonds, only the A and the C bonds exist. (e, f) The 1/1 approximant; the atoms lying on the axis and outside it occupy the positions 16(*c*) and 48(*e*), respectively. (e) The initial structure with dangling bonds for the atoms lying on the axis (the atoms lying outside the axis have four bonds). (f) Annihilation of all the dangling bonds upon phason jumps.

in this case, the structure is rotated as a whole by 90° with respect to the initial structure. As a result of this rotation, all the B-bonds are oriented along the $\langle 0\tau 1\rangle$ directions and not along the initial $\langle 01\tau\rangle$ directions. It will be shown that this global rotation can be provided by local jumps of the atoms.

PHASON DEFECTS

The unique property of the BC8 phase is the possible formation of linear defects providing the preservation of the energetically advantageous coordination number of four. The corresponding process is schematically depicted in Fig. 3. The BC8 structure can be represented by chains of atoms located on threefold axes and spaced by distances r_3 (A bonds) and τr_3 (Fig. 3a). In approaching one another, two atoms spaced by τr_3 can be displaced from their sites to form a new A bond and two dangling bonds (Fig. 3b). These dangling bonds can "propagate" in opposite directions along the chain and cause small jumps of atoms and bond switching (Fig. 3c). Upon the "annihilation" of all the dangling bonds on the crystal surface or at defect, the atomic chain is switched into a new state in which the B bonds are replaced by newly formed C bonds (Fig. 3d). All the C bonds have the $\langle 1\tau^3\tau^3\rangle$ orientation and the lengths $r_C = r_2\sqrt{5\tau + 6}/4$ intermediate between the lengths of the A and B bonds.

These jumps of the atoms are analogous to those observed in conventional quasicrystals and are called phason jumps, whereas the corresponding structural defects are called phason defects. Using the analogy between phonons and phasons, they are called *bondons*. This term combines the English and the French meanings of the word *bond* (bond and jump, respectively).

It is possible to show that not only one but any number of chains can be switched into new states with the preservation of coordination number four [25]. If all the chains parallel to one of the threefold axes are switched into another state, e.g., parallel to the [111] axis, one arrives at the structure described by the rhombohedral space group $R\bar{3}$ (which is a subgroup of the sp. gr. $Ia\bar{3}$). Such a switching was observed experimentally upon the change of the pressure as a reversible phase transition between two metastable phases—the BC8 phase and the rhombohedral phase R8 with eight atoms per unit cell [30, 31]. Switching of all the chains parallel to two different threefold axes generates the body-centered tetragonal structure with 16 atoms per unit cell [32]. The corresponding structure was given the name BT8, sp. gr. $I4_1/a$, with all the atoms being located in one general position 16(*f*). The energy and the powder diffraction data for the BT8 phase are close to those of the R8 phase, and, therefore, it is not quite clear which of these two phases is really observed in the experiment [32].

Switching of all the chains parallel to three different threefold axes yields the R8 structure again. If all the chains are switched, we arrive at the BC8 phase but with a new parameter x equal to x'_{ic}, which signifies that the small local jumps of atoms can result in the rotation of the structure as a whole by 90° with respect to the initial structure. If all the chains are switched chains randomly, i.e., in such a way that each chain can be found in one of the two states with the probability 1/2, then the disordered structure formed is described by the sp. gr. $Ia\bar{3}d$ and the diffraction pattern from this structure is similar to the diffraction patterns from amorphous structures [25]. Switching the chains in different ways, one can obtain an infinitely large number of ordered and disordered structures.

The *ab initio* calculations were performed for several structures of this type. The early computations and the corresponding references can be found in [27]. These quantum-mechanical computations of the equilibrium structures and the electronic properties of the crystals are quite reliable. It was shown that in silicon, all the BC8-based structures are metastable in comparison with either the diamond structure (under low pressures) or the β-tin structure (at high pressures) [32]. The energy of an isolated phasonlike defect is not too high, and therefore, it is possible to assume the existence of some number of these defects in real specimens of the BC8 phase. This should be taken into account in the structure analysis of these phases. It was also shown that the elastic properties of the BC8 phase are almost isotropic, as was to be expected for the approximants of icosahedral quasicrystals (the elastic properties of icosahedral quasicrystals are isotropic because of their high symmetry).

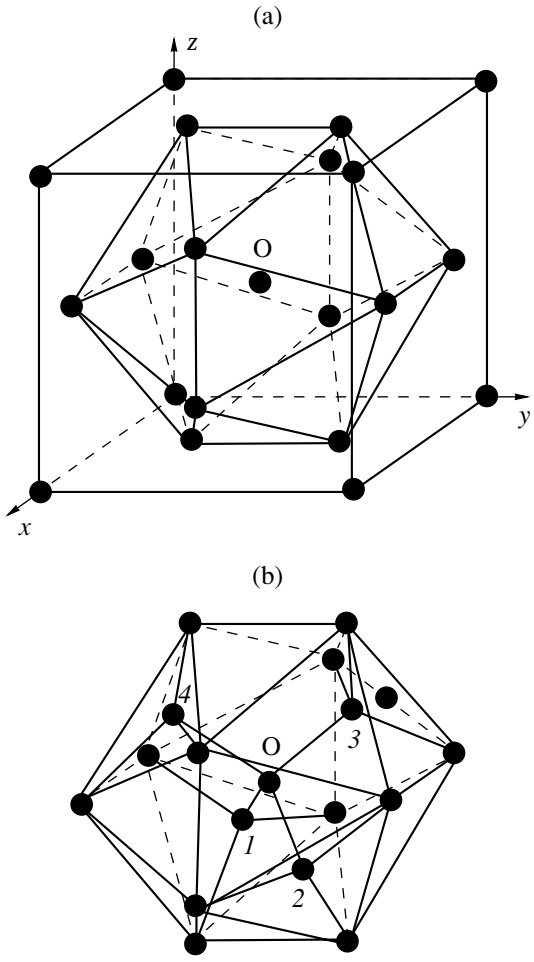

Fig. 4. (a) The A15 or V_3Si structure. Atoms are in the center and at the vertices of the cube and the icosahedron inscribed into this cube. The icosahedron is irregular, its edges are equal to the half-edge of the cube, whereas the regular icosahedron has the edge τ times shorter than the edge of circumscribed cube. The same icosahedra but rotated by 90° are located around the cube vertices. (b) The tetrahedral structure formed from the A15 structure. For simplicity, only one icosahedron with four new additional atoms (*1*, *2*, *3*, and *4*) inside it is shown; the covalent bonds are shown by solid lines.

THE 1/1 APPROXIMANT

In addition to the BC8-based structures (i.e., the approximant 1/0), it is also possible to construct the approximant 1/1 whose unit cell exceeds the unit cell of the approximant 1/0 by a factor a τ. The space group of this approximant is also $Ia\bar{3}$; 64 atoms are located in the 16(*c*) position with $x = x_{ic}$ and the 48(*e*) position with $x = (1 - 2x_{ic})/2$, $y = (2\tau - 1)x_{ic}$, and $z = x_{ic}$. This structure is also formed by atomic chains (Fig. 3e), but it is obvious that the atoms lying on the chain axes are characterized by the energetically disadvantageous coordination number—three. However, these atoms can also perform the same jumps as in the BC8 phase, which results in disappearance of all the dangling bonds (Fig. 3f). The *ab initio* calculations for carbon and silicon show that, energetically, the approximant 1/1 is less advantageous than the BC8-based structures [32, 33]. Up to now, all the attempts to construct higher-order approximants without dangling bonds have failed.

THE A15-BASED STRUCTURES

The structures related to that of the BC8 phase are not the only structures with tetrahedral coordination, high atomic density, and icosahedral motifs. One can readily see that numerous structures of this type can be obtained from the Frank–Kasper phases using a novel approach [33].

As an example, consider one of the typical Frank–Kasper phases, the so-called A15 structure (Fig. 4a), characterized by the spatial symmetry $Pm\bar{3}n$ (eight atoms per unit cell). The atoms located in the center and at the cube vertices are characterized by coordination number 12 (a distorted icosahedron), whereas the atoms located on the faces, by the coordination number 14. All the interstitials are tetrahedral. The standard method for obtaining the structures with the tetrahedral coordination is reduced to the relocation of "new" atoms into the interstitials and the removal of all the "old" atoms. As a result, one arrives at the clathrate structure with 46 atoms per unit cell described by the same space group. The atoms in this structure form slightly distorted dodecahedra around the center and the vertices of the cubic unit cell; the density of this structure is relatively low.

Here, we will use another method for transforming the A15 structure into the structure with tetrahedral coordination (Fig. 4b). We leave infact all the old atoms and place a small additional tetrahedron (four atoms) located in each icosahedron. As a result, the unit cell

contains 16 atoms in the positions 2(*a*), 6(*d*) (old atoms), and 8(*e*) (new atoms), and the symmetry of the new structure is described by the sp. gr. $P\bar{4}3n$. Obviously, the atoms in the center and at the tetrahedron vertices have four bonds (Fig. 4b). The atoms at the icosahedron vertices have one bond inside the icosahedron, but, since the symmetry of these positions is $\bar{4}$, each atom at the vertex has four such bonds from different icosahedra, which results in the formation of the structure in which all the atoms are tetrahedrally coordinated. All the bond angles exceed 90°, but differ from the ideal tetrahedral angle. The *ab initio* calculations show that, under reasonable pressures (attainable in diamond anvils) and zero temperature, the energy of this carbon phase is higher than the energy of diamond (by about 0.6 eV under the zero pressure) [33]. If this phase was more advantageous under high pressures and temperatures, this would have allowed one to explain the tetrahedral growth forms occasionally observed for diamonds, which gave rise to a lengthy discussion on its true structure (the tetrahedral growth forms are allowed for the $P\bar{4}3n$ symmetry).

It should also be noted that a tetrahedron can be inscribed into each icosahedron by ten different ways. Therefore, similar to the BC8 phase, this method allows the construction of an infinite number of both ordered and disordered structures. Of course, in many cases, the bond angles are acute and, thus, energetically unfavorable, but the *ab initio* calculations for carbon show that some of the rhombohedral structures thus obtained are energetically more advantageous than the cubic structure described by the sp. gr. $P\bar{4}3n$, although less advantageous than the diamond structure. This makes it necessary to perform new thorough studies along these lines.

CONCLUSION

Despite progress in understanding the structure of approximants, the quasicrystals with the tetrahedral coordination still remain purely hypothetical. However, the investigations performed provided the development of new methods for constructing both rather complicated crystalline and partly disordered structures with tetrahedral coordination. For some of these structures, it was possible to perform *ab initio* calculations and determine the exact atomic coordinates and the elastic and electronic properties. These structures can also be used for modeling amorphous carbon and silicon.

It should be emphasized that, recently, an experiment has been made in which the electron diffraction patterns similar to the diffraction patterns from decagonal quasicrystals were obtained from silicon specimens deposited onto mica substrates in the helium atmosphere [34] (it should be remembered that we considered here only the approximants of icosahedral quasicrystals). Despite the fact that one has to check whether this diffraction pattern is really formed due to a quasicrystal and not due to twins, we hope that this experiment would trigger new experimental studies of quasicrystals with tetrahedral coordination.

ACKNOWLEDGMENTS

The authors are grateful to V.A. Chizhikov for useful discussions, F. Mauri for his help in computations, and to T.Ya. Dmitrienko for her help in preparation of the figures.

REFERENCES

1. A. L. Mackay, Kristallografiya **26** (6), 910 (1981) [Sov. Phys. Crystallogr. **26**, 517 (1981)].
2. H. Bohr, Acta Math. **45**, 29 (1924); **46**, 101 (1925); **47**, 237 (1927).
3. R. Penrose, Math. Intell. **2**, 32 (1979).
4. D. Shechtman, I. Blech, D. Gratias, and J. W. Cahn, Phys. Rev. Lett. **53**, 1951 (1984).
5. B. K. Vainshtein, *Modern Crystallography*, Vol. 1. *Fundamentals of Crystals* (Springer-Verlag, Heidelberg, 1994), Vol. 1, Chap. 5, p. 405.
6. C. Janot, *Quasicrystals: A Primer* (Oxford Science Publ., Oxford, 1992).
7. N. Wang, H. Chen, and K. H. Kuo, Phys. Rev. Lett. **59**, 1010 (1987).
8. L. Bendersky, Phys. Rev. Lett. **55**, 1461 (1985).
9. T. Ishimasa, H.-U. Nissen, and Y. Fukano, Phys. Rev. Lett. **55**, 511 (1985).
10. D. P. Shoemaker and C. B. Shoemaker, *Aperiodicity and Order*, Ed. by M. V. Jarić and D. Gratias (Academic, Boston, 1989), Vol. 1, p. 1.
11. F. C. Frank and J. S. Kasper, Acta Crystallogr. **11**, 184 (1958); **12**, 483 (1959).
12. J. D. Bernal, Proc. R. Soc. London, Ser. A **280**, 299 (1964).
13. R. Grigorovici, Mater. Res. Bull. **3**, 13 (1968).
14. M. Kléman and J. F. Sadoc, J. Phys. Lett. **40**, L569 (1979).
15. J. F. Sadoc and R. Mosseri, Philos. Mag. B **45**, 467 (1982).
16. M. Kléman, Adv. Phys. **38**, 605 (1989).
17. R. Mosseri and J. F. Sadoc, in *Geometry in Condensed Matter Physics*, Ed. by J. F. Sadoc (World Scientific, Singapore, 1990), p. 233.
18. A. L. Mackay, Nature **315**, 636 (1985).
19. V. A. Borodin and V. M. Manichev, Zh. Éksp. Teor. Fiz. **114** (6), 2187 (1998) [JETP **87**, 1191 (1998)].
20. M. O'Keeffe, G. B. Adams, and O. F. Sankey, Philos. Mag. Lett. **78**, 21 (1998).
21. Z. Olami and S. Alexander, Phys. Rev. B **39**, 1478 (1989).

22. Y. Ishii, Acta Crystallogr., Sect. A: Found. Crystallogr. **44**, 987 (1988).
23. J. Peters and H.-R. Trebin, Phys. Rev. B **43**, 1820 (1991).
24. J. Schmitz, J. Peters, and H.-R. Trebin, Z. Phys. B **100**, 57 (1996).
25. V. E. Dmitrienko and M. Kléman, Philos. Mag. Lett. **79**, 359 (1999).
26. J. S. Kasper and S. M. Richards, Acta Crystallogr. **17**, 752 (1964).
27. J. Crain, G. J. Ackland, and S. J. Clark, Rep. Prog. Phys. **58**, 705 (1995).
28. http://cst-www.nrl.navy.mil/lattice/struk.xmol/bc8.xyz
29. V. E. Dmitrienko and M. Kléman, Mater. Sci. Eng. A **294–296**, 246 (2000).
30. J. Crain, G. J. Ackland, J. R. Maclean, *et al.*, Phys. Rev. B **50**, 13043 (1994).
31. R. O. Piltz, J. R. Maclean, J. Clark, *et al.*, Phys. Rev. B **52**, 4072 (1995).
32. V. E. Dmitrienko, M. Kléman, and F. Mauri, Phys. Rev. B **60**, 9383 (1999).
33. V. E. Dmitrienko, M. Kléman, and F. Mauri, Ferroelectrics **250**, 213 (2001).
34. R. Kamalakaran, A. K. Singh, and O. N. Srivastava, Phys. Rev. B **61**, 12686 (2000).

Translated by L. Man

Crystallography Reports, Vol. 46, No. 4, 2001, pp. 534–549. Translated from Kristallografiya, Vol. 46, No. 4, 2001, pp. 598–613.

DIFFRACTION AND SCATTERING OF ELECTRONS

Dedicated to the memory of B.K. Vainshtein

Electron Diffraction Structure Analysis—from Vainshtein to Our Days

V. V. Klechkovskaya and R. M. Imamov

Shubnikov Institute of Crystallography, Russian Academy of Sciences, Leninskiĭ pr. 59, Moscow, 117333 Russia
e-mail: klechvv@ns.crys.ras.ru

Received December 15, 2000

Abstract—The physical grounds of the modern electron diffraction structure analysis have been analyzed. Various methods and approaches developed in electron diffraction studies of various structures are considered. The results of the structure determinations of various inorganic and organic materials are discussed. © *2001 MAIK "Nauka/Interperiodica".*

INTRODUCTION

This article is written to commemorate B.K. Vainshtein and his first outstanding scientific achievement—the creation of an independent diffraction method (electron diffraction structure analysis). We have made an attempt here to generalize the results of the structural determinations of various inorganic and organic materials performed mainly by the representatives of the Russian school of the electron diffraction structure analysis.

The discovery of electron diffraction in 1927 opened the possibility for obtaining reliable data on the structure of thin films and finely dispersed crystalline materials. Many scientists demonstrated transmission electron diffraction patterns from specific objects—thin films—and reflection diffraction patterns from surfaces and compared their data with the data obtained by X-ray diffraction analysis (interplanar spacings in the lattice and visually estimated diffraction-reflection intensities [1]) and developed the methods of geometric analysis of different diffraction patterns [2] and patterns from surface structures [3]. Some researchers tried to use electron diffraction to determine the structure of molecules in gases [4, 5]. A specific encyclopedia of the knowledge accumulated over almost twenty years of studying the structures of various materials by the electron diffraction method became the monograph *Electron Diffraction* written by Pinsker [6].

From the late 1940s, a new direction known today as electron diffraction structure analysis (EDSA) was actively developed in our country. The important role in the creation and development of this new field was played by Vainshtein, who not only created this method but also established and consistently described its foundations in his famous monograph *Structure Analysis by Electron Diffraction* [7] published in 1956, which is still the guide and the manual for all those working in this field. It should be remembered that, in different times, many scientists working at the Electron Diffraction Laboratory of the Institute of Crystallography also contributed to the development of the new method—L.I. Tatarinova, I.I. Yamzin, A.N. Lobachev, S.A. Semiletov, V.F. Dvoryankin, and many others.

Vainshtein performed a number of fundamental theoretical studies concerning the formation of various types of electron diffraction patterns and the kinematical and the dynamical scattering. In cooperation with Ibers, he calculated the tables of atomic scattering factors of electrons for all chemical elements [8] and developed a simple method of allowance for the secondary scattering in the diffraction reflection intensities. He was the first to use the Fourier synthesis of the electrostatic potential for localization of atoms (including hydrogen) in various structures. These and many other important results obtained by Vainshtein [7] laid the basis of the electron diffraction structure analysis (EDSA). Vainshtein himself determined a large number of structures, among which were the pioneering studies on paraffins, where he managed to determine the positions of hydrogen atoms [9, 10] as well as urea [11] and thiourea [12]. The diketopiperazine [13] structure was determined with an accuracy compared with the accuracy of modern electron and X-ray diffraction determinations. We should like to recollect his structural studies of $BaCl_2$ [14], barium chloride hydrate [15], cobalt [16], manganese [17], nickel [18], barium bromide hydride [19], and many other compounds [20].

However, beginning from the 1960s, EDSA was developed predominantly in the Soviet Union. Most Western scientists who made attempts to use electron diffraction for structure determinations and determine reflection intensities encountered the necessity of ana-

1063-7745/01/4604-0534$21.00

lyzing the scattering nature and became rather skeptical about the use of EDSA for determining unknown complicated structures (the only exception seems to be the determination of the parameters of linear polymers and two-dimensional protein crystals, where large unit cells containing light atoms provided the reliable use of the kinematical approximation developed for thin crystals). In the following years, these scientists preferred to use high-resolution electron microscopy (HREM). It seemed then that HREM could help to solve all the problems at the atomic level which were encountered in the structural determination of thin films and objects with small unit-cell dimensions. In the past decades, HREM stopped being an "exotic" method and has become a conventional working tool in structural studies. All the advantages and disadvantages of HREM have been established. The main disadvantage of HREM is the necessity of *a priori* knowledge of an adequate atomic model of the structure, which allows the calculation of the images of the object in the multibeam approximation.

The turning point in the realization and use of all the possibilities provided by electron microscopy and electron diffraction had become Vainshtein's presentation at the 15th International Congress of the International Union of Crystallography in Bordeaux, France in 1990 in which he reviewed the results of the independent structure determinations performed by EDSA. In connection with the 80th anniversary of Vainshtein, it seems to be appropriate and useful to review the progress in EDSA achieved by Russian scientists since the publication of Vainshtein's monograph, which up to now has been scattered over numerous articles on the structure determinations of various materials, and to use these data to create the general picture of the development of the electron diffraction structure analysis.

EXPERIMENTAL METHODS FOR OBTAINING SPECIMENS AND THEIR ELECTRON DIFFRACTION PATTERNS

EDSA is generally used to study thin films of materials and allows the complete structure determinations up to the establishment of the atomic coordinates in the crystal lattice and the refinement of atomic thermal vibrations. However, this possibility often remains only theoretical. The point is that EDSA requires the use of specimens in which the constituent crystallites have some preferred orientation. The methods for specimen preparation by crystallization from solutions or deposition from suspensions are described in detail in well-known monographs [6, 7]. The technology of preparation of thin films of nitrides and carbides of the metals of VIa subgroup, hydrides of the metals of VIIIa subgroup, and oxides of the metals of the IV and V groups for electron diffraction study are described elsewhere [21–38]. Semiconductor films are usually obtained by vacuum sputtering and condensation [39].

The specimens most appropriate for studying in electron diffraction cameras at accelerating voltages ranging within 50–100 kV are crystals of about 10^{-6} cm in length. For larger crystals, the kinematic law of scattering becomes invalid and the probability of inelastic scattering in these crystals greatly increases, which essentially hinders the transition from the experimental reflection intensities to structure factors. If crystals are too small, two-dimensional diffraction can arise, which also distorts the "kinematical" reflection intensities. The optimum specimen thickness at the accelerating voltages indicated above ranges within 200–600 Å (depending on the atomic number of chemical components in the compound studied). The required crystal dimensions can be obtained by varying the conditions of specimen preparation such as the substrate temperature and the condensation rate. Yet, the situation is rather complicated, because these parameters also influence the orientation of crystallites in the film. As a result, one often has to compromise and neglect, depending on the main goal of the study, either the crystallite dimensions in the film or their orientation. Crystallite orientation in the film and the film quality provide the formation of different types of electron diffraction patterns—those from polycrystals, textures, mosaic single-crystal films or the patterns with Kikuchi lines.

Polycrystal-type electron diffraction patterns (Fig. 1) are especially valuable for precision studies—checking of the scattering law, identification of the nature of chemical bonding, and refinement of the chemical composition of the specimen—because these patterns allow the precision measurements of reflection intensities. However, two or more reflections can overlap in one ring of the pattern, especially in the cases where the material studied has large lattice parameters.

Electron diffraction patterns from oblique pattern (platelike) textures (Fig. 2) are the main experimental material for the EDSA since they have a large number of reflections, so that only one pattern can provide an almost complete three-dimensional set of diffraction reflections. The experimental data obtained from these patterns allows the determination of the atomic structure of both high- and low-symmetric crystals. One of the shortcomings of the oblique-texture diffraction patterns is the formation of the "dead cone" around the texture axis and, thus, the absence of reflections located outside the interference field of the pattern. To reduce the dead cone, one has to obtain diffraction patterns at the maximum possible tilt angles of the texture axis to the beam (60°–80°) [40]. A special method for recording the basal reflections from the oblique-textures, especially important in the refinement of the symmetry and fine details of the structure, was suggested in [41]. Another drastic shortcoming of oblique-texture patterns is the fact that, similar to reflections of polycrystal-type patterns, the crystallographically nonequivalent reflections (having equal

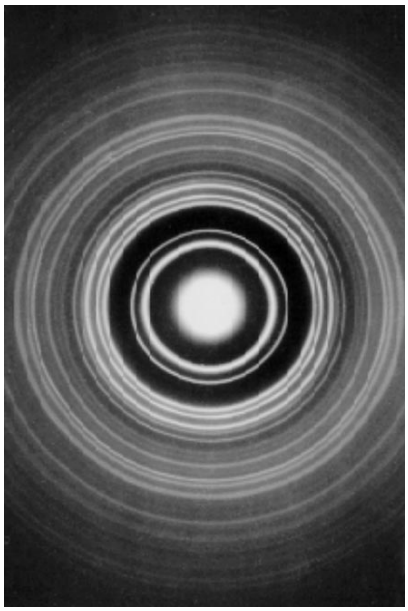

Fig. 1. Electron diffraction pattern from the polycrystalline Sb_2I_3 film.

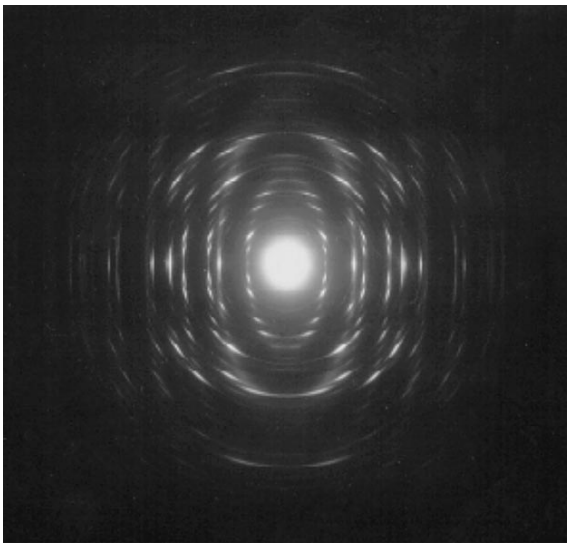

Fig. 2. Oblique-texture electron diffraction patterns from the thin film of the hexagonal modification of In_2Se_3.

interatomic spacings but different moduli of structure factors) from crystals belonging to tetragonal, rhombohedral hexagonal, and cubic systems can overlap in one reflection [42]. However, unlike the polycrystal patterns, where this shortcoming cannot be avoided, the problem for texture patterns can be solved by taking diffraction patterns from the same texture with another orientation, which allows the separation of crystallographically nonequivalent reflections. However, in practice, it is rather difficult because, as a rule, the crystals of tetragonal, rhombohedral hexagonal, and cubic systems usually have only one orientation. Thus, at the initial stage of the structure determination, one also often has to use some number of averaged moduli of structure factors. At the later stages of the structure determination (upon the establishment of the preliminary structure model), one can divide the experimental moduli of the structure factors proportionally to their calculated values for the established model. Since the number and the indices of the reflections with equal interplanar spacings are determined by the space group of symmetry, a convenient table was constructed which indicates the types of reflections on oblique-texture electron diffraction patterns that have to be separated in all the space groups of the tetragonal, orthorhombic, hexagonal, and cubic systems where such overlappings are possible [42]. The specific role of the oblique-texture type electron diffraction patterns in the study of clay minerals [43] will be considered later.

One often observes the formation of the so-called needlelike textures with the texture axis lying in the substrate plane (Fig. 3). Unlike platelike texture patterns, the needlelike patterns cannot be used for estimating intensities, because the orientations of crystal faces parallel to the substrates are not equally probable, and therefore the intensities of various zones of reflections can be distorted.

Spot-type electron diffraction patterns (Fig. 4) are formed as a result of diffraction from thin films of mosaic single crystals consisting of a large number of small, almost perfect single-crystal blocks slightly misoriented with respect to one another. These patterns are widely used for determining the symmetry and the unit-cell parameters of crystals and for studying orientational relationships [6, 7]. These patterns are obtained from the specimens prepared by condensation of molecular beams of materials onto heated NaCl cleavages, mica, and other single-crystal substrates [44–53] or by crystallization of drops of various solutions. Today, it is believed that spot-type patterns are formed due to two-dimensional diffraction from ~10^{-7}-cm-thick crystals or the multibeam dynamical scattering from sufficiently perfect 800- to 1000-Å-thick crystals. Because of the high perfection of the crystal lattice, the dynamical effects in these specimens become more pronounced. The obvious advantage of these patterns is the absence of overlapping reflections having the same spacings d_{hkl} but different Miller indices hkl and also the absence of the dead zone. There are a number of studies in which the structure determination was performed solely by the spot-type patterns [54–57]. The use of spot-type patterns proved to be very successful in the studies of organic compounds consisting of light atoms. This direction is actively being developed by American scientists [58–60].

Diffraction patterns with Kikuchi lines. As far back as 1928, studying reflection of an electron beam from the mica surface, Kikuchi obtained electron dif-

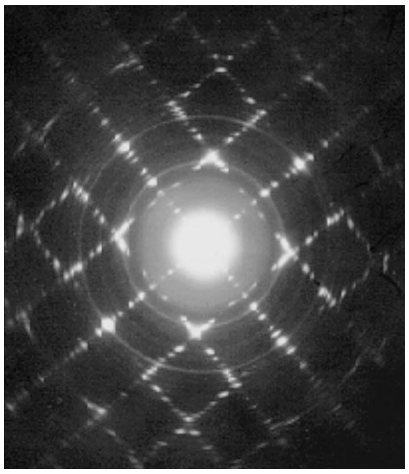

Fig. 3. Electron diffraction pattern from the needlelike $CuSbSe_2$ texture.

Fig. 4. Spot-type electron diffraction pattern from the mosaic CdTe film on the mica substrate.

fraction patterns containing along with a small number of spot reflections also pairs of parallel white and black lines [which later were termed Kikuchi lines (Fig. 5a)] and the systems of fanlike bands (Fig. 5b). The formation of Kikuchi lines and bands is caused by multiple electron scattering, and they can be interpreted only in terms of the dynamical theory. The presence or absence of Kikuchi-lines and their contrast depend on the degree of crystal perfection. Electron diffraction patterns with Kikuchi lines are widely used for the qualitative study of mosaicity of surface layers [61–64]. These pattern provide a real possibility of determining the phases of some structure factors, i.e., the partial solution of one of the most important problems of the structure analysis. This explains the constant attempts to develop the theory for interpreting Kikuchi patterns [65, 66].

PHYSICAL FOUNDATIONS OF THE EDSA METHOD

Similar to X-ray and neutron diffraction analysis, EDSA consists of four main stages—the obtaining of appropriate electron diffraction patterns (of the polycrystal, oblique texture, or single-crystal type) and their geometrical analysis, the precision evaluation of diffraction-reflection intensities, the use of the appropriate formulas for recalculation of the reflection intensities into the structure factors, and finally the solution of the phase problem.

As has already been indicated, the use of EDSA in the West was impeded because of the widespread opinion that the reflection intensities on electron diffraction patterns are distorted by dynamical effects caused by a strong interaction of electrons with the matter and, therefore, cannot be used for determination of unknown structures. Nevertheless, the structure determinations by EDSA had been made from the very first steps of its coming into being, and, thus, the structures of a large number of various inorganic and organic substances have been solved by the EDSA method, with many of

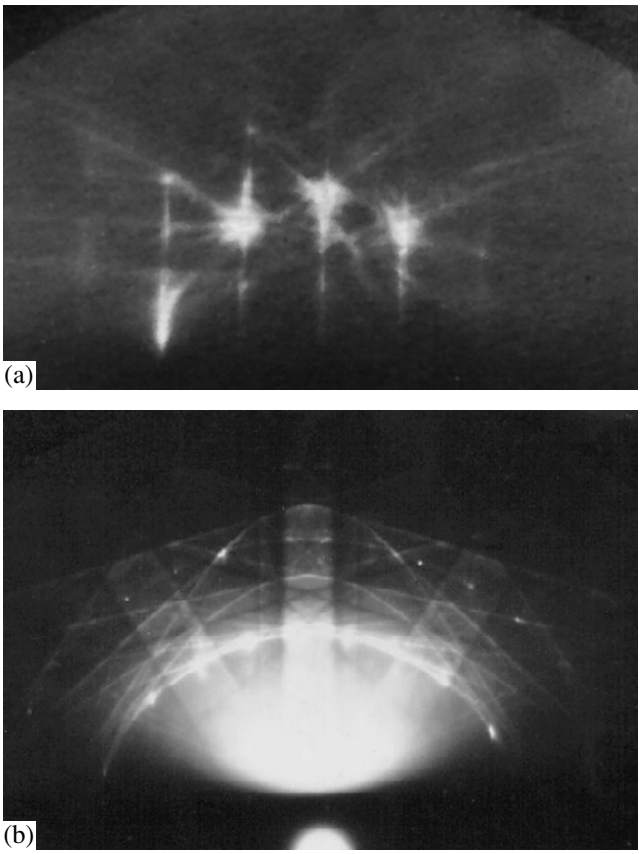

Fig. 5. Electron diffraction pattern with Kikuchi lines and bands from the surface of (a) a sapphire single crystal and (b) a Ge single crystal.

them being absolutely independent studies performed for the first time. These structural determinations were made mainly within the kinematical theory of electron scattering. However, because of the strong interaction of electrons with the matter, the dynamical effects were also possible, with the probability their occurrence increasing in the transition from polycrystal to single crystal films. Therefore, one of the most important problems of EDSA was the establishment of the relationships between the kinematical and dynamical scattering. The examination of the intensities of the rings on polycrystal-type electron diffraction patterns performed in the late 1940s [67, 68] showed that scattering by small crystallites consisting of atoms of the Periodic Table up to gold are accurately described by the kinematical theory if their linear dimensions do not exceed ~5–10^{-6} cm. The intensity I_{hkl} of diffraction reflections is determined by squared structure factors Φ_{hkl} [7] (where *hkl* are the Miller indices), i.e.,

$$I_{hkl} \sim |\Phi_{hkl}|^2. \quad (1)$$

However, if the crystal thickness t is of the order of 10^{-5} cm, scattering becomes dynamical. The checking of the applicability of the kinematical theory to scattering by crystals of moderate dimensions is made according to the theoretical relationship [69, 70]

$$A = \lambda \frac{|\bar{\Phi}|}{\Omega} t \le 1, \quad (2)$$

where $|\bar{\Phi}|$ is the average absolute value of Φ_{hkl}, Ω is the unit-cell volume, and λ is the electron wavelegnth.

According to the dynamical theory of electron scattering [7] we have

$$I_{hkl} \sim |\Phi_{hkl}|. \quad (3)$$

However, in practice, scattering is usually of the intermediate character; then

$$I_{hkl} \sim K_{\text{kin}}|\Phi_{hkl}|^2 + K_{\text{dyn}}|\Phi_{hkl}|. \quad (4)$$

The degree of scattering "dynamicity" by various materials (including the scattering by materials with unknown structure) can be estimated by comparing the curves of average intensities $I_{hkl}(\sin\theta/\lambda)$ with the Σf_{el} or Σf_{el}^2 curves in the same angular range (where f_{el} is the scattering factor of an "average" atom whose weight is averaged over the weights of all the atoms of the material). Then, introducing the corrections for the dynamic scattering, one can obtain the $|\Phi_{hkl}|$ values from the measured intensities I_{hkl}.

The fundamentals of the multibeam dynamical theory were laid by Bethe [71, 72], who also described electron scattering by the Schrödinger wave equation. In the two-beam approximation, the problem is essentially simplified—one considers the interaction between the incident wave and only one strong scattered wave (the first Bethe approximation). Then, the formula for the integrated intensity takes the form

$$\frac{I_{hkl}}{I_0 S'} = \lambda^2 \frac{|\Phi_{hkl}|^2}{\Omega^2} LD(A), \quad (5)$$

where S' is the irradiated area of the crystal and L is the factor taking into account the specimen structure. For textured specimens, L_t is determined by the formula [7]

$$L_t = \frac{t\lambda p}{2\pi R' \sin\varphi}, \quad (6)$$

where R' is the horizontal coordinate of the reflection on the oblique-texture pattern, φ is the angle of the specimen tilt to the electron beam, and p is the repetition factor (the number of reciprocal-lattice points merged in one diffraction reflection). The correction for extinction (the so-called dynamical correction) is set by the function [73]

$$D(A) = \frac{1}{A}\int_0^A J_0(2x)dx, \quad (7)$$

where $J_0(2x)$ is the Bessel function.

The dynamical correction is introduced using the graphical representation of the function $D(A)$ [27], from which one determines the A value corresponding to the best agreement between the experimental and the calculated intensities. Introducing the corrections into the intensities of several strong reflections, one selects the relative values of $D(A)$ for the averaged A value.

In the second Bethe approximation, one has to compare with the experiment not the values

$$v_{hkl} = 4\pi|\Phi_{hkl}|/\Omega \quad (8)$$

but the calculated values of

$$u_{hkl} = v_{hkl} - \sum_{g \ne 0,\, H} \frac{v_g v_{H-g}}{k^2 - k_g^2}, \quad (9)$$

where H and g are the Miller indices of strongly and weakly reflecting planes, respectively. It is clear that the multibeam solution of the Schrödinger equation is more rigorous, but, as has already been indicated, it cannot be directly used in EDSA of an unknown structure, because it is based on the use of the already known structure factors (i.e., the known structure model). The attempt to use the matrix form of the dynamical theory for polycrystal specimens was made in [74], but the authors failed to obtain the formula for direct transition from the experimental intensities to the structure factors, which is necessary for studying crystal with unknown structure.

The sufficiency of using the two-beam Bethe–Blackman approximation and the second Bethe approximation was confirmed by numerous structure determinations. The practical approach to the allowance for the dynamical scattering of electrons in thin

films is based on the assumption that the intensity of most of the reflections is described by the kinematical formula ($K_{dyn} = 0$) but that the intensities of some (usually strong) reflections can have the intensities that can differ by more than 50% from the "pure kinematical" intensities and, at the same time, also from the "pure dynamical" intensities ($K_{kin} = 0$). Assuming that the physical mechanisms of the intensity formation can be somewhat different for different reflections [75, 76], all the reflections observed on electron diffraction pattern can be divided into three groups in accordance with the method used for the transition from the experimental intensities to the structure factors. These are (i) *hkl*-type reflections with moderate and weak intensities whose structure factors are calculated in the kinematic approximation by formula (1); (ii) strong $h_0 00$, $h_0 h_0 0$, and $h_0 h_0 h_0$ "dynamic" reflections ($h_0 = 1$ or 2) whose structure factors are calculated with allowance for extinction by Eq. (5); and (iii) the higher orders of strong *h*00, *hh*0, and *hhh* reflections ($h = nh_0$, where $n = 2, 3, \ldots$) whose structure factors are calculated with due regard for the multibeam interaction in the approximation of the Bethe dynamical potentials. The practical procedure for calculating structure factors for the reflections of groups (ii) and (iii) reduces to the calculation of the "kinematical" structure factors and their subsequent correction for the dynamical scattering. Of course, this procedure is limited to the allowance for only the systematic interactions. Various methods of introducing corrections for dynamical scattering were tested on high-energy (75 keV) electron diffraction from Al, Ni, and Au polycrystal [77, 78] and ammonium bromide [79] films. The study of reflection intensities from ammonium bromide (the material with considerable difference in the atomic numbers of the constituent atoms) with an allowance for multibeam scattering was especially interesting, because it was believed [80] that such structures could be solved only within the rigorous multibeam theory. The study of ammonium bromide [79] confirmed the applicability of the kinematical theory to EDSA, on the one hand, and showed the necessity of taking into account the dynamical effects for attaining the higher accuracy and reliability of the crystallographic data, on the other hand. The nature of scattering should be taken into consideration not only for the better convergence of the experimentally observed and theoretically calculated structure factors but, mainly, for the determination, with the highest possible accuracy, of the electrostatic-potential distribution in the lattice.

Among various formulations of the theory of high-energy electron diffraction in crystals, one should indicate the formalism of Bloch waves. The characteristics of each Bloch wave can readily and graphically be interpreted in terms of physics [81]. Moreover, the wave function of an incident electron beam propagating along the principal crystallographic directions can be described with sufficient accuracy solely by two or three Bloch waves [82] that can readily be represented in the analytical form [83]. This, in turn, allows the formulation of the necessary conditions for their effective use for attaining a higher accuracy and reliability of the final structural data [84].

It should be emphasized that the success of EDSA application to the determination of atomic structures depends not only on the appropriate allowance for the nature of electron scattering by a material but, of course, also on the methods of intensity measurements and the apparatus used. In the first years of EDSA studies, the reflection intensities were estimated visually with the use of darkening scale [6]. Later, the reflection intensities were determined by microphotometric methods [7]. In the 1960s, considerable efforts were made to create systems for electrometric recording of intensities—as certain numbers of pulses—with the use of special energy filters to remove inelastically scattered electrons [85, 86]. Thus, the accuracy of intensity recording on an automated EMR-102 diffractometer (with two-dimensional scanning of diffraction patterns and a static detector designed and manufactured at the Institute of Crystallography) is about 1–2%. This allowed the study of thin layers with the accuracy sufficient for the precision determination of the electrostatic potential in the unit-cell and the study of the nature of chemical bonding in materials [87–90]. Although similar studies have been performed on materials with predominantly ionic bonding, they are undoubtedly a step forward in the development of the EDSA method and are an important contribution to the solution of the problem as to how the crystal properties are related to its structure.

A bottleneck of EDSA is the determination of phases of structure factors. Despite the fact that Vainshtein analyzed various statistical and direct methods of determining the signs of the Fourier coefficients [7], Russian researchers traditionally determined the phases by the trial and error method and widely used the Patterson function to construct trial structure models. In the 1980s, numerous attempts were made to apply the direct methods of phase determination also to high-energy electron diffraction data [91]. These methods were based on the estimation of the structure factors with the subsequent phase determination from the system of phase equations. Beginning in 1990, direct methods were used in the controlling structure determinations of inorganic and organic crystals [91–93] studied earlier by EDSA and confirmed these determinations. Unfortunately, it is only upon these studies that Western researchers recognized the importance and usefulness of numerous structural data obtained by Soviet scientists by EDSA.

FOURIER METHOD IN ELECTRON DIFFRACTION STRUCTURE ANALYSIS

The modern EDSA method is based on the Fourier series—the representation of the final result of the

structural determination as the distribution of the electrostatic potential in the unit cell of the crystal. Summing three-dimensional Fourier series over all the reciprocal-lattice points with the nonzero structure-factor moduli,

$$\varphi(xyz) = \frac{1}{\Omega}\sum_{hkl}\Phi_{hkl}\exp[2\pi i(hx + ky + lz)], \quad (10)$$

one obtains the electrostatic-potential distribution in the unit cell, which, in turn, provides the determination of all the three positional coordinates of the atoms.

The heights of the electrostatic potential on the Fourier syntheses calculated by the experimental structure factors are compared with the values of the potential at the centers of atoms of each kind calculated by the integral formula

$$\varphi(0) = G_1 = \frac{1}{2\pi^2}\int_0^\infty f(S)\exp[-B(\sin\vartheta/\lambda^2)S^2 dS = \int_0^\infty D(S)dS, \quad (11)$$

where $S = 4\pi\sin\vartheta/\lambda$ and B is the temperature factor. In practice, the value of G_1 is determined as the area under the curve $D(S)$ with due regard for the experimental series termination and the temperature factor calculated, in the first approximation [7], as $B = 3.5 \times 10^6/A_H\theta^2$, where θ is the characteristic temperature and A_H is the atomic weight multiplied by the mass of the hydrogen atom. Comparing the experimental value of the potential at the center of an atom obtained from the Fourier synthesis (in volts) and the calculated value $\varphi(0)$, one should also take into account the average internal potential equal to

$$\varphi_{av} = \frac{\Phi_{000}}{\Omega} = \frac{\sum_{i=1}^{n} f(0)}{\Omega}P, \quad (12)$$

where n is the number of atoms per unit cell, $f(0)$ is the atomic scattering factor of electrons at $\sin\vartheta/\lambda = 0$, and P is the scaling factor for transition to volts. The estimates show that the accuracy of the identification of the potential maxima for heavy atoms is ~3% and for light atoms, ~10%.

It is also possible to represent G_1 in the analytical form [7, 97, 98]. However, one should pay attention to the fact that the analytical methods so attractive for facilitating and automating the computations can be applied only in the case of the uniform termination of the series of structure factors in all directions whereas the oblique-texture electron diffraction patterns, the main experimental material for EDSA, usually give the data characterized by different series termination in different directions mainly because of the fact that some reflections (including the strong ones) are located in the dead zone [7].

In practice, the effect of the nonuniform series termination on the heights and the positions of the maxima on the Fourier maps is established from their comparison with the corresponding theoretically calculated maps constructed by the structure factors calculated for the same reflections that were used in the construction of the experimental maps. These "theoretical" maps (or syntheses) calculated either with due regard for all or only some of the constituent atoms allow the analysis of the effect of the series-termination waves on the position of each atom. The experience of electron diffraction structure determinations shows that the allowance for the nonuniform series termination complicates the procedure of the structure determination, but, under its rigorous control, yields much better results.

It should also be indicated that the preparation of specimens for EDSA by sputtering alloys and other compounds is usually accompanied by their dissociation. The inevitable difference in the elasticity of the vapors of different components can result in chemical compositions of the deposited thin film essentially different from the composition of the initial sputtered alloy and, therefore, should be determined by an independent method. This difficulty is characteristic of various objects studied by EDSA, so that the final chemical formula of the film studied should be determined in the course of the structure study, e.g., by the peak heights on the Fourier maps of the electrostatic potential.

Structure Analysis of Partly Disordered Phases

There are systems in which the specific characteristics of the electronic shells of the interacting atoms provide the formation not only of stoichiometric phases but also the phases in which some atoms occupy their positions statistically (the so-called partly disordered phases). The formation of disordered phases in such systems is the rule rather than the exception. These phases are usually characterized by a wide homogeneity ranges, a considerable scatter in the composition, and as a result also in their physical properties. These are various transition metal oxides, carbides, nitrides, and hydrides. The structure analysis of these phases was first performed by the EDSA method.

Most of the information on the structure of partly disordered phases is contained in the reflection intensities, although, in some occasions, the changes in the unit-cell parameters are also observed. The structure determination in such cases is hindered by the existence in the lattice of partly occupied positions "imitating" the decrease in the atomic number. The atomic factor takes the form wf_{at}, where $w < 1$ is the probability of the position occupancy with such atoms. Correspondingly, the structure amplitude in the kinematical approxima-

tion is determined by the formula

$$\Phi_H = \sum_{j=1}^{N}\sum_{r=1}^{s} f_j K_{jr} \exp[2\pi i(\mathbf{r}_j \cdot \mathbf{H})] \times \exp[-B_j(\sin\vartheta/\lambda)^2], \quad (13)$$

where f_j is the atomic scattering factor of electrons for the jth atom, r_j is the radius-vector of the jth atom, N is the number of atoms with different atomic numbers, s is the number of independent positions in the structure, and K_{jr} is the probability that the atom of the jth kind would occupy the rth independent position, f_jK_{jr} is the effective atomic scattering factor (Z_{eff}).

The quantity Z_{eff} leads to the necessity of localizing "a fraction of an atom" occupying a certain crystallographic position. If one has to use the least squares refinement, the use of additional parameters does not guarantee obtaining of reliable final structural data (even in the case where this procedure considerably reduces the reliability factor). Since the Fourier-potential syntheses are less sensitive to the errors in structure factors [7], the analysis of peak heights on the syntheses calculated by the experimental structure factors allows the evaluation of K_{jr} with a higher accuracy. The criterion for detecting light atoms statistically estimated by Vainshtein [7] (based on the analysis of $\Delta\varphi_{er}$, which is of the statistical nature) and using EDSA showed that using the difference Fourier maps, one can reveal the potential peaks due to hydrogen atoms in the presence of the peaks due to heavy atoms (even if the reflection intensities were estimated by the microphotometric method). Thus, it was possible to localize oxygen atoms occupying their positions with the probability 1/8 (the corresponding peak height equals ~50 V) in the presence of niobium (the peak height ~1530 V) [32] (Fig. 6).

It is seen from Eqs. (11) and (13) that the reduction of the potential-peak height can be associated not only with the appearance of the term Z_{eff} but also because of the temperature factor. However, these two factors influence the atomic scattering curve differently—the temperature factor noticeably decreases the f_j values at large angles, whereas Z_{eff} reduces the scattering power at all the angles. Therefore, when studying partly disordered phases, one has to use the effective atomic curves, which should be constructed each time and depend on the method used for the determination of the crystal structure, where the atoms give different contributions to the total intensities of reflections having different Miller indices [99].

The reliable criterion of the correct determination of the atomic coordinates and the chemical composition of the material is the "purity" of the final Fourier synthesis, i.e., the absence of spurious peaks and pronounced differences between the negative and the positive values in the area between the peaks. The final conclusions on the reliability of the results obtained can be made of upon the crystallochemical analysis of the structure thus established.

Possibilities of Electron Diffraction in Studies of the Structure of Langmuir–Blodgett Films

One of the main methods of obtaining thin organic films with a controllable molecular architecture is the Langmuir–Blodgett (LB) method [100]. The importance of LB films for nanotechnology is seen from the exponentially increasing number of publications in the last two decades. The use of polymer molecules in the architecture of LB films opens new vistas for their practical use. The Langmuir–Blodgett films are artificially constructed layer structures. The method of their preparation by the successive deposition of condensed monolayers of amphiphylic molecules with hydrophylic heads and hydrophobic tails from the aqueous subphase yields ordered platelike textures—ideal objects for EDSA.

The electron diffraction structure analysis of thin layers of chain molecules is made in the way described above. In most cases, the moduli of structure amplitudes can be determined in the kinematical approximation, because the molecules consist mainly of light atoms. The first structure determination of an LB film by EDSA was made on lead stearate films in the early 1990s [101]. Figure 7 shows the characteristic features of the diffraction patterns from an LB film consisting of long-chain molecules. One can clearly see the "layer lines" of intense reflections with the small period $c'^* = 1/c'$, where c' is the periodicity of the chain molecule, and the layer lines of weaker reflections with the large period $c^* = 1/c$ associated with packing of chain molecules into a crystal structure. If reflections on the diffraction patterns are blurred only slightly, one can also perform the structure analysis by considering the discrete reciprocal lattice of the crystal.

However, studying LB films of various materials by the EDSA, one can encounter some "unpleasant" effects—different spreading of reflections on the oblique-texture patterns [101, 102], which indicates the distortion of the ideal packing of the molecules in the film. Here, Vainshtein's monograph "Diffraction of X-rays by Chain Molecules" was an indispensable tool [103]. Although the theory of second-order distortions takes its origin in the early 1920s and was successfully developed in the 1950s by Hosemann and his research fellows, who studied X-ray scattering by liquids [104]. In this monograph, Vainshtein successfully solved a number of important problems [103].

It is well known that the aggregates of chain molecules can have various types of order, which can be considered as the distortion of the ideal crystal structure (although the chain molecules do not necessarily form crystal packings). The characteristic distortions are the shift of the molecules along their axes, the stacking faults in their packing, molecule rotation

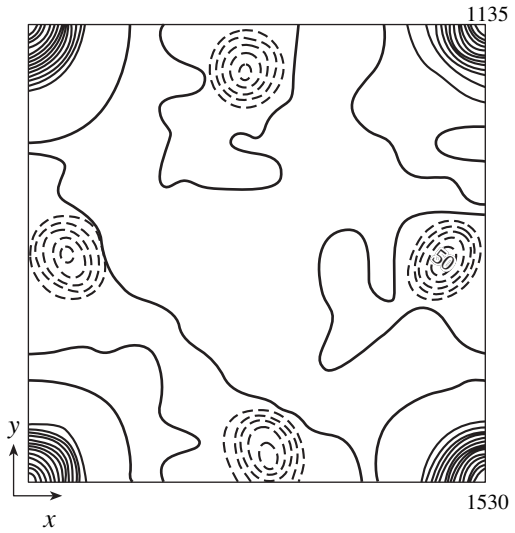

Fig. 6. Fourier-section by the (*xy*0) plane of the cubic niobium oxide (a = 3.80 Å).

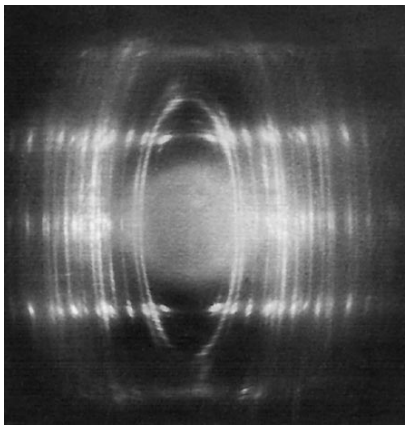

Fig. 7. Electron diffraction pattern from the Langmuir–Blodgett PbSt_2 films consisting of 20 bilayers. The angle between the sample and the beam is φ = 52°.

around the principal axis, and also their tilt and bending (the so-called second-order distortions). The diffraction phenomena associated with considerable distortions in packing of long-chain molecules are usually interpreted with the aid of the Fourier transform and the convolution function [102]. The intensities of diffraction reflections are written as products of the molecular structure factor by the convolution of the interference function $Z(\mathbf{S})$ with the squared form factor $S(\mathbf{S})$

$$I(\mathbf{S}) = |\Phi_m(\mathbf{S})|^2 \frac{1}{\Omega} \widehat{Z(\mathbf{S})|S(\mathbf{S})|^2}, \qquad (14)$$

where $\Phi_m(\mathbf{S})$ is the molecular structure factor and $\mathbf{S}$ is the reciprocal lattice vector. In principle, this formula is valid for any object, including crystals. In the latter case, Φ_m is a structure factor of the unit cell.

The starting point for considering various distortions is the allowance for the short-range order, which is determined by the shape of the structural units and the forces acting between them. If the distribution law of the nearest neighbors is established, then it can be used for obtaining the distribution function (without the rigid fixation of the equilibrium positions of all the distant neighbors). Each type of second-order distortion can be described by a certain function [103]. These distortions and the corresponding functions are shown schematically in Fig. 8. Some distortions result in blurring or even the complete disappearance of reflections (the absence of any difference between the maxima and the minima of the interference function) at a certain distance from the origin of the reciprocal space, which corresponds to the reciprocal value of the correlation length in the real space. Therefore, studying reflection blurring on electron diffraction patterns, one can qualitatively estimate the existing distortions, i.e., determine the average distance between the nearest neighbors in the *xy* plane, the correlation radius L_{corr} (the distance at which there still exists the finite probability to encounter the equivalent structural unit), and some other parameters. If the structure is completely disordered, its diffraction pattern consists of amorphous halos.

SOME RESULTS OF EDSA STUDIES

Consider the general results of the electron diffraction studies performed by the Pinsker–Vainshtein school along several main directions.

Structures of Hydrogen-Containing and Macromolecular Compounds

EDSA played an important role in localization of hydrogen atoms and establishment of the nature of chemical bonding in various organic and inorganic materials. The electron diffraction study of *n*-paraffins of the compositions $C_{18}H_{38}$, $C_{28}H_{58}$, and $C_{30}H_{62}$ provided not only the most accurate localization of hydrogen atoms in the crystal lattice and the refinement of the C–H distances (1.125 ± 0.015 Å) but also the establishment of ionization of hydrogen atoms (from the analysis of potential-peak heights on the Fourier syntheses) [9, 10, 20, 54, 105].

The precision electron diffraction determination of coordinates of hydrogen atoms in the crystal lattice of diketopiperazine [13, 106] with numerous hydrogen bonds provided the analysis of chemical bonding in this structure. The C–H distances in the CH_2 group are equal to 1.09 and 1.11 Å (±0.03 Å) and the bond angle H–C–H = 107° is close to tetrahedral (107°).

The structures of ammonium chloride, bromide, and iodide were repeatedly studied by EDSA [7, 107], The precision measurement of reflection intensities [108] allowed the refinement of the N–H distance (1.02 Å). For NH_4I, the use of difference syntheses (first, with

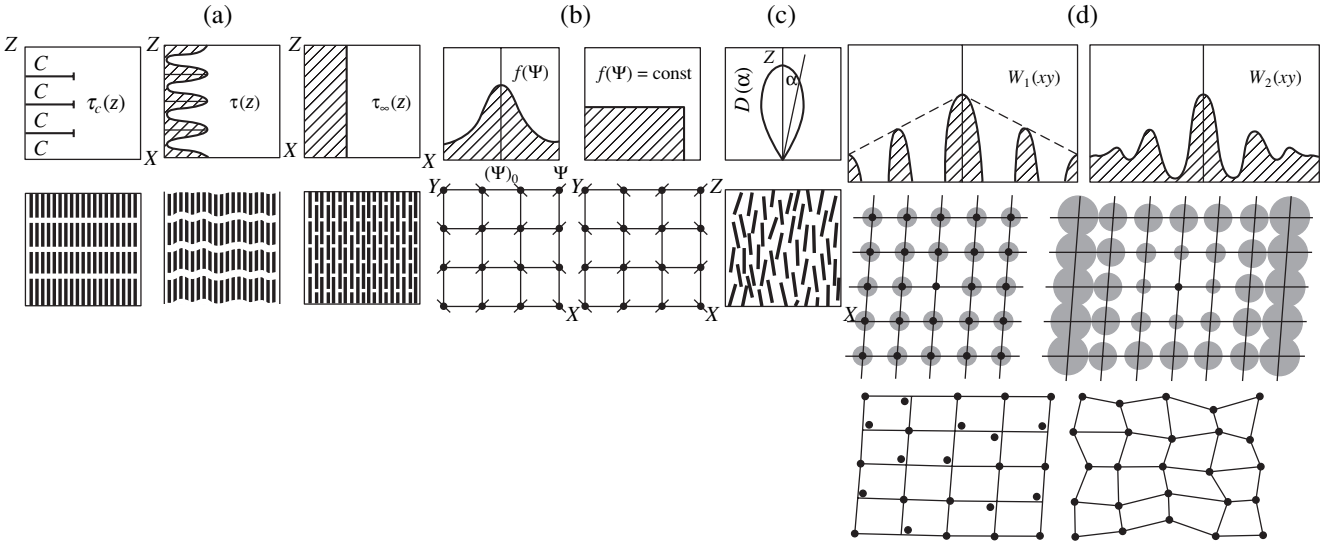

Fig. 8. Various types of distortions and the corresponding distribution functions: (a) shift function $\tau(z)$; (b) azimuthal rotation function $f(\psi)$, (c) the angular distribution function $D(\alpha)$, and (d) function of the net distortion $W(xy)$.

due regard for the contribution of iodine atoms, and then also of nitrogen atoms) [79] showed that all 16 hydrogen atoms have only one 32-multiple position in the unit cell.

The electron diffraction study of cryptohalite $(NH_4)_2SiF_6$ [109] revealed the reorientation of NH_4 groups. Despite the statistical reorientation of NH_4 groups, the three-dimensional Fourier synthesis clearly showed the presence of hydrogen atoms with the weight 1/3. The N–H distances were determined as 1.03 Å.

The efficiency of the EDSA method was demonstrated in the study of the atomic structure of mixed metal complexes with α-amino acids [110], which provided the discovery of materials containing isomers of similar and different amino acids.

At the beginning of the 1990s, the Electron Diffraction Laboratory of the Institute of Crystallography began to study Langmuir–Blodgett films. Some models of LB films constructed on the basis of X-ray reflectometry (00*l* reflections) and electron diffraction data obtained at the normal beam incidence onto the films (the *hk*0 plane) were suggested in the 1950s. Using oblique-type electron diffraction patterns and the EDSA method (Fig. 7), we managed to collect the three-dimensional set of diffraction data and performed the detailed structure determination of LB lead stearate films with the use of Patterson and the Fourier syntheses. It was established that the decisive factors in the formation of lead stearate structure of the LB films are the interactions between the carbohydrate chains caused by the "compression" of a monolayer of the stearic acid molecules on the subphase surface up to the formation of the condensed state, the interaction of lead ions with hydroxyl groups during the formation of a bilayer, and the close packing of successively applied bilayers (at the expense of CH_3 groups of hydrocarbon chains packed by the convexity-to-hollow principle). In this case, the true period along the layer normal is 96 Å [111]; i.e., it has a double value in comparison with the usually indicated value. The studies of the salts of fatty acids showed that their order in LB films directly depends on the ionic composition of the subphase [112].

In recent years, LB films are often prepared from the molecules of unusual shapes, including the polymer films. The EDSA method was successfully applied to a number of such LB films, e.g., lipids of the membrane origin [113] (phospholipids, sterols stabilizing the structures of biomembranes, etc.), discotic liquid-crystal materials [101, 102] widely used in various thin film-based sensors, polyimides [114], and other materials. The LB technology was also used to prepare the films from the cholesterol molecules with the *c*-axis normal to the substrate [102, 113]. The interpretation of the electron diffraction patterns from these films showed that, in the LB film, cholesterol is triclinic and that its unit-cell parameters coincide, within the accuracy of experimental measurements, with those determined by the X-ray diffraction analysis. Unlike the monochain aliphatic molecules, four and more aliphatic tails are located around the core in the molecules discotic liquid crystals [102]. The oblique-texture electron diffraction patterns provided the first determination of the parameters of the monoclinic and triclinic unit cells of these discotics. For tetraalkanoyloxyhydroquinone, we also determined the atomic structure.

Thus, the EDSA studies showed that the oblique-type electron diffraction patterns from LB films pro-

vide the complete description of their structural organization.

Structure of Highly Dispersed Phases

Vainshtein and his coworkers studied crystal structures of a number of finely dispersed phases by the EDSA method. In addition to the already mentioned phases [14–20], we should like to indicate the rhombohedral $PbCO_3 \cdot PbO \cdot 2H_2O$ phase [115] and the structure determination of the $CuCl_2 \cdot 3Cu(OH)_2$ salt [116] and the related $CuBr_2 \cdot 3Cu(OH)_2$ structure [117].

The unique place among the structures studied by the EDSA method belongs to low-symmetric layer minerals often encountered in nature in the finely dispersed state which can hardly be studied by the X-ray diffraction methods but which are appropriate objects for electron diffraction. As has already been indicated, these studies were performed mainly by B.B. Zvyagin (a close friend of Vainshtein from his scholastic years) and his group [41, 43, 118, 119]. The oblique-texture electron diffraction patterns proved to be an indispensable tool for solving various problems of polytypism [41, 43, 120, 121], because the electron diffraction patterns provide the establishment of the characteristics of individual layers and their mutual arrangement. We should like to mention only one of the latest studies in which electron diffractometry allowed the use of the oblique-texture patterns to refine the crystal structure of the 1*T* polytype of serpentine-type mineral lizardite [122].

The symmetry of the mineralogical objects provided the development of special methods for analysis of oblique-texture patterns from single crystals which, in the general case, belonged to the triclynic system [41]. The principles of indexing of such patterns and determining their unit cells were applied to electron diffraction patterns from single crystals forming the angle φ with the normal to the basal plane and rotated about this normal during the experiment. In this case, the measurements and the calculations are analogous to those used for oblique-texture patterns (Fig. 9). The information obtained in this case is not averaged over numerous crystals; thus, the nodal lines on the patterns from the crystal rotating in the limited angular ranges [119] do not overlap, which provides more detailed structural information. The combination of diffraction from arbitrarily oriented single crystals and their rotation along the normal to the basal plane provides the formation of a set of ellipses of spotlike reflections on the electron diffraction patterns.

Structures of Transition Metal Carbides, Nitrides, and Hydrides

EDSA was used to study metal carbides and nitrides because, first, these materials have some practically important properties such as, e.g., high refractivity; second, EDSA allows localization of light hydrogen, carbon, and nitrogen atoms in the presence of heavy metal atoms in the crystal lattice. Another factor which stimulated these studies was a relatively simple preparation of thin films of these carbides, nitrides, and hydrides convenient for the electron diffraction study. At the same time, the attempts to study these objects by EDSA encounter some difficulties associated with the unknown chemical composition of the films usually established only in the course of the structural study.

The precision electron diffraction studies of these thin films [123–127] revealed the presence of not only Ni, Pd, and Sc hydrides always present in the macrospecimens, but also of the phases never observed there. EDSA allowed the localization of carbon atoms in tungsten carbides from the difference maps of the Fourier-potential [30, 31]. The results obtained in the electron diffraction study of the crystal structure of hexagonal tungsten carbide were later confirmed by its neutron diffraction study [128]. The structures of numerous phases in the Fe–N [27], Cr–N [28], Ti–N [129], Mo–N [25, 130], and W–N [26] systems were also determined by EDSA.

Structures of Oxides of Metals of IV–VIII Groups

EDSA also proved to be very efficient for obtaining the information on the structure of oxides, the objects that can hardly be studied by any other diffraction method. The films and surface layers in which the oxidation processes proceed at high rates and to a higher degree than in the massive specimens are the appropriate objects for EDSA. The use of this method allowed not only the establishment of some new stoichiometric and nonstoichiometric phases but also shows the existence of some intermediate metastable phases existing only at certain stages of the oxidation process. EDSA provided the structure determination of a large number of transition metal oxides [32–34, 131–144] and many specific features of partly disordered compounds arising during the oxidation process. These studies allowed the establishment of successive structural rearrangements during oxidation, i.e., the reconstruction of the oxidation process at the atomic level and establishment of the specific features of oxidation depending on the experimental conditions.

The intermediate phases formed during the oxidation are characterized by a reduced density, partial filling of the atomic positions, and the formation of pseudolayers, which often result in the formation of textures. It should also be indicated that the "stability" of all the intermediate structures is provided by at least one fully occupied (100%) position in the metal sublattice. Moreover, in the regions (layers) with the considerable deficiency of atoms in both sublattices, the –*Me*–O–*Me*–O– chains are formed by the short *Me*–O bond (1.92 Å). These chains penetrate the lattice (e.g., along the *c*-axis in the δ' phase [133]) and the short *Me*–*Me* bonds in the direction normal to such layers which "fix"

the lattice as a whole. Another characteristic feature of intermediate partly disordered structures is the unusual coordination: partly filled coordination polyhedra (octahedra, dumbbels, squares, and trigonal, pentagonal, hexagonal bipyramids) around the *Me* atoms which can often be considerably distorted [32–34, 131–142].

The electron diffraction study of thin films of Bi oxides [35–38, 143, 144] revealed at least three unknown phases, which differ by the oxygen content in the lattice. During long-term storage, these phases are transformed into the tetragonal modification of the composition $Bi_2O_{2.7–2.8}$, the most stable and oxygen-rich oxide phase observed in thin films of the Bi–O system. Later, this conclusion was confirmed by the studies of oxidation kinetics in Bi films [145].

Not considering the other results of the electron diffraction study of oxides of metals of groups IV–VIII, we would only like to indicate that formation of oxide phases in the *Me*–O systems obviously depends on the position of the metal in the Periodic Table. This, in turn, indicates the dependence of the structure and properties of the oxide phases on the electronic structure of the constituent elements, screening of nuclei by valence electrons, etc.

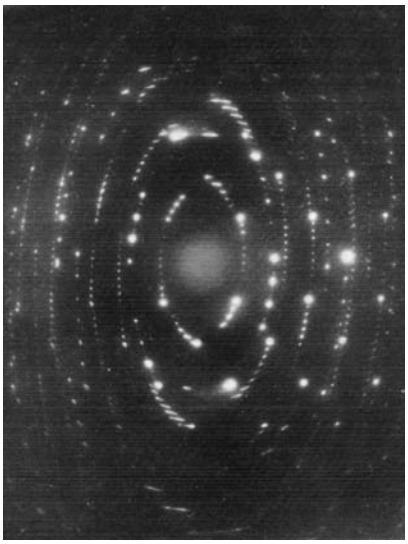

Fig. 9. Rotation electron diffraction pattern from the single crystal of trioctahedral mica, which is similar to an oblique-texture electron diffraction pattern. The rotation of the specimen within the limiting range <60° excludes the overlap of the nodal lines of *hk* reflections and provides the unique identification of the polytype 3*T* not seen on the oblique-texture pattern from the polytype 1*M*.

Structures of Binary and Ternary Semiconductors

It should be remembered that in the 1960s, during the first structural studies of binary and ternary semiconductors, the structures of many semiconductor phases had been known. The single crystals necessary for the complete X-ray diffraction analysis were not available, so that for many years, only some general ideas on the structures of many semiconductors have existed. At the same time, many of the semiconductor compounds were obtained in the form of thin films so that it was quite natural to study their structure, chemical composition, and the conditions of their formation and existence by EDSA [146–160].

Consider here only one example. EDSA revealed an unusual structure of $AgTlSe_2$ [161]: the Ag and Tl atoms formed centered hexagonal nets with six-membered rings of Se atoms forming Se_6 molecules in between them. The structure of this compound consisted of atoms with considerably different atomic numbers and was determined from the oblique-texture electron diffraction pattern. The transition to the structure factor was made by the kinematical formula. Later, the $AgTlSe_2$ structure was also studied with the use of the multibeam electron scattering [162]. Its refinement in the dynamical approximation confirmed the atomic parameters established earlier in [161]. The differences between the structure factors calculated in these two studies were insignificant. The reliability factor in the kinematical approximation was R_{h00} = 6%; the use of the dynamical approximation only slightly improved this value, R_{h00} = 4% [162]. This result had changed the negative attitude of the authors of the "dynamical study" [162] to the use of the kinematical approximation for determining reflection intensities on diffraction patterns from textured films.

It should also be indicated that EDSA allowed the refinement of the compositions of a number of $A^{III}B^{VI}$ semiconductors. The chemical composition of many phases was established only upon their complete structure determination with the analysis of the peak heights on the Fourier maps of the electrostatic potential [155].

Finally, it should be indicated that electron diffraction can also be successfully used for studying amorphous substances [163].

CONCLUSION

Thus, the above results demonstrate the possibilities of the electron diffraction structure analysis as an independent method for studying structures of thin films. Today, this opinion is shared by all those engaged in electron diffraction studies, which provides favorable conditions for the further development of EDSA. At the same time, there are numerous problems still waiting for their solution—the establishment of the nature of all the processes and phenomena occurring in scattering of high-energy electrons in thin films. It is very important to determine rigorously the contribution of diffuse scattering of electrons to the total scattering, etc. There also exist some apparatus limitations. It is necessary to design electron diffraction cameras for higher (300–400 kV) electron energies. One has to develop new effi-

cient and objective methods for recording and evaluating intensities on electron diffraction patterns of all the types, which is especially important for organic and biological objects. It is also necessary to write new specialized software for EDSA which would take into account the specific features of electron diffraction data. The combination of EDSA and electron microscopy and the experience gained in such studies would allow us to hope for further progress in this field.

ACKNOWLEDGMENTS

This study was supported by the Russian Foundation for Basic Research within the Federal Program on Support of Prominent Scientists and Leading Scientific Schools, project no. 00-15-96580.

REFERENCES

1. V. E. Lashkarev and I. D. Usyskin, Zh. Éksp. Teor. Fiz. **3**, 510 (1933).
2. P. D. Dankov, *Structure and Properties of Surface of Solids* (Akad. Nauk SSSR, Moscow, 1940).
3. P. D. Dankov, D. V. Ignatov, and N. A. Shishakov, *Electron Diffraction Studies of Oxide and Hydroxide Films on Metals* (Akad. Nauk SSSR, Moscow, 1953).
4. M. I. Davis, *Electron Diffraction in Gases* (Marcel Dekker, New York, 1971).
5. L. V. Vilkov, *Theoretical Foundations of Gas Electron Diffraction* (Mosk. Gos. Univ., Moscow, 1974), p. 127.
6. Z. G. Pinsker, *Electron Diffraction* (Akad. Nauk SSSR, Moscow, 1949; Butterworth, London, 1953).
7. B. K. Vainshtein, *Structure Analysis by Electron Diffraction* (Akad. Nauk SSSR, Moscow, 1956; Pergamon, 1964).
8. B. K. Vainshtein and J. A. Ibers, Kristallografiya **3** (2), 416 (1958).
9. B. K. Vainshtein and Z. G. Pinsker, Dokl. Akad. Nauk SSSR **72**, 53 (1950).
10. B. K. Vainshtein and A. N. Lobachev, Dokl. Akad. Nauk SSSR **120**, 523 (1958) [Sov. Phys. Dokl. **3**, 495 (1959)].
11. B. K. Vainshtein and A. N. Lobachev, Kristallografiya **6** (2), 395 (1961) [Sov. Phys. Crystallogr. **6**, 313 (1961)].
12. B. K. Vainshtein, Kristallografiya **7** (6), 960 (1962) [Sov. Phys. Crystallogr. **7**, 777 (1962)].
13. B. K. Vainshtein, Dokl. Akad. Nauk SSSR **99**, 81 (1954).
14. B. K. Vainshtein, Dokl. Akad. Nauk SSSR **60**, 1169 (1948).
15. B. K. Vainshtein and Z. G. Pinsker, Zh. Fiz. Khim. **23**, 1058 (1949).
16. B. K. Vainshtein, Dokl. Akad. Nauk SSSR **68**, 301 (1949).
17. B. K. Vainshtein, Dokl. Akad. Nauk SSSR **88**, 227 (1952).
18. B. K. Vainshtein, Zh. Fiz. Khim. **26**, 1774 (1952).
19. B. K. Vainshtein and Z. G. Pinsker, Zh. Fiz. Khim. **24**, 432 (1950).
20. B. K. Vainshtein, Q. Rev., Chem. Soc. **14** (2), 105 (1960).
21. Z. G. Pinsker and S. V. Kaverin, Kristallografiya **2** (2), 386 (1957) [Sov. Phys. Crystallogr. **2**, 380 (1957)].
22. V. I. Khitrova and Z. G. Pinsker, Kristallografiya **3** (5), 545 (1958) [Sov. Phys. Crystallogr. **3**, 551 (1958)].
23. N. V. Troitskaya and Z. G. Pinsker, Kristallografiya **4** (1), 38 (1959) [Sov. Phys. Crystallogr. **4**, 33 (1959)].
24. V. I. Khitrova and Z. G. Pinsker, Kristallografiya **5** (5), 711 (1960) [Sov. Phys. Crystallogr. **5**, 679 (1960)].
25. N. V. Troitskaya and Z. G. Pinsker, Kristallografiya **6** (1), 43 (1961) [Sov. Phys. Crystallogr. **6**, 34 (1961)].
26. V. I. Khitrova and Z. G. Pinsker, Kristallografiya **6** (5), 882 (1961) [Sov. Phys. Crystallogr. **6**, 712 (1961)].
27. G. G. Dvoryankina and Z. G. Pinsker, Kristallografiya **3** (2), 439 (1958) [Sov. Phys. Crystallogr. **3**, 439 (1958)].
28. Z. G. Pinsker and L. N. Abrosimova, Kristallografiya **3** (2), 281 (1958) [Sov. Phys. Crystallogr. **3**, 285 (1958)].
29. Z. G. Pinsker, S. V. Kaverin, and N. V. Troitskaya, Kristallografiya **2** (1), 179 (1957) [Sov. Phys. Crystallogr. **2**, 169 (1957)].
30. L. N. Butorina, Kristallografiya **5** (1), 179 (1960) [Sov. Phys. Crystallogr. **5**, 166 (1960)].
31. L. N. Butorina and Z. G. Pinsker, Kristallografiya **5** (4), 585 (1960) [Sov. Phys. Crystallogr. **5**, 560 (1960)].
32. V. V. Klechkovskaya, N. V. Troitskaya, and Z. G. Pinsker, Kristallografiya **10** (1), 37 (1965) [Sov. Phys. Crystallogr. **10**, 28 (1965)].
33. V. V. Klechkovskaya and V. I. Khitrova, *Structure, Properties and Applications of Intermetallic Compounds* (Nauka, Moscow, 1974), p. 153.
34. V. V. Klechkovskaya, Doctoral Dissertation (Inst. Kristallografii Ross. Akad. Nauk, Moscow, 1997).
35. A. A. Zav'yalova, R. M. Imamov, and Z. G. Pinsker, Kristallografiya **9** (6), 857 (1964) [Sov. Phys. Crystallogr. **9**, 724 (1964)].
36. A. A. Zav'yalova and R. M. Imamov, Kristallografiya **13** (1), 49 (1968) [Sov. Phys. Crystallogr. **13**, 37 (1968)].
37. A. A. Zav'yalova and R. M. Imamov, Kristallografiya **16** (3), 515 (1971) [Sov. Phys. Crystallogr. **16**, 437 (1971)].
38. A. A. Zav'yalova and R. M. Imamov, in *Metallides—Structure, Properties, Application* (Nauka, Moscow, 1971), p. 105.
39. S. A. Semiletov, Author's Abstracts of Doctoral Dissertation (Inst. Kristallografii Akad. Nauk SSSR, Moscow, 1969).
40. Z. G. Pinsker, Ching-Liang Chou, R. M. Imamov, and E. L. Lapidus, Kristallografiya **10** (1), 225 (1965) [Sov. Phys. Crystallogr. **10**, 225 (1965)].
41. B. B. Zvyagin, Z. V. Vrublevskaya, A. P. Zhukhlistov, O. V. Sidorenko, S. V. Soboleva, and A. F. Fedotov, *High-voltage Electron Diffraction in Studies of Layer Minerals* (Nauka, Moscow, 1979).
42. L. I. Man and R. M. Imamov, Kristallografiya **17** (4), 757 (1972) [Sov. Phys. Crystallogr. **17**, 663 (1972)].
43. B. B. Zvyagin, *Electron Diffraction Analysis of Clay Mineral Structures* (Nauka, Moscow, 1964; Plenum, New York, 1967).

44. S. A. Semiletov, Kristallografiya **1** (2), 306 (1956) [Sov. Phys. Crystallogr. **1**, 236 (1956)].
45. S. A. Semiletov, Kristallografiya **1** (5), 542 (1956) [Sov. Phys. Crystallogr. **1**, 430 (1956)].
46. R. V. Kudryavtseva, S. A. Semiletov, and G. I. Perevezentseva, Kristallografiya **12** (1), 109 (1967) [Sov. Phys. Crystallogr. **12**, 86 (1967)].
47. S. A. Semiletov and I. P. Voronina, Dokl. Akad. Nauk SSSR **152**, 1350 (1963) [Sov. Phys. Dokl. **8**, 960 (1963)].
48. S. A. Semiletov and I. P. Voronina, Kristallografiya **9** (4), 486 (1964) [Sov. Phys. Crystallogr. **9**, 405 (1964)].
49. E. V. Rakova and S. A. Semiletov, Kristallografiya **21** (1), 198 (1976) [Sov. Phys. Crystallogr. **21**, 103 (1976)].
50. S. A. Semiletov and P. S. Agalarzade, Kristallografiya **9** (4), 490 (1964) [Sov. Phys. Crystallogr. **9**, 409 (1964)].
51. V. A. Vlasov and S. A. Semiletov, Kristallografiya **12** (4), 734 (1967) [Sov. Phys. Crystallogr. **12**, 645 (1967)].
52. S. A. Aĭtkhozhin and S. A. Semiletov, Kristallografiya **10** (4), 492 (1965) [Sov. Phys. Crystallogr. **10**, 409 (1965)].
53. S. A. Semiletov and Z. A. Magomedov, Kristallografiya **12** (2), 376 (1967) [Sov. Phys. Crystallogr. **12**, 326 (1967)].
54. B. K. Vainshtein, A. N. Lobachev, and M. M. Stasova, Kristallografiya **3** (4), 452 (1958) [Sov. Phys. Crystallogr. **3**, 452 (1958)].
55. V. V. Udalova and Z. G. Pinsker, Kristallografiya **8** (4), 538 (1963) [Sov. Phys. Crystallogr. **8**, 433 (1963)].
56. A. V. Fedotov, A. P. Zhukhlistov, and B. B. Zvyagin, Izv. Akad. Nauk SSSR, Ser. Fiz. **47**, 188 (1983).
57. G. N. Tishchenko and Z. G. Pinsker, Dokl. Akad. Nauk SSSR **100**, 913 (1955).
58. D. L. Dorset, Acta Crystallogr., Sect. A: Cryst. Phys., Diffr., Theor. Gen. Crystallogr. **32**, 207 (1976).
59. B. Moss, D. L. Dorset, I. C. Wittmann, and B. Lotz, J. Polym. Sci. **22**, 1919 (1984).
60. D. L. Dorset, *Structural Electron Crystallography* (Plenum, New York, 1995).
61. L. N. Aleksandrov, É. A. Klimenko, and A. T. Klimenko, Kristallografiya **13** (6), 1098 (1968) [Sov. Phys. Crystallogr. **13**, 962 (1968)].
62. S. A. Semiletov, Kh. S. Bagdasarov, and V. S. Papkov, Fiz. Tverd. Tela (Leningrad) **10** (1), 71 (1968) [Sov. Phys. Solid State **10**, 51 (1968)].
63. M. A. Gurevich and L. A. Zhukova, Kristallografiya **13** (6), 1091 (1968) [Sov. Phys. Crystallogr. **13**, 953 (1968)].
64. L. A. Zhukova and M. A. Gurevich, *Electronography of Surface Layers and Films of Semiconducting Materials* (Metallurgiya, Moscow, 1971).
65. R. K. Karakhanyan, Kristallografiya **44** (3), 442 (1999) [Crystallogr. Rep. **44**, 402 (1999)].
66. R. K. Karakhanyan and P. L. Aleksanyan, Kristallografiya **44** (3), 438 (1999) [Crystallogr. Rep. **44**, 398 (1999)].
67. Z. G. Pinsker, Izv. Akad. Nauk SSSR, Ser. Fiz. **13**, 473 (1949).
68. I. I. Yamzin and Z. G. Pinsker, Dokl. Akad. Nauk SSSR **65**, 645 (1949).
69. Z. G. Pinsker, Acta Geol. Geogr. Univ. Comenianae Geol., No. 14, 125 (1968).
70. B. K. Vainshtein, *Modern Crystallography*, Vol. 1: *Symmetry of Crystals, Methods of Structural Crystallography*, Ed. by B. K. Vainshtein, A. A. Chernov, and L. A. Shuvalov (Nauka, Moscow, 1979; Springer-Verlag, Berlin, 1981).
71. H. Bethe, Aim. Phys. (Leipzig) **87**, 55 (1928).
72. *Fifty Years of Electron Diffraction*, Ed. by P. Goodman (Reidel, Dordrecht, 1981).
73. M. Blackan, Proc. R. Soc. London, Ser. A **73**, 68 (1939).
74. A. S. Avilov, V. S. Parmon, S. A. Semiletov, and M. I. Sirota, Kristallografiya **29** (1), 5 (1984) [Sov. Phys. Crystallogr. **29**, 1 (1984)].
75. B. K. Vainshtein, Kristallografiya **2** (2), 340 (1957) [Sov. Phys. Crystallogr. **2**, 341 (1957)].
76. B. K. Vainshtein and A. N. Lobachev, Kristallografiya **1** (4), 472 (1956) [Sov. Phys. Crystallogr. **1**, 467 (1956)].
77. V. V. Udalova and Z. G. Pinsker, Kristallografiya **17** (1), 90 (1972) [Sov. Phys. Crystallogr. **17**, 70 (1972)].
78. V. V. Udalova, Kristallografiya **20** (3), 640 (1975) [Sov. Phys. Crystallogr. **20**, 391 (1975)].
79. R. K. Karakhanyan, V. V. Udalova, R. M. Imamov, and Z. G. Pinsker, Kristallografiya **21** (5), 946 (1974) [Sov. Phys. Crystallogr. **21**, 587 (1974)].
80. J. M. Cowley, Prog. Mater. Sci. **13** (6), 267 (1967).
81. F. N. Chukhovskii and V. L. Vergasov, Acta Crystallogr., Sect. A: Found. Crystallogr. **46**, 153 (1990).
82. V. L. Vergasov and F. N. Chukhovskii, Phys. Lett. A **10**, 228 (1985).
83. V. L. Vergasov, F. N. Chukhovskiĭ, and Z. G. Pinsker, Dokl. Akad. Nauk SSSR **275**, 868 (1984).
84. V. L. Vergasov, Pis'ma Zh. Tekh. Fiz. **19**, 23 (1993) [Tech. Phys. Lett. **19**, 79 (1993)].
85. A. S. Avilov, R. M. Imamov, and Z. G. Pinsker, Izv. Akad. Nauk SSSR, Ser. Fiz. **44**, 178 (1980).
86. B. B. Zvyagin, A. P. Zhukhlistov, and V. P. Plotnikov, in *Structural Studies of Crystals*, Ed. by V. I. Simonov *et al.* (Nauka, Moscow, 1996), p. 225.
87. A. S. Avilov, Izv. Akad. Nauk SSSR, Ser. Fiz. **61**, 1934 (1997).
88. V. G. Tsirelson, A. S. Avilov, Yu. A. Abramov, *et al.*, Acta Crystallogr., Sect. B: Struct. Cryst. **B54**, 1 (1998).
89. A. S. Avilov, Z. Kitanekh, and V. G. Tsirelson, Kristallografiya **42** (4), 660 (1997) [Crystallogr. Rep. **42**, 603 (1997)].
90. A. S. Avilov, A. K. Kuligin, U. Pietsch, *et al.*, J. Appl. Crystallogr. **32**, 1033 (1999).
91. D. L. Dorset, in *Structural Studies of Crystals*, Ed. by V. I. Simonov *et al.* (Nauka, Moscow, 1996), p. 207.
92. D. L. Dorset, Acta Crystallogr., Sect. A: Found. Crystallogr. **47**, 510 (1991).
93. D. L. Dorset, Ultramicroscopy **38**, 23 (1991).
94. D. L. Dorset and H. A. Hauptman, Ultramicroscopy **1**, 195 (1976).
95. D. L. Dorset and F. Lemlin, Ultramicroscopy **33**, 227 (1990).
96. D. L. Dorset and W. T. Lhang, J. Electron Microsc. Tech. **18**, 142 (1991).

97. V. F. Dvoryankin, G. G. Dvoryankina, V. N. Kolomiĭchuk, and F. A. Brusentsev, Kristallografiya **9** (6), 730 (1964) [Sov. Phys. Crystallogr. **9**, 613 (1964)].
98. V. F. Dvoryankin and G. G. Dvoryankina, Zh. Strukt. Khim. **11** (5), 945 (1970).
99. V. I. Khitrova, Kristallografiya **11** (1), 204 (1966) [Sov. Phys. Crystallogr. **11**, 199 (1966)].
100. Yu. M. L'vov and L. A. Feĭgin, Kristallografiya **32** (3), 800 (1987) [Sov. Phys. Crystallogr. **32**, 473 (1987)].
101. B. K. Vainshtein and V. V. Klechkovskaya, Proc. R. Soc. London, Ser. A **442**, 73 (1993).
102. B. K. Vainshtein and V. V. Klechkovskaya, Kristallografiya **39** (2), 301 (1994) [Crystallogr. Rep. **39**, 256 (1994)].
103. B. K. Vainshtein, Diffraction of *X-rays by Chain Molecules* (Akad. Nauk SSSR, Moscow, 1963; Elsevier, Amsterdam, 1966).
104. R. Hosemann and S. N. Bagchi, *Direct Analysis of Diffraction by Matter* (North-Holland, Amsterdam, 1962).
105. B. K. Vainshtein and Z. G. Pinsker, Tr. Inst. Kristallogr. Akad. Nauk SSSR **10**, 14 (1954).
106. B. K. Vainshtein, Zh. Fiz. Khim. **29**, 3277 (1955).
107. B. K. Vainshtein, Tr. Inst. Kristallogr. Akad. Nauk SSSR **12**, 18 (1956).
108. A. S. Avilov, R. M. Imamov, R. K. Karakhanyan, and Z. G. Pinsker, Kristallografiya **18** (1), 49 (1973) [Sov. Phys. Crystallogr. **18**, 30 (1973)].
109. B. K. Vainshtein and M. M. Stasova, Kristallografiya **1** (2), 311 (1956) [Sov. Phys. Crystallogr. **1**, 241 (1956)].
110. I. A. D'yakon, Author's Abstract of Doctoral Dissertation (Inst. Kristallografii Akad. Nauk SSSR, Moscow, 1989).
111. G. I. Ivakin and V. V. Klechkovskaya, Izv. Akad. Nauk, Ser. Fiz. **57** (2), 30 (1993).
112. V. V. Klechkovskaya, M. Anderle, R. Antolini, *et al.*, Thin Solid Films **284/285**, 208 (1996).
113. L. L. Orekhova, L. I. Barsukov, S. V. Orekhov, and V. V. Klechkovskaya, Phys. Low-Dimens. Struct. **4/5**, 117 (1994).
114. Yu. G. Baklagina, V. P. Sklizkova, V. V. Kudryavtsev, *et al.*, Vysokomol. Soedin. **37** (8), 1361 (1995).
115. A. A. Voronova and B. K. Vainshtein, Kristallografiya **9** (1), 197 (1964) [Sov. Phys. Crystallogr. **9**, 154 (1964)].
116. A. A. Voronova and B. K. Vainshtein, Kristallografiya **3** (1), 444 (1958) [Sov. Phys. Crystallogr. **3**, 445 (1958)].
117. F. Aebi, Helv. Chim. Acta **31**, 369 (1948).
118. V. A. Drits, *Electron Diffraction and High-Resolution Electron Microscopy of Mineral Structures* (Springer-Verlag, Berlin, 1987).
119. B. B. Zvyagin, A. P. Zhukhlistov, M. G. Kyazumov, and A. M. Fominenkov, Kristallografiya **35** (3), 702 (1990) [Sov. Phys. Crystallogr. **35**, 351 (1990)].
120. B. B. Zvyagin and M. G. Kyazumov, Izv. Akad. Nauk SSSR, Ser. Fiz. **52**, 22 (1993).
121. B. B. Zvyagin, Kristallografiya **39** (2), 283 (1994) [Crystallogr. Rep. **39**, 239 (1994)].
122. A. P. Zhukhlistov and B. B. Zvyagin, Kristallografiya **43** (6), 1009 (1998) [Crystallogr. Rep. **43**, 950 (1998)].
123. Yu. P. Khodyrev, R. V. Baranova, and S. A. Semiletov, Kristallografiya **21** (6), 1245 (1976) [Sov. Phys. Crystallogr. **21**, 723 (1976)].
124. Yu. P. Khodyrev, R. V. Baranova, R. M. Imamov, and S. A. Semiletov, Kristallografiya **23** (4), 723 (1978) [Sov. Phys. Crystallogr. **23**, 405 (1978)].
125. R. V. Baranova, Yu. P. Khodyrev, R. M. Imamov, and S. A. Semiletov, Kristallografiya **25** (6), 1290 (1980) [Sov. Phys. Crystallogr. **25**, 736 (1980)].
126. S. A. Semiletov, R. V. Baranova, Yu. P. Khodyrev, and R. M. Imamov, Kristallografiya **25** (6), 1162 (1980) [Sov. Phys. Crystallogr. **25**, 665 (1980)].
127. Yu. P. Khodyrev and R. V. Baranova, Kristallografiya **25** (1), 172 (1980) [Sov. Phys. Crystallogr. **25**, 99 (1980)].
128. T. Leciejewicz, Acta Crystallogr. **14**, 200 (1961).
129. N. V. Troitskaya, Kristallografiya **10** (2), 284 (1965) [Sov. Phys. Crystallogr. **10**, 232 (1965)].
130. N. V. Troitskaya and Z. G. Pinsker, Kristallografiya **8** (4), 548 (1963) [Sov. Phys. Crystallogr. **8**, 441 (1963)].
131. V. I. Khitrova, V. V. Klechkovskaya, and Z. G. Pinsker, Kristallografiya **12** (6), 1044 (1967) [Sov. Phys. Crystallogr. **12**, 907 (1967)].
132. V. I. Khitrova and V. V. Klechkovskaya, in *Intermetallic Compounds: Structure, Properties, Applications* (Nauka, Moscow, 1971), p. 98.
133. V. I. Khitrova and V. V. Klechkovskaya, Kristallografiya **25** (6), 1169 (1980) [Sov. Phys. Crystallogr. **25**, 669 (1980)].
134. V. I. Khitrova, V. V. Klechkovskaya, and Z. G. Pinsker, Kristallografiya **17** (3), 506 (1972) [Sov. Phys. Crystallogr. **17**, 442 (1972)].
135. V. I. Khitrova, V. V. Klechkovskaya, and Z. G. Pinsker, Kristallografiya **24** (6), 939 (1979) [Sov. Phys. Crystallogr. **24**, 537 (1979)].
136. V. V. Klechkovskaya, V. I. Khitrova, and Z. G. Pinsker, Kristallografiya **24** (6), 1254 (1979) [Sov. Phys. Crystallogr. **24**, 716 (1979)].
137. V. V. Klechkovskaya, Kristallografiya **15** (2), 35 (1970) [Sov. Phys. Crystallogr. **15**, 299 (1970)].
138. V. I. Khitrova, V. V. Klechkovskaya, and Z. G. Pinsker, Kristallografiya **21** (5), 937 (1976) [Sov. Phys. Crystallogr. **21**, 535 (1976)].
139. V. I. Khitrova and V. V. Klechkovskaya, Kristallografiya **27** (4), 736 (1982) [Sov. Phys. Crystallogr. **27**, 441 (1982)].
140. V. I. Khitrova and V. V. Klechkovskaya, Kristallografiya **30** (1), 126 (1985) [Sov. Phys. Crystallogr. **30**, 70 (1985)].
141. V. V. Udalova and V. V. Klechkovskaya, *Crystallography and Crystal Chemistry* (Nauka, Moscow, 1986), p. 224.
142. A. L. Tolstikhina, V. V. Klechkovskaya, and V. N. Petrov, Kristallografiya **40** (4), 751 (1995) [Crystallogr. Rep. **40**, 695 (1995)].
143. A. A. Zav'yalova and R. M. Imamov, in *Metallides—Structure, Properties, Application* (Nauka, Moscow, 1971), p. 105.
144. A. A. Zav'yalova and R. M. Imamov, Koord. Khim. **1**, 1415 (1975).
145. G. Hapase, V. B. Tare, and A. B. Biswas, Acta Metall. **15**, 365 (1967).

146. S. A. Semiletov, Tr. Inst. Kristallogr. Akad. Nauk SSSR **11**, 121 (1955).

147. S. A. Semiletov, Kristallografiya **1** (2), 306 (1956) [Sov. Phys. Crystallogr. **1**, 236 (1956)].

148. Z. G. Pinsker, Chou Tsin Lyan, R. M. Imamov, and E. L. Lapidus, Kristallografiya **10** (1), 225 (1965) [Sov. Phys. Crystallogr. (1) (1965)].

149. B. K. Vainshtein, R. M. Imamov, and A. G. Talybov, Kristallografiya **14** (4), 703 (1969) [Sov. Phys. Crystallogr. **14**, 597 (1970)].

150. R. V. Baranova and Z. G. Pinsker, Zh. Strukt. Khim. **11**, 690 (1970).

151. L. I. Man, R. M. Imamov, and S. A. Semiletov, Kristallografiya **16** (1), 122 (1971) [Sov. Phys. Crystallogr. **16**, 94 (1971)].

152. J. H. C. Hog, H. H. Suterland, and D. G. Williams, Acta Crystallogr., Sect. B: Struct. Crystallogr. Cryst. Chem. **B29**, 1530 (1973).

153. L. I. Man, R. K. Karakhanyan, and R. M. Imamov, Kristallografiya **19** (6), 1166 (1974) [Sov. Phys. Crystallogr. **19**, 725 (1974)].

154. E. Cruclame and St. Sladoru, J. Mater. Sci. **4**, 4102 (1969).

155. L. I. Man, R. M. Imamov, and S. A. Semiletov, Krystallografiya **21** (3), 628 (1976) [Sov. Phys. Crystallogr. **21**, 355 (1976)].

156. L. I. Man, Kristallografiya **15** (3), 471 (1970) [Sov. Phys. Crystallogr. **15**, 399 (1970)].

157. Z. G. Pinsker and R. M. Imamov, Indian J. Pure Appl. Phys. **19**, 926 (1981).

158. R. M. Imamov, S. A. Semiletov, and Z. G. Pinsker, Kristallografiya **15** (2), 287 (1970) [Sov. Phys. Crystallogr. **15**, 239 (1970)].

159. Z. G. Pinsker, R. M. Imamov, and L. I. Man, Thin Solid Films **32**, 287 (1976).

160. Z. G. Pinsker, B. B. Zvyagin, and R. M. Imamov, Kristallografiya **26** (6), 1181 (1981) [Sov. Phys. Crystallogr. **26**, 669 (1981)].

161. R. M. Imamov and Z. G. Pinsker, Kristallografiya **10** (1), 199 (1965) [Sov. Phys. Crystallogr. **10**, 148 (1965)].

162. P. S. Turner and J. M. Cowley, Acta Crystallogr., Sect. A: Cryst. Phys., Diffr., Theor. Gen. Crystallogr. **25**, 475 (1969).

163. L. I. Tatarinova, *Electronography of Amorphous Substances* (Nauka, Moscow, 1972).

Translated by L. Man

Crystallography Reports, Vol. 46, No. 4, 2001, pp. 550–555. Translated from Kristallografiya, Vol. 46, No. 4, 2001, pp. 614–619.

DIFFRACTION AND SCATTERING OF ELECTRONS

Dedicated to the memory of B.K. Vainshtein

From Electron Diffraction by Clays to Modular Crystallography

B. B. Zvyagin

Institute of Geology of Ore Deposits, Petrography, Mineralogy, and Geochemistry, Russian Academy of Sciences, Staromonetnyĭ per. 35, Moscow, 109017 Russia

e-mail: zvyagin@gename.eimb.relarn.ru

Received on February 16, 2001

Abstract—Being an independent method of structure analysis, electron diffraction provides original data which are essential contributions to all the fields where this method is used. An important place of electron diffraction among other structural methods is illustrated by the results of the studies once started on clay minerals and continued on the objects extremely important for structural mineralogy, which stimulated the development of a new field—modular crystallography. *© 2001 MAIK "Nauka/Interperiodica".*

INTRODUCTION

The advent of electron diffraction as an independent method of structure analysis should be attributed to 1946, when Z.G. Pinsker gathered a team of colleagues and students from different institutions of the former USSR and organized the Electron Diffraction laboratory at the Institute of Crystallography. The atmosphere of mutual contacts and exchange of opinions allowed this team to overcome difficulties and solve the problems they encountered. The undoubtful leader of this team was B.K. Vainshtein, then a postgraduate student of the Institute of Crystallography. A postgraduate student of the Institute of Soils of the USSR Academy of Sciences, I had to master electron diffraction in application to clay minerals. Even at that time, I enjoyed the beneficial influence of the friendly relations with Vainshtein to full extent. This friendship helped me to maintain high spirit, resoluteness, and enthusiasm at the crucial moments of my life, when it seemed that montmorillonite, a structurally imperfect clay mineral, is an absolutely hopeless object for electron diffraction study.

However, fate decided to help me and provided me with specimens "saturated" with various exchange cations. This gave me a new impetus for further work. It was established that the K- and Ba-cations located between the montmorillonite layers promote layer ordering, which, in turn, gives rise to the formation of general-type reflections located on the ellipses of the oblique-texture electron diffraction patterns from montmorillonite [1]. Figure 1 shows this diffraction pattern, which is also very interesting from the historical standpoint, since it was obtained in the horizontal electron diffraction camera designed by Pinsker and is well known as a chamber with the longest specimen–screen distance (1100 mm). Two lines on the pattern are the primary-beam traces caused by a horseshoe magnet brought to the camera casing during the exposure to the electron beam. Another remarkable feature of this pattern is the fact that, as was established 37 years later, the intensity distribution indicates the coexistence of the vacant dioctahedral *trans*- and *cis*-layers in the 2 : 1 proportion [2]. Anyhow, this diffraction pattern was the starting point for the geometric analysis of oblique-texture electron diffraction patterns, the direct determination of the unit-cell parameters, and the indexing of reflections. The scheme of indexing made by Vainshtein himself is shown in Fig. 2 (at that time, he helped me to illustrate my Candidate dissertation).

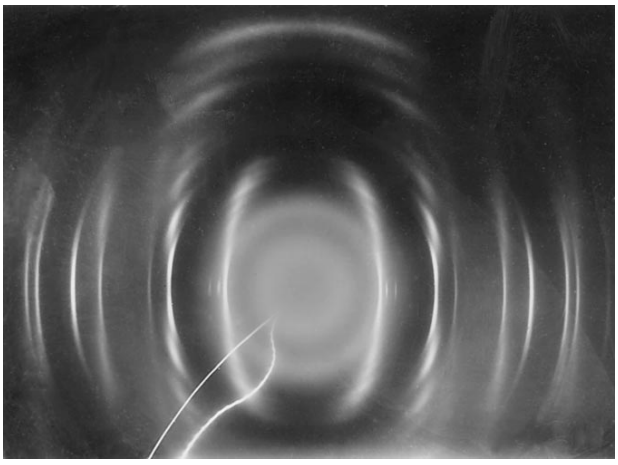

Fig. 1. Oblique-texture pattern from clay mineral montmorillonite obtained in an electron diffraction camera designed by Pinsker in 1947.

1063-7745/01/4604-0550$21.00 © 2001 MAIK "Nauka/Interperiodica"

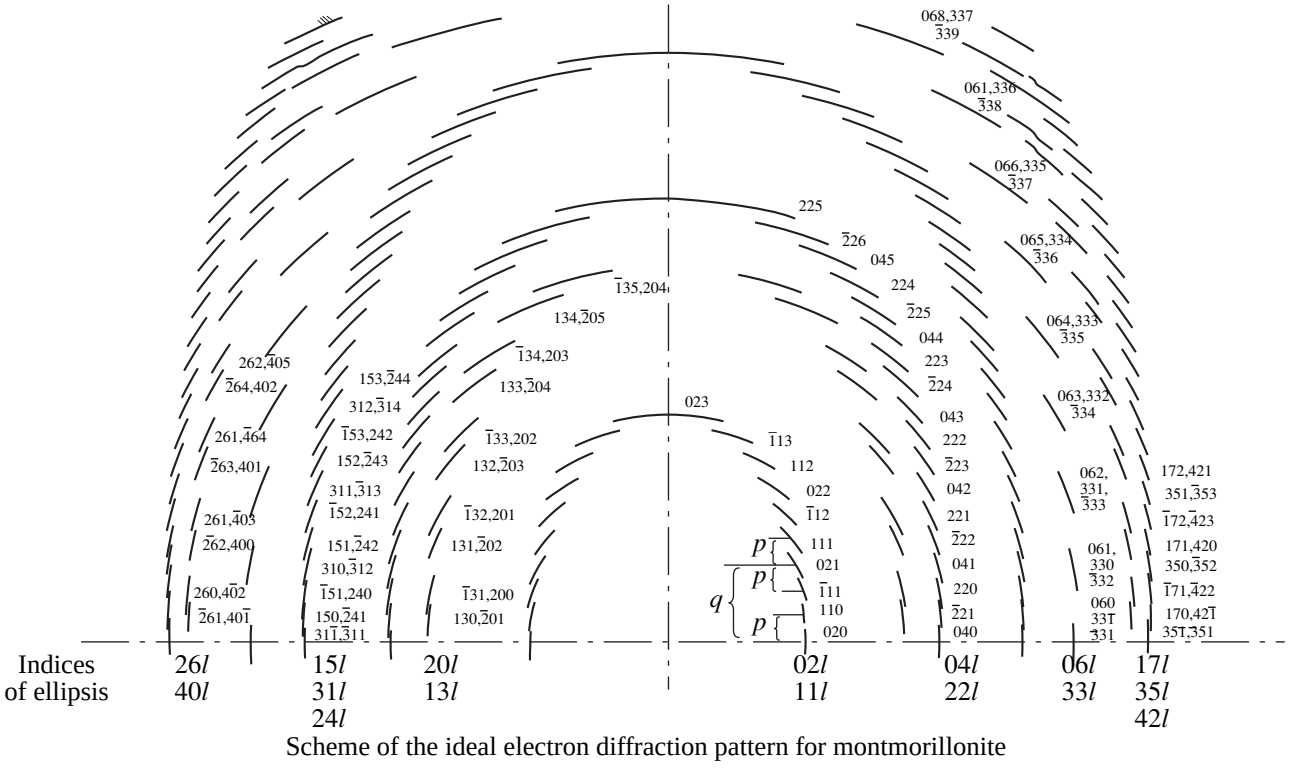

Scheme of the ideal electron diffraction pattern for montmorillonite

Fig. 2. Scheme of indexing of the oblique-texture electron diffraction pattern shown in Fig. 1 made by Vainshtein.

In the following years, Vainshtein stimulated and supported such studies. Indirect evidence of this is his joking verses written on the reprints of his articles given to me in those years: “The point is in the unit cells, but don’t forget to solve the structures,” “Don’t be afraid of the results, just analyze the structures,” “The cells were given to us from heaven, but do they substitute our luck?,” and on the reprint of the article on the remarkable electron diffraction determination of the paraffin structure: “Let paraffin be very useful to the researcher of the clays.” Even more weighty evidence of this cooperation are our joint publications—on the unique reflection of the space symmetry of crystal structures in the relationships taking into account the structure-factor phases in the reciprocal lattice [3], the fundamentals of electron diffraction structure analysis for the International Tables [4], and the article published in the two-volume edition of the International Union of Crystallography [5] on the occasion of the 50th anniversary of the discovery of electron diffraction. Giving due to the role of the electron diffraction method in the study not only of clay minerals but also of many other materials, I should like to emphasize here that Vainshtein also considerably influenced many other scientific fields.

BASIC ACHIEVEMENTS IN ELECTRON DIFFRACTION STUDY OF MINERALS

The main factors determining the efficiency of electron diffraction for studying minerals are the strong interaction of electrons with the matter, the small wavelength of high-energy electrons, and the possibility of creation of optical systems determining electron paths in various types of electron diffraction [4–8]. These features allow the study of very small amounts of materials with the exposures not exceeding several seconds. Electron diffraction patterns can be interpreted as two-dimensional sections of the reciprocal lattice. The oblique-texture electron diffraction patterns provide the most complete and detailed structural information on fine crystalline materials and can be used for efficient visual diagnostics, analysis of polytypism, and the complete structural determination of various minerals [9–12]. The complex studies combining electron-microscopy imaging and the analysis of selected-area diffraction patterns of specimens are also of great importance and allow the study of specimen heterogeneity, structural inhomogeneities in crystals, the variations in the periodicity and superperiodicity, and sometimes the refinement of crystal structures [13, 14]. Considerable progress was attained in the accuracy and reliability of the structural results due to use of electron diffractometry based on direct electrometric measurements of the reflection intensities [16–20].

Below, we illustrate the above by the results important for structural mineralogy which were obtained by the electron diffraction method. These are the first refinements of the crystal structures of highly dispersed layer silicates (phyllosilicates)—clay minerals seladonite and kaolinite [9]. The establishment of the layer

alternation in nacrite was accompanied by the theoretical derivation of all the possible polytypes formed by kaolin layers. The refinement of the structure of this clay mineral showed the anomalously small angle of the ditrigonal rotation of tetrahedra, which indicated the specific combination of interatomic forces acting onto the oxygen atoms [9, 10]. The oblique-texture electron diffraction patterns of chapmanite and bismutoferrite show that they cannot belong to orthosilicates. The analysis of these minerals provided the structural determination of the unique analogues of the kaolin polytype 1*M* in which the positions of Al-octahedra in the layers are occupied by Fe atoms and the layers are bonded to Sb or Bi atoms [10]. The oblique-texture electron diffraction patterns also provided the establishment of Fe-analogues of pyrophyllite, ferripyrophyllite 2*M*, and the related hydrated and mixed-layer phases [10].

The study of the oblique-texture electron diffraction patterns allowed the establishment of the facts which affected the nomenclature of the layer structures and provided better understanding of some fundamental concepts of crystal chemistry such as polymorphism and polytypism. Among these facts is the existence of axially symmetric dioctahedral mica layers in addition to the well-known centrosymmetric layers with vacant *trans*- or *cis*-octahedra [2, 21, 22]. Such structures with different constituent layers can be considered as individual polymorphs. The refinement of the muscovite $2M_2$ structure [10] showed that the adjacent layers with opposite parity of their azimuthal orientations are packed differently from their packing with the same parity of these orientations. The interlayer cations are located not in the octahedral (O) but in the trigonal–prismatic (P) coordination. Strictly speaking, similar structures built by equivalent main layers but different interlayers (O or P) are not individual polytypes and should be considered as pseudopolytypes.

The important advantage of oblique-texture electron diffraction patterns is that their qualitative characteristics allow one to draw important conclusions about the structure. This is especially important for layer structures, where the characteristics of the atomic arrangement in the layers and the mutual arrangement of the layers themselves can be obtained from the detailed analysis of these patterns. The data on the layer characteristics, the period of their alternation, and the lattice formed can often be obtained even without any detailed analysis of the pattern geometry and reflection intensities on such diffraction patterns. These data provide rather easy diagnostics of minerals and their polytypes. In some occasions, the interpretation of various oblique-texture electron diffraction patterns allowed the establishment of new polytypes [10, 23].

The considerable contribution to structural mineralogy came from selected-area diffraction studies in an electron microscope. This method provided the precision establishment of structural details in various serpentines represented by lizardites, antigorites with different superperiods ($A = na$), chrysotiles, *ortho*-, *clino*-, and *para*-forms with different cylindrical lattices of tubular crystals [9, 13]. The combined study of the oblique-texture and selected-area diffraction patterns allowed the establishment of a new independent kaolin polytype 2*M*—halloysite [10, 13]. The pairs of adjacent layers of this polytype and kaolinite 1TC are symmetry-equivalent. Thus, halloysite and kaolinite are classical example of polytypes which are simultaneously OD structures, contrary to dickite and kaolinite, which are not. The examples of the successful analysis of the diffraction intensities on selected-area diffraction patterns used for the complete structure determination of various minerals can be found in [14]. Thus, not only was a new type of the band silicates with the pyroxene chains condensed in the rods discovered, but the atomic positions with the aid of the Fourier syntheses were determined. The original structural data were also obtained for a number of minerals in which the layers of different (oxide and sulfide) chemical nature are capriciously combined. These studies confirmed the fundamental crystallochemical concept of hybrid minerals.

The development of the electron diffractometry marks a new stage in the structure analysis of minerals and allows one to complement the data on the lattice and the atomic arrangement with the data on the potential-field distribution characterizing the state and bonding of various atoms including the lightest hydrogen ones. In particular, electron diffractometry yielded more detailed data on muscovite, phengite, and seladonite [14–16], and revealed the differences between the internal and external hydroxyls of the layers in lizardite [19]. A fine effect of splitting of the atomic positions occupied by hydrogen in the vicinity of the three- and twofold symmetry axes was recorded in the brucite and lepidocrocite structures [18, 20].

CONCLUSIONS DRAWN FROM THE ANALYSIS OF ELECTRON DIFFRACTION DATA FOR MINERALS

As an independent method of the structure analysis based on the specific physical phenomenon, electron diffraction yields results which, being original and reflecting the characteristic features of the material associated with the distribution of the electrostatic potential, can confirm, refine, and complement the already known information. These data stimulate the development of new approaches, interpretations, and generalizations in structural mineralogy.

This concerns, first of all, the theory and practice of mineral polytypism. The identification of each new polytype stimulated the theoretical derivation of other polytypes that can be formed by the given layers with due regard for the rules of their mutual arrangement and calculation of their diffraction characteristics. Thus, new polytypes were predicted for a great variety of layer structures [9, 10, 24].

Solving the concrete problems of polytypism, we developed a simple practical method for the description and analysis of their structures—the use of the symbols of the layers and their constituent parts, their orientations and positions, and the symmetry operations. The layer sequences represented by the sequences of their symbols reveal the periodicity, symmetry, and independence or equivalence of the structures described in different settings in accordance with the rules of symbol transformations under the action of the symmetry operations characteristic of the structures [10, 25].

The experience gained in the electron diffraction studies of polytypism in minerals promoted the further development of the concepts of crystal structures which, first, were called fragmentary but, later, were interpreted more soundly as modular structures. The point is that these structures are built by several standard modules, which, in distinction from fragments, also perform some constructive function. In the general case, such modules can be infinite (in one or two dimensions) or have finite structures—layers, rods, and blocks; however, the layer structures are still the most typical and important. The possible classification of modular structures in which the layer structures occupy the central place was suggested in [26]. This classification also takes into account the particular manifestations of modularity associated with the fundamental concepts of crystal chemistry—polysomatism [27], mixed layered structures [28], hybrid layer structures [29], polytypism [30], and OD structures [31].

The above concepts were developed in the process of analyzing layer structures, although, using the analogy, they should be extended to the structures consisting of rods or blocks. At the same time, as is seen from an example of layer structures, the whole variety of modular structures will not fit into the rigid framework of the above concepts. The nomenclature status of modular structures is dependent on the choice of the building units often dictated by the author's taste and biases (clear description, manifestation of the symmetry, lattice or diffraction characteristics). The freedom of choice is also characteristic of the structures in which the layers with fixed structures are singled out in accordance with the strengths of interatomic bonds.

Operating solely with certain parts of such layers (halves of the layers, sheets of polythedra, and even atomic planes), one can derive numerous structures in which some atomic groups would have properties not inherent in the structure as a whole, but the difference between the individual groups would be lost in the consideration of the structure variety. Thus, the symmetry of cationic planes allows one to complement them with the anionic planes with the simultaneous formation of octahedral and prismatic sheets of polyhedra, but such sheets should be considered as independent types of structures. The tetrahedral sheets (T) can be equivalently adjacent to the intermediate octahedral sheet (O) with the octahedron occupancy 2/3 and the formation of TOT, centrosymmetric (CS), or axially symmetric (AS) layers with vacant *trans*- or *cis*-octahedra. These layers form individual structures of phyllosilicates.

For pure layer structures, the concept of polytypism can be somewhat simplified if one uses the equivalent layers and interlayers alternating in the same sequence (if there are several different kinds of the layers) in various structures formed with the aid of various symmetry operations not affecting their common lattice basis **ab**. This concept depends on the choice of the structure-forming layers, which can be illustrated by an example of phyllosilicates with TOT layers—micas, pyrophyllites, and chlorites (for simplicity, we assume that the bases of octahedra and the adjacent tetrahedra have the opposite orientations).

Depending on TOT layers, the whole variety of structures can be divided into two parts—the structures consisting of CS and AS layers. The differences between the layers can be considered as indicators of different polymorphs. Each polymorph has the structures with O or P interlayers. Only the structures with the equivalent layers and interlayers can be considered as polytypes, whereas the structures having different interlayers are intermediate between polytypes and polymorphs and, therefore, can be considered as pseudopolytypes.

Considering the individual T sheets oriented by their vertices along two opposite polar directions and the O sheets as independent structural units, we can consider the whole variety of structures as the variety of polytypes formed by layers of two kinds with TT interlayers being either of type O or type P obtained according to different rules of formation of adjacent T sheets. The existence of different variants of the sheets should be specified and motivated; otherwise, the manifestations of the structure polymorphism would not be seen and would be lost.

Unlike polytypism, the concept of OD structures should satisfy the additional conditions of the symmetry equivalence for the pairs of adjacent layers of the given type [31]. In fact, at the arbitrary choice of layers, such structures are singled out from the total set of polytypes and should be distinguished from one another. At the same time, there is a tendency to interpret all the polytypes as OD structures by choosing layers somewhat differently, which is usually accompanied by an increase of the number of layer kinds. Thus, instead of one TO layer in kaolins (whose fixed structure determines its mineralogical independence), layers of three kinds were used, including the plane of octahedral cations (which was "forced" to have the reduced symmetry) and the plane of hydroxyl OH groups [32]. For micas, the OD interpretation is based on two kinds of the layers—O*c* and T*et*—corresponding to the O sheet and the combination of two T sheets bordering the interlayer space (between two neighboring layers). The ideal hexagonal geometry assumed for T sheets excluded the possibility of existence of the O and P

interlayers (it was specified later as an additional effect of ditrigonalization of T sheets). In practice, it was necessary to consider polar packets formed by halves of these layers called *p* and *q* packets [33]. This identification of polytypes with OD structures is far from being convincing. The role of the chosen structural units and, especially, of individual atomic layers is rather dubious because they cannot form the whole variety of crystal structures. The same structural parts, but in other combinations, can also enter some other compounds. If the atomic interactions inside these parts and between them are of the same order of magnitude, then the mutual arrangement of these parts is not necessarily. Also, the success of such demonstration depends on the inventiveness and the skill of the authors and is still not guaranteed in all cases. Most importantly, any OD interpretation should not ignore the possible existence of layers with the fixed structure not possessing the OD properties. These layers with the fixed arrangement can form independent groups of structures that can be qualified as polymorphs, pseudopolytypes, polytypes, and in some particular cases as OD structures. The differences between these groups are objective and should not be ignored in order to avoid any distorted understanding of the real relationships between different crystal structures.

Polytypes cannot also be identified with OD structures because there exist OD structures which are not polytypes. If one can single out the regularly alternating layers of more than one kind in a framework structure, then the symmetry of individual layers allows the equivalent attachment of new layers on both sides of the already existing layers, which results in different associates of structural polyhedra providing the distinction of true polymorphs from one another. Meanwhile, the pairs of adjacent symmetrically equivalent layers also characterize polymorphs as OD structures. This is seen from the alternation of the *S* and *P* layer modules, cut out normally to the layers of close packing in the spinel and pyroxene structures, respectively [34]. If the *P* modules are related by the symmetry plane of the *S* modules, the Si-tetrahedra are incorporated into two-dimensional sheets of single tetrahedra. If the reflection operation is accompanied by the translation *a* of the module *S* equal to a half-translation of the module *P*, we arrive at the sapphirine structures with the branching chains of Si-tetrahedra [34]. Because of the possible variations of translations along the *c*-axis of *S* modules allowed by the symmetry of the *P* modules, each polymorph can have a polytype–OD variety. The dramatic differences between two OD sets of the structures with the equivalent pairs of *SP* (*PS*) modules but with different associates of Si-tetrahedra do not allows their identification with polytypes.

Striving to solve concrete problems by the simplest available methods gave rise to the formulation of the principles of the modular analysis of crystal structures [35], which includes the interpretation of the modular structures and the modular description of crystalline substances, and the establishment of the relations between the compounds with common modular characteristics. The analytical methods of structure description and the operations with these structures are of great importance because, similar to polytypes, they provide the establishment either of the independence or the equivalence of the structures described in different settings. These methods also help in determining the lattice, symmetry, and diffraction characteristics and provide the theoretical derivation (prediction) of homogeneous structures.

One of the most important elements of the modular analysis of crystal structures is the symmetry approach consistently developed in the OD theory created by Dornberger–Schiff [31]. The OD theory is based on the sound idea that the symmetry equivalence of the positions and the neighboring structure elements (layers) indicates their energy equivalence. Due to the fact that the energy equivalence is difficult to understand, it is usually ignored. In this case, it is taken into account that the interaction of the nearest parts of the structure prevails over the interaction of its more distant parts (see Appendix in [32]). The OD theory has a number of concepts and relationships which can be extended directly or indirectly (upon certain transformations) to a larger variety of modular crystal structures.

The efficiency of the modular analysis of crystal structures is demonstrated by the examples of modular series and systems in which various structures differ by layer constituent module alternation [35].

REFERENCES

1. B. B. Zvyagin and Z. G. Pinsker, Dokl. Akad. Nauk SSSR **68** (1), 65 (1949).
2. S. I. Tsipurskiĭ and V. A. Drits, Mineral. Zh. **6** (1), 9 (1984).
3. B. K. Vainshtein and B. B. Zvyagin, Kristallografiya **8** (2), 147 (1962) [Sov. Phys. Crystallogr. **8**, 107 (1962)].
4. B. K. Vainshtein and B. B. Zvyagin, in *International Tables for Crystallography*, Ed. by U. Shmueli (Kluwer, Dordrecht, 1993), Vol. B, p. 310.
5. B. K. Vainshtein, B. B. Zvyagin, and A. S. Avilov, *Electron Diffraction Techniques* (Oxford Univ. Press, Oxford, 1992), Vol. 1, Chap. 6, p. 216.
6. Z. G. Pinsker, *Electron Diffraction* (Akad. Nauk SSSR, Moscow, 1949; Butterworth, London, 1953).
7. B. K. Vainshtein, *Structure Analysis by Electron Diffraction* (Akad. Nauk SSSR, Moscow, 1956).
8. B. B. Zvyagin, Izv. Akad. Nauk, Ser. Fiz. **57** (2), 2 (1993).
9. B. B. Zvyagin, *Electron Diffraction Analysis of Clay Mineral Structures* (Nauka, Moscow, 1964; Plenum, New York, 1967).
10. B. B. Zvyagin, Z. V. Vrublevskaya, A. P. Zhukhlistov, *et al.*, *High-voltage Electron Diffraction in Study of Layer Minerals* (Nauka, Moscow, 1979).
11. B. B. Zvyagin, MSA Bull. **23** (1), 66 (1993).

12. B. B. Zvyagin, Kristallografiya **39** (2), 283 (1994) [Crystallogr. Rep. **39**, 239 (1994)].
13. G. S. Gritsaenko, B. B. Zvyagin, A. I. Gorshkov, *et al.*, *Methods of Electron Microscopy of Minerals* (Nauka, Moscow, 1969).
14. V. A. Drits, *Electron Diffraction and High-Resolution Electron Microscopy of Mineral Structures* (Nauka, Moscow, 1981; Springer-Verlag, Berlin, 1987).
15. S. I. Tsipurskiĭ and V. A. Drits, Izv. Akad. Nauk SSSR, Fiz. Zemli **41** (11), 2263 (1977).
16. S. I. Tsipurskiĭ and V. A. Drits, Mineral. Zh. **8** (3), 32 (1986).
17. B. B. Zvyagin, A. P. Zhukhlistov, and V. P. Plotnikov, *Structural Studies of Crystals* (Nauka, Moscow, 1996), p. 225.
18. A. P. Zhukhlistov, A. S. Avilov, D. Ferraris, *et al.*, Kristallografiya **42** (5), 841 (1997) [Crystallogr. Rep. **42**, 774 (1997)].
19. A. P. Zhukhlistov and B. B. Zvyagin, Kristallografiya **43** (6), 1009 (1998) [Crystallogr. Rep. **43**, 950 (1998)].
20. A. P. Zhukhlistov, Kristallografiya **46** (2001) (in press) [Crystallogr. Rep. **46** (2001) (in press)].
21. B. B. Zvyagin, V. T. Rabotnov, *et al.*, Izv. Akad. Nauk SSSR, Ser. Geol., No. 5, 121 (1985).
22. A. P. Zhukhlistov and B. B. Zvyagin, in *Proceedings of the 7th EOROCLAY Conference, Dresden, 1991*, p. 1211.
23. A. P. Zhukhlistov, B. B. Zvyagin, and T. I. Getmanskaya, Kristallografiya **46** (2001) (in press) [Crystallogr. Rep. **46** (2001) (in press)].
24. B. B. Zvyagin, Comput. Math. Appl. **16** (5–8), 569 (1988).
25. B. B. Zvyagin, *Symmetry: Culture and Science* (Washington, 1995), The Quarterly of the ISIS-Symmetry, Vol. 6, No. 3, p. 560.
26. B. B. Zvyagin, Kristallografiya **38** (1), 104 (1993) [Crystallogr. Rep. **38**, 54 (1993)].
27. J. B. Thompson, Am. Mineral. **63** (3–4), 239 (1978).
28. V. A. Drits and B. A. Sakharov, *X-ray Structure Analysis of Mixed-Layer Minerals* (Nauka, Moscow, 1976).
29. H. T. Evans, J. Allman, and R. Allman, Z. Kristallogr. **127** (1/4), 73 (1968).
30. A. R. Verma and P. Krishna, *Polymorphism and Polytypism in Crystals* (Wiley, New York, 1966; Mir, Moscow, 1969).
31. K. Dornberger-Schiff, *Gründzüge einer Theorie der OD-Strukturen aus Schichten* (Akademie-Verlag, Berlin, 1964).
32. K. Dornberger-Schiff and S. Durovic, Clays Clay Miner. **23**, 219 (1975).
33. K. Dornberger-Schiff, K.-O. Backhaus, and S. Durovic, Clays Clay Miner. **30**, 364 (1982).
34. S. Merlino and B. B. Zvyagin, Z. Kristallogr. (in press).
35. B. B. Zvyagin, *EMU Notes in Mineralogy* (Eótvós Univ. Press, Budapest, 1997), Vol. 1, Chap. 5, p. 345.

Translated by L. Man

Crystallography Reports, Vol. 46, No. 4, 2001, pp. 556–571. Translated from Kristallografiya, Vol. 46, No. 4, 2001, pp. 620–635.

DIFFRACTION AND SCATTERING OF ELECTRONS

Dedicated to the memory of B.K. Vainshtein

Precision Electron Diffraction Structure Analysis and Its Use in Physics and Chemistry of Solids

A. S. Avilov* and V. G. Tsirelson**

** Shubnikov Institute of Crystallography, Russian Academy of Sciences, Leninskiĭ pr. 59, Moscow, 117333 Russia*

e-mail: avilov@ns.crys.ras.ru

*** Department of Quantum Chemistry, Mendeleev University of Chemical Technology, Moscow, 125047 Russia*

e-mail: tsirel@muctr.edu.ru

Received February 22, 2001

Abstract—The present level of the precision electron diffraction provides the quantitative analysis of the electrostatic potential and electron density in crystals and allows us to approach the direct study of properties of solids by electron diffraction. This is demonstrated by examples of ionic compounds with an NaCl structure and a covalent Ge crystal. Using the analytical structure models of crystals, one can quantitatively characterize chemical bonding and study topological characteristics of the electrostatic potential by electron diffraction data. It is established that the internal crystal field is well structurized, whereas the topological analysis revealed some important characteristics of its structure. These data considerably enrich our knowledge on atomic interactions in crystals. © *2001 MAIK "Nauka/Interperiodica".*

INTRODUCTION

The fundamentals of the electron diffraction structure analysis of crystals based on the data of high-energy electron diffraction were formulated in Vainstein's book *Structure Analysis by Electron Diffraction* [1]. More than forty years has passed since the publication of this book, which has played the key role in the development of electron diffraction structure analysis (EDSA) as an independent physical method of studying the atomic structure of the matter. Thousands of structures of crystalline and amorphous materials and organic and inorganic compounds have been studied since then. An important role in these studies has been played by the scientists working at the Electron Diffraction Laboratory of the Institute of Crystallography founded by the late Professor Pinsker [2]. The structure determinations based on the electron diffraction data of a number of semiconductors [3–5], minerals [6, 7], organometallic and organic compounds [8–10], transition metal oxides [11], and many other materials during the passed years provide valuable information for physics and chemistry of solids, biology, and materials science.

The modern trends of the electron diffraction method and the main directions of its practical application in the period from 1950 to 1980 were reviewed in the article written by Vainshtein *et al.* [12] including the theoretical foundations, experimental methods, preparation of specimens, determination of structure factors, and the structural results. Vainshtein formulated the main features of the electron diffraction structure analysis. These are the following:

—electron scattering from the electrostatic potential of the crystal;

—strong interaction of electrons with the scattering matter;

—high intensity of diffracted beams comparable with the intensity of synchrotron radiation;

—high sensitivity of the method to the distribution of valence electrons.

Thus, one can see the main advantages of the electron diffraction method in comparison with the other diffraction methods and, in particular, the most important one—its applicability to the studies of thin films and surface layers. It is important that the objects for electron diffraction studies—thin films—are prepared much easier than single crystals and that diffusion and relaxation processes in thin films proceed much faster than in the specimens conventionally used in X-ray and neutron diffraction studies. This, in turn, allows one to fix not only the stable crystal structures but also intermediate states and metastable phases arising, e.g., during various physical and chemical processes—at various stages of redox reactions, phase transitions, and equilibrium crystal growth.

The studies performed by Vainshtein and his colleagues had stimulated the development of other electron diffraction methods, such as micro- and nanodif-

1063-7745/01/4604-0556$21.00 © 2001 MAIK "Nauka/Interperiodica"

fraction, convergent-beam electron diffraction, the method of critical voltages, etc. [13–15]. The main feature of all these methods is the possibility of studying individual microscopic single crystals or small areas of crystals, determined by the dimensions of the beam spot on the specimen. To interpret the intensities and calculate the structure factors in the methods of convergent-beam diffraction and critical voltage, one has to invoke the theory of multibeam scattering because the crystals studied are usually still rather thick. The accuracy of the determination of the structure amplitudes for low-angle reflections in these methods is 1%.

Since the main objects of EDSA are polycrystalline specimens, a large number of small crystallites (either randomly located or oriented in a certain way) are simultaneously illuminated with the beam. This creates the conditions for the formation of specific type of electron diffraction patterns with continuous rings, arcs (for textured specimens), or broadened reflections caused by the misorientation of the constituent microcrystallites (for mosaic single crystals). As a result, the diffraction pattern has a set of reflections corresponding to large scattering angles which provide the structure analysis at a high resolution.

In diffraction of high-energy (>10 keV) electrons, the effects caused by interaction between the incident electrons and the electrons of the crystal can be neglected [16]. In this case, the EDSA method provides for the obtaining of the Fourier-image of the electrostatic potential of atoms, molecules, and crystals (structure factors). The electrostatic potential determines a number of important properties of crystals, including the characteristics of atomic and molecular interactions [17]. Therefore, high-energy electron diffraction (HEED) can be used for obtaining direct information on the physical properties of crystals. It is important that, knowing the arrangement of the atoms in the unit cell of the crystal, one can calculate the electrostatic potential using the Hartree–Fock or Kohn–Sham equations [18]. Thus, the results of the electron diffraction experiment can be directly compared with the data calculated theoretically.

It should be indicated that in the standard approach, only a part of the information contained in the electron diffraction intensities is extracted. The coherent elastic scattering of high-energy electrons is provided by the electrostatic-potential distribution averaged over the thermal motion (the so-called dynamical electrostatic potential). Dividing the dynamical electrostatic potential into the vibrating atomic fragments including the nuclei within a certain structure model, one can determine the coordinates of the equilibrium points of these fragments and the characteristics of their displacements along different directions from the equilibrium points. These quantities are identified with the atomic coordinates and thermal parameters. At a high accuracy of the experiment and the structure model taking into account nonsphericity of atoms in the crystal (and, in future, also of the anharmonism of their thermal motion), one cannot only increase the accuracy of the determination of the atomic positions and the parameters of atomic thermal vibrations but also reconstruct quantitatively the continuous three-dimensional distribution of the electrostatic potential. The thermal parameters are related to the quantities used in the theory of the lattice dynamics. The electrostatic potential is related to the complete charge density by the Poisson equation. As was shown by Hohenberg and Kohn [19], the electron part of the charge density fully determines all the properties of the ground electronic states of atoms, molecules, and crystals. The electron density, which determines the characteristics of the crystal field and chemical bonding in the material is also one of the most important variables in the quantum–mechanical theory of the density functional which describes the electronic properties of the materials. The characteristics electron-density are used in various physical models. Knowing the characteristics of the electrostatic potential (determined from the electron diffraction data), one can readily pass to the studies of electron density in crystals. This fact makes the electron diffraction method very important for the physics and chemistry of solids.

PRECISION ELECTRON DIFFRACTION METHOD AND THE PERSPECTIVES OF ITS DEVELOPMENT

To provide the quantitative study of the electrostatic-potential and electron-density distributions—one of the major goals of *precision* electron diffraction—one has to develop both experimental methods for data collection and methods for processing and interpretation of these data. Thus, the main goals of precision electron diffraction structure analysis can be formulated as follows [20]:

—the development of electron diffractometry for the precise measurement of reflection intensities;

—the development of methods for taking into account extinction effects caused by multibeam scattering;

—the improvement of methods for taking into account inelastic scattering;

—the development of methods for modeling the electrostatic potential on the basis of the known experimental information and evaluation of the real accuracy of its determination;

—the development of methods for interpreting continuous distributions of electrostatic potential in terms of the physics and chemistry of solids.

The above list shows that the degree of the development of the precision electron diffraction determines the state and the possibilities of the modern electron diffraction structure analysis. In particular, the knowledge of the exact values of structure factors will also be advantageous for the use of the direct methods of structure analysis also recently applied to electron diffraction data [9].

Some progress achieved in the solution of the problems formulated above has already been considered in [20–22]. We should like to add the following. Considering the effects of primary extinction in thin films, one has to bear in mind that the dynamical effects in thin films are considerably weakened and, for the crystals of compounds formed by light elements, the kinematical approximation is still a sufficiently reliable tool even in the precision studies, which will be considered somewhat later. It is important that the extinction effects can often be taken into account in the two-beam approximation with the aid of the Blackman curve [12]. The allowance for multibeam scattering in polycrystalline and partly oriented polycrystalline films was discussed in detail elsewhere [22–24].

Inelastic scattering arises due to energy losses by diffracted electrons consumed in phonon and plasmon excitation and the interband transitions [15, 25]. For rather thick crystals, e.g., in convergent-beam electron diffraction [16], one should also take into account absorption. This is done by the introduction of the complex potential. The major contribution to the imaginary part of the structure factor comes from the thermal diffuse scattering (TDS) [26], which can be taken into account quantitatively [27, 28]. With this aim, following the initial formulation of the model of thermal diffuse scattering [29], one has to use the isotropic Debye–Waller factors and the Einstein model [30]. However, it was established [15, 31] that the intensity distributions of all the diffracted beams (except for the central beam) are only weakly sensitive on the form of the absorption function or the corresponding imaginary parts of the structure factors. Therefore, most of the studies on the verification of the relationships of the dynamical diffraction theory were performed without allowance for absorption.

Using the system of energy filtration of electrons at the filter resolution ranging within 2–3 eV, one can record diffraction patterns formed by elastically scattered electrons, which lost only a small part of their energy for excitation of phonon vibrations in the crystal. This, in turn, allows the more accurate evaluation of the thermal motion of atoms in crystals. Not going into the details of this problem, we should like to emphasize that, in the general case, TDS results in the underestimation of the heights of Bragg maxima and is pronounced both in the vicinity of these peaks and between them. The construction of a smooth background line provides only the partial allowance for the thermal diffuse scattering. It will be shown by some examples that neglect of absorption in very thin polycrystalline films of materials with small atomic numbers does not cause noticeable errors in the structure factors.

Recently, we started the systematic precision electron diffraction studies of the electrostatic potential in various crystals. The present article summarizes the latest achievements of the precision electron diffractometry and the first results of its application to quantitative studies of the electrostatic potential and electron density in crystals with ionic and covalent bonding. Some properties of the electrostatic potential are described in [17], whereas some problems of its quantitative determination in electron diffraction are considered in [15, 20, 32].

ELECTRON DIFFRACTOMETRY

The precision structure analysis of crystals and the quantitative reconstruction of the electrostatic potential requires the maximum possible set of structure factors (which would provide the high resolution of the electrostatic potential) with the statistical accuracy being at least 1–2%. Such an experimental data set was collected on an electron diffractometer designed on the basis of the EMR-102 electron diffraction camera [33] produced by the Selmi Ltd. (Sumy, Ukraine). The diffractometer is based on the well-known measurement principle [34]—a moving diffraction patters is scanned point by point by a static detector (a scintillator with a photomultiplier) (Fig. 1). Both scanning and measuring are controlled by a computer operating in the accumulation (the constant-time) mode.

To provide precision measurements, one has to use the wide dynamical range of the detector, the sufficient angular resolution, and the measuring system with a high operation speed. The electron equipment used included a scintillator with a lighting time of 4–5 ns and a high-frequency photomultiplier with a time resolution of 10 ns. This allowed electron recording with a time interval of ~15 ns, which corresponded to the average pulse repetition frequency of 60–70 MHz or the electron beam current of 10^{-11} A (under the assumption that, in the first approximation, to each electron there corresponded one pulse in the recording system). Electrons incident at higher frequencies were not recorded. To determine the degree of the system linearity, we estimated the transfer-frequency characteristic by measuring the electron beam current with the aid of a dc multiplier with a Faraday cylinder. The measurements showed that the nonlinear distortions of the system did not exceed 0.5% at the electron repetition frequency of about 1 MHz (~10^{-13} A).

Recently, the so-called charge-coupled devices or CCD-cameras have achieved great popularity in electron diffraction and electron microscopy [35, 36]. These rather expensive devices provide two-dimensional diffraction patterns and have a wide dynamical range and a high linearity. The resolution and the dimensions of the diffraction patterns studied are determined by the pixel density, i.e., are limited. Usually, CCD-cameras operate in the constant-time mode, which results in different statistical accuracies for weak and strong reflections. The use of a CCD-camera in the accumulation mode is rather difficult and reduces its main advantage—simultaneous measurement of a diffraction pattern along two directions. In our system, we

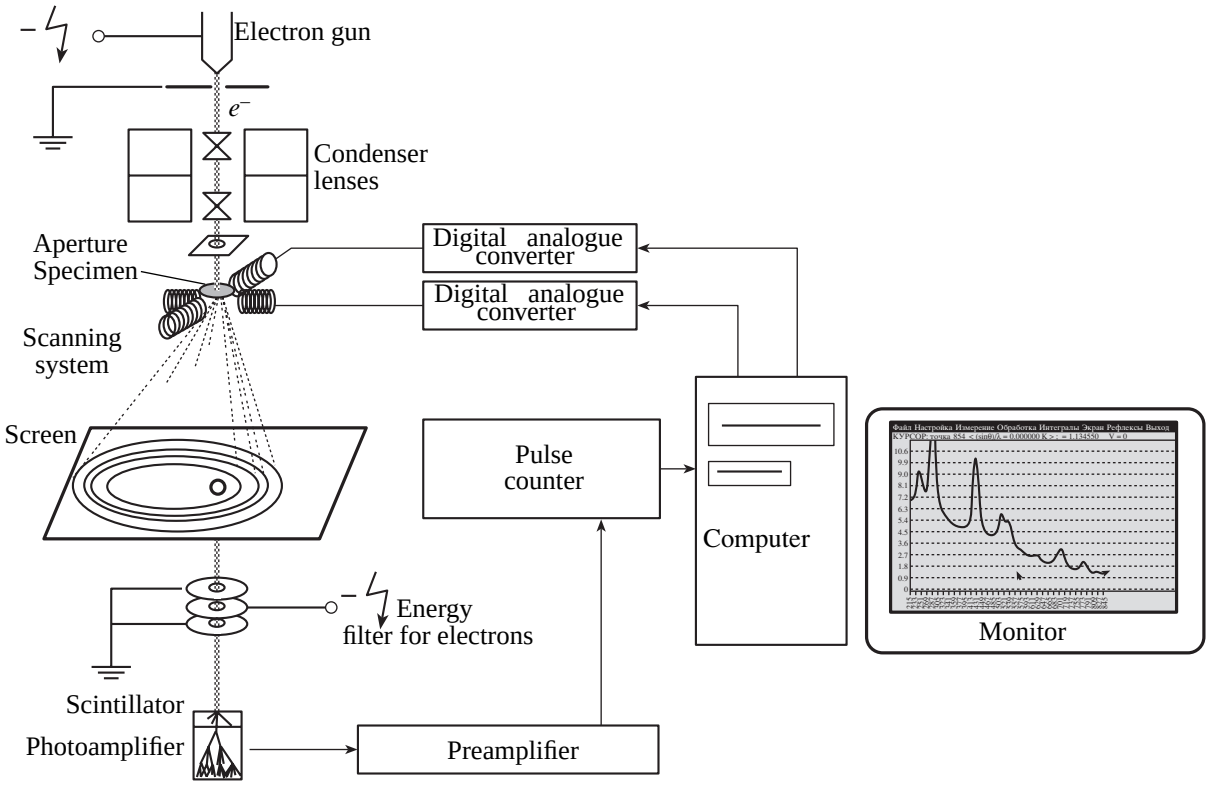

Fig. 1. Schematic of an automated electron diffractometer.

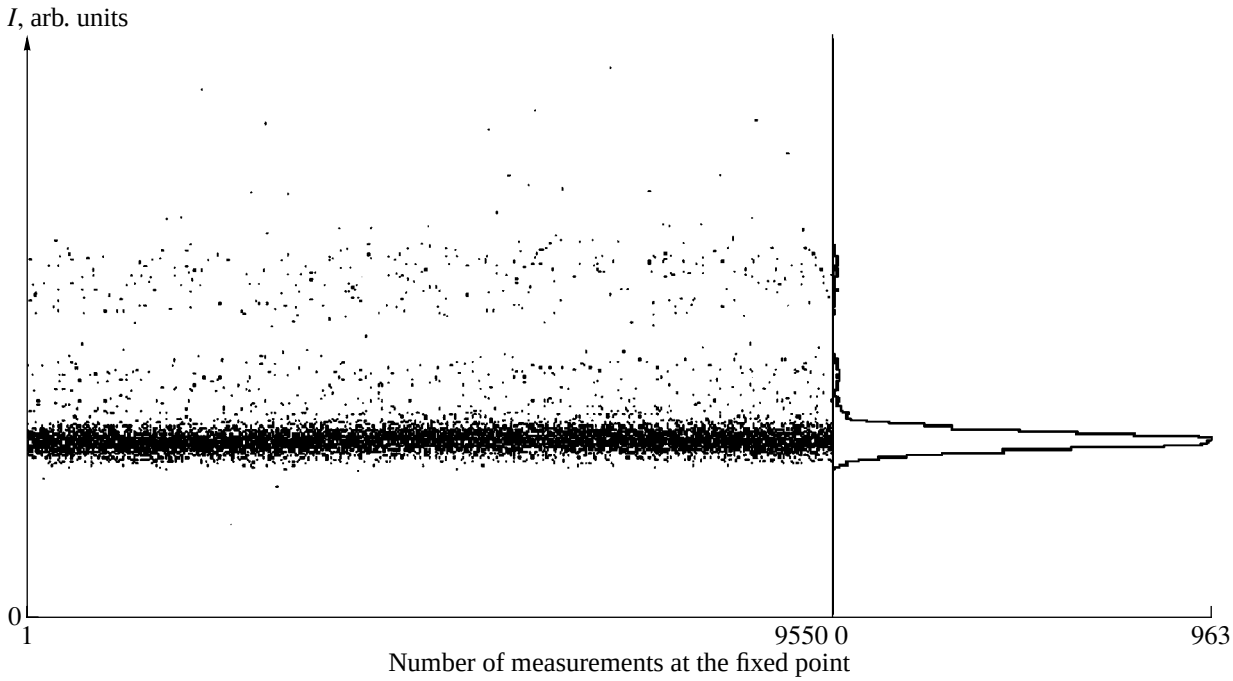

Fig. 2. Illustrating the principle of the statistic analysis of the measured signals. Each point on the left-hand part of the figure corresponds to the intensity of one packet at the fixed point of the diffraction pattern. On the right: the histogram of the intensity distribution in the packets.

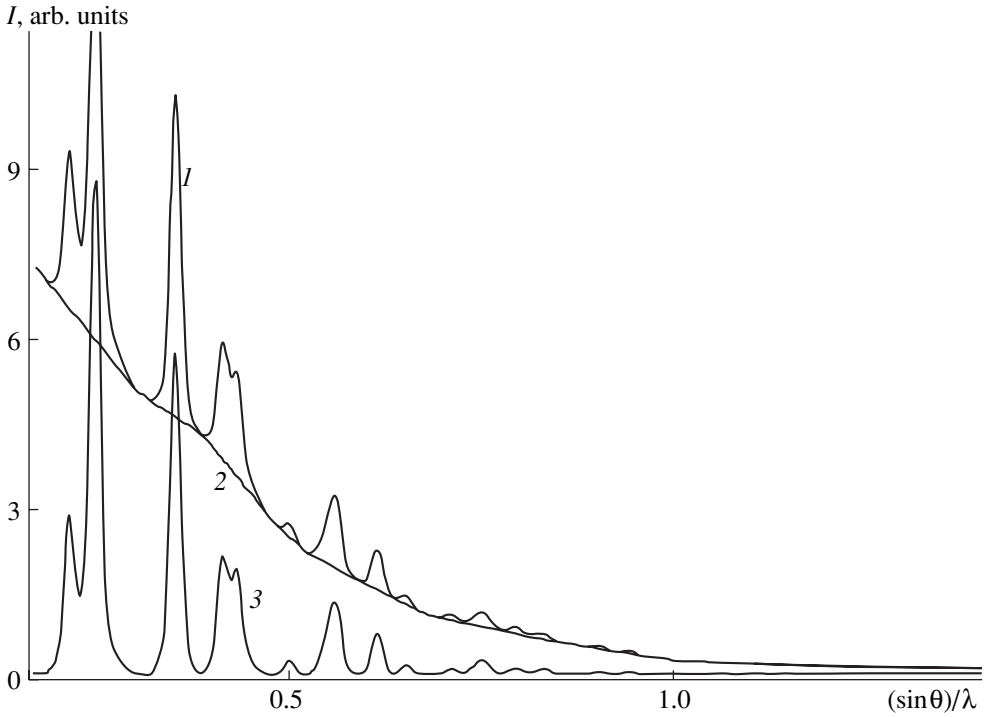

Fig. 3. Example of the one-dimensional recording of the electron diffraction pattern from a LiF polycrystal. (*1*) Experimental intensity curve, (*2*) background line, and (*3*) experimental curve with the subtracted background.

use step-by-step scanning, in which the number and the size of steps can be individually chosen for each object.

Despite the fact that the primary-beam stability is rather high (the relative current variations do not exceed 10^{-3} per 10 min), it was possible to improve it even further by dividing the intensity at each new point into the intensity continuously measured at the reference point. Moreover, to improve the measurement accuracy, we also performed the statistical analysis of the accumulated signal. Each signal was divided into several equal packets (e.g., the signal of 5×10^4 pulses was divided into 50 packets consisting of 10^3 pulses), and the measurement time was recorded for each packet. This provided the analysis of the distribution of the measuring times (Fig. 2) and the establishment of the deviations from the average time, which were determined by current instabilities in optical lenses, discharges in the electron gun, and a number of other undesirable processes. The unreliably measured packets were rejected, which considerably increased the accuracy of measurement at each point. According to the estimates made, the statistical accuracy of the intensity measurements of about 1.0–1.5% is attained at the accumulated-signal volume up to 5×10^4.

The background of incoherent scattering is described with the aid of a smooth curve (or surface) constructed by the method of a convex shell by the points between the diffraction maxima (both in the one- and the two-dimensional cases). Figure 3 shows an example of the one-dimensional record of the diffraction pattern from a polycrystalline LiF specimen upon its statistical processing and subtraction of the background. The accuracy of the subtraction of the incoherent background in this case was at least 0.5% (the energy spectrum of the background was ignored). It was shown [37] that the use of the filter of inelastically scattered electrons increases the accuracy of the background refinement.

The process of measuring and primary processing of the experimental data is schematically illustrated by Fig. 4 with the indication of the complex of the controlling computer programs. The initial measurement parameters include the choice of the necessary statistical accuracy, the type of the diffraction pattern, etc. Processing diffraction data include the statistical analysis (considered above), the separation of the overlapping diffraction peaks and the analysis of the peak shape (the profile analysis), etc. The output data include the set of structure factors ready for further use in the complex of specially written computer programs [38].

The electron diffractometer described above was used in precision studies of ionic and covalent crystals which will be considered somewhat later.

TOPOLOGICAL CHARACTERISTICS OF THE ELECTROSTATIC POTENTIAL

The development of the methods for quantitative determination of the electrostatic potential requires the methods for reconstruction of the electrostatic-poten-

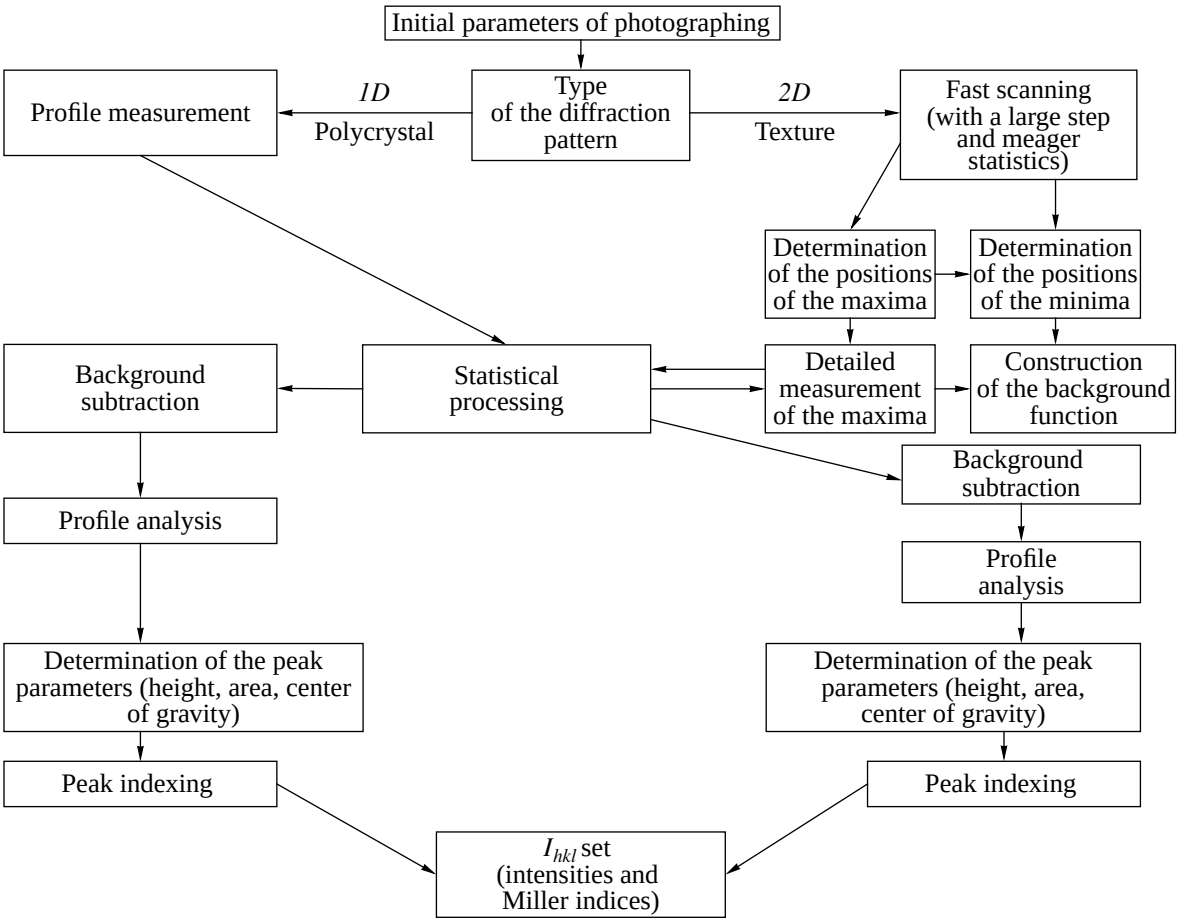

Fig. 4. Scheme of the complex of computer programs controlling diffractometer and the primary processing of the experimental intensities.

tial distribution in crystals and their interpretation. Consider in brief the main properties of the electrostatic potential [39].

The electrostatic (Coulomb) potential is a scalar function dependent on the charge density as

$$\varphi(\mathbf{r}) = \int_{-\infty}^{\infty} \{\sigma(\mathbf{r}')/|\mathbf{r}-\mathbf{r}'|\}dV'$$

and consisting of the nuclear and the electron components

$$\sigma(\mathbf{r}') = \sum Z_a \delta(\mathbf{r}' - \mathbf{R}_a) - \rho(\mathbf{r}'). \quad (1)$$

Here, Z_a and $\mathbf{R}_a$ are the nucleus charge of the atom a and its coordinates, respectively, and $\rho(\mathbf{r}')$ is the electron density. The electrostatic potential $\varphi(\mathbf{r})$ consists of the average internal potential φ_0 dependent on the shape and the structure of the crystals surface [40] and can be determined either experimentally by the method of electron holography [41] or calculated theoretically [42, 43]. The electrostatic-potential distribution reflects the features of the atomic and molecular interactions in the crystal and the characteristics of the crystal packing [17, 44]. Moreover, knowing the electrostatic potential, one can determine the electric-field gradient at nuclei (which is then used in the characteristics of the nuclear quadrupole resonance and the Mössbauer spectroscopy), diamagnetic susceptibility [45], and the refractive index of electrons [41].

The electrostatic potential of the multielectron multinuclear system has the maxima, saddle points, and minima corresponding to the positions of the nuclei, internuclear lines, atomic cycles, and closed cavities in the unit cell of the crystal. Therefore, similar to the electron density [17, 46, 47], the electrostatic potential can be characterized by the critical points with the coordinates $\mathbf{r}_c$ at which $\nabla\varphi(\mathbf{r}_c) = 0$. In terms of the topological analysis [46, 47], the critical points corresponding to the saddle points or the one- and the two-dimensional minima are denoted as (3, –1) and (3, +1) and those corresponding to the maxima and the minima as (3, –3) and (3, + 3), respectively. Here, 3 is the number of the nonzero nondegenerate eigenvalues λ_i of the Hesse matrix of the electrostatic potential, whereas the second number in parentheses is the algebraic sum of the signs of λ_i.

It is convenient to characterize the electrostatic potential by the gradient-field vector $\nabla\varphi(\mathbf{R})$ and the curvature $\nabla^2\varphi(\mathbf{R})$. It is important that these characteristics are independent of the constant φ_0. As is well known [48], the vector of the classical electrostatic field $\mathbf{E}(\mathbf{r}) = -\nabla\varphi(\mathbf{r})$ is directed along the tangent to the gradient line of the electrostatic potential at the given point, whereas the concentration of such lines passing through the unit area normal to it corresponds to the field at the given point. The pairs of the gradient lines in the field $\mathbf{E}(\mathbf{r})$ originating at the critical point (3, –1) and ending at two neighboring nuclei are determined by the eigenvectors corresponding to the only positive eigenvalue of the Hessian of the electrostatic potential at this point, λ_3. These lines connect the neighboring nuclei along which the electrostatic potential is maximal with respect to any transverse displacement. The electrostatic field $\mathbf{E}(\mathbf{r})$ acting onto the positive trial charge along the internuclear line is directed toward the critical point (3, –1) and changes its direction at this point.

The nuclei of the neighboring atoms in any crystal or a molecule are separated in the field $\mathbf{E}(\mathbf{r})$ by the surfaces satisfying the condition of the zero flow

$$\mathbf{E}(\mathbf{r})\cdot\mathbf{n}(\mathbf{r}) = -\nabla\varphi(\mathbf{r})\cdot\mathbf{n}(\mathbf{r}) = 0, \quad \forall\mathbf{r}\in\mathbf{S}_i(\mathbf{r}), \quad (2)$$

where $\mathbf{n}(\mathbf{r})$ is the unit surface normal. These surfaces determine the specific atomic regions ("atomic walleys") inside which the nucleus charge is fully screened by the electron charge. In other words, they determine the electrically neutral *bound* pseudoatoms.

The constancy of the electron-density sign leads to the positive electrostatic-potential curvature at all the points outside the nucleus: $\nabla^2\varphi(\mathbf{r}) = \lambda_1 + \lambda_2 + \lambda_3 > 0$. Since the value of λ_3 is always positive, there is the following limitation: $\lambda_1 + \lambda_2 < \lambda_3$.

Thus, in addition to the topological characteristics of the electron density, the topological characteristics of the electrostatic potential [17, 47] provide the physical information on the electrostatic field of the polycrystal. Below, we consider the first results of the topological analysis of crystals and relate the electrostatic-potential distribution obtained from the electron diffraction experiment to the description of atomic interactions in crystals.

EXPERIMENTAL

Thin polycrystalline films for an electron diffraction study in the transmission mode are prepared either by deposition from smoke in air (MgO) or by vacuum condensation onto carbon substrates with the subsequent transfer onto copper grids at room temperature (NaF, LiF, Ge). The film thickness is selected in a way to maximally reduce the effects of primary extinction, on the one hand, and to obtain high quality diffraction patterns, on the other. The average crystallite size in the films ranged within 100–300 Å. Upon checking possible preferential orientation of crystallites, the intensities of diffraction reflections were measured in an electron diffractometer at an accelerating voltage of 75 kV with the statistical accuracy of at least 1–2%. The diffraction intensities from ionic crystals were measured for reflections up to $\sin\theta/\lambda \approx 1.30$–$1.38$ Å^{-1} and from Ge crystals, up to $\sin\theta/\lambda \approx 1.72$ Å^{-1}.

The intensities of overlapping reflections were separated either with the aid of the profile analysis [33] or in accordance with the ratio of their theoretically calculated intensities. The transition from intensities to structure factors was made by the formulas of the kinematical diffraction theory. The structure factors thus obtained were reduced to the absolute scale and then used to refine the isotropic thermal parameters *B* of the atoms (Table 1). We used the standard atomic scattering functions calculated in the relativistic approximation [49]. To reduce the effect of atom nonsphericity, especially pronounced in the low-angular range, the refinement was performed by the high-angle reflections at $\sin\theta/\lambda > 0.6$–0.9 Å^{-1} (depending on the material). The experimental data for ionic crystals and Ge were further processed somewhat differently; therefore, data processing for these objects will be considered separately.

IONIC LiF, NaF, AND MgO CRYSTALS

Upon the refinement of the atomic thermal parameters, the experimental intensities were checked according to the presence of primary extinction [12]. It was revealed that the all the reflection intensities for NaF and most of the moderate-angle and all the high-angle reflection intensities for LiF and MgO are satisfactorily described within the kinematical theory. The intensities of four low-angle reflections for LiF and seven reflections for MgO were corrected for extinction in the two-beam approximation with the aid of the Blackman curve. Nevertheless, the intensities of the 400 (LiF) and 440 and 444 (MgO) reflections were underestimated because of higher order dynamical effects. Therefore, these reflections were excluded from the further refinement of the structure model.

The κ-model of the structure [50] used at the final stage of the refinement [39] was as follows. The electron structure factor *a* of each atom was expressed as the sum of the fixed component $f_{\text{core},a}$ due to the atomic core and the variable valence component $P_{\text{val},a} f_{\text{val},a}$, which took into account the charge transfer between the atoms and the expansion–compression of an ion in the crystal

$$\Phi_a(\mathbf{q}) = (\pi\Omega|\mathbf{q}|^2)^{-1}\sum\{Z_a - [f_{\text{core},a}(\mathbf{q}) + P_{\text{val},a} f_{\text{val},a}(\mathbf{q}/\kappa_a)]\}.$$

Here, $\mathbf{q}$ is the reciprocal-lattice vector, Ω is the unit-cell volume, $f_{\text{core},a}(\mathbf{q})$ and $f_{\text{val},a}$ are the X-ray atomic scattering factors for the spherically averaged atomic (ionic) core and densities of valence electrons per electron, κ_a

Table 1. Refinement of the thermal parameters and the parameters of the κ-model for binary ionic crystals

Crystal	Atom	B, Å^2	P_{val}	κ	R, %	R_w, %	φ_n^{**}	φ_{nucl}, H–Φ***	φ_{nucl}, A****
LiF	Li	1.00(2)	0.07(4)	1*	0.99	1.36	−158(2)	−159.6	−155.6
	F	0.89(1)	7.94(4)	1*			−725(2)	−727.6	−721.6
NaF	Na	0.84(2)	0.08(4)	1*	1.65	2.92	−967.5(3)	−967.5	−964.3
	F	0.934(2)	7.92(4)	1.02(4)			−731(2)	−726.8	−721.6
MgO	Mg	0.31(2)	0.41(7)	1*	1.40	1.66	−1089(3)	−1090.5	−1086.7
	O	0.34(2)	7.59(7)	0.960(5)			−609(2)	−612.2	−605.7

* Parameters have not been refined.
** Electrostatic potential at nuclei in volts.
*** Calculated for the three-dimensional potential of the periodical crystal by the Hartree–Fock method.
**** Potential calculated for atoms in [44].

are the atomic parameters responsible for the compression–extension, and $P_{val,\,a}$ are the occupancies of the atomic shells with electrons. For a better description of ions in a crystal, we used the Hartree–Fock wave functions of the valence and the core electrons of singly-charged ions (except for the F atom in LiF). The refinement of the κ-model with the final reliability factors R is indicated in Table 1. Figure 5a and 5b demonstrate the quality of the fitting procedure to the κ-model on an example of MgO. Here, Φ_{obs} is the observed structure factor, Φ_{mod} is the structure factor calculated by the parameters of the κ-model, and $\Phi_{H-\Phi}$ is the structure factor calculated by the Hartree–Fock method.

In order to estimate the experimental results independently by the nonempirical Hartree–Fock method, we calculated the electron densities for all the crystals studied with the use of the CRYSTAL95 program [51]. The accuracy of these calculations for an infinite three-dimensional crystal is about 1%. Using the theoretically calculated electron density, the Fourier transform, and the Mott–Bethe formula, we calculated the electron structure factors and compared them with the electron structure factors calculated by the parameters of the refined κ-model and reduced to the absolute zero. The comparison of these quantities is illustrated by example of MgO in Fig. 5b. It can be concluded that the average error in the determination of experimental kinematical structure factors is at a level of 1%.

Now consider the electrostatic potential and electron density calculated from the diffraction data. The construction of the electrostatic-potential distribution in high-energy electron diffraction structure analysis is usually made with the aid of the Fourier series [12, 52–53]. However, irrespective of the experimentally attained resolution, the corresponding ("dynamical") maps of the electrostatic potential are affected by the series termination—the distortion of the shape of the true peaks of the electrostatic potential and formation of spurious peaks with the intensities attaining 5–10% of the intensities of the true peaks [53]. We checked the applicability of the Lanczos factors used in the X-ray diffraction analysis for reducing the effect of the series termination and came to the conclusion that their use results in a considerable underestimation of the atomic peaks. Thus, this technique cannot be used in the quantitative analysis of the electrostatic potential. Another method for eliminating the effect of series termination consists in "building up" the experimental series with the theoretically calculated structure factors until the attainment of the resolution sufficient (although experimentally unattainable) for the satisfactory minimization of the effect of series termination.

In this connection, it should be indicated that in a number of cases involving the semiquantitative analysis of the potential-peak heights (e.g., in the identification of atoms in the unit cell), it was possible to use the integrated characteristics of the maxima or their projections onto the chosen plane, which were introduced by Vainshtein [1]. This allows one to take into account, to a certain degree, the real experimental conditions such as the series termination and the experiment temperature. However, taking into account the approximate character of the integrated characteristics and the fact that they give no information on the intermediate region between the atoms, these conditions cannot be used in the quantitative analysis of the electrostatic potential.

The method for calculating the electrostatic potential with the use of the analytical structure model (whose parameters are determined by fitting of its structure factors to the experimentally determined ones) suggested in our earlier works has a number of advantages. It is almost free of errors caused by the series termination, the experimental determination of the intensities, and the transition to the structure factors and provides the determination of the static electrostatic potential, which justifies the comparison of the experimental and theoretical results.

It is important to indicate the electrostatic potential reconstructed from the experiment should be corrected for the "self-action potential" [48]. Without such a correction, it is impossible to obtain physically valuable energies of the electrostatic interactions between the

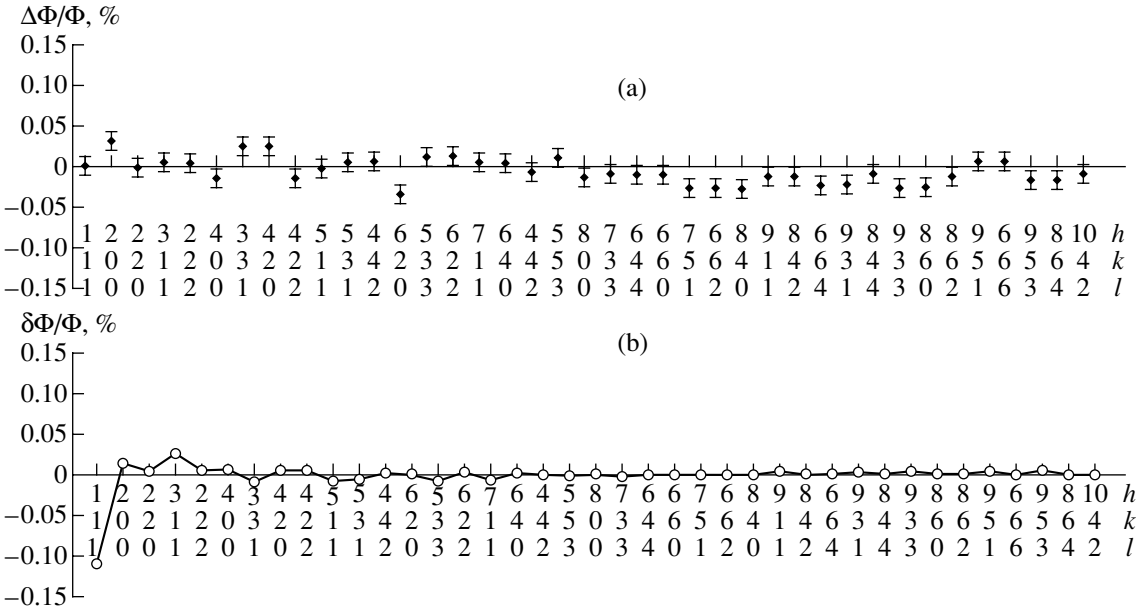

Fig. 5. Characteristics of the accuracy of the structure factors of MgO crystal. (a) The plot of relative differences between the experimental and the model structure factors calculated by the formula $\Delta = (\Phi_{obs} - \Phi_{mod})/\Phi_{mod}$ and (b) the same for the model structure factors and structure factors calculated by the Hartree–Fock method, $\delta = (\Phi_{mod} - \Phi_{H-\Phi})/\Phi_{H-\Phi}$.

nuclei and electrons in the unit cell [39]. The calculation of the electrostatic potential with the use of the analytical model allows one to take into account this effect by a simple subtraction of the corresponding contribution from the total charge density equation (1). Since the nucleus charge *a*, assumed to be a point charge, does not give any contribution to the electrostatic potential at $r' = R_a$, the electrostatic potential at point R_a is determined mainly by the electron density, with the effect of all the other nuclei being negligibly small. The corrected values of the electrostatic potential in the nucleus positions in the crystals obtained from the electron diffraction data and the use of the κ-model and calculated by the Hartree–Fock method are also indicated in Table 1. The analysis of this table shows that the experimental electrostatic potentials at the nuclei are close to those obtained in the *ab initio* calculations with both values in the crystal being different from the analogous values for free atoms [54]. It is shown [55, 56] that this difference in the electrostatic potential in the nucleus positions correlates quite well with the binding energy of 1*s* electrons. Therefore, the electron diffraction data also provide the information on bonding in crystals which is usually obtained by the method of photoelectron spectroscopy. Thus, one can conclude that the electron diffraction method can be used for quantitative determination of the binding energy of core electrons. This conclusion is worthy of special consideration.

Using the parameters of the κ-model, we calculated the values of the mean inner potential φ_0 [17, 40, 42] for all the crystals studied, which are equal to 7.07 (for LiF), 8.01 (for NaF), and 11.47 V (for MgO). The latter value is comparable with the value of 13.01(8) V obtained by the method of electron holography [41] and with the value of 12.64 V obtained in the calculation of several layers of MgO crystals by the linearized method of adjacent plane waves (LAPW) in the approximation of the local density [43].

Consider the specific features of the electrostatic-potential distribution in the main crystallographic planes of the fcc unit cell. The typical distribution of the electrostatic potential in LiF is shown in Fig. 6a. On the whole, the electrostatic potential along the cation–anion line is rather smooth with the only one-dimensional axial minimum lying at the distances of 0.93, 0.96, and 0.90 Å from the anions in LiF, NaF, and MgO crystals, respectively. These electrostatic-potential minima reflect the fact of electron-charge transfer in the crystal and, in particular, the accumulation of the excessive electron charge by anions. Indeed, the existence of these regions follows from the specific dependence of the potential of a negative ion on its distance from the nucleus (Fig. 7). Compare, e.g., LiF and NaF. The negative minima of the electrostatic potentials of individual ("removed" from the crystal) F-ions calculated with the parameters P_{val} and κ obtained from the electron diffraction experiments on LiF and NaF (see Table 1) are located at distances of 1.06 and 1.03 Å from the nucleus, respectively (Fig. 7). The positive potential of a relatively large Na ion decreases more slowly than the electrostatic potential of a Li ion, but the unit cell dimensions of NaF are much larger. As a result, the distances from the anions to the axial minima in LiF and NaF crystals are rather close.

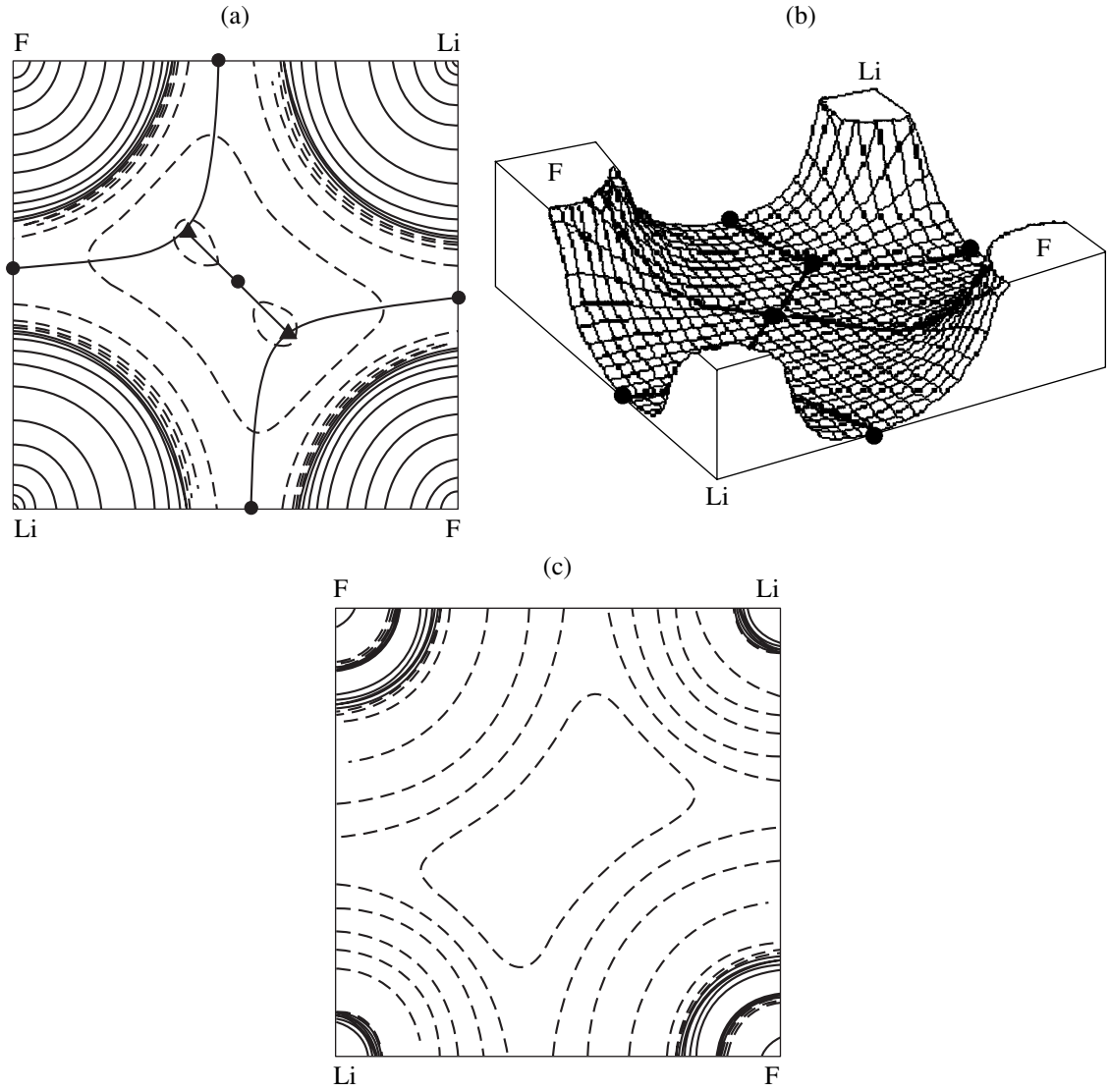

Fig. 6. Electrostatic-potential distribution for LiF in the (100) plane. The critical points (3, –1) are shown by circles, the critical points (3, +1), by triangles; (a) solid lines indicate the traces of the zero flow surfaces. (b) The three-dimensional electron density of LiF projected onto the (100) plane. The notation for the critical points is as above. (c) The map of the Laplacian $\nabla^2\varphi(\mathbf{R})$ for LiF in the (100) plane. The inner electron shells are indicated by bold lines.

The one-dimensional electrostatic-potential maxima are observed in the center of the anion–anion line in the (100) plane. They smoothly connect the pairs of two-dimensional minima located on the same line but closer to the anion positions. The existence of such two-dimensional minima is reliably confirmed by the direct calculation of the electrostatic potential by the Hartree–Fock method. The analysis shows that the more pronounced the negative charge of any isolated ion and the more the parameter $\kappa < 1$ differs from unity, the lower the negative minimum. At the same time, the minimum is shifted toward the nucleus. In the crystal, this behavior manifests itself in the formation of the regions of negative values of the electrostatic potential far from the shortest bond lengths, i.e., the so-called nonbonding directions.

It should be indicated that the analogous minima of the electrostatic potential were also recently revealed around F atoms in $KNiF_3$ [57] and O atoms in $SrTiO_3$ [58]. It should be emphasized that the appearance of the electrostatic-potential minima is a sensitive indicator of the charge transfer between atoms in the crystal.

In terms of critical points, we can state that the critical points (3, –1) in the electrostatic potential are located on the cation–anion and cation–cation lines (Fig. 6a) and are characterized by the positive curvature along the bonding lines and the negative curvature in two directions normal to the bonding lines. The two-dimensional minima located on the anion–anion line in the (100) plane correspond to the critical point (3, +1). The critical points (3, +3) are observed at the centers of cubes formed by four cations and four anions.

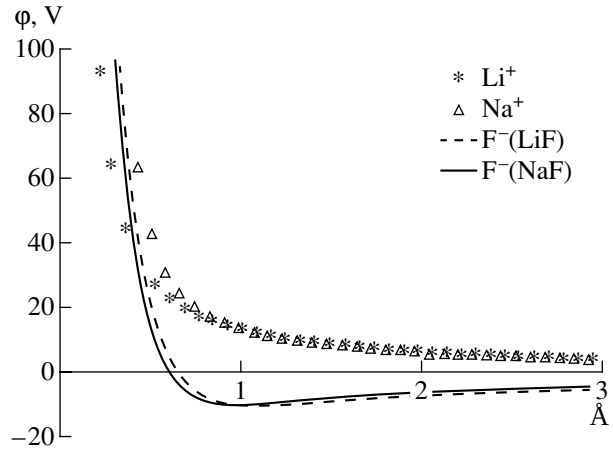

Fig. 7. Electrostatic potential as a function of the distance from the point of observation to the center of an atom for isolated ions in LiF and NaF crystals with the parameters of the κ model obtained from the electron diffraction data.

Comparing the characteristic arrangement of the critical points in the electrostatic potential and electron density in LiF (Fig. 6b), one can see that the two sets of critical points do not coincide. The critical points in the nuclear potential also differ from the critical points of the electron density [59]. These observations reflect the well known fact that the electron density and the energy of a multielectron system are only partly determined by the internal electrostatic crystal field.

Figure 6c shows the Laplacian of the electron density for LiF. The region of the positive values of the Laplacian between the nearest neighbors in the lattice and in the middle of the basal plane illustrates the outflow of electrons from these regions of the crystal toward the ion positions [47]. In this case, the region of the negative values of the electron-density Laplacian includes the valence electron shell of the fluoride ion and quantitatively characterizes the charge transfer in the ionic LiF crystal.

The electrostatic potential determining the internal electrostatic field $\mathbf{E}(\mathbf{r}) = -\nabla\varphi(\mathbf{r})$ created by all the nuclei and electrons also determines the magnitude of the classical electrostatic (single-electron) Coulomb force at the point $\mathbf{r}$. In virtue of the conditions $\nabla\varphi(\mathbf{r}_c) = 0$, the critical points of the electrostatic potential are the points at which the electric field and, thus, also the electrostatic force acting onto the charge element at the point $\mathbf{r}_c$ are equal to zero. In the nucleus positions, this is consistent with the requirements of the Hellmann–Feynman theorem [60] for the system in equilibrium. There also exist points in the internuclear space where the Coulomb force acting onto the electron-density element equals zero. Invoking the expression for the electrostatic-energy density, $w(\mathbf{r}) = (1/8\pi)[\mathbf{E}(\mathbf{r})]^2$ [48], one can see that, at the critical points of the electrostatic potential, $w(\mathbf{r})$ equals zero.

The atomic surfaces of the zero flow for the crystals studied are determined by Eq. (2) and are shown in Fig. 6a. These surfaces divide the electrostatic potential in the crystal into the atomlike regions (pseudoatoms) determined by the corresponding nuclear potential. Each element of the electron density within such a pseudoatom is attracted to "its nucleus." Therefore, the shape and the dimensions of these regions reflect the electrostatic balance between the bound atoms in the crystal. It should be emphasized that these regions are independent of the ion dimensions in the crystal determined by the electron density. Therefore, the positions of the electrostatic-potential minima on the bonding lines cannot be used to estimate the ionic radii in their traditional meaning.

The pairs of the lines of the electric-field gradient ended at the critical points (3, –1) in the electrostatic potential correspond to the shortest cation–anion and cation–cation distances in the crystal with the NaCl structure. Since the electric field and the interacting charges correspond to one another, these lines can be considered as the "images" of the electrostatic atomic interactions. It should also be noted that in the study of perovskites, the critical points (3, –1) in the electrostatic potential were also located on the Ni–F, K–F, Ni–K, and K–K lines in $KNiF_3$ [57], Ti–O, Sr–O, Ti–Sr, and Sr–Sr lines in $SrTiO_3$, and Ta–O, K–O, Ta–K, and K–K lines in $KTaO_3$ [58]. These observations show the drawback of the model of pair Coulomb interactions between all the point ions used in the calculations of the electrostatic energy of crystals [17, 61]: it reveals no gradient lines connecting anions in the field $\nabla\varphi(\mathbf{r})$. Thus, the consideration of the gradient field leads to the conclusion that the long-range Coulomb interactions between atoms having the finite dimensions have the form of the atom–atom interactions, whose structure is specific for each material or, more exactly, for each structure type.

COVALENT Ge CRYSTAL

A Ge crystal is the traditional object for verifying new theoretical and experimental methods of the solid state physics. In particular, chemical bonding in Ge was repeatedly studied by the X-ray diffraction and the Hartree–Fock methods, and the method of density functional [62–70]. As a result, the good agreement between the theoretical and experimental electron densities was attained. Consider here the first quantitative electron diffraction study of bonding in Ge based on the multipole model [71].

The intensities of 51 rings (up to $\sin\theta/\lambda \approx 1.72$ Å^{-1}) were measured. Upon the separation of the overlapping reflections with the use of the profile analysis or in accordance with their theoretical ratios, the final data set consisted of the intensities of 91 symmetrically independent reflections.

The reduction of the intensities to the absolute scale and the refinement of the isotropic temperature parameter B was performed over 59 reflections with $\sin\theta/\lambda > 0.90$ Å^{-1}. We used the relativistic atomic scattering functions [72]. The determined B value, $B = 0.546(2)$ Å^2 (R = 2.32%), was close to the value B = 0.565 Å^2 obtained in the X-ray study [67]. The corresponding Debye temperature, θ_B = 295 K, agrees quite well with the Debye temperature θ_B = 296 K obtained in [66].

The primary extinction was revealed in the intensities of the low-angle 111, 400, 440, and 620 reflections. Upon the introduction of the corresponding corrections with the aid of the Blackman curve [12], the intensities of the 440 and 620 reflections were too low in comparison with the values predicted by the kinematic theory, which is explained by an insufficiency of the extinction correction not taking into account multibeam interaction of higher orders. Therefore, these two reflections were excluded from the further refinement. The reliability factor R calculated over 89 reflections (without 440 and 620) was reduced upon the introduction of the correction for extinction from 6.40 to 2.42%.

In order to evaluate the accuracy of the electron diffraction data, we compared the low-angle electron structure factors with those calculated for a Ge crystal by the LAPW method in the approximation of the local density [67]. With this aim, we recalculated the values obtained in [67] into the electron structure factors at $B = 0.546$ Å^2. The R value obtained upon the comparison of two sets of structure factors, R = 2.07%, can be considered as the real accuracy of our experimental data.

We reduced the experimental electron structure factors Φ_{hkl} to 0 K and recalculated them into the X-ray structure amplitudes by the Mott–Bethe formula [42]. At this stage, it was established that some Φ_{hkl} values, randomly distributed over the whole reflection set, considerably differ from the corresponding theoretical values calculated in [67]. The analysis showed that these deviations resulted from small but essential errors in the background subtraction associated with the specific interpretation of the polycrystal patterns having overlapping reflections. Upon the rejection of these reflections, the final data set had 43 reflections in the range $0.15 < \sin\theta/\lambda < 1.72$ Å^{-1}.

Then, the experimental data were processed within the multipole model [73], in which the electron density of each pseudoatom is represented as

$$\rho_{at}(\mathbf{r}) = \rho_{core}(r) + P_{val}\kappa'^3\rho_{val}(\kappa' r) + \sum_{l=1}^{4}\kappa''^3 R_l(\kappa'' r)\sum_{m=-l}^{l} P_{lm} y_{lm}(\mathbf{r}/r). \quad (3)$$

The densities of the core and the spherical valence-electron shells, ρ_{core} and ρ_{val}, were described with the aid of atomic wave functions [74]. We used the radial functions in the form $R_l = r^{n_l}\exp(-\kappa'\xi r)$ with $n_3 = n_4 = 4$ ($l \le 4$) and the values of the orbital exponents ξ_{Ge} = 2.1 a.u. [68]. The Ge atom occupies the position with the symmetry $\bar{4}3m$; therefore, only the octupole (P_{32-}) and hexadecupole terms in Eq. (3) have the nonzero values, P_{40} and $P_{44} = 0.74045P_{40}$. The electron occupancies of the P_{lm} multipoles were refined by the least squares method with the use of the MOLDOS96 program [75] together with the parameter κ' responsible for the contraction–extension of the atomic valence shells (Table 2). The analysis of the parameters obtained shows that the probability of their statistically significant determination is not less than 70% (P_{40}). This result is much better than the earlier results obtained by the X-ray diffraction analysis of Ge [69] performed with the use of 13 structure factors, where the value of the parameter P_{40} was twice as small as the error of its determination.

Table 2. Parameters of multipoles obtained from the electron-diffraction data and calculated by the LAPW method [69] for Ge crystals

Parameter	Calculated from electron diffraction data	Calculated by the LAPW method
κ'	0.922(47)	0.957
P_{32-}	0.353(221)	0.307
P_{40}	−0.333(302)	−0.161
R, %	1.60	0.28
R_w, %	1.35	0.29
GOF	1.98	

The value κ' = 0.922 indicates the 8% "expansion" of the spherical part of the Ge shell in the crystal. This

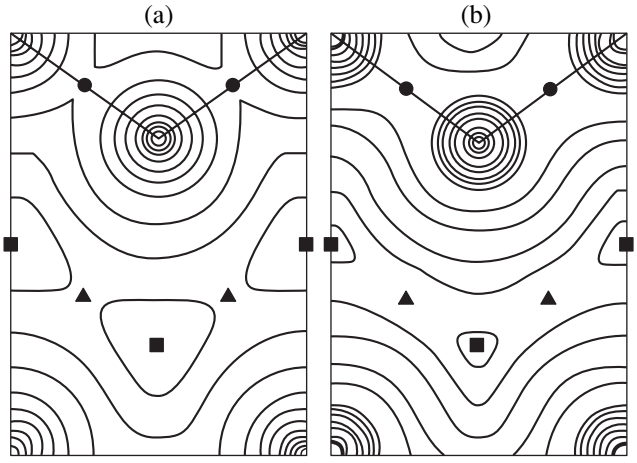

Fig. 8. Maps of the (a) electron density and (b) electrostatic-potential distribution for Ge in the (110) plane. The notation of the (3, –1) and (3, +1) critical points is the same as in Fig. 6, the critical point (3, +3) is denoted by a square.

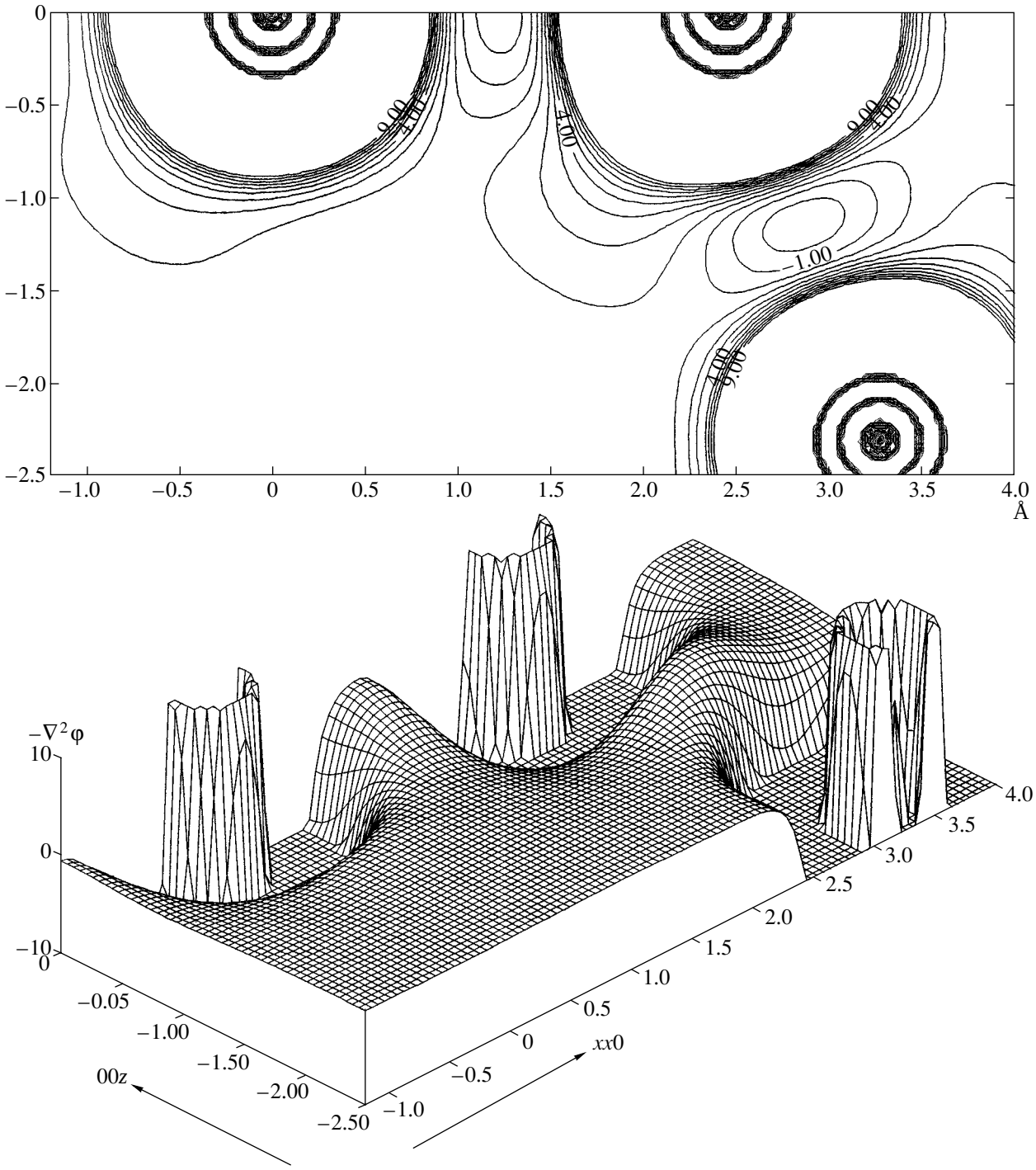

Fig. 9. Electron-density Laplacian in the (110) plane for a fragment of the Ge crystal. The upper part of the figure shows the transverse section of the Laplacian with the inner electron shells. The lower part shows the Laplacian of the same fragment with the opposite sign ($-\nabla^2\varphi(\mathbf{r})$ represented in the three-dimensional form.

agrees with the earlier results [66–68] according to which this value ranges within 4.5–17.0% depending on the method used.

As is seen from Table 2, the values of the multipole parameters determined from the corresponding electron diffraction data differ from those calculated theoretically by the LAPW method. This results in the different values of the electrostatic potentials at the critical points (3, –1). However, the topological characteristics of other critical points coincide quite well. The above discrepancy seems to be associated, first of all, with the use of the nonrelativistic wave functions for core and valence-shell electrons and valence wave functions

Table 3. Topological characteristics of electron density in Ge crystals at the bond, cage, and ring critical points

Type of the critical point and the Wyckoff position	ρ, e Å^{-3}	λ_1, e Å^{-5}	λ_2, e Å^{-5}	λ_3, e Å^{-5}	$\nabla^2\rho$, e Å^{-5}
Bond critical point	0.575(8)	−1.87	−1.87	2.04	−1.87(5)
16*c*	0.504	−1.43	−1.43	1.68	−1.18
Procrystal	0.357	−0.65	−0.65	1.85	0.55
Ring critical point	0.027(5)	−0.02	0.013	0.013	0.25(5)
16*d*	0.030	−0.02	0.014	0.014	0.26
Cage critical point	0.024(5)	0.05	0.05	0.05	0.17(5)
8*b*	0.022	0.05	0.05	0.05	0.15

Note: The first line gives the electron diffraction data, the second line, our data calculated by the LAPW method with the use of the parameters from [69] and [67]. For the critical point (3, –1). the characteristics of the procrystal are also indicated.

because of the absence of the corresponding relativistic functions and, second, with the neglect of the anharmonic thermal motion of atoms, which distorts the antisymmetric octupole term P_{32-}.

The multipole parameters obtained were used to calculate the static electron density and its Laplacian and the electrostatic potential. The (110) maps of these functions are shown in Figs. 8a, 8b, and 9. It should be indicated that the set of experimental structure factors measured up to $\sin\theta/\lambda < 1.72$ Å^{-1} provided not only the refinement of the scale and the temperature factors of Ge but also the high resolution of the electron-density and electrostatic-potential maps and the electron-density Laplacian. In particular, the electrostatic-density map revealed the electron shells of the Ge core (Fig. 9).

The topological characteristics of the critical points on the bonds (Table 3) provide the quantitative description of the well-known effect consisting in the fact that the formation of a Ge crystal is accompanied by a considerable electron-density displacement toward the Ge–Ge line. This is especially well seen from the comparison of the parameters of the electron-density curvature λ_i at the critical point (3, –1) with the analogous parameters for the procrystal (the set of noninteracting spherical atoms occupying the same positions as the atoms in the real crystal) [71]. At the same time, the electron-density curvature along the Ge–Ge line is characterized by only slight displacements of electrons toward the atomic positions. The electron density around the circular and cellular critical points is considerably reduced (Fig. 8). Unlike Si crystals [76], no nonnuclear attractors were detected on the Ge–Ge lines.

In the general case, the schemes of the location of the critical points of electron density and electrostatic potential do not coincide. However, because of the symmetry of the Ge crystal, both electrostatic potential and electron density of this crystal are homeomorphic. In this particular case, the location of the critical points of electron density and electrostatic potential are the same (Fig. 8).

CONCLUSION

Our studies showed that the well developed method of transmission high-energy electron diffraction in combination with the topological analysis of the electron density and the electrostatic potential provides the reliable quantitative information on chemical bonding in polycrystalline specimens and their bonding-dependent properties, which makes electron diffraction one of the most attractive methods in physics and chemistry solids. The reliability of the experimental results obtained is confirmed by *ab initio* calculations by the Hartree–Fock method. It is possible to outline the future development of high-energy electron diffraction. Thus, the progress in electron diffractometry consists in the use of its important advantage—high intensities of diffracted beams. This, in turn, requires the design of high-speed electron detectors, improvement of their linearity, and an increase of the dynamical range of counting. The use of polycrystal specimens with the preferable orientation of crystallites in the film (texture or oriented mosaic single crystal) would allow the separation of the overlapping reflections and obtaining more reliable diffraction data at a higher resolution. For a more thorough study of the relation between the electronic structure and the bonding-dependent physical properties of crystals, one has to consider the electron diffraction data on the potential and the electron-density distributions obtained in the precision X-ray experiment.

ACKNOWLEDGMENTS

The authors are grateful to U. Pietsch, J. Spens, A. Kulygin, and G. Lepeshov for their cooperation and B.B. Zvyagin for his constant interest in our study and valuable remarks. The study was supported by the Russian Foundation for Basic Research, project no. 01-03-33000, Deutsche Gemeinschaft (German Research Society), project no. Pi 217/13-2, and INTAS, project no. 97-32045.

REFERENCES

1. B. K. Vainshtein, *Structure Analysis by Electron Diffraction* (Akad. Nauk SSSR, Moscow, 1956; Pergamon, 1964).
2. Z. G. Pinsker, *Electron Diffraction* (Akad. Nauk SSSR, Moscow, 1949; Butterworth, London, 1953).
3. S. A. Semiletov and R. M. Imamov, in *Fifty Years of Electron Diffraction*, Ed. by P. Goodman (D. Reidel, Dodrecht, 1981), p. 309; L. I. Man, R. M. Imamov, and S. A. Semiletov, Kristallografiya **21** (3), 628 (1976) [Sov. Phys. Crystallogr. **21**, 355 (1976)].
4. Z. G. Pinsker and R. M. Imamov, Indian J. Pure Appl. Phys. **19**, 926 (1981).
5. A. S. Avilov, R. M. Imamov, and S. A. Semiletov, *Modern Electron Microscopy in Study of Matter* (Nauka, Moscow, 1982), p. 73.
6. B. B. Zvyagin, *Electron Diffraction and Structural Crystallography of Clay Minerals* (Nauka, Moscow, 1964).
7. V. A. Drits, *Electron Diffraction and High-Resolution Electron Microscopy of Mineral Structures* (Springer-Verlag, New York, 1981).
8. I. A. D'yakon, S. F. Donu, L. F. Chapurina, and A. S. Avilov, Kristallografiya **36**, 219 (1991) [Sov. Phys. Crystallogr. **36**, 126 (1991)].
9. D. L. Dorset, *Structural Electron Crystallography* (Plenum, New York, 1995).
10. B. K. Vainshtein and V. V. Klechkovskaya, Kristallografiya **39**, 301 (1994) [Crystallogr. Rep. **39**, 256 (1994)].
11. V. I. Khitrova, Kristallografiya **28**, 896 (1983) [Sov. Phys. Crystallogr. **28**, 531 (1983)].
12. B. K. Vainshtein, B. B. Zvyagin, and A. S. Avilov, in *Electron Diffraction Techniques*, Ed. by J. M. Cowley (Oxford Univ. Press, Oxford, 1992), Vol. 1, Chap. 6, p. 216.
13. J. C. H. Spence and J. M. Zuo, *Electron Microdiffraction* (Plenum, New York, 1992).
14. L. Reimer, *Transmission Electron Microscopy* (Springer-Verlag, New York, 1984).
15. J. M. Cowley, in *Electron Diffraction Techniques*, Ed. by J. M. Cowley (Oxford Univ. Press, Oxford, 1992), Vol. 1, p. 1.
16. J. C. H. Spence, in *Electron Diffraction Techniques*, Ed. by J. M. Cowley (Oxford Univ. Press, Oxford, 1992), Vol. 1, p. 360.
17. V. G. Tsirelson and R. P. Ozerov, *Electron Density and Bonding in Crystals: Theory and Diffraction Experiments in Solid State Physics and Chemistry* (Inst. of Physics, Bristol, 1996).
18. W. Kohn and L. J. Sham, Phys. Rev. A **140**, 1133 (1965); **145**, 561 (1966).
19. P. Hohenberg and W. Kohn, Phys. Rev. B **136**, 864 (1964).
20. A. S. Avilov, Kristallografiya **43**, 983 (1998) [Crystallogr. Rep. **43**, 925 (1998)].
21. V. G. Tsirelson, A. S. Avilov, Yu. A. Abramov, *et al.*, Acta Crystallogr., Sect. B: Struct. Sci. **55**, 85 (1998).
22. A. S. Avilov, Izv. Akad. Nauk SSSR, Ser. Fiz. **61**, 1934 (1997).
23. A. S. Avilov and V. S. Parmon, Kristallografiya **35**, 1249 (1990) [Sov. Phys. Crystallogr. **35**, 733 (1990)].
24. A. S. Avilov and V. S. Parmon, Kristallografiya **37**, 1379 (1992) [Sov. Phys. Crystallogr. **37**, 744 (1992)].
25. R. F. Egerton, *Electron Energy-Loss Spectroscopy in the Electron Microscope* (Plenum, New York, 1986).
26. G. Radi, Acta Crystallogr., Sect. A: Cryst. Phys., Diffr., Theor. Gen. Crystallogr. **A26**, 41 (1970).
27. L.-M. Peng, G. Ren, S. L. Dudarev, and M. J. Whelan, Acta Crystallogr., Sect. A: Fundam. Crystallogr. **A52**, 257 (1996).
28. L.-M. Peng, G. Ren, S. L. Dudarev, and M. J. Whelan, Acta Crystallogr., Sect. A: Fundam. Crystallogr. **A52**, 456 (1996).
29. C. R. Hall and P. B. Hirsch, Proc. R. Soc. London, Ser. A **286**, 158 (1965).
30. A. Weickenmeier and H. Kohl, Acta Crystallogr., Sect. A: Fundam. Crystallogr. **A47**, 590 (1991).
31. J. M. Cowley, *Diffraction Physics* (North-Holland, New York, 1981).
32. A. S. Avilov, *Methods of Structural Analysis* (Nauka, Moscow, 1989), p. 256.
33. A. S. Avilov, A. K. Kulygin, U. Pietsch, *et al.*, J. Appl. Crystallogr. **32**, 1033 (1999).
34. G. O. Bagdyk'yants and A. G. Alekseev, Izv. Akad. Nauk SSSR, Ser. Fiz. **23**, 773 (1959).
35. W. J. De Ruijter, Micron **26**, 247 (1995).
36. J. M. Zuo, Ultramicroscopy **66**, 21 (1996).
37. A. S. Avilov, R. K. Karakhanyan, R. M. Imamov, and Z. G. Pinsker, Kristallografiya **18**, 49 (1973) [Sov. Phys. Crystallogr. **18**, 30 (1973)].
38. A. K. Kulygin, G. G. Lepeshov, A. S. Avilov, and V. G. Tsirel'son, in *Proceedings of the XVIII Russia Conference on Electron Microscopy, Chernogolovka, 2000*, p. 58.
39. V. G. Tsirelson, A. S. Avilov, G. G. Lepeshov, *et al.*, J. Chem Phys. (2001) (in press).
40. M. A. O'Keeffe and J. C. H. Spence, Acta Crystallogr., Sect. A: Found. Crystallogr. **50**, 33 (1993).
41. M. Gajdardziska-Josifovska, M. McCartney, J. K. Weiss, *et al.*, Ultramicroscopy **50**, 285 (1993).
42. J. C. H. Spence, Acta Crystallogr., Sect. A: Found. Crystallogr. **49**, 231 (1993).
43. M. Y. Kim, J. M. Zuo, and J. C. H. Spence, Phys. Status Solidi A **166**, 455 (1998).
44. *Molecular Electrostatic Potentials. Concepts and Applications*, Ed. by J. S. Murray and K. Sen (Elsevier, Amsterdam, 1996).
45. N. F. Ramsey, Phys. Rev. **78**, 699 (1950).
46. M. Morse and S. S. Cairns, *Critical Point Theory in Global Analysis and Differential Geometry* (Academic, New York, 1969).
47. R. F. W. Bader, *Atoms in Molecules—A Quantum Theory* (Oxford Univ. Press, Oxford, 1990).
48. I. E. Tamm, *Fundamentals of the Theory of Electricity* (Mir, Moscow, 1979).
49. *International Tables for Crystallography*, Ed. by A. J. C. Wilson (Kluwer, Dordrecht, 1995), Vol. C.
50. P. Coppens, T. N. Guru Row, P. Leung, *et al.*, Acta Crystallogr., Sect. A **A35**, 63 (1979).

51. R. Dovesi, V. R. Saunders, C. Roetti, *et al.*, *CRYSTAL95: User's Manual* (University of Torino, Torino, 1996).
52. B. K. Vainshtein, Q. Rev., Chem. Soc. **14**, 105 (1960).
53. V. G. Tsirelson, A. S. Avilov, Yu. A. Abramov, *et al.*, Acta Crystallogr., Sect. B: Struct. Sci. **54**, 8 (1998).
54. J. Wang and V. H. Smith, Mol. Phys. **90**, 1027 (1997).
55. H. Basch, Chem. Phys. Lett. **6**, 337 (1970).
56. M. E. Schwarz, Chem. Phys. Lett. **6**, 631 (1970).
57. V. Tsirelson, Yu. Ivanov, E. Zhurova, *et al.*, Acta Crystallogr., Sect. B: Struct. Sci. **56**, 197 (2000).
58. E. Zhurova, in *Abstract of the Sagamore XII: Conference on Charge, Spin and Momentum Densities, 2000*, p. 43.
59. Y. Tal, R. F. W. Bader, and R. Erkku, Phys. Rev. A **21**, 1 (1980).
60. R. P. Feynman, Phys. Rev. **56**, 340 (1939); H. Hellmann, *Einführung in die Quanten-chemie* (Deuticke, Leipzig, 1937).
61. *Computer Modelling in Inorganic Crystallography*, Ed. by C. R. A. Catlow (Academic, San Diego, 1997).
62. *Molecular Electrostatic Potentials. Concepts and Applications*, Ed. by J. S. Murray and K. Sen (Elsevier, Amsterdam, 1996).
63. J. B. Roberto, B. W. Batterman, and D. T. Keating, Phys. Rev. B **9**, 2590 (1974).
64. C. S. Wang and B. M. Klein, Phys. Rev. B **24**, 3393 (1981).
65. T. Fukamachi, M. Yoshizawa, K. Ehara, *et al.*, Acta Crystallogr., Sect. A **A46**, 945 (1990).
66. A. S. Brown, M. A. Spackman, Z. W. Lu, *et al.*, Acta Crystallogr., Sect. A **A46**, 381 (1990).
67. Z. W. Lu, A. Zunger, and M. Deutsch, Phys. Rev. B **47**, 9385 (1993).
68. Z. W. Lu, A. Zunger, and M. Deutsch, Phys. Rev. B **52**, 11904 (1995).
69. Yu. A. Abramov and F. P. Okamura, Acta Crystallogr., Sect. A **A53**, 187 (1997).
70. A. G. Fox and R. M. Fisher, Aust. J. Phys. **41**, 461 (1988).
71. A. Avilov, G. Lepeshov, U. Pietsch, and V. Tsirelson, J. Phys. Chem. Solids (2001) (in press).
72. L. C. S. Balba, A. Rubio, J. A. Alonso, *et al.*, J. Phys. Chem. Solids **49**, 1013 (1988).
73. N. K. Hansen and P. Coppens, Acta Crystallogr., Sect. A **A34**, 909 (1978).
74. E. Clementi and C. Roetti, At. Data Nucl. Data Tables **14**, 177 (1974).
75. J. Protas, *MOLDOS96/MOLLY PC-DOS* (Univ. Nancy, 1997).
76. P. F. Zou and R. F. W. Bader, Acta Crystallogr., Sect. A **A50**, 714 (1994).

Translated by L. Man

Crystallography Reports, Vol. 46, No. 4, 2001, pp. 572–576. Translated from Kristallografiya, Vol. 46, No. 4, 2001, pp. 636–640.

DIFFRACTION AND SCATTERING OF ELECTRONS

Dedicated to the memory of B.K. Vainshtein

On the Effect of Sublattice Displacement in Visualization of Crystal Structures

V. L. Vergasov[1] and S. A. Krasnikov

Shubnikov Institute of Crystallography, Russian Academy of Sciences, Leninskiĭ pr. 59, Moscow, 117333 Russia

[1]e-mail: osv@elecdif.incr.msk.ru

Received February 12, 2001

Abstract—Electron-microscopy images of $\langle 001 \rangle$–$GeNb_9O_{25}$ obtained at the atomic resolution have been studied at the electron energy $E = 80$ keV. It is established that one of the sublattices on the image is displaced with respect to the other sublattices. The nature of this displacement is interpreted in terms of physics. The effect was studied in the formalism of Bloch waves. The important role of the valence Bloch state is also considered.

INTRODUCTION

The charge, the small mass, and the short wavelength of high-energy electrons make electron beams very sensitive to the potential of the scattering object. This explains the worldwide popularity of the electron diffraction structure analysis (EDSA) created by Vainshtein [1] on the basis of the pioneering electron diffraction studies performed by Pinsker [2]. This method has always been one of the most efficient methods of studying the structure of various materials (see the article by V.V. Klechkovskaya and R.M. Imamov in the present issue). The above factors also allowed the direct observation of the atomic structure of the matter in electron microscopy. The possibilities of this method and the difficulties encountered in the high-resolution electron microscopy are considered in detail in the well-known review article written by Vainstein [3]. One of such difficulties is associated with artefacts, i.e., the formation of images that do not correspond to the real structure of the scattering object (see review article by Hashimoto [4]). In addition to the obvious effect of the transfer function of an electron microscope on imaging, the artefacts can also be caused by a pure physical factor—the interaction of the electron beam with the potential of the crystal-lattice. However, the physical mechanism of the artefact formation could not be established for quite a long time. The question as to how the electron wave field of a crystal reflects the crystal structure is also important for a novel method of electron crystallography—electron holography—which allows the determination of both amplitude and phase characteristics of the electron wave function and which has already attained the atomic resolution [5, 6].

As an example, consider here the formation of the experimental high-resolution image of the $GeNb_9O_{25}$ structure [7], which was later interpreted as an artefact in [4].

The image of the $GeNb_9O_{25}$ lattice (Figs. 1a, 1b), which, as the authors believe, correctly reflects the material structure, was obtained by varying the transfer function of a microscope. However, a more detailed study of this image showed that the empty channels between the atomic chains (represented by white spots on the images) are located not exactly in the sites expected from the structure projection. Indeed, according to the structure model, four neighboring channels should be located along one straight line (Fig. 1a), but in the actual fact only two channels are located along this line, whereas two other channels are located along another line [7]. In other words, the groups of channels are displaced with respect to one another, which indicates the displacement of different sublattices with respect to one another on the image. It is this fact that made Hashimoto [3] consider the image obtained in [7] as an artefact.

Below, we analyze the formation of the image of this structure within the formalism of electron Bloch waves.

TRANSVERSE BLOCH WAVES AND THE STRUCTURE OF THE IMAGE

The wave function of a high-energy electron, $\Psi(\mathbf{r})$, in a crystal can be represented as a set of Bloch waves

$\Psi^j(\mathbf{r})$ [8, 9],

$$\Psi(\mathbf{r}) = \sum_{j=1}^{N} \Psi_0^{j*}\Psi^j(\mathbf{r}) = \sum_{j=1}^{N} \Psi_0^{j*}\Psi^j(x, y)\exp\{2\pi i k_z^j\}, \quad (1)$$

each of which is characterized by the excitation amplitude, Ψ_0^{j*}, the projection of the wave vector k_z^j onto the z-axis, and Bloch wave distribution in the (x, y) plane normal to the direction z of the beam incidence. Equation (1) takes into account that electrons with the kinetic energy $E \geq 100$ keV having the velocity comparable (by the order of magnitude) with the light velocity are almost insensitive to the variations in the lattice potential along the direction z of their motion and, therefore, move in the potential $V(x, y) = \bar{V}_z(x, y, z)$ averaged along z. This is equivalent to the fact that, calculating the Bloch waves, we take into account the reciprocal-lattice points (relpoints) of only one plane—the zero Laue zone. The number N includes only relpoints $\{h\}$ whose excitation errors $S_n = [K^2 - (\mathbf{K} + \mathbf{h})^2]/2K$ do not exceed the excitation errors of the relpoints from higher Laue zones, where $K = \sqrt{\mathbf{K}_0 + \bar{V}_{x,y,z}(x, y, z)}$, and $\mathbf{K}_0$ is the wave vector of the incident beam.

Then, the quantization of the energy states of electrons, $\mathbf{K} \longrightarrow \{\mathbf{k}^j\}$, occurs in the transverse potential $V(x, y)$, and these states can be conveniently characterized by the transverse energies $E_\perp^j = K^2 - (\mathbf{k}^j)^2$. Considering the energies $E_\perp^j$ and the positions of the corresponding energy levels in the potential wells $V(x, y)$, we can divide the quantum electron states into the bound $E_\perp^j \ll V_0 = \bar{V}_{x,y,z}(x, y, z)$, valence $|E_\perp^j| \approx |V_0|$, and free $E_\perp^j \gg |V_0|$ states.

The attractive feature of the method of Bloch wave in the calculation of the wave function is that, at the conventionally used electron energies $E \approx 100$ keV, the potential wells of the atomic chains are rather shallow and include, as a rule, only several bound states. Thus, the intensity distribution $J(x, y) = |\Psi(x, y)|^2$ on the crystal-lattice images is the thickness-dependent (z is the crystal thickness) superposition of several Bloch waves. It was shown in [10] that, under certain conditions, the lattice image can be formed predominantly by only one of the Bloch waves. Since the quantum energy state $\Psi^j(\mathbf{r})$ is a physical quantity which can often be observed, the nature of the distribution of this state $\Psi^j(x, y)$ inside the unit cell of the crystal allows its physical interpretation. Thus, it is clear that the bound state has the distribution maxima located in the positions determined by the coordinates of the atomic chains, and the minima in the positions between them; therefore, these states are called bound (to the atomic chains). The free states with a high transverse energy $E_\perp$ have a pronounced oscillating nature, which corresponds to an almost uniform distribution of these states inside the unit cell, because the electrons with high energy $E_\perp$ are almost insensitive to the potentials of the atomic chains. The most complicated distributions are characteristic of the states of the valence band; their characteristics include the characteristic features of the distributions of both bound and valence states, which is especially well seen for the states $E_\perp^j \approx -V_0$. As to the valence states

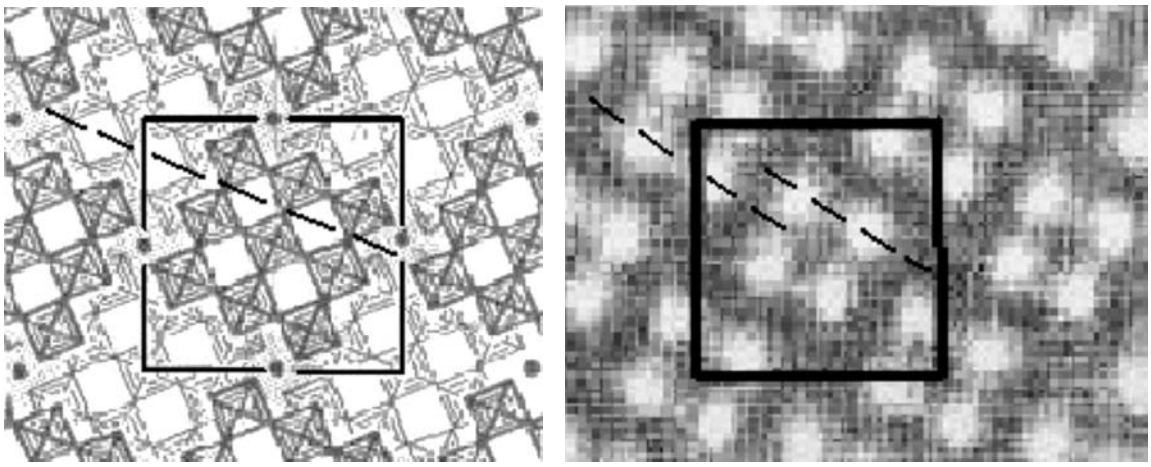

Fig. 1. (a) Structure model and (b) its image [7]; black points represent tetrahedrally located Nb–Ge atomic chains; black and grey squares denote the 3×3 blocks of the ReO_3 structure, the hatched regions indicate the so-called "tetrahedral positions" [7]. Dashed lines indicate the location of the channel.

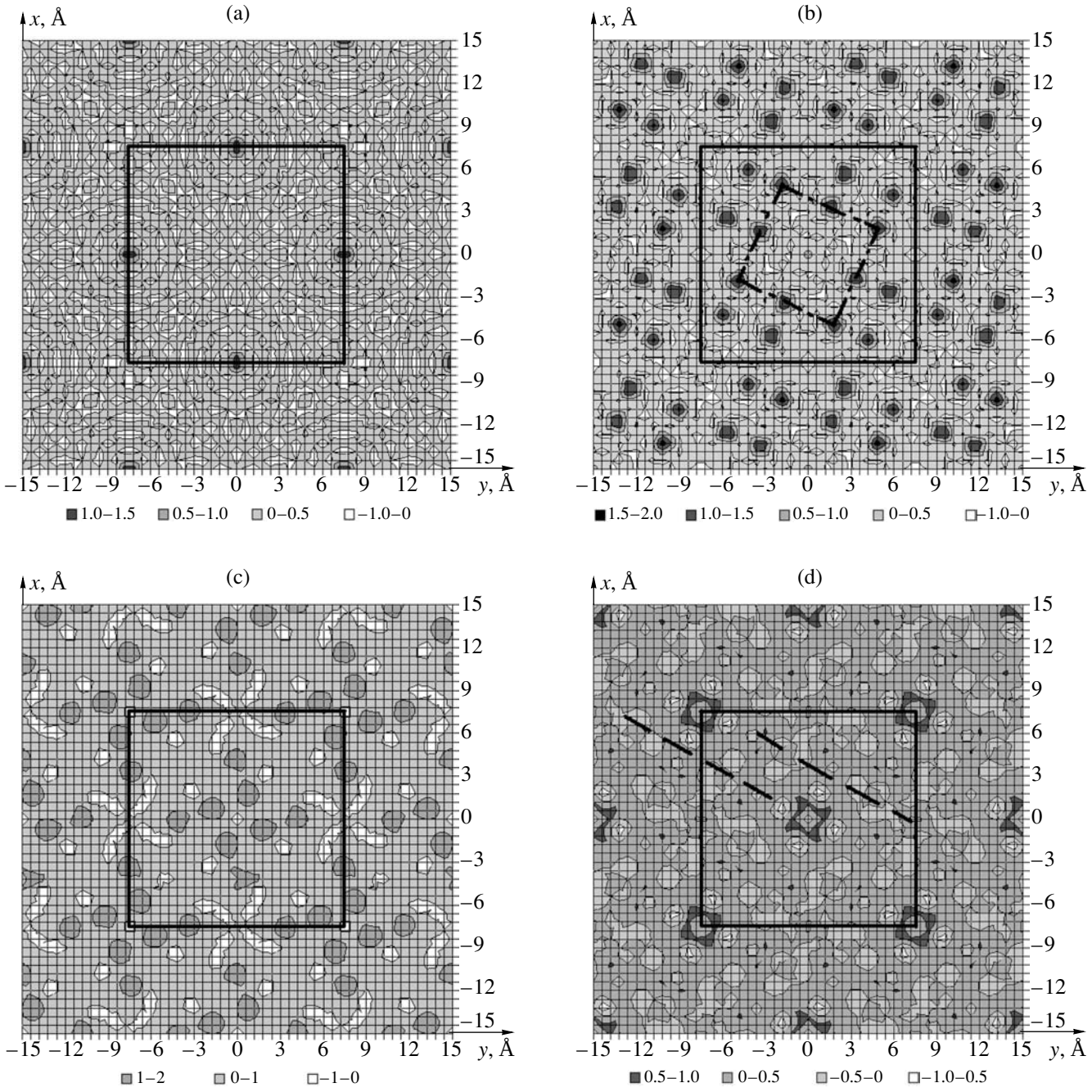

Fig. 2. Distribution of Bloch waves $\Psi^j(x, y)$ in the ⟨001⟩-$GeNb_9O_{25}$ unit cell for various j values: j equals (a) 1, (b) 2, (c) 3, and (d) 4. Solid lines indicate the unit cell. The insets on the right show the contrast gradation. The dashed line shows the position of (b) the 3×3 block and (d) the channel.

with $E_\perp^j > 0$, it is natural to assume that the maxima of the distribution density $|\Psi^j(x, y)|^2$ inside the unit cell can be determined, on the one hand, by the positions of the atomic chains (because the electrons in these states are still feel the attraction to the chains) and, on the other hand, by the positions of the interchain channels (where the electrons are equally attracted to different chains, which provides the conditions for their accumulation in this region).

STRUCTURE OF BLOCH WAVES FOR ⟨001⟩–$GeNb_9O_{25}$

Consider the structure of Bloch waves for the case under consideration. We calculated $\Psi^j(x, y)$ for $GeNb_9O_{25}$ at the electron energy E = 80 keV and N = 114. The main parameters of the Bloch waves are listed in the table. According to these data, the total occupancy of four Bloch states is $\sum_{j=1}^{4} (\Psi_0^j)^2 \geq 0.75$,

Parameters of electron Bloch waves in ⟨001⟩-$GeNb_9O_{25}$ at E = 80 keV and N = 114

Bloch wave, j	1	2	3	4
Excitation amplitude, Ψ_0^j	0.12	0.40	0.70	0.31
Transverse energy, $E_\perp^j$, eV	−155	−77	−10	8

which makes the use of only these waves sufficient for the description of the image with the corresponding accuracy. It should be indicated that the calculated parameters are in good accord with the qualitative conclusion that the highest occupancy is possessed by the states of the valence band [10, 11].

The first and deepest bound state (Fig. 2a) $\Psi^1(x, y)$ localizes the positions of the atomic chains with the highest potential, i.e., the Ge–Nb chains located in the middle of the unit-cell edges (Fig. 1a). Other chains do not localize this state, because their potentials are shallower and, therefore, cannot include such a low-lying level.

The second bound state (Fig. 2b) localizes only the structure of the 3×3 block of the structure schematically shown in Fig. 1a.

It is clear that if, under certain conditions, the image is formed by only one of these waves, the image will show only one of the crystal sublattices—the so-called effect of selective imaging [12] observed experimentally in [13].

The third Bloch state is related to the valence band $E_\perp^3 \sim V_0$ and, therefore, is characterized by a rather complicated distribution (Fig. 2c). It should only be emphasized that the sets of its extrema correspond to the positions of atomic chains in the center and at the vertices of the unit cell. Each of these sets is characterized by the symmetry axis C_4 of the space group of the crystal, $I4/m$, although the sets themselves are arranged according to the symmetry C_4V.

For us, the most interesting distribution is that of the fourth state (valence band) with the positive transverse energy (Fig. 2d).

One can readily see that the positions of the minima of the function $\Psi^4(x, y)$ coincide exactly with the positions of the white spots on the experimental image of the structure (Fig. 1b). In terms of physics, this can be interpreted as follows. The fraction of valence-band electrons with low positive transverse energies, which are in the interchain region (the channel region), is characterized by the maximum distribution density in this region. The position of this maximum is determined by the equivalent forces that attract such electrons to the nearest atomic chains. However, since in this case these chains have different average atomic numbers (i.e., the forces that attract electrons), the maximum of the electron-distribution function, $\Psi^4(x, y)$, does not coincide with the geometric center of the channel and is displaced toward the chains with the maximum atomic numbers.

In the case under consideration, this maximum is displaced toward the Nb–Ge chains (indicated by filled circles in Fig. 1a) with the maximum average atomic number. It can readily be seen that in this case, the channel centers on the $\Psi^4(x, y)$ distribution do not lie on one line any more. Therefore, if under certain conditions the lattice image is formed predominantly by the wave $\Psi^4(\mathbf{r})$ (with the opposite contrast), the corresponding image shows the so-called effect of sublattice displacement. The above consideration allows one not only to reveal the sublattice displacement but also to determine its direction. Thus, if the $\Psi^4(x, y)$ minima are displaced toward the Nb–Ge chains, the line connecting these minima in the 3×3 block should form a smaller angle with the y-axis, which was really observed in experiments.

ACKNOWLEDGMENTS

We are grateful to V.V. Klechkovskaya and E.D. Protsenko for the interest in our work and useful comments, S.V. Nikolaeva for the fruitful cooperation and discussion of the results, and K.L. Sorokina and S.N. Shkornyakov for their cooperation.

The study was supported by the Russian Foundation for Basic Research, project no. 99-03-32811 and the Federal Program on Support of Prominent Scientists and Leading Scientific Schools, project no. 00-15-96580, and the Program on Support of Young Scientists and Post Graduates, project no. 01-03-06347.

REFERENCES

1. B. K. Vainshtein, *Structure Analysis by Electron Diffraction* (Akad. Nauk SSSR, Moscow, 1956; Pergamon, Oxford, 1964).
2. Z. G. Pinsker, *Electron Diffraction* (Akad. Nauk SSSR, Moscow, 1949; Butterworth, London, 1964).
3. B. K. Vainshtein, Usp. Fiz. Nauk **152**, 75 (1987) [Sov. Phys. Usp. **30**, 393 (1987)].
4. H. Hashimoto, Ultramicroscopy **18**, 19 (1985).
5. *Electron Holography*, Ed. by A. Tonomura, L. F. Allard, *et al.* (North-Holland, Amsterdam, 1995).

6. V. L. Vergasov, Kristallografiya **43** (6), 992 (1998) [Crystallogr. Rep. **43**, 934 (1998)].
7. A. J. Skarnulis, I. Sumio, and J. M. Cowley, Acta Crystallogr., Sect. A: Cryst. Phys., Diffr., Theor. Gen. Crystallogr. **A32**, 799 (1976).
8. P. B. Hirsch, A. Howie, R. B. Nicholson, D. W. Pashley, and M. J. Whelan, *Electron Microscopy of Thin Crystals* (Butterworths, New York, 1965; Mir, Moscow, 1968).
9. F. N. Chukhovskii and V. L. Vergasov, Acta Crystallogr., Sect. A: Found. Crystallogr. **A46**, 193 (1990).
10. F. Fujimoto, in *Proceedings of the Fifth International Conference on Nigh-Voltage Electron Microscopy, HVEM, Kyoto, 1977*, p. 271.
11. Yu. Kagan, É. A. Babakhanyan, and Yu. V. Kononets, Pis'ma Zh. Éksp. Teor. Fiz. **31**, 776 (1980) [JETP Lett. **31**, 733 (1980)].
12. V. L. Vergasov, Pis'ma Zh. Tekh. Fiz. **19** (3), 23 (1993) [Tech. Phys. Lett. **19**, 79 (1993)].
13. R. Guan, H. Hashimoto, and T. Yoshida, Acta Crystallogr., Sect. B: Struct. Commun. **C40**, 109 (1984).

Translated by L. Man

Crystallography Reports, Vol. 46, No. 4, 2001, pp. 577–585. From Kristallografiya, Vol. 46, No. 4, 2001, pp. 641–650.

DIFFRACTION AND SCATTERING OF X-RAY AND SYNCHROTRON RADIATION

Dedicated to the memory of B.K. Vainshtein

Electron Microscopy of Carbon Nanotubes*

N. A. Kiselev[1] and D. N. Zakharov

Shubnikov Institute of Crystallography, Russian Academy of Sciences, Leninskiĭ pr. 59, Moscow, 117333 Russia

[1]e-mail: kiselev@ns.crys.ras.ru

Received March 7, 2001

Abstract—High-resolution electron microscopy was used to study multiwall carbon nanotubes obtained by the arc-discharge technique and double- and single-wall nanotubes produced by the arc-discharge catalytic synthesis. The structure of conical layer nanotubes obtained by the CVD technique is characterized in detail. It is established that heat treatment of nanotubes gives rise to their structural changes. The structure of nanotubes obtained by carbon evaporation in the N_2–Ar atmosphere under high pressure is determined. A new type of nano- and microtubes with surface-modulated walls is revealed. Possible applications of carbon nanotubes are reviewed. © *2001 MAIK "Nauka/Interperiodica".*

INTRODUCTION

One of the remarkable features of academician B.K. Vainshtein was his keen interest in everything new in science. We, his students, were infected by his example and also tried to follow new avenues in science. This interest gave us the impetus to study the structure of newly discovered [1] carbon nanotubes.

Carbon nanotubes are built by the so-called graphene layers. A graphene layer is the two-dimensional (2D) section by the (0001) plane of the 3D structure of hexagonal graphite. Depending of the way the graphene layer is rolled up into a tube, different types of nanotubes with different physical properties are formed. Below, we consider some types of nanotubes studied at the Laboratory of Electron Microscopy of the Institute of Crystallography in collaboration with the research Institutions engaged in their preparation. The studies were performed in a Philips EM-430ST electron microscope operated at 200 kV and a Jeol JEM-4000EX operated at 400 kV. The scanning electron microscopy studies were performed by A.B. Ormont on a low-voltage Jeol JSM-840 microscope (Institute of Radioengineering and Electronics of the Russian Academy of Sciences).

1. MULTIWALL CARBON NANOTUBES OBTAINED BY ARC-DISCHARGE TECHNIQUE

Arc-evaporation in the He atmosphere gives rise to the formation of a hard cylindrical deposit on the graphite cathode. Iijima [1] studied this deposit in a transmission electron microscope and revealed a whole range of novel graphitic structures, of which long carbon nanotubes are the most interesting. This publication triggered a large number of studies of the structure, properties and mechanisms of formation of nanotubes.

We started the electron microscopy investigations of these objects with multiwall carbon nanotubes (MWNTs) obtained at the Institute of Problems of Chemical Physics of the Russian Academy of Sciences. The structural components and the organization of carbon cathode deposits obtained under the conditions provided the efficient formation of nanotubes were studied by the methods of transmission electron microscopy (TEM), high-resolution electron microscopy (HREM), and scanning electron microscopy (SEM) [2].

The typical cross-section of a cathode deposit (Fig. 1a) reveals quasihexagonally ordered columnar structure. The columns are about 60 μm in diameter and are separated by low-density 10- to 15-μm-long spacings. Our studies show that the highest nanotube concentration is attained in the low-density intercolumnar spaces and on the side surfaces of the columns. A typical SEM image of the side surface of the intact column taken normally to the column axis (Fig. 1b) shows the structural organization of nanotubes which form the outer braid of the column. It consists predominantly of interlaced nanotubes and their bundles. A considerable part of nanotubes forming the braid lie within the angular range of 45°–75° with respect to the column and deposit axes.

An SEM image of nanotube bundles found in the space between the columns is shown in Fig. 1c. The inner part of the column inside the braid consists of various forms of graphite mixed with multilayer polyhe-

* This article was submitted by the authors in English.

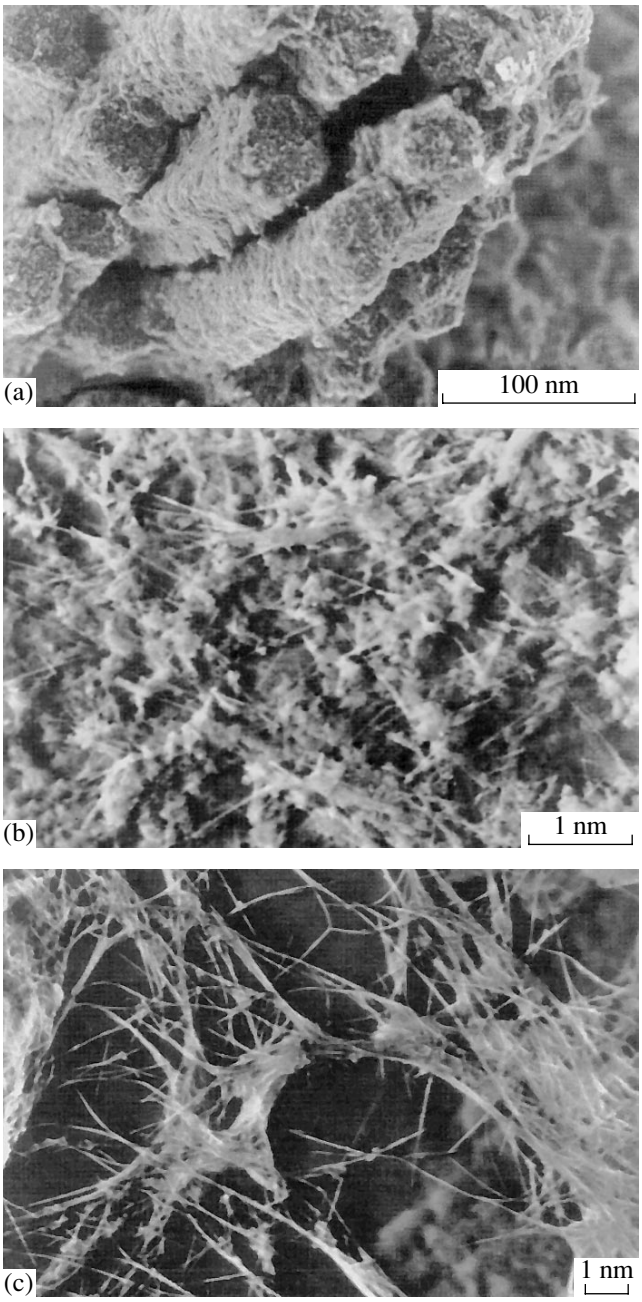

Fig. 1. SEM images of the cross section of the carbon deposit. (a) Columnar structure. (b) Lateral surface of an individual column. One can see the groups of tubes inclined to the growth axis by an angle of ~70° (the vertical line). (c) Tubes found in the space between columns. Reprinted from [2] with permission from Elsevier Science.

dral particles (MPPs) and small number of randomly oriented nanotubes. Similar columns were also observed in the deposits containing small numbers of nanotubes. Thus, the formation of columnar structures in the deposits is not the only condition for obtaining nanotubes. It can be assumed that nanotubes grow preferably on the column surfaces providing the favorable growth conditions, e.g., the suitable growth temperature. The structure of the deposit established in the present study is inconsistent with the hypothesis about the alignment of tubes along their axis, which is an essential requirement of the model proposed in [3].

The specimens for TEM and HREM studies were prepared by dispersing the core part of the deposits in acetone with the use of an ultrasonic bath. Three distinct structural components have been observed: MWNTs, MPPs, and various kinds of graphitic particles [2]. MWNTs are covered by hemispherical, conical or faceted caps; the latter variant is shown in Fig. 2a. These caps are formed only if pentamers of carbon atoms are formed inside the hexagonal net. The pentagons must also be formed at the MPP vertices (Fig. 3).

To obtain pure MWNT specimens, it is necessary to remove side products. The technique of MWNT purification based on specimen oxidation was developed in [4, 5]. Oxidation selectivity was provided by graphite intercalation with bromine. Etching selectivity was maintained by alternation of oxidation and intercalation with bromine. As a result, oxidation in the sites of distortion of C–C bonds, MPP vertices (Fig. 3), and nanotube caps attacked the polyhedral particles and burn them away. Figure 2a shows MWNT before oxidation and Fig. 2b shows similar MWNT after oxidation. It is possible to see that the cap is completely destroyed along with some of the outer graphene layers. The fragments of destroyed graphene layers fill the inner channel of the nanotube. Figure 4 shows TEM image of MWNTs after the oxidation treatment at a low magnification; one can see that a very high degree of purification is achieved.

2. SINGLE-WALL CARBON NANOTUBES OBTAINED BY ARC-DISCHARGE CATALYTIC SYNTHESIS

Single-wall carbon nanotubes (SWNTs) were first prepared by simultaneous evaporation of graphite and cobalt [5]. The SWNTs studied here were obtained at the Institute of Problems of Chemical Physics of the Russian Academy of Sciences. A channel (1 mm in diameter) drilled in the anode was filled with the mixture of Co, Ni, and C powders. As a result of arc evaporation in the He atmosphere, chamber walls are coated with a material consisting of soot, catalytic particles, and SWNTs.

The SWNTs form bundles consisting of a few dozen nanotubes. One of these bundles is shown in Fig. 5a. The upper part of the micrograph shows that the bundle consists of smaller bundles. At the site of bundle bending, one can see the nanotube fragments located along the axis. The SWNT diameter is 1.4 nm. In many instances, SWNTs “grew” radially from the catalytic particles and formed hexagonal packings with distances between the SWNT axes equal to 1.65 nm. The SWNT were purified using the special technique com-

bining two processes—treatment in acids and oxidation.

3. DOUBLE-WALL CARBON NANOTUBES

One of the principal goals of the technology of nanotube synthesis is the synthesis of only one of numerous types of carbon nanotubes, which is necessary for establishing the correlation between the structural type of nanotubes and its physical properties (electric and heat conductivities, various mechanical properties, etc.). The synthesis of only one type of nanotubes is also important for the verification of new theories.

It was decided to use not the He atmosphere but the mixed argon–hydrogen atmosphere (350 torr) and the catalysts prepared from the mixtures of Ni, Co, Fe and S powders. (This part of the study was performed in cooperation with the Institute of Problems of Chemical Physics of the Russian Academy of Sciences.) The HREM micrographs in Fig. 5b shows that most of the tubes consist of two concentric cylindrical graphene layers forming double-wall nanotubes (DWNTs) [6, 7]. Usually, the outer diameter of a DWNT ranges within 1.9 and 5 nm. The DWNTs are easily deformable. The interlayer distance measured from the tubule-wall image is 0.39 ± 0.02 nm; i.e., it exceeds that usually observed (0.34 nm) for MWNTs.

At the similar arc parameters, the temperature of the carbon plasma in Ar is considerably lower than in the He atmosphere. The temperature in the Ar arc is assumed to range within 2400–2600 K and is too low for anode evaporation of graphite. However, adding H_2 to the Ar atmosphere, one can substantially increase the rate of anode evaporation.

4. CARBON NANOTUBES FORMED BY CONICAL GRAPHENE LAYERS

Different aspects of the structure of carbon filaments and nanotubes are considered in numerous publications, e.g., [8–12]. It should be emphasized that many papers to the effect were published long before the Iijima discovery [1]. Some of the filaments described in these publications could be classified as nanotubes in accordance with their diameter. However, nanotubes obtained by the catalytic method have an imperfect structure in comparison with fullerene-related tubes observed by Iijima. These imperfect structures cannot be used (with some exceptions) in a way possible for MWNTs, DWNTs, and SWNTs.

We have studied the structure of carbon nanotubes obtained by the CVD method in the presence of the nickel catalyst at the Physical-Technological Institute in Kazan [13, 14]. The nanotubes had two main structure types. Type-I nanotubes (Fig. 6) are formed by open conical graphene layers stacked together and are, in fact, conical layer nanotubes (CLNTs). Their high-resolution micrographs show fringes corresponding to the projections of side walls of conical tubes. The interfringe spacing is 0.34 nm. The cone angle is defined as a double angle between these fringes and the tube axis and equals 6°–35°. Type-I nanotubes resemble the "bamboolike" tubes observed in [15].

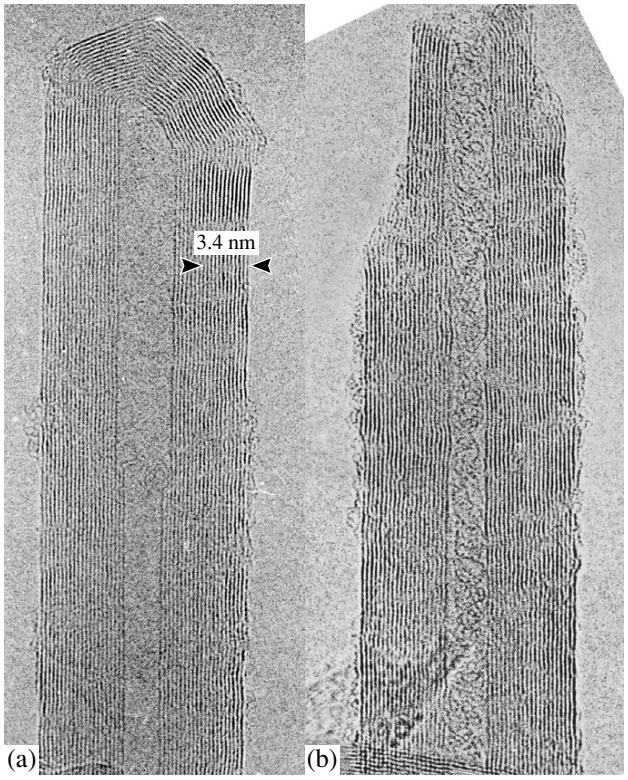

Fig. 2. Multiwall carbon nanotubes (MWNTs). (a) Tube with polyhedral cap. (b) MWNT after selective oxidation.

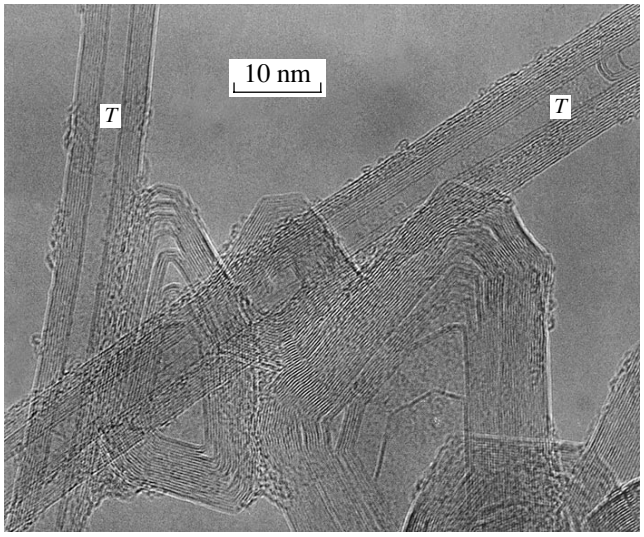

Fig. 3. Multilayer polyhedral particles and MWNTs (denoted by the letter *T*) prior to selective oxidation.

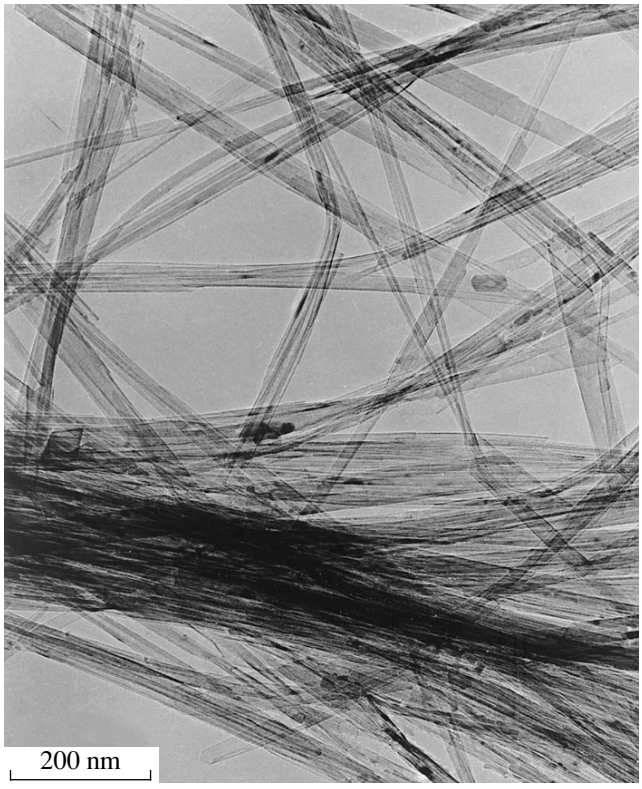

Fig. 4. Specimen of MWNTs upon selective oxidation and bromidization.

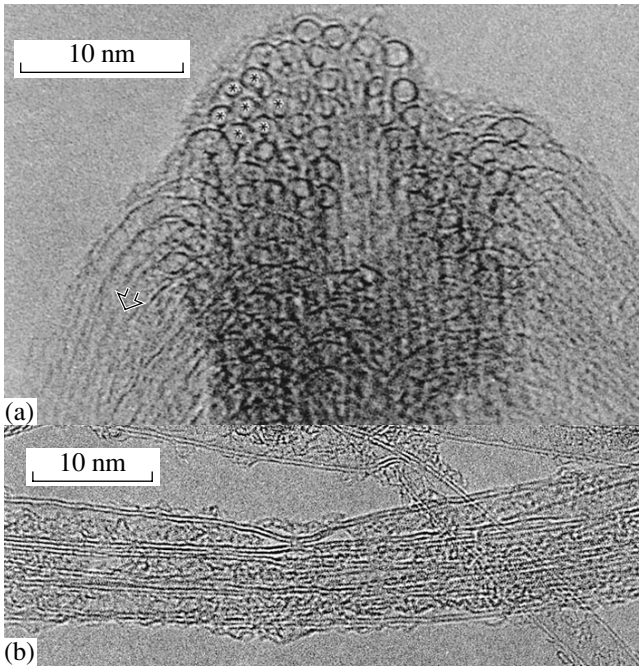

Fig. 5. (a) Bundle of SWNTs with a diameter of 1.4 nm. (b) Double-wall carbon nanotubes (DWNTs).

The characteristic feature of type-I nanotubes is open outer edges of conical graphene sheets. Many inner edges are also open, but some of them are linked by inner caps. Thus, in type-I nanotubes, the inner channel is not continuous—it is disrupted by caps. Tube walls and caps form chains of nanoballoons connected with the outer medium by interplanar spacings of the conical graphene layers. Nanotubes of type I were observed mainly at the Ni-substrate temperature ranging within 850–900°C.

Heat treatment of nanotubes in a vacuum at 1000–1400°C and the subsequent 1-h-annealing in the argon atmosphere at 1200, 2000, and 2800°C resulted in the removal of Ni catalytic particles and the modification of the microstructure. A type-I nanotube upon heat treatment at 2800°C is shown in Fig. 7. The characteristic feature of the modified microstructure is the formation of loops between the neighboring edges of graphene layers. Usually, these loops are formed either by one or several carbon layers. The degree of carbon-layer linking depends on the temperature of the heat treatment. Thus, after heat treatment at 1200°C, only a relatively small number of linked layers were observed. It is natural to assume that thermal treatment of type-I nanotubes considerably reduce the ability of gases to penetrate the inner volume of nanotubes (nanoballoons).

Type-II nanotubes are characterized by much larger cone angle (75°–80° and, in some cases, even up to 110°). After heat treatment, the shape of type-II nanotubes is not changed. Most of the inner edges are linked by loops (Fig. 8). Type-II nanotubes are usually observed at the temperature of the Ni foil equal to 600°C. These tubes resemble “fish-bone” nanotubes [16].

The early model of the mechanism of formation of carbon nanofibers was developed by Baker *et al.* [8]. The key stages of this mechanism are adsorption and decomposition of hydrocarbon on the surface of the catalyst with the yield of carbon, which is dissolved and diffuses through the bulk of the catalyst particle and, finally, precipitates at the back side of the particle to form nanotubes (or graphene layers).

Our HREM studies of almost 50 catalytic particles showed that they could be divided into three groups. At the periphery of the completely open particles, the outer polycrystalline layers were observed (Fig. 9). It was shown that the regions A and B (Fig. 9) correspond to the (201) and (113) planes of Ni_3C. The region C could tentatively be interpreted as the (111) and (200) planes of NiO.

The particles partly covered with graphene layers had no such formations except for “open” regions. Particles encapsulated with layers had no outer polycrystalline formations. The central part of these particles corresponded to the Ni lattice.

We assume that the information about the microstructure of catalytic particles is consistent with mech-

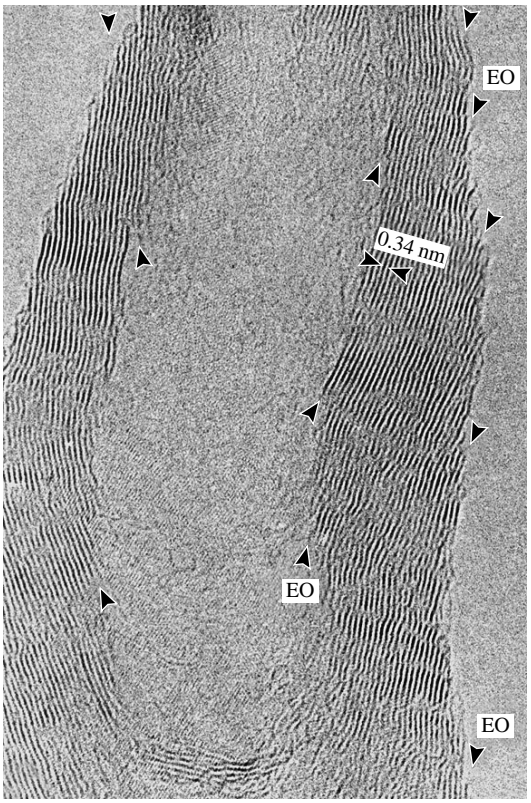

Fig. 6. Type-I conical layer nanotube (CLNT). EO indicates the edges of open graphene layers. Fringes are spaced by 0.34 nm. Reprinted from [13] with permission from Elsevier Science.

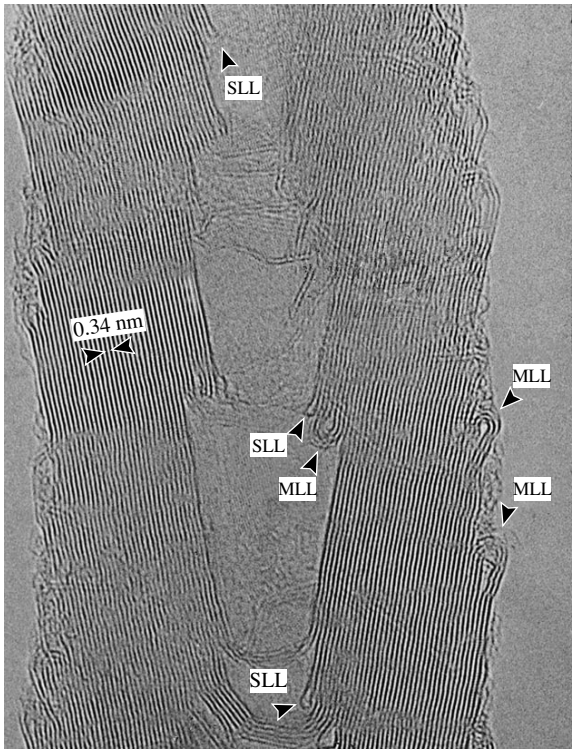

Fig. 7. Type-I heat treated CLNT. MLL are multilayer loops, SLL are single layered loops. Reprinted from [13] with permission from Elsevier Science.

anism proposed in [8, 9]. The formation of a Ni_3C nanocrystal pointed out that carbon penetrate deep into a Ni particle. If the particle is completely coated with the layers, accumulation of carbon is blocked and carbides are dissociated.

5. SURFACE MODULATED NANO- AND MICROTUBES

The experiments on resistive graphite evaporation under high gas pressure (nitrogen or nitrogen–argon mixture under the pressure of up to 1300 atm) were performed at the Technological Institute for Superhard and Novel Carbon Materials. The source of carbon vapor was the central zone of the heater with the maximum temperature 2250°C. The screen was designed in such a way that only small amount of iron was supplied to the system. Upon the experiments, black "cotton" was deposited at cool places of the heater and at the thermal screen.

The TEM examination of this black material revealed wide spectrum of nano- and microtubes of different types, including conical layer carbon nanotubes and multiwall carbon nanotubes with the pseudoperiodic variation of tube diameter and wall thickness. All these tubes had the same principle of structural organi-

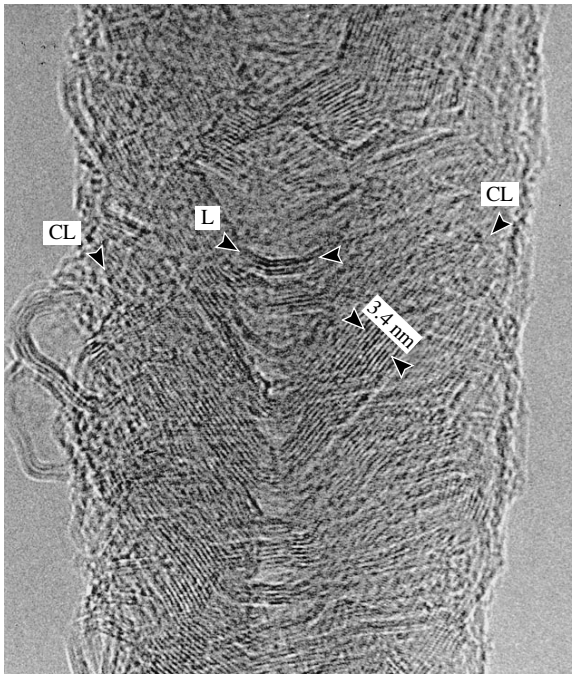

Fig. 8. Type-II CLNT. CL are the sets of conical layers. Reprinted from [13] with permission from Elsevier Science.

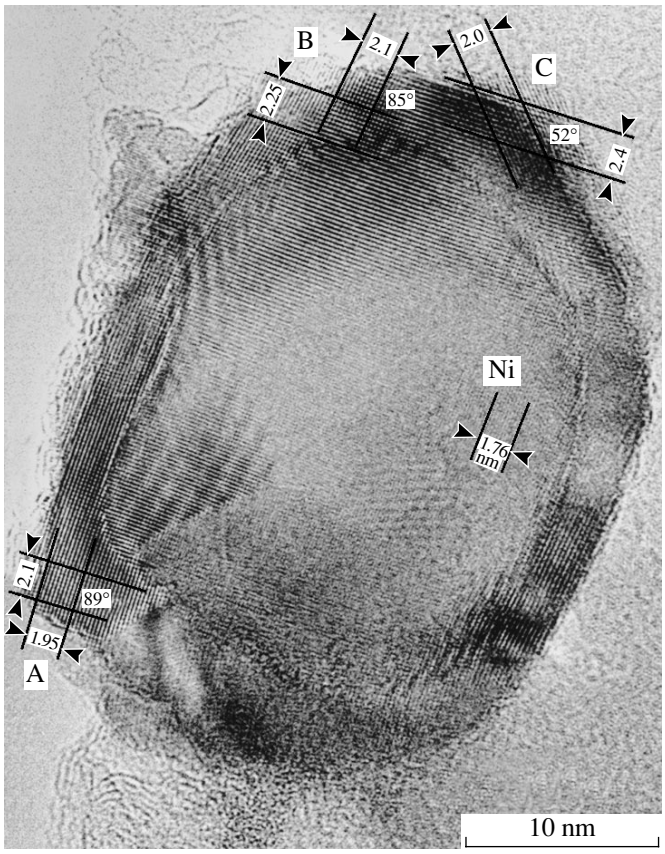

Fig. 9. Ni catalytic particle not covered with graphene layers. The regions A and B of the outer polycrystalline layer most probably correspond to Ni_3C and the region C is assumed to be NiO. Reprinted from [13] with permission from Elsevier Science.

zation—the main part of the tube wall was formed by continuous graphene layers with the adjacent layers of inner caps. Taking into consideration these features, we propose to refer to these new types of tubes as to surface-modulated nano- and microtubes, i.e., SMNTs and SMMTs, respectively [17, 18].

The TEM image of an SMNT is shown in Fig. 10. The tube diameter in this case varied from ~180 nm to 158 nm and pseudoperiodicity ranged within 90–130 nm. These SMNTs had pronounced inner caps, some of which were 2–4 times thicker than the outer walls. Caps had similar orientations, in full accordance with the motion of catalytic particles. The side part of thick caps partly formed the tube wall. This rigid part is connected with the thin flexible part of the wall. Some inner caps were faceted.

Figure 11 shows the HREM image of the cap/wall interface. The cap is formed by about 60 layers, whereas the wall, by only 10 layers. At the site of their junction, there are 70 layers. At the distance of 35–40 nm from the junction, the number of layers sharply decreases to their initial number in the wall. A small number of nanotubes are formed by five to twelve almost spherical graphene layers. In this case, the wall layers are complemented with those of the cap, but their number gradually reduces back to the initial number.

Considering the SMNT microstructure, one can assume that they are formed at melted spherical particles of the Fe catalyst in the way schematically shown in Fig. 10. (*1*) The first hemispherical graphene layer is formed as is described in [8]; (*2*) in the space between the first layer and the particle, new layers form an inner cap with well-developed side regions; (*3*) gradually, the new layers deformed the particle; (*5*, *6*) these new layers force the particle to move into a new position, where it becomes spherical again (*3*). In the case of SMNTs with "spherical" walls, the catalytic particles are assumed to move at a higher velocity and the inner caps do not have enough time to acquire a multilayer structure.

Along with SMNTs, we also observed different surface modulated microtubes with diameters up to 1000 nm. The SMNT having a moderate diameter (D_{min} = 350 nm, D_{max} = 370 nm) and a pseudoperiodicity of 260–480 nm is shown in Fig. 12a. The wall thickness varies from 18 to 22 nm depending on the position of the inner caps. Single "open" graphene layers are seen on a HREM image on the outer and the inner sides of the tube-wall profile (Fig. 12b). HREM studies of the junction of the inner caps with the tube wall marked with the letters B, C, and D showed that the number of layers increased in the junction site. Then it gradually decreased. The junction B is shown in Fig. 12b. There are 55 graphene layers in the wall at a distance of 160 nm above the junction and 10 layers in the cap joining the wall layers. At a distance of 150 nm below the junction, the number of layers increased up to 58. The total length of the region B studied by HREM is 310 nm. Most of the layers in the wall can be seen from the beginning of this region to its end. The extreme outer and inner layers extending over the whole 310-nm-long region on the image are indicated by asterisks. Most interlayers between these two are also continuous and taken together from a continuous layered structure. However, a few layers in this structure are abruptly terminated, which can be the mechanism for changing the diameter of the tube wall.

In the case of SMMTs, the catalytic particles might be of almost cylindrical shape. Carbon layers are formed on the lateral and back sides of the particles. However, the distance to the back part of the particle is larger than to its side parts and less carbon can reach this surface. That is why the inner caps in SMMTs are either very thin or even absent.

6. SOME APPLICATIONS OF CARBON NANOTUBES

Many types of carbon nanotubes have the diameter less than 10 nm (for SWNTs and DWNTs, it is about 1–5 nm). Nanotubes fall into the size range, where the

quantum effect become important; therefore, one can foresee remarkable properties of such nanotubes [19]. By this moment, many experimental studies of physical properties of carbon nanotubes and the ways of their possible application have been performed.

One of the possible MWNT application is associated with their unique mechanical properties. These nanotubes have already been used as tips for STM [20], where a single 1-μm-long MWNT was glued to the Si cantilever. Later, such nanotubes were grown directly on the cantilever of an atomic-force microscope (AFM) [21].

The first quantitative measurements of the mechanical properties of nanotubes were made on a TEM [22]. The nanotubes were deposited onto TEM grids. The specimens were located on a special holder, which enabled *in situ* heating to the temperature up to 800°C. Analyzing the amplitude of nanotubes motion depending on temperature, one managed to determine the Young's modulus (1800 GPa). A few experiments on deformation of fixed MWNTs were made with the use of the AFM probe [23]. In these experiments the bending force of nanotubes was studied as a function of displacement [23]; Young's modulus was determined to be 1.28 GPa. If these data are correct, the carbon nanotubes have the highest hardness among all known materials [19].

Taking into account the remarkable mechanical properties of carbon nanotubes, they should be considered among the first candidates being incorporated into composite materials [19].

There are two possible highly symmetric structures for nanotubes, known as the "zigzag" and "armchair" structures (see, for example, [19]). It is believed that in most nanotubes, hexagons are helically arranged around the axis. These structures are generally known as chiral. The nanotube structure is specified by the vector $\mathbf{C}_h = n\mathbf{a}_1 + m\mathbf{a}_2$, where (n, m) is a pair of integers and $\mathbf{a}_1$ and $\mathbf{a}_2$ are the basis unit-cell vectors of the graphene sheet. For all the zigzag tubes, $m = 0$; for the armchair tubes, $n = m$. The measurements performed on single SWNTs by the combined STM and scanning-tunneling spectroscopy methods showed that most of SWNTs are really chiral. The chiral tubes were found to be either semiconductor or metallic ones [24]. In [25], a field-effect transistor is described, which consists of a semiconductor SWNTs connected with two Pt electrodes on a Si/SiO_2 substrate. The transistor image was obtained with the aid of an atomic-force microscope.

Taking into consideration the high conductivity, the small diameter, and the considerable length of nanotubes, one can predict their usefulness in field emitters. Some of the pioneering studies on field emission from nanotubes are considered elsewhere [19]. The field emission experiments have been performed on individual tubes and on arrays of nanotubes.

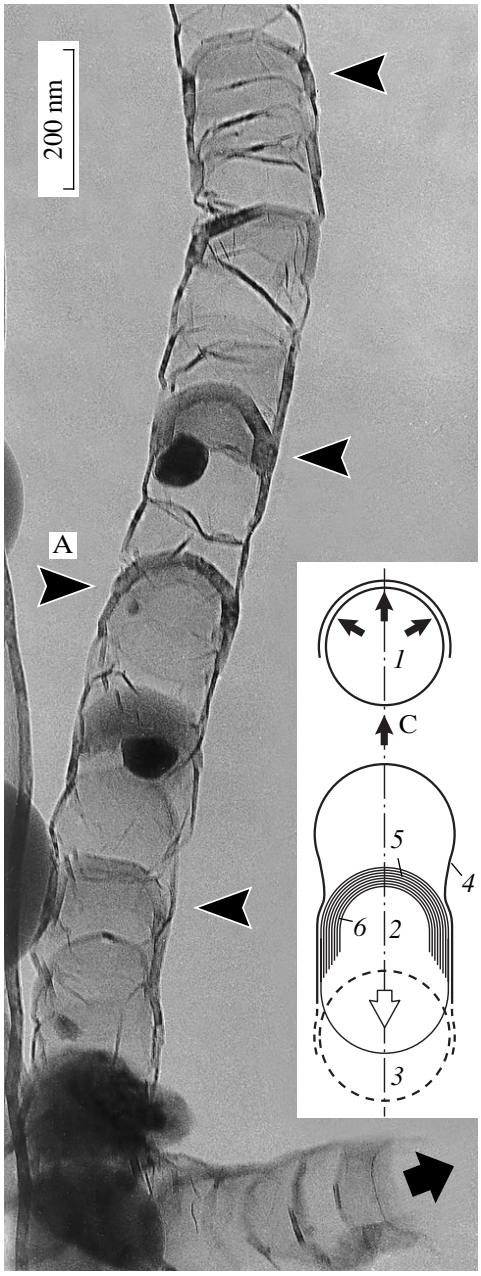

Fig. 10. Surface-modulated carbon nanotube (SMNT). Arrows indicate the inner caps which are several times thicker than the tube walls (the cap A is shown in Fig. 11). Scheme represents a tentative mechanism of formation of SWNT: (*1*) original spherical melted catalytic particle; (*2*) particle deformed by the inner carbon cap (*5*) and its side region (*6*); (*3*) the catalytic particle in a new position; (*4*) the continuous part of the wall. Black lines represent from four to ten graphene layers. Reprinted from [18] with permission from Elsevier Science.

Our investigation shows that in the case of type-I CLNTs, many nanotube ends are free from the catalytic particles. The walls of such nanotubes are ended with one to three graphene-layer edges, whose total thickness is less than 1 nm. Thus, one can assume that the

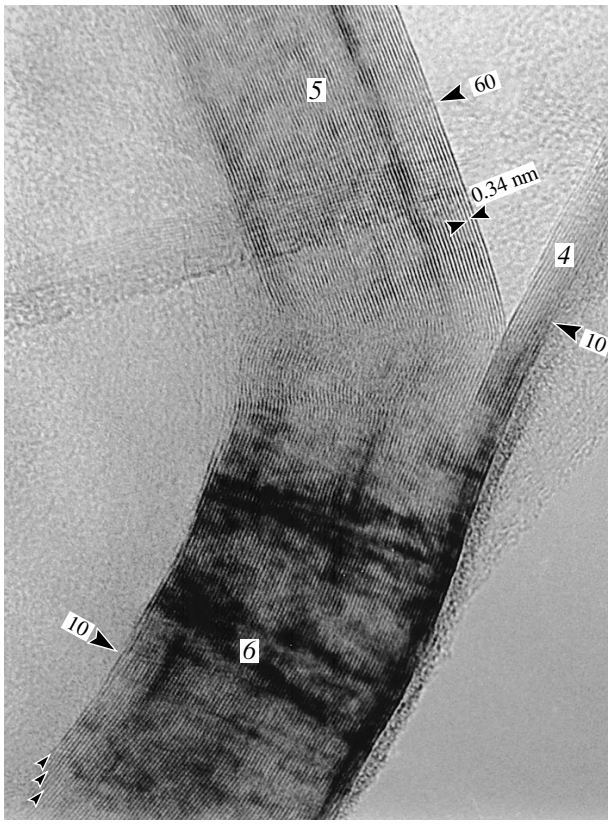

Fig. 11. HREM image of the inner cap A shown in Fig. 11. Enlarged right side of the cap. Numbers 4, 5 and 6 correspond to the continuous part of the wall, inner cap and its side region (see drawing in Fig. 10). Reprinted from [18] with permission from Elsevier Science.

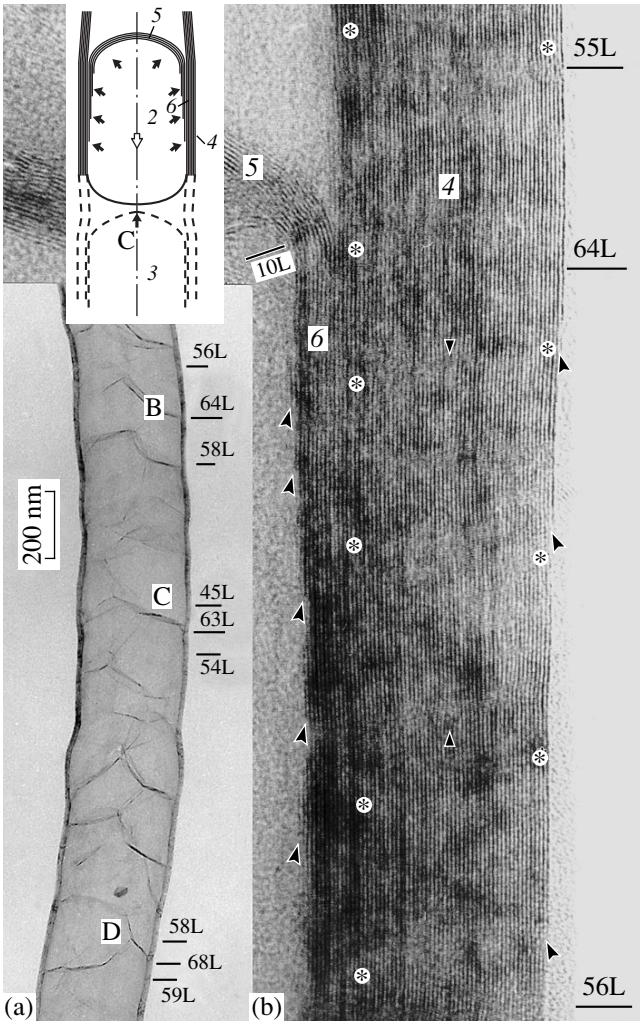

Fig. 12. Surface modulated carbon microtube (SMMT). (a) Low magnification TEM image. B, C, and D are the regions of inner caps junctions with the tube wall investigated by HREM. The number of graphene layers (L) is obtained from HREM. (b) Central part of region B in (a). Scheme shows the possible formation mechanism of an SMMT. Reprinted from [18] with permission from Elsevier Science.

coefficient β, inversely proportional to the curvature radius of such structure, should be quite pronounced.

Emission properties of type-I CLNTs layers grown on polished Ni foil at temperatures of 850–900°C were studied at the Moscow Institute of Radioengineering and Electronics. Experiments show that $E_{av} = V/d$ (where V is the voltage applied, d is the electrode–film distance) and is equal to 2–5 V/μm at β = 1000–1600 [26].

Even better characteristics (E_{av} = 1.1; β = 1600) were obtained for SWNT-based composite layers [27]. Possibly, some small SWNTs emerge to the layer surface.

One more useful feature of some types of nanotubes is their ability to absorb gases and keep them for quite a long time. Thus, it was shown [28] that SWNTs can accumulate up to 4.2 wt % of hydrogen. Type-I CLNTs can also be efficiently used for accumulating hydrogen [29].

The synthesis of one-dimensional (1D) crystals can be very important for physics and materials science. With this aim, it is very useful to encapsulate them into SWNT. In [30], SWNTs having a diameter of 1.6 nm were filled with the KI melt with the aid of a capillary method [31]; KI was mixed with SWNTs and was heated for two hours at 954°C. On the micrographs obtained along the ⟨110⟩ direction, with the ⟨001⟩ direction being parallel to the tube axis, one observes SWNTs containing KI crystals. Measurements of lattice spacings show a longitudinal contraction of KI crystal (from 0.705 to 0.695 nm) along ⟨001⟩, whereas in the cross section the lattice expansion and distortion is observed. It can be caused by the adaptation of the crystal to the radially symmetrical van der Waals surface of the confined SWNTs. Individual K and I atoms were identified from a phase image reconstructed with a modified-focal-series-restoration approach. According to HREM [32], KI forms in SWNTs with a diameter of 1.4 nm crystals consisting of two atomic layers.

CONCLUSION

The first monograph on carbon nanotubes is entitled "Carbon Nanotubes and Related Structures: New Materials for the 21st Century" [19]. Despite such an ambitious title, the author admits that it is hardly possible to foresee the future development of the science on nanotubes. The progress in this field depends on many factors, including economical factors (the reduction of the nanotube price) and the establishment of their new properties important for the fundamental science.

In conclusion, the following can be said. The nanotubes were discovered with the help of HREM, which is still the most efficient method for both studying nanotube structure and solving various technological proposes. The SEM method is an indispensable tool for surface studies of nanotube-based flat field emitters. Atomic force microscopy allows the observation of the atomic structure of SWNTs, i.e., the establishment of the helix parameters.

HREM still has many urgent interesting problems to be solved for nanotubes. One of the tendencies is seen in the study of one-dimensional crystals grown inside SWNTs. Here, it is necessary not only to work at the maximum possible resolution but also to solve the phase problem and to use the method of 3D-reconstruction seriously studied by B.K. Vainshtein for macromolecular structures.

ACKNOWLEDGMENTS

The authors should like to thank for cooperation A.S. Kotosonov (State Research Institute of Graphite), A.L. Musatov, A.B. Ormont (Institute of Radioelectronic Engineering and Electronics, RAS), A.V. Krestinin, A.P. Moravskiĭ (Institute of Problems of Chemical Physics, RAS), E.F. Kukovitskiĭ (Physical-Technological Institute, Kazan), V.B. Blank, and E.V. Polyakov (Technological Institute For Superhard and Novel Carbon Materials).

The study was supported by ISTC Projects 079 and 1024, and Russian Foundation for Basic Research, project no. 00-15-96580.

REFERENCES

1. S. Iijima, Nature **354**, 56 (1991).
2. N. A. Kiselev, A. P. Moravskiĭ, A. B. Ormont, and D. N. Zakharov, Carbon **37**, 1093 (1999).
3. D. T. Colbert, J. Zhang, S. M. McClure, *et al.*, Science **226**, 1218 (1994).
4. D. N. Zakharov, A. P. Moravskiĭ, and N. A. Kiselev, in *Proceedings of the Second National Conference on Application of X-ray, Synchrotron Radiation, Neutrons and Electrons to Study of Materials, RSNÉ-99, 1999*, p. 299.
5. D. C. Bethune, C. H. Kiang, and M. S. de Vries, Nature **365**, 605 (1993).
6. D. N. Zakharov, N. A. Kiselev, A. V. Krestinin, *et al.*, in *Proceedings of the 18th Russian Conference on Electron Microscopy, Chernogolovka, 2000*, p. 76.
7. J. L. Hutchison, N. A. Kiselev, E. P. Krinichnaya, *et al.*, Carbon **39**, 761 (2001).
8. R. T. K. Baker, M. A. Barber, P. S. Harris, *et al.*, J. Catal. **26**, 51 (1972).
9. G. G. Tibbets, J. Cryst. Growth **66**, 632 (1984).
10. E. Boellaard, D. K. DeBokx, Z. H. M. Kock, and J. W. Geus, J. Catal. **96**, 481 (1985).
11. P. E. Nolan, M. J. Schabel, D. C. Lynch, and A. H. Cutler, Carbon **33**, 79 (1995).
12. N. M. Rodríguez, A. Chambers, and R. T. Baker, Langmuir **11**, 3862 (1995).
13. N. A. Kiselev, J. Sloan, D. N. Zakharov, *et al.*, Carbon **36**, 1149 (1998).
14. D. N. Zakharov, C. P. Izraél'yants, N. A. Kiselev, *et al.*, in *Proceedings of the 18th Russian Conference on Electron Microscopy, Chernogolovka, 2000*, p. 77.
15. Y. Saito and T. Yoshikawa, J. Cryst. Growth **134**, 154 (1993).
16. X. K. Wang, R. O. Loutfy, J. C. Withers, *et al.*, in *Proceedings of the MRC'95 Fall Meeting, Boston, 1995.*
17. D. N. Zakharov, N. A. Kiselev, A. B. Ormont, *et al.*, in *Proceedings of the 18th Russian Conference on Electron Microscopy, Chernogolovka, 2000*, p. 78.
18. V. D. Blank, I. G. Gorlova, J. L. Hutchison, *et al.*, Carbon **38**, 1217 (2000).
19. P. D. Harris, *Carbon Nanotubes and Related Structures: New Materials for the 21st Century* (Cambridge Univ. Press, Cambridge, 1999).
20. H. Dai, J. H. Hafner, A. G. Riniler, *et al.*, Nature **384**, 147 (1996).
21. J. H. Hafner, C. L. Cheung, and C. M. Lieber, Nature **398**, 761 (1999).
22. M. M. J. Treacy, T. W. Ebbesen, and J. M. Gibson, Nature **381**, 678 (1996).
23. E. W. Wong, P. E. Sheehan, and C. M. Lieber, Science **277**, 1971 (1977).
24. J. W. C. Wildoer, C. Venemal, A. O. Rinzler, *et al.*, Nature **391**, 59 (1998).
25. S. J. Tans, A. R. M. Verschueren, and C. Dekuer, Nature **393**, 49 (1998).
26. A. L. Musatov, N. A. Kiselev, D. N. Zakharov, *et al.*, in *Abstracts of IEEE International Vacuum Electron Sources Conference, 2000*, p. 43.
27. J. M. Bonnard, J. P. Salvetat, T. Stökli, *et al.*, Appl. Phys. A **A69**, 2680 (1999).
28. C. Liu, Y. Y. Fan, M. Liu, *et al.*, Science **286**, 1127 (1999).
29. A. Chambers, C. Park, R. T. K. Baker, and N. M. Rodríguez, J. Phys. Chem. **122**, 4553 (1998).
30. R. R. Meyer, J. Sloan, R. E. Dunin-Borkowski, *et al.*, Science **289**, 1324 (2000).
31. J. Sloan, D. M. Wrigh, H. G. Woo, *et al.*, J. Chem. Soc. Chem. Commun. **1999**, 699 (1999).
32. J. Sloan, M. C. Novotny, S. R. Bailey, *et al.*, Chem. Phys. Lett. **329**, 61 (2000).

Crystallography Reports, Vol. 46, No. 4, 2001, pp. 586–595. Translated from Kristallografiya, Vol. 46, No. 4, 2001, pp. 651–660.

DIFFRACTION AND SCATTERING OF X-RAY AND SYNCHROTRON RADIATION

Dedicated to the memory of B.K. Vainshtein

Small-Angle X-ray Scattering Study of the Structure of Self-Organized Polymer Matrices and Formation of Imbedded Metal Nanoparticles

D. I. Svergun[1, 2], É. V. Shtykova[1], M. B. Kozin[1], V. V. Volkov[1], P. V. Konarev[1], A. T. Dembo[1], E. V. Shtykova, Jr.[1], L. M. Bronshtein[3], D. M. Chernyshov[3], O. A. Platonova[3], A. N. Yakunin[3], P. M. Valetsky[3], and A. R. Khokhlov[3, 4]

[1] *Shubnikov Institute of Crystallography, Russian Academy of Sciences, Leninskiĭ pr. 59, Moscow, 117333 Russia*

[2] *European Molecular Biology Laboratory (EMBL), Hamburg Outstation, Notkestrasse 85, Hamburg, D-22603 Germany*

[3] *Nesmeyanov Institute of Organoelement Compounds, Russian Academy of Sciences, ul. Vavilova 28, Moscow, 117813 Russia*

[4] *Physics Faculty, Moscow State University, Vorob'evy gory, Moscow, 119899 Russia*

e-mail: dsv@ns.crys.ras.ru

Received March 6, 2001

Abstract—The structures of self-organizing polymer matrices based on collapsed gels and polyoctadecylsiloxanes have been studied by the methods of conventional and anomalous X-ray small-angle scattering with the use of the laboratory and synchrotron sources of X-ray radiation. The process of formation of metal nanoparticles in such matrices is also studied, their size distributions are calculated, and the models of localization of these particles in the polymer matrices are suggested. It is shown that growth of metal particles is controlled by the structure of the polymer network and is limited by the dimensions of its cells. The electron-density profiles of polycondensed octadecylsiloxane matrices are also calculated. © *2001 MAIK "Nauka/Interperiodica".*

INTRODUCTION

In recent years, the small-angle X-ray scattering (SAXS) has become a highly informative efficient method and, for some systems, the only possible method of studying supramolecular structure both in the solid state and in solutions of various concentrations [1, 2]. An important field of SAXS application is the structural study of polymer compounds. As an object of investigation, polymers are characterized by a number of features, of which polydispersity is one of the most important. Therefore, the structure analysis of polymer systems is performed by specially developed techniques for collection and interpretation of the SAXS data, which considerably differ from the traditional methods of the structure analysis of monodisperse compounds [1–6]. Since these techniques and methods allow the simultaneous determination of the structural characteristics of the material and the size distribution of various inhomogeneities in this material, it was natural to use the SAXS method for studying the structures of self-organizing polymer matrices and the processes of formation of metal nanoparticles in these matrices.

One of the most efficient methods for studying metal-containing systems is the anomalous small-angle X-ray scattering with the use of synchrotron radiation [7, 8]. Recording the small-angle scattering curves obtained at the X-ray beam energies close to the absorption edge of the metal, one can separate scattering from metal atoms and scattering from the polymer matrix. The analysis of the contribution of each component allows the calculation of the size distribution of metal particles formed and the study of the internal structure of the polymer complex.

The idea to form metal nanoparticles in a polymer medium first arose in the study of stable self-organizing complexes of polyelectrolyte gels with oppositely charged surfactants or the so-called collapsed gels. The small-angle X-ray scattering data showed that these complexes possess a well-pronounced regular structure [9–13]. It could be assumed that the size, shape, and the size distributions of nanoparticles in such an ordered medium should be determined by the parameters and the properties of the polymer matrix. Below, we present the results obtained in the small-angle X-ray scattering studies of the internal structure of the hydrogel/surfactant complexes and the process of formation of gold

1063-7745/01/4604-0586$21.00 © 2001 MAIK "Nauka/Interperiodica"

and platinum particles in these complexes. We also analyzed the structures of the alternative polymer systems based on multilayer polyoctadecylsiloxanes [14–16] with the purposefully introduced metal nanoparticles.

EXPERIMENTAL

Samples. We prepared gel/surfactant complexes of two types: (1) cationic matrices based on the cationic polydiallyldimethylammonium chloride (PDADMACl) gel and two anionic surfactants—sodiumdodecylsulfate (SDS) and sodiumdodecylbenzylsulfonate (SDBS) and (2) anionic matrices based on the anionic gel of polymethylacrylic acid (PMA) and the cationic surfactant—cetylpyridinechloride (CPC). To provide the formation of metal nanoparticles, the collapsed gels were introduced into the solutions of metal compounds with the subsequent reduction of metal ions. The methods of preparation of gels and nanoparticles are described in detail elsewhere [17]. The sources of platinum ions were aqueous solutions of $PtCl_4$, Na_2PtCl_6, $(NH_4)_2PtCl_4$, and H_2PtCl_6. The metals in these solutions were reduced by the fast Na_2BH_4 and slow $N_2H_4 \cdot H_2O$ reducing agents. The reactive medium was water.

In addition, we also synthesized poly(octadecylsiloxane) (PODS) and hybrid PODS/CPC complexes by the method described in [16]. Then, we introduced the gold- and platinum-containing compounds ($AuCl_3$ and K_2PtCl_4 and $H_2PtCl_6 \cdot 6H_2O$, respectively) into these systems with the subsequent reduction of metal ions with the aid of Na_2BH_4, UV radiation, and the self-reduction of metal ions. The reactions for these samples were performed in water–acetone and water–ethanol mixtures by the methods described in [18].

Small-angle X-ray scattering experiment and the analysis of the data obtained. The structure of the complexes was studied by the SAXS method with the use of the laboratory and synchrotron sources of the X-ray radiation. The measurements were performed on a laboratory AMUR-K diffractometer designed at the Special Designing Bureau of the Institute of Crystallography (Moscow) at the fixed wavelength λ = 0.1542 nm in the Kratky geometry [19] using two experimental modes. The first mode provided the measurements in the momentum-transfer range $0.12 < q < 5.5$ nm^{-1} ($q = 4\pi\sin\theta/\lambda$, 2θ is the scattering angle), i.e., under scattering within relatively large angles. The second mode provided measurements in the momentum-transfer range $0.03 < q < 2.0$ nm^{-1} corresponded to the range of scattering by the largest particles in the systems studied. The average sample thickness was ~1 mm and varied along the holder; therefore, no absolute calibration of the measurements was made. The experimental data were normalized to the intensity of the incident beam, and then the correction for possible collimation distortions was introduced.

The experiments on anomalous small-angle X-ray scattering were made at the DESY Synchrotron, Hamburg, Germany (the storage ring DORIS III, the JUSIFA setup [20]). The measurements were made at different wavelengths λ, i.e., at different energies E of the incident X-ray beam [7, 21, 22]. The atomic scattering factor is determined as

$$f(E) = f_0 + f'(E) + i f''(E), \quad (1)$$

where the dispersion corrections $f'(E)$ and $f''(E)$ become essential in the vicinity of the absorption edge of the resonant atom. In our case, the measurements were made in the vicinity of L_3, the absorption band of Au and Pt atoms, at the photon energy E = 11.9 and 11.5 keV (λ = 0.104 and 0.107 nm, respectively). In order to cover the angular ranges $0.4 < q < 7.3$ and $0.08 < q < 1.5$ nm^{-1}, the sample was located at distances of 935 and 3635 mm from the detector. To reduce the parasitic scattering, the cuvette with the sample was evacuated. The PODS powders were measured in a specially designed 1-mm-thick aluminum cuvette with mica windows. The scattering curves obtained at two sample–detector distances were corrected for phonon scattering and fluorescence; then the data were reduced to the absolute units and "merged" to yield the composite curves in the angular range $0.08 < q < 7.7$ nm^{-1}.

The scattering curves $I(q, E_k)$ for each sample were measured at four different energies of the incident radiation at k = 0, 1, 2, 3 in the vicinity of the absorption edge of the respective metal. The first energy was chosen comparatively far from the absorption band (E_0 = 11.560 and 11.487 keV for the Au and Pt samples, respectively). For three energy values in the vicinity of the resonance scattering ($E_{1, 2, 3}$ = 11.870, 11.915, and 11.919 keV for Au; 11.535, 11.555, and 11.564 keV for Pt), the corrections for anomalous scattering were approximately equal to $-0.06f(E_0)$, $-0.10f(E_0)$, and $-0.20f(E_0)$, respectively. The difference between the scattering curves obtained at different energies, $\Delta_k(q) = I(q, E_0) - I(q, E_k)$, is proportional to scattering by resonant atoms. These difference curves were then used to calculate the volume distribution functions $D_V(R)$. The integral equation

$$I(q) = (\Delta\rho)^2 \int_{R_{\min}}^{R_{\max}} D_V(R) m^2(R) i_0(qR) dR \quad (2)$$

was solved with respect to $D_V(R)$ under the assumption of the spherical shape of the formed nanoparticles with the use of the GNOM program [5]. In the above equation, R is the sphere radius; $R_{\min}$ and $R_{\max}$ are the minimum and the maximum radii, $i_0(x) = \{[\sin(x) - x\cos(x)]/x^3\}^2$ and $m(R) = (4\pi/3)R^3$ are the form-factor and the sphere volume, respectively; and $x = qR$. The scattering-length density of the anomalous atoms is determined as $\Delta\rho = (N_0^2 - N_k^2)e/\nu_{at}$, where N_0 and N_k are the number of electrons which contribute to scattering far from the resonance and at $\lambda = \lambda_k$, respectively; e

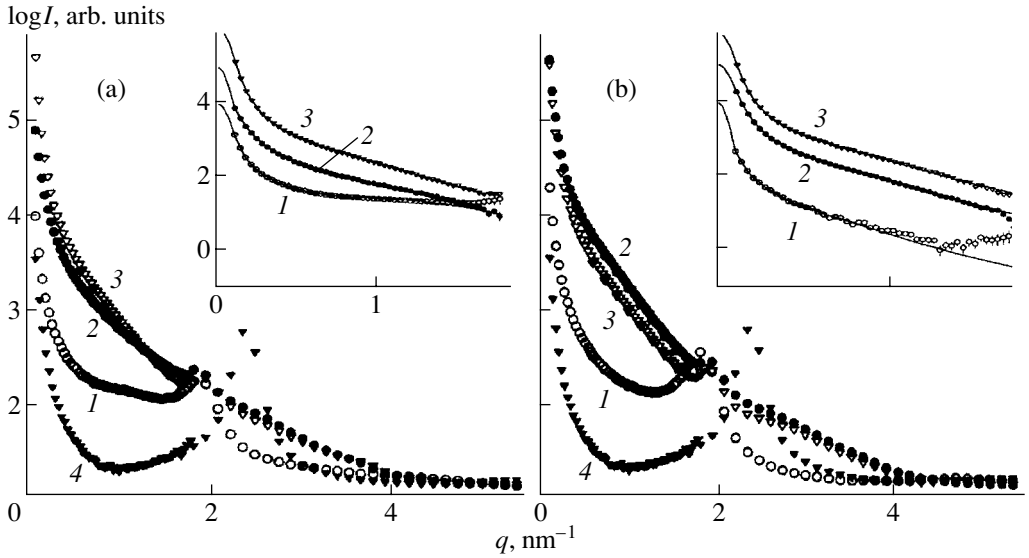

Fig. 1. Small-angle X-ray scattering curves from the PDADMACl/SDBS systems (*1*) with the introduced (a) $H_2Pt(OH)_2Cl_4$ and (b) H_2PtCl_6 compounds far from the absorption edge of Pt atoms; scattering curves upon reduction of platinum ions with the aid of (*2*, *3*) $NaBH_4$ and $N_2H_4 \cdot H_2O$, respectively, and (*4*) scattering from the initial collapsed gel.

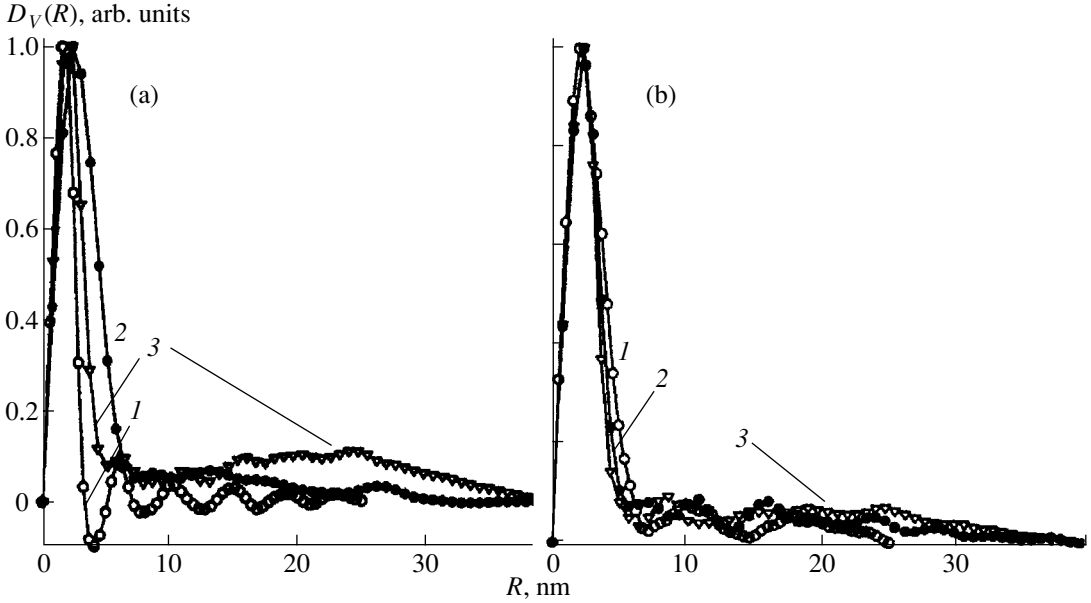

Fig. 2. Volume distribution functions for (a) $H_2Pt(OH)_2Cl_4$ and (b) H_2PtCl_6 containing PDADMACl/SDBS gels calculated by the GNOM program: (*1*) with the formed cluster compounds, (*2*, *3*) Pt-nanoparticles reduced by $NaBH_4$ and $N_2H_4 \cdot H_2O$, respectively, and normalized to unity.

is the Thompson radius of an electron; and ν_{at} is the atomic volume. At $k = 3$ (the maximum of the anomalous signal), we obtain $\Delta\rho = 6.80 \times 10^{11}$ and 6.94×10^{11} cm^{-2} for Pt and Au samples, respectively. Calculating $D_V(R)$, we used the zero value of R_{min}; the value of R_{max} was selected individually for each case of data fitting by Eq. (2). The size distributions for particles constructed by the scattering data obtained at the fixed wavelengths were calculated from the difference scattering curves between metal-containing samples and the initial polymer matrices by the method developed elsewhere [23].

The characteristics of the internal structures of polymer matrices were calculated by fitting the Gaussian profiles to those of the chosen Bragg peaks on the scattering curves with the use of the interactive PEAK program. The average crystallite size L and the degree of disorder in the system $\Delta/\bar{d}$ were determined from the

following equations [24]:

$$L = \frac{\lambda}{\beta_q \cos\theta}, \quad (3)$$

$$\Delta/\bar{d} = \frac{1}{\pi}\sqrt{\frac{\beta_q \bar{d}}{\lambda}}, \quad (4)$$

where β_q is the halfwidth of the Bragg peak in radians at the scattering angle 2θ, $\bar{d} = 2\pi/q_{max}$ is the characteristic dimensions of the ordered regions corresponding to position q_{max} the Bragg-peak, and Δ is the mean square deviation of the distance between the nearest two periodic motifs of the structure.

The centrosymmetric electron-density profile along the direction normal to the lamella plane in the multilayer structures was calculated with the use of the one-dimensional Fourier transform

$$\rho(r) = \sum_{l=1}^{N} A(q, l) q_l \cos qr = \sum_{l=1}^{N} [\pm\sqrt{S(l)}] q_l \cos qr, \quad (5)$$

where N is the number of peaks, and q_l and $S(l)$ are the position and the area of the lth Bragg peak, respectively. We considered all the possible combinations of the signs of the scattering amplitude $A(q, l)$. The most probable sign sequence was chosen upon the visual examination of the experimental electron-density profiles. To reduce the termination effect, the experimental profiles were subjected to low-frequency filtration with the period $T = 2\pi/q_N$.

DISCUSSION OF RESULTS

Hydrogel/surfactant complexes. Scattering from all the hydrogel/surfactant complexes studied showed some common features. The hydrogel collapse during its interaction with the surfactant resulted in the formation of the characteristic peak in the range of q values from 1.4 to 2.5 nm^{-1} on the scattering curve. The position of this maximum depended on the nature of the gel and the surfactant used. The introduction of metal compounds into the system reduced the peak amplitude and increased the "central scattering," which indicated the changes occurred in the internal structure of the complexes and the formation in the system of strongly scattering inhomogeneities, which could be interpreted as the formation of clusters of metal compounds. The subsequent reduction of metal ions resulted in ever more pronounced structural rearrangements and, thus, in a decrease of the characteristic-peak value with a simultaneous drastic increase of the central scattering, i.e., presumably in the formation of metal particles. All these changes in the small-angle scattering from the hydrogel/surfactant complexes are illustrated by the example of the PDAMACl/SDBS system in Fig. 1.

The inset in Fig. 1 also shows the difference anomalous small-angle scattering curves obtained by the

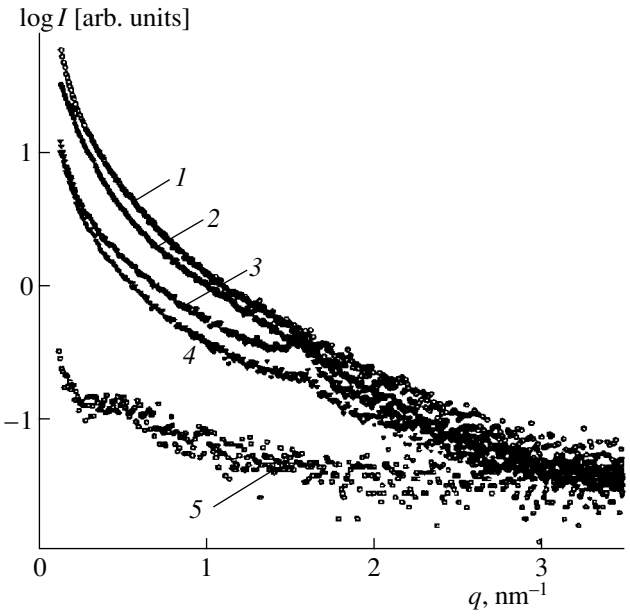

Fig. 3. Small angle scattering curves from PDADMACl/SDBS gels upon the reduction of platinum compounds with the aid of $NaBH_4$: (*1*) H_2PtCl_6, (*2*) $(NH_4)_2PtCl_4$, (*3*) Na_2PtCl_6 immediately upon reduction, and (*4*) 30 days later. The curves are scaled to scattering by an empty cell of the polymer network (*5*) in the region $q > 3$ nm^{-1}.

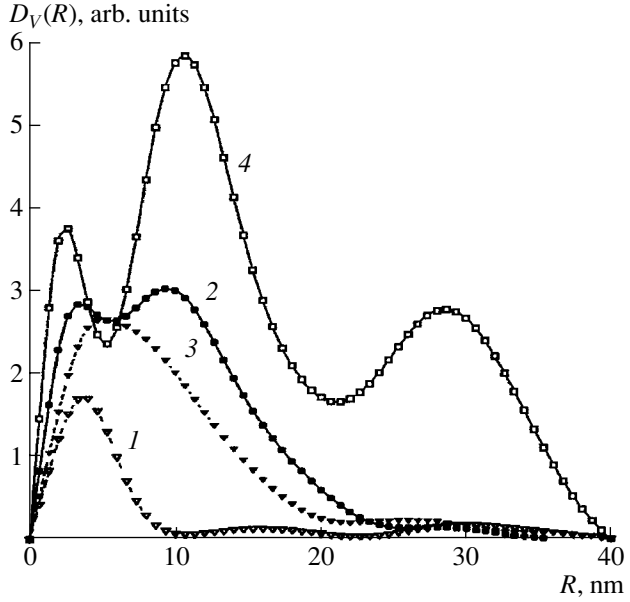

Fig. 4. Volume distribution functions in the PDADMACl/SDBS system with $HAuCl_4$ calculated by the GNOM program: (*1*) PDADMACl/SDBS system with the $HAuCl_4$ additive, (*2*) PDADMACl/SDBS system after reduction of metal ions, (*3*) PDADMACl gel upon reduction of metal ions without the use of SDS (measurements were made immediately upon the specimen preparation), (*4*) the same as (*3*) but 35 days later. For better visualization, (*1*) is multiplied by a factor of 5.

Table 1. Structural characteristics of hydrogel/surfactant complexes obtained from the traditional and anomalous small-angle X-ray scattering curves

Sample	q_{max}, nm^{-1}	$\bar{d}$, nm	L, nm	$\Delta/\bar{d}$
PDADMACl/SDBS complex				
Gel/Surfactant	2.34	2.68	27	0.10
Gel + H_2PtCl_6	1.81	3.47	33	0.10
Gel + H_2PtCl_6 + $NaBH_4$	1.64	3.84	50	0.09
Gel + H_2PtCl_6 + N_2H_4	1.91	3.29	62	0.07
Gel + $H_2Pt(OH)_2Cl_4$	1.88	3.34	38	0.09
Gel + $H_2Pt(OH)_2Cl_4$ + $NaBH_4$	1.87	3.36	74	0.07
Gel + $H_2Pt(OH)_2Cl_4$ + N_2H_4	1.94	3.24	60	0.07
PDADMACl/SDS complex				
Gel/Surfactant	1.53	4.10	31	0.12
Gel + H_2PtCl_6	1.52	4.13	29	0.12
Gel + $(NH_4)_2PtCl_4$	1.51	4.17	32	0.11
Gel + Na_2PtCl_6	1.52	4.13	38	0.11
Gel + $H_2Pt(OH)_2Cl_4$	1.58	3.98	39	0.10
Gel + Na_2PtCl_6 + $NaBH_4$	1.56	4.02	98	0.06
Gel + Na_2PtCl_6 + $NaBH_4$, upon 30-day-storage	1.58	3.97	121	0.06
PMA/CPC complex				
Gel/Surfactant, peak 1*	1.28	4.93	26	0.15
Gel/Surfactant, peak 1a	1.33	4.71	–	–
Gel + Na_2PtCl_6, peak 1	0.91	6.93	25	0.17
Gel + Na_2PtCl_6, peak 2	3.30	1.90	53	0.06
Gel + Na_2PtCl_6, peak 2a	3.10	2.03	–	–
Gel + Na_2PtCl_6 + N_2H_4, peak 1	1.33	4.71	47	0.10
Gel + Na_2PtCl_6 + N_2H_4, peak 1a	1.17	5.37	–	–
Gel + Na_2PtCl_6 + N_2H_4, peak 2	3.07	2.05	149	0.04

* For the PMC/CPC complex denote the main peaks at 1.5 and 3 nm^{-1}, respectively; the letter "a" indicates additional narrow peaks on top of the main peaks 1 and 2. For the additional peaks, only the period $\bar{d}$ was calculated.

method described above. These curves were used to calculate the size distribution function of the particles. To confirm the fact that the anomalous signal really corresponds to scattering by metal particles, we considered only those curves which satisfied two requirements: (1) the difference $\Delta_k(q)$ should be proportional to the squared anomalous correction at the kth energy and (2) the characteristic peak corresponding to the internal structure of the collapsed gel should be absent on the anomalous-scattering curve. These requirements were satisfied by all the specimens except for the complex containing $H_2Pt(OH)_2Cl_4$ prior to metal reduction; the corresponding anomalous-scattering signal was so small that, upon its subtraction, the structural peak did not completely disappear, which resulted in pronounced oscillations on the corresponding size-distribution function (Fig. 2a, curve *1*). The size distributions obtained (Fig. 2) also showed the features common for all the gel systems studied. The clusters of metal compounds penetrated the hydrogel/surfactant complexes playing the role of nuclei of metal particles whose average radius, $R \approx 2$ nm, corresponded to the radius of the main fraction of metal nanoparticles. The size distributions of clusters of metal compounds are of the monomodal nature, whereas the $D_V(R)$ functions for metals are bimodal. In this case, the fractions of larger particles (with R up to 40 nm) are formed in the presence of the $N_2H_4 \cdot H_2O$ reducing agent (slow reduction). The fast reduction of metal ions with the use of $NaBH_4$ resulted in the formation of predominantly small particles.

The stabilized effect of the polymer matrix is clearly seen on long-stored samples. Figure 3 shows the SAXS curves for samples containing platinum nanoparticles measured immediately upon sample preparation and 30 days later. The characteristic peak decreases with

time, but the initial portions of both curves almost coincide. This indicates that the particles do not change their size during storage and that considerable structural rearrangements occur in the gel. The matrix is stabilized by surfactant molecules, which is proved by the size distributions for two gold-containing systems—the collapsed gel and system without surfactants (Fig. 4). In a noncollapsed gel, nanoparticles are formed whose size distribution is of the monomodal nature (Fig. 4, curve *3*). Upon a 35-day storage, the size distribution of metal nanoparticles in this system acquired the multimodal character (Fig. 4, curve *4*) with the formation of some large particles, whereas the size of surfactant-stabilized gel did not change (Fig. 4, curve *2*).

The structural characteristics calculated from the Bragg peaks of the scattering curves for all the hydrogel/surfactant complexes studied are indicated in Table 1. The most interesting fact following from these data is the higher order degree in all the metal-containing samples in comparison with the order degree in the initial gel, despite the fact that the amplitude of the characteristic peak considerably decreases, which could have been an indication to the destruction of the gel structure. However, the Bragg-peak amplitude is proportional not only to the degree of order in the quasicrystalline zones of the gel but also to the volume of these zones in the sample. This leads to the conclusion that, during the formation of metal nanoparticles, the structural rearrangements in gel result in the formation of highly organized regions, which constitute only a small part of the total volume. One can assume that these crystalline zones are localized only around metal particles. This is confirmed by sample aging. For the PDADMACl/surfactant complex with platinum ions from Na_2PtCl_6 reduced with the aid of $NaBH_4$, the amplitude of the characteristic peak upon a 30-day-storage becomes essentially smaller (Fig. 3). At the same time, the size of the crystalline regions increases from 31 to 121 nm, whereas the degree of disorder becomes twice as low as in the initial gel containing no metal particles (Table 1).

The structural rearrangements during the formation of metal nanoparticles in the anionic gel (the PMA/CPC complex) are much more complicated (Fig. 5). Upon the introduction into the system of Na_2PtCl_6, the source of platinum ions, the sharp double peak at 1.3–1.5 nm^{-1} almost disappears (Fig. 5, curve *1*), but at the same time an intense maximum at 3.0 nm^{-1} (Fig. 5, curve *2*) is formed. The formation of platinum particles with the aid of N_2H_4 results in disappearance of the peak at 3.0 nm^{-1} and, at the same time, the restoration of the initial maximum at 1.3–1.5 nm^{-1} (Fig. 5, curve *3*). Taking into account that the collapsed PMA gel contains only about 1 wt % of platinum, i.e., one Pt ion per 50 gel monomers [12], this drastic rearrangement shows that the structure of the complex is very sensitive to the penetration of the substances interacting with the surfactant molecules. The $(PtCl_6)^{2-}$ ions

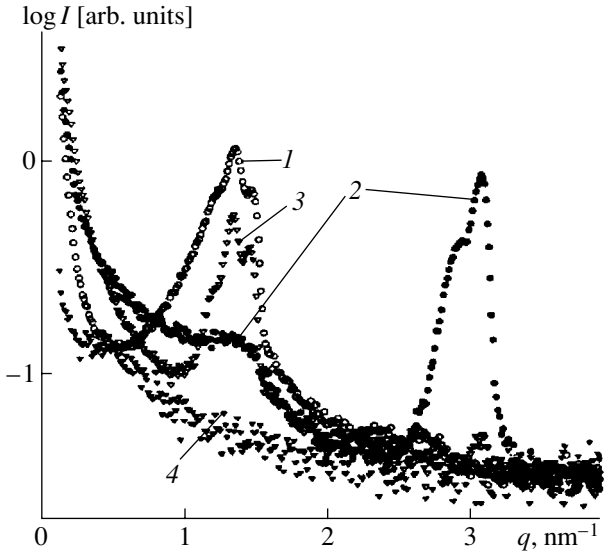

Fig. 5. Small-angle scattering curves for the PMA/CPC system: (*1*) PMA/CPC gel, (*2*) the same gel with the Na_2PtCl_6 additive, and (*3*) the same as in (*2*) upon reduction by N_2H_4. The curves are scaled to scattering by an empty cell (*4*) in the region $q > 3$ nm^{-1}.

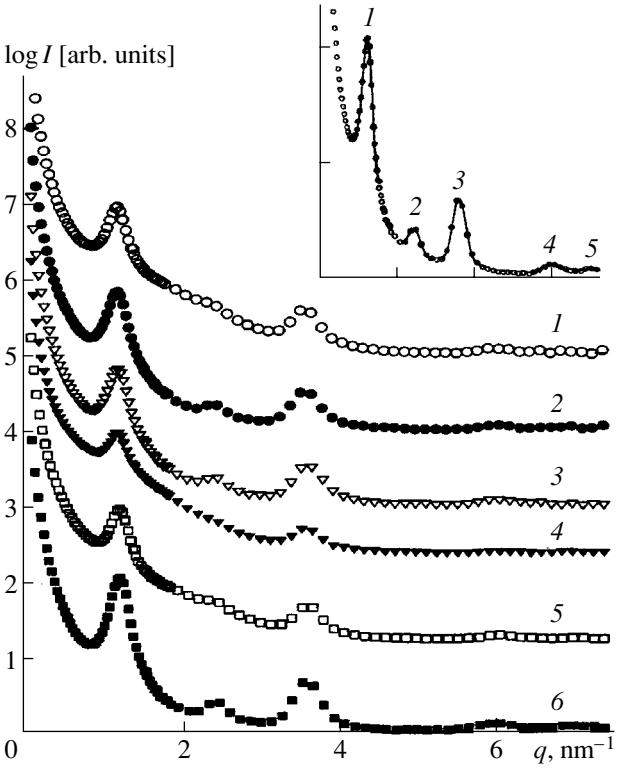

Fig. 6. Small angle scattering curves from Pt-containing PODS powders at the X-ray radiation energy far from the absorption edge: (*1*) Pt1, (*2*) Pt2, (*3*) Pt3, (*4*) Pt4, and (*5*) Pt5. The inset shows the approximation of the scattering curve for the initial PODS (symbols) by the set of the Gaussian peaks (solid lines). The peak positions are indicated by arrows. Numbers indicate the reflection orders.

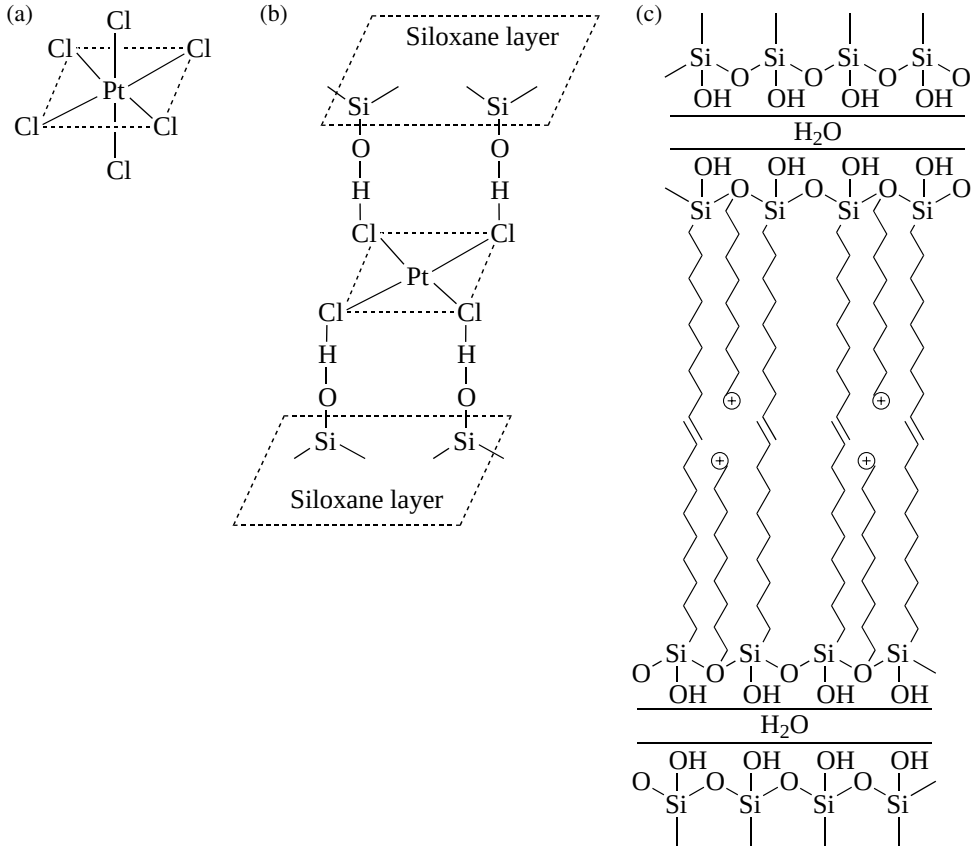

Fig. 7. (a) Geometry of the $(PtCl_6)^{2-}$ ion; (b) schematic interaction between the planar K_2PtCl_4-ion with the silanol group of the siloxane bilayer, and (c) schematic representation of the hybrid PODS/CPC complex.

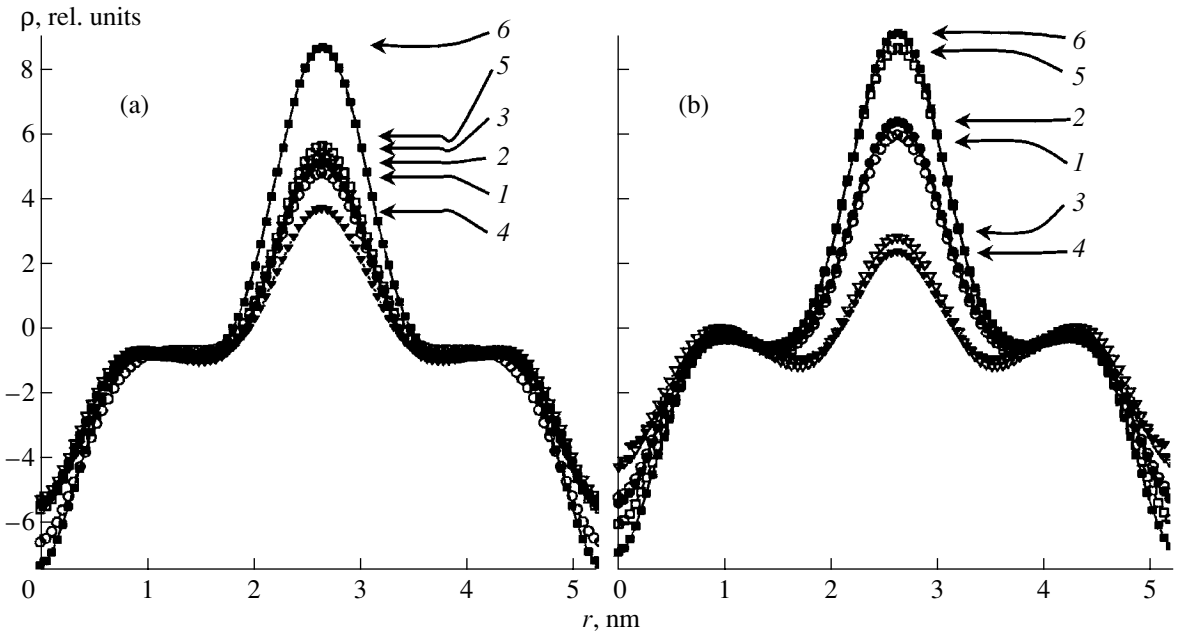

Fig. 8. Electron-density profiles normal to the multilayer plane in the PODS samples with (a) Pt nanoparticles and (b) Au nanoparticles. For better correspondence of the profiles in the around the center of the hydrocarbon chains, all the profiles are displaced with respect to each other by the same small distance.

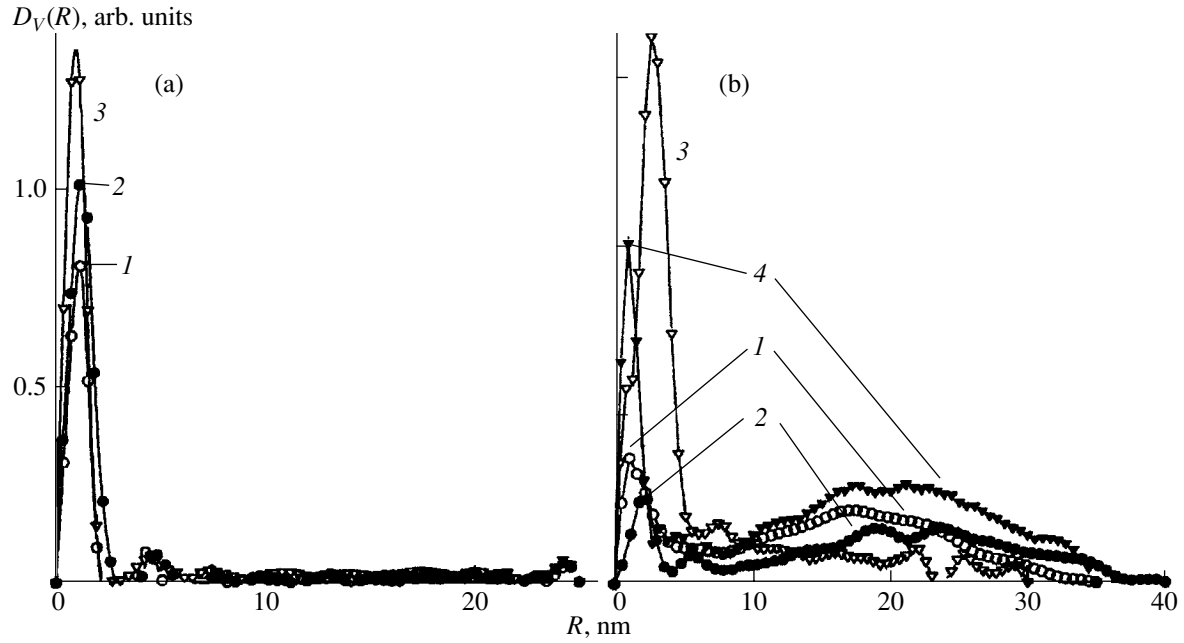

Fig. 9. Volume distribution functions of (a) Pt- and (b) Au-nanoparticle containing PODS samples. The distributions are numbered in accordance with the numbers of the Pt1–Pt5 and Au1–Au4 samples.

compete with surfactant molecules for bonding with PMA groups and thus give rise to self-assembly of free CPC molecules and formation of new structures, which, in turn, provides the appearance of a new Bragg peak. Reduction of the metal by N_2H_4 releases the bonds of $(PtCl_6)^{2-}$ ions and, thus, allows the CP cations to occupy their initial sites, which, in the final analysis, restores the gel structure. Similar to cationic gels, the degree of order in the complex increases.

Systems based on layered polycondensed octadecylsiloxanes. In comparison with the small-angle scattering from hydrogel/surfactant complexes, the small-angle scattering pattern from PODS with gold and platinum nanoparticles is enriched with Bragg peaks (Fig. 6). The location of these peaks at spacings d, $d/2$, $d/3$… indicates the lamellar nature of ordering in the polymer matrix. The fitting procedure for peaks obtained from the SAXS data for the initial PODS is illustrated by the inset in Fig. 6 (the fourth-order peak

Table 2. Structural characteristics of the initial and the metal-containing PODS complexes

Sample	Reaction medium	Reduction conditions	q_l, nm^{-1}	L, nm	$\Delta/\bar{d}$	$\bar{d}$, nm
PODS1			1.21	37	0.120	5.24 ± 0.03
PODS2			1.21	37	0.120	5.24 ± 0.03
PODS1–Pt1*	H_2O/acetone	Self-reduction	1.20	37	0.120	5.25 ± 0.03
PODS1–Pt2**	H_2O/acetone	H_2	1.21	36	0.120	5.23 ± 0.04
PODS1–Pt3	H_2O/acetone	$NaBH_4$	1.21	35	0.121	5.22 ± 0.04
PODS1–Pt4	H_2O/acetone	H_2	1.21	38	0.117	5.22 ± 0.04
PODS1–Pt5	H_2O/acetone	$NaBH_4$	1.21	36	0.120	5.22 ± 0.05
PODS1–Au1	H_2O/acetone	Self-reduction	1.21	40	0.115	5.23 ± 0.04
PODS1–Au2	H_2O/ethanol	Self-reduction	1.21	38	0.118	5.24 ± 0.04
PODS2/CPC–Au3	H_2O	$NaBH_4$	1.20	36	0.120	5.25 ± 0.08
PODS2/CPC–Au4	H_2O	UV	1.26	32	0.126	4.99 ± 0.07
PODS2/CPC–Au5	H_2O	Not reduced	1.21	37	0.120	5.23 ± 0.06

Note: PODS1 and PODS2 are two independent samples.
* K_2PtCl_4 was used for preparing PODS-Pt1.
** $H_2PtCl_6 \cdot 6H_2O$ was used for the synthesis of PODS-Pt(2–5); the PODSD-Au was prepared with the aid of $AuCl_3$.

is absent). The periodicity $d = 5.24 \pm 0.03$ nm is the same (within the experimental error) for all the samples studied and equals the thickness of fully extended $CH_3(CH_2)_{18}SiO_x$–$O_xSi(CH_2)_{18}CH_3$ bilayer. The structural characteristics of the initial and metal-containing PODS samples are indicated in Table 2. It is seen that, unlike the hydrogel/surfactant complex, the structure of the initial complex only slightly changes upon metal reduction.

The electron-density profiles along the direction normal to the lamella plane were calculated by Eq. (5). The choice of the scattering-amplitude signs was solved proceeding from the known chemical structure of PODS molecules, because the electron density should attain its maximum value at the hydrophylic center of the bilayer because of the presence of silicon atoms. Moreover, a wide interval, where the density is almost constant and which corresponds to regularly packed hydrocarbon tails of the polymer, should exist (Fig. 7). The electron-density profiles (Fig. 8) best satisfying the above-formulated requirements were obtained at the sign combination $-+---$ and $l = 1, 2, 3, 5, 6$. Because of the low resolution of the method ($2\pi/q_{max} = 1$ nm), silicon atoms shared by two neighboring monolayers yield only one electron-density peak in the bilayer center. The width of this peak equals 2 nm, which agrees quite well with the size of the smallest particles formed in these systems (Fig. 9) and confirms the assumption that the rigid polymer matrix limits growth of nanoparticles inside the siloxane bilayer. Everywhere outside the central peak, the electron density remains almost constant at a distance of 1.8 nm, which corresponds to close-packed alkyl tails. At the bilayer boundaries, the electron density drastically decreases, thus indicating the absence of any order in the boundary tail–tail contacts.

The height of the central peak for the metal-containing samples decreases in comparison with its height for the initial PODS. This is explained by the presence in the siloxane bilayer of nanoparticles, which give rise to partial deformation of the regular structure of the layer and, as a result, a decrease of the electron density in ordered regions. The maximum changes are observed for the samples with the highest quantity of small particles, which confirms the assumption about the particle formation inside the silicon bilayer. If the sample also contains some larger particles (Fig. 9), they are formed in the vicinity of alkyl tails and, possibly, also in the boundary tail–tail regions (the latter is confirmed by an increase of the electron density of the peripheral regions of the bilayer). This conclusion is also confirmed by the size distributions and the electron-density profiles obtained for the hybrid PODS/CPC complexes with large (up to 40 nm) gold particles (Figs. 8, 9) in CPC micellas located in the hydrophobic regions of the bilayer (Fig. 7), which increases their density and considerably changes the electron-density profile.

CONCLUSIONS

We had two main goals—to study in detail the structure of complicated polymer systems and the formation of metal nanoparticles in these systems and to demonstrate the possibilities of the small-angle X-ray scattering method in the analysis of such systems and processes. The joint use of the traditional and the anomalous SAXS methods provided the establishment of the structure organization of various polymer matrices at a resolution of about 1 nm and the calculation of the size-distribution functions of metal nanoparticles formed in these matrices. It is shown that all the complexes studied are highly organized nanosystems in which growth of metal particles is determined by the conditions of reduction of metal ions controlled by the structure of the polymer network and limited by the dimensions of its cells. The electron-density profiles calculated for polycondensed siloxane matrices confirm the above conclusions. The results obtained are of practical value since they open new possibilities for designing novel polymer materials with desirable properties.

ACKNOWLEDGMENTS

The authors are grateful to L.I. Man for valuable remarks.

REFERENCES

1. *Small-Angle X-ray Scattering*, Ed. by O. Glatter and O. Kratky (Academic, London, 1982), p. 515.
2. D. I. Svergun and L. A. Feĭgin, *Small-Angle X-ray and Neutron Scattering* (Nauka, Moscow, 1986).
3. D. I. Svergun and A. V. Semenyuk, Kristallografiya **32** (6), 1365 (1987) [Sov. Phys. Crystallogr. **32**, 802 (1987)].
4. A. V. Semenyuk and D. I. Svergun, J. Appl. Crystallogr. **24**, 537 (1991).
5. D. I. Svergun, J. Appl. Crystallogr. **25**, 495 (1992).
6. D. I. Svergun, J. Appl. Crystallogr. **26**, 258 (1993).
7. H. B. Stuhrmann, G. Goerigk, and B. Munk, *Anomalous X-ray Scattering*, in *Handbook on Synchrotron Radiation*, Ed. by E. Rubenstein *et al.* (Elsevier, Amsterdam, 1994), p. 555.
8. H.-G. Haubold, X. H. Wang, G. Goerigk, and W. Schilling, J. Appl. Crystallogr. **30**, 653 (1997).
9. Yu. V. Khandurina, A. T. Dembo, V. B. Rogacheva, *et al.*, Vysokomol. Soedin., Ser. A **36**, 235 (1994).
10. H. Okuzaki and Y. Osada, Macromolecules **28**, 380 (1995).
11. A. T. Dembo, A. N. Yakunin, V. S. Zaitsev, *et al.*, J. Polym. Sci., Part B: Polym. Phys. **34**, 2893 (1996).
12. L. M. Bronstein, O. A. Platonova, A. N. Yakunin, *et al.*, Langmuir **14**, 252 (1998).
13. L. M. Bronstein, O. A. Platonova, A. N. Yakunin, *et al.*, Colloids Surf., A **147**, 221 (1999).
14. W. R. Thompson and J. E. Pemberton, Langmuir **11**, 1720 (1995).
15. W. Gao and L. Reven, Langmuir **11**, 1860 (1995).

16. A. N. Parikh, M. A. Schivley, E. Koo, *et al.*, J. Am. Chem. Soc. **119**, 3135 (1997).

17. D. I. Svergun, E. V. Shtykova, M. B. Kozin, *et al.*, J. Phys. Chem. B **104**, 5242 (2000).

18. D. I. Svergun, M. B. Kozin, P. V. Konarev, *et al.*, Chem. Mater. **12**, 3552 (2000).

19. L. Yu. Mogilevskiĭ, A. T. Dembo, D. I. Svergun, and L. A. Feĭgin, Kristallografiya **29** (3), 587 (1984) [Sov. Phys. Crystallogr. **29**, 349 (1984)].

20. H.-G. Haubold, K. Gruenhagen, M. Wagener, *et al.*, Rev. Sci. Instrum. **60**, 1943 (1989).

21. H.-G. Haubold, R. Gebhardt, G. Buth, and G. Goerigk, *Resonant Anomalous X-ray Scattering*, Ed. by G. Materlik *et al.* (Elsevier, Oxford, 1994), p. 295.

22. H.-G. Haubold, J. Phys. IV **3**, 475 (1993).

23. D. I. Svergun, E. V. Shtykova, A. T. Dembo, *et al.*, J. Chem. Phys. **109** (24), 11109 (1998).

24. B. K. Vainshtein, *Diffraction of X-rays by Chain Molecules* (Akad. Nauk SSSR, Moscow, 1963; Elsevier, Amsterdam, 1966).

Translated by L. Man

Crystallography Reports, Vol. 46, No. 4, 2001, pp. 596–600. Translated from Kristallografiya, Vol. 46, No. 4, 2001, pp. 661–666.

DIFFRACTION AND SCATTERING OF X-RAY AND SYNCHROTRON RADIATION

Dedicated to the memory of B.K. Vainshtein

X-ray Microscopy of Track Membranes and Biological Objects in the Soft- and Hard-Wavelength Ranges

A. V. Andreev*, V. E. Asadchikov[1], I. A. Artyukov***, A. V. Vinogradov***, V. N. Zruev**, Yu. S. Kas'yanov***, V. V. Kondratenko****, V. E. Levashov***, B. V. Mchedlishvili**, Yu. V. Ponomarev*, A. V. Popov*****, A. A. Postnov**, S. V. Savel'ev******, R. A. Senin**, and I. I. Struk*****

** Moscow State University, Vorob'evy gory, Moscow, 119899 Russia*

*** Shubnikov Institute of Crystallography, Russian Academy of Sciences, Leninskiĭ pr. 59, Moscow, 117333 Russia*

**** Lebedev Physical Institute, Russian Academy of Sciences, Leninskiĭ pr. 53, Moscow, 117924 Russia*

***** Kharkov State Polytechnical University, ul. Frunze 21, Kharkov, 310002 Ukraine*

****** Institute of Terrestrial Magnetism, Ionosphere, and Radio Wave Propagation, Russian Academy of Sciences, Troitsk, Moscow oblast, 142092 Russia*

******* Institute of Human Morphology, Russian Academy of Medical Sciences, ul. Tsyuryupy 3, Moscow, 117418 Russia*

[1]e-mail: asad@ns.crys.ras.ru

Received March 12, 2001

Abstract—The methods used to obtain X-ray images of track membranes and various biological objects in the soft (20 nm) and hard (0.2–0.02 nm) wavelength ranges have been considered. In the range of soft X-rays, the images were obtained in a Schwarzshild microscope. In the spectral range of hard X-ray radiation, various methods were used including the use of Fresnel zone plates, asymmetric reflecting crystals, X-ray microradiography and microtomography. *© 2001 MAIK "Nauka/Interperiodica".*

INTRODUCTION

X-ray microscopy providing observation of internal details of objects, which cannot be observed in visible light and characterized by varying penetration depths and requiring the micron or submicron resolution, attracts an ever increasing amount of attention of researchers. The importance of this method is explained by the urgent necessity of *in vivo* observation of the processes occurring in tissues of the cells and organs. It is necessary to obtain X-ray images of various objects at resolution at the level of several microns or higher, to interpret these images, and then perform the three-dimensional reconstruction of the objects. These problems are closely related to the problems studied by Boris Konstantinovich Vainshtein, who was a well-known expert in the field of electron microscopy and X-ray diffraction analysis of proteins and performed the pioneering studies on three-dimensional reconstruction.

The main problem impeding the active development of the X-ray microscopy is associated with low and very close absorption coefficients of various substances in the short-wavelength range of the X-ray spectrum. The difference between the absorption coefficients increases with the wavelength, but this is accompanied by an increase of absorption. The data on X-ray absorption in some organic compounds, water, and air are presented in the table, which also indicates the data reported in [1, 2]. As the measure of absorption, we used the linear absorption coefficient μ entering the relationship $I = I_0\exp(-\mu x)$, where I_0 is the intensity of the incident radiation, I is the intensity of the transmitted radiation, and x is the sample thickness.

Thus, the selection of the X-ray wavelength is determined by the concrete experimental problem. In the present study, we used 20-nm-radiation to analyze the structure of polymer track membranes. The 0.229-nm-radiation was used to study the structures of some biological objects. The structural study of some inorganic materials were performed at the 0.07-nm-wavelength. The three-dimensional structure and shell growth and regeneration of snails were studied by the method of X-ray microtomography in the wavelength range 0.02–0.04 nm.

1063-7745/01/4604-0596$21.00 © 2001 MAIK "Nauka/Interperiodica"

X-ray absorption in organic materials (μm^{-1})

Wavelength (nm)	Material					
	water H_2O	carbohydrate $C_6H_{10}O_5$	protein $H_{65}C_{44}O_{14.5}N_{11.5}S_{0.5}$	lipid $C_{18}H_{34}O_2$	nucleic acid $H_{42}C_{25.2}O_{26.5}N_{10.5}P_{2.65}$	air
0.13	0.0006	0.0007	0.0006	0.0003	0.0014	6.4×10^{-7}
0.2	0.0022	0.003	0.002	0.001	0.005	2.4×10^{-6}
0.4	0.018	0.022	0.017	0.008	0.037	2×10^{-5}
0.8	0.126	0.158	0.113	0.065	0.169	1.42×10^{-4}
1.4	0.560	0.719	0.524	0.310	0.768	6.31×10^{-4}
2.3 (before the absorption edge)	1.733	2.259	1.67	0.996	2.422	1.95×10^{-3}

A SCHWARZSHILD MICROSCOPE

If the wavelength of the X-ray radiation exceeds 1 nm, enlarged images of objects can be obtained only with the aid of the multilayer X-ray optics. For this purpose, we modified an X-ray Schwarzshild microscope [3]. The source of X-ray radiation was a laser plasma generated in laser ablation of the target. The object was illuminated with the aid of a laser-plasma source and a condenser. The plasma was generated at focusing radiation of a YAG laser ($\lambda = 1.06 \times 10^3$ nm, $\tau = 5$ ns, $E = 0.1$ J) into a spot 0.1 mm in diameter on the surface of a solid target. The radiation of the visible range was cut off by a thin aluminum filter. The objective, the source, and the photographic film were placed into a vacuum chamber under the pressure of the order of 10^{-3} mmHg. The image was obtained using 1–10 X-ray bursts on the UF-4 photographic film.

A Schwarzshild objective consists of two (convex and concave) spherical mirrors positioned on the axis passing through their geometrical center. The characteristic feature of the concentric Schwarzshild objective is the compensation of the third-order spherical aberrations, with all the main optical parameters of the objective being determined by the radii R_1 and R_2 of the mirrors.

We used an objective with the following parameters: $R_1 = 100$ mm and $R_2 = 35$ mm, which provided the focal distance of 26.92 mm and the magnification of 21.26. The distance corresponding to the aberration compensation is $Z_0 = 28.19$ mm. The mirrors had the diameters $D_1 = 50$ mm, $D_2 = 10.6$ mm; the numerical aperture was $N_A = 0.19$.

The mirrors had multilayer Mo/Si coating ensuring the reflectivity of about 20% at wavelength 20 nm. The microscope mirrors, the condenser, and the reference flat mirror were coated simultaneously. The coating of the flat mirror was used to determine the period in the multilayer coating, which was equal to $d = 9.89$ nm; the relative thickness of the molybdenum layer in the coating was 0.34; the number of periods was equal to 20. The theoretical resolution of the objective was 100 nm, whereas the corresponding value measured on the test object (a freely hanging golden grid) was 200 nm [1, 2].

The samples were irregular (with the random pore distribution) track membranes prepared from polyethylene terephthalate (lavsan) with the pore diameter 10^3 nm (in the matrix of the thickness 2×10^4 nm) and 200 nm (in the matrix of the thickness 10^4 nm). We also studied regular track membranes with the pore diameter 500 nm and the period 1000 nm. In each case, we managed to detect the system of tracks and determine their density, which was consistent with the data of the independent electron microscopy study. It turned out that at a pore diameter less than 150 nm, the membrane became almost nontransparent because of X-ray diffraction inside the track channels. Indeed, 10^4-nm-thick polymer layer is absolutely nontransparent for radiation with the wavelength of 20 nm; thus, an individual track can be treated as a long hollow cylinder with the diameter comparable with the radiation wavelength.

The calculation of the field outside the membrane were performed by solving the parabolic wave equation numerically under the assumption that a plane monochromatic wave is incident onto an individual track (hollow cylinder) [4, 5]. The permittivity of the track membrane has the real and the imaginary parts corresponding to the known constant for wavelength of 20 nm. The calculations show a considerable decay in the transmitted-light intensity with a decrease of the pore diameter. This result is confirmed experimentally—to obtain the image of pores 200 nm in diameter, the number of bursts of the solid-state laser to expose photographic materials should be increased by a factor of about ten in comparison with the bursts for imaging pores 1000 nm in diameter. In addition, the numerical simulation shows that the tracks with the diameter less than 150 nm become nontransparent for the wavelength indicated above.

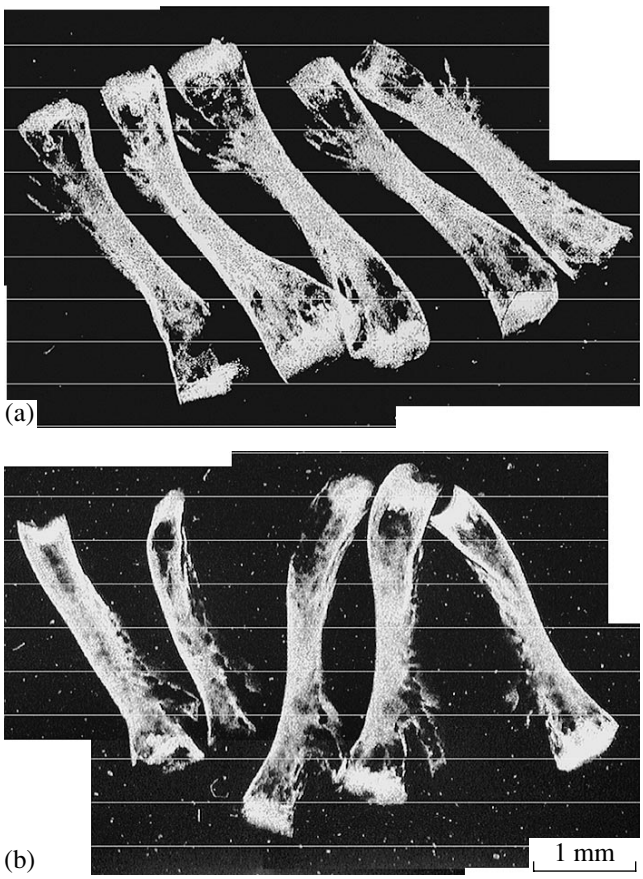

Fig. 1. The humeral bones of the newt *Pleurodeles waltlii* (Amphibia, Urodela). The photograph was obtained by the contact technique at the wavelength of 0.229 nm: (a) control group and (b) upon two-week presence aboard a BIOKOS-MOS-1887 biological satellite.

X-RAY IMAGES TAKEN AT WAVELENGTHS OF 0.229 AND 0.07 nm

The table shows that in the materials studied the change in the radiation wavelength from 0.13 to 0.4 nm (i.e., by a factor of three) results in the change in absorption by more than two orders of magnitude. The penetration depth varying in these materials from 10^4 to 10^6 nm in the 0.05–0.30 nm wavelength range makes this spectrum range appropriate for studying various biological objects, since many objects of such a thickness are nontransparent for visible light.

We should like to emphasize the following:

1. In the above wavelength range, there exist rather efficient laboratory sources of X-ray.

2. One can use as elements of X-ray optics both crystals and the conventional elements used in optics of visible light (e.g., the Fresnel zone plates).

3. Taking into account the above indicated, it is possible to study objects with considerable linear dimensions (of the order of several centimeters) at a rather high resolution (at the level of 1 μm and even higher). The studies of such objects are also of great importance for biologists as well. The attainment of high resolution for objects of the indicated linear dimensions is still hardly attainable if one uses the two-dimensional positional detectors; therefore, one has to use X-ray-sensitive films and resists.

Now consider some experimental results.

The Fresnel zone plate. Let the following parameters determine the zone positions in the zone plate: λ, f, R_0, and N, where λ is the wavelength, f is the focal distance, R_0 is the zero-zone radius, and N is the total number of the zones. Then, the radii of the remaining zones and their widths (periods) are determined by the relationships

$$R_n^2 = R_0^2 + 2\lambda f n, \quad d_n = \lambda f / R_n .$$

Using the magnetron sputtering technique, we prepared a zone plate by coating the central glass rod (mandrel) successively with copper and chromium. The mandrel diameter was equal to 10^5 nm; the total number of pairs of deposited copper and chromium layers was equal to 60. The thickness of the first zone was 458 nm and the thickness of the last one, 316 nm. The theory [6] predicts the 22% efficiency for a 6.5×10^3-nm-thick zone plate at the wavelength 0.229 nm. The real thickness was equal to 2×10^4 nm. The preparation of the zone plate is a rather complicated technological problem. In our case, the situation was even complicated since the mandrel was not ideally circular. Moreover, the interlayer roughness increased with the application of each new layer. Nevertheless, we managed to demonstrate that this zone plate provides focusing of the radiation at a distance of 10 cm.

Contact microscopy. The first X-ray images were obtained by the contact method immediately upon the discovery of X-rays in 1895 [7] (the object was in the direct contact with the X-ray sensitive film [8]). In studies of biological objects, this method was called microradiography or simply radiography [9, 10]. At present, most of the studies using contact microscopy is performed within the "water window" and only some objects require the use of shorter wavelengths of the spectrum.

However, planning the study of rather large biological objects with the linear dimensions of several centimeters at a high resolution (at the micron level), we invoked this old method, whereas the choice of the objects was dictated by the current problems of biology.

The microradiography method (including the use of stereoscopic pairs) was applied to different classes of biological objects: embryos and amphibian larvae at different stages of their development. For the first time, the X-ray data were used for the quantitative analysis of the demineralization processes occurring in skeletons of cold-blooded animals under the conditions of microgravitation (Fig. 1). We optimized the methods of sam-

ple preparation (the lyophilization conditions) and nondestructive X-ray experiment, which provided the attainment of high contrast for various biological tissues at a high resolution. We should like to emphasize that modern photographic materials really allow the attainment of the resolution as high as 10^3 nm, which was demonstrated in our study of calibrated track silver-coated membranes [$(1–2) \times 10^4$-nm-thick polymer track membranes almost do not absorb the radiation with the wavelength equal to 0.229 nm].

We illustrate our studies by the images of two groups of humeral bones of the newt *Pleurodeles waltlii* (Amphibia, Urodela) obtained by the method of X-ray microradiography at the wavelength 0.229 nm (Fig. 1). The computer processing of these images shows that upon their two-week staying under the conditions of microgravity aboard the biological *BIOKOS-MOS-1887* satellite, the bone tissue demineralization was as high as 27%.

The studies of the zone-plate properties and the use of the method of microradiography became possible only upon the design and construction of a special X-ray device, which is in fact an operating model of a universal X-ray microscope.

Obtaining enlarged with the use of an asymmetric crystal. Another optical element for obtaining enlarged images is an asymmetric crystal–monochromator [11]. This crystal ensures the formation of images with a rather high resolution and a large field of view. Also, it is much cheaper than a zone plate. Thus, the asymmetric crystal–monochromator can be used in designing laboratory X-ray microscopes.

Here, the magnification stems from the fact that the asymmetric Bragg reflection is accompanied by changes in the linear dimensions d_r of the reflected beam in comparison with dimensions d_0 of the incident beam. In the framework of geometrical optics, their ratio is determined by the equation

$$d_r/d_0 = \sin\theta_r/\sin\theta_0, \quad (1)$$

where θ_0 is the angle of incidence and θ_r is the angle of reflection.

Using Eq. (1), one can estimate the maximum possible magnification for single reflection. Assuming that $\sin\theta_r \approx 1$ and taking into account that, at the pronounced diffraction asymmetry, the minimum angle of incidence is determined by the angle of full external reflection, $\theta_c = \sqrt{|\chi_0|} \approx 4 \times 10^{-3}$ rad, we obtain that the maximum magnification is about 250.

We performed the experiments with (111) Si single crystal. The angle of crystal cut with the reflecting crystallographic planes was 5.64°, which, in accordance with Eq. (1), provides the magnification of about 20 (only in one direction, since only one monochromator was used).

We used a point source of the MoK_α radiation (the spot on the sample was about 0.05 mm in diameter) with air cooling. The width of two slit apertures was 0.250 mm. The sample was fixed on the second aperture as close as possible to the asymmetric monochromator. The monochromator was mounted on a goniometer and could be moved in the direction normal to the incident beam and rotated about two mutually perpendicular axes (one of which coincided with the normal to the front face of the crystal).

The objects were a conventional copper sample stage used in electron microscopy and a tantalum shock membrane. The sample stage was a grid with square holes with sides ~6.5×10^4 nm, the period being about 10^5 nm. The shock track membranes were tantalum foils with the array of holes $(1–7) \times 10^4$ nm in diameter. The enlarged images of objects were recorded on the UFShS photographic film.

Figure 2a shows a positive optical image; Fig. 2b shows an extended negative optical image; Fig. 2c, the negative X-ray image of test objects.

The image of the copper grid (on the right, Figs. 2b, 2c) is an array of strips separated by light spacings. Each strip corresponds to a square hole. Since the image was magnified only along one direction, the length-to-width ratio for a strip on the X-ray image corresponded to the really attained magnification and, as was expected, is about 20.

The image of shock-membrane holes also is a system of strips. All the tracks in photographs were enumerated. We managed to bring the X-ray image in correspondence with the image obtained in an optical microscope. The pore (hole) diameters obtained in the X-ray experiment are in good agreement with the electron-microscopy data. The strips indicated as *a*, *b*, 10, 12, 13 on the X-ray image had no corresponding holes in the optical pattern. The X-ray and the electron microscopy data show that these tracks have the smallest dimensions.

Thus, we showed that it is possible to obtain enlarged images of objects at the micron resolution. The images of some objects were obtained with the magnification of about 20. We also managed to obtain the enlarged images of the holes of shock track membranes with the minimum diameter on the order of 2×10^4 nm.

X-RAY MICROTOMOGRAPHY

Above, we showed that it is possible to obtain enlarged images of objects at different wavelengths. However, the complete reconstruction of their three-dimensional structure can be made only if we have a sufficient number of their projections. As was mentioned, the first step in this direction is the obtaining of stereoscopic pairs (i.e., experimental recording of two images of an object at angles differing by 4°–7°).

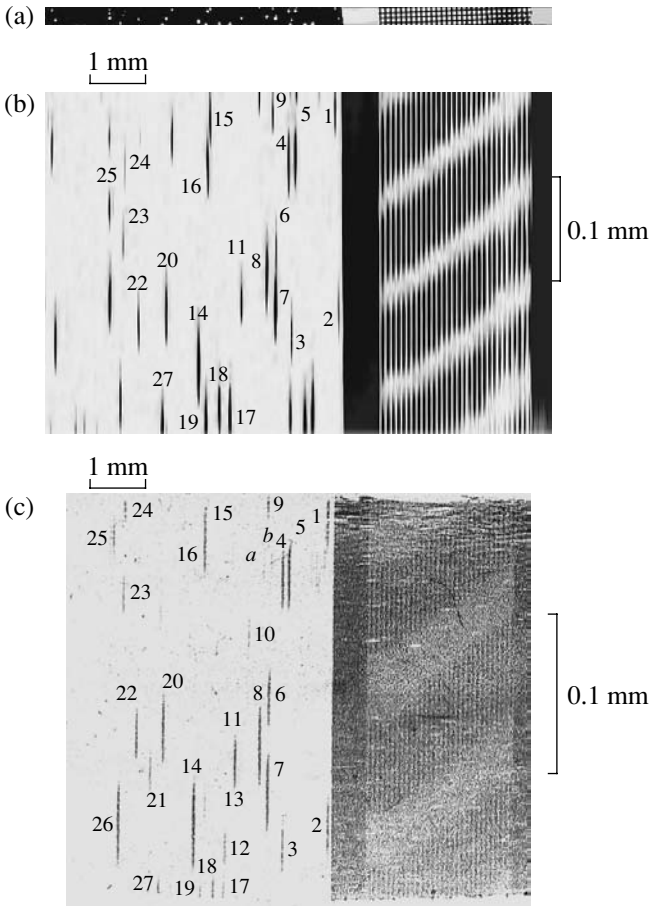

Fig. 2. The image of tantalum foil and copper grid obtained (a) in an optical microscope; (b) in optical image twenty times magnified along one direction; and (c) X-ray image obtained upon the radiation reflection from the monochromator ($\lambda = 0.07$ nm).

The problem of obtaining multiple projections of objects and the corresponding reconstruction of their spatial structure has been currently solved even in the commercially manufactured devices.

In particular, a SKYSCAN-1072 X-ray microtomograph with the probe wavelength ranging within 0.02–0.04 nm (Belgium) was successfully used to study intrinsic defects in rough diamonds [12]. We determined the spatial distribution of defects (air bubbles and graphite and metal inclusions) with the characteristic dimensions up to 20 μm. The device is supplied with the two-dimensional positional detector with 15 × 15-μm-large sensitive elements (the total number of such elements is $10^3 \times 10^3$). The three-dimensional reconstruction of the object required 135 projections. The device provides only a small (about double) magnification due to the X-ray beam divergence at the source–sample–detector path.

The biological applications of X-ray microtomography to studies of soft tissues and tumors are considered in [13].

Thus, the results presented above allow us to put forward the problem of designing an X-ray microscope–microtomograph for studying biological objects.

ACKNOWLEDGMENTS

The study was supported by the International Science and Technology Center, grant no. 918, and by the Russian Foundation for Basic Research, project no. 99-02-17336.

REFERENCES

1. P. Sayre, J. Kirz, R. Feder, *et al.*, Ultramicroscopy **2** (4), 337 (1977).
2. B. L. Henke, E. M. Gullikson, and J. C. Davis, At. Data Nucl. Data Tables **54**, 181 (1993).
3. I. A. Artyukov, V. E. Asadchikov, A. V. Vinogradov, *et al.*, Kvantovaya Elektron. (Moscow) **22** (9), 951 (1995).
4. I. A. Artyukov, V. E. Asadchikov, A. I. Vilenskiĭ, *et al.*, Dokl. Akad. Nauk **372** (5), 608 (2000) [Dokl. Phys. **45**, 248 (2000)].
5. Yu. V. Kopylov, A. V. Popov, A. V. Vinogradov, *et al.*, Opt. Commun. **118**, 619 (1995).
6. V. E. Asadchikov, V. I. Beloglazov, A. V. Vinogradov, *et al.*, Kristallografiya **44** (4), 592 (1999) [Crystallogr. Rep. **44**, 546 (1999)].
7. W. C. Röntgen, *Sitzungsberichte der Wurzburger Physik-medic* (Gesellshaft, 1895), Vol. 137, p. 41.
8. F. Ranwez, C. R. Hebd. Seances Acad. Sci. **122**, 396 (1896).
9. P. Goby, C. R. Hebd. Seances Acad. Sci. **156**, 686 (1913).
10. P. Goby, J. R. Microsc. Soc. **4**, 373 (1913).
11. A. V. Andreev, V. E. Asadchikov, B. V. Mchedlishvili, *et al.*, Pis'ma Zh. Tekh. Fiz. **73** (4), 184 (2001).
12. www.skyscan.be
13. M. J. Paulus, S. S. Gleason, S. J. Kennel, *et al.*, Neoplasia **2**, 62 (2000).

Translated by K. Kugel

Crystallography Reports, Vol. 46, No. 4, 2001, pp. 601–619. Translated from Kristallografiya, Vol. 46, No. 4, 2001, pp. 667–686.

STRUCTURE OF MACROMOLECULAR COMPOUNDS

Dedicated to the memory of B.K. Vainshtein

X-ray Studies of Biological Macromolecules at the Shubnikov Institute of Crystallography of the Russian Academy of Sciences

I. P. Kuranova

Shubnikov Institute of Crystallography, Russian Academy of Sciences, Leninskiĭ pr. 59, Moscow, 117333 Russia
e-mail: inna@ns.crys.ras.ru

Received March 7, 2001

Abstract—The results of X-ray diffraction studies of a number of proteins and the carnation mottle virus performed over a period from 1970 to 2000 at the laboratory created by Academician B.K. Vainshtein at the Shubnikov Institute of Crystallography of the Russian Academy of Sciences are surveyed. The fundamental principles of the spatial organization of protein structures are considered. The characteristic features of the three-dimensional structures of a number of various proteins performing various functions are discussed including leghemoglobin, catalases, pyrophosphatases, pyridoxal-dependent enzymes, nucleotide depolymerases, proteases, and plant toxins. The results obtained for carnation mottle virus are summarized. The contribution of X-ray diffraction studies to the understanding of mechanisms of functioning of the above macromolecules and the first stages of the crystallographic studies of nucleic-acid fragments are discussed. The present state and the prospects of studies of three-dimensional structures of macromolecules are also considered. © *2001 MAIK "Nauka/Interperiodica".*

INTRODUCTION

The development of a new field of science, which was later called biomacromolecular or biochemical crystallography, is one of the most important achievements of the twentieth century. This field of science deals with three-dimensional structures of biopolymers which are studied by the X-ray diffraction analysis. Today, this method is still the major source of the most precise and reliable information on the atomic structures of macromolecules. The data on macromolecules in crystals can also be extended, with a high degree of accuracy, to macromolecules in solutions. The knowledge of atomic structures is also important from the theoretical standpoint for the further understanding of proteins; their structural organization; self-assembly of macromolecules and their ensembles; and also mechanisms of their functioning, the structure–function relationships, and evolution of macromolecules. From the practical standpoint, the results of the crystallographic studies are widely used in biotechnology, gene engineering, medicine, and pharmacology for the directional search for highly efficient drugs and their design. Knowing the structure and the functions of proteins and using the methods of protein engineering, one can design molecules possessing new properties by using the principles of construction of natural proteins. This also provides better understanding of the evolution of living organisms. If the new century is to be the age of biology, it cannot be imagined without extensive studies of three-dimensional macromolecular structures.

The first steps in the protein crystallography go back to the first X-ray diffraction pattern of pepsin crystals obtained by Bernal in 1934 [1], who was the first to show that all protein molecules have the same structures and are arranged in the crystal in the ordered way. However, the detailed interpretation of these X-ray diffraction patterns became possible only in 1954, when Green, Ingram, and Perutz proposed the method for solving the phase problem in the X-ray diffraction analysis of proteins [2]. This method was given the name of multiple isomorphous replacement. It is based on the use of heavy-atom derivatives of proteins for the phase determination. In 1958, Kendrew applied this method to the calculation of the electron density synthesis of myoglobin first at 6 Å resolution [3] and then at 2 Å resolution [4]. At the same time, Perutz obtained the electron density synthesis for hemoglobin at 5.5 Å resolution [5]. The achievements in the crystallography of natural molecules won due recognition of the international scientific community and J.C. Kendrew and M.F. Perutz (1962) and D.M. Crowfoot Hodgkin (1964) were awarded the Nobel prize for chemistry.

This new actively developing field of science using the complex physical method for solving important biological problems could not but attract the attention of B.K. Vainshtein. Being a physicist, he became aware of the importance and the prospects of this direction and created the Laboratory of Protein Structures at the Institute of Crystallography of the Russian Academy of Sciences still in 1959–1960. The laboratory started

1063-7745/01/4604-0601$21.00

working when nobody applied X-ray diffraction analysis to biocrystals in the Soviet Union, and molecular biology itself was only at the very beginning of its development.

To examine the mechanisms of the processes occurring in living organisms at the molecular level, it was necessary to study the structures of biomolecules; to reveal and characterize their functionally important fragments; to compare the structures of the same molecules in different functional states; and, thoroughly analyzing the results, to elucidate establish the correlation between their structures and functions. These complicated problems could be solved only by the combined efforts of experts working in various fields of science, first of all, physicists, chemists, and biologists. To accomplish this goal, it was necessary to educate and train skilled experts, who should understand each other and to coordinate their efforts. Considering molecular biology from the viewpoint of a physicist, Vainshtein realized the importance of such a combined approach. Vainshtein, in cooperation with V.A. Engelhardt and A.S. Spirin, organized scientific schools on molecular biology first in Dubna and then in Zvenigorod, where the lecturers and the participants were physicists, chemists, and biologists. These schools have played an important role in recruiting young scientists to molecular biology. The scientific contacts thus established made it possible to set up a number of joint projects with participation of various institutes on studies of protein structures and functions. Many samples were prepared and supplied by the scientists from the Institute of Protein Research of the Russian Academy of Sciences (Pushchino, Moscow oblast), the Institute of Virusology, the Engelhardt Institute of Molecular Biology of the Russian Academy of Sciences, the Bach Institute of Biochemistry of the Russian Academy of Sciences, etc. Vainshtein invited to his laboratory numerous physicists, chemists, biologists, and mathematicians, who mastered the sophisticated methods of X-ray diffraction analysis. This collaboration proved to be very fruitful. In addition to the X-ray diffraction analysis, other physical methods for studying macromolecules were used, such as electron microscopy and small-angle X-ray scattering. Later these two methods have become individual branches of crystallography.

X-ray diffraction studies of biomolecules require the use of expensive instruments, advanced computational facilities, and stations of molecular graphics. The Institute of Crystallography has all the necessary facilities for structure studies including modern diffractometers, program packages for X-ray data processing and solution of protein structures [6], and methods for protein purification and preparation of protein single crystals. Thus, almost all protein single crystals studied at the Instituted of Crystallography were grown in the laboratory headed by Vainshtein. For these years, more than 40 three-dimensional structures of both native proteins and their complexes with functional ligands have been studied; the structure of carnation mottle virus has been established. The laboratory also started the crystallographic studies of nucleic-acid fragments Vainshtein himself initiated the research of many proteins and took an active part in their solutions. He was interested in symmetry of macromolecules and biocrystals, the methods of three-dimensional object reconstruction from its electron-microscopy projections, and the phase determination by the direct methods by the electron microscopy data on viruses [7–11]. The organizational support and Vainshtein's interest in all the studies have always contributed to the successful results. The enormous scientific contracts established by Vainshtein provided the supply with most interesting objects for research. The studies performed at the laboratory received the recognition of the international crystallographic community. A number of studies were carried out in cooperation with the leading world's laboratories working in protein crystallography with the use of powerful X-ray sources at the Synchrotron Radiation Source in Daresbury (England) and at the European Molecular Biology Laboratory (EMBL) in Hamburg (Germany), modern computing facilities, and graphics stations thanks to the courtesy of our scientific partners (M. Perutz, G. Dodson, K. Wilson, M. Rossman, R. Huber, T. Blundell, and many other).

Below, we survey some data on the atomic structures of macromolecules obtained at the Institute of Crystallography under the directorship of Vainshtein. The theory and the methods of X-ray diffraction analysis are beyond the scope of this review. The goal of this review article was to show how the information on the structures of biomacromolecules brings us to an understanding of the mechanisms of their functioning and provides the establishment of the evolutionary relations between these biomacromolecules.

LEVELS OF STRUCTURAL ORGANIZATION IN PROTEINS

Protein molecules are characterized by several levels of structural organization. The primary structure is the sequence of 20 different amino acids covalently bound via peptide bonds to form a polypeptide chain. The polypeptide chain is folded into an ordered three-dimensional globule stabilized by noncovalent interactions between main- and side-chain atoms of amino acid residues. The secondary structure of the protein is formed via hydrogen bonding of NH and CO groups of the polypeptide chain. Generally, the polypeptide chain is folded into α-helices and β-sheets consisting of parallel or antiparallel polypeptide chains adopting extended conformations (β-strands) (Fig. 1). These sheets can be twisted and, in the limiting case, can form a closed cylindrical structure called a barrel (Fig. 2). Hydrophobic interactions are of considerable importance in the formation and stabilization of globular structures. Thus, nonpolar residues in an aqueous medium are located inside the globule and form a compact core to exclude unfavorable contacts with the polar

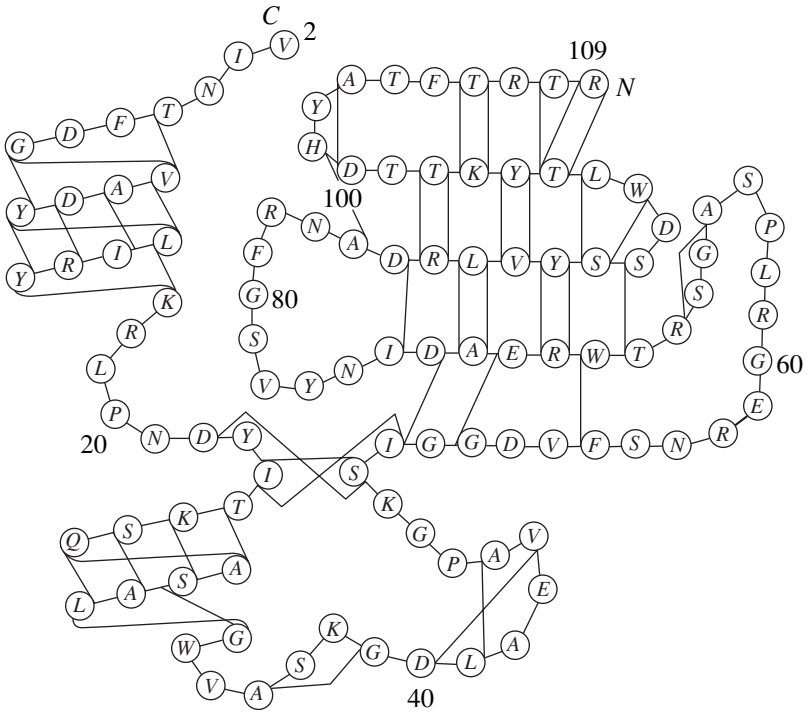

Fig. 1. Scheme of hydrogen bonding in a ribonuclease *Bi* molecule [52]. Hydrogen bonds secondary-structure elements (β-sheet and α-helices) are indicated.

solvent. As a result, secondary-structure elements linked by irregular polypeptide-chain fragments form a unique three-dimensional (tertiary) structure. A large number of proteins consist of more than one polypeptide chain (subunit). The constituent chains can be identical or nonidentical. The polypetide chains linked by noncovalent interactions (van der Waals, hydrogen, or ionic bonds) form the quaternary structure (Fig. 3). The geometrically isolated compact globular units within the molecule linked to the remaining portion of the protein by irregular regions of the polypeptide chain are called domains (Fig. 4). In an aqueous medium, the protein molecule retains its unique architecture and undergoes only insignificant conformational changes depending on pH of the solution or the presence of particular low-molecular-weight components. In the crystal, a large number (up to several hundreds) of water molecules are bound to residues of the protein molecule located on the surface. Since protein crystals contain from 40 to 70% water, the protein structures in the solution and in the crystal are virtually identical. The relatively rigid three-dimensional structure ensures the fixed spatial arrangement of the amino acid residues involved in the formation of the catalytic (active) center, where substrate binding and the enzymatic reaction or interactions with other components of the cell medium proceed (Fig. 5). In some cases, catalysis proceeds with the participation of a cofactor bound to the protein molecule either by a covalent bond or by noncovalent interactions.

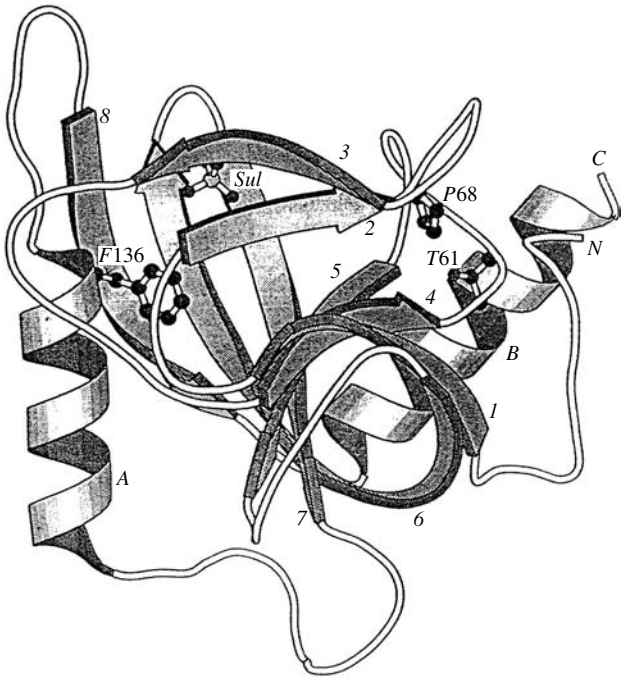

Fig. 2. Ribbon model of the pyrophosphatase subunit from *Thermus thermophilus* [64]. The origin and the end of the polypetide chain are indicated by *N* and *C*, respectively. The β-strands are indicated by numbers *1–8*. The α-helices are labeled with *A* and *B*. The bound sulfate group is located in the active center. One can see three invariant amino acid residues outside the active center. The cylindrical β-barrel can be seen.

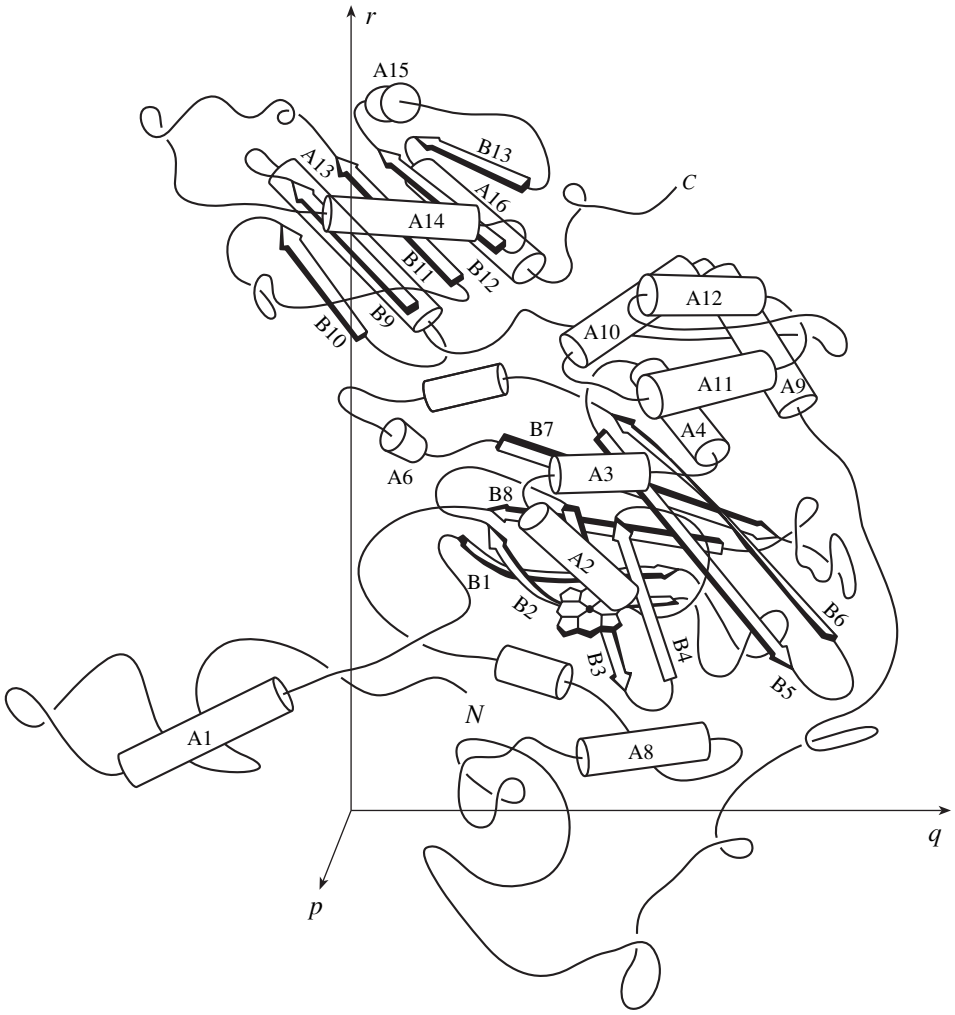

Fig. 3. Polypetide-chain folding in the catalase molecule from *Penicillum vitale* [27]. The twofold symmetry axes of the molecule are denoted by *p*, *q*, and *r*. The origin and the end of the polypetide chain are labeled with *N* and *C*, respectively. The α-helices are depicted as cylinders. The β-strands are depicted by arrows. The heme is shown as a planar group. The *C*-terminal domain is a compact fragment of the polypeptide chain shown at the figure top.

A primary protein structure can be established by chemical methods or from the consideration of the nucleotide sequence in the gene coding the particular protein. The secondary structure is identified by optical methods. The number of subunits in the protein molecule can be determined from the molecular weight. X-ray diffraction studies provide the most detailed information on the macromolecule including the coordinates of all non-hydrogen atoms. These data allow one to compare the polypeptide-chain topologies in various proteins and follow the evolutionary relations between proteins belonging to different families. A knowledge of the nature and the geometry of the residues forming the active center in the native protein and in its complexes with analogues of substrates allows one to make some conclusions about the mechanism of catalysis and provides the insight into the character of the conformational changes accompanying the enzyme functioning. The surface topology and the structure of the active center are also important for attaining targeted drug delivery and designing construction proteins with the desired propertied by the methods of gene engineering.

LEGHEMOGLOBIN

The structure of leghemoglobin (Lb) was the first protein structure established at the Institute of Crystallography. Proteins belonging to the hemoglobin family perform the function of oxygen storage and transport. These proteins were formed on Earth upon the formation of an oxygen atmosphere and oxygen-consuming organisms. Hemoglobins contain a prosthetic group, namely, the heme responsible for their functioning. In all hemoglobins, this group has the same structure–that of protoporphyrin IX. The iron atom in the center of porphyrin adopts the maximum coordination number (six) and holds two axial ligands and four equatorial

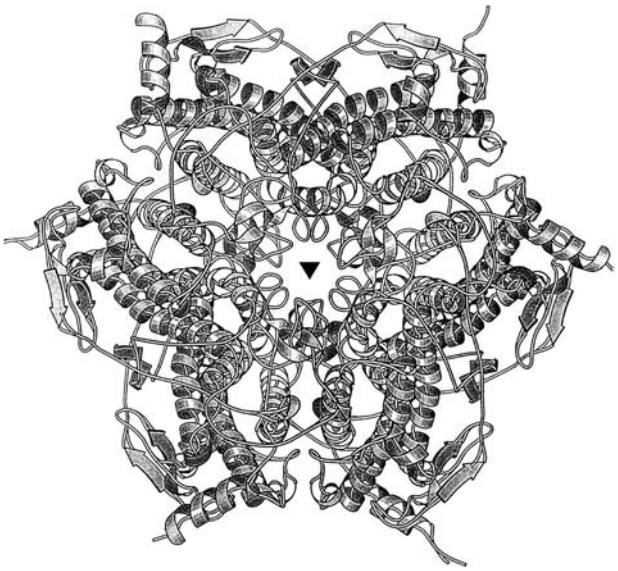

Fig. 4. Ribbon model of the tertiary structure of the dimanganese catalase molecule from *Thermus thermophilus* consisting of six subunits [36]. The threefold axis is indicated by a triangle.

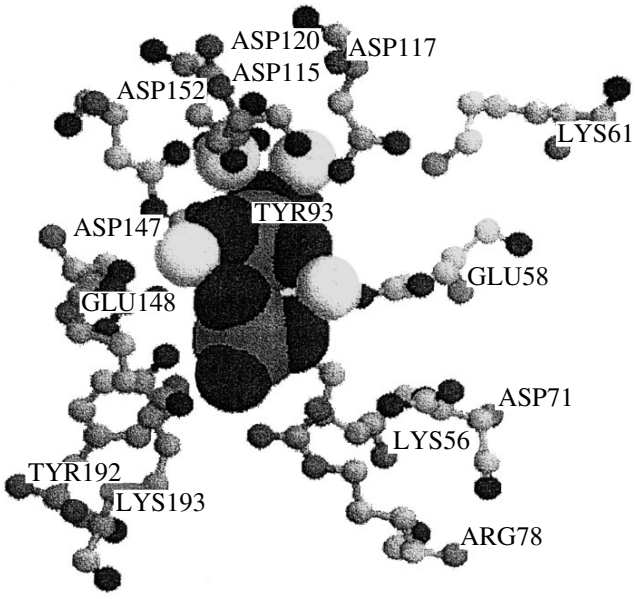

Fig. 5. Fragment of the active center of pyrophosphatase from *Saccharomyces cerevisiae* with bound Mn^{2+} ions (empty spheres) and two phosphate groups (tetrahedra) [61].

ligands. One of the axial sites is occupied by the imidazole ring of proximal histidine through which the heme group is linked to the protein. Molecular oxygen is the second axial *in vivo* ligand. Because of the crucial importance of aerobic respiration, hemoglobins are being extensively studied by different methods. Proteins of this family were the first that have been studied by the methods of X-ray diffraction analysis. X-ray studies demonstrated that all the hemoglobins are characterized by the same polypeptide-chain folding, which was formed during myoglobin folding.

It was believed that hemoglobins could be found only in animals. Leghemoglobins, which were discovered in higher plants, where they perform the function of fixation of atmospheric nitrogen, can be considered as a separate evolutionary branch of hemoglobins. In nodules of fabaceous plants inoculated with bacteria *Rhizobium*, these monomeric hemoglobins provide oxygen diffusion to nitrogen-fixing bacteroids. Because of a high oxygen affinity, leghemoglobin maintains the concentration of O_2 sufficient for oxidative phosphorylation and, at the same time, low enough so that it does not cause inactivation of the nitrogenase complex acting under anaerobic conditions. In the presence of excessive oxygen, the iron atom of the heme group is transformed into the oxidized ferric state so that the protein cannot bind molecular oxygen any more; however, it can bind charged diatomic ligands.

Leghemoglobin was isolated from root nodules of yellow lupin and was separated into individual components. Leghemoglobin crystals suitable for X-ray diffraction study were grown from pure preparation [12]. The three-dimensional structure was established by the isomorphous replacement method first at 5 Å and then at 2.8 Å resolution [13–15].

Even the low-resolution data provided the evidence that the polypeptide-chain folding of Lb is analogous to that observed for animal myoglobins [16] (Fig. 6). Eight α-helices linked by irregular regions form the same characteristic folding (Fig. 6). The homology of the structures of plant and animal hemoglobins suggests that their common precursors existed more than 1.3 billion years ago, when plants and animals started developing separately. This indicates that the three-dimensional structure is exceptionally conservative, which is seen against the background of considerable changes of the primary structure.

Despite the fact that all hemoglobins contain the same heme group, the homologous amino acid sequences, and are characterized by the same polypeptide-chain folding, representatives of this family are characterized by the oxygen affinites differing by a factor more than 10^5, which corresponds to the change in the binding energy of O_2 by 7 kcal/mol. Leghemoglobin possesses a high oxygen affinity because of a high value of the rate constant oxygen-complex of formation and the moderate rate of its dissociation.

One of the goals of the X-ray diffraction analysis of Lb at high resolution was to reveal the structural characteristics responsible for its functional behavior. The studies of Lb performed at the Institute of Crystallography attracted the attention of Perutz and Huber, who performed the pioneering studies of hemoglobins, and the subsequent investigations were performed within the framework of international cooperation. The refine-

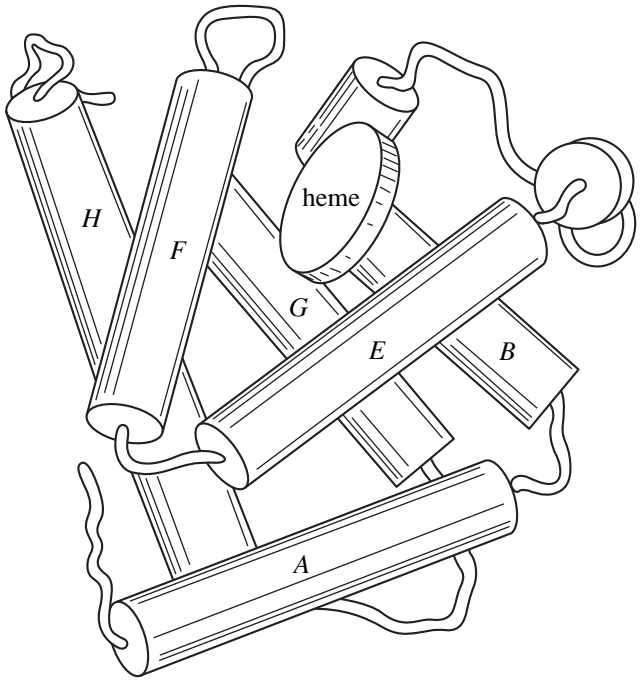

Fig. 6. Structure of the leghemoglobin molecule [15]. The α-helices shown as cylinders are labeled with Latin letters. The arrangement of eight helices typical of all hemoglobins is shown. The heme is represented by a disk located between the *E* and *F* helices. The distal and proximal cavities are situated above and below the heme, respectively.

ment of the structure of ferric Lb at 2 Å resolution from the X-ray data collected on crystals grown from the ammonium acetate buffer showed that the acetate ion occupies the position of the sixth ligand coordinated to the iron atom [17]. The complexes of ferric and ferrous Lb with diatomic molecules and ions (CN^-, F^-, NO, and CO) and bulky organic molecules (nitrobenzene and nicotinic acid) were prepared and studied at high resolution [18–20]. Nicotinic acid is present in root nodules and is probably involved in *in vivo* control over the oxygen affinity of the protein. The X-ray data sets collected on crystals under anaerobic conditions and also in the presence of oxygen traces made it possible to study Lb in the deoxy and oxy states [21].

The analysis of the three-dimensional structures of the Lb complexes with different ligands demonstrated that the ability of Lb to bind bulky ligands is explained by the larger size of the cavity in which the functional ligand is located in comparison to that for myoglobin and the mobility of the distal histidine residue, which closes the entrance to the heme pocket. The cavity of the heme pocket increases because of the displacement of the heme group by 3.5 Å toward the *G* and *H* helices (Fig. 6). The mobility of the distal histidine accounts for the high rate of oxygen-complex formation. Yet another unique characteristic of the Lb structure is the rotational freedom of proximal histidine. This residue in deoxy-Lb oscillates between two alternative orientations, whereas in oxy-Lb it is rigidly fixed and approaches the porphyrin plane. The rigid position of the proximal histidine in the oxy form leads to a decrease in the rate of dissociation in the oxygen complex. In spite of the larger distal cavity, the molecule of carbon monoxide in Lb is inclined to the heme plane like in all the other hemoglobins. This geometry is unfavorable for CO binding resulting in the preferential oxygen binding. This property, common to all hemoglobins, prevents protein inhibition by carbon monoxide is formed *in vivo* upon decomposition of porphyrin.

CATALASES

Heme catalases. Catalases belong to another family of heme-containing proteins. Catalases are highly efficient enzymes with high molecular weights (250–300 kDa). They catalyze decomposition of hydrogen peroxide to water and oxygen. This process is fastest among all the enzymatic reactions known up to date (the rate constant $k = 10^7$ M^{-1} s^{-1}).

Catalases are present in the systems in which cell respiration involving cytochromes occur, i.e., in which oxygen reduction results in formation of hydrogen peroxide, toxic for living cells. Hence, the main function of catalase is to protect the cell and its components against the destructive effect of hydrogen peroxide. Catalases were found in all plants, animals, and in most of aerobic bacteria. The corresponding reaction involves two hydrogen peroxide molecules. The first molecule bound to the heme acts as a two-electron oxidizer and gives up its electrons to the second hydrogen peroxide molecule bound to the heme.

The structures of two heme catalases from the fungus *Penicillum vitale* [22–30] and the microorganism *Micrococcus lysodeikticus* [31–33] were first solved at 3 Å resolution and then were refined at 2 and 1.5 Å, respectively. Catalase from *Penicillum vitale* was the first protein whose crystals were grown by the ultracentrifugation method developed at the Institute of Crystallography [26].

The protein crystallized in the sp. gr. $P3_12_1$ had rather large unit-cell parameters ($a = b = 144.4$ Å, $c = 133.8$ Å). When the study of catalase from *Penicillum vitale* was started, there were no data on the structures of the enzymes of this family; therefore, the phases of the structure factors were determined by the isomorphous replacement method. There were no data on the primary protein structure either, and the amino acid sequence was initially determined from an electron-density synthesis. Later, it was compared with the amino acid sequence established by chemical methods.

A catalase molecule consists of four subunits and is described by the symmetry 222. The *N*-terminal segment of each subunit (Fig. 3) contains one α-helical region (*A*1) extended toward adjacent subunits and forming numerous contacts with them. The *N*-terminal segment is followed by three compact domains. The

heme-containing domain includes a β-barrel built by eight antiparallel β-strands and seven α-helices (the α + β domain). Another much smaller domain consists of four α helices located in the vicinity of the helices of the first domain. The third *C*-terminal domain consists of five parallel β-strands alternating with α-helices (Fig. 3). This domain is of the α/β type and is topologically similar to flavodoxin (the flavodoxin domain). Eighty percent of amino acid residues are located in ordered secondary-structure regions, and the remaining residues belong to the *N*-terminal segment and two irregular fragments located between the domains.

The quaternary enzyme structure is very unusual. Four subunits are arranged in such a way that the *N*-terminal segment of the polypetide chain of each subunit passes through the loop linking the heme-containing and helical domains of the adjacent subunit.

The heme group represents the center, in which the enzymatic reaction proceeds. The heme group in catalases is not necessarily protoporphyrin IX—some catalases have modified protoporphyrins. In particular, the catalase from *Penicillum vitale* contains the heme *d*, more stable against oxidative destruction.

The arrangement of the heme and the heme environment are conservative in all the catalases. Similar to hemoglobins, the heme in catalases is linked to the protein only via noncovalent interactions and is "hidden" inside the globule at a distance of about 20 Å from the molecule surface. Tyrosine on the proximal side of the heme and histidine and asparagine on its distal side are involved in catalysis. The deprotonated oxy group of tyrosine serves as a proximal ligand coordinated to the iron atom of the heme group. Apparently, the negatively charged oxygen atom of the phenol group of this residue is of great importance for maintaining the high degree of iron oxidation.

The heme pocket on the distal side is formed mainly by hydrophobic residues, with only the functionally important histidine and asparagine residues being polar. The ring of distal histidine is almost parallel to the porphyrin plane. This arrangement differs from the arrangement of distal histidine in hemoglobins, cytochromes, and peroxidases and is apparently associated with the enzymatic activity of catalases. The distal cavities of some catalases, in particular, the catalase from *Micrococcus lisodeikticus*, contain water molecules.

To reveal the heme side where the ligand is coordinated, the crystals of the complex of catalase from *Penicillum vitale* with the 3-amino-1,2,4-triazole inhibitor were studied by X-ray analysis at 1.8 Å resolution. The inhibitor is covalently bound to the imidazole ring of the conservative distal histidine residue. The inhibitor does not interact with the iron atom of the heme and is elongated toward the asparagine residue in the distal cavity. This arrangement prevents the penetration of a hydrogen peroxide molecule to the reaction center of the enzyme and, thus, provides the inhibition effect.

One more interesting characteristic of the catalase molecule is the presence of large cavities and channels. The largest spherical cavity has the radius of almost 7 Å. The cavities do not emerge to the molecule surface. At least some of these cavities are of the functional importance, because they ensure substrate diffusion to the reaction center. Two (major and minor) channels provide passages to the distal cavity, in which a substrate, reaction products, or an inhibitor can be located. The major channel is 30 Å in length; its diameter at the molecule surface reaches 15 Å. With an approach to the reaction site, this cone-shaped channel becomes narrower; hence, large molecules have only the limited access to the heme. The inner channels surfaces are lined with hydrophobic residues.

Comparing this catalase with other catalases, we see that the most substantial differences are associated with the presence (catalase from *Penicillum vitale*) or absence (catalase from *Micrococcus lysodeikticus*) of the *C*-terminal domain with the flavodoxin-like topology. The catalases of various origins also differ in the presence or absence of the NADPH-binding center. It exists in some catalases not containing the *C*-terminal domain, i.e., not having the region with the topology providing nucleotide binding. Despite the fact that these enzymes are well studied and their structures are known, the role of NADPH in catalase functioning is not quite clear; hence, their further investigations are of obvious interest.

On the whole, the heme-containing catalases are characterized by the unique spatial organization which remained intact throughout the evolutionary period. This polypeptide-chain folding, common to all the studied heme catalases, is called the catalase-type folding. The comparison of the properties of two heme proteins—leghemoglobin and catalase—clearly shows the pronounced dependence of the heme properties on the protein globule nature. Thus, the heme group performs different functions in different proteins.

Dimanganese catalase. Unlike the enzymes described above, the catalase isolated from the thermophilic bacterium *Thermus thermophilus* belongs to another family of catalases in which the active center has two manganese ions instead of the heme group [34]. Dimanganese catalases isolated from a number of bacteria are less studied than heme-containing enzymes. Apparently, the occurrence of non-heme catalases is associated with the specific conditions of existence of thermophilic bacteria. These bacteria function at about 80°C, the temperature at which proteins are usually denaturated.

The three-dimensional structure of a dimanganese catalase from *Thermus thermophilus* was established at a 3- and 1.0-Å resolution [35, 36]. A dimanganese catalase molecule with the molecular weight of 200 kDa consists of six identical subunits forming a hexamer with the symmetry 32 (Fig. 4). The EPR studies showed that both manganese ions can exist in different oxida-

Fig. 7. Ribbon model of the polypeptide chain of aspartate aminotransferase [38].

tion states and can change the oxidation state under the action of oxidizing and reducing agents. The structures of two forms of catalase—native and inhibited with chloride ions—were established. The atomic models at a 1-Å resolution were refined to *R* factors of 9.8 and 10%, respectively. The molecule core consists of four parallel α-helices with two manganese ions in between. The manganese ions are spaced by 3.6 Å. The active center lies deeply inside the monomer between four major helices and is connected with the surrounding solution by two channels. The coordination spheres of the manganese ions are characterized. The high-resolution X-ray data provided the analysis of the electron-density distribution in the active center of the enzyme and the establishment of several possible positions of side chains depending on the oxidation state of the manganese ions. The amino acid residues of the active center in the native enzyme and in its complex with the chloride ion can have different conformations. The analysis of the structures revealed the possible binding sites of hydrogen peroxide, which in turn allowed one to suggest a spatial mechanism of hydrogen peroxide decomposition [36].

PYRIDOXAL-DEPENDENT ENZYMES

The pyridoxal-dependent enzymes contain pyridoxal-5'-phosphate (the active form of the vitamin B_6) as a cofactor. These enzymes control numerous processes of amino-acid metabolism by catalyzing transamination; aldol cleavage; racemization; α-, β-, and γ-elimination; etc. The catalysis by these enzymes involves a number of successive stages and is accompanied by conformational changes [37]. Because of the reversibility of the reactions catalyzed by aminotransferases, the enzymes of this group can be used as highly specific catalysts for preparing ultrapure amino-acid samples.

The study of the three-dimensional structure of cytosolic aspartate aminotransferase (AATF; transaminase) was started in 1976 in cooperation with the Engelhardt Institute of Molecular Biology of the Russian Academy of Sciences. Aspartate aminotransferase catalyzes the reversible transfer of the amino group from aspartate to ketoglutarate. The enzyme consists of two identical subunits.

The three-dimensional structure of the enzyme in the pyridoxal form was established at 2.8 Å resolution [38, 39]. The ribbon model of the enzyme is shown in Fig. 7. Each subunit consists of one large and one small domains linked by irregular polypeptide chains. The large domain consists of a strongly bent β-sheet formed by seven strands and is surrounded with α-helices located on both sides. The small domain consists of the closely located *N*- and *C*-terminal regions of the polypeptide chain. Two active centers occupy a deep cavity at the interface between the subunits, so that the amino acid residues of both domains of one subunit and the large domain of the other subunit are involved in the formation of each active center. Pyridoxal-5'-phosphate participating in the transfer of the amino group is bound to the large domain, the most stable fragment of the structure. The coenzyme is located at the bottom of the cavity of the active center at a distance of almost 10 Å from the molecule surface. One of the coenzyme sides "looks" at the β-sheet so that its mobility is limited by the van der Waals interactions with the β-sheet. The opposite side of the coenzyme is accessible to the solvent. The phosphate group is linked to the enzyme via hydrogen bonds.

In the pyridoxal form of the enzyme, the subunits linked to each other predominantly by hydrogen bonds can adopt either an open or a closed conformation, which differ by the position of the small domain. In the open form, the small domain is located for from the active center, whereas in the closed form, it is located close to the active center. In the complex of the enzyme with 2-oxoglutarate [40], the latter interacts with amino acid residues of both subunits adopting the closed conformation. If 2-oxoglutarate is removed from the crystal, the small domain of one subunit is displaced from the active center and the conformation of this subunit becomes open.

Other pyridoxal-dependent enzymes, namely, tyrosine phenol-lyases from *Citobacter freundi* and *Erwina herbicola* and tryptophanase from *Proteus vulgaris* have similar quaternary structures. These enzymes exist as tetramers. Tyrosine phenol-lyase catalyzes β-elimination of tyrosine and provides the formation of phenol and pyruvate. This enzyme can be used to synthesize tyrosine and its physiologically active analogues, e.g., 3,4-oxyphenylalanine used in the treatment of Parkinson's disease.

The structures of both native tyrosine phenol-lyase [41–43] and its complex with the quasi-substrate *N*-(5'-phosphopyridoxyl)-*L*-tyrosine [44] were also estab-

lished. In the complex with the quasi-substrate, the tyrosine fragment of the substrate adopts two major conformations. In one of these conformations, the phenol ring of tyrosine is parallel to the pyridine ring of the coenzyme, whereas in the other conformation these fragments are perpendicular to one another. Presumably, the former and latter conformations correspond to the initial and the final stages of the catalytic event. It was also found that cofactor binding is accompanied by a decrease in the distance between the large and the small domains by 1.4 Å, whereas binding of the pseudosubstrate causes additional narrowing of the interdomain cleft by 3 Å. The X-ray structural data allowed one to propose the model of conformational changes occurring in the passage from the free enzyme to the stage simulating the completion of the catalytic event.

Tryptophanase catalyzes the decomposition of tryptophan into indole, pyruvate, and ammonia. The structure of tryptophanase was solved by the molecular replacement method at 2.1 Å resolution. Similar to tyrosine phenol-lyase, the potassium ions necessary for enzymatic activity in tryptophanase were localized between the subunits. These ions provide the active conformation of the large domain [45–47].

The analysis of the three-dimensional structures of pyridoxal-dependent enzymes revealed the conformational changes for the protein globules and the coenzyme upon the catalysis, which allowed one to follow the conformational changes accompanying the transformation of the pyridoxal form of the enzyme into the pyridoxamine form. A more detailed spatial mechanism of this complicated multistage reaction was proposed. Despite the low homology of the amino acid sequences, the principal characteristics of the polypeptide-chain folding turned out to be similar to those observed for cytosolic aspartate aminotransferase, namely, dimers in the tetramer resemble the dimer of AATF (Fig. 7).

NUCLEOTIDE DEPOLYMERASES

The X-ray diffraction studies of proteins involved in interactions with nucleic acids are of considerable interest. Nucleotide depolymerases belonging to enzymes of the nucleic-acid metabolism play the key role in the "processing" of genetic information. These enzymes cleave phosphodiester bonds between nucleotides without the formation of free phosphate and produce mono- and oligonucleotides. DNases and RNases are involved in all the reactions associated with conversion of nucleic acids providing utilization of macromolecules; inactivation of foreign DNA; and selective cleavage of some bonds in the molecule necessary for transcription, replication, recombination, and processing of different types of nucleic acids. In biochemical assays, these enzymes are used for the determination of nucleotide sequences of nucleic acids. Since these enzymes exhibit antiviral and antitumor properties, they are widely used in biotechnologies.

Ribonuclease *A* is a classical representative of the RNase family. It is widely used in the therapy of some virus diseases, for example, virus encephalitis. With the accumulation of information on the properties of these enzymes and a better understanding of the mechanism of their catalysis, these proteins are found ever increasing range of application.

The well-studied pyrimidine-specific pancreatic ribonuclease *A* (RNase *A*) catalyzes hydrolysis of phosphodiester bonds in RNA predominantly located next to the pyrimidine nucleotides. Hydrolysis with the use of this enzyme proceeds in two stages. First, oligonucleotides with the terminal 2',3'-cyclic phosphate fragment are formed, which is followed by its hydrolysis to yield 3'-phosphate. In addition to classical RNase *A*, a large number of microbial and fungal ribonucleases with the molecular weights of 10000–12000 Da are known. Unlike RNase *A* specific to the pyrimidine base, these enzymes are generally specific to guanine. Among them are fungal ribonucleases C_2, Ap_1, Pb_1, and Th_1 [48–51] and bacterial ribonuclease *Bi* [52]. The three-dimensional structures of the polypeptide chains of bacterial and fungal nucleases have many characteristics in common. Guanyl-specific RNase belongs to proteins of the ($\alpha + \beta$) type. The molecule core is formed by a β-sheet consisting of 4–5 strands covered with one or two α-helices. The amino acid residues involved in the active center are distributed among the β-sheet and the adjacent fragments of the structure. Since the structure-specificity relationships are especially important in the studies of the structures of ribonucleases, both native enzymes and their complexes with nucleotides were structurally studied. The refinement of the structure of the complex of ribonuclease Pb_1 with the reaction product (guanyl nucleotide) at high resolution showed that the nucleotide is bound to the recognition loop of the enzyme by four hydrogen bonds between the atoms of the base and the atoms of the recognition groups of the enzyme. All the amino acid residues involved in these interactions were established. Only two atoms of the adenine ring can participate in the formation of the necessary hydrogen bonds, whereas the guanine base forms four such bonds; this allows the enzyme to "recognize" these nucleotides.

Unlike the structural studies of DNases and RNases, investigations of nucleases, which do not exhibit specificity to the chemical nature of the carbohydrate component, are scarce. In this connection, the study of extracellular endonuclease from the pathogenic gram-negative bacterium *Serrata marcescens* (nuclease *Sm*) is of great interest. This protein is stable to incubation in 4 M urea and in 0.01 M β-mercaptoethanol and, therefore, can be used for removing undesirable nucleic acids. Nuclease *Sm* is a sugar-nonspecific metal-dependent enzyme which exhibits the maximum activity in the presence of magnesium ions and (with a partial loss of the catalytic activity) in the presence of manganese ions. This enzyme catalyzes cleavage of 3'-phosphodi-

ester bonds in single- and double-stranded DNA and RNA to form 5'-phosphorylated nucleotides. It is a structural homologue of the superfamily of nucleotide depolymerases isolated from different prokaryotes and eukaryotes. The endonuclease molecule exists as a dimer consisting of two identical subunits with a molecular weight of 30 kDa. The three-dimensional structure of nuclease *Sm* was solved by the isomorphous replacement method and refined at 1.7 Å resolution [53]. This enzyme is the only well studied representative of the homologous family of related proteins. The amino acid residues essential for catalysis were localized in the active center of the enzyme. The magnesium–water cluster was revealed, and the ligands in the inner and outer coordination spheres of the magnesium ion were found. The role of different amino acid residues of nuclease *Sm* in catalysis was established in the studies of mutant forms of the protein and the comparison with amino acid residues of the related proteins. The DNA-binding center of the protein was localized with the aid of simulation and computer graphics. The consideration of the structure refined at a 1.7-Å resolution and the data on the three-dimensional structures and properties of the related enzymes allowed one to suggest the spatial scheme of the reaction catalyzed by nuclease *Sm* [54–56]. This reaction proceeds according to the S_N2 mechanism.

PYROPHOSPHATASES

Inorganic pyrophosphatases belong to enzymes involved in the phosphorus exchange. These enzymes transfer the phosphate groups and are involved in the processes accompanying the biological conversion of the energy in living organisms. The enzymes of this class are divided into two large families with substantially different properties and functions. Hydrolysis of the macroergic phosphoanhydride bond in inorganic pyrophosphate (PPi) with the formation of orthophosphate is the major reaction catalyzed by soluble pyrophosphatases. Pyrophosphate is formed as a product of biosynthetic reactions involving ATP and is of great importance for cell metabolism. The pyrophosphate concentration affects the level of cyclo-AMP, the reproduction and expression of the genetic information, the processes of tissue mineralization, etc. Hydrolytic cleavage of pyrophosphate following its formation in the reactions of biosynthesis leads to the consumption of two high-energy bonds per newly formed bond in the biopolymer, which makes the biosynthesis of DNA, RNA, and proteins practically irreversible. More complex membrane pyrophosphatases present in mitochondrial membranes or chromatophores of photosynthetic bacteria catalyze energy-dependent synthesis of PPi. The subsequent hydrolysis of PPi under the action of membrane pyrophosphatases is accompanied by the proton transfer through the membrane and the appearance of the membrane potential. It was shown that the reactions of oxygen isotope exchange and phosphate exchange catalyzed by soluble pyrophosphatase also proceed with formation of intermediate enzyme-bound pyrophosphate. Therefore, in the absence of an external energy source, soluble pyrophosphatases catalyze the formation of the macroergic pyrophosphate bond in the active center. Hence, these rather simple enzymes can serve as convenient models for studying general characteristics of hydrolysis and synthesis of the pyrophosphate bond. Pyrophosphatases attract considerable attention because of their widespread occurrence and remarkable properties.

All inorganic pyrophosphatases are metal-dependent enzymes because they exhibit activity only in the presence of divalent metal ions. Magnesium is the best activator, whereas calcium, uranyl, terbium, and fluoride ions are inhibitors of pyrophosphatases.

Inorganic yeast pyrophosphatase from *Saccharomyces cerevisiae* was the first enzyme of this family whose three-dimensional structure was established by the molecular replacement method. The structures of the free form and its complex with metal ions were determined at 3 Å resolution [57–61]. The structure of its complex with the reaction products was established at a 2.4-Å resolution [62].

Pyrophosphatase from a thermophilic strain of the bacterium *Thermus thermophilus* has the highest thermal stability of all presently known pyrophosphatases [63]. The enzyme was isolated, characterized, and studied by X-ray diffraction analysis at a 2-Å resolution using the molecular replacement method [64]. The electron density for the active center of the subunit of the pyrophosphatase from *Thermus thermophilus* is shown in Fig. 8. The study of *E. coli* pyrophosphatase is under way. For this enzyme, the gene sequencing was carried out and a number of site mutants was obtained [65–67].

Inorganic pyrophosphatase from yeast *Saccharomyces cerevisiae* exists as a dimer of two identical subunits related by the noncrystallographic twofold axis. The polypeptide-chain folding of one subunit is shown in Fig. 9. Analysis of this folding showed that the enzyme belongs to the proteins of the $(\alpha + \beta)$ type. About one-half of the amino acid residues of the polypeptide chain are involved in extended β-strands, with some of them forming a system of antiparallel sheets. The molecule core consists of a barrel formed by five strands surrounded by four helices located on the subunit surface. In a dimer, one of these helices is hidden. The remaining part of the molecule consists of the β-sheet formed by four long and three short strands. Later, it was found that the arrangement of the barrel and two helices is the same in all the structurally studied pyrophosphatases (Fig. 2).

The comparison of this molecule with the topologically similar molecules showed that the five-strand β-barrel also exists in a number of proteins performing different functions. Generally, these are nucleotide-binding proteins containing pyrophosphate binding

sites. This phenomenon can be interpreted by two different ways. First, it might be that pyrophosphatases and some nucleotide-binding proteins have a common precursor. It can also be assumed that the independent evolution of these proteins gave rise to the formation of the β-barrel as a stable structural type. A shell-shaped cleft at the barrel surface surrounded by loops forms a potential binding site suitable for many ligands.

Initially, the active center was localized considering the positions of four uranyl ions in the crystals of the pyrophosphatase complex with these ions. The detection of four bound ions instead of two or three allowed the refinement of the early kinetic schemes of catalysis performed by pyrophosphatase.

The active center of the enzyme is located in the cavity bounded inside by the β-sheet and the wall of the barrel and limited outside by the longest α-helix and two flexible loops. One of these loops contains a conservative arginine residue. Another loop contains several residues of dicarboxylic amino acids. The active center is formed predominantly by polar residues, most of which are dicarboxylic acids serving as potential ligands for metal ions. The enzyme also contains a cluster formed by the basic amino acid residues involved in phosphate binding. All pyrophosphatases characterized by this type of polypeptide-chain folding have 17 conservative amino acid residues located in the cavity of the active center. Using the results of X-ray diffraction studies, some conservative residues were replaced and the resulting mutants of the enzyme were studied. The positions of four manganese ions and two phosphate groups were localized in the pyrophosphatase complex with the reaction products (manganese ions and phosphate) (Fig. 5). The results of X-ray diffraction analysis made it possible to differentiate the ions initially bound to the enzyme and the ions added together with the substrate. The spatial scheme of the enzymatic reaction was proposed. According to the results of the biochemical assays, this reaction proceeds by the S_N2 mechanism.

The comparison of the three-dimensional structures of pyrophosphatases from *Thermus thermophilus* and *E. coli* revealed the causes of the high thermal stability of the former enzyme [68]. Both enzymes exist as *D*3 hexamers, crystallize in the same space group, and have close unit-cell parameters. However, the interactions between oligomers in these enzymes are substantially different, with the number of contacts between the subunits in pyrophosphatase from *Thermus thermophilus* being much larger than in pyrophosphatase from *E. coli*. The presence of additional ionic and hydrophobic interactions between the subunits makes the hexamer of pyrophosphatase from *Thermus thermophilus* more compact, and the size of the surface hidden in this enzyme is 16% larger than in the enzyme from *E. coli*.

The structures of active centers in all three pyrophosphatases are similar. Apparently, the enzymatic reactions proceed by the same mechanism. The studies

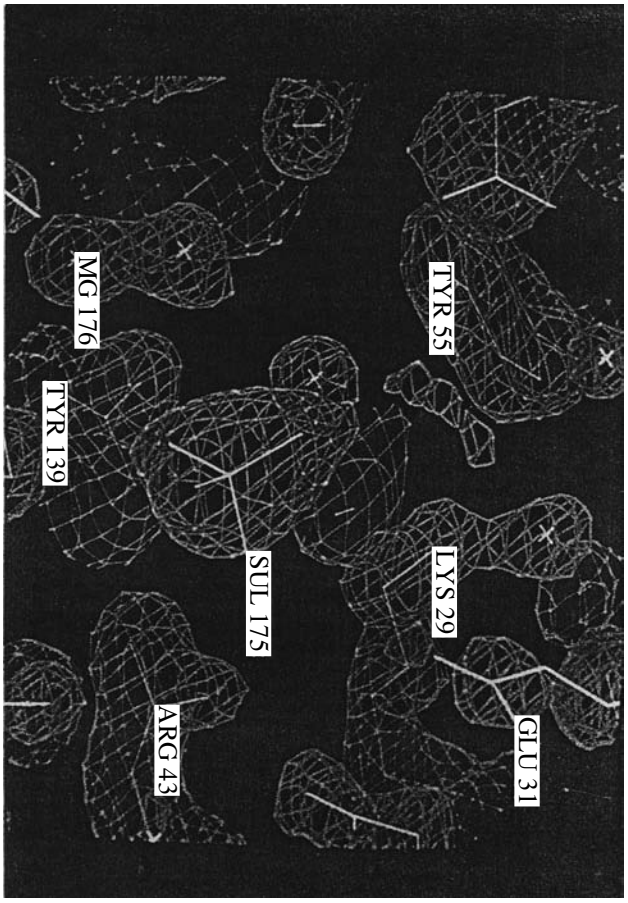

Fig. 8. Electron-density fragment of the subunit of pyrophosphatase from *Thermus thermophilus*. The amino acid residues and the phosphate group bound in the active center are fitted into the electron density [64].

of a number of mutants of pyrophosphatase from *E. coli* showed that even a single mutation causes local structural changes about the substituted residue and, more importantly, affects the conformations of the distant side chains thus changing the enzymatic activity of the protein.

In the experiments on crystallization of pyrophosphatase from *E. coli*, the special procedures were developed to improve the quality of crystals for low-temperature X-ray diffraction studies. With this aim, several cycles of rapid reversible freezing–thawing of the crystals were performed in a cryosolution at different concentrations of the precipitating salt. As a result, the low-temperature X-ray data were collected up to a 1.0-Å resolution [69].

X-ray diffraction study of the complex of *E. coli* pyrophosphatase with inhibiting calcium ions and potassium pyrophosphate at a 1-Å resolution and the biochemical assays provided the establishment of the causes of enzyme inactivation with calcium ions. It was found that potassium pyrophosphate is located in the active center, so that no adjacent water molecules can

Fig. 9. Polypetide-chain folding of inorganic pyrophosphatase from *Saccharomyces cerevisiae*. The bound metal ions and phosphate groups are located in the active center [61].

be involved in the nucleophilic attack on the phosphorus atom of the pyrophosphate molecule.

Taking into account the contribution of X-ray diffraction studies of pyrophosphatases to the understanding of their function, it can be concluded that the present knowledge on the mechanism of catalysis by pyrophosphatase is gained mainly to the achievements in X-ray diffraction analysis.

PROTEASES

Serine proteases of the chymotrypsin and subtilysine families are widespread in living organisms. These enzymes perform polypeptide and protein cleavage, promote the transformation of zymogens into the active forms of enzymes, and are involved in processing of a number of viruses. Proteases are widely used in the analysis of amino acid sequences in proteins; in the synthesis of biologically active peptides and proteins; and in industry as components of detergents and in the cases, where it is necessary to provide resistance to the aggressive media and temperature. The protease family is extensively studied to establish the mechanisms of catalysis and specificity and to elucidate the evolutionary relations within this large class of enzymes.

Carboxypeptidase (CPT) from *Thermoactinomyces vulgaris* belongs to metalloenzymes containing a zinc ion in the active center. This exopeptidase catalyzes hydrolysis of the *C*-terminal residue of the polypeptide substrate. Carboxypeptidase shows a low homology (27–30%) with mammalian carboxypeptidases *A* and *B*. This protein is remarkable for its mixed (*A* + *B*) substrate specificity characteristic of pancreatic carboxypeptidases *A* and *B*. Carboxypeptidases *A* and *B* cleave peptide bonds following the hydrophobic residues and basic amino acid residues, respectively, whereas CPT cleaves both types of bonds. Similar to other proteins from *Thermoactinomyces vulgaris*, the thermal stability of CPT is enhanced in the presence of calcium ions.

The structure of the enzyme was established at a 2.35-Å resolution by the molecular replacement method in combination with the isomorphous replacement method [70]. Carboxypeptidase appeared to be a spatial homologue of pancreatic carboxypeptidases, despite the low homology between their primary structures. The molecule core consists of a six-strand mixed β-sheet surrounded by seven α-helices (Fig. 10). The structure of the active center is similar to that of the pancreatic enzymes. The amino acid residues involved in catalysis and binding of the *C*-terminal carboxyl group of the substrate are fully conservative. Similar to pancreatic enzymes, the five-coordinate zinc ion in CPT is surrounded by the oxygen atoms of the carboxyl group of glutamic acid, the nitrogen atoms of two histidine residues, and a water molecule. Proceeding from this fact, it can be assumed that the catalytic mechanism proposed for pancreatic enzymes is also valid for all the carboxypeptidases. The analysis of the amino acid substitutions in the pocket, which are responsible for the primary specificity, provided the explanation of the mixed (*A* + *B*) enzyme specificity. The charged residue *Asp*253 replacing the sterically equivalent glycine residue in carboxypeptidase *A* is responsible for the *B* specificity of CPT. This residue can recognize the positive charge of the substrate. The *A* specificity is provided by the small size of the pocket and by the fact that contacts with the polar residue *Asp*253 unfavorable for binding a hydrophobic residue are partly compensated by the formation of the hydrogen bond between *Asp*253 and *Thr*255. The high thermal stability is explained by the binding of two calcium ions.

Thermitase from *Thermoactinomyces vulgaris* is extracellular serine proteinase belonging to enzymes of the subtilysine type. Its homology with subtilysines reaches 44%. The enzyme exists as a monomer, its polypeptide chain consists of 279 residues. Similar to all subtilysines, thermitase exhibits a broad spectrum of specificities. However, it predominantly cleaves peptide bonds following bulky hydrophobic residues.

The structure of thermitase was solved at a 1.4-Å resolution using the combination of the isomorphous and the molecular replacement methods [71]. The molecule core consists of the eight parallel strands forming a twisted β-sheet and five α-helices. The catalytic triad (*Ser*225, *His*71, and *Asp*28) is common to all serine proteases. In the absence of the substrate, the cleft of the active center is substantially hydrated. The central β-sheet contains a loop formed by the residues from 60 to 65 with the calcium ion. The thermal stability of

thermitase is enhanced due to the presence of the bound calcium ions and a large number of hydrophobic and ionic interactions. A characteristic feature of the enzyme is the presence of an 11-Å-long channel occupied by water molecules. The channel origin lies in the vicinity of the *N*-terminus at the enzyme surface of the molecule, passes through its center to the *C*-terminal region. The channel contains five water molecules, which form contacts with many atoms of the protein. Apparently, the water molecules bound in the vicinity of the active center stabilize the enzyme structure in the absence of the substrate.

HUMAN GROWTH HORMONE SOMATOTROPIN

Somatotropin is the polypeptide hormone isolated from hypophysis. This protein exhibits both lactogenic and growth activities. Despite a high homology in the primary structures, these hormones are species-specific; i.e., the hormones active in animals are inactive in humans. Attempts over many years to crystallize the growth hormone have failed apparently due to the heterogeneity of samples isolated from hypophysis. The successful synthesis of human and animal somatotropins of bacteria by the methods of gene engineering provides an essentially new source of obtaining homogeneous hormone samples. A strain of bacteria *E. coli* is used as the hormone producer.

The three-dimensional structure of human somatotropin prepared by the methods of gene engineering, was studied at 3.0 Å resolution [72–73]. Knowledge of the three-dimensional structure gave an impetus to the studies of the hormone interactions with receptors and the attempts to construct efficient analogues of somatotropin on the basis of the achievements of gene engineering.

PLANT TOXINS

Toxins found in various parts of the plants distant in systematics, inhibit the protein synthesis in the cells of eukaryotes by inactivating ribosomes. The best studied proteins of this family are ricin, abrin, viscumin, and ricin agglutinin. This class of proteins attracts ever growing interest, because plant toxins serve as the basis for constructing targeted-delivery cytostatics, i.e., immunotoxins. The action of toxins begins with binding with the receptor. The transfer of the catalytic subunit of toxins through a membrane is followed by modification of ribosomes, which results in termination of the protein synthesis. Since the function and the mechanism of toxin action remain unclear, the studies of their three-dimensional structures are important for solving fundamental problems, designing a new generation of drugs with selective cytotoxic effect, and searching for the methods of enhancing the activity of cytotoxic action of immunotoxins.

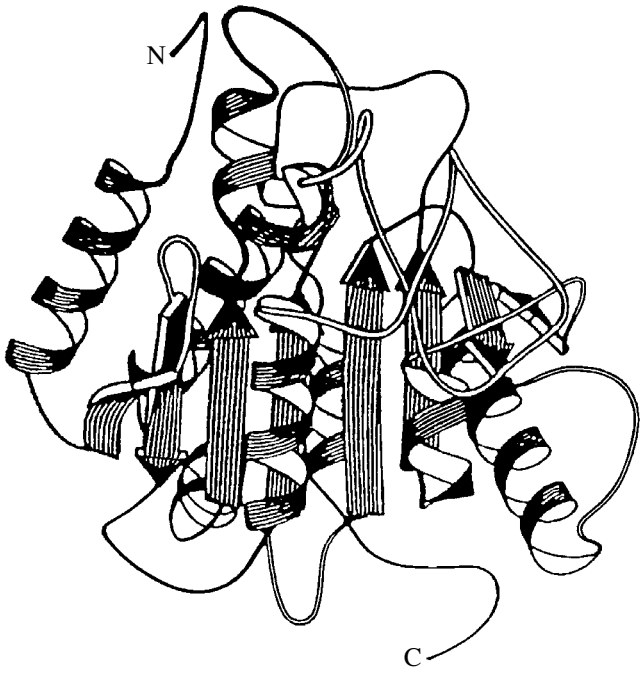

Fig. 10. Ribbon model of the carboxypeptidase molecule from *Thermoactinomyces vulgaris* [70]. One can see the extended β-sheet and the α-helices surrounding it.

Recently, the three-dimensional structures of viscumin *MLI* from *Viscum album* (*Mictletoe*) [74] and ricin agglutinin from *Ricinus communis* [75] were established at 3.5- and 3.6-Å resolutions, respectively. Both structures were solved by the molecular replacement method. Immunotoxins of the viscumin family are glycoproteins consisting of two subunits with approximately equal molecular weights. These subunits perform different functions. One subunit is, in fact, lectin and has two binding sites of β-*D*-galactose. The other catalytically active subunit (subunit *A*) is a highly specific *N*-glucosidase, modifying 28*S* RNA of the 60*S* subunit of ribosomes. Penetrating into the cell cytoplasm, the *A* subunit terminates the protein synthesis. Immunotoxins based on the *A* subunit are more active than other analogous enzymes by a factor of about 50 and, therefore, are used in medicine. In a dimer, the catalytic and binding subunits are linked by a disulfide bond. The structure was solved by the molecular replacement method at 3.5 Å resolution. It was found that a viscumin molecule is an associate of two ricin-like molecules forming a tetramer of the *AB–BA* type with the molecular twofold symmetry axis. The tetramer is formed mainly because of strong hydrophobic and polar interactions. The domain structures of both subunits were established. The *A* subunit consists of three domains. The *B* (binding) subunit consists of β-strands and loops and forms two topologically identical domains symmetric with respect to the local twofold axis. Each domain, in turn, consists of three quasi-equivalent subdomains. These subdomains

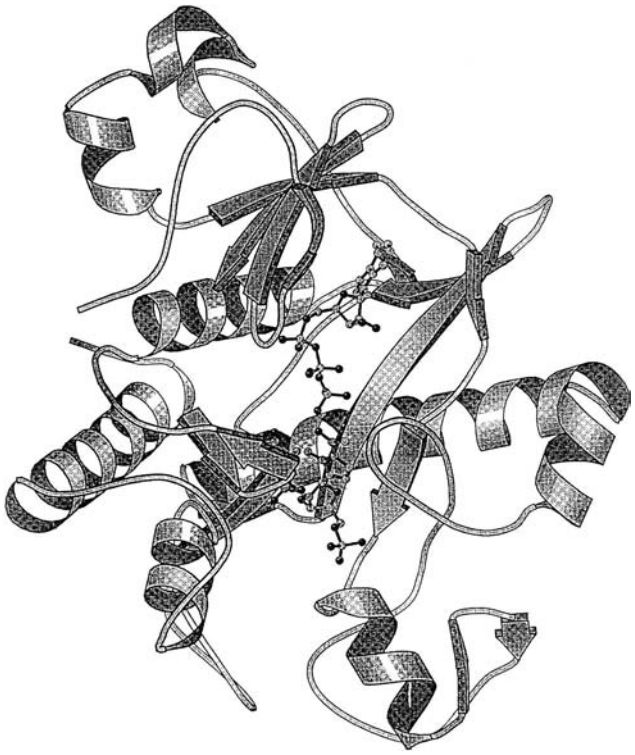

Fig. 11. Molecule of SAICAR synthase with the bound substrate and ATP [77].

are formed from the equally long fragments of the primary structure.

Similar to ricin, ricin agglutinin from *Ricinus communis* belongs to lectins. Ricin is specifically bound to galactoso- and *N*-acetylgalactosoamino-containing oligosaccharides, whereas ricin agglutinin recognizes only galactoso-containing sugars. Similar to viscumin, ricin agglutinin exists as a tetramer consisting of two *AB* dimers. Two dimers are linked into a tetramer by a disulfide bridge of the *BAAB* type. The single mutation of *Tyr*248 (in ricin) to *His*248 (in ricin agglutininin) in the *B* subunit results in the fact that the second domain of ricin agglutinin loses its carbohydrate-binding activity. The agglutininating activity of ricin agglutinin is approximately 62 times higher than that of ricin. At the same time, the toxicity of ricin agglutinin is lower by three orders of magnitude than that of ricin. Apparently, the different toxicities are associated with the change in the hydrophobicity degree of some regions of the polypetide chain caused by the amino acid substitutions.

SAICAR SYNTHASE

Phosphoribosylsuccinocarboxamideaminoimidazole synthase (SAICAR synthase) is involved in the biosynthesis of purines and catalyzes the seventh stage of the total ten stages of the process. Under the action of the enzyme, a nitrogen atom is incorporated into the purine ring in the presence of substrates (phosphoribosylcarboxyaminoimidazole and aspartate), ATP, and magnesium ions. The biosynthesis of purines, the most important components of the cell metabolism, is of great importance. Purines are the components of nucleic acids and also of cofactors of many enzymes. The studies of their biosynthesis provide a deeper insight into the central pathways of the metabolism and help to design efficient chemotherapeutic agents. SAICAR synthase is the second structurally studied enzyme participating in purine biosynthesis.

The protein exists as a monomer with the molecular weight of 36 kDa. Its three-dimensional structure was solved by the isomorphous replacement method and refined at a 1.9-Å resolution [76, 77]. The polypeptide chain of the enzyme forms three domains. The first two domains are of the ($\alpha + \beta$) type, each consisting of the five-strand antiparallel right-twisted β-sheet and α-helices located on one side of the sheet. The third domain consists of two closely spaced α-helices. The active center is located inside the long deep cleft, whose walls are lined with amino acid residues of all the three domains. Twenty-four fully conservative amino acid residues are located in the cavity of the active center. Being an ATP-dependent enzyme, the SAICAR synthase has binding sites of adenine base and phosphate groups in the active center. The ATP molecule is aligned along the phosphate-binding loop, in the way observed earlier in protein kinase and *D*-alanine–*D*-alanine ligase (Fig. 11). It is remarkable that binding of adenine base occurs via the formation of hydrogen bonds only with the nitrogen and the oxygen atoms of the main chain, whereas the side chains of amino acids do not participate in these bonds. Hence, the binding region do not contain any conservative residues. Therefore, all attempts to identify this region only by comparing amino acid sequences have failed. The topological analysis of the individual domains showed that the polypeptide-chain folding of the *N*-terminal domain is similar to that found in the family of protein kinases. The ATP-binding region contains the topological motif typical of actin and cyclo-AMP-dependent protein kinases and ligases. Being taken together, these enzymes comprise a new superfamily of mononucleotide-binding proteins.

CARNATION MOTTLE VIRUS

Viruses are complex biocompounds with the molecular weights of several million of Daltons and consist of the protein coat (capsid) and molecules of genomic RNA or DNA. Viruses generally can be readily crystallized. Many viruses are highly symmetric associations, the fact especially attractive to crystallographers. The three-dimensional structure of the carnation mottle virus has first been studied by electron microscopy and small-angle X-ray scattering [78–80]. The three-dimensional structure of the virus has been originally established at a 18-Å resolution using the results of the three-dimensional reconstruction of the spatial model

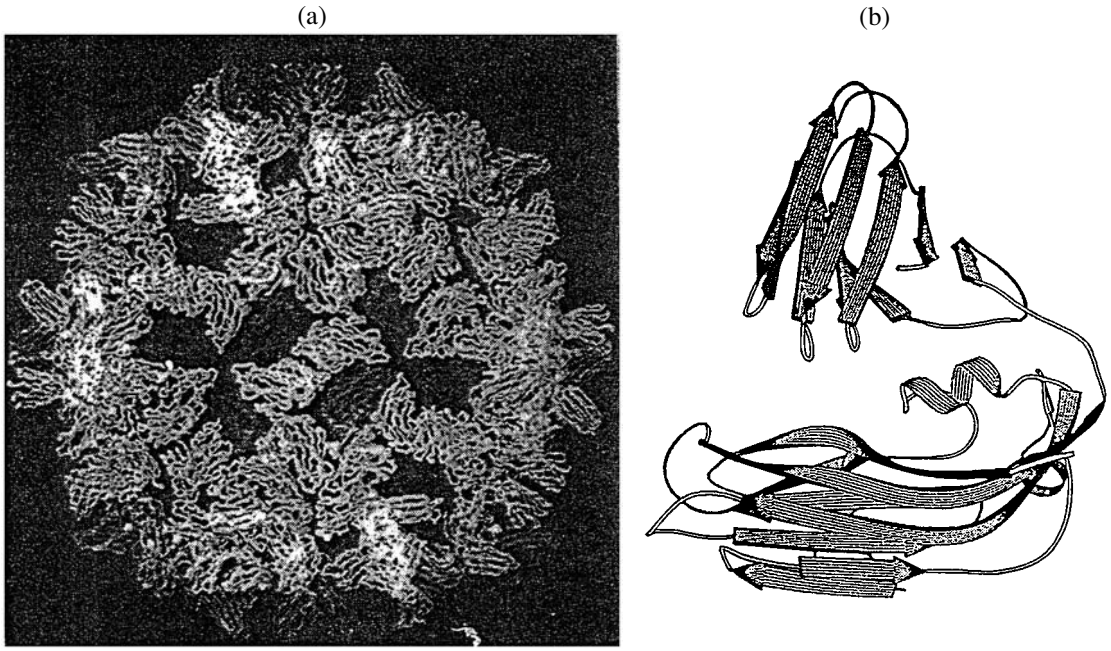

Fig. 12. Packing of subunits in the coat of carnation mottle virus (CMtV) [82]. (a) The *A* subunits are grouped around the fivefold axis; the *B* subunits are grouped about the twofold quasi-symmetry axis; the *C* subunits are related by twofold axes of the icosahedron. (b) Ribbon model of the *A*/*B* subunit of the capsid protein; the *P* and *S* domains are situated at the top and the bottom of the figure.

of the virus with the aim to determine the phases by direct methods [81]. X-ray diffraction studies of viruses have become possible only with the aduent of new sources of powerful X-ray radiation (apparatus with a rotating anode, synchrotrons), high-performance computers, and efficient methodological approaches to the solution of the phase problem. The structural studies of spherical viruses clearly showed that they have canyons or several cavities, in which amino acid residues participating in binding with the receptor are hidden. These cavities are located around the fivefold axis of an icosahedral particle. Because of this arrangement, the regions providing binding with the cell are inaccessible to all the attacks of antibodies. In other viruses, the region of interaction with a cell receptor is protected by a mobile extended polypeptide-chain loop located in the vicinity of the fivefold axis. Knowledge of the real structure of the virus capsid allows the directional synthesis of compounds preventing the addition of a virus particle to the cell and the preparation of synthetic vaccines and vaccines obtained by the methods of gene-engineering, whose activity is based on the complementary principle with respect to the virus surface.

Carnation mottle virus belongs to the group of small spherical plant viruses with single-stranded RNA. The protein coat (capsid) of the virus is composed of 180 identical subunits with the molecular weight of 37.787 Da each. The subunits are related by the icosahedral symmetry $T = 3$. The molecular weight of the virus is $(7.6–7.7) \times 10^6$ Da. The complete three-dimensional X-ray diffraction data set was collected within 12 h. from four crystals using synchrotron radiation (EMBL, Hamburg) to a 3.2-Å resolution. The structure was solved by the molecular replacement method using the molecule of the coat protein of the tobacco mosaic virus as the starting model and then was refined at a 3.2-Å resolution [82–83]. The comparison of three chemically identical *A*, *B*, and *C* subunits in the icosahedral asymmetric unit of the unit cell ($T = 3$) revealed that packing of these subunits in the virus capsid leads to the changes in the conformation and arrangement of the elements of the secondary structure in the subunits. Each subunit consists of two major ordered domains—the *S* domain containing 170 amino acid residues and the *P* domain with the fragments being extended into the solution. Both domains are linked via a flexible loop (Fig. 12). The *P* domain is less ordered than the *S* domain (the average *B* values differ by almost a factor of two). The *P* domain contains two antiparallel β-sheets. The principal structural motif of the *S* domain can be represented by eight antiparallel strands forming the β barrel consisting of two β-sheets, one of which is twisted. In addition to the β-strands, the *S* domain contains two helical regions. The structures of both domains are similar to the corresponding structures observed in the capsid protein of the tobacco mosaic virus. The *C* subunit contains the coordinated calcium ion. The authors believed that the calcium ion triggers the mechanism of self-association of the subunits. The results of the biochemical assays on dissociation and reassociation of virus particles demonstrated that this process is reversible within wide ranges of pH

Macromolecules studied at the Institute of Crystallography of the Russian Academy of Sciences

Protein	Molecular weight, Da	Space group	Resolution, Å	References
Deoxyleghemoglobin	17000	$B2$	1.8	[21]
Complexes of leghemoglobin with	–	–		–
acetate	17000	$B2$	1.4	[17]
nitrobenzene	17000	$B2$	2.0	[16]
nicotinic acid	17000	$B2$	2.0	[16]
aquomet	17000	$B2$	2.0	[16]
oxygen	17000	$B2$	1.7	[21]
CO	17000	$B2$	1.8	[20]
NO	17000	$B2$	1.8	[20]
isoquinoline	17000	$B2$	1.9	[93]
Inorganic pyrophosphatase from *Saccharmoyces cerevisiae*	64000	$P2_1$	3.0	[60]
Complex of inorganic pyrophosphatase from *Saccharomyces cerevisiae* with MnPi	64000	$P2_12_12_1$	2.4	[62]
Inorganic pyrophosphatase from *Thermus thermophilus*	120000	$R3_2$	2/0	[64]
Inorganic pyrophosphatase from *E. coli*	120000	$R3_2$	2.0	[65]
Complex of inorganic pyrophosphatase from *E. coli* with Mn and Eu ions	12000	$R3_2$	2.0	[95]
Complex of inorganic pyrophosphatase from *E. coli* with CaPPi	120000	$R3_2$	1.0	[67]
Human somatotropin	22000	$P4_32_12$	3.0	[73]
Endonuclease *Sm*1	26700	$P2_12_12_1$	1.7	[56]
Aspartate aminotransferase	90000	$P2_12_12_1$	2.0	[40]
Complex of tyrosine phenol-lyase from *Erwina herbicola* with Na ions:	200000	$P6_222$	3.2	[43]
holoenzyme with potassium ions	200000	$P6_222$	3.1	[43]
holoenzyme with ammonium ions	200000	$P6_222$	2.7	[43]
tryptophanase from *Proteus vulgaris*	210000	$P2_12_12_1$	1.7	[46]
Ricin agglutinin	130000	$P3_2$	3.6	[74]
Viscumin *ML*1	120000	$P6_222$	2.5	[75]
Neurotoxin from venom of Central Asian cobra	7800	$P2_12_12_1$	1.9	[91]
Spherical carnation mottle virus	6802000	123	3.2	[82]
Uridine phosphorylase from *E. coli*	165000	$P2_1$	2.5	[94]
Ribonuclease C_2	11000	$P2_1$	1.75	[51]
Ribonuclease C_2	11000	$P2_1$	1.35	[51]
Ribonuclease Ap_1	11000	$P2_1$	1.08	[53]
Ribonuclease Ap_1 (phosphate-free)	11000	$P2_1$	1.8	[53]
Complex of ribonuclease with 3,5-guanosine-diphosphate	11000	$P2_1$	1.8	[48]
Ribonuclease Th_1	11000	$P3_22_1$	1.6	[51]
Ribonuclease Th_1 (ACG)	11000	$P3_22_1$	2.2	[51]
Ribonuclease Pb_1	11000	$I222$	1.4	[48]
Ribonuclease Pb_1 (ACG)	11000	$C222_1$	2.0	[48]
Complex of binase with 3'-GMP	12000	$P2_12_12_1$	1.8	[52]
Thermitase from *Thermoactinomyces vulgaris*	29000	$P2_12_12_1$	1.4	[71]
Carboxypeptidase from *Thermoactinomyces vulgaris* *Thermoactinomyces vulgaris*	35000	$P6_322$	3.0	[70]
SAICAR synthase from *Saccharomyces cerevisiae*	36000	$P2_12_12_1$	1.91	[76]
Catalase from *Penicillum vitale*	300000	$P3_121$	2.0	[28]
Catalase from *Thermus thermophilus*	210000	$P2_13$	1.0	[36]
Catalase from *Micrococcus lysodeikticus*	220000	$P4_22_12$	1.5	[31]
Formate dehydrogenase from *Pseudomonas* Sp. 101, holoenzyme	800000	$P2_12_12_1$	2.5	[92]
Formate dehydrogenase from *Pseudomonas* Sp. 101, apoenzyme	800000	$P2_1$	1.8	[92]

values, ionic strength, and the salt concentrations. Apparently, the mobility of the virus coat can be attributed to the presence of a large hole in the vicinity of threefold axes and weak contacts along these axes. The results of X-ray diffraction studies and the biochemical assays confirmed that the dimer plays the role of morphological species in the virus self-association. This process starts with the formation of the RNA complex with the minor protein. The addition of dimers to the initial intermediate via the charge interactions with the participation of the calcium ion.

CRYSTALLOGRAPHIC STUDIES OF DNA FRAGMENTS

The discovery of the *Z* form of DNA in the late 1970s marked the advent of a new field of biomolecular crystallography dealing with DNA structures. Soon thereafter, the studies along this line were also initiated at the Institute of Crystallography [84–90]. The *in vivo* DNA molecules form compact structures in contact with each other and also protein molecules. A knowledge of the fine DNA structure and the character of its changes under the influence of the nearest environment is of great importance for understanding the biological processes with the participation of DNA and the detailed analysis of the mechanisms of its functioning.

Investigations of the fine structure and conformational variability of DNA by the X-ray diffraction analysis of various crystalline modifications of DNA fragments were aimed at elucidating of the changes in the double-helix conformation under the influence of its nearest environment. Different crystalline modifications of DNA fragments of the same composition represent a convenient system for studying the structure of the DNA fragment surrounded by other molecules. With the aim of obtaining the same DNA fragment in different crystalline modifications, an essentially new approach to crystallization of oligonucleotide duplexes was developed. The analysis of the experimental phase diagrams for the duplex–spermine system allowed the construction of the theoretical model which described the behavior of two-component crystallization systems. This model allowed one to follow the dependence of the composition of the resulting oligonucleotide complexes as a function of the length of the oligonucleotide and the concentrations of the reagents added. The regions where the crystals of certain composition would be expected to grow were localized in the phase diagrams. For a number of oligonucleotides of different lengths and compositions, these crystalline modifications were really obtained in the theoretically predicted regions. Then these modifications were studied by the X-ray diffraction analysis. The comparison of the conformations of the equivalent fragments in different crystalline modifications showed that the DNA double helix is highly flexible and that its conformation is noticeably changed under the influence of the nearest environment. The changes in the axis bending, the angles of inclination of the base pairs to the helix axis, and the helical angles for the base pairs result in the changes of the accessibility exposure of the active groups located on the molecule surface. These *in vivo* changes in the surface properties allow DNA molecules to interact with each other and with other cell components in in various ways. A number of new conformations of the double helix intermediate between the *A*, *B*, and *Z* forms of DNA were revealed. A series of successive changes finally resulting in the closure of the major groove in the *A* form of DNA were followed.

The crystallographic studies showed that DNA can undergo conformational changes, due to which it can selectively interact with various molecules involved in the metabolism.

The macromolecules studied at the Laboratory of Protein Structure of the Institute of Crystallography are listed in the table.

CONCLUSIONS

Presently, the studies of the three-dimensional structures of biomacromolecules acquire an ever increasing importance. Both experimental and theoretical aspects of the X-ray diffraction analysis are extensively developed. Powerful synchrotron radiation sources provide the study of smaller crystals. Because of the continuous spectrum of the synchrotron radiation, one can use anomalous scattering most efficiently. Large X-ray data sets can be simultaneously measured with the use of two-dimensional positional detectors. Complete X-ray data sets can be collected within a fraction of a second by the Laue method with the use of white beam generated by a synchrotron. This, in turn, provides the possibility to follow the proceeding of the enzymatic reaction in the crystal. A combination of the methods of isomorphous replacement and multiple-wave anomalous scattering facilitates the extraction of the information on phases. The techniques of X-ray studies at cryogenic temperatures makes it possible to reduce the radiative damages and improve the quality of the final X-ray diffraction data. The vigorous development of computing facilities and special-purpose software (automated crystallographic program packages, graphics programs, new algorithms, etc.) and the total time of data processing, structure solution, and refinement are considerably reduced. The improvement of the procedures for protein purification, the use of recombinant samples, and the possibility of crystallization under the microgravitational conditions enabled one to prepare almost perfect biomolecular crystals, which in turn provided the solution of more complicated macromolecules and their ensembles by the methods of X-ray diffraction analysis.

ACKNOWLEDGMENTS

I am grateful to V.R. Melik-Adamyan and K.M. Polyakov for helpful discussion and valuable

advice. The study was supported by the Russian Foundation for Basic Research, project no. 99-03-33051.

REFERENCES

1. J. D. Bernal and D. Crowfoot, Nature **133**, 794 (1934).
2. D. W. Green, V. M. Ingram, and M. F. Perutz, Proc. R. Soc. London, Ser. A **255**, 287 (1954).
3. J. C. Kendrew, G. Bodo, H. M. Dintzis, *et al.*, Nature **181**, 662 (1958).
4. J. C. Kendrew, R. E. Dickerson, and B. E. Strandberg, Nature **185**, 422 (1960).
5. M. F. Perutz, M. G. Rossman, A. G. Guillis, *et al.*, Nature **185**, 416 (1960).
6. A. A. Vagin, Candidate's Dissertation in Physics and Mathematics (Inst. Kristallografii Akad. Nauk SSSR, Moscow, 1989).
7. B. K. Vainshtein, in *Problems of the Theory of Symmetry in Application to Macromolecules and Biocrystals* (Nauka, Moscow, 1987), p. 9.
8. B. K. Vainshtein, Usp. Fiz. Nauk **152** (1), 75 (1987) [Sov. Phys. Usp. **30**, 393 (1987)].
9. B. K. Vainshtein and A. B. Goncharov, Dokl. Akad. Nauk SSSR **287**, 1131 (1986) [Sov. Phys. Dokl. **31**, 278 (1986)].
10. A. B. Goncharov, B. K. Vainshtein, and A. I. Ryskin, Kristallografiya **32** (5), 858 (1987) [Sov. Phys. Crystallogr. **32**, 504 (1987)].
11. B. K. Vainshtein, Comput. Math. Appl. B **12**, 237 (1986).
12. I. P. Kuranova, A. I. Grebenko, N. V. Konareva, *et al.*, Biokhimiya **41**, 1603 (1975).
13. B. K. Vainshtein, E. G. Harutyunyan, I. P. Kuranova, *et al.*, Nature **254**, 163 (1975).
14. B. K. Vainshtein, É. G. Harutyunyan, I. P. Kuranova, *et al.*, Dokl. Akad. Nauk SSSR **216**, 690 (1975).
15. B. K. Vainshtein, É. G. Harutyunyan, I. P. Kuranova, *et al.*, Kristallografiya **23** (3), 517 (1978) [Sov. Phys. Crystallogr. **23**, 287 (1978)].
16. B. K. Vainshtein, I. P. Kuranova, É. G. Harutyunyan, *et al.*, Bioorg. Khim. **6**, 684 (1980).
17. É. G. Harutyunyan, I. P. Kuranova, B. K. Vainshtein, *et al.*, Kristallografiya **25** (1), 80 (1980) [Sov. Phys. Crystallogr. **25**, 43 (1980)].
18. É. G. Harutyunyan, I. P. Kuranova, A. B. Tovbis, *et al.*, Kristallografiya **25** (3), 526 (1980) [Sov. Phys. Crystallogr. **25**, 302 (1980)].
19. I. P. Kuranova, A. V. Teplyakov, G. V. Obmolova, *et al.*, Bioorg. Khim. **8**, 1625 (1982).
20. E. H. Harutyunyan, T. N. Safonova, I. P. Kuranova, *et al.*, J. Mol. Biol. **264**, 152 (1996).
21. E. H. Harutyunyan, T. N. Safonova, I. P. Kuranova, *et al.*, J. Mol. Biol. **251**, 104 (1995).
22. B. K. Vainshtein, V. R. Melik-Adamyan, V. V. Barynin, *et al.*, Dokl. Akad. Nauk SSSR **246**, 220 (1979).
23. B. K. Vainshtein, V. R. Melik-Adamyan, V. V. Barynin, *et al.*, Dokl. Akad. Nauk SSSR **250**, 242 (1980).
24. B. K. Vainshtein, V. R. Melik-Adamyan, V. V. Barynin, *et al.*, Acta Crystallogr., Sect. A: Cryst. Phys., Diffr., Theor. Gen. Crystallogr. **37**, C29 (1981).
25. B. K. Vainshtein, V. R. Melik-Adamyan, V. V. Barynin, *et al.*, Nature **293**, 411 (1981).
26. B. K. Vainshtein, V. R. Melik-Adamyan, V. V. Barynin, *et al.*, J. Mol. Biol. **188**, 63 (1986).
27. V. R. Melik-Adamyan, V. V. Barynin, A. A. Vagin, *et al.*, J. Mol. Biol. **188**, 49 (1986).
28. V. R. Melik-Adamyan, V. V. Barynin, A. A. Vagin, *et al.*, Kristallografiya **32** (3), 638 (1987) [Sov. Phys. Crystallogr. **32**, 372 (1987)].
29. V. R. Melik-Adamyan, V. V. Barynin, A. A. Vagin, *et al.*, Kristallografiya **32** (3), 653 (1987) [Sov. Phys. Crystallogr. **32**, 382 (1987)].
30. V. R. Melik-Adamyan, A. I. Grebenko, V. V. Barynin, *et al.*, Dokl. Akad. Nauk SSSR **306**, 620 (1989) [Sov. Phys. Dokl. **34**, 404 (1989)].
31. G. N. Murshudov, V. R. Melik-Adamyan, A. I. Grebenko, *et al.*, FEBS Lett. **312**, 127 (1992).
32. G. N. Murshudov, A. I. Grebenko, V. V. Barynin, *et al.*, J. Biol. Chem. **271**, 8863 (1992).
33. V. V. Barynin and V. R. Melik-Adamyan, Kristallografiya **27** (5), 981 (1982) [Sov. Phys. Crystallogr. **27**, 588 (1982)].
34. M. M. Barynin, A. A. Vagin, V. R. Melik-Adamyan, *et al.*, Dokl. Akad. Nauk SSSR **288**, 877 (1986) [Sov. Phys. Dokl. **31**, 457 (1986)].
35. V. V. Barynin, A. A. Vagin, V. R. Melik-Adamyan, *et al.*, Dokl. Akad. Nauk SSSR **306**, 620 (1989) [Sov. Phys. Dokl. **34**, 404 (1989)].
36. S. V. Antonyuk, V. R. Melik-Adamyan, A. N. Popov, *et al.*, Kristallografiya **45** (1), 111 (2000) [Crystallogr. Rep. **45**, 105 (2000)].
37. A. E. Braunshteĭn, É. G. Harutyunyan, and V. N. Malashkevich, Mol. Biol. **19**, 196 (1985).
38. V. V. Borisov, S. N. Borisova, N. I. Sosfenov, *et al.*, Dokl. Akad. Nauk SSSR **250**, 288 (1980).
39. V. V. Borisov, S. N. Borisova, G. I. Kachalova, *et al.*, in *Transaminases*, Ed. by P. Christen and D. E. Metzler (Wiley, New York, 1985), p. 155.
40. V. N. Malashkevich, B. V. Strokopitov, V. V. Borisov, *et al.*, J. Mol. Biol. **247**, 111 (1995).
41. A. A. Antson, B. V. Strokopytov, G. N. Murshudov, *et al.*, Kristallografiya **37** (1), 82 (1992) [Sov. Phys. Crystallogr. **37**, 40 (1992)].
42. A. A. Antson, B. V. Strokopytov, G. N. Murshudov, *et al.*, FEBS Lett. **302**, 256 (1992).
43. A. A. Antson, B. V. Strokopytov, T. V. Demidkina, *et al.*, Acta Crystallogr., Sect. A: Found. Crystallogr. **46**, C132 (1990).
44. A. A. Antson, T. V. Demidkina, P. Gollnick, *et al.*, Biochemistry **32**, 4195 (1993).
45. S. V. Pletnev, A. A. Antson, N. I. Sinitsyna, *et al.*, Kristallografiya **42** (5), 877 (1997) [Crystallogr. Rep. **42**, 809 (1997)].
46. M. N. Isupov, A. A. Antson, E. J. Dodson, *et al.*, J. Mol. Biol. **276**, 603 (1998).
47. M. Isupov, I. Dementieva, I. Zakomirdina, *et al.*, in *Biochemistry of Vitamin B_6 and PQQ*, Ed. by G. Marino, G. Samnia, and F. Bossa (Birkchauser Verlag, Basel, 1987).

48. A. G. Pavlovskiĭ, B. V. Strokopytov, and S. N. Borisova, Dokl. Akad. Nauk SSSR **292**, 1253 (1987).
49. K. M. Polyakov, B. K. Vainshtein, G. N. Tishchenko, *et al.*, Dokl. Akad. Nauk SSSR **273**, 1383 (1983) [Sov. Phys. Dokl. **28**, 988 (1983)].
50. A. G. Pavlovskiĭ, B. V. Strokopytov, S. N. Borisova, *et al.*, Kristallografiya **31** (3), 476 (1986) [Sov. Phys. Crystallogr. **31**, 279 (1986)].
51. K. M. Polyakov, B. M. Strokopytov, B. K. Vainshtein, *et al.*, Kristallografiya **32** (4), 918 (1987) [Sov. Phys. Crystallogr. **32**, 539 (1987)].
52. A. G. Pavlovskiĭ, R. G. Sanishvili, S. N. Borisova, *et al.*, Kristallografiya **34** (1), 137 (1989) [Sov. Phys. Crystallogr. **34**, 79 (1989)].
53. J. Sevcik, R. G. Sanishvili, K. M. Polyakov, *et al.*, Trends Biochem. Sci. **15**, 158 (1990).
54. V. Yu. Lunin, V. M. Levdikov, S. V. Shlyapnikov, *et al.*, FEBS Lett. **412**, 217 (1997).
55. S. V. Shlyapnikov, E. V. Blagova, V. M. Levdikov, *et al.*, Mol. Biol. **33**, 454 (1999).
56. S. V. Shlyapnikov, V. V. Lunin, M. Perbandt, *et al.*, Acta Crystallogr., Sect. D: Biol. Crystallogr. **56**, 567 (2000).
57. I. P. Kuranova, E. A. Smirnova, V. V. Makhaldiani, *et al.*, Dokl. Akad. Nauk SSSR **258**, 1245 (1981).
58. I. P. Kuranova, S. S. Terzyan, A. A. Voronova, *et al.*, Bioorg. Khim. **9**, 1611 (1983).
59. É. G. Harutyunyan, S. S. Terzyan, A. A. Voronova, *et al.*, Dokl. Akad. Nauk SSSR **258**, 1480 (1981).
60. S. S. Terzyan, A. A. Voronova, E. A. Smirnova, *et al.*, Bioorg. Khim. **10**, 1469 (1984).
61. I. P. Kuranova, Biokhimiya **53**, 1821 (1988).
62. E. G. Harutyunyan, I. P. Kuranova, B. K. Vainshtein, *et al.*, Eur. J. Biochem. **239**, 220 (1996).
63. I. P. Kuranova, G. V. Obmolova, and N. V. Konareva, Dokl. Akad. Nauk SSSR **295**, 1013 (1987).
64. A. V. Teplyakov, G. V. Obmolova, I. P. Kuranova, *et al.*, Protein Sci. **3**, 1098 (1994).
65. E. G. Harutyunyan, V. Yu. Oganessyan, N. N. Oganessyan, *et al.*, Biochemistry **36**, 7754 (1997).
66. S. M. Avaeva, E. V. Rodina, N. N. Vorob'eva, *et al.*, Biokhimiya **63**, 797 (1998).
67. S. M. Avaeva, N. N. Vorob'eva, S. A. Kurilova, *et al.*, Biokhimiya **65**, 442 (2000).
68. T. Salminen, A. Teplyakov, Yu. Kancare, *et al.*, Protein Sci. **5**, 1014 (1996).
69. V. R. Samigina, S. V. Antonyuk, V. S. Lamzin, *et al.*, Acta Crystallogr., Sect. D. Biol. Crystallogr. **56**, 595 (2000).
70. A. Teplyakov, K. Polyakov, I. Kuranova, *et al.*, Eur. J. Biochem. **208**, 281 (1992).
71. A. V. Teplyakov, I. P. Kuranova, B. K. Vainshtein, *et al.*, J. Mol. Biol. **214**, 261 (1990).
72. S. N. Borisova, A. G. Pavlovskiĭ, B. K. Vainshtein, *et al.*, Dokl. Akad. Nauk SSSR **301**, 474 (1988).
73. A. G. Pavlovskiĭ, S. N. Borisova, B. V. Strokopitov, *et al.*, Dokl. Akad. Nauk SSSR **305**, 861 (1989) [Sov. Phys. Dokl. **34**, 280 (1989)].
74. A. G. Tonevitskiĭ, D. E. Temyakov, E. C. Sweeney, *et al.*, Kristallografiya **41** (6), 1018 (1996) [Crystallogr. Rep. **41**, 966 (1996)].
75. E. V. Vernoslova, N. V. Konareva, A. M. Mikhaĭlov, *et al.*, Kristallografiya **44** (4), 630 (1999) [Crystallogr. Rep. **44**, 582 (1999)].
76. V. M. Levdikov, A. I. Grebenko, V. V. Barynin, *et al.*, Kristallografiya **41** (2), 293 (1996) [Crystallogr. Rep. **41**, 275 (1996)].
77. V. M. Levdikov, V. V. Barynin, A. I. Grebenko, *et al.*, Structure (London) **6**, 363 (1998).
78. E. Yu. Morgunova, A. S. Kaftanova, A. V. Kulinin, *et al.*, Dokl. Akad. Nauk SSSR **276**, 119 (1984) [Sov. Phys. Dokl. **29**, 357 (1984)].
79. A. T. Dembo, E. Yu. Morgunova, B. V. Mchedleshvili, *et al.*, Kristallografiya **32** (6), 1414 (1987) [Sov. Phys. Crystallogr. **32**, 831 (1987)].
80. E. Yu. Morgunova, A. M. Mikhaĭlov, Yu. V. Nekrasov, *et al.*, Dokl. Akad. Nauk SSSR **299**, 1129 (1988) [Sov. Phys. Dokl. **33**, 239 (1988)].
81. E. Yu. Morgunova, A. M. Mikhaĭlov, A. I. Nikitenko, *et al.*, Dokl. Akad. Nauk SSSR **305**, 489 (1989).
82. E. Yu. Morgunova, A. M. Mikhaĭlov, and B. K. Vainshtein, Mol. Biol. **27**, 371 (1993).
83. E. Yu. Morgunova, Z. Dauter, E. Fry, *et al.*, FEBS Lett. **338**, 267 (1994).
84. L. V. Malinina, V. V. Makhaldiani, B. K. Vainshtein, *et al.*, Dokl. Akad. Nauk SSSR **248**, 229 (1985).
85. L. V. Malinina, V. V. Makhaldiani, B. K. Vainshtein, *et al.*, Mol. Biol. **21**, 529 (1987).
86. L. V. Malinina, V. A. Tereshko, A. A. Vagin, *et al.*, Mol. Biol. **21**, 1142 (1987).
87. V. A. Tereshko and L. V. Malinina, Mol. Biol. **23**, 1163 (1989).
88. L. Malinina, V. Tereshko, Z. Ivanova, *et al.*, J. Cryst. Growth **110**, 252 (1991).
89. V. Strokopitov and L. Malinina, J. Biomol. Struct. Dyn. **11**, 1049 (1994).
90. D. E. Klimenko, B. K. Chernov, and L. V. Malinina, J. Biomol. Struct. Dyn. **13**, 529 (1995).
91. A. M. Mikhaĭlov, A. V. Nikitenko, and E. V. Chetverina, Bioorg. Khim. **17**, 372 (1991).
92. V. S. Lamzin, Z. Dauter, E. G. Harutyunyan, *et al.*, J. Mol. Biol. **236**, 759 (1994).
93. É. G. Harutyunyan, J. Deisenhofer, and A. V. Teplyakov, Dokl. Akad. Nauk SSSR **270**, 732 (1983).
94. E. Yu. Morgunova, A. M. Mikhailov, A. N. Popov, *et al.*, FEBS Lett. **367**, 183 (1995).
95. É. G. Harutyunyan, I. Yu. Oganessyan, N. N. Oganessyan, *et al.*, Kristallografiya **41** (1), 84 (1996) [Crystallogr. Rep. **41**, 77 (1996)].

Translated by T. Safonova

Crystallography Reports, Vol. 46, No. 4, 2001, pp. 620–625. Translated from Kristallografiya, Vol. 46, No. 4, 2001, pp. 687–691.

STRUCTURE OF MACROMOLECULAR COMPOUNDS

Dedicated to the memory of B.K. Vainshtein

X-ray Diffraction Study of the Complexes of SAICAR Synthase with Adenosinetriphosphate

S. V. Antonyuk*, A. I. Grebenko*, V. M. Levdikov*, D. V. Urusova*, V. R. Melik-Adamyan*, V. S. Lamzin, and K. S. Wilson****

** Shubnikov Institute of Crystallography, Russian Academy of Sciences, Leninskiĭ pr. 59, Moscow, 117333 Russia*

e-mail: mawr@ns.crys.ras.ru

*** European Molecular Biology Laboratory, EMBL Hamburg Outstation, c/o DESY, Notkestrasse 85, Hamburg, 22603 Germany*

Received December 28, 2000

Abstract—The three-dimensional structures of two enzyme–substrate complexes of SAICAR synthase from the yeast *Saccharomyces cerevisiae* with adenosinetriphosphate (ATP) prepared under different conditions were studied by X-ray diffraction analysis and then refined. An enzyme molecule was shown to contain two binding sites of ATP. One of these sites is located in the central cavity of the enzyme molecule and apparently binds the ATP molecule directly involved in the enzymatic reaction. In the complexes, the phosphate groups of ATP occupying this site adopt different conformations depending on the Mg^{2+} concentration. The functional role of the second binding site located at a distance of approximately 15 Å from the first site away from the central enzyme cavity has not been understood as yet. It might be that the second site perform the regulatory role in enzyme functioning. *© 2001 MAIK "Nauka/Interperiodica".*

INTRODUCTION

SAICAR synthase (phosphoribosylsuccinocarboxamideaminoimidazole synthase, EC 6.3.2.6) is an enzyme catalyzing the seventh stage of the biosynthesis of purine nucleotides in the living organisms. The enzymatic reaction involves the synthesis of 5'-phosphoribosyl-4-(*N*-succinocarboxamide)-5-aminoimidazole (SAICAR) from 5'-phosphoribosyl-4-carboxy-5-aminoimidazole (CAIR) and aspartic acid in the presence of Mg^{2+} ions accompanied by hydrolysis of adenosinetriphosphate (ATP) to yield adenosinediphosphate (ADP) and inorganic phosphate. The substrate specificity of SAICAR synthase was examined by various biochemical methods and was shown that Mg^{2+} ions are necessary for the reaction occurrence. However, at high concentrations, these ions inhibit the enzymatic reaction [1].

The three-dimensional structure of the native enzyme SAICAR synthase from yeast *Saccharomyces cerevisiae* has been established earlier by the multiple isomorphous-replacement method and refined to the *R* factor of 0.154 at 1.9 Å resolution [2, 3]. The assumption about the binding site of ATP in the SAICAR synthase molecule was made based on the data of the analysis of the three-dimensional structure of the enzyme and comparison of the SAICAR synthase structure with the known structures of other ATP-binding proteins. This assumption has been confirmed by the preliminary study of the crystals of the complex of SAICAR synthase with ATP [3]. In the present study, we refined the binding site and the mode of binding of the ATP molecule based on the results of X-ray diffraction analysis of two crystal structures of two complexes prepared at different Mg^{2+} concentrations by different methods.

MATERIALS AND METHODS

Crystallization of SAICAR-Synthase Complexes with ATP

Crystals of the first enzyme–substrate complex (SATP-I) were prepared by cocrystallization by the vapor-diffusion hanging-drop method at room temperature. The droplets consisted of the protein solution (24 mg/mL), 1 M ammonium sulfate, 0.04 M aspartic acid, 0.05 M ATP, 0.01 M $MgCl_2$, and 0.05 M *Tris*-HCl buffer (pH 7.5). The reservoir solution consisted of 2.25 M ammonium sulfate, 0.04 M aspartic acid, 0.05 M ATP, 0.01 M $MgCl_2$, and 0.05 M *Tris*-HCl buffer (pH 7.5).

The crystals of the second complex (SATP-II) were prepared by soaking the crystals of the native enzyme in the solution consisting of 2.25 M ammonium sulfate, 0.1 M ATP, 0.04 M 5'-phosphoribosyl-5-amino-4-imidazole carboxamide (AICAR), 0.04 M Asp, 0.04 M

1063-7745/01/4604-0620$21.00 © 2001 MAIK "Nauka/Interperiodica"

Fig. 1. Arrangement of two binding sites of ATP in a molecule of SAICAR synthase.

$MgCl_2$, and a 0.05 M Tris-HCl buffer (pH 7.5). In order to determine simultaneously also the binding site of another substrate of SAICAR synthase, we added some AICAR to the solution. However, we failed to determine it apparently because of an insufficient AICAR concentration.

The crystals of the complexes grew to the sizes of 0.5–1.0 mm; they belong to the sp. gr. $P2_12_12_1$. The unit-cell parameters of the crystals grown are given in Table 1.

X-ray Data Collection

The X-ray diffraction data sets were collected from crystals of the enzyme–substrate complexes using synchrotron radiation (the DORIS storage ring, the beam energy 4.5 GeV; EMBL, Hamburg) and an Imaging Plate detector. The X-ray diffraction data for the crystals of SATP-I and SATP-II were collected at room temperature and 100 K, respectively. The solution in which the crystals were kept prior to the low-temperature X-ray study contained 30% saturated solution of glucose, 2.5 M ammonium sulfate, 0.04 M aspartic acid, 0.01 M $MgCl_2$, and 0.05 M Tris-HCl buffer (pH 7.5). The experimental data were processed by the

Table 1. Statistical characteristics of X-ray diffraction data sets collected from crystals of the SATP-I and SATP-II complexes

Complexes	SATP-I	SATP-II
Wavelength, Å	0.98	0.906
a, *b*, *c*, Å	69.77, 74.19, 76.0	61.48, 63.05, 79.82
Number of measured reflections	25206	59439
Number of measured reflections, Å	13.82–2.05	24.74–1.4
Last resolution shell, Å	2.09–2.05	1.42–1.4
R_{int}	0.07	0.085
Set completeness, %	98.5	97.0
Completeness of the last resolution shell, %	98.5	97.4
Redundancy	4.0	4.08
$\langle I\rangle/\langle\sigma\rangle$	17.0	15.6
$\langle I\rangle/\langle\sigma\rangle$ in the last resolution shell	3.6	6.7

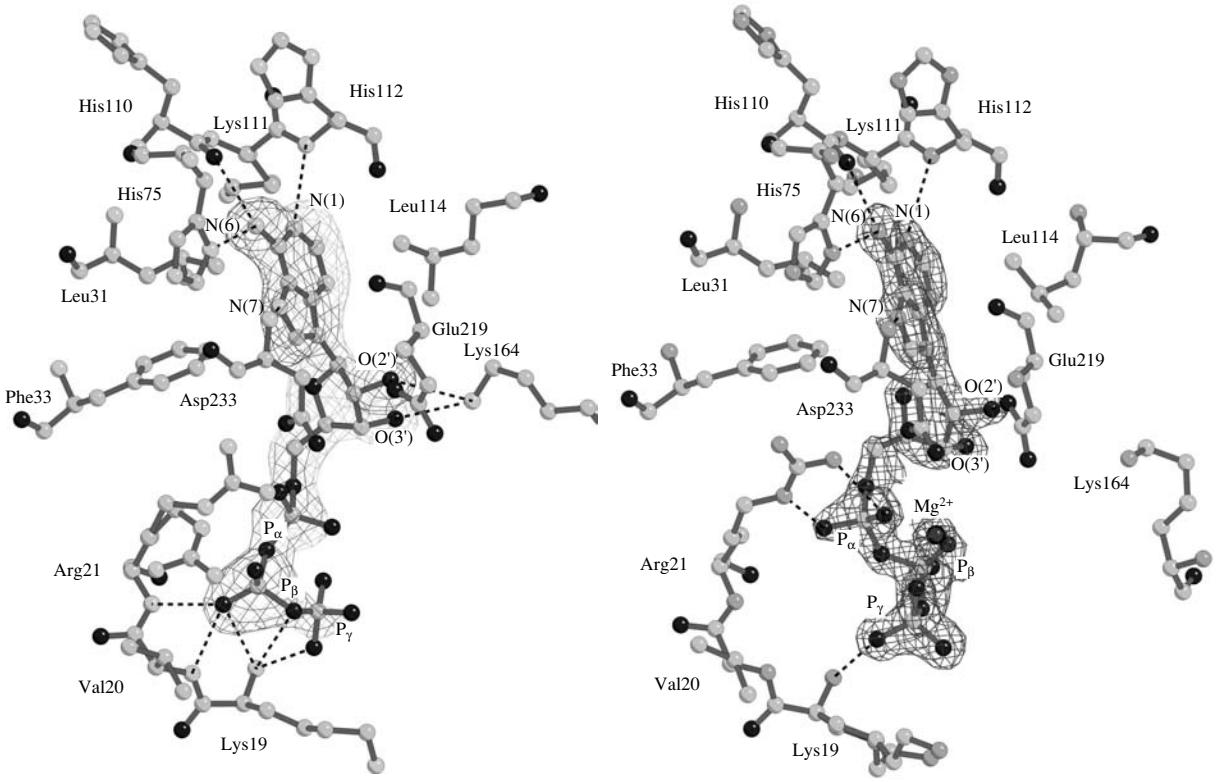

Fig. 2. Difference electron-density (omit) synthesis in the region of the main binding site of ATP in (a) the SATP-I complex and (b) the SATP-II complex. The contours are drawn at the 3σ levels. (The residue Val232 mentioned in the text is omitted, since it is located above the drawing plane.)

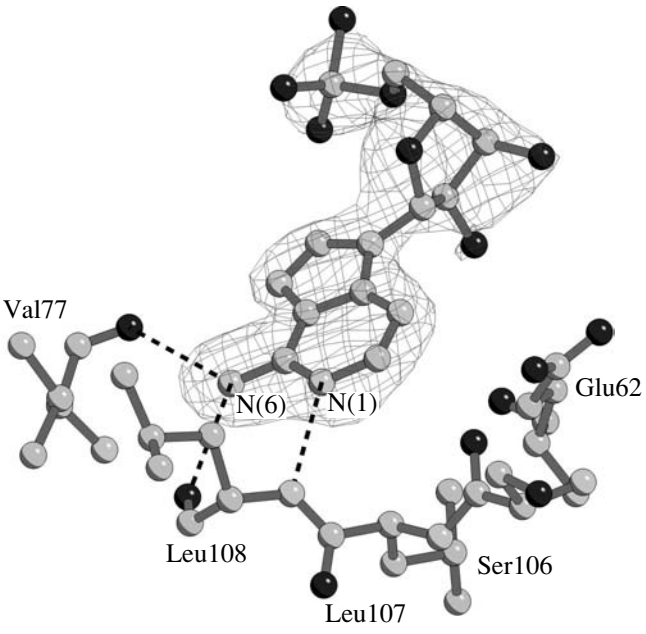

Fig. 3. Difference electron-density distribution about the ATP molecule located in the additional binding site of the SATP-II complex. The difference electron-density synthesis corresponds to the omit synthesis at the 3σ level.

DENZO/SCALEPACK program package [4]. The statistical characteristics of X-ray data collection are given in Table 1.

Determination of the Structures of the Enzyme–Substrate Complexes

The crystals of SATP-I and the native enzyme are described by the same sp. gr. $P2_12_12_1$. However, their unit-cell parameters are substantially different (a = 69.8 Å, b = 74.2 Å, c = 76.0 Å for SATP-I and a = 62.4 Å, b = 63.4 Å, c = 81.2 Å for the native enzyme). Therefore, the structure of this complex was solved by the molecular replacement method using the AMORE program [5] from the CCP4 crystallographic program package [6]. The translation and rotation functions were calculated using the model of the native-enzyme and the X-ray diffraction data in the resolution range from 8.0 to 4.0 Å. The refinement of the rigid-body model at 3.0 Å resolution converged to R = 34.2% and the correlation coefficient 69.1%.

The unit-cell parameters of the SATP-II crystals differ only slightly from those of the native crystals of SAICAR synthase because the former crystals were obtained by soaking. Therefore, we used as the starting

model in the refinement of the SATP-II complex the structure of the native enzyme solved at a 1.9-Å resolution in [3].

The atomic models of the complexes were refined by the least-squares method using the PROLSQ [7] and REFMAC [8] program packages. The positions of the solvent molecules were localized by the ARP automated procedure [9]. The atomic model of an enzyme molecule was constructed and corrected using the FRODO [10] and O [11] graphics program packages. The manual improvement of the model was based on the analysis of the difference Fourier syntheses calculated with the $(3F_o - 2F_c, \varphi_c)$, $(2F_o - F_c, \varphi_c)$, and $(F_o - F_c, \varphi_c)$ coefficients, where F_o and F_c are the observed and calculated moduli of the structure factors, respectively, and φ_c are the their phases calculated from the atomic model. The omit syntheses were calculated with the $(F_o - F_c, \varphi_c)$ coefficients, but the contributions of the atoms of ATP to F_c and φ_c were ignored.

The parameters and the statistical characteristics of the refined models of the enzyme-substrate complexes of SAICAR synthase are given in Table 2.

The atomic coordinates of the ATP molecules bound to the enzyme were determined from the difference electron-density syntheses constructed after the initial stages of the refinement and then were included into the refinement along with the atomic coordinates of a protein molecule.

Table 2. Statistical characteristics of the refined models of the SAICAR synthase complexes

Complexes	SATP-I	SATP-II
R-factor, %/number of reflections	16.3/23714	14.0/53447
R_{free} factor/N_{free}	21.9/1022	20.6/5989
DPI, Å [12]	0.16	0.072
Number of protein atoms	2449	2513
Number of solvent atoms	273	557
Number of atoms of ATP, *A*	31	31
Number of atoms of ATP, *B*	31	23
Rms for bond lengths:		
1–2	0.011	0.015
1–3	0.035	0.034
1–4	0.050	0.035
$\langle B \rangle$-factor for main-chain atoms, Å^2	21.7	17.3
$\langle B \rangle$-factor for side-chain atoms, Å^2	30.5	22.0
$\langle B \rangle$-factor for water molecules, Å^2	46.2	36.7

RESULTS AND DISCUSSION

The analysis of the difference electron-density syntheses calculated for both complexes demonstrated that a molecule of SAICAR synthase has two binding sites of ATP molecules labelled with *A* and *B* (Fig. 1).[1] The corresponding electron densities are shown in Figs. 2 and 3, respectively.

The ATP molecule occupying the main binding site (*A*) in the complexes is located in the interdomain cavity of SAICAR synthase and is aligned along the central cavity of the enzyme molecule. Both complexes have the same arrangement of the adenine base of ATP and the ribose ring. The adenine base adopts the *anti* conformation with respect to the ribose ring and is located in the hydrophobic pocket formed by the residues Leu114 and Val232 located on one side of the interdomain cavity and by the residues Leu31 and Phe33 located on the other side of this cavity. The binding specificity of the adenine ring is achieved via the formation of the N(1)···N His112, N(6)···O His110, and N(7)···N Asp233 hydrogen bonds (Figs. 2a, 2b, Table 3). It is remarkable that all three bonds are formed by the main-chain atoms and do not require the presence of conservative residues. The position of the ribose ring of ATP adopting the C(3')-*endo* conformation is stabilized by the O(2')···O(*E*2) Glu219 hydrogen bond in both complexes and by the O(2')···N(Z) Lys164 and O(3')···N(Z) Lys164 hydrogen bonds in the SATP-I complex.

At the same time, the arrangements of the phosphate groups of the ATP molecule in the two complexes are substantially different. In the SATP-I complex, the position of the β-phosphate group of ATP corresponds to the position of the SA1 sulfate ion in the native enzyme [3]. The conformations of the amino acid residues Lys19, Val20, and Arg21 forming a turn of the polypeptide chain in the phosphate-binding loop are such that the amino groups of these residues are aligned in the same direction. Three hydrogen bonds between the O(1*B*) atom of the β-phosphate group and the main-chain nitrogen atoms of these residues are formed (Fig. 2a). Rather pronounced thermal parameters for the atoms of phosphate groups and the corresponding difference electron-density syntheses indicate high mobilities of these atoms in the complexes. High mobilities of the phosphate groups of ATP may be important in the interactions with other enzyme substrates. The higher electron density at the β-phosphate group in comparison with the electron density at the other phosphate groups and the fact that the side chain of Arg21 occupies two positions (in the first one, the guanidine group of Arg21 forms impermissibly short

[1] All the figures were drawn with the use of the BOBSCRIPT program [13].

Table 3. Hydrogen bonds between the atoms of the enzyme and ATP in the SATP-I and SATP-II complexes

Atoms	Bond length, Å	
	SATP-I	SATP-II
Major binding site of ATP		
NLys19···O(3*G*)	2.87	2.95
NLys19···O(1*B*)	3.19	
NLys19···O(3*B*)	3.16	
NVal20···O(1*B*)	2.72	
NArg21···O(1*B*)	2.64	
N(*E*)Arg21···O(1*A*)		2.82
N(*H*2)Arg21···O(2*B*)		3.13
N(*D*1)His75···N(6)	2.69	2.83
OHis110···N(6)	3.02	2.93
NHis112···N(1)	3.06	3.30
N(*Z*)Lys164···O(3')	3.31	
N(*Z*)Lys164···O(2')	3.06	
O(*E*2)Glu219···O(2')	2.70	2.44
NAsp233···N(7)	3.13	3.16
Additional binding site of ATP		
OVal77···(N6)	2.81	2.8
OLeu108···N(6)	2.93	2.88
NLeu108···N(1)	3.01	2.96

contacts with the O(2*A*) atom of the α-phosphate group) can be attributed to possible sulfate-ion impurity occupying the position of the β-phosphate group.

In the SATP-II complex, the arrangement of the phosphate groups differs from that observed in SATP-I. In SATP-II, these groups are characterized by a higher electron density on the difference syntheses. Two nitrogen atoms of the guanidine group of Arg21 form hydrogen bonds with two oxygen atoms of α-phosphate, with the β-phosphate group being excluded from hydrogen bonding with atoms of the protein molecule; the γ-phosphate group forms one hydrogen bond, O(3*G*)···N Lys19 (Fig. 2b). These differences are caused by the presence of a magnesium ion forming coordination bonds with the oxygen atoms of all the three phosphate groups of ATP in the SATP-II complex. The presence of magnesium ions in the SATP-II complex is associated with the complex preparation from the solution with the magnesium-ion concentration four times higher than their concentration in the solution, used for preparation of the SATP-I complex. It can be assumed that the binding of magnesium ions to the phosphate groups of ATP reduced the mobility of the latter and inhibits the reaction. This assumption agrees with the results of the biochemical studies of SAICAR synthase, which demonstrated that the enzymatic activity at the Mg^{2+} ion concentrations exceeding 30 mM [1] decreases.

As was mentioned above, the analysis of the difference electron-density syntheses for the SATP-I complex and for the native enzyme revealed, along with the main binding site, an additional binding site of an ATP molecule. This additional site is located in a small cavity of the amino-terminal domain of SAICAR synthase (site *B*, Fig. 1). In this case, the atoms of the adenine base of ATP form the contacts with the enzyme molecule, whereas the phosphate groups are extended toward the solvent surrounding the enzyme molecule.

The purine base in this position is fixed by hydrogen bonds with the atoms of the main chain of the Val77 and Leu108 amino acid residues (Fig. 3, Table 3). The atomic thermal parameters and the difference electron density syntheses indicate that the closer the ATP atoms to the phosphate groups, the higher their mobility. The β- and γ-phosphate groups of ATP extended into the solvent have too high mobility; hence, these atoms were excluded from the refinement.

In the SATP-II complex, the difference electron-density synthesis also showed the existence of the second binding site of ATP. However, its density was lower than that in the case of SATP-I despite the higher ATP concentration during the preparation of the SATP-II complex. This can be associated with the fact that SATP-I crystals were obtained by cocrystallization, whereas SATP-II crystals were obtained by soaking the crystals in the solution with ATP; thus, the access to the second site could have been hindered by the adjacent protein molecules in the crystal.

The functional role of the second binding site of ATP in a SAICAR synthase molecule has not been understood as yet. The second site might play a regulatory role for enzyme functioning.

ACKNOWLEDGMENTS

This study was supported by the European Molecular Biology Organization (EMBO, grant no. PX310-1998) and by the Russian Foundation for Basic Research, project nos. 99-04-48570, 99-02-16191, and 00-15-96633).

REFERENCES

1. K. V. Ostanin, V. V. Alenin, V. D. Domkin, and M. N. Smirnov, Biokhimiya **54**, 1265 (1989).
2. V. M. Levdikov, A. I. Grebenko, V. V. Barynin, *et al.*, Kristallografiya **41** (2), 293 (1996) [Crystallogr. Rep. **41**, 275 (1996)].
3. V. M. Levdikov, V. V. Barynin, A. I. Grebenko, *et al.*, Structure (London) **6**, 363 (1998).

4. Z. Otwinowski and V. Minor, Methods Enzymol. **276**, 307 (1997).
5. J. Navaza, Acta Crystallogr., Sect. A: Fundam. Crystallogr. **A50**, 157 (1994).
6. Collaborative Computational Project, Number 4, Acta Crystallogr., Sect. D: Biol. Crystallogr. **50**, 760 (1994).
7. J. H. Konnert and W. A. Hendrickson, Acta Crystallogr., Sect. A: Cryst. Phys., Diffr., Theor. Gen. Crystallogr. **A36**, 344 (1980).
8. G. N. Murshudov, A. A. Vagin, and E. J. Dodson, Acta Crystallogr., Sect. D: Biol. Crystallogr. **53**, 240 (1997).
9. V. S. Lamzin and K. S. Wilson, Acta Crystallogr., Sect. D: Biol. Crystallogr. **49**, 129 (1993).
10. T. A. Jones, J. Appl. Crystallogr. **11**, 268 (1978).
11. T. A. Jones, J. Y. Zou, S. W. Cowan, and M. Kjeldgaard, Acta Crystallogr., Sect. A: Found. Crystallogr. **47**, 110 (1991).
12. W. J. Cruickshank, in *Macromolecular Refinement: Proceedings of the CCP4 Study Weekend, 1996*, p. 11.
13. R. M. Esnouf, J. Mol. Graphics **15**, 132 (1997).

Translated by T. Safonova

Crystallography Reports, Vol. 46, No. 4, 2001, pp. 626–630. Translated from Kristallografiya, Vol. 46, No. 4, 2001, pp. 692–697.

STRUCTURE OF MACROMOLECULAR COMPOUNDS

Dedicated to the memory of B.K. Vainshtein

Crystallographic Aspects of Functioning of Adenosine Triphosphatase as a Macromolecular Biomachine

S. A. Pikin

Shubnikov Institute of Crystallography, Russian Academy of Sciences, Leninskiĭ pr. 59, Moscow, 117333 Russia

Received January 30, 2001

Abstract—The structural characteristics and the properties of nanoscopic biological objects functioning as rotational molecular "machines" of the type of F-adenosine triphosphatase (F_0F_1-ATPase) are described in terms of physics. The fundamental relationships between the dynamic characteristics of such machines are established, as well as the kinetic coefficients in the equations relating the generalized forces acting in these molecular machines and the generalized currents. It is shown that the one-to-one correspondence between the directions of the current flowing through the biomembrane, the chemical reactions at the catalytic sites of the "stator," and the revolution of the machine "rotor" is dictated by the symmetry of the protein subunits. *© 2001 MAIK "Nauka/Interperiodica".*

INTRODUCTION

Boris Konstantinovich Vainshtein was an enthusiast about the structural studies of proteins, enzymes, and biological objects and made great efforts to solve numerous problems presented by nature, including those of the structure and functioning of living cells. He considered as one of the most important goals the establishment of the physical laws governing the protein crystallography and providing a large variety of the properties and functions of the cells whose evolution has continued for billions of years. Admiring Vainshtein's efforts in the propaganda of the combined physical-biological approach in the research of proteins, I dedicate this article to his memory.

This article is aimed at the establishment of the general physical laws governing the structure and the properties of the so-called rotational macromolecular machines by an example of their most characteristic representative—the adenosine triphosphatase enzyme.

Enzymes of the F-adenosine triphosphatase (F_0F_1-ATPase) type are unique molecular "machines" functioning in the cell membranes of plants, animals, and bacteria and catalyzing the formation of adenosine triphosphate (ATP)—a universal source of energy for numerous processes occurring in living cells [1–3]. The F_0F_1-ATPase (or ATP-synthase) enzyme consists of two main parts—the F_1 part containing catalytic sites and the F_0 part connecting the F_1 part with the membrane. It was established that the proton transport through the membrane in the F_0 part governs the ATP formation in the F_1 part. During ATP hydrolysis, the terminal phosphate group is released with the simultaneous formation of adenosine diphosphate (ADP) so that the evolved energy can "participate" in other reactions. Vice versa, this additional energy can also be used to attach a phosphate group to ADP and, thus, provide the ATP synthesis.

The detailed chemical and structural study of ATP-synthase allowed the establishment of the mechanism of its functioning [2]. The F_1 part consists of three α- and three β-subunits and one γ- and one ε-subunit. The ATP synthesis occurs at β-subunits forming an immobile "stator" of the machine, whereas the connected γ- and ε-subunits form its "chiral rotor" [4, 5], which is of great importance for understanding the mechanism of functioning of this molecular machine. The γ- and ε-subunits rotate inside the cylinder formed alternatively either by α or β subunits. This rotation is governed by the ionic current and induces the structural changes in the β-subunits located at the angular distances of 120° from each other, thus giving rise to the periodic change of the catalytic activity of subunits. Different machines of this type have different charge carriers, e.g., hydrogen, sodium, or potassium ions [6, 7]. The rotor revolution was observed experimentally in [8].

CRYSTALLOGRAPHY OF ATP-SYNTHASE

Figure 1 schematically shows ATP-synthase incorporated into a lipid membrane [1–5]. It is seen that the rotor consisting of γ- and ε-subunits has an elongated screwlike shape similar to the shape of anisotropic chiral molecules in low-molecular liquid crystals. The

1063-7745/01/4604-0626$21.00 © 2001 MAIK "Nauka/Interperiodica"

dimension of such a macromolecular formation (a "rotor") in the direction of its long axis is about 10 nm; i.e., it is three times longer than the length of a liquid-crystal molecule. Similar to liquid crystals [9], the rotor orientation can be characterized by the unit vector **n** (the so-called director) lying on a straight line connecting the most distant points of the rotor.

The directions ±**n** are physically equivalent, and therefore, all the physical quantities characterizing the rotor should be the combinations of the even number of the director components. Figure 1 also shows that the director **n** deviates from the membrane normal **z** for a certain small angle θ (at least in the functioning machine).

The projection of the machine onto the plane of the membrane (Fig. 2) clearly shows the elements providing the anisotropy of the β-subunits and the rotor. Thus, the length of the projection of the director $\mathbf{n}_\perp$ is approximately equal to the value of θ. Moreover, the rotor is characterized by a steric or an electric dipole $\mathbf{P}_\gamma$ in the membrane plane, which can be of the same physical nature as in the chiral smectic liquid crystals of type *C*—the point symmetry C_2 of the chiral rotor should inevitably result in the appearance of polarization $\mathbf{P}_\gamma$ normal to the director component $\mathbf{n}_\perp$ [9, 10]. Of course, the anisotropy of the rotor shape can be more complicated, e.g., because of the biaxiality of the macromolecule, the existence of quadrupole moments, etc. However, even the simplest assumption made above has important consequences.

Figure 2 schematically shows the anisotropy of β-subunits in the model suggested by Paul Boyer [1, 3]. At each moment, three β-subunits exist in three different conformational or deformational states: open (O), tight (T), and loose (L). With a rotor revolution by 120°, these states of the β-subunit alternatively change one another. The T-state possesses the minimum free energy; the O-state, the maximum free energy; and the L-state corresponds to the intermediate energy values. In the O-state, the ATP molecule can either freely leave the β-subunit or "enter" its catalytic site. In the T-state, the strongly bound ATP molecule can spontaneously be split into ADP and inorganic phosphate group Pi in the process of hydrolysis or, vice versa, in the process of the ADP synthesis, the phosphate group Pi can form ATP strongly bound to the catalytic site. In the L-state, the Pi group can either be removed or, vice versa, can be bound to the catalytic site. The removal of ATP from the T-state and binding of Pi in the L-state require considerable energy consumption (of about 20 k_BT [11], where T is the temperature and k_B is the Boltzmann constant). Vice versa, the binding of ATP in the T-state and the removal of Pi in the L-state results in an evolution of the same energy.

The Boyer model allows one to assume that, in the O-state, the strongest interaction takes place between the rotor and the β subunit, which at this moment possesses the maximum electric or steric dipole moment

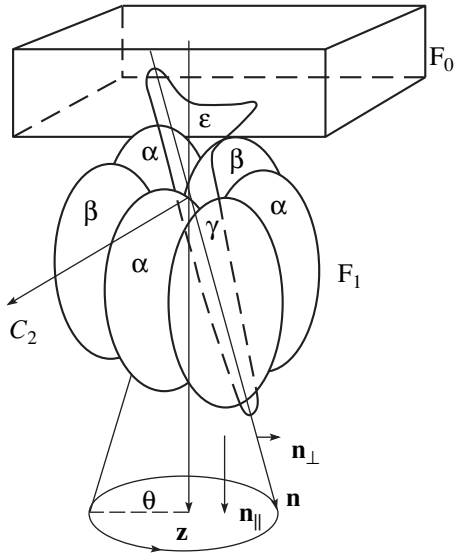

Fig. 1. Schematic view of ATP-synthase. One can see the F_0 part attached to the membrane and the F_1 part connected with the α-, β-, γ-, and ε-subunits and the orientation of the director **n** and its components $\mathbf{n}_\parallel$ and $\mathbf{n}_\perp$ with respect to the membrane normal **z**, with the polar axis C_2 being parallel to the membrane plane and normal to $\mathbf{n}_\perp$. The director revolves over the surface of a cone with the opening angle 2θ.

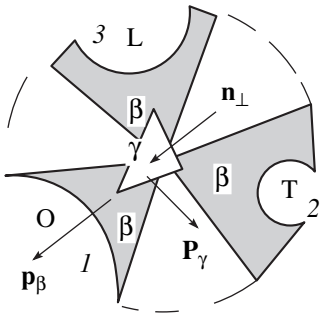

Fig. 2. Schematic location of the γ-subunit, three β-subunits, and the vectors $\mathbf{n}_\perp$, $\mathbf{p}_\beta$, and $\mathbf{P}_\gamma$ projected onto the membrane plane in a molecular machine. The change in the shape is maximal for the first β-subunit (in the O-state) and is weaker for two other β-subunits (in the L- and T-states).

$\mathbf{p}_\beta$, whereas the T-state has the highest symmetry (there is no dipole). For the proper functioning of the machine, the vectors $\mathbf{p}_\beta$ and $\mathbf{P}_\gamma$ or their components should necessarily be mutually orthogonal, as is the case shown in Fig. 2. It is also possible to foresee the situation where the dipoles of the β-subunits would be directed along the tangent to the circumference of the stator, with the rotor dipole being oriented along its radius similar to the director component $\mathbf{n}_\perp$. In the latter case, the dipole $\mathbf{P}_\gamma$ is parallel to $\mathbf{n}_\perp$, which has nothing to do with the rotor chirality. Below, we consider some of the consequences that follow from the structure of the machine described above.

TRANSPORT EQUATIONS AND KINETIC COEFFICIENTS IN THE ISOTHERMAL CHIRAL ROTATIONAL BIOMACHINE

The states of the molecular machine are isothermal, i.e., in equilibrium at each given temperature as in the case of linear machines considered by Prost [12]. Functioning of a rotational machine can be conveniently described within the formalism of generalized forces and currents suggested for liquid crystals [9, 10]. In our case, the machine functioning is driven by the forces which are, the electrochemical gradient **E** in the membrane, the velocity **N** of the mechanical motion of the rotor, and the difference Δ between the chemical potentials, which is, in fact, the measure of the change in free energy per "fuel" ATP molecule.

In the state of chemical equilibrium, Δ is zero; it is positive if the ATP molecules are in excess and is negative if the ADP molecules are in excess. The forces **E**, **N**, and Δ provide the formation of the following generalized currents: the electric-current density **j**, the mechanical force **g** applied to the rotor, and the average rate u of "fuel" consumption (i.e., the average number of ATP molecules bound and hydrolyzed per unit time, with u being positive). The rate u becomes negative if ADP molecules are bound, thus providing the ATP synthesis. The mechanical force **g** includes the force of viscous friction arising in the rotor revolution in the hydrophobic cavity of the stator.

In the general case, the $\mathbf{j}(\mathbf{E}, \mathbf{N}, \Delta)$, $\mathbf{g}(\mathbf{E}, \mathbf{N}, \Delta)$, and $u(\mathbf{E}, \mathbf{N}, \Delta)$ dependences are nonlinear, because the machine is functioning far from the state of the chemical equilibrium ($\Delta > k_BT$). However, the consideration of the linear mode ($\Delta < k_BT$) is rather useful and leads to a number of qualitative conclusions. Within the linear approximation, the following relationships are valid [13]:

$$\mathbf{j} = \sigma\mathbf{E} + \nu(\mathbf{n}\times\mathbf{N}) + \mathbf{e}\Delta, \tag{1a}$$

$$u = -\mathbf{e}\mathbf{E} - \mathbf{v}\mathbf{N} + \lambda\Delta, \tag{1b}$$

$$\mathbf{g} = \nu(\mathbf{n}\times\mathbf{E}) + \gamma\mathbf{N} + \mathbf{v}\Delta. \tag{1c}$$

The above equations include the kinetic coefficients chosen in such a way that the rate $\dot{S}$ of energy dissipation is positively defined, i.e.,

$$\dot{S} = \mathbf{j}\mathbf{E} + u\Delta + \mathbf{g}\mathbf{N} = \sigma E^2 + \gamma N^2 + \lambda\Delta^2, \tag{2}$$

where the conductivity coefficient σ, viscosity γ, and the coefficient λ are positive. The appearance of the pseudoscalar coefficient ν in Eqs. (1) is dictated by the "rotor chirality," with the product $(\mathbf{n}\times\mathbf{N})$ being a pseudoscalar and the product $\nu(\mathbf{n}\times\mathbf{N})$ being a true scalar. It should be indicated that the director components, $\mathbf{n} = \mathbf{n}_\parallel + \mathbf{n}_\perp$ ($\mathbf{n}^2 = 1$), approximately satisfy the relationships

$$n_\perp^2 = n_x^2 + n_y^2 \approx \theta^2, \quad n_\parallel^2 = n_z^2 \approx 1. \tag{3}$$

The director velocity is $\mathbf{N} = d\mathbf{n}/dt = (\boldsymbol{\Omega}\times\mathbf{n})$, where the pseudoscalar $\boldsymbol{\Omega}$ is the angular velocity of the rotor.

$$\begin{aligned} &\Omega_z \neq 0, \quad \Omega_x = \Omega_y = 0, \\ &N_x = -n_y\Omega_z, \quad N_y = n_x\Omega_z, \quad N_z = 0. \end{aligned} \tag{4}$$

The formalism originally suggested for the description of liquid crystals [9, 10] is also quite useful for solving our problem.

The electrochemical gradient **E** consists of two terms corresponding to the changes in the transmembrane potential Φ and the transmembrane proton concentration C (pH),

$$\mathbf{E} = -\nabla\Phi - \kappa C^{-1}\nabla C, \tag{5}$$

where $\kappa = k_BT/Q$ is the constant and Q is the ion charge. In the state of chemical equilibrium, i.e., at $C = C_0\exp(-\Phi/\kappa)$, the "field" **E** disappears. Strictly speaking, one also has to take into account in Eqs. (1) an additional current of proton diffusion at $\nabla C \neq 0$ and the corresponding kinetic coefficients. In what follows, we assume that the gradient ∇C is induced in the F_0 part and is independent of the F_1 part.

The kinetic coefficient **e** is the polar vector describing an interaction as a result of which the consumption of the ATP fuel by the machine provides the appearance of an electric current and a mechanical motion. In accordance with the model considered here, in the absence of rotor inclination ($\theta = 0$) should provide the disappearance of this interaction. Thus, the vector **e** can be determined by the interactions between the $\mathbf{p}_\beta$ and $\mathbf{P}_\gamma$ dipoles. If the value of $\mathbf{P}_\gamma$ is determined by the rotor chirality, the vector **e** is two-dimensional and oriented along the twofold axis C_2. It is related to the director by the following equations:

$$\mathbf{P}_\gamma = \mu\boldsymbol{\xi}, \quad \xi_x = n_zn_y, \quad \xi_y = -n_zn_x, \tag{6a}$$

$$P_{\gamma x} = \mu n_zn_y, \quad P_{\gamma y} = -\mu n_zn_x, \tag{6b}$$

where the piezoelectric modulus μ is proportional to the chirality parameter [10]. Thus, the vector **e** can be represented in the form

$$\mathbf{e} = c(\mathbf{p}_\beta\times\boldsymbol{\xi}), \tag{7}$$

where c is the constant and **e** plays the role of the rotating moment [cf. with the first term in the right-hand part of Eq. (1c)] and goes to zero at $\theta = 0$. If the dipole $\mathbf{P}_\gamma$ is parallel to $\mathbf{n}_\perp$ and does not result from the rotor chirality and inclination, then the vector **e** can be written as $\mathbf{e} = cn_z(\mathbf{p}_\beta\times\mathbf{n}_\perp)$, where the vector $\mathbf{p}_\beta$ is directed along the tangent to the stator circumference.

The same physical reasons provide the relation of the polar vector **v** to **n**, $\mathbf{P}_\gamma$, and $\mathbf{p}_\beta$. At small θ angles, the only expression for the vector **v** has the form

$$\mathbf{v} = b\mu(\mathbf{n}\times\mathbf{e}) = -b\mu\boldsymbol{\xi}(\mathbf{n}_\perp\mathbf{p}_\beta) = -b\mathbf{P}_\gamma(\mathbf{n}_\perp\mathbf{p}_\beta), \tag{8}$$

where b is the constant, which, being multiplied by **N** [cf. with Eq. (2)], yields a physical quantity independent of the director sign ($\pm\mathbf{n}$). In our consideration, the products $(\mathbf{p}_\beta \times \boldsymbol{\xi})$ and $(\mathbf{n}_\perp \mathbf{p}_\beta)$ in Eqs. (7) and (8) are the constant parameters of the machine, because, during the interactions between the rotor and the β-subunits in the O-states, the mutual orientations of all the above vectors in each of the three β-subunits remain constant during rotor revolution. For such O-states, the machine parameter is the quantity $(\mathbf{n}_\perp \mathbf{p}_\beta) = \theta p_\beta$. It should also be indicated that the kinetic coefficient **v** is the quantity of the second order of smallness with respect to the small angle θ. If the dipole $\mathbf{P}_\gamma$ is parallel to $\mathbf{n}_\perp$ and the dipole $\mathbf{p}_\beta$ is normal to $\mathbf{n}_\perp$, then the vector **v** can be written in the form $\mathbf{v} = -b\mathbf{p}_\beta(\mathbf{P}_\gamma \mathbf{n}_\perp)$; in other words, this kinetic coefficient should necessarily include the combination of the three above vectors.

According to the model considered here, the strong interaction between the dipoles $\mathbf{p}_\beta$ and $\mathbf{P}_\gamma$ and the rotor chirality induce the directional rotor revolution in the machine in the presence of an ionic current. We should like to emphasize the importance of the symmetry factor—the interaction energy has the term of the type $\nu(\mathbf{p}_\beta \times \mathbf{P}_\gamma)\mathbf{o}$ (provided by chirality) only if the electrochemical gradient and the ionic current determine a certain specific direction $\mathbf{o} = \mathbf{E}/E$ in the machine.

USEFUL WORK DONE BY ROTATIONAL BIOMACHINE

A machine does a certain mechanical work if the product **gN** is negative. If the product $u\Delta$ is negative, the machine generates a chemical energy; if the product **jE** is negative, it generates the electric energy. Thus, ATP-synthase can function in several nonpassive regimes. If $u\Delta > 0$, $\mathbf{gN} < 0$, and $\mathbf{jE} < 0$, the machine uses the energy of the heat bath and generates the mechanical rotation and the electric current by using excessive ATP in the process of hydrolysis (i.e., at $u > 0$ and $\Delta > 0$).

The rotor revolution with a constant angular velocity Ω_z takes place if the moments of forces provided by viscosity and field effect compensate each other, i.e., if $(\mathbf{g} \times \mathbf{n}) = 0$. In this case, the machine does not do any mechanical work. It follows from Eqs. (1) and (6)–(8) that

$$\gamma\Omega_z = \nu E_z - b\mu\Delta(\mathbf{p}_\beta \mathbf{n}_\perp) n_z. \quad (9)$$

If the dipole $\mathbf{P}_\gamma$ is parallel to $\mathbf{n}_\perp$ and does not result from the rotor chirality and inclination and the vector $\mathbf{p}_\beta$ is directed along the tangent to the circumference of the stator, then

$$\gamma\Omega_z = \nu E_z - b\Delta(\mathbf{p}_\beta \times \mathbf{n}_\perp)_z(\mathbf{P}_\gamma \mathbf{n}_\perp). \quad (10)$$

The second pseudovector in the right-hand side of Eq. (10) is necessarily the combination of three vectors and provides the contribution to the angular velocity of the rotor only at a finite value of Δ. The latter case is of great importance for machines with the structure characterized by a considerable tilt of the director, i.e., $\mathbf{n}_\parallel \longrightarrow 0$, $\mathbf{n}_\perp \longrightarrow \mathbf{n}$, which resembles the structure of a cholesteric liquid crystal. Possibly, the machines functioning in some bacteria with rotating protein flagella [14] elongated in the $\mathbf{n}_\perp$ direction correspond to such a model. The rotation velocity in this case is determined by Eq. (10): $\gamma\Omega_z \approx \nu E_z - b\Delta p_\beta P_\gamma$. It should be emphasized that the results obtained indicate the only possible way of machine operation: the directions of the angular velocity **Ω** and the current **j** are strictly defined. The ATP synthesis should result in the reversal of the **Ω** and **j** directions.

If a rotor revolves with a constant velocity, no mechanical work is done ($\mathbf{gN} = 0$) but, as follows from Eqs. (1) and (9), the machine generates an electric current if $\mathbf{jE} < 0$ at the finite values of E_z. In this case, j_z is given by the equation

$$j_z = \sigma E_z - c\Delta p_\beta \theta n_z + \nu\theta^2\Omega_z. \quad (11)$$

For the machines functioning in bacteria with flagella, the electric-current density is

$$j_z = \sigma E_z + \nu\Omega_z. \quad (12)$$

If the changes in the membrane potential and ion concentration become equivalent (i.e., the system is far from the chemical equilibrium), they give independent contributions to the moment of forces associated with the field **E**. No such equivalence is possible at the concentration changes corresponding to the following Δ in the chemical potentials:

$$C \equiv \tilde{C}(z) \approx C_0 \exp\left[\frac{1}{\kappa}\left(-\Phi + \frac{c p_\beta \theta \Delta z}{\sigma}\right)\right]. \quad (13)$$

It should be noted that due to ion diffusion, the "field" **E** can quickly disappear with an approach of $\tilde{C}(z)$ to $C_0\exp(-\Phi/\kappa)$ in the situation where the velocity Ω_z and the current density j_z are equal to zero. Indeed, in this case, the specific direction **o** related to the vectors **j** and **E** in the membrane disappears, and therefore, the forces inducing the directional motion of the rotor and the changes in the shape of the β-subunits also disappear, whereas the θ deviations become random. If the rotor tilt θ and, therefore, the polarization $\mathbf{P}_\gamma$ arise due to the consumed energy Δ, then the finite values of θ and $\mathbf{P}_\gamma$ exist only during chemical reactions and then relax to the zero values. If the relaxation time is less than that necessary for the jump of the rotor toward those β-subunits at which the chemical reactions occur, then θ and $\mathbf{P}_\gamma$ should go to zero. The value of $\mathbf{p}_\beta$ should also go to zero. Thus, $\tilde{C}(z)$ can quickly relax to the distribution $C_0\exp(-\Phi/\kappa)$ at $j_z = \Omega_z = 0$.

It is seen from Eqs. (11) and (12) that the machine stops generating the current ($j_z = 0$) under a certain critical condition, which, at relatively weak fields and

small tilt angles of the rotor has the form

$$\sigma n_z E_z \approx c\Delta p_\beta \theta. \quad (14)$$

The experiment shows that the rotor revolution and the current flow in the ATP-synthase are initiated and completed almost simultaneously. Then, it follows from Eqs. (9) and (11) that the parameters σ, ν, b, and c are related as

$$b\mu\sigma \approx c\nu. \quad (15)$$

It seems that the above relationship results from the selection of biomachines with appropriate parameters in the course of evolution [15]. This condition signifies that j_z and Ω_z are related as

$$\Omega_z = \frac{\nu j_z}{\gamma\sigma + (\nu\theta)^2}, \quad (16)$$

which reminds the expression for the well-known Lehmann effect in chiral liquid crystals [9] and can be explained by the same physical nature of both phenomena.

For the molecular machines functioning in bacteria with $\mathbf{n}_\perp \longrightarrow \mathbf{n}$, i.e., with $|\mathbf{n}_\perp| \approx 1$, relationship (15) seems to be invalid, and, in accordance with Eqs. (10) and (12), the quantities j_z and Ω_z cannot have zero values simultaneously. Nevertheless, the causes discussed above should provide the cessation of the current flow upon the cessation of the rotor (flagellum) revolution, e.g., because p_β and E_z become zero in the absence of the directional interaction between the rotor and the β-subunits. In this case, the machine "behaves" in a random manner [it was noticed that the change of the direction of revolution results in flagellum unbinding, in other words, the notion of a director looses any sense (14)]. However, after certain time, the directions of the flagellum rotation and the ion motion can be restored because of difference Δ in the chemical potentials and the attainment of the admissible p_β and E_z values (in this case, a new machine orientation in the space is independent of its initial orientation [14]).

The efficiency η of the above machines (determined as the ratio of the generated electric energy to the consumed chemical energy) is very high. Thus, the electric efficiency for ATP synthase is [13]

$$\eta = -\frac{j_z E_z}{u\Delta} \approx \frac{c\Delta p_\beta \theta n_z E_z - \sigma E_z^2}{\lambda\Delta^2 + c\Delta p_\beta \theta n_z E_z}. \quad (17)$$

If the machine generates the chemical energy at the expense of the consumed electrical energy, then the chemical efficiency is the quantity reciprocal to Eq. (17). One can readily see that the maximum efficiency η_{max} is independent of E_z; it has a rather low value at small θ angles and is close to unity at relatively high θ-values ($\theta^2 \gg \lambda\sigma/c^2 p_\beta^2$). In a similar way, for machines functioning in bacteria, the efficiency is determined by Eqs. (1), (10), and (12) and becomes almost unity at relatively high values of the p_β and P_γ dipoles (where $bp_\beta P_\gamma \gg \sqrt{\lambda\sigma E}$).

CONCLUSIONS

An attempt has been made to interpret functioning of the rotational biomachines of the ATP-synthase type in terms of physics. The structure and the properties of such nanoscopic objects are described in terms of the general principles of symmetry. We also took into account the polarization properties of chiral materials and considered the transport equations, taking into account the kinetics of the structural parameters and the ionic currents in such biological objects. It is shown that the latter objects can be described within the formalism used in the physics of liquid crystals. The expressions for the angular rotor velocity and the electric-current density in such biomachines are obtained. These expressions depend on the main structural and chemical parameters of these molecular machines. It is also shown that the characteristics of such macromolecular machines provide their high efficiencies.

ACKNOWLEDGMENTS

This study was supported by the Russian Foundation for Basic Research, project no. 00-02-17801.

REFERENCES

1. P. D. Boyer, Biochim. Biophys. Acta **1140**, 215 (1993).
2. J. P. Abrahams, A. G. Leslie, R. Lutter, and J. E. Walker, Nature **370**, 621 (1994).
3. P. D. Boyer, Annu. Rev. Biochem. **66**, 717 (1997).
4. W. Junge, D. Sabbert, and S. Engelbrecht, Ber. Bunsen-Ges. Phys. Chem. **100**, 2014 (1996).
5. B. Schulenberg, F. Wellmer, H. Lill, *et al.*, Eur. J. Biochem. **249**, 134 (1997).
6. P. Dimroth, H. Wang, M. Grabe, and G. Oster, Proc. Natl. Acad. Sci. USA **96**, 4924 (1999).
7. W. Junge, Proc. Natl. Acad. Sci. USA **96**, 4735 (1999).
8. H. Noji, R. Yasuda, M. Yoshida, *et al.*, Nature **386**, 299 (1997).
9. P. G. De Gennes, *The Physics of Liquid Crystals* (Clarendon Press, Oxford, 1974; Mir, Moscow, 1977).
10. S. A. Pikin, *Structural Transformations in Liquid Crystals* (Gordon and Breach, New York, 1991).
11. J. Weber and A. E. Senior, Biochim. Biophys. Acta **1319**, 19 (1997).
12. F. Julicher, A. Ajdari, and J. Prost, Rev. Mod. Phys. **69**, 1269 (1997).
13. S. Pikin and W. Haase, Zh. Éksp. Teor. Fiz. **119** (1), 199 (2001) [JETP **92**, 174 (2001)].
14. V. P. Skulachev, Soros. Obraz. Zh., No. 9, 2 (1998).
15. A. Blair, L. Ngo, J. Park, *et al.*, Microbiology **142**, 17 (1996).

Translated by L. Man

Crystallography Reports, Vol. 46, No. 4, 2001, pp. 631–635. Translated from Kristallografiya, Vol. 46, No. 4, 2001, pp. 698–702.

STRUCTURE OF ORGANIC COMPOUNDS

Dedicated to the memory of B.K. Vainshtein

Synthesis and Crystal Structure of 3,10-Dimethyl-10*H*-Dibenzo[*b*,*e*]iodinium Tetrafluoroborate

N. E. Zhukhlistova*, G. N. Tishchenko*†, T. P. Tolstaya, and L. D. Asulyan****

** Shubnikov Institute of Crystallography, Russian Academy of Sciences, Leninskiĭ pr. 59, Moscow, 117333 Russia*
e-mail: nez@ns.crys.ras.ru
*** Moscow State University, Vorob'evy gory, Moscow, 119899 Russia*

Received July 5, 2000

Abstract—The crystal and molecular structures of a chiral cyclic iodonium salt, namely, 3,10-dimethyl-10*H*-dibenzo[*b*,*e*]iodinium tetrafluoroborate, is solved by the direct method (a = 20.678(5) Å, b = 20.738(5) Å, c = 8.408(2) Å, γ =120.404(5)°, Z = 4, sp. gr. $P2_1/b$).[1] The crystals of the title compound consist of the iodonium cations and the BF_4^- anions. The benzene rings *A* and *B* of the cations are planar. The angles between these rings are 56.1(4)° and 58.3(4)° in two independent molecules, and the rings are virtually coplanar with the corresponding halves of the central heterocycle *C* adopting the I,C(3)-boat conformation. The structural units are packed in the crystal so that each I atom forms short contacts with the fluorine atoms of two independent anions.

INTRODUCTION

Recently, two cyclic iodonium salts containing an asymmetric carbon atom in the cation, namely, 3-methyl-10*H*-10-(4-tolyl)dibenzo[*b*,*e*]iodinium tetrafluoroborate and the salt containing the same cation and the anion of (–)-mono-(*N*-α-phenylethyl)amide of maleic acid, have been synthesized [1]. In the present study, we synthesized another cyclic iodonium salt with the asymmetric carbon atom in the cation, namely, 3,10-dimethyl-10*H*-dibenzo[*b*,*e*]iodinium tetrafluoroborate, and determined its crystal and molecular structures.

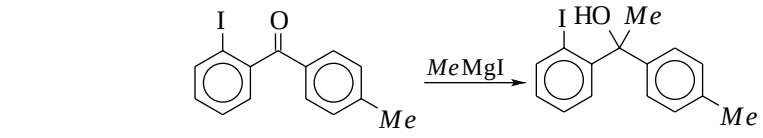

I **II**

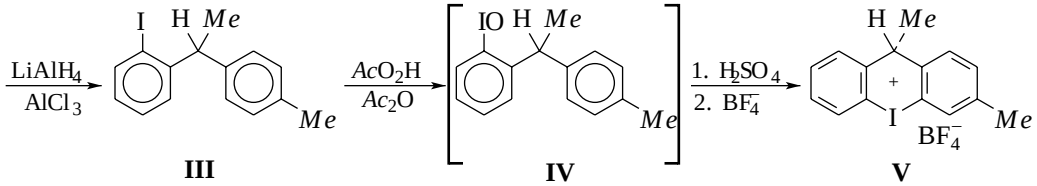

III **IV** **V**

Salts with these structures can possess interesting stereochemistry (in the series of iodonium compounds, the stereochemistry is poorly known), because their cations contain not only the asymmetric center but also a plane which passes through the iodonium atom and the asymmetric carbon atom and separates two asymmetric moieties of the molecule. Consequently, it can *a priori* be assumed that four optical isomers (or two diastereomeric racemates) may exist. With the aim of examining this assumption and establishing the structure of salt **V**, we performed X-ray diffraction study of this salt and determined the geometric parameters of its

† Deceased.

[1] According to the nomenclature accepted in *Chemical Abstracts*, an iodonium cation containing the I atom incorporated into a six-membered ring is called iodinium.

cation. However, as can be seen from the data considered below, the molecule of the title compound exists only as two mirror isomers. Apparently, this fact is associated with the characteristic features of cyclization of iodoarene **III** into iodonium salt **V**, which gives rise to only two antipodes. In both antipodes, the bridging hydrogen atom is directed inward the nonplanar central ring adopting a boat conformation, which, in turn, is determined exclusively by steric factors. This is all the more true for the iodonium salt described earlier in [1], namely, for 3-methyl-10*H*,10-(4-tolyl)dibenzo[*b*,*e*] iodinium tetrafluoroborate containing the bulkier substituent in the bridge.

EXPERIMENTAL

3,10-Dimethyl-10*H*-dibenzo[*b*,*e*]iodinium tetrafluoroborate (V). A solution of 2-iodo-4'-methylbenzophenone (**I**) (32.2 g, 0.1 mol) [1] in anhydrous ether (50 ml) was slowly added to a transparent solution of methylmagnesium iodide, which was prepared from magnesium (3.6 g, 0.15 g-at.) and iodomethane (9.3 ml, 0.15 mol), in anhydrous ether (350 ml) at 0°C. The reaction mixture was stirred for 1.5 h, kept for one day (TLC control), and decomposed with an excess of 30% acetic acid. After standard treatment, the resulting 2-iodophenyl-4-tolylmethylcarbinol (**II**) (IR spectrum: 3600–3100 (ν_{OH}), 1600 cm^{-1} (ν_{Ar})) was reduced as described previously [2] using the complex of lithium aluminohydride with aluminum chloride, which has been prepared from $LiAlH_4$ (6.59 g, 0.17 mol) and $AlCl_3$ (46.73 g, 0.35 mol) in anhydrous ether. After standard treatment, the resulting 2-iodophenyl-4-tolylmethylmethane (**III**) was dissolved in acetic anhydride (35 ml). Then, a 27% solution of peracetic acid (83 ml) was added dropwise to the reaction solution at 0°C, and the mixture was kept at 20°C for 12 h to obtain a solution of the iodoso derivative (**IV**). Concentrated sulfuric acid (35 ml) was slowly added dropwise with stirring to the reaction mixture at 0°C, and the mixture was kept at 20°C for one day and poured onto ice. Then, NH_4BF_4 (30 g, 0.29 mol) was added to the resulting solution of 3,10-dimethyl-10*H*-dibenzo[*b*,*e*]iodinium hydrosulfate, and the mixture was stirred until NH_4BF_4 was dissolved. 3,10-Dimethyl-10*H*-dibenzo[*b*,*e*]iodinium tetrafluoroborate **V** was extracted with a *Me*NO_2–$CHCl_3$ mixture (3 : 1, v/v). The extract was dried, the solvents were distilled off *in vacuo*, and the residue was reprecipitated with ether from acetone and recrystallized from alcohol. Salt **V** was obtained in a yield of 11.23 g (28% with respect to iodoketone **I**). A solution of salt **V** in CH_2Cl_2 was passed through a layer (h = 7–10 mm, d = 15 mm) of Al_2O_3; the filtrate was concentrated to the minimum volume and salt **V** (mp 178–179°C) was precipitated with ether.

For $C_{15}H_{14}BF_4I$, anal. calcd. (%): C, 44.16; H, 3.46.

Found (%): C, 44.31; H, 3.46.

Colorless transparent well-faceted monoclinic crystals of **V** were grown from a mixture of ethanol and water (1 : 1) at room temperature. The crystallographic data are as follows: a = 20.678(5) Å, b = 20.738(5) Å, c = 8.408(2) Å, γ =120.404(5)°, sp. gr. $P2_1/b$, Z = 4, M = 408, and V = 3109.7(13) $Å^3$. The X-ray diffraction data were collected on a Synthex $P2_1$ diffractometer ($\theta/2\theta$ scan mode, CuK_α radiation, graphite monochromator) at room temperature. A total of 5476 reflections were measured, and processing them gave 4024 independent nonzero structure amplitudes (θ_{max} = 56.08°).

The structure was determined by the direct method using the SHELXS86 program package [3]. The unit cell contains two independent cations (**Va** and **Vb**) and two BF_4^- anions. Most of atoms were located from the *E* synthesis. The remaining non-hydrogen atoms were revealed after the phase refinement (SHELXS86 [3]). The hydrogen atoms were placed in calculated positions. The non-hydrogen atoms were refined in the anisotropic approximation, and the hydrogen atoms were refined using the riding-atom model. The final R factors were 0.074 and 0.089 for 3017 reflections with $I > 2\sigma(I)$ and for all 4024 independent reflections, respectively. The large R factors are attributable to the large thermal vibrations of the F atoms of the anions. However, an attempt to locate these atoms more precisely using the statistics failed. The atomic coordinates and thermal parameters for the structure are given in the table.

RESULTS AND DISCUSSION

The crystal structure **V** consists of the heterocyclic iodonium cations and the BF_4^- anions. The structure of one of the independent $C_{15}H_{14}I^+$ cations (**Va**) is shown in Fig. 1. The benzene rings *A* and *B* are planar to within 3σ. The dihedral angles between the rings *A* and *B* are 56.1(4)° and 58.3(4)° in **Va** and **Vb**, respectively. These rings are virtually coplanar with the corresponding halves of the central heterocycle *C* adopting the I,C(3)-boat conformation. Similar structures of the cations were observed in 10-oxodibenzo[*b*,*e*]iodinium tetrafluoroborate (**VI**) and 10*H*-dibenzo[*b*,*e*]iodinium tetrafluoroborate (**VII**) [4]. These cations differ only by the dihedral angles between the rings *A* and *B* (27.5° and 46.4° in **VI** and **VII**, respectively). The folding angles of the central ring *C* along the I…C(13) line are 56.5(5)° and 55.2(4)° in cations **Va** and **Vb**, respectively (30.7° and 45.7° in molecules **VI** and **VII**, respectively). Therefore, a comparison of the folding angles in three compounds containing different substituents at the C(13) atom demonstrated that this angle depends on the nature of the substituents in the bridging group. The angle increases from 30.7° (the carbonyl group) to 45.7° (the CH_2 group) [4] and then to 56.5(5)° or 55.2(4)° (the $CHCH_3$ group in **Va** and **Vb**, respectively). The deviations of the I, C(13), and C(14) atoms

Atomic coordinates and thermal parameters

Atom	*x*/*a*	*y*/*b*	*z*/*c*	U_{eq}
		Molecule **Va**		
I(1)	0.38148(5)	0.22821(6)	0.62527(12)	0.0744(4)
C(1)	0.4778(8)	0.3224(9)	0.5336(18)	0.071(4)
C(2)	0.4683(10)	0.3770(9)	0.4620(18)	0.077(4)
C(3)	0.5336(11)	0.4377(9)	0.402(2)	0.095(5)
C(4)	0.6014(11)	0.4382(9)	0.405(2)	0.090(5)
C(5)	0.6058(8)	0.3826(9)	0.484(2)	0.079(5)
C(6)	0.5454(9)	0.3236(9)	0.5450(17)	0.071(4)
C(7)	0.4171(8)	0.1576(8)	0.5333(18)	0.067(4)
C(8)	0.3642(9)	0.0898(8)	0.4669(18)	0.078(4)
C(9)	0.3918(10)	0.0432(10)	0.406(3)	0.105(6)
C(10)	0.4652(11)	0.0691(10)	0.411(2)	0.095(6)
C(11)	0.5168(9)	0.1363(9)	0.475(2)	0.078(4)
C(12)	0.4936(7)	0.1839(7)	0.5452(16)	0.061(3)
C(13)	0.5477(8)	0.2581(8)	0.6296(17)	0.068(4)
C(14)	0.6284(9)	0.2719(10)	0.6417(19)	0.087(5)
C(15)	0.3366(11)	−0.0301(10)	0.334(3)	0.124(8)
		Molecule **Vb**		
I(2)	0.11482(5)	0.34522(5)	0.87596(12)	0.0730(4)
C(1')	0.0168(9)	0.3413(9)	0.9658(17)	0.075(4)
C(2')	0.0288(10)	0.4078(9)	1.040(2)	0.084(5)
C(3')	−0.0369(12)	0.4009(11)	1.102(2)	0.095(6)
C(4')	−0.1059(10)	0.3356(10)	1.097(2)	0.080(4)
C(5')	−0.1086(9)	0.2747(9)	1.024(2)	0.080(4)
C(6')	−0.0485(7)	0.2753(7)	0.9522(16)	0.057(3)
C(7')	0.0776(9)	0.2361(9)	0.9651(18)	0.074(4)
C(8')	0.1302(9)	0.2224(10)	1.039(2)	0.081(5)
C(9')	0.1071(12)	0.1547(11)	1.0990(18)	0.086(5)
C(10')	0.0289(10)	0.1017(10)	1.090(2)	0.085(5)
C(11')	−0.0217(9)	0.1172(8)	1.0199(19)	0.074(4)
C(12')	0.0010(8)	0.1878(7)	0.9522(16)	0.060(3)
C(13')	−0.0518(8)	0.2090(8)	0.8703(17)	0.071(4)
C(14')	−0.1290(8)	0.1429(9)	0.850(2)	0.091(5)
C(15')	0.1579(11)	0.1320(12)	1.165(3)	0.112(7)
B(1)	0.1960(10)	0.0465(12)	0.752(3)	0.089(6)
F(11)	0.2522(7)	0.1102(7)	0.773(2)	0.180(7)
F(12)	0.1321(7)	0.0372(10)	0.790(2)	0.181(7)
F(13)	0.2051(12)	−0.0041(10)	0.826(4)	0.275(14)
F(14)	0.1914(11)	0.0363(17)	0.588(3)	0.294(16)
B(2)	0.3040(11)	0.3505(12)	0.761(4)	0.104(9)
F(21)	0.2480(8)	0.3570(10)	0.774(2)	0.182(6)
F(22)	0.3681(7)	0.4041(9)	0.783(2)	0.197(8)
F(23)	0.2941(10)	0.2915(12)	0.839(4)	0.252(12)
F(24)	0.3095(16)	0.3342(19)	0.604(4)	0.338(19)

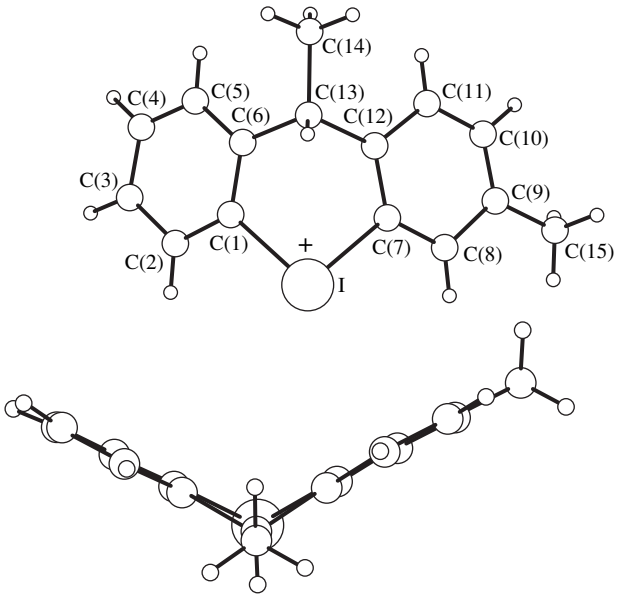

Fig. 1. Conformation of the 3,10-dimethyl-10*H*-dibenzo[*b*,*e*]iodonium cation (two mutually perpendicular projections).

from the mean plane passing through the remaining four atoms of the ring *C* are 0.86(2), 0.67(2), and 0.66(3) Å, respectively, in cation **Va** and –0.86(2), –0.64(2), and –0.69(3) Å, respectively, in cation **Vb**. The C(15) methyl group of cation **Va** lies in the plane of the ring *B* (the deviation is 0.02(3) Å), whereas the deviation of this group in **Vb** is –0.11(3) Å. The corresponding bond lengths in **Va** and **Vb**, as a rule, have close values and are similar to analogous bond lengths in salts **VI** and **VII** [4] and in 4,2'-iodonio-3-phenyl-1,2-benzoisoxazole (**VIII**) [5]. It should be noted that sharp asymmetry of the I–C bonds observed in molecules **VI** and **VII** [4] is absent in the molecule of the title compound. The I–C bond lengths are 2.107(14) and 2.092(14) Å in molecule **Va** and 2.125(15) and 2.124(16) Å in molecule **Vb** (the average I–C distance in **V** is 2.11 Å). Noteworthy are only slight differences in the C–C bond lengths in two independent molecules **Va** and **Vb**. Shortening of the C(5)–C(6) bond in molecule **Va** [1.33(2) Å] compared to that in molecule **Vb** [1.38(2) Å] is accompanied by the corresponding elongation of the C(6)–C(13) bond [1.56(2) and 1.51(2) Å, respectively]. The C(8)–C(9) and C(9)–C(10) bonds differ noticeably in length. In molecule **Va**, the C(8)–C(9) bond is longer [1.44(2) Å] and the C(9)–C(10) bond is shorter [1.33(3) Å] than those in **Vb** [1.33(2) and 1.42(2) Å, respectively]. The C(13)–C(14) bond lengths differ insignificantly [1.55(2) and 1.50(2) Å in molecules **Va** and **Vb**, respectively].

For the most part, the bond angles in both molecules have close values. Only the C(10)–C(9)–C(15) bond angle in molecule **Va** [124(2)°] is larger than that in molecule **Vb** [119.5(17)°], which is accompanied by a decrease in the C(8)–C(9)–C(15) bond angle in molecule **Va** [118.0(17)°] and the corresponding increase in this angle in molecule **Vb** [123.3(19)°]. The C–I–C bond angles are 90.7(6)° and 90.5(6)° (the corresponding angles in molecules **VI** and **VII** [4] and in salt **VIII** [5] are 93°, 92°, and 95.6(1)°, respectively).

The crystal structure of **V** is shown in Fig. 2. The structural units are packed in the crystal so that each

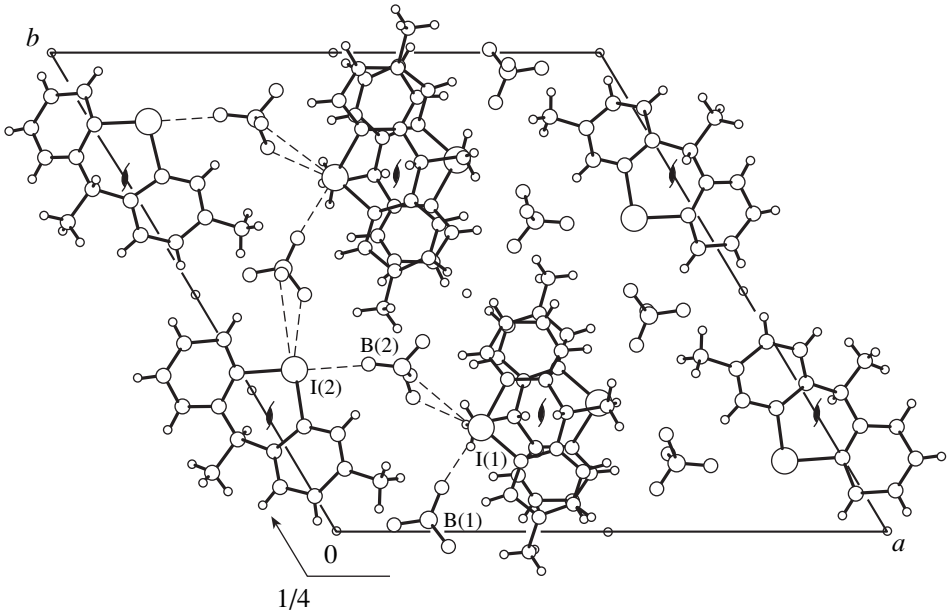

Fig. 2. Crystal packing of ions projected along the *c*-axis.

I atom forms short contacts with the fluorine atoms of two independent anions. The I(1)…F(11) and I(2)…F(21) distances [2.84(1) and 2.78(1) Å, respectively] are close to those found in [4]. Other I···F contacts, namely, I(1)···F(24) [3.22(4) Å], I(1)···F(23) [3.26(2) Å], I(2)···F(13) (x, y + 0.5, $-z$ + 1.5) [3.20(3) Å], and I(2)···F(14) (x, y + 0.5, $-z$ + 1.5) [3.46(3) Å], even though substantially larger than the aforementioned two contacts, are noticeably smaller than the sum of the van der Walls radii (2.20 and 1.33 Å for I and F, respectively [6]; or 2.15 and 1.35 Å for I and F, respectively [7]). It is known that the effective radius of an atom decreases if this atom bears a positive charge [8]. For I^+, the interatomic radius is 1.7 Å [5]. The sum of this radius and the anionic radius of the fluorine atom (which is equal to the van der Waals radius) approximates the I^+···F distances observed in structure **V**. Therefore, these distances correspond to Coulomb (ionic or ion–dipole) interactions. The angular (two covalent bonds) coordination of the I atom is completed with these contacts to a distorted tetragonal pyramid. The C(1), C(7), F(11), and F(23) atoms (cation **Va**), which are located in the base of the pyramid, are coplanar to within 0.037 Å. The I and F(24) atoms deviate from the mean plane of the base by 0.09(1) and 1.61(4) Å, respectively. In cation **Vb,** the distortions are more significant. The average deviation of the C(1'), C(7'), F(21), and F(13) (x, y + 0.5, $-z$ + 1.5) atoms located in the base of the pyramid is 0.11 Å. The iodine atom deviates from the base of the pyramid by 0.03(1) Å (i.e., it lies virtually in the plane of the base), and the apical F(14) atom (x, y + 0.5, $-z$ + 1.5) deviates from this plane by 1.74(4) Å.

The BF_4^- group acts as a bridge (through the fluorine atoms) between the iodonium atoms of two cations. One of the anions links two independent cations. The resulting fragments related by the *b* plane form infinite chains consisting of the cations and anions, which are extended along the *b* axis. The second anion links the aforementioned fragments. In the unit cell, both independent cations **Va** and **Vb** are located virtually perpendicular to the twofold screw axes. Cations **Va** and **Vb** related by these axes are packed in stacks along this direction, the central rings of the cations in the adjacent stacks formed by independent cations being bent in opposite directions. The distances between the cations in the stacks are equal to *c*/2. In each stack, the rings *A* and *B* of one cation overlap with the rings *B* and *A*, respectively, of another cation. The I atoms are virtually projected onto the C(14) atoms of the methyl groups so that the chains consisting of the alternating I atoms and methyl groups are observed along the *c*-direction. The stacks of molecules **Va** related by the inversion centers are located along the *b* direction. The stacks of molecules **Va** and **Vb** alternate along the *a* direction.

In the tetrahedral BF_4^- anions, the B–F bonds are nonequivalent and their lengths lie in the range of 1.24(2)–1.39(3) Å, which is comparable with the values reported previously for the BF_4^- ion [4]. Although a particular regularity is observed in the B–F bond lengths in both independent anions, it is risky to attribute the differences in the B–F bond lengths to I···F interactions, because the thermal vibrations of the F atoms are large, and some of their positions could be split. In the crystal structure, several contacts between the F atoms and the hydrogen atoms, which do not fall into the scheme of van der Waals interactions, are observed in addition to the aforementioned shortened F···I contacts. The sums of the van der Waals radii of the C and F atoms and of the H and F atoms are 3.17 and 2.64 Å, respectively [6]. The F···H and F···C contacts lie in the ranges 2.39–2.56 and 3.17–3.32 Å, respectively. The C–H–F angles range from 131.4° to 151.9°.

ACKNOWLEDGMENTS

We thank Yu.V. Nekrasov for his help in collecting X-ray diffraction data.

REFERENCES

1. T. P. Tolstaya, A. N. Vanchikov, E. V. Vinnik, and L. D. Asulyan, Khim. Geterotsikl. Soedin., No. 8, 1112 (1999).
2. J. Blackwell and W. J. Hickinbottom, J. Chem. Soc., No. 3, 1405 (1961).
3. G. M. Sheldrick, *SHELXS86: Program for the Solution of Crystal Structures* (Univ. of Göttingen, Göttingen, 1986).
4. Z. G. Aliev, L. O. Atovmyan, L. D. Egorova, *et al.*, Izv. Akad. Nauk SSSR, Ser. Khim., No. 5, 1042 (1985).
5. A. S. Batsanov, V. N. Petrov, Yu. T. Struchkov, *et al.*, Izv. Akad. Nauk SSSR, Ser. Khim., No. 10, 2309 (1985).
6. B. K. Vainshtein, V. M. Fridkin, and V. L. Indenbom, *Modern Crystallography*, Vol. 2: *Structure of Crystals*, Ed. by B. K. Vainshtein, A. A. Chernov, and L. A. Shuvalov (Nauka, Moscow, 1979; Springer-Verlag, Berlin, 1995, 2nd ed.).
7. L. Pauling, *The Nature of the Chemical Bond* (Cornell Univ. Press, New York, 1960, 3rd ed.).
8. S. S. Batsanov, *Structural Chemistry: Findings and Relationships* (Dialog–Mos. Gos. Univ., Moscow, 2000).

Translated by T. Safonova

Crystallography Reports, Vol. 46, No. 4, 2001, pp. 636–641. Translated from Kristallografiya, Vol. 46, No. 4, 2001, pp. 703–709.

Dedicated to the memory of B.K. Vainshtein

Refinement of the Atomic Structure of CdTe Single Crystals

M. Kh. Rabadanov, I. A. Verin, Yu. M. Ivanov, and V. I. Simonov

Shubnikov Institute of Crystallography, Russian Academy of Sciences, Leninskiĭ pr. 59, Moscow, 117333 Russia

Received September 11, 2000

Abstract—A comparative refinement of the anharmonic and disordered models of the atomic structure was performed based on precision X-ray diffraction data sets collected from a CdTe single crystal at 295, 376, 491, and 583 K. Although both models provide the asymmetric contributions of Cd and Te to the structure factors, the anharmonic model seems to be more advantageous. © *2001 MAIK "Nauka/Interperiodica".*

INTRODUCTION

Cadmium telluride belongs to high energy-gap $A^{II}B^{VI}$ semiconductors. Single crystals of CdTe are widely used for construction of X-ray- and gamma-radiation-detectors having considerable advantages over conventional silicon- and germanium-based detectors. Thus, they possess a high stopping power and allow measurements at room temperature. Another important application of CdTe single crystals is their use as substrates for growth of epitaxial $Hg_xCd_{1-x}Te$ films for detectors in the infrared range. Recent studies showed that CdTe possesses the most pronounced electrooptical coefficient in the IR region of all the $A^{II}B^{VI}$ and $A^{III}B^{V}$ semiconductors, which opens new possibilities the use of CdTe as a photorefractive material.

Single crystals of CdTe are crystallized in the sphalerite structure type (sp. gr. $F\bar{4}3m$) with the basis Cd and Te atoms occupying the 4*a* (0 0 0) and 4*c* (1/4 1/4 1/4) positions, respectively (Fig. 1). The structure consists of sharing-vertices $[CdTe_4]$-tetrahedra forming a three-dimensional framework. Formally, the structure can also be considered as a framework built of the $[TeCd_4]$-tetrahedra. The X-ray diffraction studies of sphalerite-type singles crystals showed the asymmetric contributions of Cd and Te to the structure factors, which can be explained by two causes. First, these contributions can correspond to different physical models of the structure. In one of these models, the asymmetry of the atomic contributions is associated with the anharmonicity of thermal vibrations of atoms occupying the above special positions. Second, the asymmetry can be attributed to small static atomic displacements. In the latter case, the atoms statistically occupy several positions in the vicinity of the ideal atomic positions in the sphalerite structure. There are adherents of both anharmonic [2, 3] and disordered models [4, 5]. The asymmetric contributions produce only a slight effect on the

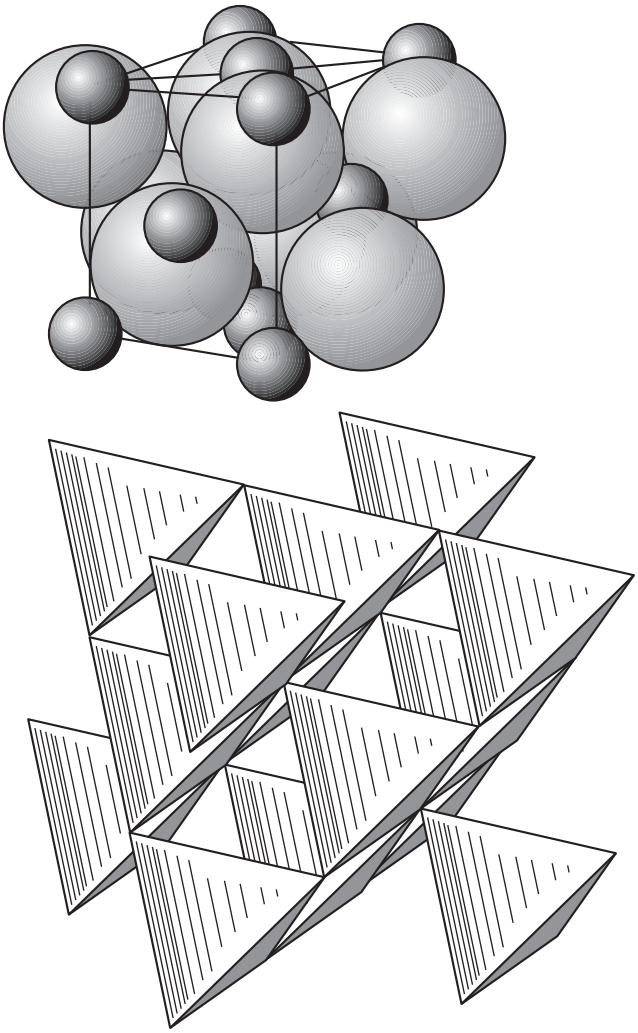

Fig. 1. Two representations of the atomic model of the CdTe structure [1].

1063-7745/01/4604-0636$21.00 © 2001 MAIK "Nauka/Interperiodica"

Table 1. Details of X-ray diffraction experiment, measured data, and the refined unit-cell parameters of a CdTe single crystal

T, K	295	376	491	583
a, Å	6.4827(8)	6.4861(8)	6.4894(9)	6.4920(6)
μr	2.598	2.595	2.591	2.587
Scanning range	$1.2 + 0.35\tan\theta$	$1.3 + 0.35\tan\theta$	$1.1 + 0.35\tan\theta$	$1.3 + 0.35\tan\theta$
Detector window, mm	3×1	6×3	6×3	6×3
$\sin\theta/\lambda$, Å^{-1}	0.15–1.14	0.15–1.14	0.15–1.14	0.15–1.09
Number of measured reflections	3442	998	1530	1303
Number of independent reflections	214	207	188	152
R_{int}	2.28	1.96	2.64	2.89

structure factors. These contributions can be interpreted within the frameworks of both models of the crystal structure. For example, in the detailed study of the sphalerite-type structure [6, 7], preference was given to the anharmonicity model, whereas in [8], the model with the disordered atomic arrangement was favored.

Below, we refine and analyze possible structural models of CdTe crystals, namely, an ideal sphalerite structure with harmonic atomic thermal vibrations, a similar structure but taking into account the anharmonic components of atomic thermal vibrations, and a model with split atomic positions. The least squares refinement of the sphalerite model (based on the X-ray diffraction data) revealed strong correlations between the structural parameters, which considerably complicates the problem. The present study was aimed at the precision X-ray diffraction investigation of CdTe single crystals at different temperatures and the solution of the problem whether it is possible to make the unique choice between the two physically different models of the CdTe structure.

X-RAY DIFFRACTION STUDY AND DATA PROCESSING

Single crystals of CdTe were grown by the Obreimov–Shubnikov method in BN crucibles sealed into quartz ampules under a pressure of 10^{-7} torr. The axial temperature gradient was 2–3 K/cm and the cooling rate was 0.5 K/h. The synthesis of CdTe crystals is described in detail elsewhere [9].

A specimen with a diameter of 0.286(8) mm providing the best X-ray diffraction pattern was chosen from CdTe single crystals ground to spheres. The X-ray diffraction data sets were collected on an automated four-circle CAD-4 Enraf-Nonius diffractometer (MoK_α radiation, graphite monochromator, $\theta/2\theta$ scanning technique) at four temperatures—295, 376, 491, and 583 K. The specimen temperature was maintained with the use of an attachment described in [10]. The stable operation of the diffractometer and of the temperature attachment was checked every 60 min by measuring the intensities of two reference reflections. The specimen orientation at high temperatures was checked and refined after measurement of each 100 reflections. The experimental conditions and the results of X-ray studies are indicated in Table 1.

The orientation matrix and the unit-cell parameters were refined based on 24 of symmetrically equivalent 844-type reflections ($\theta = 32°$). The reflection intensities were corrected for the Lorentz and the polarization factors, absorption, and thermal diffuse scattering of the X-ray radiation. The first- and the second-order corrections for thermal diffuse scattering were calculated based on the elastic constants of the crystal by the TDSCOR program [11]. We used the elastic constants at room temperature obtained in [12]. Their temperature changes were calculated by the equations common to all the crystals with the sphalerite structure [13]. The CdTe density is 5.86 g/cm^3 [12]. The total corrections for thermal diffuse scattering depending on $\sin\theta/\lambda$ at four different temperatures are indicated in Fig. 2. Their values are rather high. The extinction parameter was introduced by the Becker–Coppens formalism (the isotropic type 1; the Lorentz distribution of the blocks of mosaics), because other methods of taking into account extinction resulted in higher reliability factors.

REFINEMENT OF STRUCTURE MODELS OF CdTe

The structural parameters of CdTe single crystals were refined by the least-squares and X-ray diffraction data using the PROMETHEUS program package [14, 15]. The complete refinement was performed for the structural models with the anharmonic atomic thermal vibrations and split atomic positions. At the first stage of the study, the model of the ideal structure with harmonic thermal atomic vibrations was refined. This model is characterized by four parameters—the coefficient of $|F|_{exp}$ reduction to the absolute scale, the extinction coefficient, and two parameters corresponding to isotropic harmonic thermal vibrations of Cd and Te atoms. The number of independent structure amplitudes used in the refinement at each temperature is indicated in Table 1. The minimum number (152) of structure amplitudes was measured at 583 K. The final weighted/standard reliability factors (R_w and R, respec-

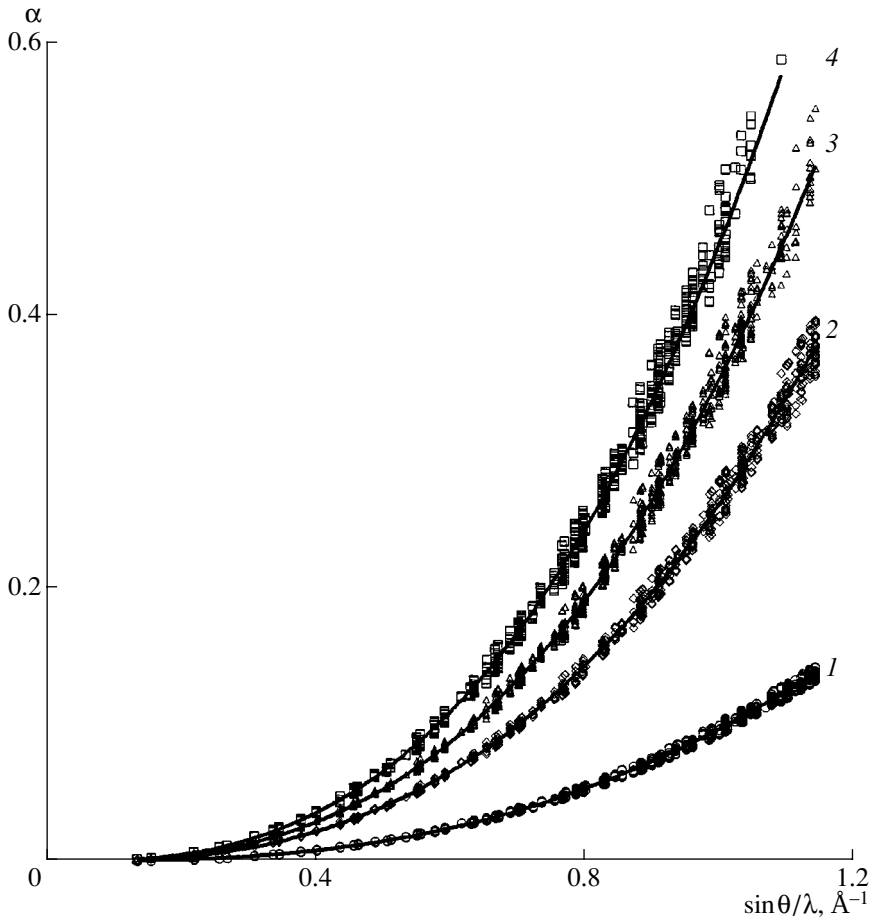

Fig. 2. Corrections α for thermal diffuse scattering depending on $\sin\theta/\lambda$ at different temperatures. Curves *1–4* correspond to T = 295, 376, 491, and 583 K, respectively.

tively) at T = 295, 376, 491, and 583 K were 1.25/1.27, 1.56/1.76, 1.64/1.98, and 1.67/2.05%, respectively. The $(1\bar{1}0)$ section of the zeroth electron-density synthesis at 583 K is shown in Fig. 3. The body diagonal of the unit cell with the basis Cd and Te atoms lies in this section. The presence of residual electron-density maxima in this section characterizes the above-mentioned asymmetric contributions of the Cd and Te atoms to the structure amplitudes.

In the models with anharmonic atomic thermal vibrations, the anharmonicity was taken into account by expanding the probability-density function of displacements of atoms from their equilibrium positions into the Gram–Charlier series. Initially, we took into account in the refinement only the expansion terms up to the sixth order, but only the third- and fourth-order expansion terms appeared to be physically significant (c_{123}, $d_{1111} = d_{2222} = d_{3333}$, and $d_{1122} = d_{1133} = d_{2233}$ for each atom). Below, all the results with allowance for the anharmonicity considered below are obtained in this approximation.

Strong correlations did not allow us to refine independently the third-order anharmonic parameters of atomic thermal vibrations of Cd and Te atoms. The environments of both Cd and Te atoms are characterized by the same geometry. All the Cd–Te bonds are of the same character. The atomic numbers of Cd and Te atoms (Z_{Cd} = 48 and Z_{Te} = 52), which influence first of all the harmonic components of vibrations, are rather close. Thus, it was possible to assume that the third-order anharmonic components of atomic thermal vibrations of Cd and Te atoms have equal magnitudes. The total number of the parameters in the refinement of the anharmonic structure model is equal to 9; i.e., there are at least 16 independent structure amplitudes per parameter to be refined even at T = 583 K.

The refinement in the anharmonic approximation based on the data sets collected at T = 295, 376, 491, and 583 K yielded the final R_w/R factors equal to 0.96/0.92, 1.29/1.39, 1.19/1.38, and 1.26/1.54, respectively. The R-factors for the anharmonic model were substantially lower (25% of the average R factor) than those obtained in the refinement of the harmonic model. The Hamilton tests [16] indicated the high significance of the results obtained. The difference maps of the probability density of the occurrence of atoms at the given point of the space in the process of the thermal motion were constructed based on the anharmonic

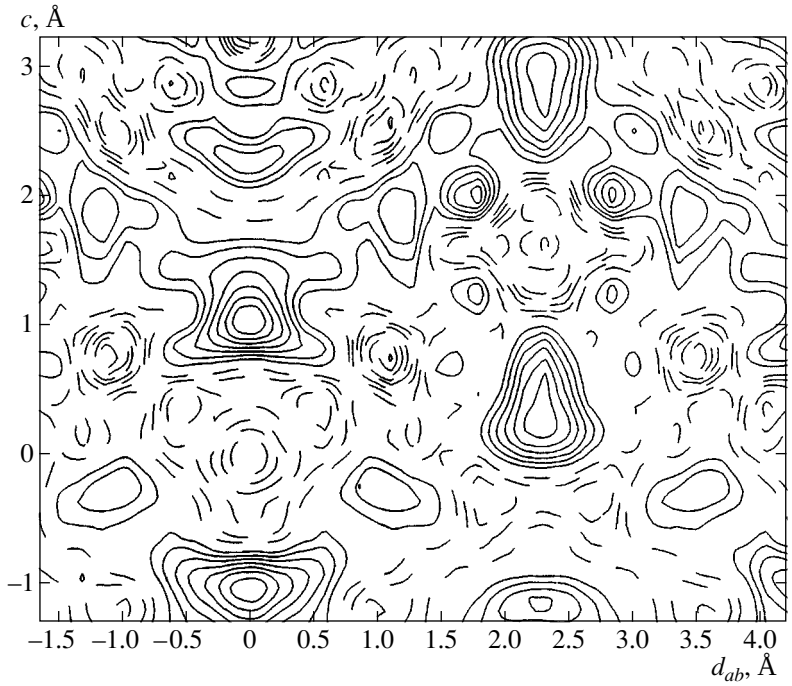

Fig. 3. The $(1\bar{1}0)$ section of the zeroth electron-density synthesis constructed upon subtraction of the structure model of CdTe with isotropic harmonic atomic thermal vibrations at $T = 583$ K. The positive and the negative contours are shown by solid and dashed lines, respectively. The isolines are drawn at constant intervals on a relative scale.

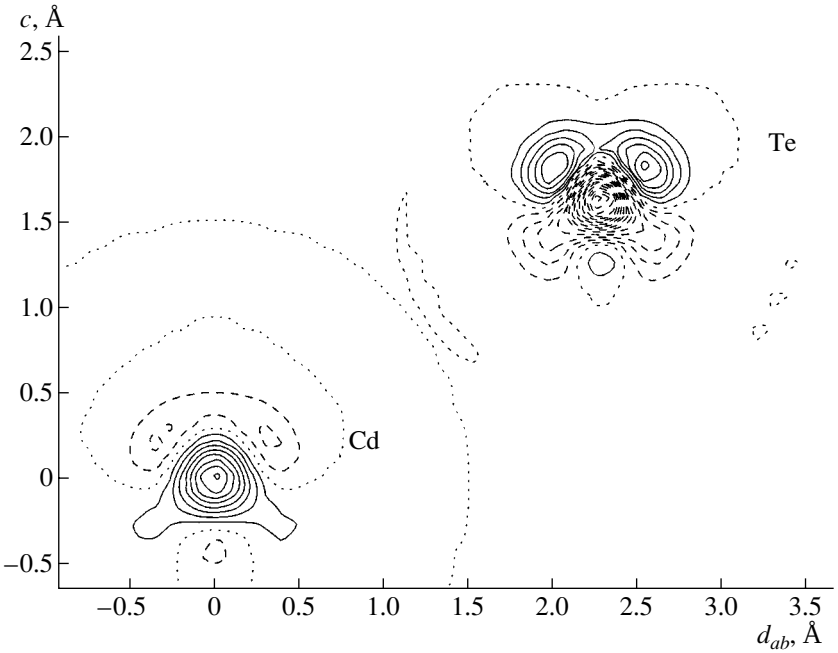

Fig. 4. The $(1\bar{1}0)$ section of the anharmonic component of the probability density-distribution for location of Cd and Te atoms at different points of the space during thermal vibrations. The isolines are drawn at constant intervals on a relative scale.

parameters using the Fourier transformation. The $(1\bar{1}0)$ section of the distribution of Cd and Te atoms is shown in Fig. 4. These maps indicate that the maximum anharmonicity of thermal vibrations is observed along the [111] direction. For Cd atoms, this line passes through the face center of the $[CdTe_4]$-tetrahedron and also Cd and Te atoms. The negative probability densities for Cd and Te atoms observed on a Cd–Te bond indicate the natural asymmetry in the elongation and shortening of this bond in the course of atomic thermal vibrations.

At the final stage of the study, the disordered structure model with split atomic positions was refined.

Table 2. Results of the refinement of the atomic models of a CdTe single crystal

T, K		$u_{11} \times 10^5$, Å^2		$u_{12} \times 10^5$, Å^2		c_{123}, Å^3 d^{Cd}_{1111}, d^{Cd}_{1122}, d^{Te}_{1111}, d^{Te}_{1122}, Å^4	x_{Cd} and x_{Te}	S	R_w/R
		Cd	Te	Cd	Te				
295	a*	2376(6)	1679(3)					1.12	1.25/1.27
	b**	2429(12)	1629(7)			−0.00045(5) 0.00021(10) 0.00019(4) −0.00037(4) −0.000052(19)		0.87	0.96/0.92
	c***	2275(9)	1340(4)	291(50)	−131(21)		−0.0056(1) 0.2586(1)	0.92	1.02/0.98
376	a*	3055(15)	2149(9)					1.10	1.56/1.76
	b**	3151(21)	2094(11)			−0.0008(1) 0.00084(10) 0.00052(26) −0.00021(9) −0.00019(4)		0.90	1.29/1.39
	c***	2768(17)	1778(5)	324(56)	−238(38)		−0.0090(1) 0.2589(1)	0.91	1.29/1.43
491	a*	4095(11)	2862(6)					1.17	1.64/1.98
	b**	4153(25)	2787(11)			−0.000167(13) −0.00009(32) 0.00068(14) −0.00060(11) −0.00021(5)		0.82	1.19/1.38
	c***	3794(15)	2300(6)	474(42)	−183(33)		−0.0093(1) 0.2609(1)	0.80	1.15/1.37
583	a*	4997(20)	3486(9)					1.24	1.67/2.05
	b**	5105(32)	3407(15)			−0.000203(20) 0.00108(52) 0.00072(22) −0.00058(7) −0.00029(7)		0.91	1.26/1.54
	c***	4503(18)	2812(9)	360(53)	−203(31)		−0.0109(2) 0.2618(1)	0.90	1.22/1.48

* Harmonic model.

** Model with anharmonic atomic thermal vibrations.

*** Model with the disordered arrangement of atoms.

Indirect evidence in favor of this model is the information on the formation of the ferroelectric phase in Zn-doped CdTe crystals [17]. It is reasonable to associate the ferroelectric phase transition with small atomic displacements. The question about the directions of the atomic displacements from the positions of the ideal sphalerite structure was answered upon the analysis of the difference maps of the probability-density distribution showing the location of the atoms at the particular points of space which were constructed using the anharmonic atomic thermal vibrations. It is seen from Fig. 4 that Cd and Te atoms can be displaced only along the [111] axis in opposite directions from the Cd–Te bond. Four threefold symmetry axes are intersected at the center of a regular [$CdTe_4$]-tetrahedron. In different tetrahedra, the atoms are displaced with the equal prob-

ability only along one of these axes. In each tetrahedron, the equal Cd–Te distances characteristic of the ideal sphalerite structure become unequal. The atoms displaced along the threefold symmetry axis from the special positions (0 0 0) and (1/4 1/4 1/4) with the point symmetry $\bar{4}3m$ acquire the coordinates (*xxx*) and the point symmetry 3*m*. The harmonic atomic thermal vibrations in these positions are characterized by ellipsoids of revolution; the initial position is split into four positions occupied with the probabilities 0.25, which are located at the vertices of a regular tetrahedron. This model is characterized by eight structural parameters to be refined. In this case, strong correlations between the displacements and the parameters of harmonic atomic thermal vibrations hindered in the refinement. The problem was solved by stepwise scanning [18] of the coordinates (*xxx*) with a step of $\Delta x = 0.0005$. The refinement of the disordered model in the approximation of harmonic atomic thermal vibrations at T = 295, 376, 491, and 583 K yielded the R_w/R factors equal to 1.02/0.98, 1.29/1.43, 1.15/1.37, and 1.22/1.48, respectively.

The Hamilton tests demonstrated that the results obtained for the model with split atomic positions are also significant as compared to those for the ideal harmonic model. It is difficult to choose between the anharmonic and the disordered models by comparing the refinement results for these models from the formal estimates alone (the R factors and the Hamilton tests). Both models provide asymmetric contributions of Cd and Te to the structure amplitudes of the CdTe crystals. Evidently, this conclusion is valid for the precision of X-ray data obtained in our study and the series termination determined by the maximum value of $\sin\theta/\lambda$ equal to 1.14 $Å^{-1}$.

The main difference between the model with split atomic positions and the anharmonic model reduces to the formation of different Cd–Te distances. At 583 K, all Cd–Te distances in the anharmonic model are equal, 2.809(1) Å, whereas the distances in the disordered model range within 3.064(1)–2.726(1) Å. If all the new atomic positions in the disordered model are occupied with the equal probability (0.25), one can readily evaluate the probabilities of formation of each Cd–Te distance in the above range. The probability of the formation of the distance Cd–Te = 3.064 Å is 1/16, the probabilities of the formation of the distances equal to 2.903, 2.889, and 2.734 Å are 3/16, and the probability of formation of Cd–Te = 2.726 Å is 6/16. In terms of crystal chemistry, the substantial scatter in the Cd–Te bond lengths in CdTe is hardly probable. For comparison, the data on the refinement of the anharmonic and the disordered models are given in Table 2.

The data on the structure of the matrix CdTe crystal obtained in this study will be used as the starting information for further studies of CdTe doped with different elements. We consider as the starting model of undoped CdTe crystal the model characterized by a substantial anharmonicity of atomic thermal vibrations. In terms of physics, the maximum anharmonicity observed in the case of atomic thermal vibrations along threefold axes of a $[CdTe_4]$-tetrahedron is quite justified. Vibrations of an atom located in the tetrahedron center lying on the line connecting the tetrahedron vertex with the center of the opposite face cannot obey the harmonic law, because the quantitative changes in the lengths of the bonds from the atom located at the tetrahedron vertex to three atoms forming the opposite face are essentially different.

ACKNOWLEDGMENTS

We are grateful to V.N. Molchanov and A.P. Dudka for the valuable remarks and the useful discussion.

The study was supported by the Federal Program on Support of Prominent Scientists and Leading Scientific Schools, project no. 00-15-96633.

REFERENCES

1. N. V. Belov, *Structure of Ionic Crystals and Metal Phases* (Akad. Nauk SSSR, Moscow, 1947), p. 60.
2. B. T. M. Willis and A. W. Pryor, *Thermal Vibrations in Crystallography* (Cambridge Univ. Press, Cambridge, 1975).
3. W. F. Kuhs, Acta Crystallogr., Sect. A: Found. Crystallogr. **48**, 80 (1992).
4. B. T. M. Willis, Proc. R. Soc. London, Ser. A **274**, 122 (1963).
5. A. A. Vaĭpolin, Fiz. Tverd. Tela (Leningrad) **15**, 1223 (1973) [Sov. Phys. Solid State **15**, 823 (1973)].
6. M. Sakata, S. Hoshino, and J. Harada, Acta Crystallogr., Sect. A: Cryst. Phys., Diffr., Theor. Gen. Crystallogr. **A30**, 655 (1974).
7. M. Kh. Rabadanov, Kristallografiya **40** (3), 505 (1995) [Crystallogr. Rep. **40**, 460 (1995)].
8. A. A. Vaĭpolin, Fiz. Tverd. Tela (Leningrad) **27** (12), 3620 (1985) [Sov. Phys. Solid State **27**, 2180 (1985)].
9. Yu. M. Ivanov, J. Cryst. Growth **194**, 309 (1998).
10. F. Tuinstra and G. M. Fraase Storm, J. Appl. Crystallogr. **11**, 257 (1978).
11. A. P. Dudka, M. Kh. Rabadanov, and A. A. Loshmanov, Kristallografiya **34** (4), 818 (1989) [Sov. Phys. Crystallogr. **34**, 490 (1989)].
12. *Physics and Chemistry of II–VI Compounds*, Ed. by M. Aven and J. S. Prener (North-Holland, Amsterdam, 1967; Mir, Moscow, 1970).
13. S. Nikanorov and Y. Burenkov, Acta Crystallogr., Sect. A: Cryst. Phys., Diffr., Theor. Gen. Crystallogr. **A34**, S285 (1978).
14. U. H. Zucker, E. Peterthaler, W. F. Kuhs, *et al.*, J. Appl. Crystallogr. **16**, 398 (1983).
15. L. A. Muradyan, M. I. Sirota, I. P. Makarova, and V. I. Simonov, Kristallografiya **30** (2), 258 (1985) [Sov. Phys. Crystallogr. **30**, 148 (1985)].
16. W. S. Hamilton, Acta Crystallogr. **18**, 502 (1965).
17. R. Weil, R. Nkum, E. Muranevich, *et al.*, Phys. Rev. Lett. **62** (23), 2744 (1989).
18. L. A. Muradyan, S. F. Radaev, and V. I. Simonov, *Methods of Structure Analysis* (Nauka, Moscow, 1989), p. 5.

Translated by T. Safonova

Crystallography Reports, Vol. 46, No. 4, 2001, pp. 642–646. Translated from Kristallografiya, Vol. 46, No. 4, 2001, pp. 710–714.

STRUCTURE OF INORGANIC COMPOUNDS

Dedicated to the memory of B.K. Vainshtein

Refinement of the $K_{0.96}Ti_{0.96}Nb_{0.04}OPO_4$ Structure

O. A. Alekseeva*, M. K. Blomberg, V. N. Molchanov*, I. A. Verin*, N. I. Sorokina*, T. Yu. Losevskaya***, V. I. Voronkova***, and V. K. Yanovskiĭ*****

** Shubnikov Institute of Crystallography, Russian Academy of Sciences, Leninskiĭ pr. 59, Moscow, 117333 Russia*
e-mail: vladimol@ns.crys.ras.ru
*** Department of Physics, University of Helsinki, Siltavuorenpenger 20 I, P.O. Box 9, Helsinki, FIN-00014 Finland*
****Moscow State University, Vorob'evy gory, Moscow, 119899 Russia*
Received October 18, 2000

Abstract—The structure of a $K_{0.96}Ti_{0.96}Nb_{0.04}OPO_4$ single crystal was established by the methods of the X-ray diffraction analysis. Additional positions of K atoms were established. In the superionic state, these atoms provide ionic transport in the crystals. © *2001 MAIK "Nauka/Interperiodica".*

INTRODUCTION

The present work continues the studies of the atomic structures and physical properties of the crystals of Nb-doped potassium titanyl phosphate $KTiOPO_4$ (KTP) crystals [1–4]. Earlier [1], it was found that $K_{1-x}Ti_{1-x}Nb_xOPO_4$ single crystals with the 4% niobium concentration crystallized from flux in the K_2O–TiO_2–Nb_2O_5–P_2O_5 system are orthorhombic (sp. gr. $Pna2_1$) with the unit-cell parameters a = 12.814(2) Å, b = 6.408(1) Å, c = 10.587(2) Å. The crystal structure of $K_{0.90}Ti_{0.96}Nb_{0.04}OPO_4$ [1] consists of (Ti,Nb)O_6-octahedra sharing vertices with the PO_4-tetrahedra, which form the three-dimensional framework with wide helical channels along the c-axis. These channels are filled with potassium cations with the 89 and 90% occupancies of the K(1) and K(2) positions, respectively. The substitution of tetravalent titanium atoms by pentavalent niobium atoms provides the formation of additional vacancies in the K(1) and K(2) positions. The number of such vacancies exceeds the number that could be expected from the condition of conservation of electroneutrality and the valences other ions.

STRUCTURE REFINEMENT

The structure of the single crystals of the compound was refined using the JANA-96 program package [5] and the X-ray diffraction data set collected earlier on an automated CAD-4F Enraf-Nonius diffractometer in [1].

The atomic coordinates, the anisotropic thermal parameters, and the occupancies of the crystallographic positions refined in [1] by the PROMETHEUS [6] program package were used as a starting model in our refinement. The reliability factors for this model are R = 2.25% and R_w = 2.81%. The occupancies of the crystallographically independent positions of the potassium cations are 0.89 and 0.90 for K(1) and K(2), respectively. All the Nb atoms (4%) enter only the Ti(1) positions. The residual-density peaks in the vicinity of the (Ti,Nb)(1), Ti(2), K(1), and K(2) positions were observed on difference electron-density syntheses constructed for the above model (Fig. 1). The most pronounced peak was located at a distance of 1.71 Å from the K(2) atom.

Then, we refined the structural parameters using the model with the split K(2) position (R = 1.96% and R_w = 2.37%). The occupancies of the potassium positions of the potassium atoms were $q_{K(1)} = 0.899$, $q_{K(2)} = 0.858$, and $q_{K(3)} = 0.108$. Thus, the chemical formula should be close to $K_{0.94}Ti_{0.96}Nb_{0.04}OPO_4$. The obtained positional parameters were used to construct a difference electron-density synthesis. The section in which the K(2) and K(3) atoms are located (x = 0.394) is shown in Fig. 2. The above formula of the specimen shown that the fulfillment of the condition of electroneutrality requires the presence of the additional amount of potassium (2%) in the structure.

The section of the electron-density synthesis showing the K(1) atom (Fig. 1) also reveals an additional position appropriate for the location of 2% of potassium atoms. However, the attempt to use the split K(1) position failed because of the close (at a distance of about 0.61 Å) residual electron-density peak in the vicinity of this position. Therefore, we had to take into account the anharmonicity of thermal vibrations of K(1) atoms by expanding the probability density function of the displacements of atoms from their equilib-

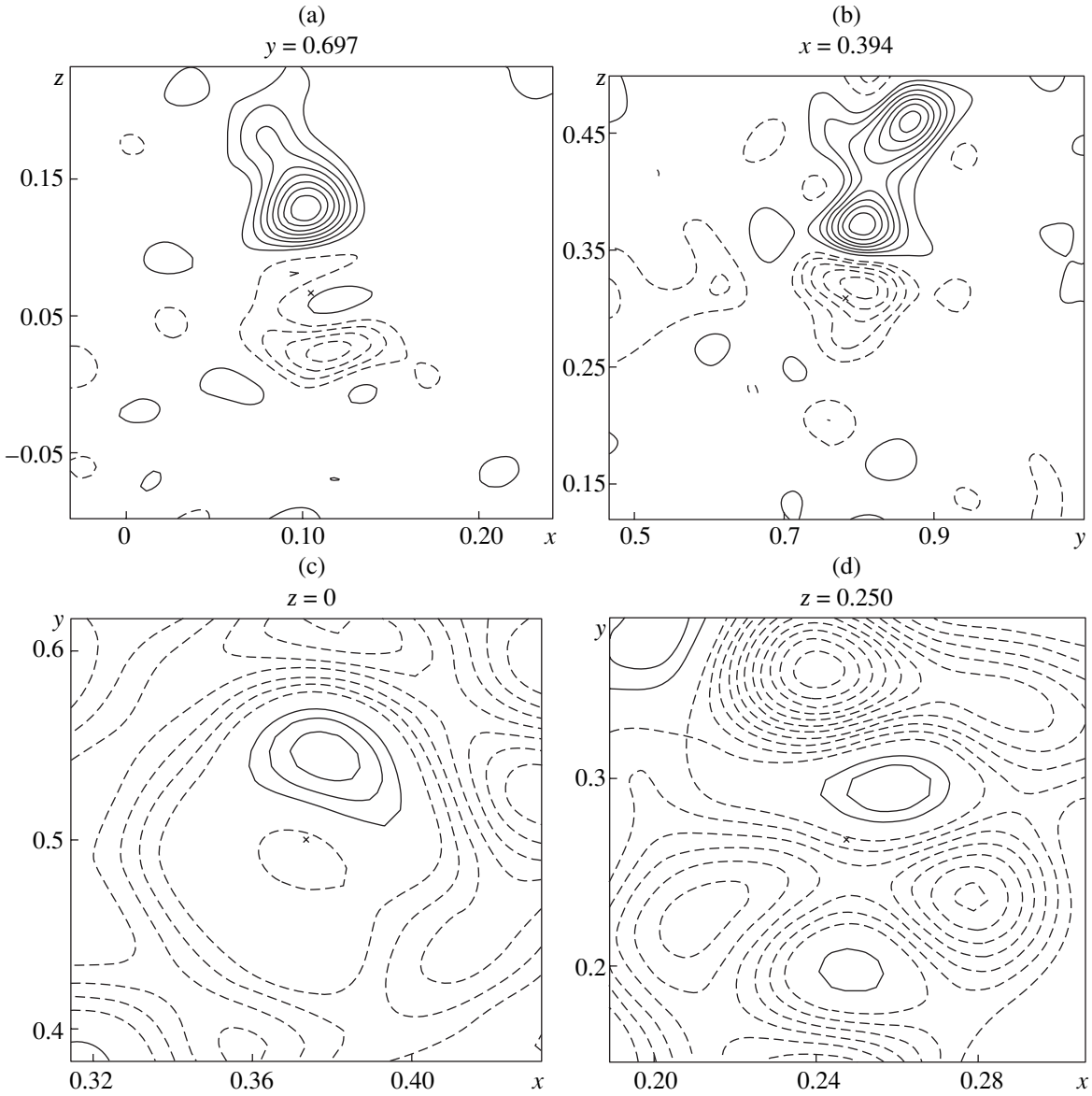

Fig. 1. Difference electron-density syntheses for the structure model refined with allowance for anisotropic thermal parameters for all the atoms: (a) the section passing through the K(1) atom; (b) the section passing through the K(2) atom; (c) the section passing through the (Ti,Nb)(1) position; and (d) the section passing through the Ti(2) atom.

rium positions into the Gram–Charlier series, and retained the terms up to the fourth order. At this stage of the refinement, the reliability factors were $R = 1.75\%$ and $R_w = 2.15\%$.

The difference electron density-syntheses constructed for the model taking into account the anisotropic thermal vibrations had the residual electron-density peaks in the vicinity of the Ti and Nb (Fig. 1) and also K(2) and K(3) positions (Fig. 2). These syntheses can be interpreted using two different models: (a) a model with split positions of the corresponding atoms or (b) the model taking into account the anharmonicity of thermal vibrations of the Ti and Nb atoms statistically occupying one position and the K(2) and K(3) atoms. Low values of the residual electron-density peaks and their location in close proximity to the atomic positions did not allow the refinement of the first model. Examination of the second model demonstrated that the expansion terms up to the fourth order should be retained. The sections of difference electron-density syntheses for the structure model refined with due regard for the anharmonic thermal vibrations of the K and Ti atoms are shown in Fig. 3. The final R factors are $R = 1.45\%$ and $R_w = 1.92\%$ (2699 reflections with $|F| > 3\sigma(F)$ for 269 refined parameters). The coordinates of the basis atoms, the occupancies q of the crystallographic positions, and the equivalent isotropic thermal parameters B_{eq} are given in the table.

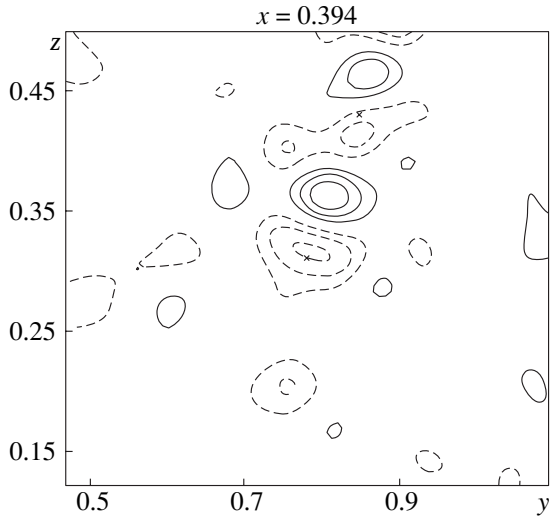

Fig. 2. Difference electron-density synthesis for the structure model with the statistical distribution of potassium atoms over two independent K(2) and K(3) positions. The section at passing through the K(2) and K(3) atoms (x = 0.394).

RESULTS AND DISCUSSION

A fragment of the $K_{0.96}Ti_{0.96}Nb_{0.04}OPO_4$ structure is shown in Fig. 4. The structure channels are occupied by potassium cations with the occupancies for the K(1), K(2), and K(3) positions equal to 90, 86, and 11%, respectively. Potassium atoms in different positions are characterized by different coordination numbers, namely, 9, 8, and 7, for the K(1), K(2), and K(3) positions, respectively. The average K–O distances for K(1), K(2), and K(3) atoms are also different (2.935, 2.848, and 2.974 Å, respectively). The existence of a chain of positions suitable for location of K atoms along the framework channels and a noticeable amount of vacancies account for the transport of K cations in the channels along the *c*-axis. Thus, the model of disordered potassium cations in the $K_{0.96}Ti_{0.96}Nb_{0.04}OPO_4$ structure explains the superionic properties of these crystals with the K^+-ion conductivity ($\sigma_{33} = 5 \times 10^{-2}\ \Omega^{-1}\ cm^{-1}$ at 300°C).

Atomic coordinates, position occupancies (q), and equivalent isotropic thermal parameters B_{eq} (Å^2) for the $K_{0.96}Ti_{0.96}Nb_{0.04}OPO_4$ structure

Atom	*x*/*a*	*y*/*b*	*z*/*c*	*q*	B_{eq}
Ti(1)	0.37240(3)	0.49967(7)	0	0.918(1)	0.46(1)
Nb(1)	0.37240(3)	0.49967(7)	0	0.081	0.46(1)
Ti(2)	0.24713(4)	0.26707(7)	0.2504(1)	1.000	0.61(1)
P(1)	0.49833(1)	0.33697(2)	0.25941(8)	1.000	0.44(0)
P(2)	0.18148(1)	0.50169(3)	0.51157(8)	1.000	0.46(0)
K(1)	0.10468(7)	0.6968(1)	0.0688(1)	0.899(1)	2.16(3)
K(2)	0.3800(1)	0.7786(2)	0.3102(2)	0.858(2)	1.39(6)
K(3)	0.397(1)	0.886(3)	0.430(1)	0.108(2)	13.36(47)
O(1)	0.48611(6)	0.4851(1)	0.1486(1)	1.000	0.75(1)
O(2)	0.51022(5)	0.4673(1)	0.3820(1)	1.000	0.76(1)
O(3)	0.40077(4)	0.1995(1)	0.2790(1)	1.000	0.63(1)
O(4)	0.59402(4)	0.1947(1)	0.2409(1)	1.000	0.70(1)
O(5)	0.11241(5)	0.3111(1)	0.5400(1)	1.000	0.69(1)
O(6)	0.11214(6)	0.6916(1)	0.4862(1)	1.000	0.75(1)
O(7)	0.25286(5)	0.5400(1)	0.6272(1)	1.000	0.76(1)
O(8)	0.25341(5)	0.4612(1)	0.3981(1)	1.000	0.75(1)
O(9)	0.22382(5)	0.0412(1)	0.3888(1)	1.000	0.69(1)
O(10)	0.22461(9)	−0.0352(1)	0.6419(1)	1.000	0.68(1)

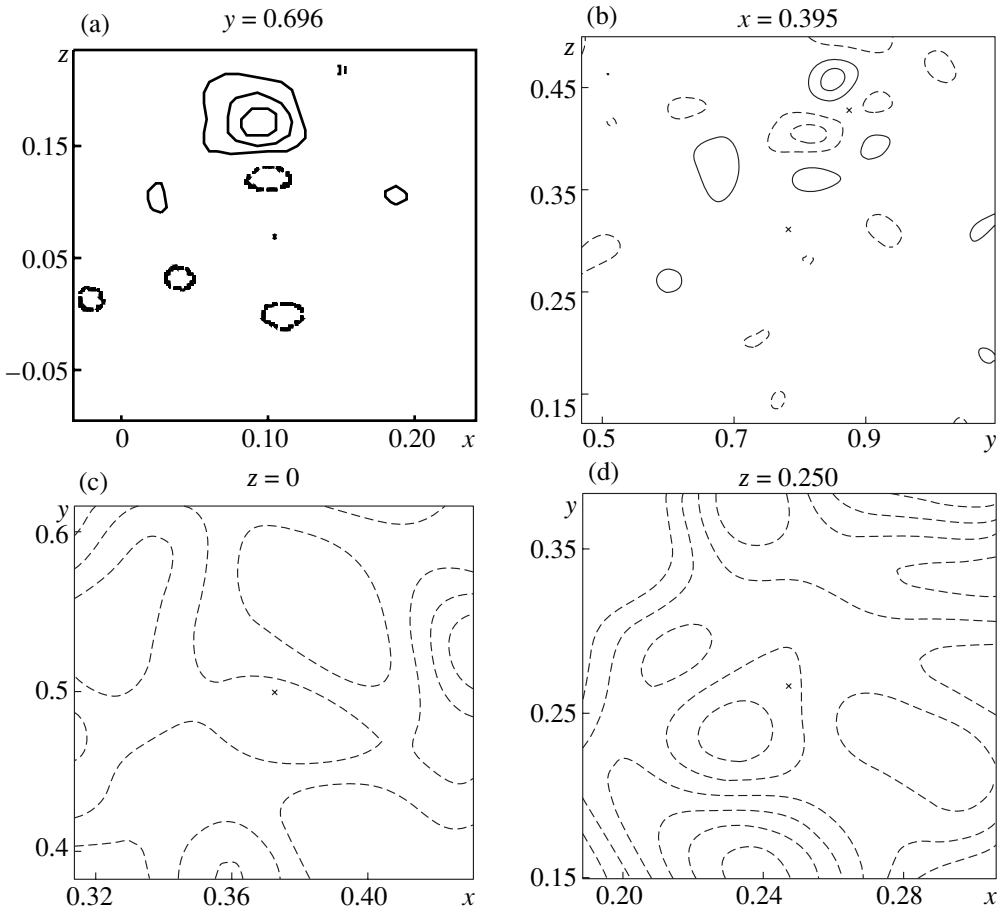

Fig. 3. Difference electron-density syntheses for the structure model refined with allowance for the anharmonicity of thermal vibrations of the K and Ti atoms: (a) the section passing through the K(1) atom; (b) the section passing through the K(2) and K(3) atoms; (c) the section passing through the (Ti,Nb)(1) position; and (d) the section passing through the Ti(2) atom.

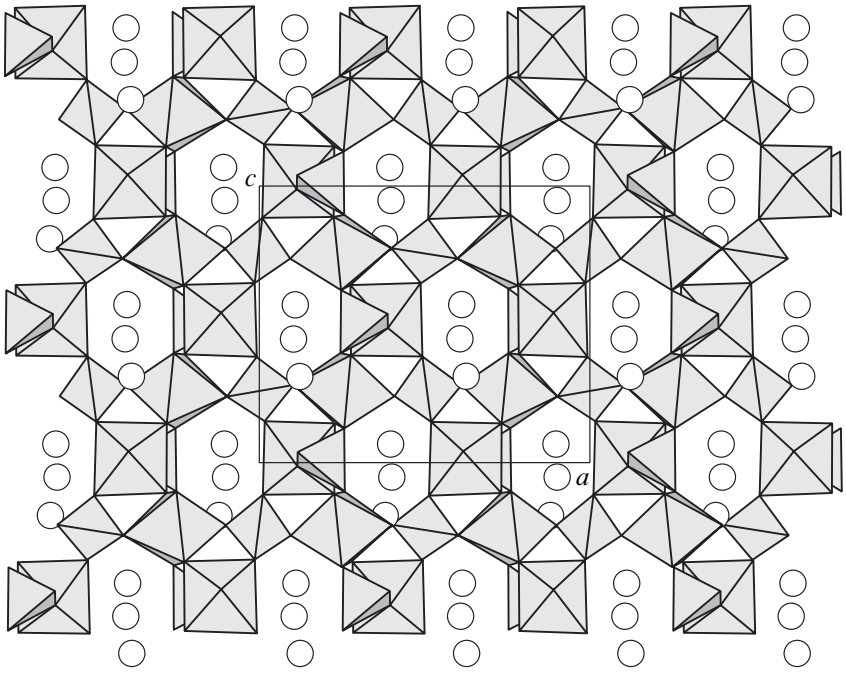

Fig. 4. Fragment of the $K_{0.96}Ti_{0.96}Nb_{0.04}OPO_4$ crystal structure projected onto the *ac* plane;Ti(Nb) and P atoms are located in octahedra and tetrahedra, respectively; K atoms are indicated by circles.

As follows from the earlier study of $K_{1-x}Ti_{1-x}Nb_xOPO_4$ ($x \sim 0.03$) single crystals [1], the unit-cell parameters *a* and *b* increase with the temperature. At 620°C, the crystal undergoes the translational-type ferroelectric phase transition. It should be mentioned that the parameter *c* is virtually insensitive to a temperature rise. A similar behavior of the parameter *c* is also observed at lowering of the temperature. Thus, the unit-cell parameters of the $K_{0.96}Ti_{0.96}Nb_{0.04}OPO_4$ single crystals at 20 K are $a = 12.796(5)$ Å, $b = 6.394(3)$ Å, $c = 10.592(7)$ Å.

ACKNOWLEDGMENTS

This study was supported by the Russian Foundation for Basic Research (project nos. 00-02-16059 and 00-02-17802) and by the Council on Leading Scientific Schools (project no. 00-15-96633).

REFERENCES

1. T. Yu. Losevskaya, O. A. Alekseeva, V. K. Yanovskiĭ, *et al.*, Kristallografiya **45** (5), 809 (2000) [Crystallogr. Rep. **45**, 739 (2000)].
2. O. A. Alekseeva, N. I. Sorokina, M. K. Blomberg, *et al.*, Kristallografiya **46** (2), 215 (2001) [Crystallogr. Rep. **46**, 176 (2001)].
3. P. A. Thomas and B. E. Watts, Solid State Commun. **73**, 97 (1990).
4. G. Moorthy, F. J. Kumar, C. Subramanian, *et al.*, Mater. Lett. **36**, 266 (1998).
5. V. Petricek and M. Dusek, *JANA-96: Crystallographic Computing System* (Institute of Physics, Praha, 1996).
6. B. H. Lucker, E. Perentaller, W. E. Kuhs, *et al*., J. Appl. Crystallogr. **16**, 358 (1983).

Translated by T. Safonova

Crystallography Reports, Vol. 46, No. 4, 2001, pp. 647–653. Translated from Kristallografiya, Vol. 46, No. 4, 2001, pp. 715–721.

STRUCTURE OF INORGANIC COMPOUNDS

Dedicated to the memory of B.K. Vainshtein

Modular Structure of a Potassium-Rich Analogue of Eudialyte with a Doubled Parameter *c*

R. K. Rastsvetaeva* and A. P. Khomyakov**

** Shubnikov Institute of Crystallography, Russian Academy of Sciences, Leninskiĭ pr. 59, Moscow, 117333 Russia*

e-mail: rast@ns.crys.ras.ru

*** Institute of Mineralogy, Geochemistry, and Crystal Chemistry of Rare Elements, ul. Veresaeva 15, Moscow, 121357 Russia*

Received July 17, 2000

Abstract—The structure of a new potassium-rich representative of the eudialyte group described by the idealized formula $Na_{27}K_8Ca_{12}Fe_3Zr_6[Si_{52}O_{144}](O,OH,H_2O)_6Cl_2$ was established by the methods of the X-ray diffraction analysis (R = 0.045, 3900 reflections). The unit-cell parameters are a = 14.249(1) Å, c = 60.969(7) Å, V = 10 720.3 Å^3, sp. gr. $R3m$. The structure of the mineral is characterized by in-layer order in cation arrangement resulting in doubling of the parameter c and the formation of two different modules, of which one corresponds to composition and structure of eudialyte (with an admixture of kentbrooksite) and the other is the derivative of alluaivite. © *2001 MAIK "Nauka/Interperiodica".*

Eudialyte, a zirconium silicate of a complicated varying composition, occurs in agpaitic rocks of the Kola Peninsula and other regions. It is of the most important rare-metal minerals and plays the role of a concentrator not only of zirconium but also of hafnium; yttrium; heavy and light lanthanides; and (in some varieties) also of niobium, tantalum, tungsten, and strontium. The combination of these rare elements in eudialyte attracts to it considerable attention as a complex useful mineral. The knowledge of the crystallochemical characteristics of the minerals of the eudialyte group can be very useful when designing technological processes for enrichment and processing of eudialyte ores. In recent years, the structures of more than 30 minerals of this group have been established by the Russian, Danish, and Canadian researchers. Recently, four of these minerals (in addition to two minerals studied earlier—eudialyte proper and alluaivite) were given their own names—kentbrooksite, khomyakovite, manganokhomyakovite, and oneillite. However, the study of new specimens, including the mineral in question, showed that many problems concerning eudialyte are still unsolved. Also, the general crystallochemical formula and the classification of the minerals of this group proposed in [1] require the further refinement.

The analogue of eudialyte considered below was discovered in intensely mineralized alkaline ultraagpaitic pegmatites from the Rasvumchorr mountain of the Khibiny massif. The mineral was discovered as impregnations of irregularly shaped grains 1–2 mm in size and their aggregates with the diameters ranging

Table 1. Crystallographic data and details of the X-ray diffraction experiment

Characteristic	Data and conditions
Unit-cell parameters, Å	a = 14.249(1), c = 60.969(7)
Unit-cell volume, Å^3	V = 10720.34
Density, g/cm^3: ρ_{calc}; ρ_{obs}	2.84; 2.86
Sp. gr.; Z	$R3m$; 3 (for the idealized formula)
Radiation; λ, Å	Mo$K\alpha$; 0.71073
Crystal dimensions, mm	0.35 × 0.25 × 0.20
Diffractometer	Enraf-Nonius
Scanning mode	ω/2θ
sinθ/λ, Å^{-1}	<0.81
Ranges of the indices of measured reflections	$-22 < h < 19$, $0 < k < 22$, $0 < l < 98$
R_{av} over equivalent reflections	0.024
Total number of reflections	10354 $I > 2\sigma(I)$
Number of independent reflections	3917 $F > 5\sigma(F)$
Program used for computations	AREN [2]
Program used for introduction of the absorption correction	DIFABS [3]
Number of independent positions	95
R factor upon anisotropic refinement	0.045

Table 2. Atomic coordinates, equivalent thermal parameters, multiplicities (Q), and occupancies (q) of the positions

Atom	x/a	y/b	z/c	Q q	B_{eq}, Å^2
Zr(1)	0.1675(1)	0.3350(1)	0.0833(1)	9 1	1.58(2)
Zr(2)	0.0004(1)	0.5002(1)	0.2480(1)	9 1	1.56(1)
Ca(1)	0.0720(1)	0.6661(1)	0.1659(1)	18 1	1.52(1)
Ca(2)	–0.0003(1)	0.2616(1)	–0.0009(1)	18 1	1.55(1)
Si(1)	0.3253(1)	0.0563(1)	0.1182(1)	18 1	1.8(1)
Si(2)	0.2522(1)	0.1261(1)	0.2940(1)	9 1	1.3(1)
Si(3)	0.0629(1)	0.3434(1)	0.2835(1)	18 1	1.4(1)
Si(4)	0.5967(1)	0.4033(1)	0.2910(1)	9 1	1.2(1)
Si(5)	0.0717(1)	0.1434(1)	0.0411(1)	9 1	1.6(1)
Si(6)	0.4042(1)	0.5958(1)	0.2066(1)	9 1	1.4(1)
Si(7)	0.5413(1)	0.4587(1)	0.1279(1)	9 1	2.1(1)
Si(8)	0.2636(1)	0.5272(1)	0.1259(1)	9 1	1.6(1)
Si(9)	0.0046(1)	0.6084(1)	0.0489(1)	18 1	1.4(1)
Si(10)	0.1245(1)	0.2490(1)	0.2037(1)	9 1	1.6(1)
Si(11)	0.4152(2)	0.2076(1)	0.0378(1)	9 1	1.7(1)
Si(12)	0.3389(1)	0.0639(1)	0.2141(1)	18 1	1.4(1)
Si(13)	0	0	0.1934(1)	3 0.81(1)	1.7(1)*
Si(14)	0	0	0.2871(1)	3 1	1.7(1)
Si(15)	0.6667	0.3333	0.0458(1)	3 0.83(1)	1.7(1)
Si(16)	0.6667	0.3333	0.1182(5)	3 0.17(2)	2.8(3)
Al	0	0	0.1885(5)	3 0.19(1)	2.6(4)*
*TM***	0.6667	0.3333	0.1440(1)	3 0.60(2)	2.9(1)*
Fe(1)	0.3292(3)	0.1646(2)	0.1667(1)	9 0.63(1)	1.6(1)
Fe(2)	0.3892(20)	0.1946(20)	0.1639(10)	9 0.10(1)	1.6(2)*
Mn	0.2711(20)	0.1356(20)	0.1672(10)	9 0.12(1)	2.0(4)*
K(1)	0.0943(1)	0.1886(1)	0.1433(1)	9 1	3.5(1)
K(2)	0.1028(1)	0.2056(1)	0.3291(1)	9 0.67(1)	2.0(1)
K(3)	0.5635(1)	0.1270(1)	0.0045(1)	9 0.67(1)	1.7(1)
K(4)	0.1710(7)	0.0855(5)	0.0823(1)	9 0.22(1)	2.2(1)
Na(1*a*)	0.0922(4)	0.5461(2)	0.3020(1)	9 0.70(1)	2.4(1)
Na(1*b*)	0.4283(5)	0.5717(5)	0.3067(2)	9 0.30(1)	2.4(2)
Na(2)	0.2150(4)	0.1075(3)	0.0771(1)	9 0.78(1)	2.7(1)
Na(3)	0.2138(2)	0.4276(2)	0.0296(1)	9 1	3.3(2)
Na(4)	0.4429(2)	0.5571(2)	0.0904(1)	9 1	4.6(2)
Na(5)	0.5683(2)	0.4317(2)	0.1905(1)	9 1	3.2(1)
Na(6)	0.2201(2)	0.4402(4)	0.2428(1)	9 1	4.3(1)
Na(7*a*)	0.4802(8)	0.2401(6)	0.2505(1)	9 0.44(3)	3.1(5)
Na(7*b*)	0.4294(11)	0.2147(8)	0.2583(1)	9 0.56(1)	5.2(2)
Na(8*a*)	0.1491(16)	0.0146(23)	0.2476(3)	18 0.22(1)	6.0(6)
Na(8*b*)	0.1624(10)	0.0812(7)	0.2438(2)	9 0.56(1)	8.2(3)
Na(9*a*)	0.5036(7)	0.2518(5)	0.0870(1)	9 0.89(1)	8.7(1)
Na(9*b*)	0.5863(30)	0.1726(30)	0.0766(10)	9 0.11(2)	4(1)*
Na(10)	0.2034(21)	0.1017(15)	0.1684(3)	9 0.15(1)	2.7(4)
Na(11)	–0.0018(11)	0.4991(8)	0.0040(1)	9 0.33(2)	2.3(3)

Table 2. (Contd.)

Atom	*x*/*a*	*y*/*b*	*z*/*c*	*Q q*	B_{eq}, Å^2
O(1)	0.3534(6)	0.1767(4)	0.1093(1)	9 1	2.2(2)
O(2)	0.3058(6)	0.1529(4)	0.3170(1)	9 1	2.2(2)
O(3)	0.5161(2)	0.0322(3)	0.1519(1)	9 1	1.5(2)
O(4)	0.3839(3)	0.2798(3)	0.0541(1)	18 1	1.9(1)
O(5)	0.0698(3)	0.3696(3)	0.3089(1)	18 1	1.7(2)
O(6)	0.0308(4)	0.2584(4)	0.1045(1)	18 1	2.7(2)
O(7)	0.3090(6)	0.1545(4)	0.2233(1)	9 1	2.3(3)
O(8)	0.1010(4)	0.4078(4)	0.0651(1)	18 1	2.7(2)
O(9)	0.0593(4)	0.1186(5)	0.2043(2)	9 1	4.8(4)
O(10)	0.5675(2)	0.1350(4)	0.2666(1)	9 1	2.6(3)
O(11)	0.2403(3)	0.4806(4)	0.1016(1)	9 1	2.9(3)
O(12)	0.3057(3)	0.2531(3)	0.1445(1)	18 1	1.8(2)
O(13)	0.5544(2)	0.4456(2)	0.3108(1)	9 1	1.5(2)
O(14)	0.2708(2)	0.5416(3)	0.2042(1)	9 1	1.6(2)
O(15)	0.0378(3)	0.6312(3)	0.0235(1)	18 1	2.2(2)
O(16)	0.3707(3)	0.2918(3)	0.1888(1)	18 1	2.0(2)
O(17)	0.1224(5)	0.0612(3)	0.0409(1)	9 1	2.1(3)
O(18)	0.5428(5)	0.2714(3)	0.2931(1)	9 1	2.3(3)
O(19)	0.0556(3)	0.2911(3)	0.2192(1)	18 1	1.3(1)
O(20)	0.5132(2)	0.0264(3)	0.0565(1)	9 1	1.7(2)
O(21)	0.3946(3)	0.6054(3)	0.1273(1)	9 1	2.5(2)
O(22)	0.0954(2)	0.1908(4)	0.0654(1)	9 1	2.0(2)
O(23)	0.0727(3)	0.6363(3)	0.2679(1)	18 1	1.7(1)
O(24)	0.1582(3)	0.3164(4)	0.2755(1)	9 1	2.0(3)
O(25)	0.4381(4)	0.3617(4)	0.2290(1)	18 1	2.6(2)
O(26)	0.5452(5)	0.2726(3)	0.0358(1)	9 1	2.6(2)
O(27)	0.1128(3)	0.2256(4)	0.0218(1)	9 1	2.4(3)
O(28)	0.2201(2)	0.4402(4)	0.1451(1)	9 1	2.2(2)
O(29)	0.1038(5)	0.5519(3)	0.1880(1)	9 1	1.9(3)
O(30)	0.2810(4)	0.2285(3)	0.2782(1)	18 1	2.3(2)
O(31)	0.6074(3)	0.2148(4)	0.1265(1)	9 1	2.5(2)
O(32)	0.4375(6)	0.3843(5)	0.1130(1)	18 1	4.4(3)
O(33)	0.1204(5)	0.0602(4)	0.2984(1)	9 1	2.4(3)
O(34)	0.1518(3)	0.3036(4)	0.1801(1)	9 1	2.5(3)
O(35)	0.4284(2)	0.5716(2)	0.2307(1)	9 1	2.1(3)
O(36)	0.3574(4)	0.1787(3)	0.0145(1)	9 1	1.7(3)
Cl(1)	0.3333	0.6667	0.3088(1)	3 0.88(5)	3.3(2)
Cl(2)	0	0	0.1147(2)	3 0.55(1)	3.8(2)
Cl(3*a*)	0.3333	0.6667	0.0240(1)	3 0.78(5)	3.2(3)
Cl(3*b*)	0.3333	0.6667	0.0535(4)	3 0.22(1)	3.1(4)*
OH(1)	0	0	0.2615(2)	3 1	3.0(3)
OH(2)	0.6667	0.3333	0.0725(1)	3 0.83	1.7(1)
OH(3)	0.6667	0.3333	0.0922(14)	3 0.17(1)	7(1)
OH(4)	0.5540(30)	0.2770(30)	0.1663(10)	9 0.23(2)	3.1(5)*
OH(5)	0.6667	0.3333	0.1696(15)	3 0.39(5)	4.2(5)*
OH(6)	0.1046(4)	0.0523(4)	0.1686(10)	9 0.19(1)	2.7(8)*
OH(7)	0	0	0.1681(10)	3 0.81(1)	4.0(5)*
$H_2O(1)$	0.3333	0.6667	0.2609(10)	3 0.50(7)	3.5(8)*
$H_2O(2)$	0.6667	0.3333	0.2192(10)	3 1	6.3(5)
$H_2O(3)$	0.3333	0.6667	0.0727(10)	3 0.54(7)	3.6(8)*
$H_2O(4)$	0.3333	0.6667	0.5	3 0.30(6)	4(1)*

* Isotropic thermal parameters.

** Hereafter, the positions simultaneously occupied by the tetrahedrally and octahedrally coordinated cations.

Table 3. Characteristics of coordination polyhedra

Position	Coordination number	Cation–anion distances, Å		
		limiting		average
Zr(1)*	6	2.046	2.128	2.091
Zr(2)*	6	2.017	2.073	2.058
Ca(1)*	6	2.295	2.413	2.370
Ca(2)*	6	2.312	2.422	2.336
Si(13)	4	1.544	1.606	1.591
Si(14)	4	1.550	1.637	1.615
Si(15)	4	1.618	1.620	1.619
Si(16)	4	1.54	1.58	1.55
Al	6	1.752	1.772	1.762
*TM**	4	1.53	1.81	1.74
*TM**	6	1.809	1.945	1.88
Fe(1)	4	1.988	2.092	2.04
Fe(2)	5	2.038	2.155	2.12
Mn	5	2.03	2.35	2.16
Na(1*a*)*	6	2.403	2.923	2.556
Na(1*b*)	6	2.34	2.90	2.68
Na(2)	8	2.483	2.805	2.665
Na(3)	6	2.401	2.917	2.585
Na(4)	8	2.543	2.787	2.645
Na(5)	7	2.510	2.993	2.765
Na(6)	8	2.511	2.702	2.633
Na(7*a*)	7	2.47	2.98	2.63
Na(7*b*)	8	2.52	2.76	2.64
Na(8*a*)	7	2.19	3.04	2.44
Na(8*b*)	8	2.19	3.02	2.77
Na(9*a*)	8	2.19	3.00	2.74
Na(10)	5	2.40	2.84	2.60
Na(11)	4	2.10	2.37	2.24
K(1)	8	2.66	3.11	2.82
K(2)	7	2.58	3.07	2.83
K(3)	7	2.66	3.10	2.85
K(4)	7	2.47	2.88	2.61

* The compositions of the mixed positions (Z = 1): Zr(1) = 7.2Zr + 1.8Ti; Zr(2) = 8.82Zr + 0.18(Hf,Ta); Ca(2) = 17Ca + 0.9Sr + 0.1Ce; *TM* = 2.1Si + 0.3Nb; Na(1*a*) = 4.9Na + 1.4Sr.

from 0.3–0.5 to 2 cm. The bright pink grains are uniaxial transparent positive crystals with n_p = 1.598 and n_g = 1.600, with the vitreous luster and a conchoidal fracture. The chemical analysis showed that the empirical formula (with respect to the sum of the anions equal to 152; Z = 3) of the mineral can be written as

$$Na_{27.10}(K_{7.93}Ba_{0.03})_{\Sigma 7.96}(Ca_{11.29}Sr_{0.74}Ce_{0.04})_{\Sigma 12.07}\cdot(Fe_{2.32}Mn_{0.42})_{\Sigma 2.74}(Zr_{5.69}Ti_{0.30}Hf_{0.04})_{\Sigma 6.03}\cdot(Si_{51.53}Al_{0.20}Nb_{0.16}Ta_{0.01})_{\Sigma 51.9}O_{146.14}OH_{1.86}Cl_{2.29}(H_2O)_{1.71}.$$

The idealized formula can be written as $Na_{27}K_8Ca_{12}Fe_3Zr_6Si_{52}O_{144}(O,OH,H_2O)_6Cl_2$. The mineral is characterized by a substantially elevated potassium content (6.12 wt % of K_2O as opposed to 0.5–1.0 wt % typical of eudialytes) and a reduced iron content (2.73 wt % of FeO as opposed to 5–7 wt % typical of eudialytes).

The X-ray diffraction data were collected from a tapered single crystal, whose characteristics and the details of the X-ray diffraction study are indicated in Table 1.

At present, two minerals of the eudialyte group with the doubled unit cells are known—alluaivite described by the sp. gr. $R\bar{3}m$ [4] and a titanium-rich analogue of eudialyte described by the acentric space group $R3m$ [5]. Proceeding from the fact that the composition of the latter mineral is close to the composition of the mineral under study, we assumed that these two minerals are isostructural and, therefore, used the known coordinates of the framework atoms determined in [5] as the starting model for the structure determination. The positions of all intraframework atoms were determined from a number of Fourier syntheses. At the final stage, we also managed to localize the positions with low occupancies from the difference electron-density synthesis. Upon placing the admixture atoms over various positions and the use of the mixed atomic scattering curves, the R-factor was rather low and the crystallochemical characteristics of all the atoms were established reliably. The final atomic coordinates are listed in Table 2. The main characteristics of coordination polyhedra (except for the Si-tetrahedra of the rings) are listed in Table 3.

The eudialyte structure type is based on the three-dimensional framework of three- and nine-membered Si,O-rings linked to each other through discrete Zr-octahedra and six-membered rings of Ca,O-octahedra. The cavities of the mixed framework are occupied by differently charged cations and anions of different sizes. The ordered arrangement of these atoms in the xy (horizontal) plane results in lowering of the symmetry to $R3$, whereas the ordered arrangement along the vertical direction (the long z-axis) results in doubling of the parameter c. In this case, the unit cell is doubled mainly because ordering of Fe and Na atoms occupying the positions of the planar square and of Fe and K atoms in two subpositions adjacent to this square along the threefold axis. The character of such ordering allows one to consider the structure of the new mineral as consisting of three modules, which have the following geometric prototypes: alluaivite (Fig. 1), eudialyte (Fig. 2), and kentbrooksite–"barsanovite" (Fig. 3). The former two modules build the major part of the structure, whereas the latter one complements the structure (10%) and is statistically present in the eudialyte module.

Although the composition of the alluaivite module does not allow one to consider it as the direct analogue

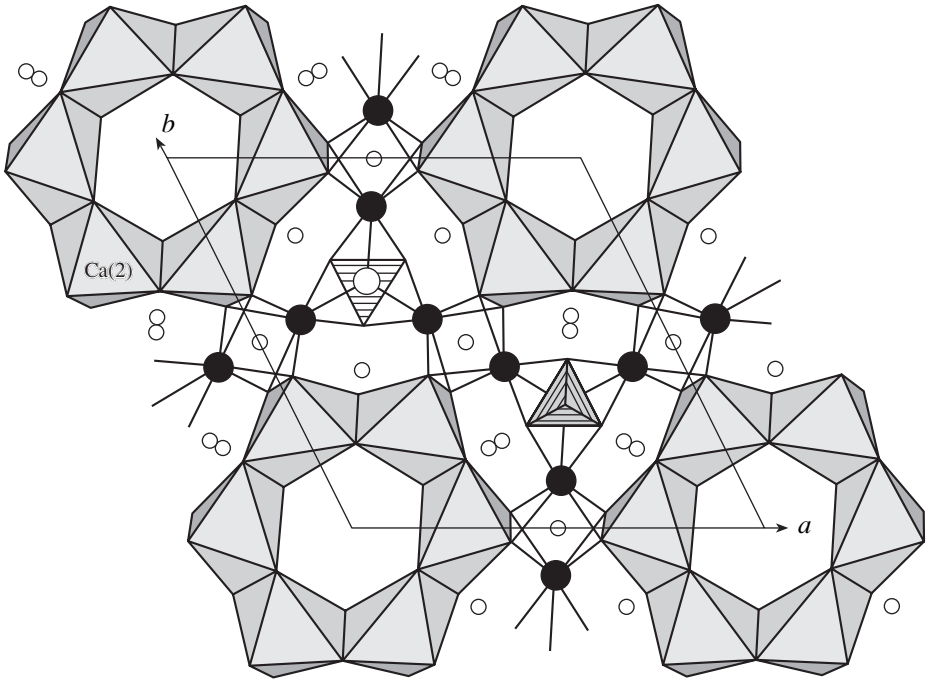

Fig. 1. Cationic layer in the structure of potassium-rich eudialyte corresponding to the "alluaivite" module projected onto the (001) plane; Si-tetrahedra are hatched with solid lines; the Na, Cl, and K atoms are indicated by small and large empty and filled circles, respectively.

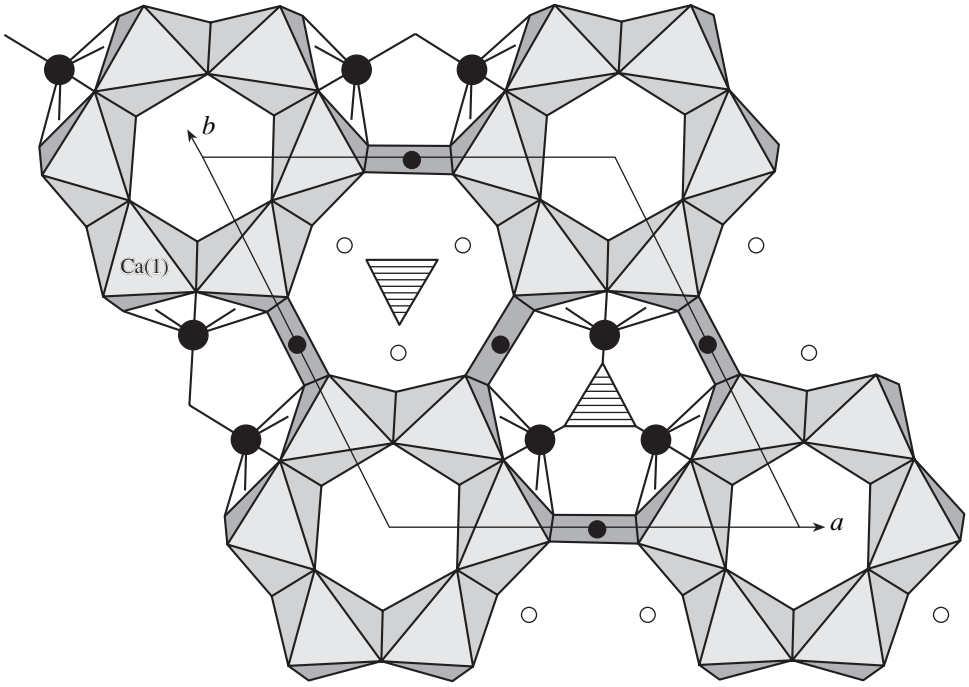

Fig. 2. Cationic layer corresponding to the eudialyte module; Fe atoms are indicated by small filled circles; for the further notation, see Fig. 1.

of alluaivite because most of Ti atoms in this module are substituted by Zr atoms, the characteristic structural features of alluaivite are clearly seen in this module. Thus, there are no Fe atoms either in the square center or in the adjacent five-vertex polyhedra constructed on the basis of this square. These positions in the alluaivite structure are occupied by Na atoms, which considerably increase the dimensions of the square, whereas the

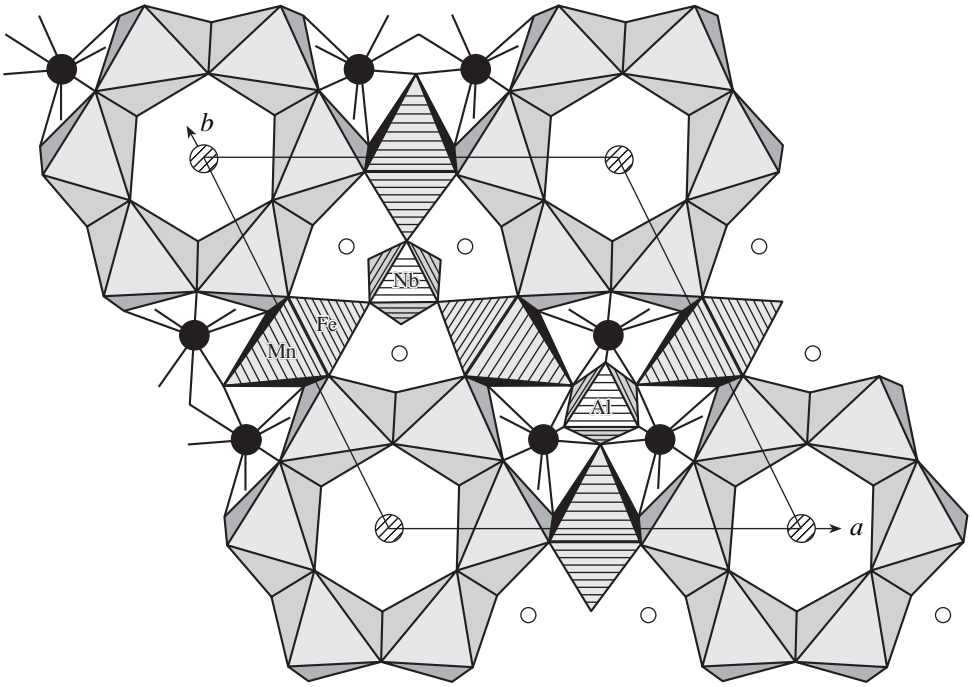

Fig. 3. Cationic layer corresponding to the kentbrooksite–barsanovite module; the clusters of polyhedra are hatched with solid lines; Na and K atoms are represented by small empty and large filled circles, respectively; H_2O molecules are represented by hatched circles.

compact hemioctahedra are transformed into large seven-vertex polyhedra related by the center of inversion. A higher potassium content in the new mineral provides the partial replacement of Na by K in all the three modules, and especially in the alluaivite module in which 12 potassium atoms occupy the seven-vertex polyhedra described above. Another characteristic feature of the "alluaivite" module is the high silica content: the positions in the centers of both nine-membered silicon–oxygen rings are occupied by Si atoms; as a result, these rings are transformed into ten-membered tetrahedral "platforms."

The isomorphous replacement of Na by K in two other modules occurs in the positions characterized by the highest isomorphous capacity of all the Na positions in the eudialyte structure (which was denoted as Na(4) in [1]).

The main characteristics of the composition and modular structure of the mineral are reflected in its crystallochemical formula ($Z = 1$):

$$\{[Zr_{8.82}(Hf,Ta)_{0.18}][Ca_{18}][Si_{72}O_{216}][Si_{4.5}(OH)_{4.5}Al^{[VI]}_{0.6}\cdot$$
$$Nb_{0.3}\square_{0.6}O_2(OH)_{0.7}][Fe^{[IV]}_{5.7}Fe^{[V]}_{0.9}Mn^{[V]}_{1.1}Na^{[V]}_{1.3}(OH)_{0.6}]\cdot$$
$$[K_9Na_{36}][(H_2O)_{5.4}Cl_{1.65}]\}\{[Zr_{7.7}Ti_{1.3}][Ca_{17}Sr_{0.9}Ce_{0.1}]\cdot$$
$$[Si_{72}O_{216}][Si_{5.5}\square_{0.5}(OH)_{5.5}][Na^{[IV]}_3K^{[VII]}_6K^{[VII]}_6]\cdot$$
$$[Na_{41.6}K_2Sr_{1.4}][Cl_{5.6}(H_2O)_{1.6}]\},$$

in which the formulas in braces correspond to the eudialyte (including kentbrooksite) and alluaivite modules, respectively. The formulas in brackets show the composition of the key positions. The coordination numbers of the cations are indicated by Roman numerals in brackets. The modules correspond to the structural fragments whose *z*-coordinate ranges from –0.05 to 0.11 and from 0.11 to 0.27 Å. These modules form a two-layer sheet with the thickness of about 20.3 Å. These sheets are multiplied along the threefold axis by the law of the *R* lattice and form the structure of the mineral with the doubled parameter *c*, i.e., $c = 61$ Å.

Comparing the new mineral with alluaivite [4] and titanium-rich eudialyte [5], we can see that the main cause of doubling of the parameters *c* is the process of ordering of cations of only one type, namely, the additional Si atoms or impurity Ti atoms, respectively. Despite of the fact that the Fe atoms in titanium-rich eudialyte also tend to be ordered over the positions of the square and the [Ti_3Al]-cluster, the maximum ordering of the cationic layers is observed only in the structure of the potassium-rich representative of this group. The ordered substitution of a number of cations within one framework leads to regular displacements of oxygen atoms from their positions and, hence, to changes in the configurations of Si-tetrahedra and Ca-octahedra forming this framework. In view of this fact, the framework of the mineral studied, similar to the framework of titanium-rich eudialyte, can be considered as a proportionally modulated framework with the modulation wave propagating along the *c*-axis and the modulation vector being equal to the parameter *c*.

Thus, the new mineral is the first representative possessing the modular structure in the eudialyte group. This mineral does not fall into the classification of eud-

ialytes proposed earlier [1]. Indeed, this mineral cannot be considered as a member of the isomorphous eudialyte–kentbrooksite series, because it simultaneously is eudialyte, alluaivite, and partly kentbrooksite (barsanovite). Taking into account the tendency for cationic ordering in the structure of titanium-rich eudialyte, one can expect the discovery of other minerals composed of modules–prototypes of the already described minerals of the eudialyte group. Vice versa, we can expect the discovery of minerals, whose compositions and structures would be similar to each of the above modules, e.g., to the alluaivite module of the structure considered above.

ACKNOWLEDGMENTS

The study was supported by the Russian Foundation for Basic Research, project no. 99-05-65035.

REFERENCES

1. O. Johnsen, J. D. Grice, and R. A. Gault, Eur. J. Mineral. **10**, 207 (1998).
2. V. I. Andrianov, Kristallografiya **32** (1), 228 (1987) [Sov. Phys. Crystallogr. **32**, 130 (1987)].
3. N. Walker and D. Stuart, Acta Crystallogr., Sect. A: Found. Crystallogr. **39** (2), 158 (1983).
4. R. K. Rastsvetaeva, A. P. Khomyakov, V. I. Andrianov, and A. I. Gusev, Dokl. Akad. Nauk SSSR **312** (6), 1379 (1990) [Sov. Phys. Dokl. **35**, 492 (1990)].
5. R. K. Rastsvetaeva, A. P. Khomyakov, and G. Chapius, Z. Kristallogr. **214**, 271 (1999).

Translated by T. Safonova

Crystallography Reports, Vol. 46, No. 4, 2001, pp. 654–658. Translated from Kristallografiya, Vol. 46, No. 4, 2001, pp. 722–726.

Dedicated to the memory of B.K. Vainshtein

Bulk Photovoltaic Effect in Noncentrosymmetric Crystals

V. M. Fridkin

Shubnikov Institute of Crystallography, Russian Academy of Sciences, Leninskiĭ pr. 59, Moscow, 117333 Russia

Received February 28, 2001

Abstract—The theory and the experimental characteristics of the bulk photovoltaic effect in ferroelectric and piezoelectric crystals first observed at the Institute of Crystallography have been reviewed. I dedicate this review to the memory of B.K. Vainshtein whose help in performing these works was really inestimable. © *2001 MAIK "Nauka/Interperiodica".*

INTRODUCTION

Illumination of crystals (or polycrystalline media) in the range of intrinsic and extrinsic absorption gives rise to photocurrents and photovoltages. If the circuit is closed (the short-circuited electrodes), one records the photocurrent J; if the circuit is open, the photovoltage U_{ph} or the corresponding field E_{ph} (Fig. 1). This phenomenon is known as the photovoltaic effect.

Until recently two types of the photovoltaic effect have been known. The first, Dember effect is caused by a nonuniform illumination of the crystal, e.g., by strong absorption of light. In this case, the photovoltaic effect is associated with diffusion of photoexcited (nonequilibrium) carriers and the variations in the mobility of holes and electrons. The second type of the photovoltaic effect is associated with separation of nonequilibrium carriers at crystal inhomogeneities. The well-known example here is the photovoltaic effect at the p–n transitions. It is this effect that is used in solar batteries. Thus, the photovoltaic effect recorded up to now was associated either with inhomogeneity in crystals or with its nonuniform illumination. Both phenomena have one common property—the photovoltage observed in a crystal (or at a p–n transition) does not exceed the band gap, i.e., a value of several volts.

In the second half of the 1960s, a new effect was discovered—bulk photovoltaic effect [1]. This effect arises under illumination of crystals (or polycrystalline media) having no center of symmetry. Contrary to the manifestations of the photovoltaic effects observed earlier, the bulk photovoltaic effect is observed their uniform crystals under a homogeneous illumination, which, therefore, was named the bulk photovoltaic effect. The latter has two characteristic features. First, its value depends on the light polarization and, second, the photovoltage in a crystal can reach several tens of thousands of volts, i.e., exceed the band gap by several orders of magnitude. Since the bulk photovoltaic effect can be observed in noncentrosymmetric crystals, it can be recorded for only 20 point (piezoelectric) symmetry groups. In other words, the bulk photovoltaic effect is inherent only in piezoelectric and ferroelectric crystals.

In this respect, the bulk photovoltaic effect is an analogue of the effect of change of parity in the case of weak interactions. In the low-temperature experiments on Co^{90} performed by C.H. Wu, the electric current appeared as a result of the neutron decay in a magnetic field L.D. Landau was the first to assume that the effect of the change in parity is associated with the asymmetry of world.

PHENOMENOLOGY OF THE BULK PHOTOVOLTAIC EFFECT

By analogy with the nonlinear optics, the bulk photovoltaic effect can be termed the non-linear photonics. The allowance for the quadratic dependence of the current J on the field due to the light wave with the unit vector $\mathbf{e}$ for linearly (L) and circularly (C) polarized light leads to the equation:

$$J_i = G^L_{ijl} e_j e^*_l I + iG^c_{il}[\mathbf{ee}^*]_i I, \qquad (1)$$

where I is the light intensity.

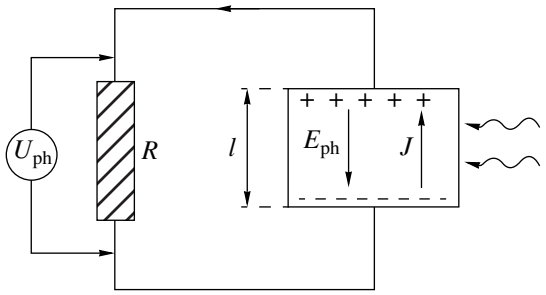

Fig. 1. Schematic of measurements of the photovoltaic current J and photovoltage U_{ph}.

1063-7745/01/4604-0654$21.00 © 2001 MAIK "Nauka/Interperiodica"

The first term in Eq. (1) describes the bulk photovoltaic effect for the linearly polarized light, and G^L_{ijl} is the tensor of the third rank. The operation of the three-dimensional inversion shows that the linear bulk photovoltaic effect is nonzero only in noncentrosymmetric crystals, and G^L_{ijl} is the conventional piezoelectric tensor. The second term in Eq. (2) describes the bulk photovoltaic current for a crystal illuminated with a circularly-polarized light, whereas the second-rank tensor G^c_{il} has the nonzero value only for gyrotropic (optically active) noncentrosymmetric crystals. It follows from Eq. (1) that the current J_i depends on the light polarization.

If the electrodes are disconnected, the current J_i generates the photovoltage (see Fig. 1),

$$U_{ph} = J_i l/(\sigma_d + \sigma_{ph}), \quad (2)$$

where σ_d and σ_{ph} are the darkconductivity and the photoconductivity, respectively, and l is the distance between the electrodes. If either darkconductivity or and photoconductivity is low, the photovoltaic current J_i generates a high voltage in the electrodes, which is proportional to the distance between electrodes and is not limited by the band gap.

ON THE MICROSCOPIC NATURE OF THE BULK PHOTOVOLTAIC EFFECT

The microscopic bulk photovoltaic effect is associated with the violation of the principle of the detailed balancing for photoexcited (nonequlibrium) carriers in noncentrosymmetric crystals. The principle of the detailed balancing suggests that the probability $W_{kk'}$ of the electron transition from the state with a momentum k' to a state with the momentum k is equal to the probability of the reverse transition: $W_{kk'} = W_{k'k}$. Up to now, it was believed that this principle is fulfilled in electron kinetics of solids, although there are some cases (foreseen by Boltzmann) where it is violated. In centrosymmetric crystals (such as, Ge or Si), this principle is fulfilled and the photovoltaic effect is of the conventional nature. In noncentrosymmetric crystals, $W_{kk'} \neq W_{k'k}$ and the violation of the principle of the detailed balancing gives rise to an asymmetric momentum distribution for nonequlibrium electrons (or holes), which results in the appearance of the photovoltaic current in homogeneous crystals or in uniformly illuminated ones. Figure 2 schematically illustrates the violation of the principle of detailed balancing in noncentrosymmetric crystals. This can be caused by inelastic scattering of carriers from asymmetric centers (Fig. 2a), excitation of impurity centers with an asymmetric potential (Fig. 2b), or the hopping mechanism acting between the asymmetrically distributed centers (Fig. 2c). Figure 3 provides the interpretation of the bulk photovoltaic effect in gyrotropic crystals. Spin-orbital splitting of the valence band

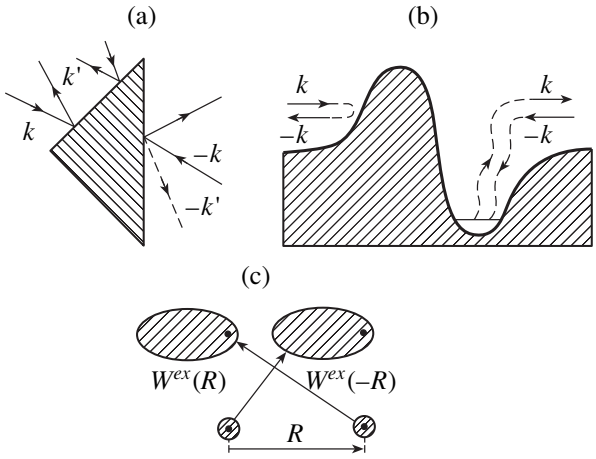

Fig. 2. Illustrating violation of the principle of the detailed balancing in noncentrocymmetric crystals.

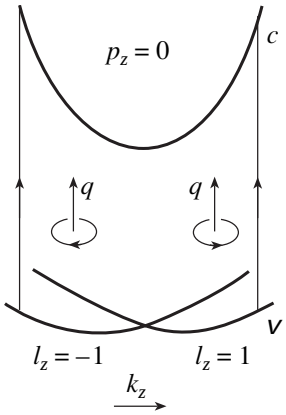

Fig. 3. To the formation of bulk photovoltaic effect in gyrotropic crystals.

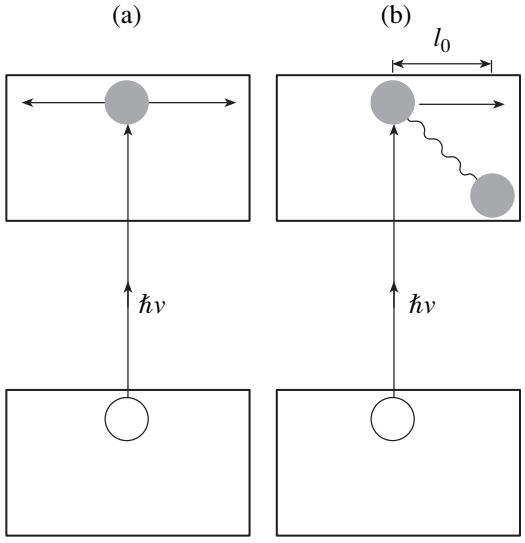

Fig. 4. (a) Symmetric distribution of nonequilibrium carriers in a centrocymmetric crystal; (b) asymmetric distribution of nonthermalized carriers in a noncentrocymmetric crystal.

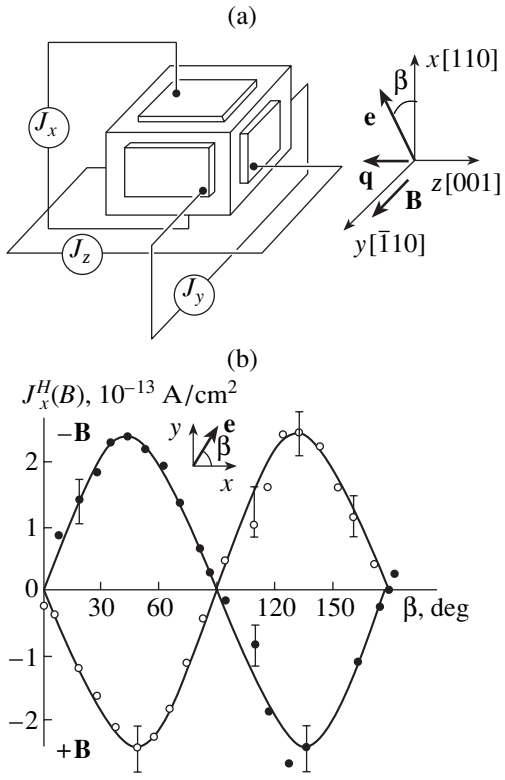

Fig. 5. (a) Schematic of measurements of the bulk photovoltaic current in polarized light in a magnetic field. (b) Dependence of the Hall-component of the bulk photovoltaic current in a cubic ZnS crystal on the angle of light polarization for two directions of the magnetic field.

(ν) results in excitation of electrons with a momentum $k_z < 0$ clockwise circularly-polarized light ($l_z = -1$), whereas the counterclockwise circularly-polarized light ($l_z = 1$) excites electrons with a momentum $k_z > 0$. Thus, changing the sign of the circular light polarization, one can change the direction of the bulk photovoltaic current. This was first made experimentally in tellurium crystals [1] and can also be made for all the gyrotropic crystals.

Independently of the microscopic mechanism, the bulk photovoltaic effect is associated with the excitation in a crystal of the so-called nonthermalized electrons (holes) (Fig. 4). Figure 4a illustrates the intrinsic excitation of a centrosymmetric crystal. It is seen that the electron distribution in the band is symmetric and there is no current. The excitation of a noncentrosymmetric crystal (Fig. 4b) provides the asymmetric momentum distribution for electrons (shown by an arrow). The photoexcited nonthermalized electrons lose the energy and descend to the band bottom, which results in the shift l_0. An amplitude of the tensor component G^L has the form

$$G^L = el_0\xi^{ex}\varphi(\hbar\nu)^{-1}. \quad (3)$$

Here, φ is the quantum yield, ξ^{ex} is the parameter characterizing the excitation asymmetry and depending on the mechanism of violation of the principle of detailed balancing, and e is the electron charge. The lifetime of an electron in the nonthermalized state, $\tau_{nth} \approx 10^{-12}$ s, is small in comparison with the lifetime of a nonequilibrium thermalized electron, $\tau_{th} \approx 10^{-6}$ s. Nevertheless, l_0 can reach the values of order of several angstroms, since the mobility of a nonthermalized electron, μ_{nth}, is very high in comparison its mobility in the nonthermalized state, μ_{th}:

$$\mu_{nth} = e(m^*)^{-1}\tau_0 \approx el_0(\hbar k_0)^{-1}. \quad (4)$$

High μ_{nth} values are provided by a small effective mass of an electron, m^*, (τ_0 is the thermalization time).

Thus, if is clear that the bulk photovoltaic effect provides the transformation of the light energy into electric. However, the efficiency η of this transformation is very low. It is easy to see that

$$\eta \approx \tau_{nth}/\tau_{th} = 10^{-6}–10^{-4}. \quad (5)$$

Thus, the main application field of the bulk photovoltaic effect is photorefraction and photorefractive optics which use intense fields generated in piezo- and ferroelectric crystals.

EXPERIMENTAL OBSERVATION OF THE BULK PHOTOVOLTAIC EFFECT

The schematic of the experimental observation of the bulk photovoltaic effect is shown in Fig. 5a. A crystal is illuminated with a polarized light with the wavevector **q**. The vector **e** of the light polarization forms an angle β with the x-axis. If the bulk photovoltaic effect is studied in a current mode, the currents J_x, J_y, and J_z are measured along the crystallographic directions x, y and z, respectively. If the measurements are also made in a magnetic field (see below), the vector **B** denotes the magnetic field intensity. According to Eq. (1), the rotation of the polarization vector **e** of the light results in oscillations of the bulk photovoltaic current, i.e., in its dependence on the β angle; the type of oscillations depends on the crystal symmetry and the direction of the incident light beam. Figure 6 shows the angular dependences of the photocurrent for trigonal (3m) $LiNbO_3$: Fe, cubic p-GaAs, and trigonal (3 : 2) quartz crystals with different concentrations of F-centers.

In lithium niobate and quartz, the bulk photovoltaic effect is of the extrinsic nature; i.e., it is caused by excitation of F^{+2} centers in the former crystal and of color centers in the latter one. In p-GaAs, the bulk photovoltaic effect is of the intrinsic nature, i.e., is caused by an interband transitions of the carriers. In ferroelectric crystals (Fig. 6a), there are certain directions along which the bulk photovoltaic effect is observed in the natural light. In piezoelectric crystals (see Figs. 6b, 6c), such directions are absent and the bulk photovoltaic

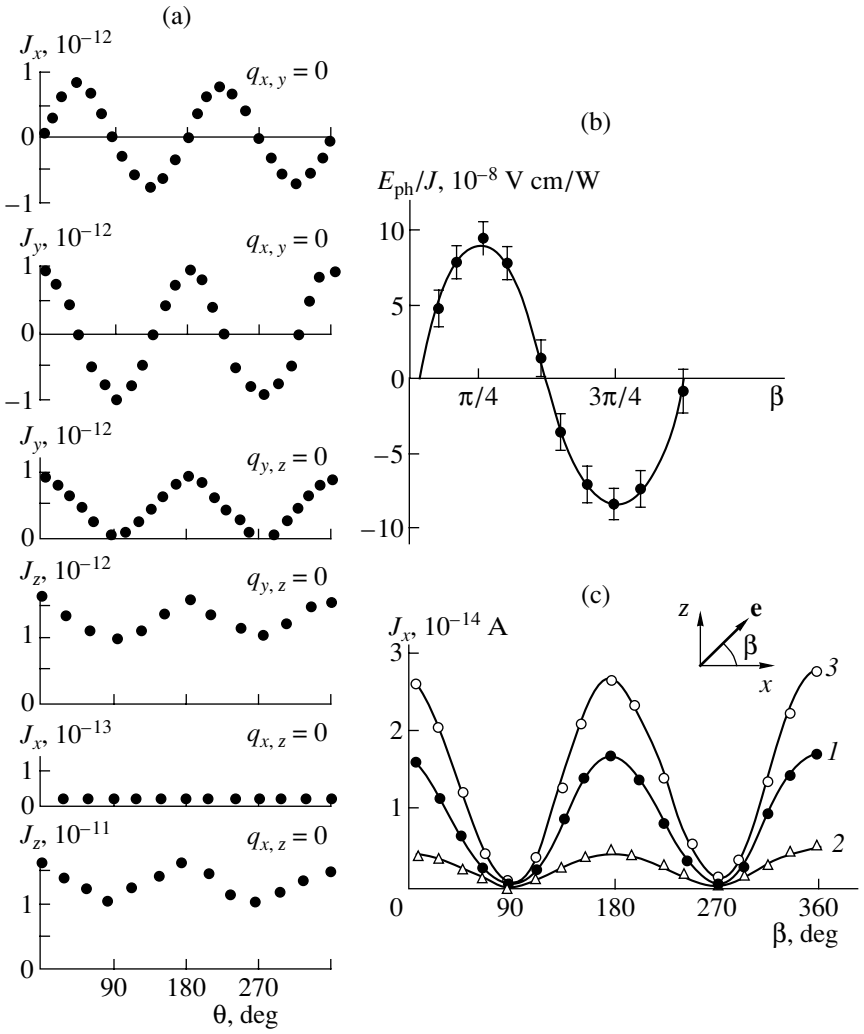

Fig. 6. Angular dependences of the bulk photovoltaic current in (a) $LiNbO_3$: Fe; (b) *p*-GaAs; and (c) quartz crystals.

effect is observed only in polarized light. All these symmetric characteristics follow from Eq. (1). In semiconductors with a high conductivity (GaAs), the bulk photovoltaic effect provides low voltages only slightly different from the band gap (2–3 V). However, in dielectric crystals with low darkconductivity and photoconductivity ($LiNbO_3$), the bulk photovoltaic effect provides rather intense fields. At higher light intensities in $LiNbO_3$: Fe, the electric fields attain the fields $\sim 10^4$ V cm^{-1}. In some cases, these fields are limited by the breakdown of the ambient air.

MAGNETOPHOTOVOLTAIC EFFECT IN NONCENTROSYMMETRIC CRYSTALS

The bulk photovoltaic current should give rise to an effect similar to the Hall effect. This conclusion can be drawn proceeding from high values of nonthermalized-carrier mobility. To observe this effect, referred to as the magnetophotovoltaic effect [1], one has to illumi-

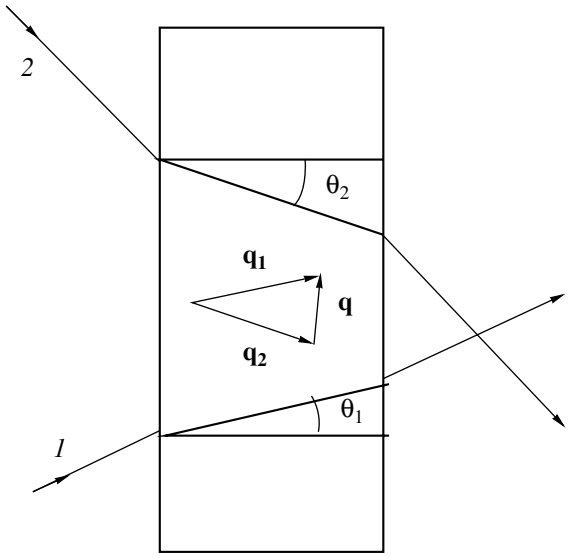

Fig. 7. Two-beam coupling in a photorefractive crystal.

Mobilities of thermalized and nonthermalized carriers

	μ_{th}, $cm^2\ V^{-1}\ s^{-1}$	μ_{nth}, $cm^2\ V^{-1}\ s^{-1}$
ZnS	10^{-2}	10^2
$LiNbO_3$: Fe	10^{-6}	10^3
$Bi_{12}SiO_{20}$	10^{-6}	10^2

nate piezoelectric or ferroelectric crystals with polarized light in a magnetic field (Fig. 5a). By analogy with Eq. (1), the magnetophotovoltaic current $J_i(\mathbf{B})$ can also be observed in both linearly and a circularly polarized light. Figure 5b shows the Hall current $J_x^H(\mathbf{B})$ in a cubic ZnS crystal (point symmetry $3/\bar{4}$) illuminated along [001] as a function of the polarization angle β for two directions of the magnetic field (see Fig. 5a). As is seen, the Hall component rigorously follows the angular dependence determined by the crystal symmetry. This experiment allows the determination of the mobility of nonthermalized carriers using the ratio of the component of the Hall current $J_x(\mathbf{B})$ to the photovoltaic current J_z,

$$\mu_{nth} = (1/B)J_x(\mathbf{B})/J_z. \quad (6)$$

The table lists the μ_{th} and μ_{nth} values for ZnS, $LiNbO_3$: Fe, and $Bi_{12}SiO_{21}$ crystals. The μ_{th} values determined from the conventional Hall effect or determined indirectly are taken from the related publications, whereas the μ_{nth} values are measured with the aid of the magnetophotovoltaic effect [1]. It is seen from the table that the mobility μ_{nth} of nonthermalized carriers exceeds the μ_{th} value be several orders of magnitude, which provides the experimental detection of the photovoltaic effect. In order words, the observation of the bulk photovoltaic effect is possible under two conditions—the use of a noncentrosymmetrical crystal and the excitation of nonthermalized states.

PHOTOREFRACTION AND PHOTOREFRACTIVE OPTICS

As was stated above, the low efficiency of the bulk photovoltaic effect makes the conversion of light energy into electric energy impossible. However, intense electric fields generated by crystals which manifest the bulk photovoltaic effect are used in photorefraction and photorefractive optics [2]. It should be indicated that the effect of photorefraction was observed several years before the discovery of the bulk photovoltaic effect. The use of KDP-based electrooptical modulators revealed their light-induced damages. It turned out that illumination of KDP crystals with light changed their birefringence. This effect was later called photorefraction, but it was interpreted only upon the discovery of the bulk photovoltaic effect [1]. The illumination of a piezoelectric or a ferroelectric crystal with applied disconnected electrodes generates the bulk photovoltaic current and the electric field (see Eq. (2)). Because of the linear electrooptical effect, this field changes birefringence. The photorefractive effect is stable because the field is induced by the charge-carriers captured by deep traps. The effect of photorefraction laid the basis for photorefractive optics and three-dimensional holography. At present, photorefractive optics is an independent scientific discipline. We consider here in brief only the principle it is based on.

Figure 7 shows a noncentrosymmetric crystal illuminated with two coherent polarized light beams (*1* and *2*) incident onto the crystal surface at a certain angle. The interference of these beams provides a sinusoidal distribution of the light intensity in the crystal bulk, whereas the bulk photovoltaic effect provides the formation of the corresponding photovoltage and birefringence distributions. The change of the refractive index gives rise to the formation of a phase grating the beam diffraction from it. Diffraction provides the energy transfer and redistribution between the beams. In turn, this creates new media for a three-dimensional phase holography, enhancement of the image contrast, improves filters, etc. However, one should not forget that the bulk photovoltaic effect is only one of the possible mechanisms of photorefraction. In some photorefractive crystals, other mechanisms of the charge transfer are possible, such as photoconductivity in external fields and diffusion.

REFERENCES

1. B. I. Sturman and V. M. Fridkin, *The Photovoltaic and Photorefractive Effects in Noncentrosymmetric Materials* (Gordon and Breach, Philadelphia, 1992).
2. *Photorefractive Materials and Their Applications*, Ed. by P. Günter and J.-P. Huignard (Springer-Verlag, Berlin, 1988), Vols. I, II.

Translated by T. Dmitrieva

Crystallography Reports, Vol. 46, No. 4, 2001, pp. 659–664. Translated from Kristallografiya, Vol. 46, No. 4, 2001, pp. 727–732.

PHYSICAL PROPERTIES OF CRYSTALS

Dedicated to the memory of B.K. Vainshtein

Domain Structure in $CsDSO_4$ Crystals

L. F. Kirpichnikova*, M. Polomska, and B. Hilczer****

** Shubnikov Institute of Crystallography, Russian Academy of Sciences, Leninskiĭ pr. 59, Moscow, 117333 Russia*
e-mail: Luba@ns.crys.ras.ru
*** Institute of Molecular Physics, Polish Academy of Sciences, Smoluchowskiego 17, 60-17 Poznan, Poland*

Received February 20, 2001

Abstract—A complex study of domain structure of $CsDSO_4$ crystals has been performed over a wide temperature range. The effect of internal and external stresses and the PO_4 impurity on the kinetics of domain growth is considered. The behavior of the domain structure of the $CsDSO_4$ crystals is compared with martensite phase transformations. A model of crystal-lattice transformations in various phases is suggested, including an intermediate phase with the unknown symmetry of $CsDSO_4$ crystals. © *2001 MAIK "Nauka/Interperiodica".*

According to [1–6], deuterated $CsDSO_4$ (CDS) crystals containing more than 50% of deuterium have an improper superprotonic–ferroelectric first-order phase transition, $I4_1/amd$–$P2_1/c$, at T_s = 412 K, which is accompanied by considerable spontaneous deformations. The unit-cell parameters of the superprotonic tetragonal phase are $a_1 = b_1$ = 5.729 Å and c_1 = 14.21 Å; the parameters of the monoclinic ferroelectric phase at room temperature are a_2 = 7.789 Å, b_2 = 8.146 Å, c_2 = 7.726 Å, β = 110.87°. The superprotonic phase transition can be observed in a 10- to 20-nm-thick subsurface layer at 395 K, i.e., 17 K below T_s [7]. The optical–polarization studies of the domain structure in CDS [8–11] shows that the transition into a superprotonic phase during heating occurs at $T_s\uparrow$ = 421 K, whereas during subsequent cooling, it occurs at $T_s\downarrow$ = 417 K. It was also revealed that a new domain structure is formed at the temperature 3–4 K below $T_s\uparrow\downarrow$. A considerable change in the domain structure is observed during an increase and decrease of the temperature with a thermal hysteresis ΔT = 7 K. At a temperature 3 K lower than T_s, the conductivity starts gradually increasing by 1.5–2.0 orders of magnitude, and the transition into the superprotonic phase is accompanied by an additional abrupt increase in conductivity by two orders of magnitude [8]. Crystallographic modeling of the (100) domain wall on the (001)-cut shows that considerable displacements of Cs atoms (up to 2.5 Å) and the rotation of SO_4 tetrahedra occur, in fact, at a temperature 3 K lower than the temperature of the superprotonic transition [10]. The changes in domain pattern observed below T_s are consistent with the anomalous behavior of the thermal expansion coefficients in the vicinity of T_s [11]. With an increase of the temperature, a gradual linear decrease of thermal expansion coefficient on the (001)-cut is observed, and at a temperature 3 K lower than T_s, the thermal expansion coefficient goes to zero. Then, at $T_s\uparrow$, it increase in a jumpwise manner from zero to 10^{-4} K^{-1}. It was assumed that there exists an intermediate ferroelastic phase in the vicinity of T_s and a hypothetical intermediate cubic phase–prototype [12]. This idea is consistent with the data of the group-theoretic analysis [13–15]. The tables [13] describing various sequences of possible ferroelastic phase transitions do not indicate the ferroelectric phase transition $I4_1/amd$ (D_{4h}^{19})–$P2_1/c$ (C_{2h}^5). The theoretical consideration of the symmetries of phases formed in $CsHSO_4$ and $CsDSO_4$ crystals under high pressures and their possible changes during condensation of various components of an order parameter was made in [14, 15].

The present study was undertaken for further study of the domain structure of CDS crystals and generalization and systematization of the observed changes, which would provide the better understanding of the processes occurring in the vicinity of the phase transition and accompanied by disappearance of a spontaneous deformation and appearance of a considerable conductivity.

EXPERIMENTAL

The optical studies of the domain structure in CDS crystals were performed in polarized light with the aid of a VTO 232 M1 videosystem over a wide temperature range. The samples were placed onto a THMS 600 heating stage. The precise control, programmed change, and stabilization of the temperature were made

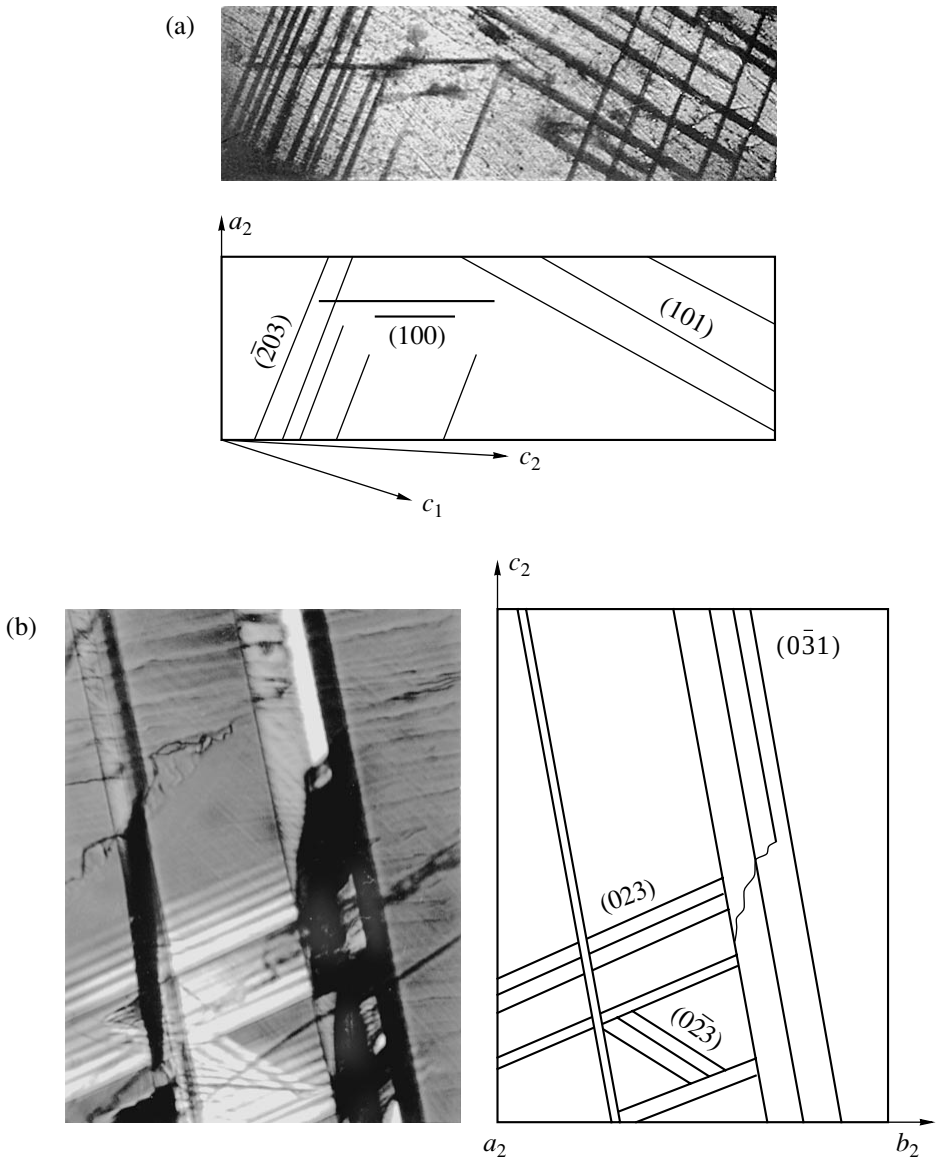

Fig. 1. Photographs and schematic drawing of the domain structure induced by external stresses in a CDS crystal at room temperature on the (a) (010)-cut; (b) (100) cleavage; a_2, b_2, c_2 are the crystallographic axes of the monoclinic $P2_1/c$ phase, c_1 is the axis of the tetragonal phase, $I4_1/amd$.

with the aid of a TMS91 system (LINKAM, UK). The changes in domain structure were recorded onto a video cassette, visualized on a TV screen, and also photographed. The temperature was controlled within an accuracy of 0.01 K.

EXPERIMENTAL RESULTS

The as-grown CDS crystals are usually in the single-domain state. The domain structure at room temperature can be formed by applying an external mechanical stress. The compression applied to the (010)-cut results in the appearance of inclined domains with the $(\bar{2}03)$ and (101) walls and cracks along the (100) cleavage plane (Fig. 1a). The mechanical factors applied to the (001)-cut provide the formation of (100)-type domain walls. The external stress applied to the (100) cleavage gives rise to the formation of bright colored (023), $(0\bar{2}3)$, and $(0\bar{3}1)$ domains. With an increase of the applied stress, the latter domains first slightly widen and they are "stabilized" by the cracks appearing near domains (Fig. 1b). Thin domains caused by the comparatively low stresses disappear upon their removal or become "annealed" similar to defects with an increase of the temperature.

A domain structure spontaneously appears on a single-domain (010)-cut during heating at the temperature $T_s\uparrow$–3 K (Fig. 2a) and, during cooling, upon passing the

superprotonic phase at $T_s\downarrow$ (Fig. 2b). The orientation of domains formed in the vicinity of T_s differs from those formed at room temperature by 15°–20°. It is clearly seen that some domains form angles equal to 30° or 60°. The width of the domains formed in the intermediate phase remains almost constant; the change in temperature is accompanied by formation of new smaller domains.

The introduction to crystals of 5 mol % of PO_4 impurity results in a fast increase of the domain width in the intermediate phase (contrary to their in "pure" crystals) with an increase of the temperature. The impurity distorts and "weakens" the crystal lattice and reduces the coercive stress of a crystal and favors the appearance of a possible side motion of domain walls under the action of the internal stresses. The increase of PO_4 content up to 10 mol % results in the gradual disappearance of the intermediate phase.

If a sufficient number of the $(\bar{2}03)$ and (101) domains are formed under the effect of an external stress on the (010)-cut of CDS crystal at room temperature, then an increase of temperature gives rise to the formation of bright color stripes at 418 K indicating the appearance of high internal stresses. As is seen from Fig. 3, the domain walls formed at room temperature become thin in the intermediate phase and disappear against the background of the constantly varying strained state of the sample. The domain structure formed at room temperature seems to be related to a pronounced deformations of crystal lattice. This causes large internal stresses in the intermediate phase, hinders the rearrangement of the crystal lattice and the appearance of new domains, and also distorts the pattern of the phase transitions.

As was shown in [8], the first cycle of the temperature change does not provide the domain formation on the (100)-cut in the intermediate phase during heating; one observes only the movement of the phase front at 418 K; however, by lowering the temperature to T_s from the superprotonic phase at $T_s\downarrow$, the domains appear. If the temperature increases only up to 420 K (1 K lower than $T_s\uparrow$) (not entering the range of the superprotonic phase) and starts cooling the sample, the domains reappear (Fig. 4a). It should be indicated that the domains are formed very quickly, almost instantaneously. With the change in the temperature, smaller domains are formed, which results in twinning; and the domains almost stop growing in width (Fig. 4b). The wedgelike shape of the twins indicates the presence of high internal stresses in the vicinity of domains. If lowering the temperature is stopped, the twinning process decays, but the further temperature reduction provides the formation of new smaller domains. At 411 K, the movement of the second phase front is observed, which indicates the first-order transition from the intermediate ferroelectric phase to the ferroelectric phase existing down to liquid nitrogen temperatures. After the passage of the second phase front (at $T_s\downarrow - 3$ K), the bright sample color disappears; it becomes gray and turbid (Fig. 4c). At room temperature, the sample has, along with transparent areas, some opaque areas of decomposed subsurface layer (which can readily be polished off) and the traces of the "frozen" domains of the intermediate phase remaining as the defect areas. It seems that the mobility of interphase boundary of the second-phase front is high in comparison with the mobility of domain walls, so that after the completion of the phase transition, the low-temperature phase still preserves the "frozen" areas of domain structure of the intermediate

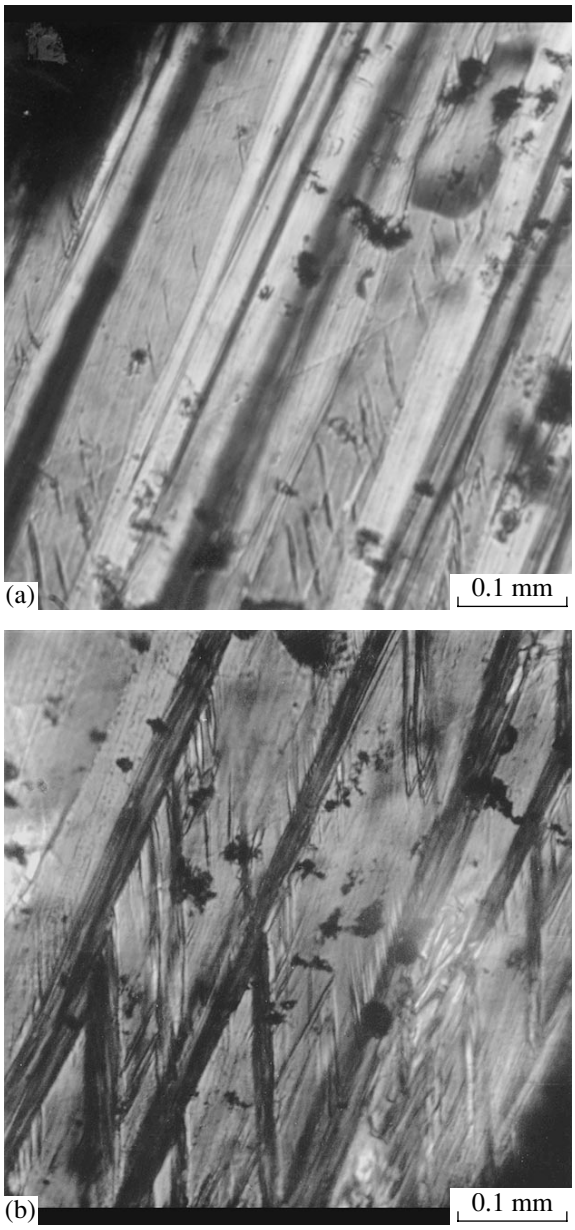

Fig. 2. Photographs of the domain structure formed in a single-domain sample on the (010)-cut of the intermediate phase in a CDS crystal: (a) during heating; (b) during cooling after passing the superprotonic phase.

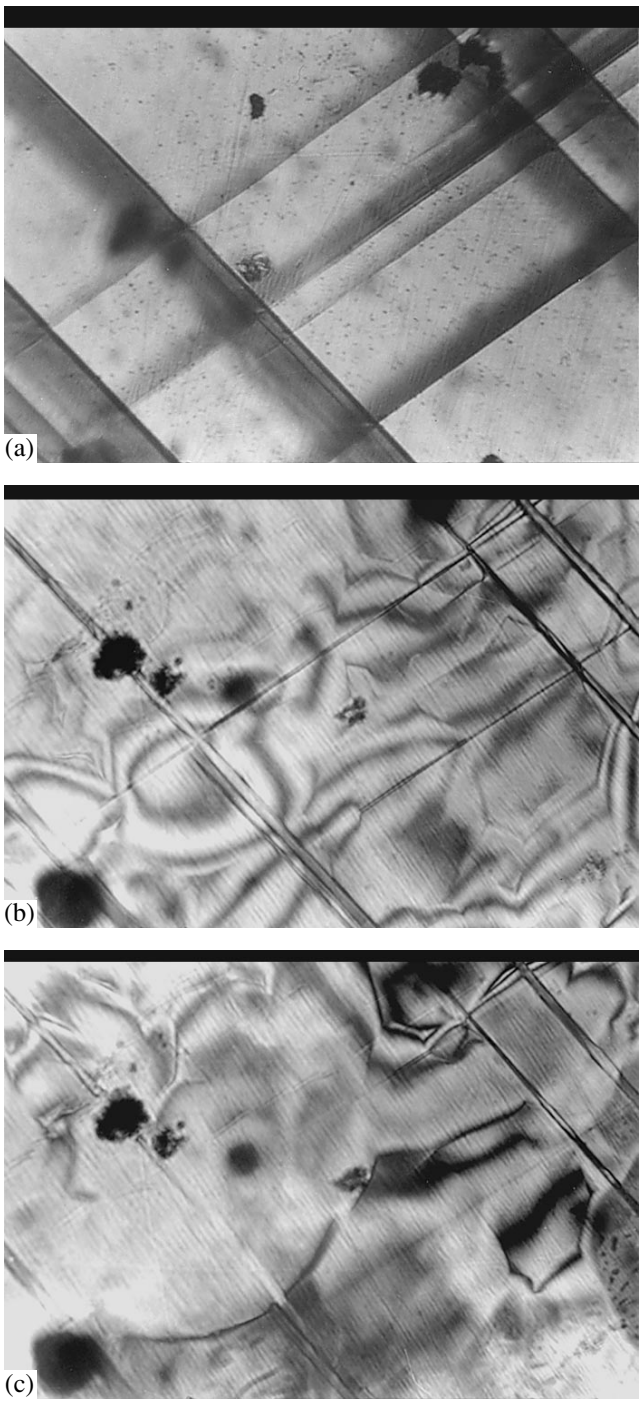

Fig. 3. The changes in the (010)-cut of a CDS crystal with the (203) and (101) domains formed by the external mechanical stresses at room temperature at different temperatures: (a) 300; (b) 418; (c) 419 K.

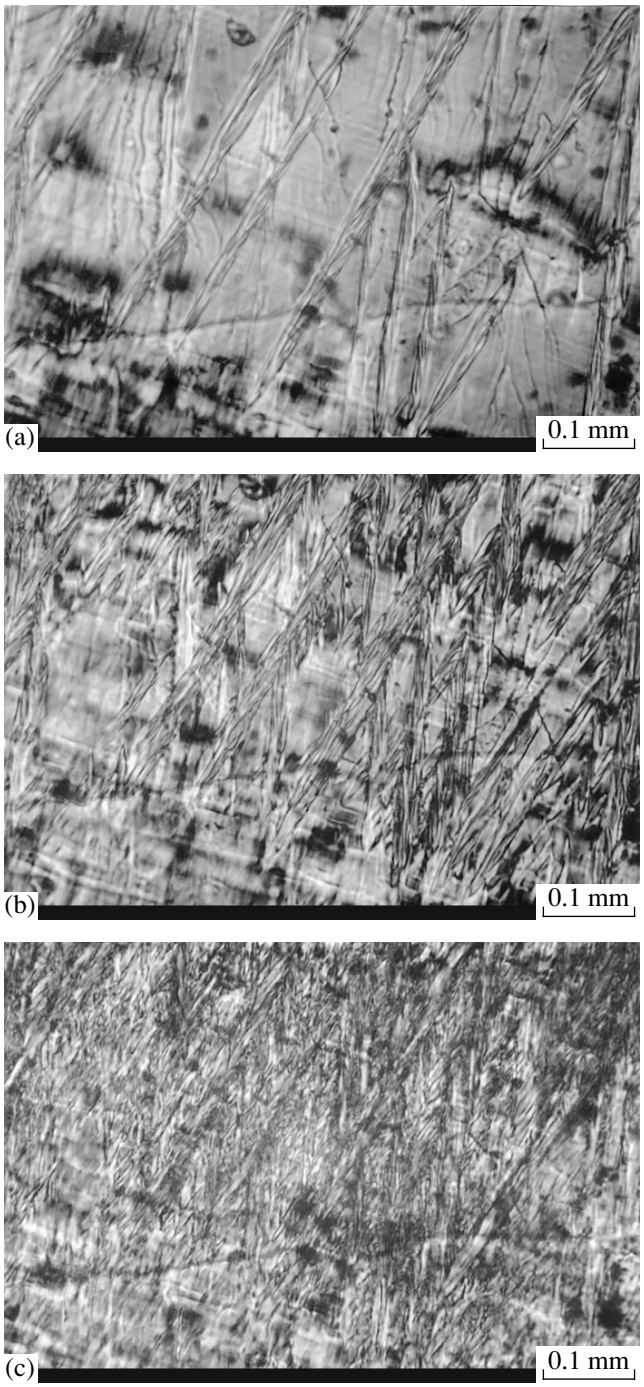

Fig. 4. Photographs of the domain structure on the (100)-cut of a CDS crystal formed in the intermediate phase during cooling at different temperatures: (a) 417; (b) 416; (c) 414 K.

phase corresponding, to a certain extent, to the equilibrium structure formed at $T_s - 3$ K. Applying a mechanical stress, one can obtain a new domain typical of the monoclinic ferroelectric phase existing at room temperature near the "frozen" domain (Fig. 5). The orientations of these domains differ by 15°–20°. A multiple heating–cooling cycle in the vicinity of a superprotonic phase transition provides the formation of additional defects in a crystal, intensifies the internal stresses, smears the pattern of transitions and the changes in the domain structure, and increases the time necessary for domain restructuring.

DISCUSSION AND CONCLUSIONS

The analysis of the domain structure, its changes, the corresponding X-ray data [2–4, 11] and theoretical studies [14] led us to the model of possible changes in the crystal lattice of CDS crystals in phase transitions in the vicinity of T_s (Fig. 6). At room temperature, a CDS crystal is in the monoclinic phase, $P2_1/c$, with coordinate axes a_2, b_2, c_2. At T_s – 3 K, the crystal undergoes the transition into the intermediate phase, with the axes being parallel to the diagonal of the (001) face of the monoclinic cell. The unit cell of the intermediate phase (a_{int}, b_{int}, c_{int}) is shown by the dotted line in Fig. 1. At T_s, the transition into the tetragonal phase (a_1, b_1, c_1) takes place. We assume that if the directions of the a_{int}, b_{int}, and c_{int} axes coincide with the directions of the a_1, b_1, c_1 axes, the intermediate phase is most probably orthorhombic or, possibly, tetragonal (depending on the ratio of the lattice parameters). If these axes do not coincide, the intermediate phase is monoclinic. Unfortunately, the X-ray studies still cannot answer the question about the intermediate-phase symmetry because of complications in measuring the crystal with constantly varying domain structure in the narrow temperature range of intermediate-phase existence. A number of possible orientational states in CDS crystals, the domain shapes, and the angular correlation between them, the crystallographic features, and the domain indices (at room temperature) point to the existence of a threefold axis in a prototype phase. Taking into consideration the tetragonal symmetry of the superprotonic phase, all these facts favor the cubic symmetry of the prototype phase. The crystallographic axes (a_c, b_c, c_c) of the hypothetical cubic phase are parallel to the diagonals in the (001) face of the tetragonal crystal.

The measurements of the electrical properties [16] showed that the resistance of the crystal at room temperature is $(4–5) \times 10^6$ Ω; the resistance of the superprotonic phase, about 60 Ω; and that of the intermediate phase, $(5–6) \times 10^3$ Ω. The activation energy of the superprotonic phase is 0.29–0.33 and that of the intermediate phase, 0.77 eV. Thus, the number of free charge carriers in the intermediate phase is small, but they seem to be "blocked." Since the barriers are low, they can easily move. The intermediate phase can hardly be called superprotonic; rather, it can be regarded as a certain intermediate state.

The domain structure in the intermediate phase spontaneously formed under the action of internal stresses reminds the domain structure induced by the external mechanical stresses at room temperature but rotated by 15°–20°. The indexing of intermediate-phase domains is hindered because of the unknown unit-cell parameters of this phase. The narrow temperature range of intermediate-phase existence and varying number and shape of domains hinder the X-ray studies in this range.

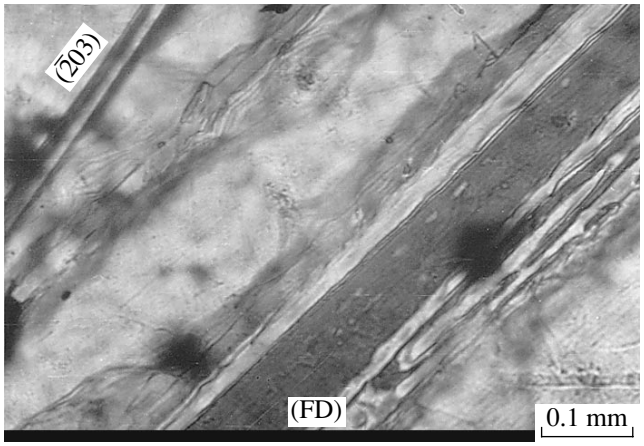

Fig. 5. Photograph of the (010)-cut of a CDS crystal with a "frozen" domain (FD) structure formed in the intermediate phase and the (203) domain induced by mechanical stresses upon thermal tests.

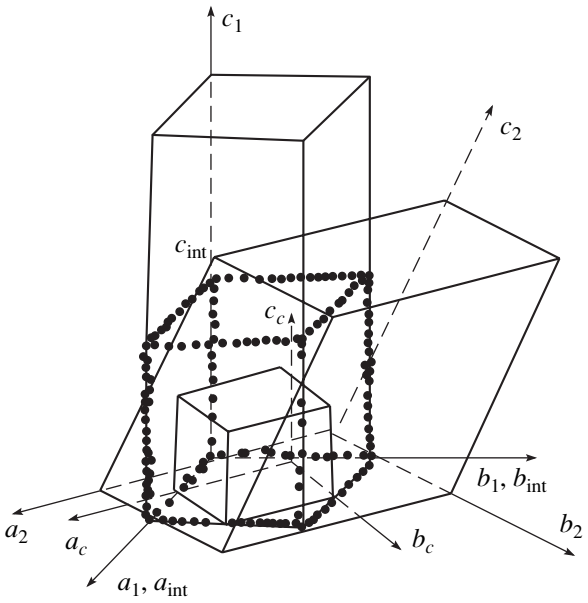

Fig. 6. A model of possible changes in the crystal lattice in a CDS crystal occurring in phase transitions from the low-temperature ferroelastic monoclinic phase (crystallographic axes a_2, b_2, c_2) to the tetragonal phase (axes a_1, b_1, c_1) via the intermediate phase (dotted line); a_c, b_c, c_c are the directions of crystallographic axes of the hypothetical prototype cubic phase.

The internal stresses, impurities, and regions with defects modify the processes occurring in the vicinity of superprotonic phase. Thus, the domain structure of the intermediate phase can be studied only on high-quality crystals.

The ferroelastic phase transition in CDS crystals is associated with the pronounced spontaneous deformation comparable with the spontaneous deformations observed in martensite transformations. The formation

of characteristic triangular domains, the reversibility of twinning, and the character of the variations in the domain structure with temperature are similar to the behavior of the domain structure in martensite transformations. In both cases, the first-order transition takes place, which is accompanied by the thermal hysteresis, the reversibility of the martensite transformation, and the phase-front motion. In both CDS crystals and in martensite transformations, twinning is interpreted with the invocation of the cubic phase-prototype (real or hypothetical), which determines a specific triangular shape of the domain structure. The considerable spontaneous deformation in CDS crystals, the rotation of the crystal lattice in twinning, the internal stresses in the vicinity of domains, and the features of the phase-transition kinetics result in the formation of supercooled region of existence of the high-temperature intermediate phase. The decisive role in the formation of domain structure and domain switching in ferroelastics is played by the elastic energy of the crystals in the field of external and internal stresses and the surface energy of domain walls. The "martensite features" observed in ferroelastic phase transitions are understandable—all these features should be inherent in all the transformations caused by spontaneous deformation.

ACKNOWLEDGMENTS

This study was supported by the Russian Foundation for Basic Research, project no. 00-12-17095-a and the Committee of Scientific Studies, project no. 2 P03 B024.

REFERENCES

1. A. I. Baranov, L. A. Shuvalov, and N. M. Shchagina, Kristallografiya **29** (6), 1203 (1984) [Sov. Phys. Crystallogr. **29**, 706 (1984)].
2. R. A. Dilanyan, V. Sh. Shekhtman, A. I. Baranov, *et al.*, Fiz. Tverd. Tela (Leningrad) **26** (2), 587 (1986) [Sov. Phys. Solid State **28**, 328 (1986)].
3. B. V. Merinov, A. I. Baranov, B. A. Maksimov, *et al.*, Kristallografiya **31** (3), 450 (1986) [Sov. Phys. Crystallogr. **31**, 264 (1986)].
4. B. V. Merinov, A. I. Baranov, and L. A. Shuvalov, Kristallografiya **32** (1), 86 (1987) [Sov. Phys. Crystallogr. **32**, 47 (1987)].
5. A. I. Baranov, Izv. Akad. Nauk SSSR, Ser. Fiz. **51** (12), 2146 (1987).
6. Ph. Colomban, M. Pham-thi, and A. Novak, Solid State Ionics **2**, 125 (1986).
7. A. V. Belushkin, M. A. Adams, S. Hull, *et al.*, Solid State Ionics **77**, 91 (1995).
8. L. F. Kirpichnikova, M. Polomska, Ya. I. Volyak, *et al.*, Pis'ma Zh. Éksp. Teor. Fiz. **55**, 297 (1996) [JETP Lett. **63**, 912 (1996)].
9. L. Kirpichnikova, B. Hilczer, M. Polomska, *et al.*, Ferroelectrics **190**, 7 (1997).
10. L. Kirpichnikova, B. Hilczer, M. Polomska, *et al.*, J. Korean Phys. Soc. **32**, S796 (1998).
11. R. A. Dilanyan and V. Sh. Shekhtman, Fiz. Tverd. Tela (Leningrad) **29** (12), 3577 (1987) [Sov. Phys. Solid State **29**, 2049 (1987)].
12. L. Kirpichnikova, M. Polomska, and B. Hilczer, Ferroelectrics **221**, 85 (1999).
13. J. C. Toledano and P. Toledano, Phys. Rev. B **21**, 1139 (1980).
14. V. S. Shakhmatov, Kristallografiya **36** (4), 1021 (1991) [Sov. Phys. Crystallogr. **36**, 575 (1991)].
15. V. S. Shakhmatov, Kristallografiya **38** (6), 176 (1993) [Crystallogr. Rep. **38**, 805 (1993)].
16. L. Kirpichnikova, A. Pawlowski, M. Polomska, and B. Hilczer, Solid State Ionics **125**, 171 (1999).

Translated by A. Zalesskiĭ

Crystallography Reports, Vol. 46, No. 4, 2001, pp. 665–672. Translated from Kristallografiya, Vol. 46, No. 4, 2001, pp. 733–741.

Dedicated to the memory of B.K. Vainshtein

Optical and Nonlinear Laser Properties of the $\chi^{(3)}$-Active Monoclinic α-$KY(WO_4)_2$ Crystals

A. A. Kaminskii*, A. F. Konstantinova*, V. P. Orekhova*, A. V. Butashin*, R. F. Klevtsova, and A. A. Pavlyuk****

** Shubnikov Institute of Crystallography, Russian Academy of Sciences, Leninskiĭ pr. 59, Moscow, 117333 Russia*

e-mail: afkonst@usa.net

*** Institute of Inorganic Chemistry, Siberian Division, Russian Academy of Sciences, pr. Akademika Lavrent'eva 3, Novosibirsk, 630090 Russia*

Received February 16, 2001

Abstract—Monoclinic α-$KRE(WO_4)_2$ crystals are grown. Their structure is described in two crystallographic settings. The principal refractive indices are determined and the coefficients and characteristic wavelengths are used for calculating refractive indices by the Selmeyer formulas. The data on the anisotropic parametric Raman generation in these crystals under the picosecond pumping are discussed. *© 2001 MAIK "Nauka/Interperiodica".*

INTRODUCTION

The family of lasing monoclinic tungstates α-$KRE(WO_4)_2$ (RE = Y and Ln) crystals activated by trivalent lanthanide ions Ln^{3+} was discovered at the Shubnikov Institute of Crystallography (Moscow) and the Institute of Inorganic Chemistry (Novosibirsk) more than thirty years ago [1].

Since that time, the stimulated radiation emission in these crystals has been obtained for a large number of intermultiplet $4f^N$–$4f^N$ channels of lanthanide ions within a wide wavelength range. Currently, the set of these crystals and activator Ln^{3+} ions is rather large and is intensely increasing. The generalized diagram of the laser generation channels in Pr^{3+}, Nd^{3+}, Dy^{3+}, Ho^{3+}, Er^{3+}, Tm^{3+}, Yb^{3+} in some α-$KRE(WO_4)_2$ crystal matrices is presented in Fig. 1 [2–16].[1] In the near-infrared (IR) range, the laser generation was observed at wavelengths from 0.85 to 2.9 μm and in the optical range at the wavelengths 0.57 and 0.66 μm for $^4F_{9/2} \longrightarrow {}^6H_{13/2}$ and $^4F_{9/2} \longrightarrow {}^6H_{11/2}$ channels of Dy^{3+} ions (the result of the most recent studies [16]). The α-$KRE(WO_4)_2$ tungstates also exhibit a pronounced optical cubic nonlinearity [17–25] and can be used in various devices based on the effect of stimulated Raman scattering.

Despite promising properties of these crystals for various applications, their characterization is far from exhaustive. Thus, there are no data on their refractive indices, one of the most important optical characteristics of crystals. In the present study, we determined the dispersion of refractive indices of one representative of the tungstate family, namely, α-$KY(WO_4)_2$ and also obtained new data on the parametric Raman generation under the picosecond pumping for this crystal. We also considered the structure of α-$KY(WO_4)_2$ crystals, since it was described in two different crystallographic settings, which gave rise to a number of inconsistencies in the interpretation of the optical and lasing properties of these crystals.

GROWTH OF α-$KY(WO_4)_2$ CRYSTALS

The $KY(WO_4)_2$ compound congruently melts at 1080°C and has a layered structure similar to that of the orthorhombic $KY(MoO_4)_2$ crystal. At 1010°C, the crystal undergoes the polymorphous structural transformation into the monoclinic α-$KY(WO_4)_2$ phase [26]. The monoclinic α-$KY(WO_4)_2$ crystals cannot be grown from the stoichiometric melt by the conventional Czochralski technique because of the complete decomposition of single crystals upon the above polymorphous transformation. Therefore, the crystals were grown by the low-gradient Czochralski technique from the potassium ditungstate ($K_2W_2O_7$) flux [27] in a setup with the two-zone heater under the precision temperature control (±0.1°C). To maintain the necessary supersatura-

[1] The first study on the laser generation of Yb^{3+} ions in the α-$KY(WO_4)_2$ and α-$KGd(WO_4)_2$ crystals was reported by A.A. Kaminskii at the International Symposium Modern Problems in Laser Physics in Novosibirsk in September 1996 and, as a remark, at the International Conference "Euro/CLEO-97" in Hamburg in 1997 (see also [13]).

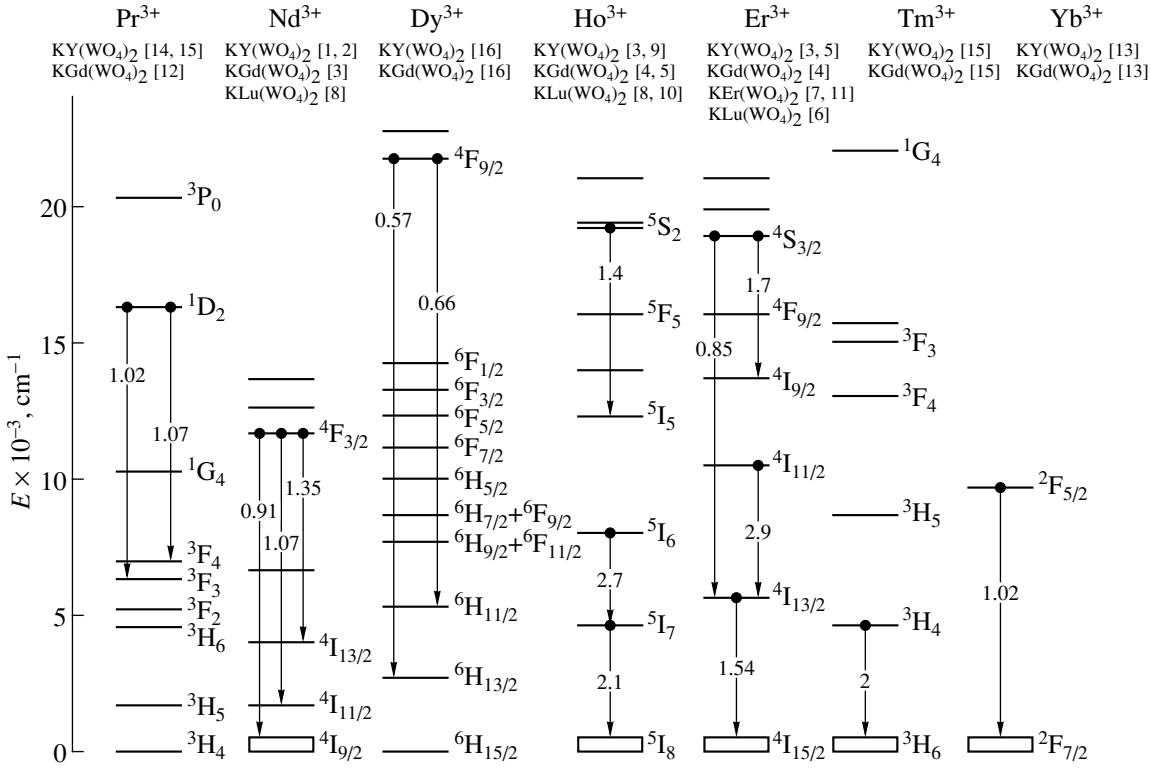

Fig. 1. Laser $4f^N$–$4f^N$ transitions for Ln^{3+} ions in monoclinic α-$KRE(WO_4)_2$ crystals (the generation wavelength ranges are indicated in μm).

tion in the flux, it was continuously cooled by the paired analog temperature controllers ZTA-1 according to the solubility curves for $KY(WO_4)_2$ in potassium ditungstate using the special program. The crystals were pulled along the twofold axis at the rate of about 0.2 mm/h; the seed was rotated at a velocity of 50–90 rev/min in the low-gradient temperature field (0.5–1 deg/cm). The habit of the α-$KY(WO_4)_2$ crystals thus grown with the volume of up to 50 cm^3 is formed mainly by the {100}, {010}, and {001} pinacoidal and {110} and {011} prismatic faces. Some physical characteristics α-$KY(WO_4)_2$ crystals are indicated in Table 1 and can be found in [28].

Table 1. Some physical characteristics of an α-$KY(WO_4)_2$ crystal

Melting point	~1080°C
Density	6.565 g cm^{-3}
Specific heat	~500 J kg^{-1} deg^{-1}
hermal conductivity	~0.03 W cm^{-1} deg^{-1}
Thermal expansion	~4.6×10^{-6} deg^{-1}
Microhardness on the Mohs scale	4–5
Optical transparency*	~0.34–5.5 μm
Band gap	~3.83 eV
Thermooptical coefficient *dn*/*dT*	~0.4×10^{-6} deg^{-1}

* Optical transparency for a 1-mm-thick sample.

THE CRYSTAL STRUCTURE OF α-$KY(WO_4)_2$

The structure of a α-$KY(WO_4)_2$ crystal, which belongs to the centrosymmetric class 2/*m* of the monoclinic sp. gr. C_{2h}^6, $Z = 4$ (for the *C*2/c crystallographic setting), was described in [29]. This space group has two crystallographic settings (*I*2/*c* and *C*2/*c*); therefore, we present the monoclinic unit-cell parameters in both *I* and *C* settings in Table 2. Since the unit cell in the *I* setting better corresponds to the crystal habit, the further consideration is made for this setting. The basis vectors (**a**, **b**, **c**) and ($\mathbf{a}_1$, $\mathbf{b}_1$, $\mathbf{c}_1$) in *I* and *C* settings of the monoclinic unit cell of the α-$KY(WO_4)_2$ structure and

Table 2. X-ray characteristics of an α-$KY(WO_4)_2$ crystal in two settings

Crystal setting	*I*2/*c*	*C*2/*c*
Unit-cell parameters (Å)	$a = 8.05$	$a_1 = 10.64$
	$b = 10.35$	$b_1 = 10.35$
	$c = 7.54$	$c_1 = 7.54$
Monoclinicity angle (deg)	$\beta = 94$	$\beta_1 = 130.5$

the corresponding atomic coordinates (x, y, z) and (x_1, y_1, z_1) are related in the following way:

$$\mathbf{a}_1 = \mathbf{a} + \mathbf{c}, \quad \mathbf{b}_1 = -\mathbf{b}, \quad \mathbf{c}_1 = -\mathbf{c},$$

$$\begin{bmatrix} x \\ y \\ z \end{bmatrix} = \begin{bmatrix} 1 & 0 & 0 \\ 0 & -1 & 0 \\ 1 & 0 & -1 \end{bmatrix} \begin{bmatrix} x_1 \\ y_1 \\ z_1 \end{bmatrix}. \quad (1)$$

The atomic coordinates and interatomic distances of the α-KY$(WO_4)_2$ structure for both settings are listed in Tables 3 and 4.

In the α-KY$(WO_4)_2$ structure (Fig. 3), the oxygen and the tungsten atoms occupy the general positions having no symmetry elements (C_1), whereas the Y and K atoms are located on twofold rotation axes (C_2). Oxygen atoms form three types of polyhedra: a distorted octahedron around the W atom, polyhedra with eight vertices around the Y atoms, and polyhedra with twelve vertices around the K atoms (Fig. 3b). The structure has a doubled band formed by W octahedra along the *c*-axis. The W–O distances in the octahedron are not equivalent and form the groups 4 + 1 + 1 or 5 + 1. However, considering the W atom as being coordinated with only the four or five nearest O atoms, we see that this W atom is located either almost on the edge of a rather distorted tetrahedron or lies almost in the plane of the square face of a tetragonal pyramid. Thus, the octahedral coordination of the W atom seems to be the most reasonable. The second large fragment of the structure is the band formed by *Y*-eight-vertex edge-sharing polyhedra parallel to the *a*-axis. The size of YO_8 polyhedra are consistent with the ionic radii of Y^{3+}. The three-dimensional framework of the α-KY$(WO_4)_2$ type structure is formed by two aforementioned vertex- and edge-sharing fragments of the structure arranged almost perpendicular to one another. The structure voids are filled with the large potassium atoms.

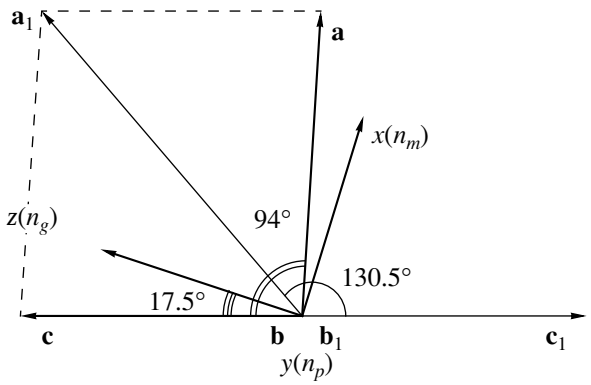

Fig. 2. The relation between basis vectors of the monoclinic unit cell in the α-KY$(WO_4)_2$ structure in the *I* (**a**, **b**, **c**) and *C* ($\mathbf{a}_1$, $\mathbf{b}_1$, $\mathbf{c}_1$) settings and the directions of principal axes (*x*, *y*, *z*) of the optical indicatrix (**b** is perpendicular to the figure plane and directed from the observer; $\mathbf{b}_1$ is directed toward the observer).

Table 3. Positions of basis atoms in the α-KY$(WO_4)_2$ structure in two settings

Crystal setting	*I*2/*c*			*C*2/*c*		
Atomic coordinate	*x*/*a*	*y*/*b*	*z*/*c*	x_1/a_1	y_1/b_1	z_1/c_1
W	0.1962	0	0.4603	0.1962	0	0.2359
Y	0.50	0.2275	0.75	0	0.2725	0.75
K	0.50	0.808	0.75	0	0.692	0.75
O_1	0.3727	0.080	0.552	0.122	0.580	0.174
O_2	0.0242	−0.108	0.053	0.029	0.108	0.976
O_3	0.2740	−0.158	0.398	0.222	0.342	0.120
O_4	0.1882	0.073	0.255	0.185	0.927	0.930

Table 4. Main interatomic distances in the α-KY$(WO_4)_2$ crystal structure

Octahedron WO_6		Polyhedron YO_8		Polyhedron KO_{12}	
W–O_1	1.78	Y–$O_1 \times 2$	2.31	K–$O_4 \times 2$	2.84
O_4	1.72	$O_2 \times 2$	2.28	$O_{4'} \times 2$	2.86
O_3	1.84	$O_3 \times 2$	2.31	$O_1 \times 2$	2.80
O_2	1.93	$O_{3'} \times 2$	2.71	$O_2 \times 2$	3.07
$O_{2'}$	2.14	⟨Y–O⟩	2.40	$O_3 \times 2$	3.12
$O_{4'}$	2.36			$O_{1'} \times 2$	3.31
⟨W–O⟩	1.96			⟨K–O⟩	3.00

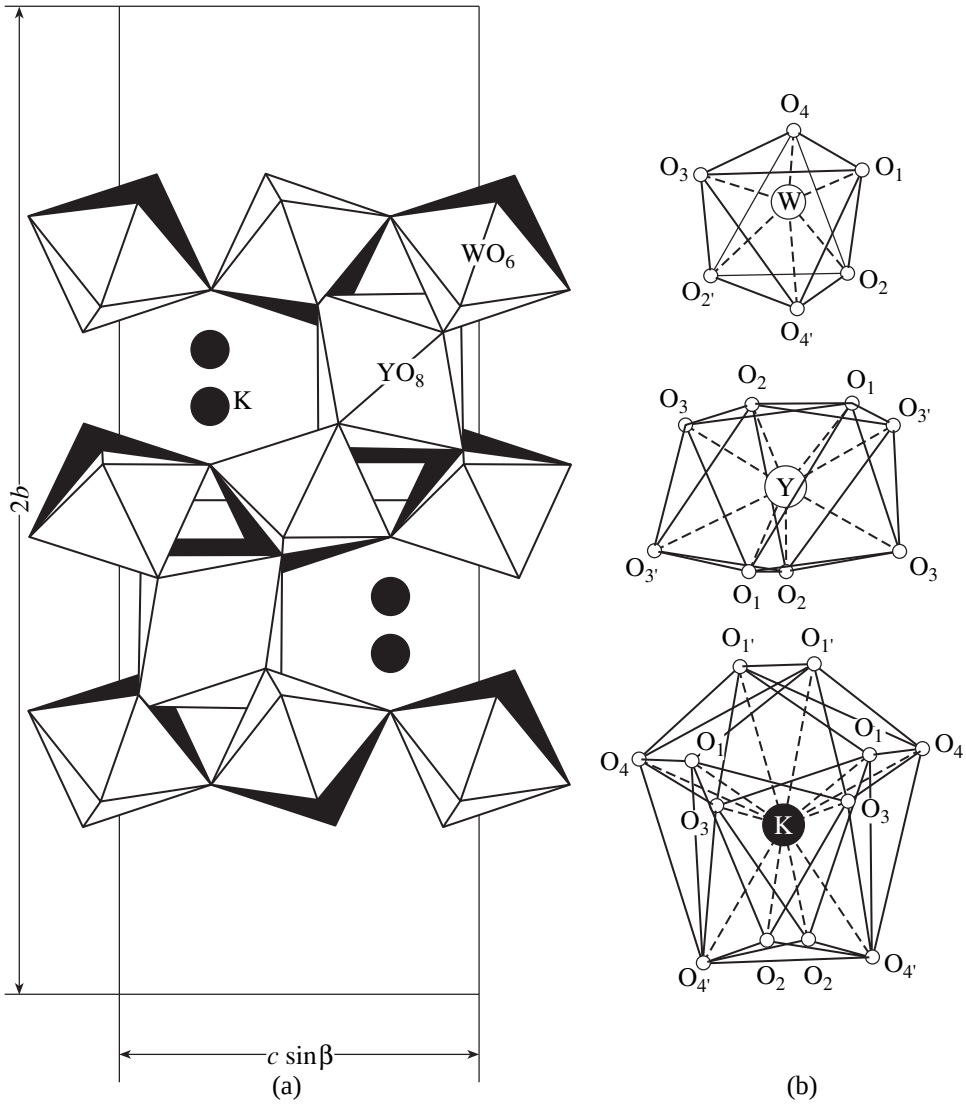

Fig. 3. The α-$KY(WO_4)_2$ crystal structure: (a) projection along the *a*-axis, the polyhedra of the next level are blackened; (b) the structures of WO_6, YO_8, and KO_{12} polyhedra, the metal–oxygen distances are shown by dashed lines (their values are indicated in Table 4).

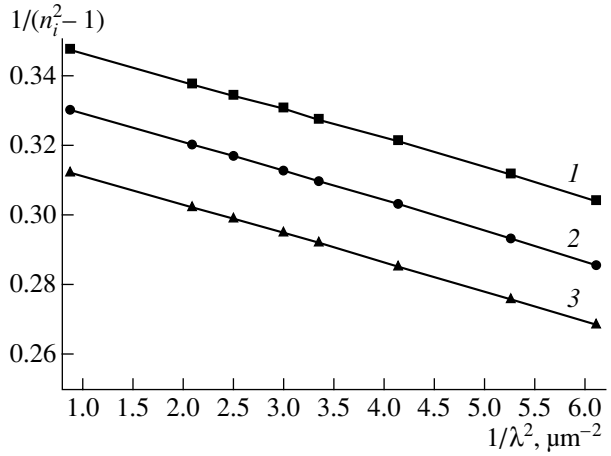

Fig. 4. $1/(n_i^2 - 1)$ versus $1/\lambda^2$ for an α-$KY(WO_4)_2$ crystal: (*1*) $1/(n_p^2 - 1)$; (*2*) $1/(n_m^2 - 1)$; (*3*) $1/(n_g^2 - 1)$.

REFRACTIVE INDICES OF A α-$KY(WO_4)_2$ CRYSTAL

The refractive indices of α-$KY(WO_4)_2$ crystals were measured by the technique of the least beam deviation within the wavelength range 0.405–1.064 μm on a GS-5 goniometer at room temperature [30]. Since the α-$KY(WO_4)_2$ crystal is biaxial, the measurements were made on specially prepared two prisms with refraction angles $\alpha_1 = 40.421°$ and $\alpha_2 = 40.218°$. The "refraction edges" of both prisms were parallel to the *y*-axis of the crystal indicatrix ($y \parallel b$), whereas the *yz* and *yx* symmetry planes of the indicatrix bisect the refraction angles formed by the polished faces of the corresponding prisms. The rotation angle of the optical indicatrix in the crystallographic axes of the *I* setting is determined as $\angle cz = 17.5° \pm 0.5°$ (see Fig. 2). The prism aperture equals 2 cm^2, the accuracy of the orientation is 0.5°.

Table 5. Principal refractive indices n_p, n_m, n_g and birefringence for an α-$KY(WO_4)_2$ crystal

Wavelength λ (μm)	n_p	n_m	n_g	$n_m - n_p$	$n_g - n_m$	$n_g - n_p$
0.405	2.0704	2.1217	2.1738	0.0513	0.0521	0.1034
0.436	2.0516	2.1003	2.1508	0.0487	0.0505	0.0992
0.491	2.0277	2.0738	2.1223	0.0461	0.0485	0.0946
0.546	2.0128	2.0568	2.1042	0.0440	0.0474	0.0914
0.579	2.0058	2.0491	2.0955	0.0433	0.0464	0.0897
0.633	1.9972	2.0392	2.0848	0.0420	0.0456	0.0876
0.691	1.9907	2.0312	2.0764	0.0405	0.0452	0.0857
1.064	1.9688	2.0065	2.0507	0.0377	0.0442	0.0819

The first prism was used to measure the refractive indices n_p and n_g; the second one, the refractive indices n_p and n_m.

The light sources were a PRK-4 mercury lamp and He–Ne (λ = 0.633 μm) and Nd lasers (λ = 1.064 μm). The measured refractive indices and birefringences are indicated in Table 5. The refractive indices were measured within the accuracy of ±0.0002 in the wavelength range 0.436–0.633 μm. At λ = 0.405 μm and λ = 1.064 μm, the measurement accuracy was lower: ±0.0008. The refractive indices n_p measured on both prisms coincided within ±0.0002, which demonstrates their accurate orientations of prisms.

All the refractive indices measured on the α-$KY(WO_4)_2$ crystals, including the mean refractive index $n_0 = (n_p + n_m + n_g)/3$, can be approximated by the single-term Selmeyer dispersion formula

$$n_i^2 - 1 = K_i\lambda^2/(\lambda^2 - \lambda_i^2), \quad (2)$$

where K_i and λ_i are the coefficients and the corresponding wavelengths for $i = p, m, g, 0$ and λ is the wavelength of the incident light. The plots of the functions $1/(n_i^2 - 1) = (\lambda^2 - \lambda_i^2)/K_i\lambda^2$ are presented in Fig. 4. All the functions are linear and, therefore, are well approximated by straight lines. The coefficients K_i and corresponding λ_i are indicated in Table 6. The axis of the optical indicatrix n_p coincides with y (i.e., it is parallel to crystallographic axis b); n_m coincides with x, and n_g, with z (Fig. 2). The angle between the optical axes lying in the yz plane is equal to 2β. The angle β is calculated by the equation

$$\tan\beta = [n_g^2(n_m^2 - n_p^2)/n_p^2(n_g^2 - n_m^2)]^{1/2}. \quad (3)$$

As a result, we find that β = 45.825° at λ = 0.405 μm, β = 44.949° at λ = 0.579 μm, and β = 43.598° at λ = 1.064 μm. Since, within the whole wavelength range, the angle β is close to 45°, the crystal is neither positive nor negative, and its optical properties are far from those characteristic of uniaxial crystals.

The refractive indices determined in this study are lower than those reported in [31] for the α-$KY(WO_4)_2$ crystals. In fact, the refractive indices in [31] were obtained by a less accurate method based on the transmission spectra of the polarized light on Er^{3+}-doped samples. Also, unlike the experiments in [31], the direction of crystal indicatrix n_p was parallel to crystallographic b-axis (b coincided with the twofold axis and the pulling direction during crystal growth).

ANISOTROPIC PARAMETRIC RAMAN GENERATION

The parametric Raman generation in α-$KY(WO_4)_2$ crystals was excited according the resonatorless single-pass scheme using picosecond pumping pulses of an $Y_3Al_5O_{12}$: Nd^{3+} laser at wavelengths of about 1.06 μm and 0.53 μm (second harmonic). The samples were prepared in the form of polished parallelepipeds with the dimensions about $10 \times 12 \times 25$ mm^3 and the longest edge being parallel to the b-axis (two other edges were almost parallel to the a- and c-axes). The experimental conditions were similar to those reported elsewhere [21]. The orientational spectra of the parametric Raman generation in the α-$KY(WO_4)_2$ crystal and the identification of the Stokes and anti-Stokes components are shown in Figs. 5 and 6, where the notation of the type $b(cc)b$ are used for the geometry of the experiment: the first and fourth characters denote the directions (crystallographic axes) of pumping-radiation propagation and the detection of the radiation emitted by the crystal,

Table 6. Calculated K_i and λ_I values in Eq. (2) for the principal refractive indices n_p, n_m, n_g and of mean refractive index n_0 for α-$KY(WO_4)_2$ crystal

n_i	K_i	λ_I, μm
n_p	2.8134935	0.1529056
n_m	2.9568303	0.1591855
n_g	3.1278346	0.161512
n_0	2.9660389	0.157844

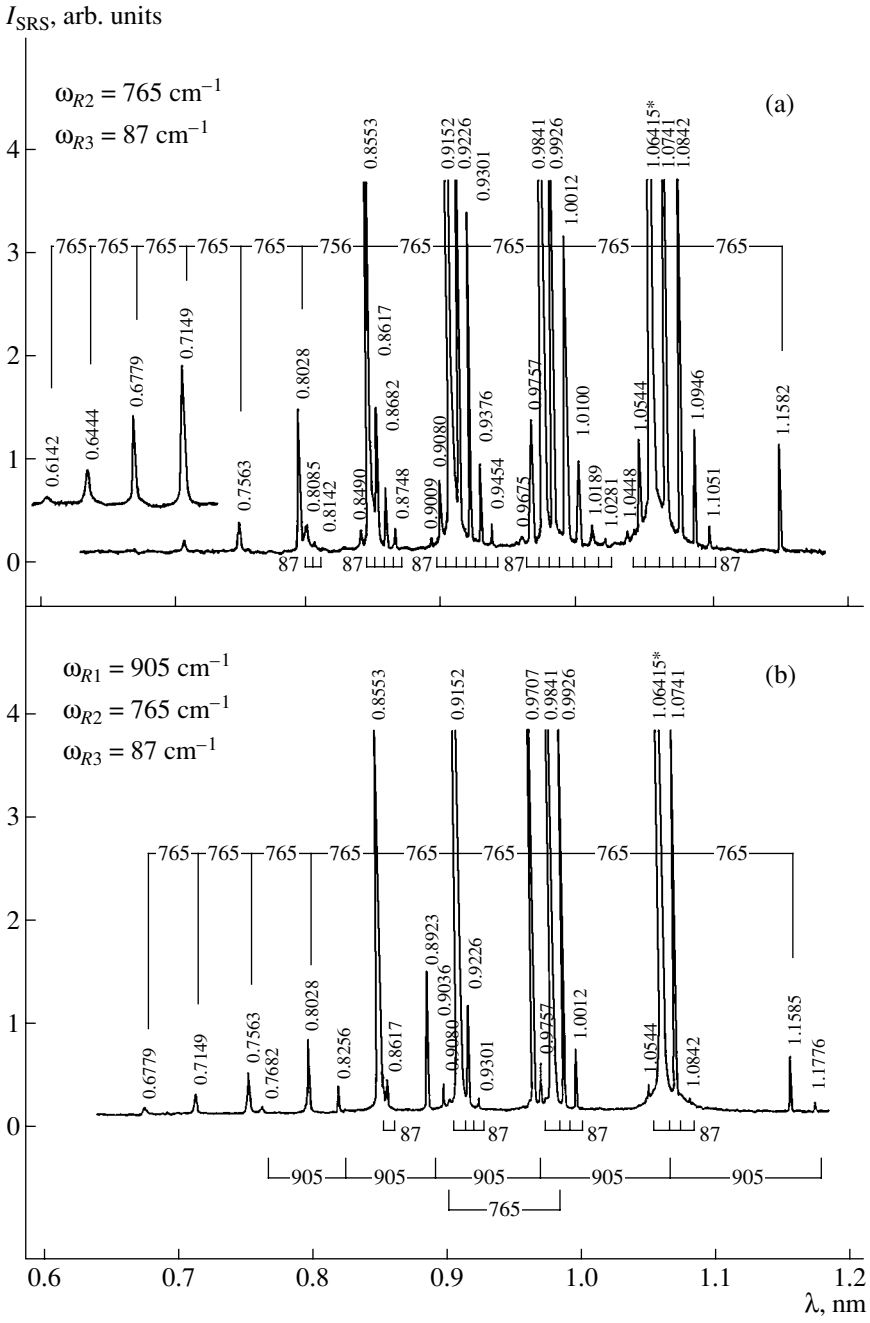

Fig. 5. The spectra of stimulated Raman scattering (SRS) for α-KY$(WO_4)_2$ at 300 K in the excitation geometry: (a) *a*(*cc*)*a*; (b) *b*(*cc*)*b* (the wavelengths are indicated in μm). The brackets below indicate the relation of SRS-active vibrational modes in the crystal to the Stokes and anti-Stokes emission lines, the corresponding energies are given in cm^{-1}. The asterisk marks the pumping wavelength.

respectively; the second and third characters correspond to the polarization of these radiations. SRS-active vibrational modes of the crystal have the energies ω_{R1} = 905, ω_{R2} = 765, and $\omega_{R3} \approx 87$ cm^{-1} and correspond to the most intense lines of the orientational spectra of spontaneous Raman scattering from the α-KY$(WO_4)_2$ crystal at 300 K. The value ω_{R1} = 905 cm^{-1} corresponds to the maximum energy of the optical phonons observed in the spectra. Under the same experimental conditions, we also determined the steady-state Raman gain coefficient for vibrational modes with ω_{R1} and ω_{R2}. Its maximum value for the first Stokes line is $g_{ssR} \approx 3.6$ cm g W^{-1} (because of the pronounced optical anisotropy of the crystal). In contrast to the $\chi^{(3)}$-nonlinear tungstate crystals with the scheelite ($CaWO_4$) structure, where the SRS-active modes are reliably related to the full-symmetry A_g vibrations of the isolated tetrahedral $[WO_4]^{2-}$ anions

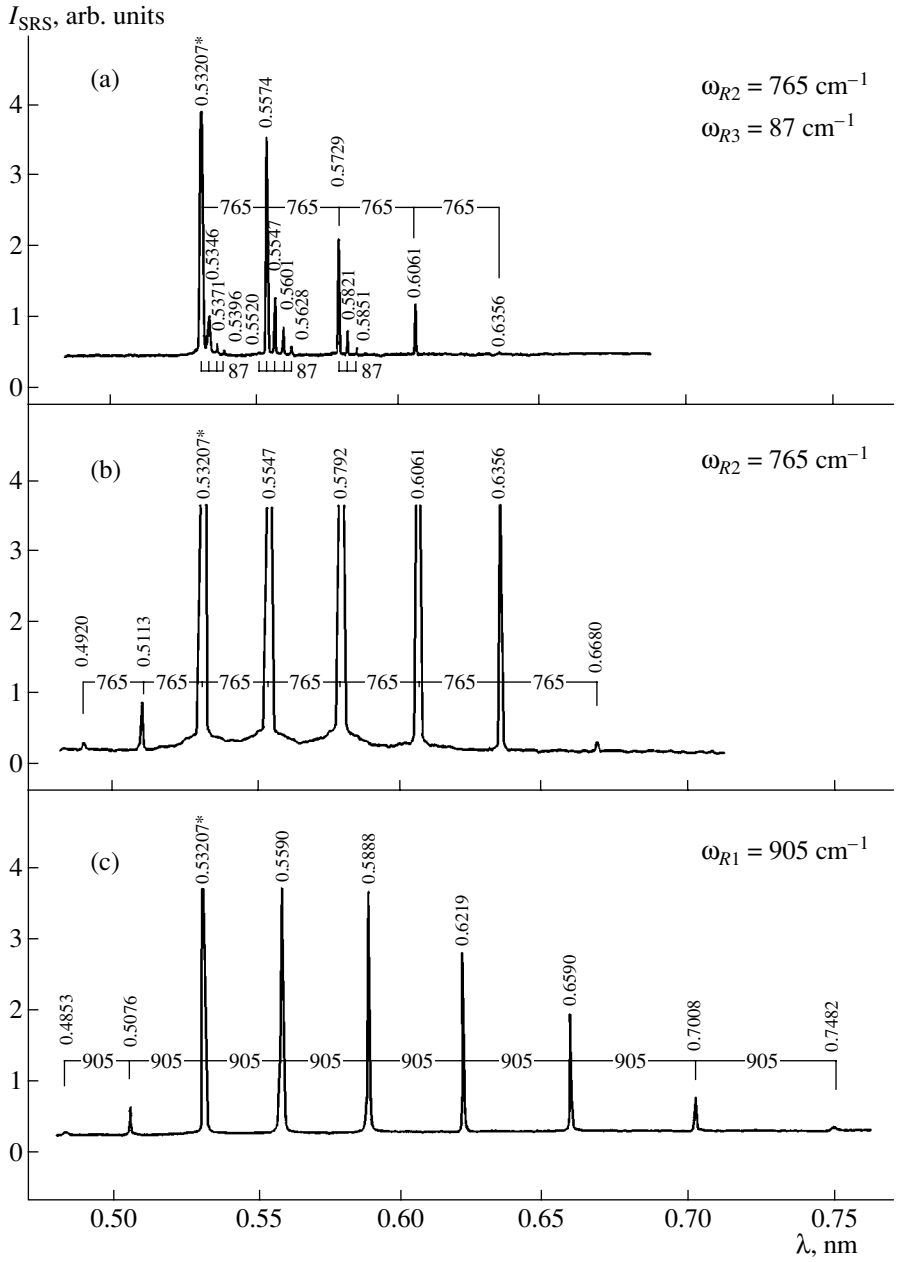

Fig. 6. The spectra of stimulated Raman scattering (SRS) for α-KY$(WO_4)_2$ at 300 K in the excitation geometry: (a) *a*(*cc*)*a*; (b) *b*(*cc*)*b*; (c) *b*(*aa*)*b*. For notation see Fig. 5.

[32], in α-KY$(WO_4)_2$ crystals, no such coupling was reliably established because of the complexity of their structure. One can state that two SRS-active modes of the α-KY$(WO_4)_2$ crystals with the energies ω_{R1} = 905 cm^{-1} and ω_{R2} = 765 cm^{-1} are explained by internal W–O vibrations in the double bands formed by vertex- and edge-sharing W-octahedra [33].

CONCLUSION

In the end of the 1960s, B.K. Vainshtein, then the director of the Shubnikov Institute of Crystallography and the Chairman of the Scientific Council on Formation and Structure of Crystals of the USSR Academy of Sciences, recommended to one of the authors (A.A. Kaminskii) to establish the cooperation in searching for new lasing crystals with the Institute of Inorganic Chemistry of the Siberian Division of the USSR Academy of Sciences. He said that the Siberian Institute of Inorganic Chemistry is a well-developed institution with the research lines very close to those of the Institute of Crystallography. He also said his own people work there. It was a hint to P.V. Klevtsov, an ex-post-graduate student of the Institute of Crystallogra-

phy. Later, Klevtsov took an active part in our research work and was a coauthor of our pioneering publications on lasing tungstates.

It should be indicated that the progress in the studies of these crystals made in the last decade is also explained, to a large extent, by our cooperation in the Open Joint Laboratory *Laser Crystals and Precision Laser Systems*, one of whose founders was Vainshtein. All this clearly illustrates an extremely diverse and broad spectrum of Vainshtein's scientific interests. We consider the possibility to participate in this issue of *Kristallografiya* dedicated to the memory of Academician B.K. Vainshtein as a great honor. We are grateful to the fate which gave us the opportunity to enjoy Vainshtein's support and interest in our research.

ACKNOWLEDGMENTS

We are grateful to Academician F.A. Kuznetsov, director of the Institute of Inorganic Chemistry, Siberian Division, Russian Academy of Sciences, without whose support and collaboration this study would not be possible.

Our studies of α-$KY(WO_4)_2$ crystals were supported by the Russian Foundation for Basic Research and by the State Programs *Fundamental Spectroscopy* and *Optics: Laser Physics* of the Russian Ministry of Industry, Science, and Technology.

REFERENCES

1. A. A. Kaminskii, P. V. Klevtsov, and A. A. Pavlyuk, Phys. Status Solidi A **5** (2), K79 (1971).
2. A. A. Kaminskii, P. V. Klevtsov, L. Li, and A. A. Pavlyuk, IEEE J. Quantum Electron. **8** (3), 457 (1971).
3. A. A. Kaminskii, A. A. Pavlyuk, P. V. Klevtsov, *et al.*, Izv. Akad. Nauk SSSR, Neorg. Mater. **13** (3), 582 (1977).
4. A. A. Kaminskii, A. A. Pavlyuk, I. F. Balashov, *et al.*, Izv. Akad. Nauk SSSR, Neorg. Mater. **13** (8), 1541 (1977).
5. A. A. Kaminskii, A. A. Pavlyuk, I. F. Balashov, *et al.*, Izv. Akad. Nauk SSSR, Neorg. Mater. **14** (12), 2256 (1978).
6. A. A. Kaminskii, A. A. Pavlyuk, N. R. Agamalyan, *et al.*, Izv. Akad. Nauk SSSR, Neorg. Mater. **15** (8), 1496 (1979).
7. A. A. Kaminskii, A. A. Pavlyuk, T. I. Butaeva, *et al.*, Izv. Akad. Nauk SSSR, Neorg. Mater. **15** (3), 541 (1979).
8. A. A. Kaminskii, A. A. Pavlyuk, N. R. Agamalyan, *et al.*, Izv. Akad. Nauk SSSR, Neorg. Mater. **15** (12), 2092 (1979).
9. A. A. Kaminskii, A. A. Pavlyuk, Chan Ngok, *et al.*, Dokl. Akad. Nauk SSSR **245** (3), 575 (1979) [Sov. Phys. Dokl. **24**, 201 (1979)].
10. A. A. Kaminskii, A. G. Petrosyan, V. A. Fedorov, *et al.*, Dokl. Akad. Nauk SSSR **260** (1), 64 (1981) [Sov. Phys. Dokl. **260**, 846 (1981)].
11. A. A. Kaminskii, A. A. Pavlyuk, F. I. Polyakova, *et al.*, Dokl. Akad. Nauk SSSR **268** (4), 856 (1983) [Sov. Phys. Dokl. **28**, 154 (1983)].
12. A. A. Kaminskii, S. N. Bagaev, and A. A. Pavlyuk, Phys. Status Solidi A **151** (2), K53 (1995).
13. A. V. Kuleshov, A. A. Lagatsky, A. V. Podlipensky, *et al.*, Opt. Lett. **22** (16), 1317 (1997).
14. A. A. Kaminskii and A. A. Pavlyuk, Neorg. Mater. **31** (11), 1500 (1995).
15. A. A. Kaminskii, L. Li, A. V. Butashin, *et al.*, Jpn. J. Appl. Phys. **36** (2A), L107 (1997).
16. A. Kaminskii, U. Hommerich, D. Temple, *et al.*, Jpn. J. Appl. Phys. **39** (3A/B), L208 (2000).
17. K. Andryunas, Yu. Vishchakas, V. Kabelka, *et al.*, Pis'ma Zh. Éksp. Teor. Fiz. **42** (8), 333 (1985) [JETP Lett. **42**, 410 (1985)].
18. A. A. Kaminskii, in *Proceedings of International Workshop "Tungstate Crystals," Università degli Studi La Sapienza, Rome, 1998*, p. 249.
19. A. A. Kaminskii, *Raman Scattering—70 Years of Researches* (Fiz. Inst. Ross. Akad. Nauk, Moscow, 1998), p. 206.
20. A. A. Kaminskii, H. J. Eichler, K. Ueda, *et al.*, Appl. Opt. **38** (21), 4533 (1999).
21. A. A. Kaminskii, K. Ueda, H. J. Eichler, *et al.*, Jpn. J. Appl. Phys. **37** (8A), L923 (1998).
22. A. A. Kaminskii, H. J. Eichler, J. Fernández, *et al.*, Jpn. J. Appl. Phys. (in press).
23. A. M. Ivanyuk, M. A. Ter-Pogosyan, P. A. Shakhverdov, *et al.*, Opt. Spektrosk. **59** (5), 950 (1985) [Opt. Spectrosc. **59**, 572 (1985)].
24. A. A. Kaminskii, N. S. Ustimenko, S. N. Bagaev, *et al.*, Dokl. Akad. Nauk **359** (2), 179 (1998) [Dokl. Phys. **43**, 148 (1998)].
25. A. A. Lagatsky, A. Abdolvand, and N. V. Kuleshov, Opt. Lett. **25** (9), 616 (2000).
26. P. V. Klevtsov and R. F. Klevtsova, Zh. Strukt. Khim. **18** (3), 419 (1977).
27. A. A. Pavlyuk, Ya. V. Vasiliev, L. Yu. Kharchenko, *et al.*, in *Proceedings of the Asia Pacific Society for Advanced Materials, APSAM-92, Shanghai, China, 1993*, p. 164.
28. A. A. Kaminskii, *Crystalline Lasers: Physical Processes and Operating Schemes* (CRC Press, Boca Raton, 1996).
29. S. V. Borisov and R. F. Klevtsova, Kristallografiya **13** (3), 517 (1968) [Sov. Phys. Crystallogr. **13**, 420 (1968)].
30. N. M. Melankholin, *Methods of Studying the Optical Properties of Crystals* (Nauka, Moscow, 1970).
31. N. N. Mit'kina, A. A. Pavlyuk, R. A. Puko, *et al.*, Izv. Akad. Nauk SSSR, Neorg. Mater. **26** (7), 1564 (1990).
32. S. P. S. Porto and J. F. Scott, Phys. Rev. **157** (3), 716 (1967).
33. L. Mocalik, J. Hanuza, and A. A. Kaminskii, J. Mol. Struct. **555** (1–3), 289 (2000).

Translated by K. Kugel

Crystallography Reports, Vol. 46, No. 4, 2001, pp. 673–679. Translated from Kristallografiya, Vol. 46, No. 4, 2001, pp. 742–747.

Dedicated to the memory of B.K. Vainshtein

Configurations of the Zero-Birefringence and Zero-Dichroism Lines of Electromagnetic Waves in Weakly Anisotropic Crystals

V. I. Alshits, V. N. Lyubimov, and L. A. Shuvalov

Shubnikov Institute of Crystallography, Russian Academy of Sciences,
Leninskiĭ pr. 59, Moscow, 117333 Russia
e-mail: Alshis@ns.crys.ras.ru

Received February 15, 2000

Abstract—Configurations of two types of lines—those of zero birefringence and zero dichroism—drawn by the end of the directional vector of the wave normal over the unit sphere, which correspond to the coincident phase velocities or the absorption coefficients of isonormal electromagentic waves in weakly anisotropic crystals, have been studied analytically. It is shown that under the conditions of weak dielectric anisotropy, even slight changes in anisotropy result in the dramatic deformation of the lines of both types. The corresponding evolution of the configurations with the change of the anisotropy parameters is considered by example of absorptive orthorhombic crystals. © *2001 MAIK "Nauka/Interperiodica".*

INTRODUCTION

Two types of wave surfaces play an important role in the description of the optical properties of absorptive crystals—the surface of refractive indices (equivalent to the surface of reciprocal phase velocities) and the surface of absorption coefficients of electromagnetic waves [1–3], with both being two-sheet surfaces. The sheets are intersected along certain cones, which, in the general case of triclinic crystals, are the surfaces of the 24th order [4–7]. The intersection of the sheets of the refractive-index surface determines the directions along which the phase velocities of isonormal waves coincide, i.e., the directions of zero birefringence. The analogous line of self-intersection of the absorption-coefficient surface sets the directions of the zero dichroism along which the intensities of both propagating isonormal waves decrease in the same way.

The complexity of the general equations describing these intersections hinders their analytical study. Only particular cases of such intersections were calculated numerically [1, 4–7]. At the same time, the analytical description of the conditions of existence of circular cones, which correspond to such intersections in absorptive optically uniaxial crystals, was considered in [8, 9]. Below, we examine analytically the geometry of more complicated intersections of the surface sheets for low-symmetric crystals both weakly anisotropic and weakly absorptive. Interest in such crystals is associated, in particular, with the fact that the sheets of the wave surfaces in these crystals are close to each other. Under such conditions, even slight changes in the material characteristics of the crystals, e.g., their complex permittivity, give rise to dramatic changes in the geometry of the sheet intersections and configurations of the optical axes. Thus, in a conventional biaxial crystal, weak absorption only slightly splits all the optical axes [10]. If a biaxial crystal is close to an isotropic medium, then even weak (but isotropic) absorption can result in a considerable splitting of the optical axes [11]. This sensitivity of the optical characteristics of such media to small variations in the material parameters motivated the present study. Below, we follow the evolution of the configuration of the zero-birefringence and zero-dichroism lines with the variation of the material characteristics of the crystals with the focus on the instances, where, for certain relationships of the parameters, the change in the topology of these lines bears the sign of a catastrophe.

EQUATIONS OF THE ZERO-BIREFRINGENCE AND ZERO-DICHROISM LINES

As the initial relationship, consider the general equation which describes the dependence of refractive indices n and absorption coefficients n' on the direction of the wave normal $\mathbf{m}$ ($\mathbf{m}^2 = 1$) of an electromagnetic wave [2]

$$N^4\varepsilon_{\mathbf{m}} - N^2(\bar{\varepsilon}_t - \bar{\varepsilon}_{\mathbf{m}}) + |\hat{\varepsilon}| = 0, \qquad (1)$$

where $N = n + in'$ is the complex refractive index; $\hat{\varepsilon}$ is the complex permittivity tensor; $|\hat{\varepsilon}|$ is the determinant of this tensor; and the subscript t denotes the tensor trace, $\bar{\varepsilon}_t = \mathrm{trace}\hat{\bar{\varepsilon}}$, where $\hat{\bar{\varepsilon}}$ is the tensor adjoint with respect to $\hat{\varepsilon}$. Here, the convolution of an arbitrary tensor $\hat{A}$ with the vector $\mathbf{m}$ is denoted as $\mathbf{m} \cdot \hat{A}\,\mathbf{m} = A_{\mathbf{m}}$. To

single out the dielectric anisotropy essential for our further consideration, we represent the tensor $\hat{\varepsilon}$ as a sum of its spherical part $(\varepsilon_1 + i\varepsilon_1')\hat{I}$ (where $\hat{I}$ is the unit matrix) and the anisotropic "addition" $\hat{\delta} = \hat{d} + i\hat{d}'$. For weak absorption and small anisotropy parameters, Eq. (1) has the following solutions (in the first order of small parameters $\hat{\delta}$ and ε_1'):

$$N_\pm = n_1 + in_1' + \frac{1}{4\sqrt{\varepsilon_1}}(\delta_t - \delta_\mathbf{m} \pm R), \tag{2}$$

where

$$\begin{aligned} n_1 &= \sqrt{\varepsilon_1}, \quad n_1' = \varepsilon_1'/2\sqrt{\varepsilon_1}, \\ R^2 &= (\delta_t - \delta_\mathbf{m})^2 - 4\bar{\delta}_\mathbf{m} \equiv D + iD'. \end{aligned} \tag{3}$$

Specifying the expressions for the real and the imaginary parts of Eqs. (3) for R^2, we obtain

$$D(\mathbf{m}) = (d_t - d_\mathbf{m})^2 - (d_t' - d_\mathbf{m}')^2 - 4(\bar{d}_\mathbf{m} - \bar{d}_\mathbf{m}'), \tag{4}$$

$$\begin{aligned} D'(\mathbf{m}) &= 2(d_t' - d_\mathbf{m}')(d_t - d_\mathbf{m})) \\ &- 4[2(\hat{d}'\hat{d})_\mathbf{m} - (\hat{d}'\hat{d})_t - d_t'd_\mathbf{m} - d_\mathbf{m}'d_t + d_t'd_t]. \end{aligned} \tag{5}$$

It should be emphasized that, writing Eqs. (2)–(5), we assumed that the components of the tensors $\hat{d}$ and $\hat{d}'$ are quantities of the same order of magnitude.

As is seen from Eqs. (2) and (3), under the conditions that $D'(\mathbf{m}) = 0$, the line $D(\mathbf{m}) \le 0$ on the sphere $\mathbf{m}^2 = 1$ corresponds to the directions of the wave normal $\mathbf{m}$ along which $\mathrm{Re}R = 0$. Therefore, the isonormal waves have the same refractive indices, $n_+ = n_-$. In a similar way, under the condition $D'(\mathbf{m}) = 0$, the line $D(\mathbf{m}) \ge 0$ corresponds to the same values of the absorption coefficients of isonormal waves, $n_+' = n_-'$. At the point $D(\mathbf{m}) = 0$, both lines smoothly converge. The common point of these lines corresponds to the coincidence of the refractive indices and the absorption coefficients of the isonormal waves, and the corresponding direction $\mathbf{m}$ becomes the direction of the optical axis. Here, we mean the optical axes of the general type, the so-called circular axes [2].

Along with the solution lines of the equation $D'(\mathbf{m}) = 0$, which include with five points of the sign reversal of function $D(\mathbf{m})$ (these points correspond to the optical axes), there can also exist the closed lines of zero birefringence (or zero dichroism) such that the function $D(\mathbf{m})$ along these lines does not pass through the zero value and is either negative or positive. Earlier, these lines were described for optically uniaxial absorptive crystals [8, 9]. However, the analysis shows that solution lines exist only because of the transverse anisotropy of these media and disappear at any infinitely small perturbation of the tensor $\hat{\varepsilon}$ eliminating the transverse isotropy.

It is seen from Eq. (5) that the lines of zero birefringence and zero dichroism in the approximation considered here are described by the fourth-order algebraic equation with respect to the components of the vector $\mathbf{m}$. This equation is the sum of the products of the type $(m_i m_j)$ and $(m_i m_j m_k m_l)$ and the $\mathbf{m}$-independent term the coefficients of these combinations can be represented as the ratios of small parameters. If these ratios tend to zero, the above relationships becomes uncertainties of the 0/0 type. It is obvious that even small changes in the parameters of dielectric anisotropy produce a considerable effect on the coefficients of the above equation, which, in turn, should dramatically change the configurations of the lines studied, including the positions of the optical axes. It should also be indicated that the solutions of Eq. (5) ($D'(\mathbf{m}) = 0$) are the same irrespective of any proportional changes in the tensors $\hat{d}$ and $\hat{d}'$. However, in this case, the degeneracy points corresponding to the roots of Eq. (4) ($D(\mathbf{m}) = 0$) change their positions along the line $D'(\mathbf{m}) = 0$.

Below, we consider absorptive orthorhombic crystals, for which the general equations are essentially simplified and the behavior of the zero-birefringence and zero-dichroism lines can readily be studied analytically.

RELATIONSHIPS FOR ORTHORHOMBIC CRYSTALS

For orthorhombic crystals, both real and imaginary parts of the permittivity tensor $\hat{\varepsilon}$ are simultaneously reduced to the diagonal form. In this case, the anisotropic part, $\hat{\delta} = \hat{d} + i\hat{d}'$, of the tensor $\hat{\varepsilon}$ acquires the form

$$\hat{d} = \begin{bmatrix} 0 & 0 & 0 \\ 0 & d_2 & 0 \\ 0 & 0 & d_3 \end{bmatrix}, \quad \hat{d}' = \begin{bmatrix} 0 & 0 & 0 \\ 0 & d_2' & 0 \\ 0 & 0 & d_3' \end{bmatrix}. \tag{6}$$

The anisotropy parameters introduced here are uniquely related to the principal refractive indices n_i and the principal absorption coefficients n_i' by the relationships

$$d_j = 2n_1(n_j - n_1), \quad d_j' = 2n_1(n_j' - n_1'), \tag{7}$$

where $n_j = \sqrt{\varepsilon_1} + d_j/2\sqrt{\varepsilon_1}$ and $n_j' = (\varepsilon_1' + d_j')/2\sqrt{\varepsilon_1}$ ($j = 2, 3$), and the index n_1 and the coefficient n_1' were introduced in Eqs. (3).

It is convenient to introduce the spherical coordinate system (angles ϑ and φ). Then, the vector $\mathbf{m}$ can be written as $\mathbf{m} = (m_1, m_2, m_3) = (\sin\vartheta\cos\varphi, \sin\vartheta\sin\varphi, \cos\vartheta)$, and the general equation, $D'(\vartheta, \varphi) = 0$, of the

lines we are interested in reduces to the following equation relating the angles ϑ and φ:

$$\sin^2\varphi_\pm = \frac{1}{2p\sin^2\vartheta}[2p - 1 - \cos^2\vartheta \pm \sqrt{(1+\cos^2\vartheta)^2 - 4p(q\sin^4\vartheta + 2\cos^2\vartheta)}]. \quad (8)$$

Here,

$$p = \frac{\gamma\gamma'}{\gamma+\gamma'}, \quad q = \frac{1}{\gamma+\gamma'}, \quad (9)$$

where

$$\gamma = \frac{d_2}{d_3} = \frac{n_2 - n_1}{n_3 - n_1}, \quad \gamma' = \frac{d_2'}{d_3'} = \frac{n_2' - n_1'}{n_3' - n_1'}. \quad (10)$$

In this case, the equation for D acquires the form

$$D(\vartheta,\varphi) = d_3^2\{m_2^4 g_1 - 2m_2^2[g_1 - g_2(1+\cos^2\vartheta)] + g_1 - 2g_2\sin^2\vartheta + g_3\sin^4\vartheta\}, \quad (11)$$

where

$$g_1 = \gamma^2 - \xi^2(\gamma')^2, \quad g_2 = \gamma - \xi^2\gamma', \quad g_3 = 1 - \xi^2, \quad \xi = \frac{d_3'}{d_3} = \frac{n_3' - n_1'}{n_3 - n_1}. \quad (12)$$

The points of the sign reversal of $D(\mathbf{m})$ on the line $D'(\mathbf{m}) = 0$, which correspond to the optical axes, can readily be expressed in terms of the anisotropy parameters used here proceeding from the general relationships derived in [2]. For four directions of the optical axes denoted here as $\mathbf{m}^{++}$, $\mathbf{m}^{+-}$, $\mathbf{m}^{-+}$, and $\mathbf{m}^{--}$, we have

$$\mathbf{m}^{\pm\pm} = \frac{2}{1 + |r_1|^2 + |r_2|^2} \times \{\pm\mathrm{Re}(r_1), \pm\mathrm{Im}(r_1^* r_2), \mathrm{Re}(r_2)\}, \quad (13)$$

$$1/r_1 = \sqrt{1 - \frac{1+i\xi}{\gamma + i\xi\gamma'}}, \quad 1/r_2 = \sqrt{1 - \frac{\gamma + i\xi\gamma'}{1+i\xi}}. \quad (14)$$

The angular coordinates of all the four optical axes for orthorhombic crystals are

$$(\vartheta_0, \pm\varphi_0), \quad (\vartheta_0, \pm\varphi_0 + \pi). \quad (15)$$

Similar to the case of transparent crystals, at $\varphi_0 = 0$, the optical axes "collapse" pairwise and the crystal becomes optically biaxial.

In correspondence with Eq. (8), the configurations of the lines $D'(\mathbf{m}) = 0$ on the sphere $\mathbf{m}^2 = 1$ depend on two parameters—γ and γ', which are, in fact, the ratios of small quantities [see Eq. (10)]. Therefore, even small changes in anisotropy [see Eq. (6)] can considerably influence the structure of the lines under consideration. Below, we consider the changes in the structure of these lines. The coordinates of the optical axes on the lines described by Eq. (8), which are determined by Eqs. (13)–(15), also depend on the parameter ξ from Eq. (12), which is also the ratio of small quantities. The change in the parameter ξ (at the given γ and γ' values) gives rise to the displacement of the points corresponding to the optical axes along the line described by Eq. (8).

As is seen from Eq. (8), different combinations of the parameters p and q on the sphere $\mathbf{m}^2 = 1$ can result in the existence of two or four closed lines that pass through eight points $\pm\mathbf{m}^{\pm\pm}$ at which the sign reversal of the function $D(\vartheta, \varphi)$ described by Eq. (11) takes place, in full accordance with the symmetry of an orthorhombic crystal. Passing through each of the eight points of the emergence of the optical axes on the sphere $\mathbf{m}^2 = 1$, the zero-birefringence line ($D < 0$) is transformed into the zero-dichroism line ($D > 0$). Figures 1 and 2 show a number of various possible configurations of these lines and the ways of their possible mutual topological transformations. Their evolution will be considered in more detail in the following sections by studying some simplified situations that admit clear analytical solutions.

EVOLUTION OF THE LINES IN THE CASE WHERE A CRYSTAL IS SIMILAR TO AN OPTICALLY UNIAXIAL MEDIUM

The optical properties of an orthorhombic crystal are close to those of a uniaxial medium if, e.g., the parameters γ and γ' given by Eq. (10) are small. Then the angle ϑ is also small, so that all the lines studied are grouped in the vicinity of the direction $\mathbf{m}$ coinciding with [001]. Under these conditions, Eqs. (8) and (11) are essentially simplified and take the form

$$\vartheta_\pm^2 = (\gamma/2)(\eta+1)\cos 2\varphi \pm \sqrt{(\eta+1)^2\cos^2 2\varphi - 4\eta}], \quad (16)$$

$$\eta = \gamma'/\gamma,$$

$$D(\vartheta,\varphi) = d_3^2[g_1 - 2g_2\vartheta^2\cos 2\varphi + g_3\vartheta^4]. \quad (17)$$

The parameters g_1 and g_2 in Eq. (16) are small, $g_1 \sim \gamma^2$ and $g_2 \sim \gamma$.

Analyzing the curves described by Eqs. (16) and (17), it is convenient to use the following relationships:

$$\vartheta_\pm^2(\varphi = 0) = \begin{cases}\gamma \\ \gamma'\end{cases}, \quad \vartheta_\pm^2(\varphi = \pi/2) = \begin{cases}-\gamma \\ -\gamma'\end{cases}, \quad (18)$$

$$D(\vartheta^2 = \gamma, \varphi = 0) = D(\vartheta^2 = -\gamma, \varphi = \pi/2) = -[d_3\gamma\xi(\eta-1)]^2 \le 0, \quad (19)$$

$$D(\vartheta^2 = \gamma', \varphi = 0) = D(\vartheta^2 = -\gamma', \varphi = \pi/2) = [d_3\gamma(\eta+1)]^2 \ge 0. \quad (20)$$

Different inequality signs in relationships (19) and (20) indicate that the function $D(\vartheta, \varphi)$ described by Eq. (17)

and determined on the line described by Eq. (16) goes to zero in the range $0 \le \varphi \le \pi/2$ (the respective point on the line corresponds to the direction of the optical axis).

Figure 1a illustrates the evolution of the curves with the change of the parameters $\eta = \gamma'/\gamma$ and γ. Stereographic projections *1–7* correspond to an increase of the parameter η from $-\infty$ to ∞ under the condition $\gamma > 0$; sequence *7–12–1* also corresponds to an increase of η in the same range but at $\gamma < 0$ (at $\eta \longrightarrow \pm\infty$, it is assumed that $|\gamma| \ll |\gamma'| \ll 1$). The passage through the critical value $\gamma = 0$ corresponds to the rotation of all the curves through the angle $\pi/2$ around the [001] direction, because initial equations (16) and (17) are invariant with respect to the changes $\gamma \longrightarrow -\gamma$ and $\varphi \longrightarrow \varphi + \pi/2$. Thus, at $\gamma = 0$, a considerable rearrangement takes place—a transition of the catastrophe type. Splitting of the lines (the transformation of two closed loops into four) occurs at $\eta = \pm\infty$ (projections *1* and *7*) and also at $\eta = 0$ (projections *3* and *9*). At $\eta = 1$, four closed loops are contracted into points and the crystal becomes optically biaxial (projections *5* and *11*).

The configurations studied are divided into stable (not changing their topological structure at small variations in the anisotropy parameters) and unstable areas (not possessing this property). The former are indicated by bold circles; the characteristic feature of the latter is the existence of intersections, which disappear at configuration perturbations.

The division of the closed curves into the portions corresponding to zero birefringence, on the one hand, and portions corresponding to zero dichroism, on the other hand, can readily be made with the aid of inequalities (19) and (20). The motion of the points separating these portions (these points are determined by the zeroes of the function $D(\vartheta, \varphi)$ described by Eq. (17) and corresponds to the optical axes) can easily be followed, e.g., at $\eta = -1$, where the closed curve is a circumference (the particular case of projection *2*), and Eqs. (16) and (17) take the form

$$\vartheta^2(\varphi) \equiv \gamma, \quad D(\vartheta, \varphi) \equiv 2d_3^2\gamma^2(1 + \xi^2) \times\left(\frac{1 - \xi^2}{1 + \xi^2} - \cos 2\varphi\right); \quad 0 \le \varphi \le 2\pi. \tag{21}$$

Then, the angular coordinates of the optical axes φ_0 are set by the following equations (Fig. 1b):

$$\sin^2\varphi_0 = \xi^2/(1 + \xi^2). \tag{22}$$

If $\eta = 0$, the closed curves disintegrate (projection *3*) and we obtain

$$\vartheta^2(\varphi) = \gamma\cos 2\varphi, \quad D(\vartheta, \varphi) = d_3^2\gamma^2(1 + \xi^2) \times\left(\frac{1}{1 + \xi^2} - \cos^2 2\varphi\right); \quad 0 \le \varphi \le \pi/4. \tag{23}$$

The angular coordinates of the optical axes are also determined by Eq. (22) with the change $\varphi_0 \longrightarrow 2\varphi_0$.

It should be indicated that splitting of the optical axis of an absorbing optically uniaxial crystal caused by a small anisotropic perturbation occurs anomalously sharply (this was indicated in [11]). Thus, it is seen from Eqs. (18) that splitting of the optical axis parallel to the [001] direction is of the order of $\vartheta \sim \sqrt{|\gamma|} \sim \sqrt{|\gamma'|}$, so that the derivatives $\partial\vartheta/\partial\gamma$ and $\partial\vartheta/\partial\gamma'$ go to infinity at $\gamma, \gamma' \longrightarrow 0$. This signifies that small changes in the anisotropy parameters γ and γ' give rise to considerably more pronounced changes in the angle ϑ, namely, $\vartheta\sqrt{|\gamma|} \gg |\gamma|$ at $|\gamma| \ll 1$. Using the value $\gamma \sim \gamma' \approx 0.01$ for the numerical estimations, we obtain $\vartheta \approx 0.1$ ($\sim 6^0$).

The situations analogous to that considered above, can arise in orthorhombic crystals in the vicinity of the direction **m** close to [010] (at $\gamma, \gamma' \longrightarrow \infty$) and in the vicinity of the direction **m** close to [100] (at $\gamma, \gamma' \longrightarrow 1$).

EVOLUTION OF THE LINES ON THE SPHERE $\mathbf{m}^2 = 1$

Figure 2a shows the scheme of various mutual transformations of the lines on the sphere $\mathbf{m}^2 = 1$ at different combinations of the anisotropy parameters. Not going into the details of all the possible transformations shown in Fig. 2a, we consider here only the sequence of projections *1–6* for which $d_2' \equiv 0$, i.e., the projections for which $\gamma' \equiv 0$ but $d_3' \ne 0$. In this case, the equation $D'(\vartheta, \varphi) = 0$ has only one parameter γ and is reduced to a rather compact relationship between the angles ϑ and φ:

$$\sin^2\varphi = \frac{1 - (\sin^2\vartheta)/\gamma}{1 + \cos^2\vartheta}. \tag{24}$$

Now, we have

$$D(\vartheta, \varphi) = d_3^2[(m_2^2\gamma)^2 + 2(m_2^2\gamma)(1 + \cos^2\vartheta - \gamma) + (\sin^2\vartheta - \gamma)^2 - \xi^2\sin^4\vartheta]. \tag{25}$$

With due regard for the above equations and the relationship

$$D(\vartheta = 0, \varphi) = d_2^2 \ge 0, \tag{26}$$

one can follow the evolution of the line with an increase of the parameter γ from $-\infty$ to $+\infty$. Here, attention is attracted to the transitions of the catastrophe type, during which the closed curves undergo discontinuity at the critical values $\gamma = \pm\infty$ (projection *1*) and $\gamma = 1$ (projection *5*).

At $\gamma = 0$, the crystal passes through the optically uniaxial state, and the zero-birefringence and zero-dichroism lines "shrink" into points (projection *3*).

The position of the optical axes on the given curve depends on the parameter ξ [see Eq. (25)]. The variation of this parameter gives rise to the motion of the points corresponding to the optical axes along the given

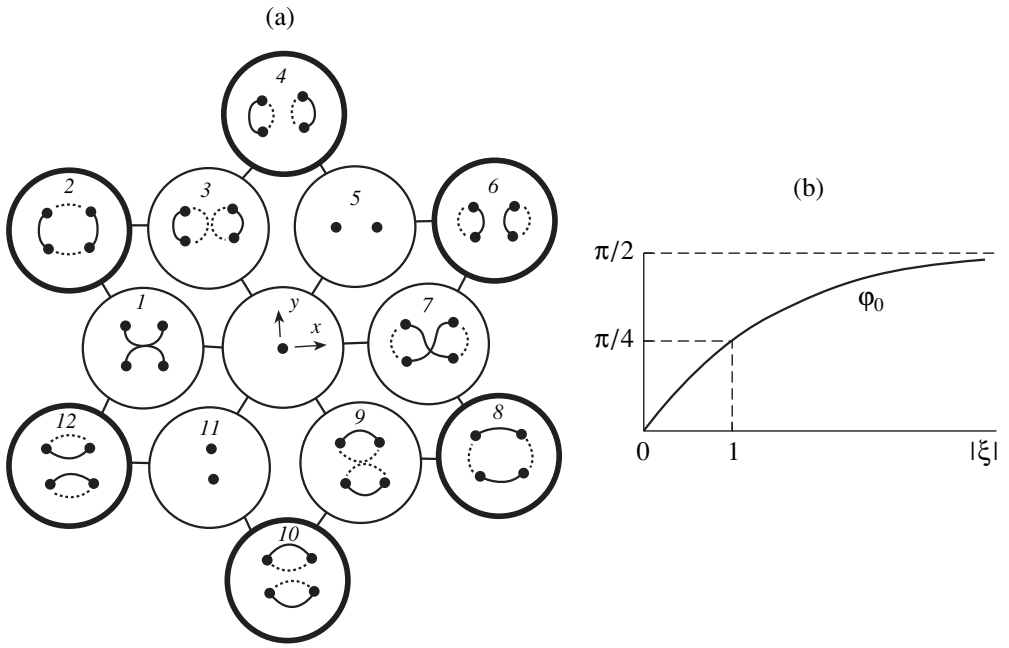

Fig. 1. Possible configurations of the zero-birefringence and zero-dichroism lines in orthorhombic crystals similar to optically uniaxial media: (a) evolution of the zero-birefringence (solid lines) and zero-dichroism (dashed lines) lines with the variation of η and γ (filled circles correspond to the optical axes) and (b) angular coordinates of the optical axes as functions of ξ at $\eta = -1$ (projection *2* in Fig. 1a for the case, where the closed curves are circumferences).

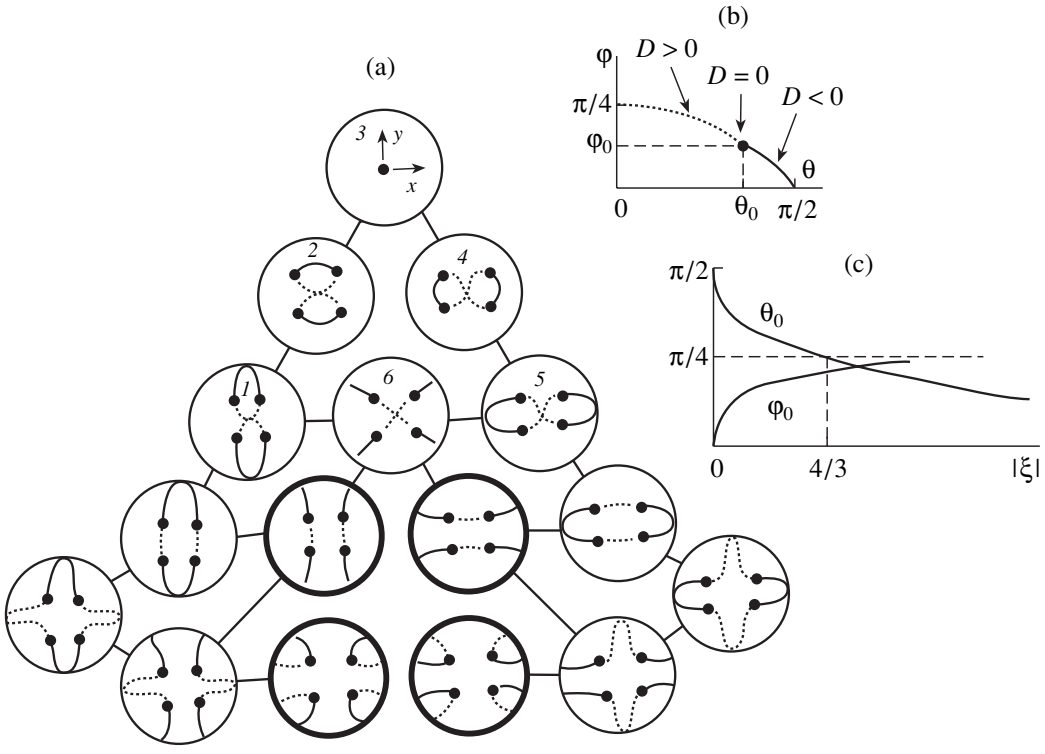

Fig. 2. Possible configurations of the zero-birefringence and zero-dichroism lines in orthorhombic crystals on the sphere $\mathbf{m}^2 = 1$: (a) evolution of the lines with the variation of the anisotropy parameters; (b) the zero-birefringence and zero-dichroism lines corresponding to the case $\gamma = 1$ and $\gamma' \equiv 0$ (projection *5* in Fig. 2a) as functions of the angular coordinates ϑ and φ; and (c) angular coordinates of the optical axes as functions of ξ for the zero-birefringence and zero-dichroism lines shown in projection *5* in Figs. 2a and 2b.

curve. For a better visualization, consider the case $\gamma = 1$ (projection *5*), where the curve shape is set by the equations

$$\tan^2\varphi = \cos^2\vartheta \quad (27)$$

and the motion of the optical axes along this curve determined by the parameter ξ is described by the formula

$$|\xi| = \left|\frac{d_3'}{d_3}\right| = \frac{2\cot^2\vartheta_0}{1+\cos^2\vartheta_0}. \quad (28)$$

The above characteristics are shown in Figs. 2b and 2c. The similar dependences are characteristic of the case $\gamma = \pm\infty$ (projection *1*) upon the changes $\varphi \longrightarrow \pi/2 - \varphi$ and $d_3 \longrightarrow d_2$. It is seen from Fig. 2c that the derivatives $\partial\vartheta_0/\partial|\xi|$ and $\partial\varphi_0/\partial|\xi|$ go to infinity at $|\xi| \longrightarrow 0$, when the crystal passes through the optically uniaxial state: here, the optical axis undergoes anomalous splitting along the direction parallel to [100]. One can see that a similar situation also takes place at $|\xi| \longrightarrow \infty$: here, the anomaly is observed with respect to the small parameter $1/|\xi| \longrightarrow 0$, and the optical axis parallel to the direction [001] is split.

OPTICALLY POSITIVE AND NEGATIVE CRYSTALS UNDER THE CONDITIONS OF WEAK ABSORPTION ANISOTROPY

At $\hat{d}' = 0$ and $\varepsilon_1' \neq 0$, the absorptive crystal is optically biaxial—the orientations of the optical axes are determined only by the parameters d_2 and d_3, as in transparent crystals. If the components of the tensor $\hat{d}$ are much less than the components of the tensor $\hat{d}'$, then each of the two optical axes is split into two new circular optical axes, but the value of this splitting is quite small [10]. Under these conditions, the concept of optically positive and negative crystals remains valid despite the fact that it was introduced only for transparent crystals [3]. These crystals are considered to be optically positive if the angle $2\vartheta_0$ between their optical axes is less than $\pi/2$ (the bisector of this angle coincides with that of the principal axes of the permittivity tensor, which is characterized by the maximum eigenvalue of this tensor). If the angle $2\vartheta_0$ exceeds $\pi/2$, the crystals are considered to be optically negative.

If the components of the tensor $\hat{d}'$ are considerably less than the components of the tensor $\hat{d}$, then, ignoring the small corrections, we can state that the angle between the pairs of split optical axes is determined only by the relationships between the parameters d_2 and d_3, i.e., by the values of $\gamma = d_2/d_3$ [see Eq. (10)].

Now, consider the situation, where n_3 has the maximum magnitude of all the three principal refractive indices. Here, two variants are possible. In the first variant, $n_1 < n_2$, so that $n_1 < n_2 < n_3$ and $0 < \gamma < 1$. In this case, the angle between the pairs of split optical axes $2\vartheta_0$ is determined by the equations

$$\tan\vartheta_0 = \sqrt{G}, \quad G = \gamma/(1-\gamma). \quad (29)$$

The initial (unsplit) optical axes lie in the *xz* plane, whereas the *z*-axis is the bisector of the angle $2\vartheta_0$, so that if $0 < \gamma < 1/2$, the crystal is optically positive, but if $1/2 < \gamma < 1$, the crystal is optically negative.

In the second variant $n_2 < n_1$, so that now $n_2 < n_1 < n_3$ and $\gamma < 0$. Then, $G = -\gamma$ in Eq. (29); the initial optical axes lie in the *yz* plane; the crystal is optically positive at $-1 < \gamma < 0$ and optically negative at $\gamma < -1$.

Qualitatively similar situations also arise at some other relationships between the principal refractive indices (the maximum value is possessed either by n_1 or n_2).

DISCUSSION

Thus, we have obtained the basic equations describing the configurations of the zero-birefringence and zero-dichroism lines of isonormal electromagnetic waves for weakly anisotropic and weakly absorptive crystals of an arbitrary symmetry. All the configurations considered above depend solely on the parameters of dielectric anisotropy. We have followed the evolution of these configurations with the change of the anisotropy parameters. Despite the smallness of the changes in the anisotropy parameters, the configurations undergo considerable changes and the catastrophe-type transitions take place.

The lines considered here are characterized by alternative zero-birefringence and zero-dichroism portions. The junction points of these portions correspond to the directions of the optical axes. At the same time, completely different intersections of the wave surfaces of electromagnetic waves were described in [8, 9]—in optically uniaxial absorptive crystals, these lines on the sphere $\mathbf{m}^2 = 1$ are circumferences. Such a circumference corresponds either solely to the zero birefringence or solely to the zero dichroism of isonormal waves. The optical axis does not pass through these lines; instead, it passes through the centers of these circumferences and is parallel to the principal symmetry axis.

Thus, absorption cannot be reduced to a mere decrease of the intensities of the propagating electromagnetic waves in crystals; it also gives rise to the formation of specific phenomena, one of which has been described in this article.

ACKNOWLEDGMENTS

The authors are grateful to E.A. Evdischenko and A.F. Konstantinova for a number of useful remarks. The study was supported by the Russian Foundation for Basic research, project no. 98-02-16069.

REFERENCES

1. A. F. Konstantinova, B. N. Grechushnikov, B. V. Bokut', and E. G. Valyashko, *Optical Properties of Crystals* (Nauka i Tekhnika, Minsk, 1995).
2. F. I. Fedorov, *The Theory of Gyrotropy* (Nauka i Tekhnika, Minsk, 1976).
3. Yu. I. Sirotin and M. P. Shaskolskaya, *Fundamentals of Crystal Physics* (Nauka, Moscow, 1975; Mir, Moscow, 1982).
4. A. M. Goncharenko and F. I. Fedorov, Kristallografiya **3** (5), 587 (1958) [Sov. Phys. Crystallogr. **3**, 592 (1958)].
5. A. M. Goncharenko, Kristallografiya **4** (3), 393 (1959) [Sov. Phys. Crystallogr. **4**, 365 (1960)]; Kristallografiya **4** (5), 727 (1959) [Sov. Phys. Crystallogr. **4**, 688 (1960)]; Kristallografiya **4** (6), 849 (1959) [Sov. Phys. Crystallogr. **4**, 807 (1960)]; Kristallografiya **7** (1), 133 (1962) [Sov. Phys. Crystallogr. **7**, 108 (1962)].
6. S. V. Grum-Grzhimaĭlo, N. N. Fomichev, F. I. Fedorov, and A. M. Goncharenko, Kristallografiya **6** (1), 67 (1961) [Sov. Phys. Crystallogr. **6**, 54 (1961)].
7. A. M. Goncharenko, S. V. Grum-Grzhimaĭlo, and F. I. Fedorov, Kristallografiya **9** (4), 589 (1964) [Sov. Phys. Crystallogr. **9**, 504 (1964)].
8. V. I. Alshits, V. N. Lyubimov, W. Gierulski, and A. Radowicz, Kristallografiya **45** (6), 1068 (2000) [Crystallogr. Rep. **45**, 985 (2000)].
9. V. I. Alshits and V. N. Lyubimov, Kristallografiya **45** (6), 1075 (2000) [Crystallogr. Rep. **45**, 991 (2000)].
10. V. I. Alshits and V. N. Lyubimov, Kristallografiya **45** (4), 731 (2000) [Crystallogr. Rep. **45**, 670 (2000)].
11. V. I. Alshits, V. N. Lyubimov, A. Radowicz, and L. A. Shuvalov, Kristallografiya **46** (3), 504 (2001) [Crystallogr. Rep. **46** (2001)].

Translated by L. Man

Crystallography Reports, Vol. 46, No. 4, 2001, pp. 680–686. Translated from Kristallografiya, Vol. 46, No. 4, 2001, pp. 749–755.

LIQUID CRYSTALS

Dedicated to the memory of B.K. Vainshtein

Structure and Thermal Fluctuations in Thin Films of Smectic Liquid Crystals

B. I. Ostrovskii[1]* and W. H. de Jeu[2]**

** Institute of Crystallography, Russian Academy of Sciences, Leninskiĭ pr. 59, Moscow, 117333 Russia*

*** FOM-Institute AMOLF (Institute of Atomic and Molecular Physics), Kruislaan 407, 1098 SJ Amsterdam, The Netherlands*

[1]e-mail: ostr@cea.ru

[2]e-mail: dejeu@amolf.nl

Received February 23, 2001

Abstract—Thermal fluctuations of the smectic layers in freely suspended thin liquid crystalline films have been studied by the methods of X-ray diffraction and reflectometry. The fluctuation dynamics is studied by the methods of photon correlation spectroscopy with the use of a source of coherent synchrotron radiation. In freely suspended smectic films, the typical relaxation times are of the order of several microseconds. In thin liquid crystalline films, the simultaneous damped and oscillatory behavior was observed for the layer undulations. *© 2001 MAIK "Nauka/Interperiodica".*

INTRODUCTION

Although liquid crystals (LCs) have already been known for more than a century, they were long considered as an amusing scientific incident having no direct relation to the development of physics of condensed matter. The dramatic change in the attitude to liquid crystals occurred in the early 1960s. At that time, it became evident that liquid crystals form a large variety of phases with unusual properties and fill the gap between solid crystals and isotropic liquids. Vainshtein was among the first scientists who started working along this direction. The systematic study of the structure of liquid crystals also started in the 1960s and became a natural continuation of the fundamental studies of the structure of chain molecules such as proteins, nucleic acids, rubbers, and other natural and synthetic polymers. The tendency to parallel packings of chain molecules stems from their geometry and results in anisotropy in their properties along and normally to the axis of their preferred orientation [1]. This opens the possibility to the study of the structure of liquid crystals proper.

In 1963, B.K. Vainshtein and I.G. Chistyakov published a series of articles on liquid crystals [2]. Unlike conventional three-dimensional crystals, whose structure can be described by the periodic density function $\rho(\mathbf{r})$, the structure of partly ordered systems such as liquid crystals requires the consideration of mutual correlations of the position and orientations of the molecules, $\langle\rho(\mathbf{r})\rho(\mathbf{r}')\rangle$ [3, 4]. To describe the structure of a liquid crystal (LC), the so-called function of the intermolecular distances was introduced.[1] The methods for reconstructing this function from the X-ray scattering data in application to liquid crystals were developed in [2].

First, the structural studies of smectic phases were performed. In smectics, there is no translational invariance along the long axes of the molecules, which manifests itself in the one-dimensional density modulation in three-dimensional liquids. These systems exhibit strong thermal fluctuations. Ideal three-dimensional crystals are characterized by a true long-range order in the atomic (molecular) arrangement, whereas in the systems with the one- or the two-dimensional periodicity this order is destroyed by thermal fluctuations [3]. In the mid-1930s, Landau and Peierls showed that thermal fluctuations in the layer positions "smear" the long-range order in smectic LCs. However, this "smearing" is weak (logarithmic) so that the smectic samples of finite size remain stable. Nevertheless, there are differences between smectics and systems with the true long-range order. These differences can be seen from the decrease of the positional correlations at long distances by a power law. The relevant phenomena were thor-

[1] The function of the intermolecular distances, or the Patterson function, has maxima at the points corresponding to the most frequently repeated intermolecular distances. The physical sense of this function is analogous to that of the density–density correlation function $g_2(\mathbf{r})$, used in physics of condensed matter.

1063-7745/01/4604-0680$21.00 © 2001 MAIK "Nauka/Interperiodica"

oughly studied in the precision X-ray experiments on the measurement of the structure factor of the smectic LCs [5–7]. However, these experiments provided the data solely on the static properties of the density correlation function. At the same time, almost no information on the dynamics of thermal fluctuations in the positions of the smectic layers was known until recently. The situation started improving only in the last few years, when the new methods of studying the dynamics of the disordered systems by means of the coherent X-rays were developed. If a coherent radiation is incident onto the fluctuating medium, the scattered radiation forms the so-called speckle pattern reproducing the instantaneous scatter location with regard for the phase relationships between them. The scatter motion gives rise to the corresponding changes in the speckle pattern, which thus can provide an information on the system dynamics. The photon correlation spectroscopy allows one to measure the time autocorrelation function of the intensity of the scattered radiation. For the visible light, the above technique (the dynamical light scattering) is well known [8]. For X-rays, the study of coherent dynamical scattering became possible only with the advent of the powerful sources of synchrotron radiation of the third generation [9, 10]. Unlike the dynamical light scattering, the X-ray correlation spectroscopy allows the study of the dynamical scattering on the molecular scale. These experiments provide valuable information on the characteristics of the relaxation processes in molecular ordered media and complement the data obtained in the structural studies.

Below, we report the results of the recent studies of the static and dynamic properties of freely suspended smectic films. Unlike the bulk samples, the smectic films are characterized by discrete spectra of relaxation modes of the layer displacements, which depend on the film thickness and surface parameters. In freely suspended smectic films, the characteristic relaxation times are on the order of several microseconds. In thin smectic films, the simultaneous damping and oscillatory of behavior was observed. The latter phenomenon is associated with the contribution provided by the surface to the free energy of the system. This contribution is most pronounced for thin films. We also consider the structure and the properties of polymer liquid crystalline films, and the prospects of the use of the dynamical X-ray scattering for studying polymers and biological and lipid membranes.

STATIC PROPERTIES OF SMECTIC FILMS

The formation of a smectic phase is associated with the appearance of the one-dimensional layer order in a liquid (Fig. 1). Such a structure can be obtained by translation of a layer along the *z*-axis for a distance corresponding to the layer period *d* (~2–3 nm). Now the question as to whether the one-dimensional order can be extended for an infinitely large distance arises. It is well known that even in solids, the thermal motion of atoms gives rise to their displacement from the equilibrium positions. In smectics, thermal fluctuations result in much larger layer displacements from the given positions. These deviations are described with the use of the parameter $u_z = u(\mathbf{r})$, which characterizes the layer displacement along the layer normal (*z*-axis). In the harmonic approximation, the functional of the free energy of the smectic corresponding to the layer distortion has the form [11, 12]

$$F = \frac{1}{2}\int d^3r\left[B\left(\frac{\partial u(r)}{\partial z}\right)^2 + K(\Delta_\perp u(r)^2)\right] + \frac{1}{2}\gamma\int d^2r(\nabla_\perp u(r_\perp, z = \pm L/2))^2. \quad (1)$$

Here, the subscript "⊥" designates the directions lying in the smectic-layer plane; *K* and *B* are the volume elastic constants corresponding to bending and compression of the smectic layers, respectively; and γ is the surface-tension coefficient. The last term in Eq. (1) represents the surface contribution to the free energy of the smectic film of the thickness *L* [13, 14]. To obtain the spectrum of the eigenmodes of the bulk smectic sample, we have to pass to the Fourier components of displacements $u(\mathbf{r})$ and apply the equation

$$\langle u(\mathbf{q})^2\rangle = k_B T/(Bq_z^2 + Kq_\perp^4). \quad (2)$$

Here, the term Bq_z^2 is associated with the mode of compression–dilation along the normal to smectic layers, while $Kq_\perp^4$ is associated with the bending mode (Fig. 1). We should like to draw attention to the absence of the term $\sim q_\perp^2$ in the denominator of Eq. (2). Physically, the reason is the absence of the crystalline ordering within the smectic layer, which permits sliding of the liquid layers. The characteristic features of the mode structure of the smectic described by Eq. (2) pro-

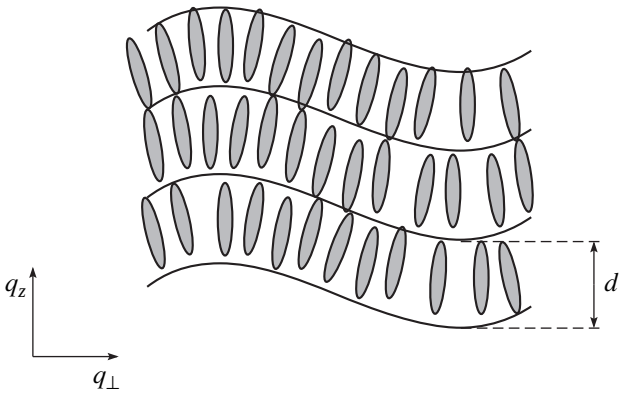

Fig. 1. The smectic *A* phase of liquid crystals. The bending mode is shown in which the layer period remains constant; q_z and $q_\perp$ are the components of the wave vector along the layer normal and in the layer plane, respectively.

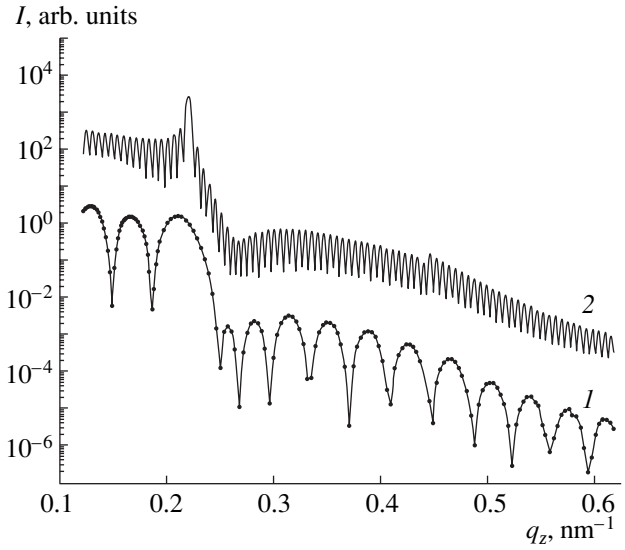

Fig. 2. The reflection curves of (*1*) 6- and (*2*) 43-layer-thick freely suspended films of the smectic liquid crystal 40.8. For clearer presentation, the curves are shifted by two decades.

vide instability of the smectic layers at long distances: at $\mathbf{r} - \mathbf{r}' \longrightarrow \infty$, the correlator of the layer displacements $\langle u(\mathbf{r})u(\mathbf{r}')\rangle$ is divergent [3]. This signifies that the fluctuations in the positions of smectic layers smear the long-range order of an infinite system. Thus, the mean–square layer displacement,

$$\langle u^2(\mathbf{r})\rangle = \frac{k_B T}{(2\pi)^3}\int \frac{d^3q}{Bq_z^2 + Kq_\perp^4} = \frac{k_B T}{8\pi(KB)^{1/2}}\ln\frac{L}{d}, \quad (3)$$

diverges logarithmically with an increase of the sample dimension L. However, this divergence is weak and the amplitude of the layer displacement for laboratory samples does not exceed $\sigma = \langle u^2(r)\rangle^{1/2} \approx 0.4$–$0.7$ nm. In terms of the relative displacements, $\sigma/d \approx 15\%$; in other words, the layers do exist.

The characteristics of the static structure factor of smectic LCs can be studied directly in the X-ray experiments on freely suspended films of various thicknesses. In freely suspended smectic films, the layers are parallel to the plane of the opening which bounds the film [15]. The film is not broken down due to the elastic response to dilation (compression) of the layers along the surface normal to the film. Such films are highly homogeneous, although their thickness can vary from two to several hundreds of molecular layers.

Studying freely suspended smectic films, one uses the geometry of reflection at glancing angles (X-ray reflectometry). Within the range of the X-ray wavelengths used ($\lambda \approx 0.1$ nm), the refractive index n is less than unity: $n = 1 - \delta$ (for organic materials, $\delta \approx 3 \times 10^{-6}$). Despite the smallness of δ, the classical phenomena of reflection and interference at the air–LC interface are observed in the small-angle range. The reflection curves $R(q_z)$ for freely suspended smectic films from a *N*-(4-*n*-butoxybenzylidene)-4-*n*-octylaniline (40.8) are shown in Fig. 2.[2] The reflection curve $R(q_z)$ falls down by the law $\sim q_z^{-4}$, determined by the Fresnel formulas. In addition, one also observes in freely suspended smectic films the simultaneous interference of the rays reflected from the front and the back surfaces (isoclinic fringes) and diffraction from the smectic layers. At a large number of the layers, one observes intense Bragg maxima at the reciprocal-lattice points $q_{zn} = 2\pi n/d$. The final reflection pattern from the freely suspended smectic film is the result of the interference of the isoclinic fringes and the Bragg peaks.

The positions of the interference maxima allow one to determine the total thickness of the freely suspended smectic film. The analysis of the reflection curves is based on the exact (matrix) solution of the Fresnel equations for reflection from a multilayer system [16]. The electron density of each smectic layer is determined by the convolution of the projections of the electron density of molecules onto the *z*-axis with the Gaussian of width σ_i, which describes the smearing of the centers of gravity of the molecules in the *i*th layers caused by thermal fluctuations of the layer positions [17–19]. The resulting distribution of the rms displacement amplitudes σ_i across the freely suspended films of different thicknesses in the smectic-*A* and crystalline-*B* phases of the 40.8 compound are shown in Fig. 3 (only one half of the centrosymmetric profile is presented). The fluctuations in the layer displacements at the free surfaces are suppressed irrespectively of their thicknesses. This is the consequence of the fact that the surface contribution to the free energy of the system prevails in the vicinity of the interface. The theoretical calculations made for a smectic film of finite dimensions show that the layer fluctuations at the free surface of the smectic are suppressed if $\nu = \gamma/(KB)^{1/2} > 1$ [13, 14]. For a 40.8 liquid crystal, the use of the elastic constants $K \approx 10^{-11}$ N and $B \approx 10^7$ N/m^2 and the surface-tension coefficient $\gamma \approx 0.02$ N/m yields $\nu = 2$, in close agreement with the experimental data. In the smectic *A* phase, the amplitude of thermal fluctuations at the film center increases with its thickness, which is the direct confirmation of the Landau–Peierls instability (3). Vice versa, upon the transition into the low-temperature crystalline *B* phase, the fluctuation amplitude in the center of the freely suspended smectic film stops being dependent on the thickness. It is consistent with the appearance of the term $C_{44}q_\perp^2$ in the dispersion law for the elastic modes of the three-dimensional crystal, which excludes the Landau–Peierls instability [3] (C_{44} is the shear elastic modulus in the *xy* plane).

[2] With lowering of the temperature, a 40.8 liquid crystal shows the following sequence of phases: I (78°C) N (63.5°C) Sm*A* (48.5°C) Cr*B*, where I, N, Sm*A*, and *B* indicate isotropic, nematic, smectic *A*, and crystalline *B* phases, respectively.

DYNAMICS OF THERMAL FLUCTUATIONS

The above results concerned the static properties of the density correlation function in smectic films. What can be stated about the dynamics of thermal fluctuations of the smectic layers? The related problems can be solved with the use of the X-ray photon correlation spectroscopy in the X-ray wavelength range. Prior to the discussion of the experiment, consider the dynamics of the layer systems. A set of the hydrodynamic equations describing the dynamics of the smectic phases is considered by Kats and Lebedev [20] and de Gennes and Prost [11]. For the case of thermal fluctuations in the layer positions, the linearized hydrodynamic equation is written as

$$\rho_0 \frac{\partial^2 u(r)}{\partial t^2} = \eta_3 \frac{\partial}{\partial t} \nabla_\perp^2 u(r) + (B\nabla_z^2 - K\Delta_\perp^2) u(r), \quad (4)$$

where ρ_0 is the LC density and η_3 is the viscosity coefficient corresponding to shear of smectic layers with respect to one another. Equation (4) is, in fact, the second Newton law written for the layer displacements u along the layer normal (z-axis). The left-hand side of the equation describes inertia; the right-hand terms describe the viscous friction and the elastic force acting onto the smectic layers. In discussing the layer dynamics of the bulk LC samples, the term describing inertia can be omitted because of the smallness of the dimensionless parameter $\rho_0 K/\eta_3^2 \approx 10^{-4}$–$10^{-6}$. As a consequence, the equation of smectic-layer motion is essentially simplified, while the time-dependent layer displacement correlation function proves to be overdamped and is described by a simple relaxation equation having the form [11, 20]

$$\langle u(\mathbf{q}, t) u^*(\mathbf{q}, 0) \rangle \sim \exp(-t/\tau_q) \quad (5)$$

with the characteristic relaxation times

$$\tau_q = \eta_3 q_\perp^2 / (Bq_z^2 + Kq_\perp^4). \quad (6)$$

According to Eq. (6), the spectrum of the relaxation modes of a bulk smectic is continuous. Considering the dynamic properties of the smectic films of finite dimensions one also has to take into account the appropriate boundary and initial conditions. Then the spectrum of the relaxation modes becomes discrete. In the long-wavelength limit ($q_\perp \longrightarrow 0$), it has the only relaxation time [21, 22]

$$\tau_1 = \eta_3 L / 2\gamma. \quad (7)$$

At the typical values of the quantities in Eq. (7), $\eta_3 \approx 0.04$ kg/m s and $\gamma \approx 0.02$ N/m, and the film thickness L of the order of a micron (10^{-6} m), we arrive at the characteristic relaxation times of the order of several microseconds. Equation (7) was verified for thick freely suspended smectic films in experiments on the dynamical scattering of light in the range of soft X-rays [23].

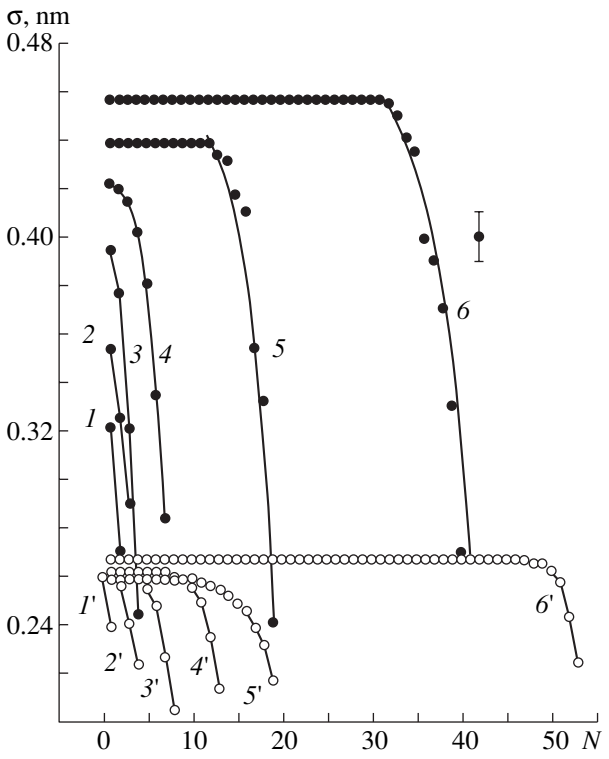

Fig. 3. Fluctuation profiles of the smectic *A* phase films at ~63°C (filled circles) consisting of (*1*) 5, (*2*) 6, (*3*) 8, (*4*) 15, (*5*) 38, and (*6*) 80 layers and in the crystalline *B* phase films of the compound 40.8 at ~47°C (open circles) consisting of (*1*') 3, (*2*') 8, (*3*') 16, (*4*') 26, (*5*') 38, and (*6*') 107 layers, obtained by simulation of the reflection curves [*N* is the layer position (its number)].

In thin freely suspended smectic films, the dynamics of layer fluctuations was studied by means of the photon correlation spectroscopy with the use of hard (8 keV) X-ray radiation [24]. The measurements were made on the undulator beam line ID10A (Troika I) at the European Synchrotron Radiation Facility (ESRF, Grenoble). To obtain the coherent radiation from the undulator (a partly coherent source), one has to provide the validity of the monochromatic plane-wave approximation at the site of sample location. Therefore, the size of the first slit placed at a distance of $R = 46$ m from the sample did not exceed $s = 0.9$ mm. This provided the so-called transverse coherence length (along the wave front) $\xi_{th} = (\lambda R/2s) \approx 4$ μm in the horizontal (scattering) plane [25]. In the vertical direction, the transverse coherence length ξ_{tv} was limited by the collimating aperture 12 μm in diameter (Fig. 4a). An analyzing 40×40 μm^2-large aperture was placed in front of the detector at a distance of 1.2 m from the sample. The monochromator was a Si (111) crystal with the transmission $\Delta\lambda/\lambda \approx 1 \times 10^{-4}$. The ~15% coherence was determined from contrast measurements of the Fraunhofer diffraction pattern from the collimating aperture taken in the absence of the sample.

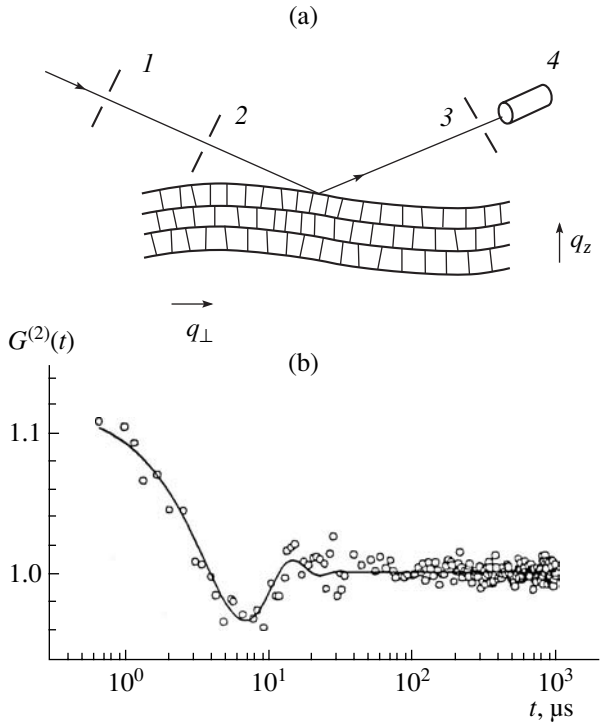

Fig. 4. (a) Scheme of the experiment for measuring dynamical structure factor of smectic LCs with the use of coherent X-ray radiation: (*1*) the collimating aperture providing the coherent component of the beam, (*2*) the guard slit protecting from the parasitic scattering from the edges of the previous slit, (*3*) the detector or "analyzing" aperture, and (*4*) the detector. (b) The normalized autocorrelation time function for the freely suspended smectic liquid-crystal film consisting of 95 layers (~0.3 nm) at $T \approx 50$°C; the solid line is the approximation by model (8).

The intensity–intensity time correlation function $G^{(2)}(q, t) = \langle I(\mathbf{q}, 0)I(\mathbf{q}, t)\rangle$ was measured with the aid of a fast digital correlator at the reciprocal-space point $q_z = 2\pi/d \approx 2.2$ nm^{-1} corresponding to the first Bragg peak of the layer structure. Under the conditions of our experiment, the function $G^{(2)}(q, t)$ is specified by the time-dependent layer displacement–displacement correlation function $G(\mathbf{q}, z, z', t) = \langle u(\mathbf{q}_\perp, z, 0)u^*(\mathbf{q}_\perp, z', t)\rangle$. The exact expression for the function $G(\mathbf{q}, z, z', t)$ is given in [22]. Despite the considerable losses of intensity associated with the beam collimation, the coherent-scattering volume $(\xi_{th}/\sin\theta_B) \times \xi_{tv} \times L \approx 500$ μm^3 was sufficient for the reliable recording of the time autocorrelation function to the microsecond time range (θ_B is the Bragg angle of beam incidence onto the sample ~1.5°).

The time autocorrelation function $G^{(2)}(t)$ measured on the freely suspended film of the 40.8 compound in the smectic *A* phase is shown in Fig. 4b. The function $G^{(2)}(t)$ shows the decay of the fluctuations in the layer displacements on the microsecond time scale and, at the same time, the oscillatory behavior with the typical times on the order of ten microseconds. The measurements are well described by the formula

$$G^{(2)}(t) = 1 + A\cos(\omega t)\exp(-t/\tau), \qquad (8)$$

where the amplitude *A* is determined by the degree of coherence, whereas the relaxation and the oscillation times τ are equal to ≈6 and $2\pi/\omega \approx 16$ μs, respectively.

It should be emphasized that in our experiments, the projection of the wave vector onto the layer normal was equal to $q_z = 2\pi/d \approx 2.2$ nm^{-1}, which exceeds by a factor of 100 the range of the wave vectors in the experiments on the dynamic scattering of visible light. At the same time, the range of the wave vectors $q_\perp = 2\pi/r_\perp$ corresponding to the layer-bending mode was much longer—from $r_\perp$ close to the molecular dimensions to the macroscopic values of the order of tens of micrometers and was determined mainly by the diffractometer resolution along $q_\perp$ (≈10^{-4} nm^{-1}).

At first glance, the oscillatory mode in the dynamics of thermal fluctuations of the smectic layers in the freely suspended films seems to be inconsistent with the theoretical conclusions and the experimental results [23]. However, this is only an apparent contradiction. The point is that the neglect of the term describing inertia in Eq. (4) is justified only if $\rho_0 K/\eta_3^2 \ll 1$. For bulk samples, this parameter is really very small (~10^{-4}–10^{-6}), because the expression of free energy has no term proportional to $q_\perp^2$. However, for thin freely suspended films, the situation is different because of the presence of the additional surface contribution, $\gamma q_\perp^2$ [13, 14]. In the static case, this leads to suppression of the amplitudes of the layer fluctuations at the free surface of liquid crystals. In dynamics, the surface contribution prevails over the energy of the bending mode $Kq_\perp^4$ in the long-wavelength limit ($q_\perp \longrightarrow 0$), and the inertia term becomes more important [21, 22]. The estimations show that the transition from the surface to the bulk mode takes place at the limiting value $q_{\perp c} \approx 2 \times 10^{-3}$ nm^{-1}. With due regard for the inertia term in Eq. (4), the reciprocal relaxation time corresponding to the fundamental mode of the freely suspended smectic film can be written as follows [22]:

$$\frac{1}{\tau_1} = \pm i\left(\frac{2\gamma}{\rho_0 L}\right)^{1/2} q_\perp + \frac{\eta_3}{2\rho_0} q_\perp^2. \qquad (9)$$

Thus, the relaxation time of the layer fluctuations becomes complex for $q_\perp < q_{\perp c}$, with its real part providing attenuation and the imaginary part being responsible for oscillations of the time correlation function. Since the instrumental resolution in the experiment is of the same order of magnitude as $q_{\perp c}$, the oscillations of the $G^{(2)}(t)$ function should be observable for rather thin films as well (Fig. 4b).

THE PROSPECTS FOR FURTHER RESEARCH

The experiments performed showed that the methods of the photon correlation spectroscopy based on the coherent radiation sources can be extended to the X-ray wavelengths. This offers the unique opportunity to study the comparatively fast dynamic processes in the structured organic films on the molecular distance scale. It should be remembered that Raman and Mandelstam–Brillouin scattering in the visible range provide an information on the long-wavelength ranges of the phonon spectra of the crystals. These methods are used to study fast processes on the atomic and molecular level (10^7–10^{14} Hz). To study comparatively slow processes (1–10^6 Hz) with the characteristic scale of the order of the wavelength of the visible light, the dynamical light scattering is widely used. In particular, it was used in the study of thermal fluctuations of the director orientation in nematic liquid crystals [11]. To study fast processes in the condensed media (10^9–10^{12} Hz) on the scale of molecular length, one traditionally uses inelastic neutron scattering. The dynamical X-ray scattering allows one to study rather slow processes (10^{-2}–10^7 Hz) with the characteristic inhomogeneity scale of the molecular length (10^{-1}–10^3 nm).

The promising objects for studying the dynamic processes on a molecular scale are polymer liquid crystals in which the LC fragments are attached to the main polymer chain via flexible spacers. These phases are the unique combinations of the liquid-crystal order with specific polymer properties. The flexible main polymer chain and the spacers provide the necessary degree of freedom for LC fragments for the self-assembly into the LC phases of various symmetry, including the smectic phases [26]. At present, little is known about the dynamics of such systems, although it can provide an extremely important information on the effect of the conformation of the main polymer chain on the liquid crystalline ordering. The studies of the dynamics of the surfactant solutions forming lyotropic lamellar phases are also of great interest. These are model membranes based on the aqueous phospholipid solutions forming the lipid bilayers alternating with aqueous interlayers [27, 28]. Another important direction is the dynamics of lipid membranes with the imbedded DNA molecules. In particular, linear DNA molecules and certain mixtures of the cationic liposomes can be self-assembled into two-dimensional smectic phases imbedded into lipid bilayers [29]. These systems allow the simulation of DNA transport via cellular membranes. There are some other types of self-assembly of molecules, including those resembling smectic membranes, which exist in amphiphilic associating polyelectrolytes [30, 31]. These substances are characterized by mutually excluding properties provided by the presence of the antagonistic hydrophilic and hydrophobic groups in one polymer. Thin films of such polymers are obtained from the aqueous solutions of polyelectrolytes.

Concluding the article, we should like to emphasize that our knowledge about the dynamic behavior of comparatively simple smectic films is still far from exhaustive. With the enrichment of our knowledge about these films, the focus of such studies would be shifted toward more complicated membrane systems important for biology.

ACKNOWLEDGMENTS

We are grateful to A. Shalaginov for valuable discussion of the theoretical aspects of our study and to A. Fera, I. Dolbnya, R. Opitz, and G. Grübel for their participation in the experiments and fruitful discussions. This study was supported by the Russian Foundation for Basic Research, project no. 00-03-33174.

REFERENCES

1. B. K. Vainshtein, *Diffraction of X-rays by Chain Molecules* (Nauka, Moscow, 1963, p. 372; Elsevier, Amsterdam, 1966).
2. B. K. Vainshtein and I. G. Chistyakov, *Problems of Modern Crystallography* (Nauka, Moscow, 1975), p. 12.
3. L. D. Landau and E. M. Lifshitz, *Statistical Physics* (Nauka, Moscow, 1976; Pergamon, Oxford, 1980).
4. M. A. Osipov and B. I. Ostrovskii, Crystallogr. Rev. **3**, 113 (1992).
5. J. Als-Nielsen, J. D. Litster, J. D. Birgeneau, *et al.*, Phys. Rev. B **22**, 312 (1980).
6. C. R. Safinya, D. Roux, G. S. Smith, *et al.*, Phys. Rev. Lett. **57**, 2718 (1986).
7. V. M. Kaganer, B. I. Ostrovskii, and W. H. de Jeu, Phys. Rev. A **44**, 8158 (1991).
8. *Photon Correlation and Light Beating Spectroscopy*, Ed. by H. Z. Cummins and E. R. Pike (Plenum, New York, 1974; Mir, Moscow, 1978).
9. S. Dierker, NSLS Newslett., July 1, 1 (1995).
10. D. L. Abernathy, G. Grübel, S. Brauer, *et al.*, J. Synchrotron Radiat. **5**, 37 (1998).
11. P. G. de Gennes and J. Prost, *Physics of Liquid Crystals* (Clarendon Press, Oxford, 1992, 2nd ed.), p. 597.
12. S. A. Pikin, *Structural Transformations in Liquid Crystals* (Nauka, Moscow, 1981; Gordon and Breach, New York, 1991).
13. R. Holyst, Phys. Rev. A **44**, 3692 (1991).
14. A. Shalaginov and V. P. Romanov, Phys. Rev. E **48**, 1073 (1993).
15. P. Pieranski *et al.*, Physica A (Amsterdam) **195**, 364 (1993).
16. I. I. Samoilenko, O. V. Konovalov, L. A. Feigin, *et al.*, Kristallografiya **44**, 347 (1999) [Crystallogr. Rep. **44**, 310 (1999)].
17. E. A. L. Mol, J. D. Schindler, A. N. Shalaginov, and W. H. de Jeu, Phys. Rev. E **54**, 536 (1996).
18. A. Fera, D. Sentenac, B. I. Ostrovskii, *et al.*, Phys. Rev. E **60**, R5033 (1999).
19. A. Fera, I. Dolbnya, R. Opitz, *et al.*, Phys. Rev. E **63**, 020-601R (2001).

20. E. I. Kats and V. V. Lebedev, *Dynamics of Liquid Crystals* (Nauka, Moscow, 1988).
21. A. Ponierewski and R. Holyst, Phys. Rev. E **58**, 2027 (1998).
22. A. N. Shalaginov and D. E. Sullivan, Phys. Rev. E **62**, 699 (2000).
23. A. C. Price, L. B. Sorensen, S. D. Kevan, *et al.*, Phys. Rev. Lett. **82**, 755 (1999).
24. A. Fera, I. Dolbnya, G. Grubel, *et al.*, Phys. Rev. Lett. **85**, 2316 (2000).
25. M. Born and E. Wolf, *Principles of Optics* (Pergamon, Oxford, 1969; Nauka, Moscow, 1973).
26. *Liquid-Crystal Polymers*, Ed. by N. A. Plate (Plenum, New York, 1993).
27. V. G. Ivkov and G. I. Berestovskiĭ, *Dynamical Structure of Lipid Bilayer* (Nauka, Moscow, 1981).
28. Yu. M. L'vov and L. A. Feĭgin, *Problems of Crystallography* (Nauka, Moscow, 1987), p. 126.
29. T. Salditt, I. Koltover, J. O. Radler, and C. R. Safinya, Phys. Rev. Lett. **79**, 2582 (1997).
30. F. Millet, J. J. Benattar, and P. Perrin, Phys. Rev. E **60**, 2045 (1999).
31. I. I. Potemkin, V. V. Vasilevskaya, and A. R. Khokhlov, J. Chem. Phys. **111**, 2809 (1999).

Translated by A. Zolot'ko

Crystallography Reports, Vol. 46, No. 4, 2001, pp. 687–689. Translated from Kristallografiya, Vol. 46, No. 4, 2001, pp. 756–758.

Dedicated to the memory of B.K. Vainshtein

On the Variation of the Impurity Composition in LaF_3 Crystals Grown by the Bridgman–Stockbarger Method

E. A. Krivandina, Z. I. Zhmurova, and B. P. Sobolev

Shubnikov Institute of Crystallography, Russian Academy of Sciences, Leninskiĭ pr. 59, Moscow, 117333 Russia

Received February 10, 2000

Abstract—Single crystals of the composition LaF_3 with CeF_3, YF_3, and SrF_2 impurities have been grown by the Bridgman–Stockbarger method in a graphite crucible with six cells. The CeF_3 concentration has been measured in the LaF_3 charge prior to the growth experiment and in the grown LaF_3 crystals upon it. It is shown that, depending on the growth conditions, the CeF_3 concentration can change during crystallization from 25% of its initial concentration in the charge up to 550%. © *2001 MAIK "Nauka/Interperiodica".*

INTRODUCTION

Multicomponent metal fluoride-based single-crystalline materials are promising for various fields of science and technology. However, sometimes the crystals having the same compositions but grown in different experiments have considerably differing properties [1, 2], which up to now has not been uniquely interpreted. We believe that this discrepancy can be associated with different growth conditions in these experiments.

To facilitate the search for new fluoride single crystals and increase the rate of their growth, one often uses crucibles consisting of several growth cells. This allows the simultaneous growth of several crystals with different basic composition and different concentrations of activating impurities [3]. The physical properties of the crystals thus grown can differ considerably. Thus, the question may arise whether the composition of the crystals grown in such experiments corresponds to the composition of the initial charge in each cell or the crystallization provides the redistribution of impurities in different cells. The probable transfer of impurity between different cells during growth of fluoride crystals has not been studied as yet despite the fact that the crystal growth can be accompanied by considerable mass losses.

The present study was undertaken to answer the above questions for the case of multicomponent fluoride crystals grown from melt by the Bridgman–Stockbarger method.

EXPERIMENTAL

We studied LaF_3 single crystals with CeF_3, YF_3, and SrF_2 impurities grown in an open graphite crucible with six cells. The impurity redistribution was studied on CeF_3, since this impurity can readily be detected from the corresponding absorption spectrum (the $5d \longrightarrow 4f$ electron transitions). Crystals were grown on a KRF-1 setup (designed and manufactured at the Special Designing Bureau of the Institute of Crystallography of the Russian Academy of Sciences) in a helium atmosphere (P = 1.5 atm) with Teflon as the fluorinating agent. The initial reagents were of 99.95 wt % purity. The composition of the initial charge and the CeF_3 concentration in it prior to crystallization are indicated in table. The 1–2 mm^3-large granules of the components were melted in the fluorinated atmosphere and loaded into a crucible. The charge was heated at a rate of 1500 deg/h until its complete melting. Then the melt was homogenized for one hour at overheating of about 50°C. In the growth process, the crucible was lowered with a velocity of 5.3 ± 0.5 mm/h. The crystals grown were 12 mm in diameter and from 15 to 16 mm in length. The mass loss during growth ranged from 4 to 5 wt %.

The growing LaF_3 crystals can be contaminated with cerium by two different ways—either from the gas phase formed during evaporation of CeF_3 from the crucible cells containing a cerium-activated charge or from the cold parts of the heater and thermal shields covered with condensate particles in the course of previous experiments with cerium-containing melts. Therefore, we performed two types of experiments: (I) crystallization in the setup thoroughly cleaned from all the possible deposits and annealed at 1500°C and (II) crystallization in a setup earlier used for melting 500 g of CeF_3.

The presence of CeF_3 in the grown crystals was detected from the optical transmission spectra recorded on a Perkin-Elmer spectrophotometer in the wave-

1063-7745/01/4604-0687$21.00 © 2001 MAIK "Nauka/Interperiodica"

Change of CeF_3 concentration during crystallization

Experiment	Cell	Composition of initial charge	CeF_3 concentration, mol %		$\frac{C_2-C_1}{C_1} \times 100\%$
			in charge, C_1	upon crystallization, C_2	
I	1	LaF_3 + CeF_3	0.0035	0.0055	+57
	2		0.0080	0.0055	–31
	3		0.0110	0.0085	–22
	4		0.0160	0.0125	–22
	5		0.0210	0.0156	–26
	6	LaF_3 + 0.02 mol % YF_3	0.0010	0.0025	+150
II	1	LaF_3 + CeF_3	0.0060	0.0105	+75
	2		0.0060	0.0105	+75
	3		0.0120	0.0165	+37.5
	4		0.0120	0.0105	–12.5
	5	LaF_3 + 0.01 mol % YF_3	0.0010	0.0065	+550
	6	LaF_3 + 1.0 mol % SrF_2	0.0010	0.0060	+500

length range from 200 up to 300 nm at room temperature. The specimens were prepared from the parts of the crystals cut out from the portions of the boule located directly above its conelike part.

The specimens were the disks 12 mm in diameter and 2.0 ± 0.1 mm in thickness with the following surface characteristics: roughness R_z = 0.05, planarity N = 3–5, and plane-parallelity $Q < 0.3°$. It is well known (see, e.g., [4]) that the presence of CeF_3 in crystals can be detected from the presence of the absorption bands at the wavelengths λ = 207, 218, 235, and 245 nm. The calibration curves of the transmission intensity depending on the CeF_3 concentration in the crystalline specimens were constructed only for the absorption bands λ = 218 and 235 nm, where the Buger–Beer law is valid. The method provides the determination of the CeF_3 concentration within (0.001–0.021) ± 0.0005 mol %.

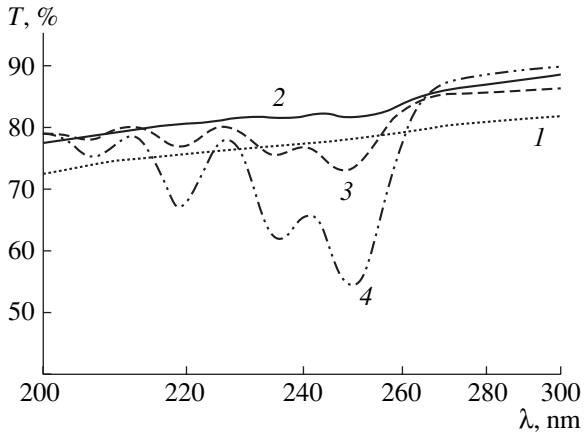

Transmission spectra of (*1*) LaF_3 + 0.02 mol % YF_3 and (*2*) LaF_3 + 1 mol % SrF_2 in the absence of CeF_3 impurity in the initial charge, (*3*) LaF_3 + 0.02 mol % YF_3 upon experiment I, and (*4*) LaF_3 + 1 mol % SrF_2 upon experiment II.

EXPERIMENTAL RESULTS

The data on the CeF_3 concentration in the initial charge and in the specimens cut out from the boules crystallized in both experiments are listed in the table. It is seen that in the course of experiment I, cesium is redistributed between the cells via the gas phase. In cells 2–5, where the CeF_3 concentration in the charge exceeded 0.0080 mol %, its concentration in the crystal decreased, on average, by 25%. In cells 1 and 6, where the initial CeF_3 concentration was lower than 0.0035 mol %, its concentration in the crystals increased by more than 50%.

Experiment II resulted in the mechanical contamination of the crystals with cerium. However, instead of an expected decrease in the cerium concentration because of its evaporation as was the case in experiment I, we observed a considerable increase of the CeF_3 concentration in all the cells except for cell 4. In the cells with the charge nominally free of cerium (0.0010 mol % CeF_3), a multiple increase of its concentration in the grown crystals was observed.

Comparing the character of the changes in the transmission spectra from the crystals LaF_3 + 0.02 mol % YF_3 and LaF_3 + 1.0 mol % SrF_2 grown under "pure conditions" (in the absence of CeF_3 in the charge) with the transmission spectra from the crystals of the same compositions grown in experiments I and II (cells 6), we see (figure) that, in the first case, the absorption bands at λ = 207, 218, 235, and 245 nm are practically absent, whereas in the second case, these bands are clearly seen

and indicate a considerable increase in the CeF_3 concentration.

It follows from the data obtained that, during crystal growth, both the contamination due to transfer of the component–activator via the gas phase and the mechanical contamination of the melt with condensate particles containing cerium trifluoride from the cold parts of the setup take place. Thus, both the above factors should be taken into account in growth of crystals of refractory fluorides. One should also be extremely careful in choosing charge compositions for growth of crystals which then will be used for studying and interpreting their physical properties.

ACKNOWLEDGMENTS

The authors are grateful to A.P. Shtyrkova for her help in recording the transmission spectra of crystalline specimens. The study was supported by the Russian Foundation for Basic Research, project no. 99-02-18067.

REFERENCES

1. J. M. Reau, C. Lucat, G. Compet, *et al.*, J. Solid State Chem. **17** (1–2), 123 (1976).
2. M. Svantner, E. Mariani, P. P. Fedorov, *et al.*, Cryst. Res. Technol. **16** (5), 617 (1981).
3. E. A. Krivandina, Z. I. Zhmurova, G. V. Berezhkova, *et al.*, Kristallografiya **40** (4), 741 (1995) [Crystallogr. Rep. **40**, 686 (1995)].
4. C. Pedrini, B. Moine, J. C. Gacon, and B. Jacquier, J. Phys.: Condens. Matter **4** (24), 5461 (1992).

Translated by L. Man

Crystallography Reports, Vol. 46, No. 4, 2001, pp. 690–695. Translated from Kristallografiya, Vol. 46, No. 4, 2001, pp. 759–764.

Dedicated to the memory of B.K. Vainshtein

Striation in Ge Single Crystals Grown from Melt under Vibrations and Weak Heat Convection

V. I. Strelov, V. S. Sidorov, and B. G. Zakharov

Space Materials Research Center, Shubnikov Institute of Crystallography, ul. Akademicheskaya 8, Kaluga, Moscow oblast, 248033 Russia

Received March 28, 2000

Abstract—The influence of vibrations on the formation of mictohomogeneities of the properties in Ga-doped Ge single crystals grown by the method of directional crystallization with the axisymmetric upper heat supply has been studied in earth experiments. It has been established that vibrations provide the formation of inhomogeneities in the dopant distribution in the grown crystals. *© 2001 MAIK "Nauka/Interperiodica".*

INTRODUCTION

It has been predicted theoretically [1] and confirmed experimentally [2] that the nonstationary thermogravitational convection in crystal growth from melts by the method of directional crystallization under the earth conditions should give rise to oscillations in the temperature and the velocities of the mass flows in the vicinity of the crystal–melt interface [3]. In the final analysis, this results in the variations in the crystallization rate and formation of microinhomogeneities in the dopant distribution. Under the conditions of microgravitation, the intensity of thermogravitational convection dramatically decreases, which provides favorable conditions for growing single crystals with highly homogeneous properties [4]. However, one has to take into account that under the microgravitation conditions, the processes of heat and mass transfer are essentially dependent on various mass forces existing under the conditions of the space flight. The residual microaccelerations, as well as the microaccelerations caused by the changes in the space-craft orientation and various vibrational effects, can considerably change the hydrodynamics of the melt and give rise to inhomogeneous dopant distribution in the crystal. The level of these microaccelerations can vary over a wide range—from 10^{-2} to 10^{-6} g_0 [5].

In this connection, the successful growth of single crystals with homogeneous properties requires the thorough optimization of the space experiments still in earth experiments with the aim to determine the effect of vibrational and other dynamic factors on the crystal properties and predict possible effect of these factors on the nature of convective flows under the microgravitation conditions. The conditions for performing earth experiments at reduced thermogravitational convection cannot fully imitate the convection under the microgravitation conditions, but still allow the optimization of the structure and the intensity of convective processes occurring in space. This, in turn, allows the prediction of some of the possible effects taking place in space, e.g., the influence of vibrations on heat and mass transfer under the microgravitation conditions.

METHODOLOGY OF EXPERIMENTS ON CRYSTAL GROWTH

In earth experiments on crystal growth with the lateral or lower heat supply, the main source of nonstationarities in the convective processes occurring in the melt is the considerable radial temperature gradients. The numerical computations showed that, in this case, growth from melt is accompanied by the formation of a multivortex flow pattern with the maximum intensity in the subsurface region [6]. With a decrease of the melt level, the flows of different intensities in various directions at the crystallization front give rise to the changes in the dopant distribution. Thus, in order to obtain the flows and heat and mass transfer that would form a low-intensity monovortex flow pattern in the melt, one has to vary the control parameters and, first of all, the thermal ones.

In practice, this can be attained by using predominantly axisymmetric upper heat supply to the crystal. Figure 1 schematically shows two variants of the thermal blocks–crystallizers with the given thermal growth parameters for the vertical Bridgman method. In the first case (Fig. 1a), considerable radial temperature gradients (predominantly lateral heat supply $\Delta T_R \approx 25$–30°C/cm) could provide the steady-state mode of heat convection; therefore, the grown crystals are characterized by inhomogeneous dopant distribution over the ingot length (Fig. 2a; $\Delta C/C = 10\%$, where C is the dopant concentration). In the second case (Fig. 1b, the

1063-7745/01/4604-0690$21.00

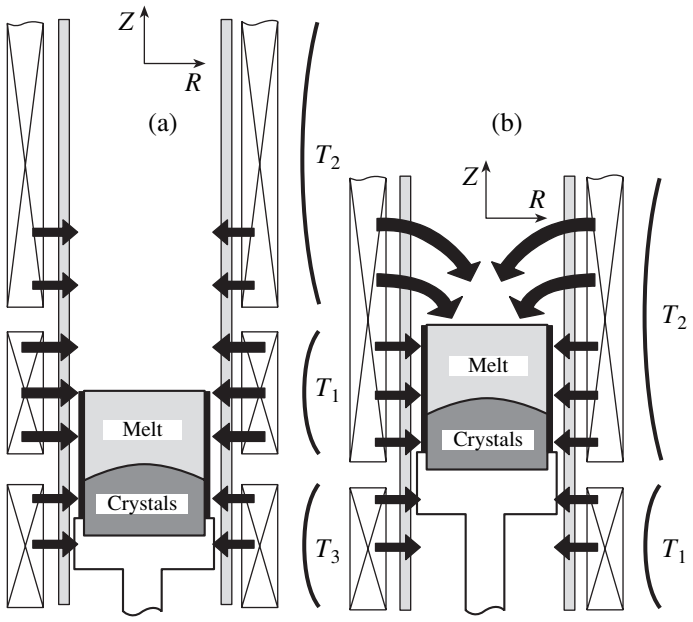

Fig. 1. Block-diagram of a crystallizer: (a) mode of natural thermogravitational convection with the lateral heat supply ($T_1 > T_2 > T_3$, $\Delta T_R \approx 25$–30°C/cm, $\Delta T_Z \neq$ const, crystallization front is convex toward the melt); (b) the mode of weak thermogravitational convection with the axial heat supply from above ($T_2 > T_1$, $\Delta T_R \approx 2$–3°C/cm, T_Z = const (20–30°C/cm), crystallization front is convex toward the crystal).

conditions of the reduced thermogravitational convection), the low radial temperature gradients are formed (Fig. 2b, predominantly axial heat supply from above $\Delta T_R \approx 1.5$–2.5°C/cm), the melt is characterized by the steady-state mode of heat convection, and the properties of the crystals thus grown are much more homogeneous ($\Delta C/C = 4\%$). The change in the geometry of the heat supply to the melt is clearly seen from the change in the geometry of the crystallization front—from the front pronouncedly convex toward the melt (Fig. 1a) in the first case (Δh = 1.5–2.0 mm) to the front slightly convex toward the crystal (Fig. 1b) in the second case (Δh = 0.2–0.5 mm).

Simultaneously with the creation of the conditions for the reduced thermogravitational convection, we also applied an axial temperature field moving at a constant velocity (without translation of the specimen or the heater translation), which allowed us to avoid noncontrollable vibrations caused by the translation mechanism. Moreover, the constancy of the axial temperature gradient ΔT_Z the maintenance of the created convective flows.

Using the provided thermal modes of the reduced thermogravitational convection, we studied the influence of natural and forced vibrations on the heat- and mass transfer in the melt. Figure 3 shows the block diagram of an experimental automated *Zona-03* setup for growing semiconductor crystals by the vertical Bridgman method in the mode of controlled vibrations. The setup induces vibrations over the wide range of amplitudes and frequencies which acting onto the melt [7]. Heater *1* provides the axial heat supply, whereas heater *2* plays the role of a thermostat and provides the constancy of the boundary conditions in the lower part of the crystal. Controlling thermocouples *4*, *5*, and *6* measure the axial and radial temperature gradients, whereas accelerometers *8* record the translational, torsional, and librational vibrations along the three directions. Electromagnetic vibrator *9* generates the translational (in the frequency range 0.5–200.0 Hz and the amplitude range up to $10^{-1}\ g_0$) vibrations (applied to a crystal and the melt above it) orthogonal to the crystallization front. Electromagnetic vibrator 10 generates torsional vibrations around the crystal axis (in the frequency range 0.5–200 Hz and the amplitude range up to $10^{-1}\ g_0$).

Figure 4a illustrates the growth mode (according to the specially developed algorithm and the program of the automated control of the crystallization process maintaining the temperature within ±0.1°C) with the set thermal parameters. Stage I consists of heating and initiation of the melting process with the attainment of the set mode within four hours. Stage II consists of maintaining the attained temperature for 2.0–2.5 h in order to homogenize the melt and provides the steady-state values of the thermal parameters. Stage III consists of 5- to 6-h-long growth under the given axial and radial temperature gradients. Stage IV reduces to slow melt cooling within 3.0 to 3.5 h. And, finally, stage V reduces to fast cooling of the melt down to room temperature. Thermocouples *4* and *5* are in contact with the melt surface and record the beginning of melting and the end of crystallization from the changes in the slope

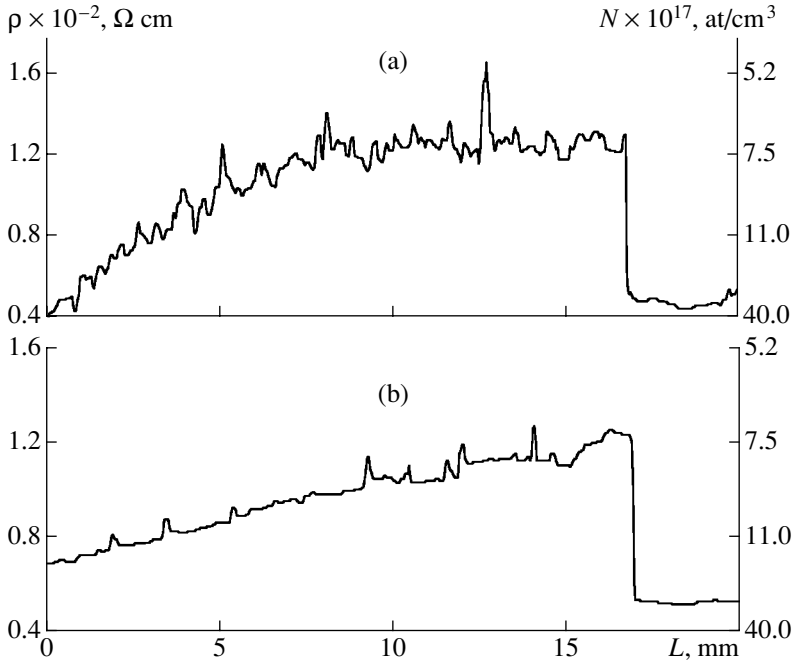

Fig. 2. Resistivity distribution over the specimen length: (a) lateral heat supply, (b) predominantly axial heat supply from above.

of the temperature profile (Figs. 4b, 4c). The information thus obtained is used to determine the averaged growth rate (ranging in our experiments from 4 to 6 mm/h).

EFFECT OF VIBRATIONS ON CRYSTAL MICROINHOMOGENEITY

In the experiments under the conditions of weak heat convection, the background of natural vibrations ranged within the frequencies 0.1–40.0 Hz and the amplitudes attained the values up to 6×10^{-3} g_0. The analysis of microinhomogeneities of Ge single crystals (up to 24 mm in diameter and 40 mm in length) grown under the above conditions showed homogeneous Ga-dopant distribution without striation [$(1–2) \times 10^{19}$ at/cm^{-3}) over the whole crystal length and its diameter within $\Delta C/C = 2\%$ (Fig. 5). Thus, the experiments indicate that the conditions of weak thermogravitational convection gives rise to the creation of favorable convective modes of heat and mass transfer providing, in turn, the homogeneous dopant distribution in the crystal bulk.

We performed a number of experiments for investigating the effect of vibrations normal to the crystallization front and characteristic of the real conditions aboard space crafts on the microinhomogeneity of the crystals grown over wide ranges of amplitudes and frequencies characteristic of the reduced thermogravitational convection ($\Delta T_R \approx 1.5–2.5$°C/cm and $\Delta T_Z \approx 25–30$°C/cm). The frequencies of vibrations "transferred" to the melt varied from 0.5 to 200 Hz, whereas the amplitude of microaccelerations ranged from 10^{-4} to 10^{-1} g_0. No striation was observed in the whole amplitude and frequency ranges studied, because normal vibrations gave rise to displacement of both crystal and the melt above it as a whole without any change in the flow pattern during growth (i.e., at the given level of

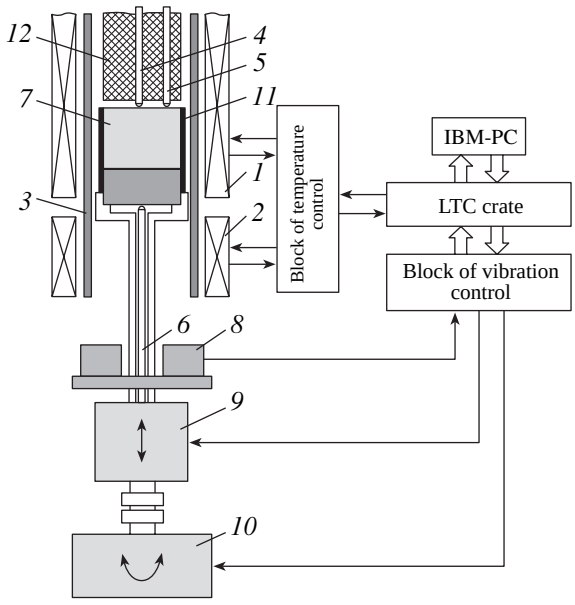

Fig. 3. Block-diagram of a *Zona-03* setup for crystal growth: (*1*, *2*) heaters, (*3*) quartz tube, (*4–6*) thermocouples, (*7*) melt, (*8*) accelerometers, (*9*) electromagnetic vibrators generating normal vibrations, (*10*) electromagnetic vibrator generating torsional vibrations, and (*11*, *12*) graphite tube.

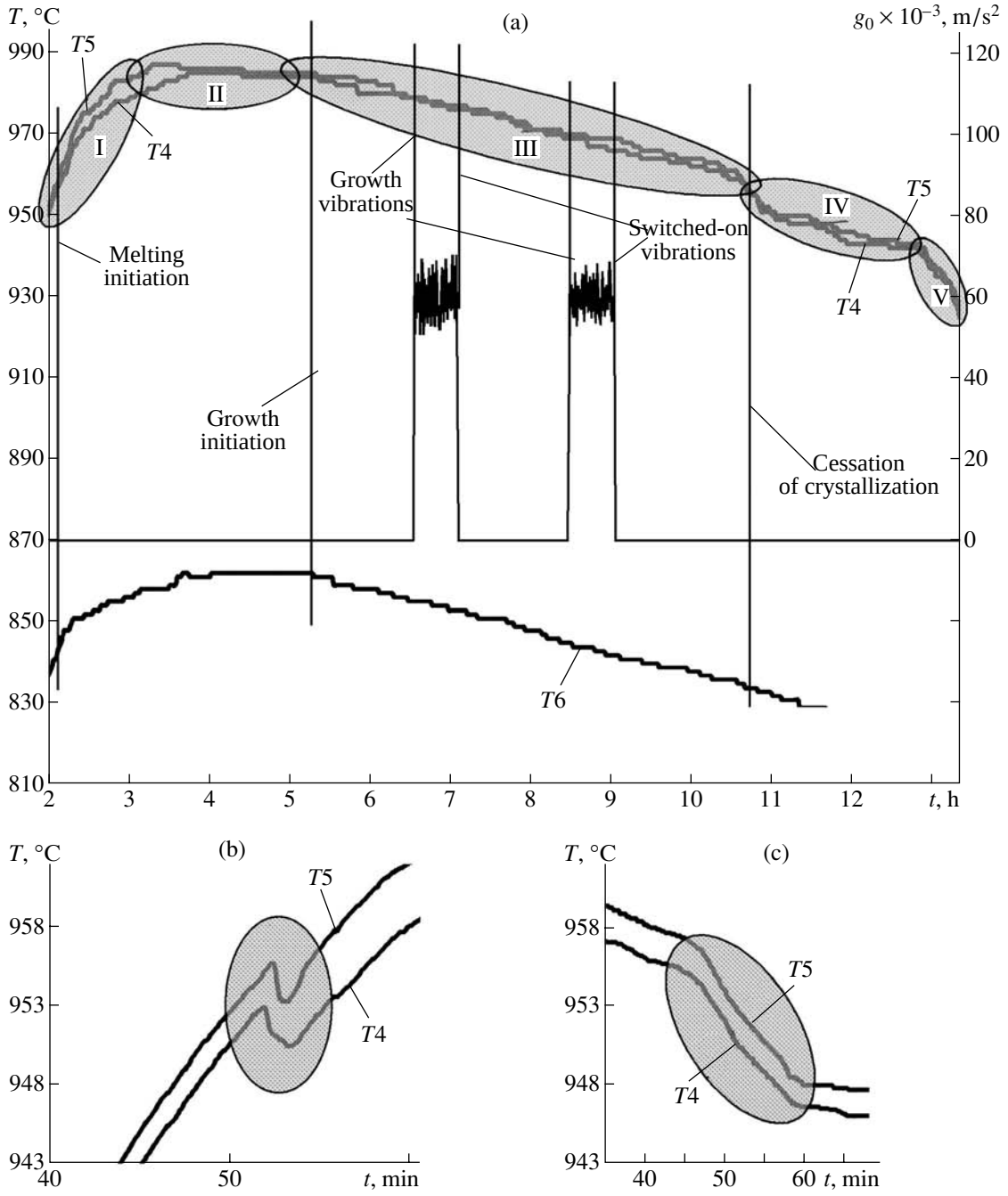

Fig. 4. Modes of crystal growth: (a) growth mode, (b) mode of melting initiation, (c) mode of crystallization cessation.

vibrations, the melt can be considered as an incompressible liquid).

The application of torsional vibrations around the axis of a growing crystal considerably changed the striation pattern. Figure 6 shows some regions of the crystal under 30-min-long vibrations at the frequency 3 Hz and the amplitude $(3–5) \times 10^{-2}$ applied two times one hour apart. It is seen that these vibrations give rise to microinhomogeneities in the dopant distribution. These are two characteristic 2.5- to 3.0-mm-long series of stria. In this case, striation is caused by shear-induced melt displacement in the direct vicinity of the crystallization front, which changes the steady-state character of the convective flow. In turn, this results in temperature variations at the crystallization front and the oscillations in the growth rate. In the final analysis, this causes the formation of microinhomogeneities in the dopant distribution.

The series of experiments provided the determination of the range of the amplitude–frequency character-

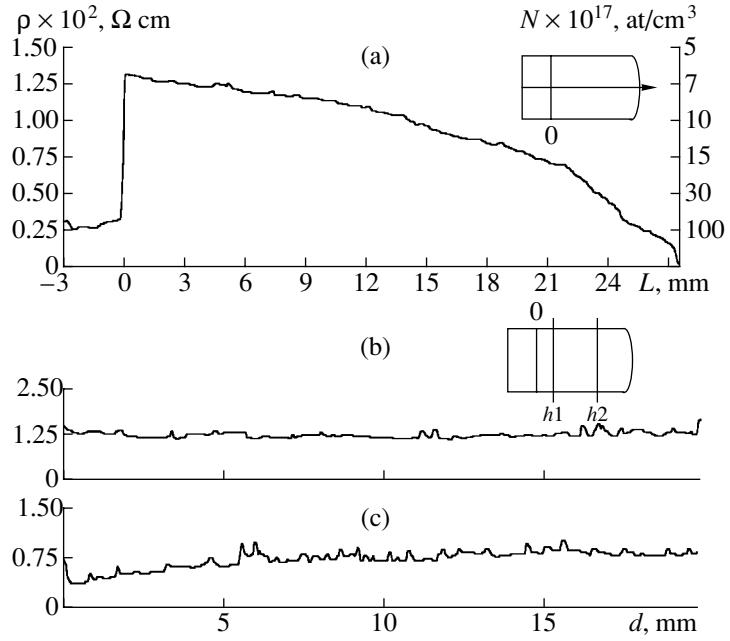

Fig. 5. Spreading-resistance distribution along (a) the specimen axis, (b) the specimen diameter at a height of 5 mm from the seed, and (c) the specimen diameter at a height of 20 mm from the seed.

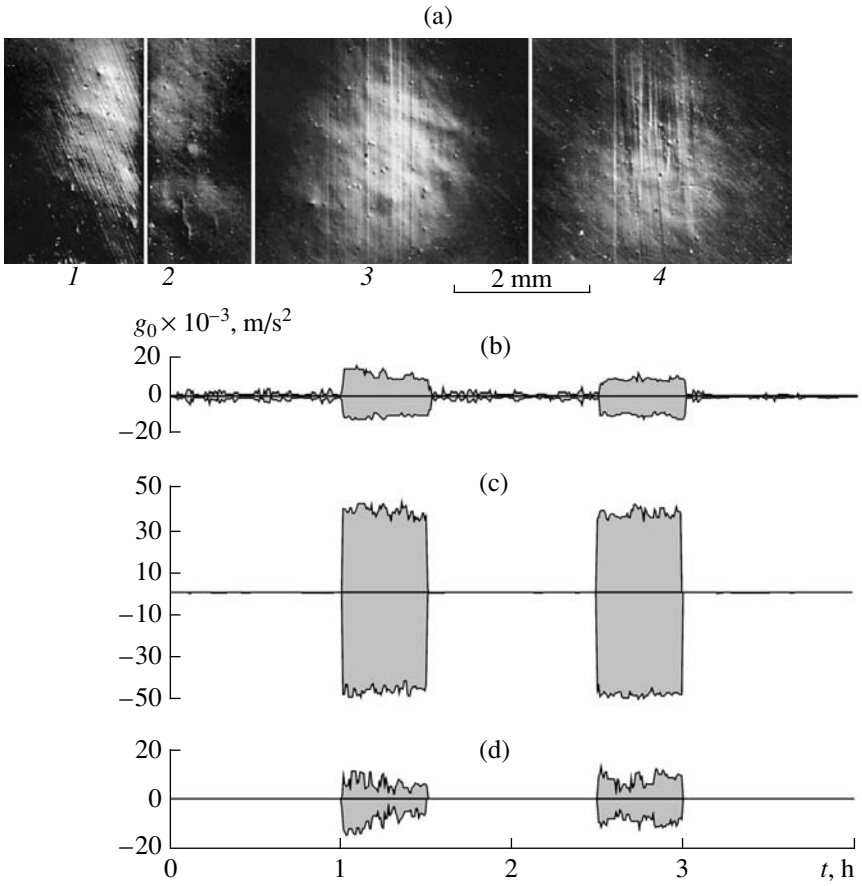

Fig. 6. Microinhomogeneities in Ga-doped (2×10^{19}) Ge single crystal caused by torsional vibrations: (a) micrographs of a crystal cut parallel to the [111] axis: (*1*) seed, (*2*) interface, (*3*, *4*) region of the crystal grown under the torsional vibrations, (b) accelerations at the detector of translational vibrations, (c) accelerations at the detector of torsional vibrations, and (d) accelerations at the detector of librational vibrations.

Formation of striation in Ga-doped Ge single crystals under the effect of applied torsional vibrations

Frequency	Amplitude		
	$<5\times10^{-3}\,g_0$	$(5–10)\times10^{-3}\,g_0$	$>10\times10^{-3}\,g_0$
0.5–100 Hz	–	– +	+

Note: Signs + and – indicate the presence and the absence of striation in single crystals grown under the action of torsional vibrations.

istics of torsion vibrations affecting the homogeneity of the dopant distribution. It was established that, irrespectively of the frequency (in the frequency range studied from 0.5 to 100.0 Hz), the vibrations with an amplitude exceeding $10^{-2}\,g_0$ applied to the melt cause the formation of inhomogeneities. The vibrations with the amplitude less than $5\times10^{-3}\,g_0$ (also irrespectively of the frequency) did not cause any composition microinhomogeneities (no striation was revealed). In other words, the vibrations of this level produce no effect on the thermal-flow pattern in the melt. The vibrations with the amplitude $(5–10)\times10^{-3}\,g_0$ correspond to the transitional region. The main results obtained in our experiments are listed in the table.

CONCLUSIONS

The thermal conditions for crystal growth with the axisymmetric upper heat supply providing the mode of weak thermal convection have been determined and implemented in the earth experiments. It has been established that under the conditions of weak thermogravitational convection, the favorable convection modes of heat and mass transfer are attained, which provides microhomogeneous dopant distribution in the crystal bulk. It is shown experimentally that vibrations normal to the crystallization front in the wide amplitude and frequency range (0.5–200.0 Hz and 10^{-4}–$10^{-1}\,g_0$, respectively) affect neither the processes of heat and mass transfer in the melt nor the homogeneity of the dopant distribution in the crystal. It is also shown experimentally that, at the accelerations exceeding $10^{-2}\,g_0$, the torsional vibrations result in the formation of microinhomogeneities in growing crystals.

ACKNOWLEDGMENTS

This study was supported by the Russian Foundation for Basic Research, project no. 00-02-16394.

REFERENCES

1. P. K. Volkov, B. G. Zakharov, and Yu. A. Serebryakov, J. Cryst. Growth **204**, 475 (1999).
2. V. I. Strelov, V. S. Sidorov, and B. G. Zakharov, in *Proceedings of the Third International Conference ICSS, Obninsk, 1999*, p. 180.
3. M. G. Milvidskiĭ, A. V. Kartavykh, É. S. Kopeliovich, and V. V. Rakov, Nauka Rossii, No. 1, 4 (1999).
4. A. V. Kartavykh, É. S. Kopeliovich, M. G. Milvidskiĭ, and V. V. Rakov, Kristallografiya **43** (6), 1136 (1998) [Crystallogr. Rep. **43**, 1075 (1998)].
5. A. V. Kartavykh, É. S. Kopeliovich, M. G. Milvidskiĭ, and V. V. Rakov, Kristallografiya **42** (4), 755 (1997) [Crystallogr. Rep. **42**, 694 (1997)].
6. P. K. Volkov and B. G. Zakharov, Dokl. Akad. Nauk **361** (5), 616 (1998) [Phys. Dokl. **42**, 423 (1998)].
7. V. S. Sidorov, B. G. Zakharov, Yu. A. Serebryakov, *et al.*, Prib. Tekh. Éksp., No. 2, 148 (1999).

Translated by L. Man

Crystallography Reports, Vol. 46, No. 4, 2001, pp. 696–697. Translated from Kristallografiya, Vol. 46, No. 4, 2001, pp. 765–766.

PERSONALIA

Yuriĭ Andreevich Osipyan (on the Occasion of His Seventieth Birthday)

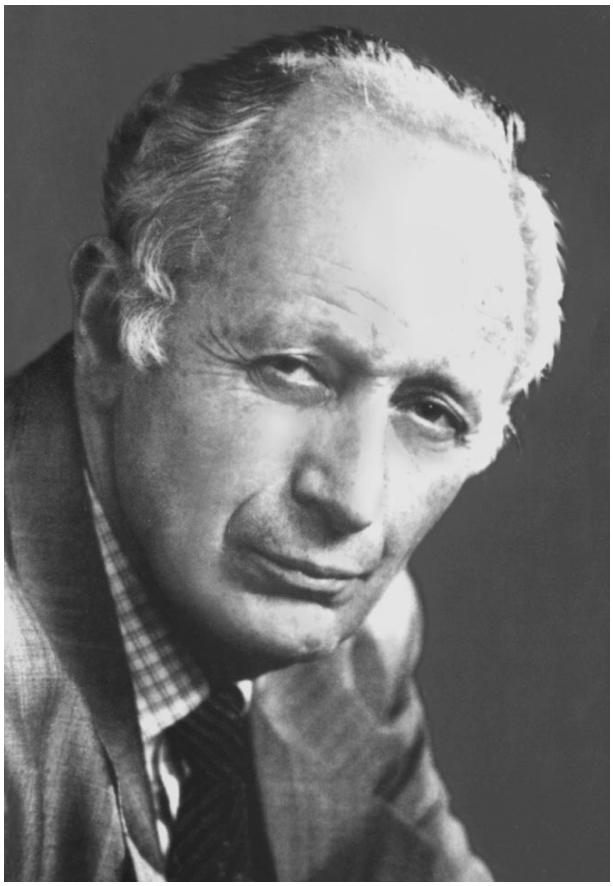

This year, Academician Yuriĭ Andreevich Osipyan, an outstanding Russian physicist and director of the Institute of Solid State Physics of the Russian Academy of Sciences, celebrates his seventieth birthday.

Osipyan was born on February 15, 1931, in Moscow. In 1555, he graduated from Moscow Institute of Steel and Alloys and began working at the Research Institute of Ferrous Metallurgy under the guidance of G.V. Kurdyumov. The subject of his first studies related to the theory of martensite transitions in alloys at low temperatures.

The brilliant experimental studies on the interaction of electrons with extended defects performed by Osipyan in the 1960's gave an impetus to the development of a new direction in crystal physics. In the same period, Osipyan discovered the effect of optic excitation on plastic properties of semiconductors, the so-called photoplastic effect. Later, Osipyan and his students discovered the electroplastic effect, the existence of clusters of dangling valent bonds at dislocation cores in silicon, the electron spin resonance, and the spin-dependent electron recombination at dislocations.

Osipyan made a considerable contribution to science of dislocations, which was initially a somewhat exotic part of the theory of elasticity of continuous media and has transformed into the important constituent part of modern solid state physics. Today, there is no need to prove that dislocations determine to a large extent not only the mechanical but also many thermodynamic, optic, electric, and magnetic properties of crystals.

Physics of dislocations in crystals is not the only field where Osipyan obtained outstanding results. He is also well known with his works on high-temperature superconductivity and fullerenes, a new form of carbon.

Osipyan also made an important contribution to the materials science by the crystallographic studies performed on the *Mir* space station. Osipyan and his coworkers simulated the processes of crystal growth using the theory of similarity under the microgravity conditions. Osipyan is the head of the Section of the Space Technology and Materials Science of the Coordination Research and Technological Council of the Russian Aviation and Space Agency and the Russian Academy of Sciences.

Osipyan has made a lot for the development of science in our country. He has played an important role in the organization of the Institute of Solid State Physics of the Russian Academy of Sciences in Chernogolovka (Moscow oblast). He was one of the scientific advisers in the Gorbachev administration and, for many years, a vice president of the USSR Academy of Sciences. Today, Osipyan is the member of the Presidium of the Russian Academy of Sciences and the Bureau of the Department of General Physics and Astronomy of this Academy; he is the chairman of the Scientific Council on Physics of Condensed Matter of the Russian Academy of Sciences, the chairman of the National Committee of Russian Crystallographers, the editor-in-chief of the journals *Poverkhnost* (Surface: X-ray, Synchrotron, and Neutron Studies) and *Kvant* (Quantum) and the member of the editorial boards of *Kristallografiya* (Crystallography Reports) and several other Russian and international journals.

1063-7745/01/4604-0696$21.00 © 2001 MAIK "Nauka/Interperiodica"

Osipyan is the member of several foreign academies and scientific societies. In the period from 1990 to 1994, he was the president of the International Union of Pure and Applied Physics (IUPAP). Today, he is a member of the Committee on Space Research (COSPAR) and the European Physical Society.

Osipyan scientific activity was highly evaluated and he was awarded with the Lebedev Gold Medal and the International Karpinskii Prize and Gold Medal. He has been awarded an honorary title of Hero of the Socialist Labor and decorated with numerous state decorations—three Lenin Orders, three Orders of Red Banner of Labor, and the Order for Merits before Russia (in 1999).

Being a benevolent, delicate, and charming person, Osipyan enjoys the respect and love of all the colleagues and friends.

The Editorial Board and the staff of *Kristallografiya* congratulate Yuriĭ Andreevich Osipyan with his birthday and wish him good health and many years of fruitful scientific activity.

Courtesy of Journal *Poverkhnost*

Photograph of Yu.A. Osipyan is reproduced due to courtesy of Journal *Poverkhnost* (no. 2, 2001).

Translated by L. Man

Crystallography Reports, Vol. 46, No. 4, 2001, pp. 698–699. Translated from Kristallografiya, Vol. 46, No. 4, 2001, pp. 767–768.

IN MEMORIAL

To the Hundredth Anniversary of Georgiĭ Glebovich Lemmlein

On August 23, 2001, Georgiĭ Glebovich Lemmlein, an outstanding mineralogist and crystallographer, would have been 100 years old. He was born in Zurich, where his parents completed their higher education. His father was a physicist and his mother, a teacher.

Lemmlein spent his childhood in Tilfis, Georgia, whose nature and historical monuments he had known, remembered, and loved for all his life. It is there, in Georgia, that he made his first geological–mineralogical expeditions.

The years of Lemmlein studies at the university coincided with the years of the revolution. Studying in Tiflis (today Tbilissi), he seldom attended lectures and preferred learning by books and working at laboratories, thus simultaneously earning his living.

In the autumn of 1924, Lemmlein entered the Geological–Mineralogical Faculty of the Leningrad State University. Under the influence of A.V. Shubnikov, then the head of the Mineralogical Museum, Lemmlein became interested in crystallography. He was happy to help his remarkable chief and became enthusiastic over the organization of the Crystallographic Laboratory, the future Institute of Crystallography of the USSR Academy of Sciences. He was charmed with the world of "dead nature"—the kingdom of minerals—not only because it gave food for thought but also because he received esthetic pleasure from it. Lemmlein always combined the deep mind of a scientist with the emotional nature of an artist. He was deeply absorbed into science and, at the same time, collected gems and engravings. After his death, his colleagues fulfilled his wish and gave his famous collection of gems to the State Hermitage in Leningrad (where he was a councellor for many years) and his collection of engravings, to the Pushkin Museum of Fine Arts in Moscow.

Great interest in crystal morphology in the 1920's and 1930's was caused first of all by his curiosity and wish to reconstruct the natural conditions of mineral formation. At the same time, he also enjoyed consulting engineers–practitioners (for many years, he was an official consultant of the Mineralogical Trust no. 13).

In 1929, Lemmlein wrote his classical article on secondary inclusions in minerals. He showed that gaseous–liquid inclusions are the result of crack healing. This allowed him to consider and use inclusions as indicators of the geological conditions existed during mineral formation. The great importance for the development of this direction was a cycle of studies performed by Lemmlein and his student P.V. Klevtsov. In 1954, they constructed the first thermodynamic diagrams of state for a number of ternary water–salt systems.

In 1938, Lemmlein, being at the near-polar Urals, managed to make a remarkable collection of minerals, which is now stored at the Mineralogical Museum of the Russian Academy of Sciences. Lemmlein's attention was bound to quartz crystals, which he had studied for three decades and which had allowed him to make the morphological discoveries and generalizations that forwarded him to the leading positions in mineralogy. His studies of quartz crystallography, its formation, the transformations of inclusions in quartz, the thermodynamic properties of salt systems, the equilibrium shape of crystals, etc., have been highly evaluated by Russian and foreign scientists. The studies of quartz performed in the period between 1939 and 1942 were generalized

1063-7745/01/4604-0698$21.00 © 2001 MAIK "Nauka/Interperiodica"

in his doctoral dissertation entitled *Morphogenetic Investigation of Quartz*.

In 1945, while studying the superfine relief of crystal surfaces, Lemmlein developed a new method for determining the elements of a superfine relief—the so-called dew method. The discovery of the spiral relief of crystals, making the film on on spiral growth of crystals, and the discovery of the dew method gave him an impetus for performing direct physical experiments on crystal growth.

Still in 1934, Lemmlein experimentally showed that a prick or a scratch made on the face of a growing crystal gives rise to the appearance of vicinal pyramids and their fast tangential growth. Returning to these experiments in 1945, Lemmlein established for the first time, the spiral structure of vicinals on silicon carbide. This phenomenon made the basis of the modern theory of crystal growth. Unfortunately, Lemmlein had not come to the idea (had not had the sense) that growth pyramids are formed around dislocations. At that time, dislocations were still poorly studied, and some people in our country were even inclined to consider them as a "bourgeois concept" (happily, on a smaller scale than the theory of resonance in intermolecular bonds). Independently of Lemmlein, dislocations were associated with crystal growth only four years later by C. Frank, who is thus considered to be the "father" of the dislocation theory of crystal growth. It is a pity that Lemmlein does not not share this honor with Frank since his animated cartoon film (drawn by him himself) showed the motion of monomolecular steps around a dislocation in the way Lemmlein saw it mentally with his mind's eye and which was later fully confirmed by theory and direct growth experiments.

The studies performed by Lemmlein at the beginning of the 1950s had become known in the United States, and in 1958 Lemmlein was invited to the first scientific meeting on crystal growth organized by the *General Electric* in Schenectady, New York. Lemmlein did not get the permission to go to the United States, but his contribution was highly evaluated by all the colleagues even in his absence.

The 1950s evidenced the use of the technology of quartz growth on an industrial scale, the design and construction of a special apparatus for Verneuil growth of ruby single crystals. Not personally taking part in these works, Lemmlein consulted the people who were directly engaged in these works. His knowledge was extremely useful for all those who started the crystal growth on the industrial scale.

In 1952–1953, a new film was ready, this time not a cartoon but the documentary film on the layer–spiral growth of paratoluidine and P-methylnaphthalene from vapors with many accompanying phenomena. This became possible because of strong birefringence and large lattice parameters of these platelike crystals along the plate normal. The film taken by Lemmlein and his student E.D. Dukova had became the highlight of the programs of numerous scientific meetings. Thus, everybody could see how crystals grow and answer many questions raised by Shubnikov in his pamphlet *How Crystals Grow.*

The same strive for passing from the mental reconstruction from morphology data to the direct observation of various processes in crystals and on their surfaces led Lemmlein and his student M.O. Kliya to the experiments on the acquisition of the equilibrium shape by the NH_4Cl crystal in the closed volume of the solution. The idea of the experiment dated back to the first love of Lemmlein—the direct observation of inclusions in crystals.

In his scientific studies, Lemmlein always tried to achieve high accuracy both in observations and measurements and their interpretation. This explains his strive for quantitative understanding of physics of various processes. It also manifested itself in the coloring distribution around the radioactive inclusions in quartz and in the observations of twisted quartz. Studying the elementary processes of crystal growth, he supported the attempts to create the physical theory of crystal growth made by A.A. Chernov, who graduated then from the Physics Faculty of the Moscow State University and entered the laboratory headed by Lemmlein.

Lemmlein possessed all the best qualities of a classical scientist. He had a deep searching mind, imagination, and associative thinking; the gift of observation; a keen sense of beauty; and the inventiveness of a real experimentalist. He was a man of broad education and deep culture; a connoisseur of objects of high esthetic and intellectual value; and was a highly intelligent, delicate, and noble man.

Translated by L. Man